NOVEMBER 2019

AJNR

VOLUME 40 • PP 1791–1976

AJNR

AMERICAN JOURNAL OF NEURORADIOLOGY

NOVEMBER 2019
VOLUME 40
NUMBER 11
WWW.AJNR.ORG

THE JOURNAL OF DIAGNOSTIC AND INTERVENTIONAL NEURORADIOLOGY

MR features of primitive neuroectodermal tumors and pineoblastomas

ASL techniques in moyamoya

Microgravity affects human brain structure

Official Journal ASNR • ASFNR • ASHNR • ASPNR • ASSR

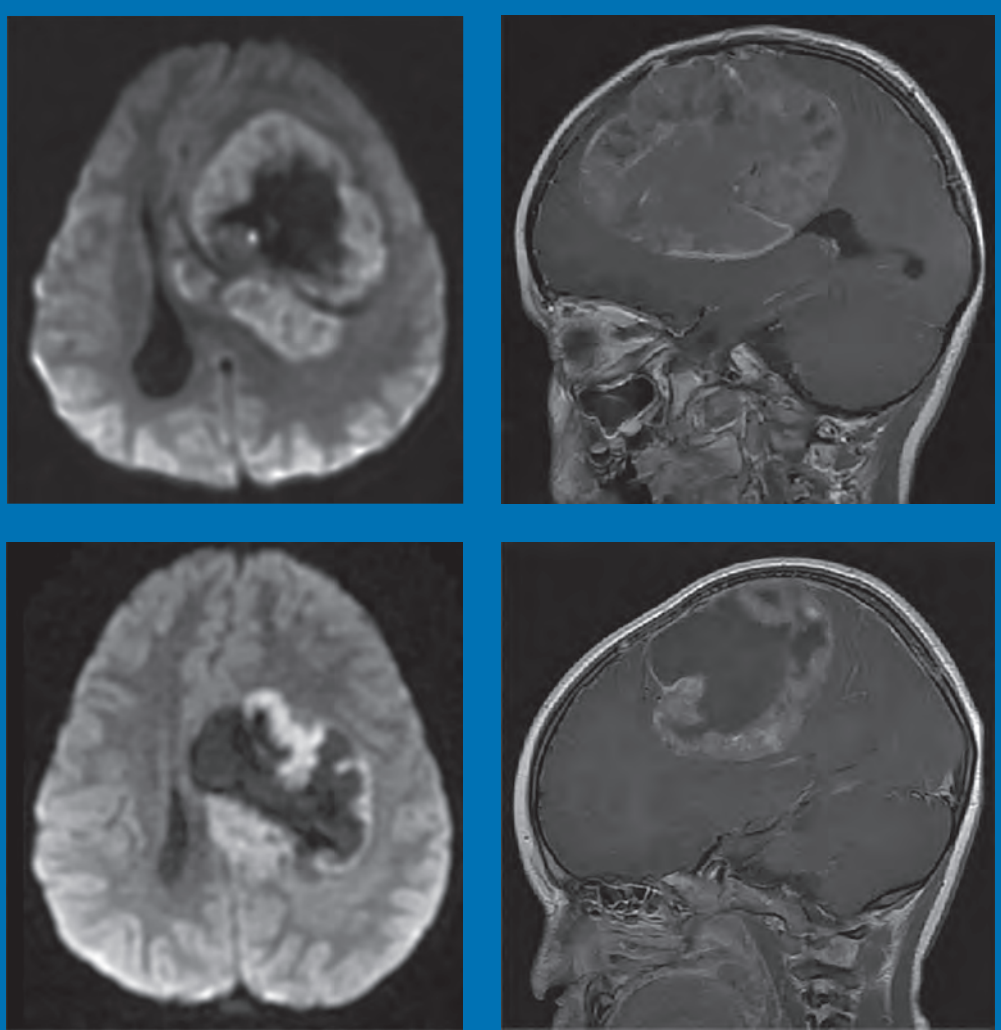

WEB®

Aneurysm Embolization System

MicroVention® delivers the first intrasaccular solution for wide neck bifurcation aneurysms.

The **world leader** and **first PMA-approved device** in an important new category of intrasaccular flow disruptors.

The WEB® System is a safe and effective single-device solution for treating wide neck bifurcation aneurysms.

SL Device

SLS Device

Contact a MicroVention sales associate to learn more about integrating the WEB® device into your practice.

MicroVention® TERUMO

MicroVention Worldwide Innovation Center
35 Enterprise
Aliso Viejo, CA 92656 USA
PH +1.714.247.8000

MicroVention UK Limited PH +44 (0) 191 258 6777
MicroVention Europe, S.A.R.L. PH +33 (1) 39 21 77 46
MicroVention Deutschland GmbH PH +49 211 210 798-0

microvention.com

DOTAREM®
(gadoterate meglumine) Injection

REAL-WORLD TESTED.
REAL-WORLD PROVEN.

The Dotarem® safety profile has been tested and proven in both studies and 30 years of global clinical use.*

0.007% **Spontaneously Reported Worldwide Adverse Events. (>50 million doses)[3-10]**

Dotarem remains an industry standard for contrast imaging with a low incidence of immediate adverse events for patients of all ages.[2-10]

1 Dotarem®
The first and only macrocyclic and ionic GBCA molecule.[1]

A low incidence of adverse events can help your patient focus on what matters most in their life.

Guerbet | COMMITTED

For more information on Dotarem, please see Full Prescribing Information including Boxed Warning and Medication Guide

IMPORTANT SAFETY INFORMATION[1]

WARNING: NEPHROGENIC SYSTEMIC FIBROSIS (NSF)

Gadolinium-based contrast agents (GBCAs) increase the risk for NSF among patients with impaired elimination of the drugs. Avoid use of GBCAs in these patients unless the diagnostic information is essential and not available with non-contrasted MRI or other modalities. NSF may result in fatal or debilitating fibrosis affecting the skin, muscle and internal organs.

- The risk for NSF appears highest among patients with:
  - Chronic, severe kidney disease (GFR < 30 mL/min/1.73m2), or
  - Acute kidney injury.
- Screen patients for acute kidney injury and other conditions that may reduce renal function. For patients at risk for chronically reduced renal function (e.g. age > 60 years, hypertension, diabetes), estimate the glomerular filtration rate (GFR) through laboratory testing.
- For patients at highest risk for NSF, do not exceed the recommended DOTAREM dose and allow a sufficient period of time for elimination of the drug from the body prior to any re-administration.

Indications and Usage

DOTAREM® (gadoterate meglumine) injection is a prescription gadolinium-based contrast agent indicated for intravenous use with magnetic resonance imaging (MRI) in brain (intracranial), spine and associated tissues in adult and pediatric patients (including term neonates) to detect and visualize areas with disruption of the blood brain barrier (BBB) and/or abnormal vascularity.

Contraindications

History of clinically important hypersensitivity reactions to DOTAREM.

Warnings and Precautions

- Hypersensitivity Reactions: Anaphylactic and anaphylactoid reactions have been reported with DOTAREM, involving cardiovascular, respiratory, and/or cutaneous manifestations. Some patients experienced circulatory collapse and died. In most cases, initial symptoms occurred within minutes of DOTAREM administration and resolved with prompt emergency treatment.
- Before DOTAREM administration, assess all patients for any history of a reaction to contrast media, bronchial asthma and/or allergic disorders. These patients may have an increased risk for a hypersensitivity reaction to DOTAREM.
- Administer DOTAREM only in situations where trained personnel and therapies are promptly available for the treatment of hypersensitivity reactions, including personnel trained in resuscitation.
- Gadolinium Retention: Gadolinium is retained for months or years in several organs. The highest concentrations have been identified in the bone, followed by brain, skin, kidney, liver and spleen. The duration of retention also varies by tissue, and is longest in bone. Linear GBCAs cause more retention than macrocyclic GBCAs.
- Consequences of gadolinium retention in the brain have not been established. Adverse events involving multiple organ systems have been reported in patients with normal renal function without an established causal link to gadolinium retention.
- Acute Kidney Injury: In patients with chronically reduced renal function, acute kidney injury requiring dialysis has occurred with the use of GBCAs. The risk of acute kidney injury may increase with increasing dose of the contrast agent; administer the lowest dose necessary for adequate imaging.
- Extravasation and Injection Site Reactions: Ensure catheter and venous patency before the injection of DOTAREM. Extravasation into tissues during DOTAREM administration may result in tissue irritation.

Adverse Reactions

- The most common adverse reactions associated with DOTAREM in clinical trials were nausea, headache, injection site pain, injection site coldness and rash.
- Serious adverse reactions in the Postmarketing experience have been reported with DOTAREM. These serious adverse reactions include but are not limited to: arrhythmia, cardiac arrest, respiratory arrest, pharyngeal edema, laryngospasm, bronchospasm, coma and convulsion.

Use in Specific Populations

- **Pregnancy:** GBCAs cross the human placenta and result in fetal exposure and gadolinium retention. Use only if imaging is essential during pregnancy and cannot be delayed.
- **Lactation:** There are no data on the presence of gadoterate in human milk, the effects on the breastfed infant, or the effects on milk production. However, published lactation data on other GBCAs indicate that 0.01 to 0.04% of the maternal gadolinium dose is present in breast milk.
- **Pediatric Use:** The safety and efficacy of DOTAREM at a single dose of 0.1 mmol/kg has been established in pediatric patients from birth (term neonates ≥ 37 weeks gestational age) to 17 years of age based on clinical data. The safety of DOTAREM has not been established in preterm neonates. No cases of NSF associated with DOTAREM or any other GBCA have been identified in pediatric patients age 6 years and younger.

You are encouraged to report negative side effects of prescription drugs to the FDA. Visit www.fda.gov/medwatch or call 1-800-FDA-1088.
Please see the full Prescribing Information, including the patient Medication Guide, for additional important safety information.
*Dotarem was launched globally in 1989 and approved by the FDA for use in the US in 2013.

References:

1. Dotarem [package insert]. Princeton, NJ: Guerbet LLC; July 2019. **2.** Internal data as of May 2019. **3.** de Kerviler E et al. Adverse reactions to gadoterate meglumine: review of over 25 years of clinical use and more than 50 million doses. Invest Radiol. 2016 Sep;51(9):544-51. **4.** Briand et al. Efficacy and safety of the macrocyclic complex Gd-DOTA in Children: Results of a Multi-Centre Study. Proceedings of the 29th Congress ofthe European Society of Pediatric Radiology. 1992; 128 **5.** Briand Y. Daily Paediatric Use of MRI Contrast Agents: Results of a Multi-Centre Survey. Proceedings of the 29th Congress of the European Society of Pediatric Radiology. 1992. **6.** Ishiguchi T & Takahashi S. Safety of gadoterate meglumine (Gd-DOTA) as a contrast agent for magnetic resonance imaging: results of a post-marketing surveillance study in Japan. Drugs R D. 2010;10(3):133-45. **7.** Emond S & Brunelle F. Gd-DOTA administration at MRI in children younger than 18 months of age: immediate adverse reactions. Pediatr Radiol. 2011 Nov;41(11):1401-6. **8.** Maurer M et al. Tolerability and diagnostic value of gadoteric acid in the general population and in patients with risk factors: results in more than 84,000 patients. Eur J Radiol. 2012 May;81(5):885-90. **9.** Soyer et al. Observational Study on the Safety Pro le of Gadoterate Megluminein 35,499 Patients: The SECURE Study. J. Magn. Reson. Imag. 2017; 45, 988-997 **10.** Radbruch A et al. Gadolinium retention in the dentate nucleus and globus pallidus is dependent on the class of contrast agent. Radiology. 2015 Jun;275(3):783-97.

GU09191202

stryker

The shape of **something better**

Being better means always being ahead

At Stryker, we invest heavily to create better technology that elevates outcomes. The result? We continue to make history, make a difference and make healthcare better, unlike any other company in the VCF space.

strykerIVS.com/VCF

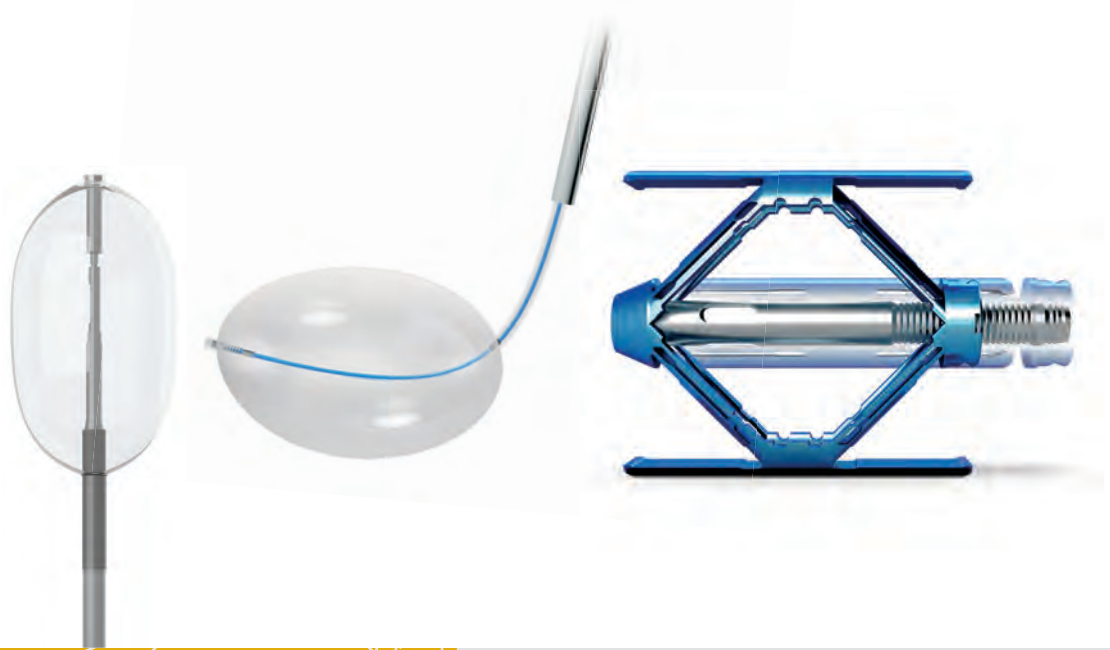

Bone cement: Complications with the use of bone cement are rare. Serious adverse events, some with fatal outcome, associated with the use of bone cements for vertebroplasty, kyphoplasty and sacroplasty include myocardial infarction, cardiac arrest, cerebrovascular accident, pulmonary embolism, and cardiac embolism. Although it is rare, some adverse events have been known to occur up to one year post-operatively. Additional risks exist with the use of bone cement. Please see the IFU for a complete list of potential risks.

D0000018655 |

Introducing

Eclipse 2 L

DUAL LUMEN BALLOON CATHETER

Balt's Access Portfolio Delivers Unique Solutions

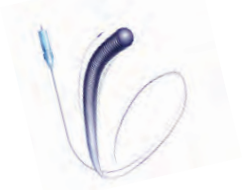

Hybrid GUIDEWIRES

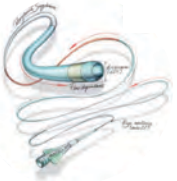

Magic®

FLOW-DEPENDENT MICROCATHETER SERIES

BALLAST LONG SHEATH 6F 088

Visit www.balt-usa.com to learn more

Balt USA
29 Parker, Irvine, CA 92618 • tel 949.788.1443 fax 949.788.1444 • balt-usa.com

balt
inspiring innovation

stryker

The results say it all

Now **PMA** approved

Clinically proven

84.7%
Primary efficacy endpoint

Safe

4.4%
Primary safety endpoint

Durable

3.8%
Retreatment rate

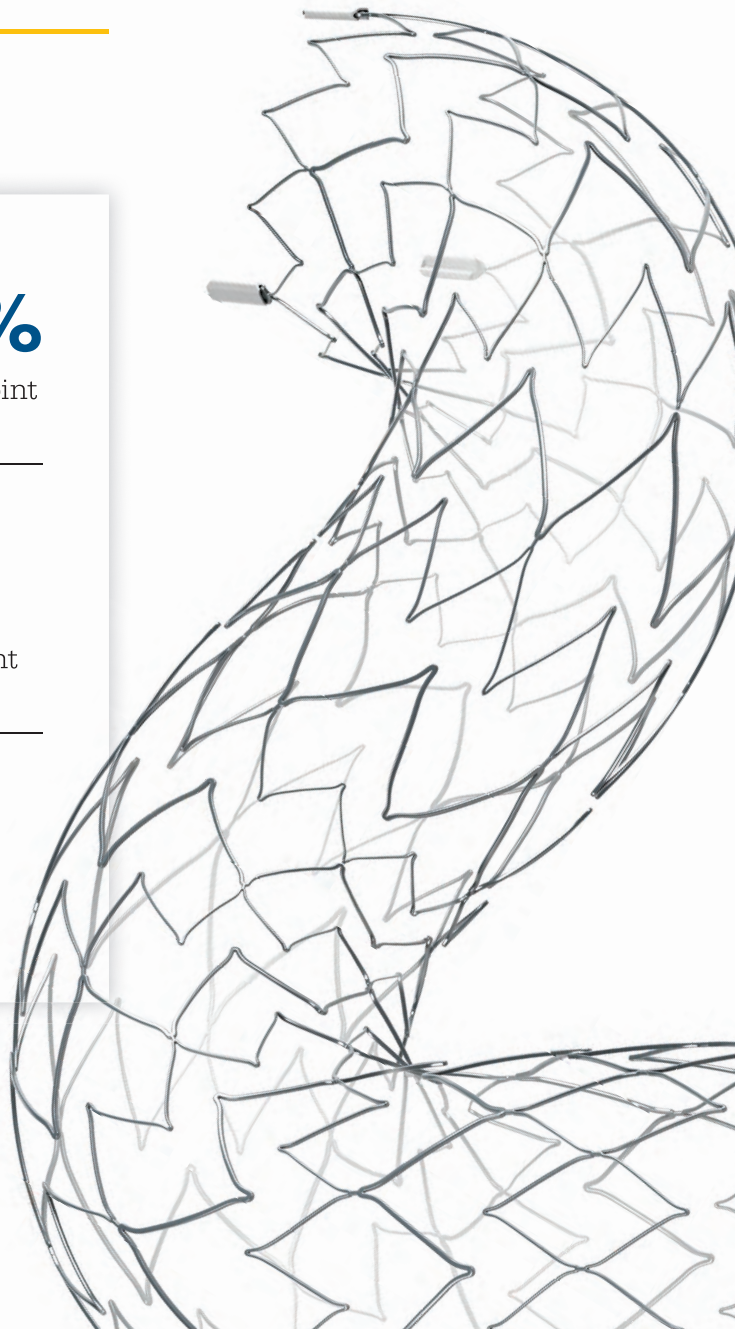

The ATLAS IDE Study is the largest of its class with **182 patients treated.**

Neuroform Atlas®
Stent System

AJNR

CALL FOR AJNR EDITORIAL FELLOWSHIP CANDIDATES

ASNR and **AJNR** are pleased once again to join efforts with other imaging-related journals that have training programs on editorial aspects of publishing for trainees or junior staff (<5 years on staff), including **Radiology** (Olmsted fellowship), **AJR** (Figley and Rogers fellowships), **JACR** (Bruce J. Hillman fellowship), and **Radiologia**.

2020 Candidate Information and Requirements

GOALS

- Increase interest in editorial and publication-related activities in younger individuals.
- Increase understanding and participation in the AJNR review process.
- Incorporate into AJNR's Editorial Board younger individuals who have previous experience in the review and publication process.
- Fill a specific need in neuroradiology not offered by other similar fellowships.
- Increase the relationship between "new" generation of neuroradiologists and more established individuals.
- Increase visibility of AJNR among younger neuroradiologists.

ACTIVITIES OF THE FELLOWSHIP

- Serve as Editorial Fellow for one year. This individual will be listed on the masthead as such.
- Review at least one manuscript per month for 12 months. Evaluate all review articles submitted to AJNR.
- Learn how electronic manuscript review systems work.
- Be involved in the final decision of selected manuscripts together with the Editor-in-Chief.
- Participate in all monthly Senior Editor telephone conference calls.
- Participate in all meetings of the Editors during the annual meetings of ASNR and RSNA and the Radiology Editors Forum as per candidate's availability. The Foundation of the ASNR will provide $2000 funding for this activity.
- Evaluate progress and adjust program to specific needs in annual meeting or telephone conference with the Editor-in-Chief.
- Embark on an editorial scientific or bibliometric project that will lead to the submission of an article to AJNR or another appropriate journal as determined by the Editor-in-Chief. This project will be presented by the Editorial Fellow at the ASNR annual meeting.
- Serve as liaison between AJNR and ASNR's Young Professionals Network. Participate in meetings and telephone calls with this group. Design one electronic survey/year, polling the group regarding readership attitudes and wishes.
- Recruit trainees as reviewers as determined by the Editor-in-Chief.
- Organize and host a Fellows' Journal Club podcast.
- Serve as Guest Editor for an issue of AJNR's News Digest with a timely topic.

QUALIFICATIONS

- Be a fellow in neuroradiology from North America, including Canada (this may be extended to include other countries).
- Be a junior faculty neuroradiology member (<5 years) in either an academic or private environment.
- Be an "in-training" or member of ASNR in any other category.

APPLICATION

- Include a short letter of intent with statement of goals and desired research project. CV must be included.
- Include a letter of recommendation from the Division Chief or fellowship program director. A statement of protected time to perform the functions outlined is desirable.
- Applications will be evaluated by AJNR's Senior Editors prior to the ASNR meeting. The name of the selected individual will be announced at the meeting.
- Applications should be received by March 2, 2020 and sent to Ms. Karen Halm, AJNR Managing Editor, electronically at khalm@asnr.org.

AJNR go green

AJNR urges American Society of Neuroradiology members to reduce their environmental footprint by voluntarily suspending their print subscription.

The savings in paper, printing, transportation, and postage directly fund new electronic enhancements and expanded content.

The digital edition of *AJNR* presents the print version in its entirety, along with extra features including:

- **Publication Preview**
- **Case Collection**
- **Podcasts**
- **The *AJNR* News Digest**
- **The *AJNR* Blog**

It also reaches subscribers much faster than print. An electronic table of contents will be sent directly to your mailbox to notify you as soon as it publishes.

Readers can search, reference, and bookmark current and archived content 24 hours a day on www.ajnr.org.

ASNR members who wish to opt out of print can do so by using the AJNR Go Green link on the *AJNR* Website (http://www.ajnr.org/content/subscriber-help-and-services). Just type your name in the email form to stop print and spare our ecosystem.

We're Inside Every Great Neuroradiologist!

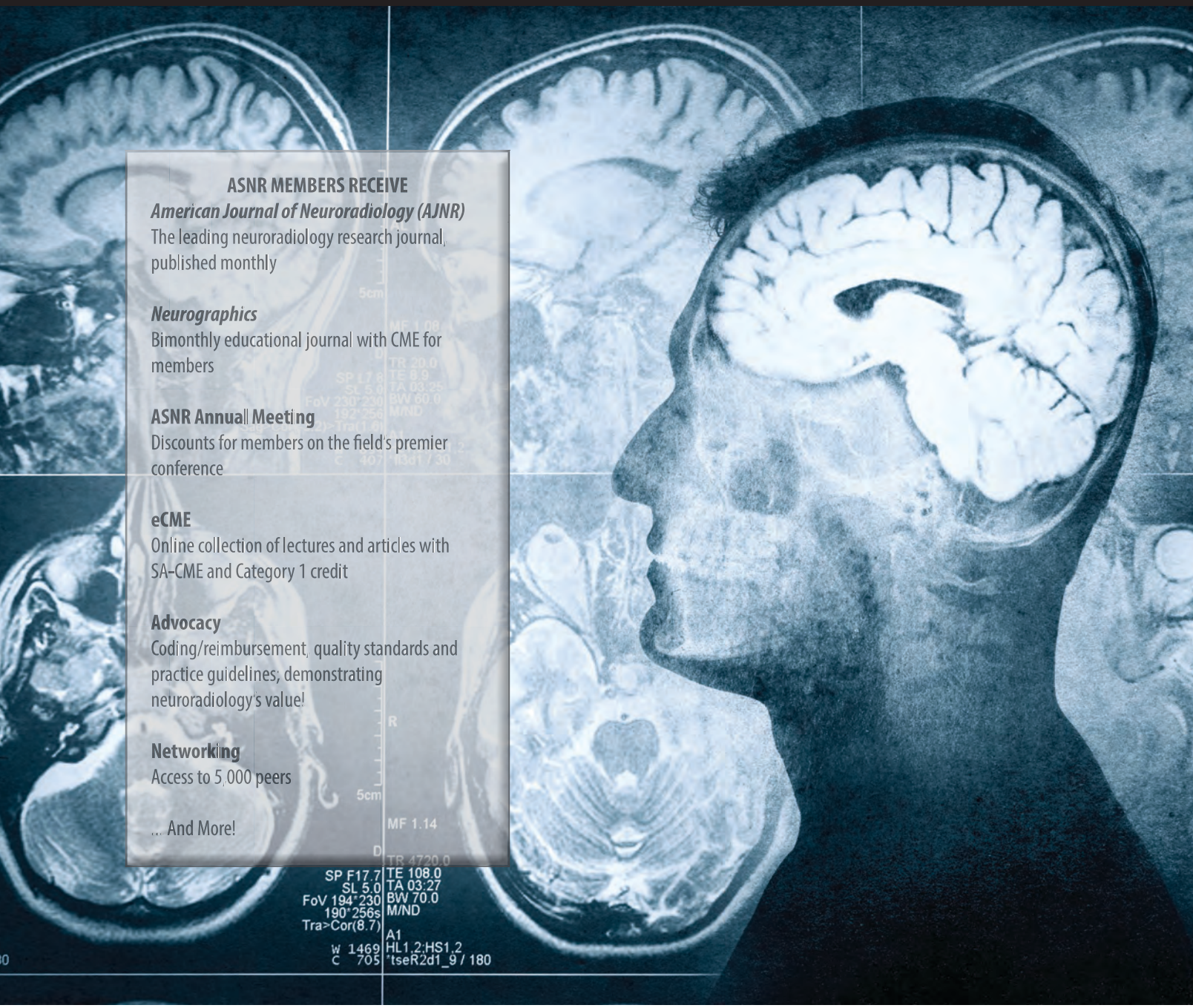

Join the leaders in neuroradiology today!
Learn more at www.asnr.org/join

ASNR
American Society of Neuroradiology

800 Enterprise Dr., Suite 205, Oak Brook, IL 60523 • (630)574-0220 • membership@asnr.org • www.asnr.org

PS Form 3526 — **Statement of Ownership, Management, and Circulation (All Periodicals Publications Except Requester Publications)**

1. Publication Title	2. Publication Number	ISSN	3. Filing Date
AMERICAN SOCIETY OF NEURORADIOLOGY/AJNR-AMERICAN JOURNAL OF NEURORADIOLOGY	532630		09/30/2019

4. Issue Frequency	5. Number of Issues Published Annually	6. Annual Subscription Price
MONTHLY	12	$ 410.00

7. Complete Mailing Address of Known Office of Publication
800 ENTERPRISE DRIVE
SUITE 205
OAK BROOK, DU PAGE, IL 60523

Contact Person KAREN HALM
Telephone (630) 574-1487 Ext. 238

8. Complete Mailing Address of Headquarters or General Business Office of Publisher
800 ENTERPRISE DR STE 205
OAK BROOK, IL 60523-4216

9. Full Names and Complete Mailing Addresses of Publisher, Editor, and Managing Editor

Publisher *(Name and complete mailing address)*
Ame. Society of Neuroradiology
800 ENTERPRISE DR
STE 205
OAK BROOK, IL 60523

Editor *(Name and complete mailing address)*
Ame. Society of Neuroradiology
800 ENTERPRISE DR
STE 205
OAK BROOK, IL 60523

Managing Editor *(Name and complete mailing address)*
Ame. Society of Neuroradiology
800 ENTERPRISE DR STE 205
OAK BROOK, IL 60523-4216

10. Owner *(Do not leave blank. If the publication is owned by a corporation, give the name and address of the corporation immediately followed by the names and addresses of all stockholders owning or holding 1 percent or more of the total amount of stock. If not owned by a corporation, give names and addresses of the individual owners. If owned by a partnership or other unincorporated firm, give its name and address as well as those of each individual owner. If the publication is published by a nonprofit organization, give its name and address.)*

Full Name	Complete Mailing Address
Am. Society of Neuroradiology	800 ENTERPRISE DRIVE, SUITE 205, OAK BROOK, IL 60523

11. Known Bondholders, Mortgagees, and Other Security Holders Owning or Hoding 1 Percent or More of Total Amount of Bonds. Mortgages, or Other Securities. If none, check box [X] None

Full Name	Complete Mailing Address

PS Form **3526**, September 2007 *(Page 1)* — **PRIVACY NOTICE:** See our privacy policy on *www.usps.com*

13. Publication Title	14. Issue Date for Circulation Data Below
AMERICAN SOCIETY OF NEURORADIOLOGY/AJNR-AMERICAN JOURNAL OF NEURORADIOLOGY	09/06/2019

15. Extend and Nature of Circulation			Average No. Copies Each Issue During Preceding 12 Months	No. Copies of Single Issue Published Nearest to Filing Date
a. Total Numbers of Copies *(Net press run)*			3001	2875
b. Paid Circulation *(By Mail and Outside the Mail)*	(1)	Mailed Outside County Paid Subscriptions Stated on PS Form 3541*(include paid distribution above nominal rate, advertiser's proof copies, and exchange copies)*	2513	2351
	(2)	Mailed In-County Paid Subscriptions Stated on PS Form 3541*(include paid distribution above nominal rate, advertiser's proof copies, and exchange copies)*	0	0
	(3)	Paid Distribution Outside the Mails Including Sales Through Dealers and Carriers, Street Vendors, Counter Sales, and Other Paid Distribution Outside USPS	232	226
	(4)	Paid Distribution by Other Classes of Mail Through the USPS *(e.g. First-Class Mail)*	0	0
c. Total Paid Distribution *(Sum of 15b (1), (2), (3), (4))*			2745	2577
d. Free or Nominal Rate Distribution *(By Mail and Outside the Mail)*	(1)	Free or Nominal Rate Outside County Copies included on PS Form 3541	0	0
	(2)	Free or Nominal Rate In-County Copies included on PS Form 3541	0	0
	(3)	Free or Nominal Rate Copies Mailed at Other Classes Through the USPS *(e.g. First-Class Mail)*	0	0
	(4)	Free or Nominal Rate Distribution Outside the Mail *(Carriers or other means)*	40	37
e. Total Free or Nominal Rate Distribution *(Sum of 15d (1), (2), (3), (4))*			40	37
f. Total Distribution *(Sum of 15c and 15e)*			2785	2614
g. Copies not Distributed			216	261
h. Total *(Sum of 15f and 15g)*			3001	2875
i. Percent Paid *((15c / 15f) times 100)*			98.56 %	98.58 %

16. If total circulation includes electronic copies, report that circulation on lines below.		
a. Paid Electronic Copies	0	0
b. Total Paid Print Copies*(Line 15C)* + Paid Electronic Copies	0	0
c. Total Print Distribution*(Line 15F)* + Paid Electronic Copies	0	0
d. Percent Paid*(Both Print and Electronic Copies)*	0.00 %	0.00 %

☐ I Certify that 50% of all my distributed copies (Electronic and Print) are paid above a nominal price.

17. Publication of Statement of Ownership

[X] If the publication is a general publication, publication of this statement is required. Will be printed in the 11/13/2019 issue of this publication. ☐ Publication not required.

18. Signature and Title of Editor, Publisher, Business Manager, or Owner	Title	Date
Karen E. Halm	Managing Editor	09/30/2019 11:44:16 AM

I certify that all information furnished on this form is true and complete. I understand that anyone who furnishes false or misleading information on this form or who omits material or information requested on the form may be subject to criminal sanctions (including fines and imprisonment) and/or civil sanctions (including civil penalties).

PS Form **3526**, September 2007 *(Page 2)* — **PRIVACY NOTICE:** See our privacy policy on *www.usps.com*

MicroVention®
TERUMO

NE AND DONE

INDICATIONS FOR USE:

The WEB Aneurysm Embolization System is indicated for use at the middle cerebral artery (MCA) bifurcation, internal carotid artery (ICA) terminus, anterior communicating artery (AComm) complex, or basilar artery apex for the endovascular treatment of adult patients with saccular, wide neck bifurcation intracranial aneurysms with dome diameter from 3 mm to 10 mm and either neck size 4 mm or greater or the dome-to-neck ratio is greater than 1 and less than 2.

The WEB Aneurysm Embolization System is contraindicated for patients with known bacterial infection that may interfere with or negatively affect the implantation procedure and patients with known hypersensitivity to nickel. For complete indications, contraindications, potential complications, warnings, precautions, and instructions, see instructions for use (IFU provided with the device).

The VIA® Catheter is intended for the introduction of non-liquid interventional devices (such as stents/_ ow diverters) and infusion of diagnostic (such as contrast media) or non-liquid therapeutic agents into the neuro, peripheral, and coronary vasculature. The VIA Catheter is contraindicated for use with liquid embolic materials, such as n-butyl 2-cyanoacrylate or ethylene vinyl alcohol & DMSO (dimethyl sulfoxide). The VIA Catheter is contraindicated for use in the pediatric population (<22 yrs of age).

Caution: Federal law restricts these devices to sale by or on the order of a physician.

CE 0297

Neuroform Atlas® Stent System

RX ONLY

See package insert for complete indications, contraindications, warnings and instructions for use.

Indications for use

The Neuroform Atlas Stent System is indicated for use with neurovascular embolization coils in the anterior circulation of the neurovasculature for the endovascular treatment of patients ≥ 18 years of age with saccular wide-necked (neck width ≥ 4 mm or a dome-to-neck ratio of < 2) intracranial aneurysms arising from a parent vessel with a diameter of ≥ 2.0 mm and ≤ 4.5 mm.

Contraindications

- Patients in whom the parent vessel size does not fall within the indicated range.
- Patients in whom antiplatelet and/or anticoagulation therapy (e.g., aspirin and clopidogrel) is contraindicated.
- Patients who have not received anti-platelet agents prior to stent implantation.
- Patients with an active bacterial infection.
- Patients in whom angiography demonstrates the anatomy is not appropriate for endovascular treatment due to conditions such as:
- Severe intracranial vessel tortuosity or stenosis;
- Intracranial vasospasm not responsive to medical therapy.
- Patients in whom a pre-existing stent is in place in the parent artery at the target intracranial aneurysm location.

Potential adverse events

The potential adverse events listed below, as well as others, may be associated with the use of the Neuroform Atlas Stent System or with the procedure:

- Aphasia
- Allergic reaction to Nitinol metal and medications
- Aneurysm perforation/rupture, leak or contrast extravasation
- Blindness
- Cardiac arrhythmia
- Coil herniation through stent into parent vessel
- Cranial neuropathy
- Death
- Embolus
- Headache
- Hemiplegia
- Hemorrhage (i.e., intracerebral, subarachnoid, retroperitoneal, or in other locations)
- Hydrocephalus
- In-stent stenosis
- Infection
- Ischemia
- Mass effect
- Myocardial infarction
- Neurological deficit/intracranial sequelae
- Pseudoaneurysm
- Reaction to radiation exposure (i.e., alopecia, burns ranging in severity from skin reddening to ulcers, cataracts, or delayed neoplasia)
- Reactions to anti-platelet/anti-coagulant agents
- Renal failure
- Seizure
- Stent fracture, migration/embolization, or misplacement
- Stent thrombosis
- Stroke
- Transient ischemic attack
- Vasospasm
- Vessel occlusion or closure including parent vessel or non-target side-branches
- Vessel perforation/rupture, dissection, trauma or damage
- Vessel thrombosis
- Visual impairment
- Other procedural complications including but not limited to anesthetic and contrast media risks, hypotension, hypertension, access site complications (including pain, hematoma, local bleeding, local infection, and injury to the artery (i.e. dissection), vein, or adjacent nerves)
- Unplanned intervention

Warnings

Contents supplied STERILE using an ethylene oxide (EO) process. Do not use if sterile barrier is damaged. If damage is found, call your Stryker Neurovascular representative.

For single use only. Do not reuse, reprocess or resterilize. Reuse, reprocessing or resterilization may compromise the structural integrity of the device and/or lead to device failure which, in turn, may result in patient injury, illness or death. Reuse, reprocessing or resterilization may also create a risk of contamination of the device and/or cause patient infection or cross-infection, including, but not limited to, the transmission of infectious disease(s) from one patient to another. Contamination of the device may lead to injury, illness or death of the patient.

After use, dispose of product and packaging in accordance with hospital, administrative and/or local government policy.

- This device should only be used by physicians who have received appropriate training in interventional neuroradiology or interventional radiology and preclinical training on the use of this device as established by Stryker Neurovascular.
- Persons allergic to nickel titanium (Nitinol) may suffer an allergic response to this stent implant.
- Higher adverse event rates may be experienced for distal aneurysms located in the anterior and middle cerebral arteries.
- Do not use device to treat patients with ruptured intracranial aneurysms within a minimum of 30 days from the aneurysm rupture.

Cautions / precautions

- Take all necessary precautions to limit X-ray radiation doses to clinical operators by using sufficient shielding, reducing fluoroscopy times, and modifying X-ray technical factors whenever possible.
- The Neuroform Atlas stent may create local field inhomogeneity and susceptibility artifacts during magnetic resonance angiography (MRA), which may degrade the diagnostic quality to assess effective intracranial aneurysm occlusion.
- Safety and effectiveness of the Neuroform Atlas Stent System in patients below the age of 18 has not been established.
- The benefits may not outweigh the risks of device use in patients with small and medium asymptomatic extradural intracranial aneurysms, including those located in the cavernous internal carotid artery.
- Carefully weigh the benefits vs. risks of device treatment for each individual patient based on their medical health status and risk factors for intracranial aneurysm rupture during their expected life time such as age, comorbidities, history of smoking, intracranial aneurysm size, location, and morphology, family history, history of prior asymptomatic subarachnoid hemorrhage (aSAH), documented growth of intracranial aneurysm on serial imaging, presence of multiple intracranial aneurysms, and presence of concurrent pathology. The benefits may not outweigh the risks associated with device use in certain patients; therefore, judicious patient selection is recommended based on clinical practice guidelines or tools to assess the life time risk of intracranial aneurysm rupture.

Safety Information Magnetic Resonance Conditional

Non-clinical testing and analysis have demonstrated that the Neuroform Atlas Stent is MR Conditional alone, or when overlapped with a second stent, and adjacent to a Stryker Neurovascular coil mass. A patient with the Neuroform Atlas Stent can be safely scanned immediately after placement of this implant, under the following conditions:

- Static magnetic field of 1.5 and 3.0 Tesla
- Maximum spatial gradient field up to 2500 Gauss/cm (25 Tesla/m)
- Maximum MR system reported whole body averaged specific absorption rate of 2 W/kg (Normal Operating Mode) and head averaged specific absorption rate of 3.2 W/kg.

Under the scan conditions defined above, the Neuroform Atlas Stent is expected to produce a maximum temperature rise of 4 °C after 15 minutes of continuous scanning. The Neuroform Atlas Stent should not migrate in this MRI environment.

In non-clinical testing, the image artifact caused by the device extends approximately 2 mm from the Neuroform Atlas Stent when imaged with a spin echo pulse sequence and 3 Tesla MRI System. The artifact may obscure the device lumen. It may be necessary to optimize MR imaging parameters for the presence of this implant. See additional precaution related to the image artifact from the implant in the "Precautions" section of this labeling.

Stryker Neurovascular
47900 Bayside Parkway
Fremont, CA 94538

strykerneurovascular.com

Date of Release: MAY/2019

EX_EN_US

AXS Catalyst® Distal Access Catheter

RX ONLY

See package insert for complete indications, complications, warnings, and instructions for use.

Indication for use as a conduit

The AXS Catalyst Distal Access Catheter is indicated for use in facilitating the insertion and guidance of appropriately sized interventional devices into a selected blood vessel in the peripheral and neurovascular systems. The AXS Catalyst Distal Access Catheter is also indicated for use as a conduit for retrieval devices.

Indication for use as a revascularization device

The AXS Catalyst Distal Access Catheter is indicated for use in the revascularization of patients with acute ischemic stroke secondary to intracranial large vessel occlusive disease (in the internal carotid, middle cerebral - M1 and M2 segments, basilar, and vertebral arteries) within 8 hours of symptom onset. Patients who are ineligible for intravenous tissue plasminogen activator (IV t-PA) or who failed IV t-PA are candidates for treatment.

Device description when use as a revascularization device

The AXS Universal Aspiration System is composed of the following components:

- AXS Catalyst Distal Access Catheter
- AXS Universal Aspiration Tubing
- Medela Dominant Flex Pump
- AXS Universal Liner Set

The AXS Universal Aspiration System is designed to remove thrombus from the neurovasculature using continuous aspiration.

The AXS Catalyst Distal Access Catheter delivers aspiration from the Medela Dominant Flex Pump directly to the site of the occlusion to remove the clot. The AXS Catalyst Distal Access Catheter is a sterile, single lumen, variable stiffness catheter. The catheter shaft has a hydrophilic coating to reduce friction during use, includes a radiopaque marker on the distal end for angiographic visualization, and includes a luer hub on the proximal end allowing attachments for flushing and aspiration. It is packaged with a Rotating Hemostasis Valve (RHV), Tuohy Borst Valve with Sideport, and Peel Away Introducer. The Rotating Hemostasis Valve and Tuohy Borst valve with sideport are used for flushing, insertion of catheters, and aspiration. The peel away introducer sheaths are designed to protect the distal tip of the catheter during insertion into the RHV or Tuohy Borst. The AXS Catalyst Distal Access Catheter is the only component of the AXS Universal Aspiration System that is used intravascularly.

AXS Universal Aspiration System
The AXS Universal Aspiration Tubing serves as a conduit to supply vacuum from the Medela Dominant Flex Pump to the distal tip of the AXS Catalyst Distal Access Catheter. The AXS Universal Aspiration Tubing provides a connection between the sterile and non-sterile environments. The proximal end of the AXS Universal Aspiration Tubing is connected to the AXS Universal Liner Set (outside of the sterile environment) while the distal end of the AXS Universal Aspiration Tubing is connected to the AXS Catalyst Distal Access Catheter (inside the sterile environment). The AXS Universal Liner Set is connected to the Medela Dominant Flex Pump (also outside of the sterile environment).

The Medela Dominant Flex Pump is designed to generate vacuum for the AXS Universal Aspiration System. When used as part of the AXS Universal Aspiration System, the AXS Catalyst Distal Access Catheter requires a minimum vacuum pressure of -68 kPa [-20.08 in Hg] from the Medela Dominant Flex Pump. The Medela Dominant Flex Pump is reusable, non-sterile, and intended to be utilized outside of the sterile environment.

The AXS Universal Liner Set is provided non-sterile and consists of an individually packaged canister liner and a ClotFinder specimen cup. The AXS Universal Liner Set is offered with and without a desiccant. The AXS Universal Liner Set is single-use and the repository for aspirated material.

Contraindications

None known.

Adverse events

Potential adverse events associated with the use of catheters or with the endovascular procedures include, but are not limited to:

- Access site complications
- Allergic reaction
- Aneurysm perforation
- Aneurysm rupture
- Death
- Embolism (air, foreign body, plaque, thrombus)
- Hematoma
- Hemorrhage
- Infection
- Ischemia
- Neurological deficits
- Pseudoaneurysm
- Stroke
- Transient Ischemic Attack
- Vasospasm
- Vessel dissection
- Vessel occlusion
- Vessel perforation
- Vessel rupture
- Vessel thrombosis

Use of device requires fluoroscopy which presents potential risks to physicians and patients associated with x-ray exposure. Possible risks include, but are not limited to, the following:

- Alopecia
- Burns ranging in severity from skin reddening to ulcers
- Cataracts
- Delayed neoplasia

Warnings for both indications

Contents supplied STERILE using an ethylene oxide (EO) process. Do not use if sterile barrier is damaged. If damage is found, call your Stryker Neurovascular representative.

For single use only. Do not reuse, reprocess or resterilize. Reuse, reprocessing or resterilization may compromise the structural integrity of the device and/or lead to device failure which, in turn, may result in patient injury, illness or death. Reuse, reprocessing or resterilization may also create a risk of contamination of the device and/or cause patient infection or cross-infection, including, but not limited to, the transmission of infectious disease(s) from one patient to another. Contamination of the device may lead to injury, illness or death of the patient.

After use, dispose of product and packaging in accordance with hospital, administrative and/or local government policy.

- Limited testing has been performed with solutions such as contrast media, and saline. The use of these catheters for delivery of solutions other than the types that have been tested for compatibility is not recommended.
- Not intended for use with power injectors.
- If flow through catheter becomes restricted, do not attempt to clear catheter lumen by infusion. Doing so may cause catheter damage or patient injury. Remove and replace catheter.
- Never advance or withdraw an intravascular device against resistance until the cause of the resistance is determined by fluoroscopy. Movement of the device against resistance could dislodge a clot, perforate a vessel wall, or damage the device.

Additional warning for revascularization indication only

- Excessive aspiration may cause patient complications.

Precautions

- Carefully inspect all devices prior to use. Verify size, length, and condition are suitable for the specific procedure. Ensure the catheter's labeled outer diameter is smaller than the treatment vessel diameter. Do not use a device that has been damaged in any way. Damaged device may cause complications.
- To control the proper introduction, movement, positioning and removal of the catheter within the vascular system, users should employ standard clinical angiographic and fluoroscopic practices and techniques throughout the interventional procedure.
- Use the product prior to the "Use By" date printed on the label.
- To prevent thrombus formation and contrast media crystal formation, maintain a constant infusion of appropriate flush solution through catheter lumen.
- Torquing the catheter may cause damage which could result in kinking or separation of the catheter shaft.

Stryker Neurovascular
47900 Bayside Parkway
Fremont, CA 94538

strykerneurovascular.com

Date of Release: MAY/2019

EX_EN_US

stryker

Trap more.

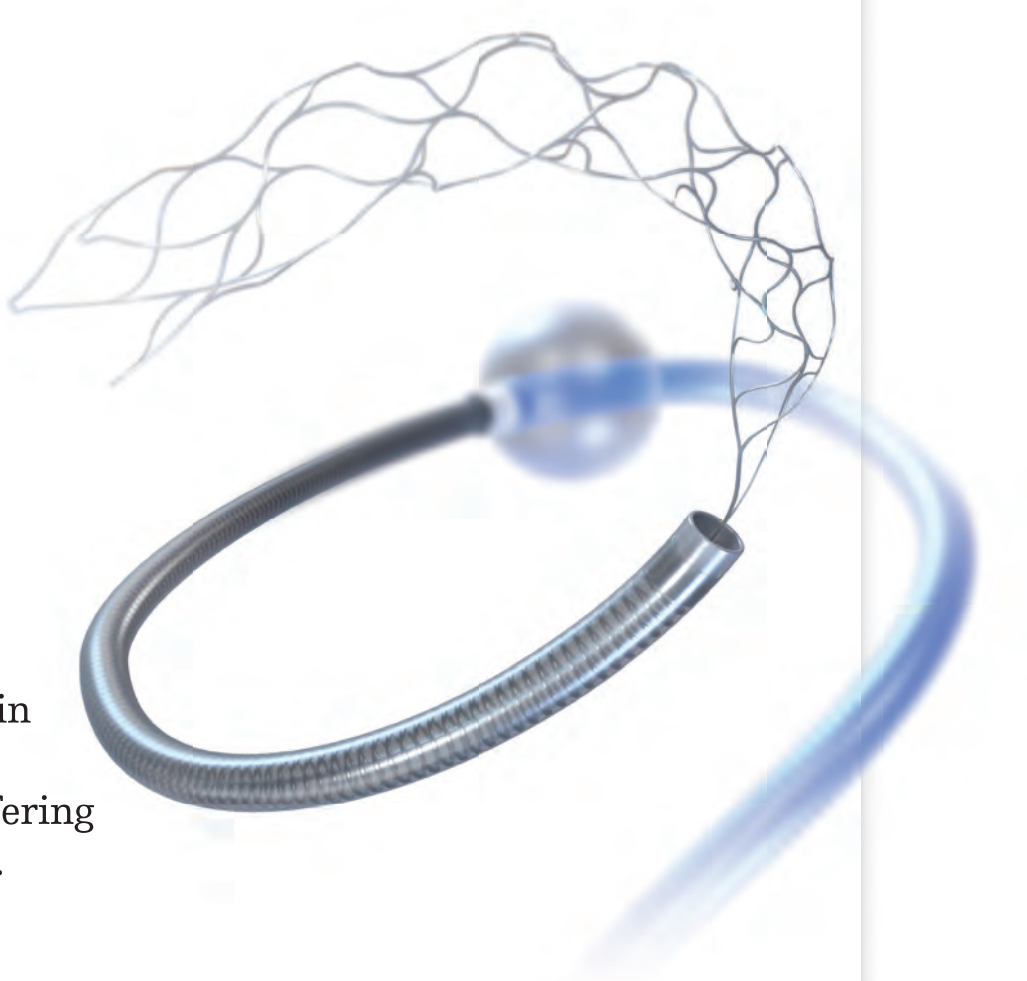

Empowering first pass retrieval with the new 0.068in lumen CAT 7 Distal Access Catheter, offering ultimate versatility.

AXS Catalyst® 7
Distal Access Catheter

CAT 7 lumen is bigger than CAT 6 lumen.

AJNR

AMERICAN JOURNAL OF NEURORADIOLOGY

NOVEMBER 2019
VOLUME 40
NUMBER 11
WWW.AJNR.ORG

Publication Preview at www.ajnr.org features articles released in advance of print. Visit www.ajnrblog.org to comment on AJNR content and chat with colleagues and AJNR's News Digest at http://ajnrdigest.org to read the stories behind the latest research in neuroimaging.

AJNR (Am J Neuroradiol ISSN 0195–6108) is a journal published monthly, owned and published by the American Society of Neuroradiology (ASNR), 800 Enterprise Drive, Suite 205, Oak Brook, IL 60523. Annual dues for the ASNR include $170.00 for journal subscription. The journal is printed by Cadmus Journal Services, 5457 Twin Knolls Road, Suite 200, Columbia, MD 21045; Periodicals postage paid at Oak Brook, IL and additional mailing offices. Printed in the U.S.A. POSTMASTER: Please send address changes to American Journal of Neuroradiology, P.O. Box 3000, Denville, NJ 07834, U.S.A. Subscription rates: nonmember $410 ($480 foreign) print and online, $320 online only; institutions $470 ($540 foreign) print and basic online, $935 ($1000 foreign) print and extended online, $380 online only (basic), extended online $825; single copies are $35 each ($40 foreign). Indexed by PubMed/Medline, BIOSIS Previews, Current Contents (Clinical Medicine and Life Sciences), EMBASE, Google Scholar, HighWire Press, Q-Sensei, RefSeek, Science Citation Index, SCI Expanded, Meta/CZI and ReadCube.

ONLINE FEATURES

LETTERS

BOOK REVIEWS *R.M. Quencer, Section Editor*

Please visit www.ajnrblog.org to read and comment on Book Reviews.

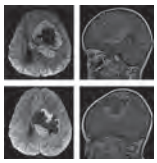

Axial DWI (*top left*) and sagittal postcontrast T1-weighted (*top right*) images in a 4-year-old girl with a molecular diagnosis of high-grade glioma show a large mass centered in the left frontal lobe with prominent necrotic/cystic areas centrally and diffusion restriction and heterogeneous enhancement. Axial DWI (*bottom left*) and sagittal postcontrast T1-weighted (*bottom right*) images in a 4-year-old boy with a molecular diagnosis of ependymoma demonstrate a large mass centered deep in the left hemisphere with prominent necrotic/cystic areas centrally, diffusion restriction, and heterogeneous enhancement with a very similar appearance to the prior patient with different molecular diagnoses.

AJNR

AMERICAN JOURNAL OF NEURORADIOLOGY

Publication Preview at www.ajnr.org features articles released in advance of print. Visit www.ajnrblog.org to comment on AJNR content and chat with colleagues and AJNR's News Digest at http://ajnrdigest.org to read the stories behind the latest research in neuroimaging.

NOVEMBER 2019 • VOLUME 40 • NUMBER 11 • WWW.AJNR.ORG

Official Journal:
American Society of Neuroradiology
American Society of Functional Neuroradiology
American Society of Head and Neck Radiology
American Society of Pediatric Neuroradiology
American Society of Spine Radiology

Title: Mechanical Password. Mixing the analog world with the digital world: Instead of having electronic passwords, the BEST way to protect information is still the dear old lock!

Guido Guglielmi, MD, former professor in residence at University of California, Los Angeles and Chairman of Interventional Neuroradiology, University of Roma, Italy, Rome, Italy

Mixed Solid and Cystic Mass in an Infant

J.C. Benson, D. Summerfield, J.B. Guerin, D. Kun Kim, L. Eckel, D.J. Daniels, and P. Morris

ABSTRACT

SUMMARY: Desmoplastic infantile tumors are rare supratentorial brain tumors that occur in pediatric patients. Desmoplastic infantile tumors are made up of 2 subtypes: desmoplastic infantile gangliogliomas and desmoplastic infantile astrocytomas. Desmoplastic infantile tumors are often identifiable on imaging on the basis of multiple characteristics. Nevertheless, pathologic analysis is required to confirm the diagnosis, particularly when the imaging features are atypical. Here, the radiology findings, surgical approach and subsequent management, and pathology of a desmoplastic infantile ganglioglioma are described.

ABBREVIATIONS: DIA = desmoplastic infantile astrocytoma; DIG = desmoplastic infantile ganglioglioma; DIT = desmoplastic infantile tumor

Brief History

The patient is a 3-month-old girl, born at 37 weeks' gestation after delivery was induced following the discovery of a 2-vessel umbilical cord. No intracranial or calvarial abnormalities had been reported on prenatal sonography. She presented with recent-onset episodic lower left facial grimacing accompanied by decreased responsiveness. She also had progressive macrocephaly with a head circumference at the 96th percentile, severe frontal bossing, palpable splaying of the calvarial sutures, and a bulging anterior fontanelle.

Imaging

MR imaging showed a massive lesion in the right cerebral hemisphere with both cystic and solid components (Fig 1). The cystic aspects made up most of the mass and had a thin internal septation. The lobulated solid components were located centrally near the brain stem and were T2 isointense and heterogeneous with avid enhancement. Associated mass effect was present, including a leftward midline shift, right lateral ventricular effacement, and right basal ganglia and brain stem compression. Confluent T2 hyperintensity within the parenchyma posterior to the mass represented edema and/or gliosis. The cerebral aqueduct was compressed, causing left lateral and third ventricular dilation, though with minimal periventricular edema.

The cystic component of the mass appeared to be extra-axial, evidenced by buckling and compression of the adjacent normal cortex. However, the solid components appeared to be at least partially intra-axial, with complete absence of normal temporal lobe parenchyma.

A massive, predominately cystic supratentorial mass presenting in an infant was suggestive of a desmoplastic infantile tumor (DIT), which includes both desmoplastic infantile gangliogliomas (DIGs) and astrocytomas (DIAs). However, mild-to-moderate restricted diffusion was seen within the solid components of the lesion, which would be atypical for this tumor (Fig 1). An infantile glioblastoma was also considered, given the shared imaging characteristics of both tumors and intralesional restricted diffusion. Other diagnostic considerations were thought to be less likely, including an embryonal tumor with multilayered rosettes, atypical teratoid/rhabdoid tumor, supratentorial ependymoma, and pleomorphic xanthoastryocytoma.

No metastases were present in the spine, and the patient underwent gross total resection of the tumor 2 days after presentation.

Operative Report

A near-gross total resection of the tumor was completed via a right craniotomy. The superficial cystic wall was thin and easily entered (Fig 2). The solid portion of the tumor was highly vascular and was firmly adherent to the adjacent parenchyma in several areas, particularly the right lateral brain stem. The tumor itself was firm and rubbery, consistent with a desmoplastic tumor, making the tumor difficult to aspirate and even challenging to cut. The right carotid artery and right middle cerebral artery were directly on the tumor and required careful separation. The tumor

Received July 25, 2019; accepted after revision August 7.

From the Departments of Radiology (J.C.B., J.B.G., D.K.K., L.E., P.M.), Pathology (D.S.), and Neurosurgery (D.J.D.), Mayo Clinic, Rochester, Minesotta.

Please address correspondence to John C. Benson, MD, Mayo Clinic, Department of Radiology, 723 6th St SW, Rochester, MN 55902; e-mail: benson.john3@mayo.edu

http://dx.doi.org/10.3174/ajnr.A6226

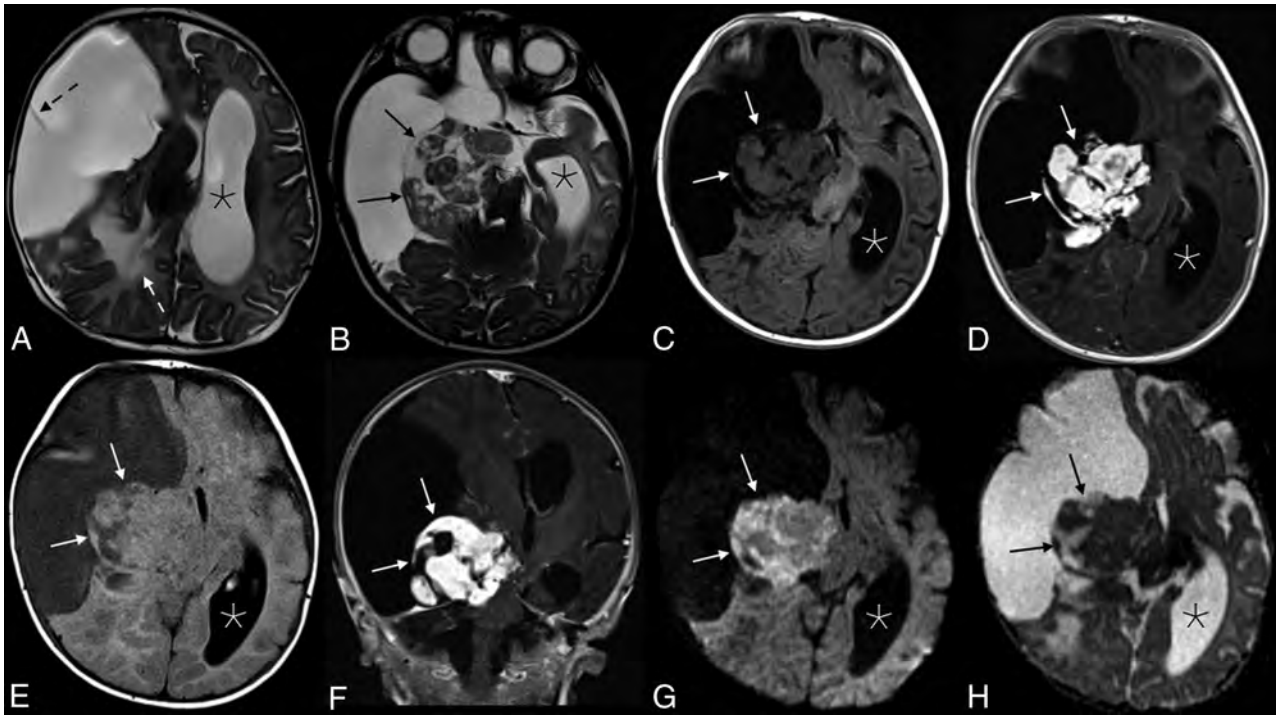

FIG 1. Appearance of the solid tumor component on various sequences. Axial T2 (*A* and *B*), axial T2 FLAIR (*C*), and T1 FLAIR (*D*) images showed a predominantly cystic mass in the right cerebral hemisphere with a heterogeneous solid component (*black arrows* in *B*, and *H*; *white arrows* in *C–G*) along the medial aspect of the tumor margin. A single thin septation was present within the cystic component (*dashed black arrow, A*). There is significant associated mass effect with T2 hyperintensity in the adjacent right parietal lobe white matter (*white dashed arrow, A*), a leftward midline shift, and compression of the right basal ganglia, brain stem, and right cerebral and middle cerebellar peduncles. The left lateral ventricle (*asterisks*) and third ventricle (not shown) were obstructed, causing marked ventricular dilation. Avid enhancement of the solid component is demonstrated in the axial (*D*) and coronal (*E*) T1WI + Gadolinium images. Heterogeneous mild intralesional restricted diffusion (*G* and *H*) is atypical for these tumors.

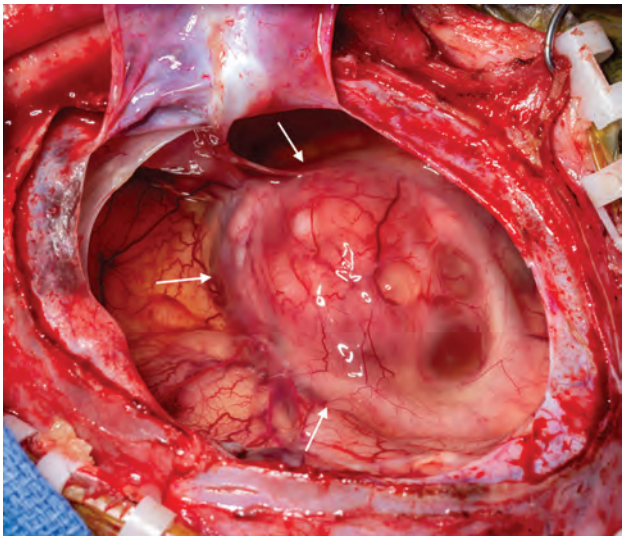

FIG 2. Intraoperative photograph of the tumor, after opening and draining of the cystic portion. The remaining mixed solid and cystic nodule is seen along the medial aspect of the tumor (*arrows*).

circumferentially surrounded the intersection of the right cranial nerve III and posterior cerebral artery, and a small amount of tumor was left at this location. The tumor came out piecemeal after careful dissection around these structures.

Diagnosis: Desmoplastic Infantile Ganglioglioma

Pathology. Histologically, DIGs and DIAs are considered histologic variants of a single World Health Organization grade I entity, with complete surgical resection resulting in long-term survival.[1] Both have a prominent glial cell component characterized by desmoplasia with abundant extracellular matrix production and a fibroblast-like morphology (Fig 3). The distinction between DIG and DIA is made by the identification of a ganglion (neuronal) cell component, which is required for the diagnosis of the ganglioglioma entity. Methylation profiling studies of these tumors support both morphologies representing the same disease process, and long-term follow-up shows a similar prognosis.[2] Some tumors show a minor component of poorly differentiated small round blue cells. However, this is not required for the diagnosis and was not present in this case. Finally, the proliferation rate of these tumors is typically low (<2%).[1]

Photomicrographs of the tumor are presented in Fig 3, highlighting the desmoplastic component. The presence of rare synaptophysin-positive cells (ganglion cells) is sufficient for the diagnosis of DIG, and the glial fibrillary acidic protein (positive cells [glial cells]) is abundant. Tumor DNA was analyzed with a targeted 150 gene neuro-oncology next-generation sequencing panel (including *BRAF*, *FGFR1*, *IDH1*, *IDH2*, and *NF1*). Two variants of unknown significance were identified; however, no pathogenic mutations were identified. The Ki-67 labeling index, which is a marker of proliferative activity, was low in this tumor,

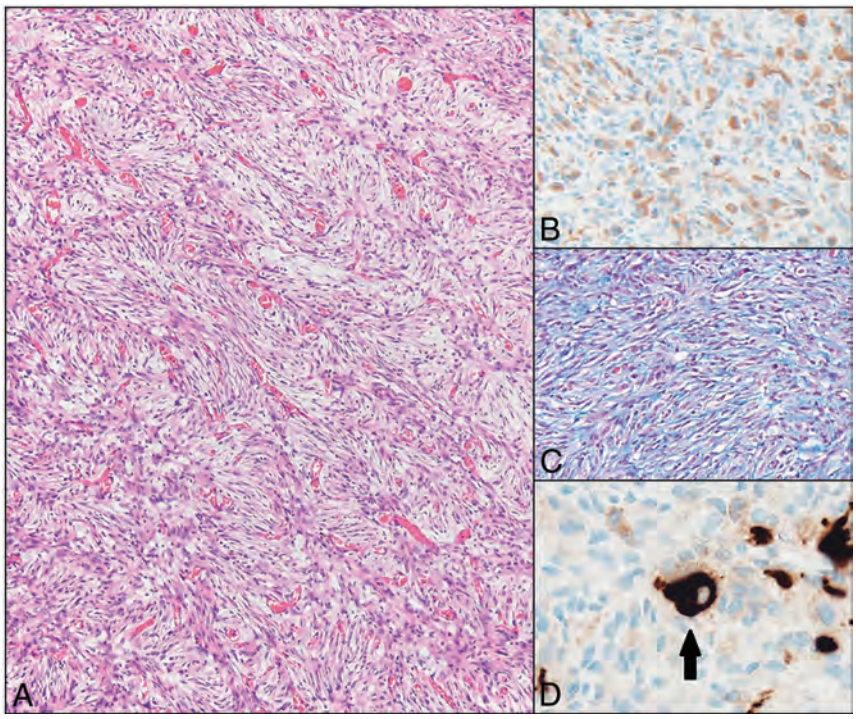

FIG 3. Hematoxylin eosin–stained photomicrograph demonstrates the characteristic fascicular/storiform arrangement of the prominent spindle-shaped glial component of the tumor (*A*, scaled from 100×). These cells are glial fibrillary acid protein positive (confirming their glial origin) (*B*, scaled from 200×), and an abundant pericellular connective tissue network is highlighted by the methyl blue component of a Mason trichrome stain (*C*, scaled from 100×). Rare ganglion cells are present (*arrow*), which are highlighted by Synaptophysin immunostaining (*D*, scaled from 400×).

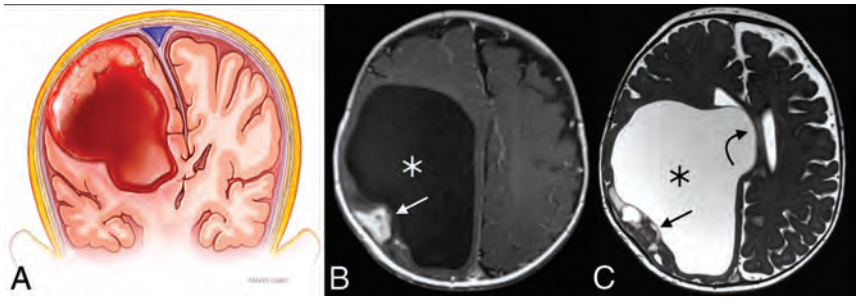

FIG 4. Illustration (*A*) and example (*B* and *C*) of a DIT with typical features. The tumors are exclusively supratentorial and voluminous and are made up of both cystic (*asterisks*) components and a peripheral mural nodule (*straight arrows*). Significant associated mass effect and midline shift (*curved arrow*) are often present. Illustration (*A*), Used with permission of Mayo Foundation for Medical Education and Research. All rights reserved.

which supports the diagnosis of a DIG. *BRAF* mutations, which were absent in this tumor, are found in a minority of DITs. These histologic and molecular features are characteristic of a DIG.

DISCUSSION

DIGs are benign intra-axial CNS tumors.[3,4] They are rare, accounting for 0.5%–1.0% of intracranial tumors.[5,6] Nearly all DIGs occur in patients younger than 18 months of age with a median age at diagnosis of 5–6 months, though noninfantile cases have been reported.[3,7-10] The male/female ratio is 1.7.[3] Most commonly, patients present with macrocephaly related to the size of the lesion and associated mass effect. Resulting seizures and other neurologic deficits may also occur.[7] Despite the aggressive appearance of many DIGs on imaging, the prognosis of these tumors is often favorable, and surgical resection tends to be curative, though the voluminous size and high vascularity of these tumors can contribute to significant intraoperative blood loss.[9-13] Although benign, extremely rare case reports do exist of DITs with malignant transformation as well as cerebrospinal metastases.[14,15]

Multiple characteristic features make DITs recognizable entities on imaging, though the differentiation between DIG and DIA requires histologic analysis. The tumors are invariably supratentorial, contain solid and cystic components, and are often of substantial size.[5,9] Involvement of multiple lobes is common, with a predilection for the frontoparietal regions.[16,17] The solid component tends to be located peripherally, along the dural side of the tumor, and is usually T2 iso-/hypointense to gray matter with avid enhancement (Fig 4).[9,10] Typically, the dura or leptomeninges adjacent to the solid nodule or both demonstrate enhancement.[9] Extremely rare purely solid and nonenhancing DIGs have been reported, as have DIGs in a suprasellar location.[18]

In the index case, the radiologic diagnosis was complicated by the presence of intralesional restricted diffusion. A review by Bader et al[19] found no evidence of restricted diffusion in their 3 cases of DIT, and in only 1 of 32 DIT cases in a related review of the published literature. Infantile glioblastoma multiforme, conversely, had restricted diffusion in 2/2 of the cases reviewed by Bader et al, and in 2/2 tumors in 18 prior publications reviewed by Bader et al. The mural nodule in our case was also located medial to the cystic component, which is a known, albeit rare, appearance of DIT.[9] Nevertheless, the imaging characteristics of the presented case were overall highly suggestive of a DIT. The solid aspects of the mass demonstrated avid enhancement in our case, while infantile glioblastoma multiforme tends to enhance heterogeneously.[19]

Because of both the benignity of the tumor and the near-complete surgical resection, the neurosurgery team elected to proceed with a watch-and-wait approach. The patient had a right-sided cranial nerve III palsy, which was not unexpected because the residual tumor was near the third cranial nerve; this is expected to improve with time. The patient is scheduled to have follow-up imaging every 3 months for the first year; follow-up intervals will then be lengthened if the imaging findings are stable. If growth of the residual tumor is observed, the patient will likely need to undergo either a repeat resection or radiation therapy. An excellent long-term prognosis is expected.

Case Summary

- Imaging highly suggestive of a DIT (DIG/DIA): voluminous cystic mass with a peripheral mural nodule in an infant younger than 18 months of age
- Atypical features include central/medial location of solid component and intralesional restricted diffusion
- The main differential consideration is infantile glioblastoma multiforme, which tends to enhance heterogeneously
- Less likely diagnostic considerations: supratentorial ependymoma, embryonal tumor with multilayered rosettes, atypical teratoid/rhabdoid tumor, and pleomorphic xanthoastryocytoma
- Mass effect related to the tumor often requires urgent neurosurgical intervention; the surgical goal is to safely resect as much as possible and open CSF pathways.

Disclosures: Padraig Morris—*UNRELATED*: *Royalties*: textbook, Lippincott, Williams, & Wilkins.

REFERENCES

1. Gessi M, Zur Muhlen A, Hammes J, et al. **Genome-wide DNA copy number analysis of desmoplastic infantile astrocytoma and desmoplastic infantile gangliogliomas.** *J Neuropathol Exp Neurol* 2013; 72:807–15 CrossRef Medline
2. Wang AC, Jones DTW, Abecassis IJ, et al. **Desmoplastic infantile ganglioglioma/astrocytoma (DIG/DIA) are distinct entities with frequent BRAFV600 mutations.** *Mol Cancer Res* 2018;16:1491–98 CrossRef Medline
3. Ho CY, Gener M, Bonnin J, et al. **Diffusion, perfusion, and histopathologic characteristics of desmoplastic infantile ganglioglioma.** *J Radiol Case Rep* 2016;10:1–13 CrossRef Medline
4. Tamburrini G, Colosimo C, Giangaspero F, et al. **Desmoplastic infantile ganglioglioma.** *Childs Nerv Syst* 2003;19:292–97 CrossRef Medline
5. Tenreiro-Picon OR, Kamath SV, Knorr JR, et al. **Desmoplastic infantile ganglioglioma: CT and MRI features.** *Pediatr Radiol* 1995; 25:540–43 CrossRef Medline
6. Taranath A, Lam A, Wong C. **Desmoplastic infantile ganglioglioma: a questionably benign tumour.** *Australas Radiol* 2005;49: 433–37 CrossRef Medline
7. Romero-Rojas AE, Diaz-Perez JA, Lozano-Castillo A. **Desmoplastic infantile ganglioglioma with late presentation.** *Neuroradiol J* 2013; 26:649–54 CrossRef Medline
8. Gupta A, Karthigeyan M, Gupta K, et al. **Atypical imaging in a desmoplastic non-infantile astrocytoma.** *Childs Nerv Syst* 2017;33:517–20 CrossRef Medline
9. Derinkuyu BE, Ucar M, Borcek AO, et al. **Non-infantile variant of desmoplastic ganglioglioma: conventional and advanced MR imaging characteristics.** *Neuroradiol J* 2015;28:259–63 CrossRef Medline
10. Gelabert-Gonzalez M, Serramito-García R, Arcos-Algaba A. **Desmoplastic infantile and non-infantile ganglioglioma: review of the literature.** *Neurosurg Rev* 2011;34:151–58 CrossRef Medline
11. Lababede O, Bardo D, Goske MJ, et al. **Desmoplastic infantile ganglioglioma (DIG): cranial ultrasound findings.** *Pediatr Radiol* 2001; 31:403–05 CrossRef Medline
12. Qaddoumi I, Ceppa EP, Mansour A, et al. **Desmoplastic noninfantile ganglioglioma: report of a case.** *Pediatr Dev Pathol* 2006;9:462–67 CrossRef Medline
13. Sperner J, Gottschalk J, Neumann K, et al. **Clinical, radiological and histological findings in desmoplastic infantile ganglioglioma.** *Child's Nerv Syst* 1994;10:458–63 CrossRef Medline
14. Darwish B, Arbuckle S, Kellie S, et al. **Desmoplastic infantile ganglioglioma/astrocytoma with cerebrospinal metastasis.** *J Clin Neurosci* 2007;14:498–501 CrossRef Medline
15. Loh JK, Lieu AS, Chai CY, et al. **Malignant transformation of a desmoplastic infantile ganglioglioma.** *Pediatr Neurol* 2011;45:135–37 CrossRef Medline
16. VandenBerg SR. **Desmoplastic infantile gangliogliomas and desmoplastic cerebral astrocytoma of infancy.** *Brain Pathol* 1993;3:275–81 CrossRef Medline
17. Ng THK, Fung CF, Ma LT. **The pathological spectrum of desmoplastic infantile gangliogliomas.** *Histopathology* 1990;16:235–41 CrossRef Medline
18. Naylor RM, Wohl A, Raghunathan A, et al. **Novel suprasellar location of desmoplastic infantile astrocytoma and ganglioglioma: a single institution's experience.** *J Neurosurg Pediatr* 2018;22:397–403 CrossRef Medline
19. Bader A, Heran M, Dunham C, et al. **Radiological features of infantile glioblastoma and desmoplastic infantile tumors: British Columbia's Children's Hospital experience.** *J Neurosurg Pediatr* 2015;16:119–25 CrossRef Medline

MRI Features of Histologically Diagnosed Supratentorial Primitive Neuroectodermal Tumors and Pineoblastomas in Correlation with Molecular Diagnoses and Outcomes: A Report from the Children's Oncology Group ACNS0332 Trial

A. Jaju, E.I. Hwang, M. Kool, D. Capper, L. Chavez, S. Brabetz, C. Billups, Y. Li, M. Fouladi, R.J. Packer, S.M. Pfister, J.M. Olson, and L.A. Heier

ABSTRACT

BACKGROUND AND PURPOSE: Supratentorial primitive neuroectodermal tumors and pineoblastomas have traditionally been grouped together for treatment purposes. Molecular profiling of these tumors has revealed a number of distinct entities and has led to the term "CNS-primitive neuroectodermal tumors" being removed from the 2016 World Health Organization classification. The purpose of this study was to describe the MR imaging findings of histologically diagnosed primitive neuroectodermal tumors and pineoblastomas and correlate them with molecular diagnoses and outcomes.

MATERIALS AND METHODS: Histologically diagnosed primitive neuroectodermal tumors and pineoblastomas were enrolled in this Children's Oncology Group Phase III trial, and molecular classification was retrospectively completed using DNA methylation profiling. MR imaging features were systematically studied and correlated with molecular diagnoses and survival.

RESULTS: Of the 85 patients enrolled, 56 met the inclusion criteria, in whom 28 tumors were in pineal and 28 in nonpineal locations. Methylation profiling revealed a variety of diagnoses, including pineoblastomas ($n = 27$), high-grade gliomas ($n = 17$), embryonal tumors ($n = 7$), atypical teratoid/rhabdoid tumors ($n = 3$), and ependymomas ($n = 2$). Thus, 39% overall and 71% of nonpineal tumor diagnoses were discrepant with histopathology. Tumor location, size, margins, and edema were predictors of embryonal-versus-nonembryonal tumors. Larger size and ill-defined margins correlated with poor event-free survival, while metastatic disease by MR imaging did not.

CONCLUSIONS: In nonpineal locations, only a minority of histologically diagnosed primitive neuroectodermal tumors are embryonal tumors; therefore, high-grade glioma or ependymoma should be high on the radiographic differential. An understanding of molecularly defined tumor entities and their relative frequencies and locations will help the radiologist make more accurate predictions of the tumor types.

ABBREVIATIONS: ATRT = atypical teratoid/rhabdoid tumor; EP = ependymoma; ET = embryonal tumor; ETMR = embryonal tumor with multilayered rosettes; GBM = glioblastoma multiforme; HGG = high-grade glioma; HGNET = high-grade neuroepithelial tumor; MB = medulloblastoma; NOS = not otherwise specified; PBL = pineoblastoma; PNET = primitive neuroectodermal tumor

Historically, supratentorial primitive neuroectodermal tumor of the central nervous system (CNS–PNET) and pineoblastoma (PBL) have been considered embryonal tumors (ETs) histopathologically, similar to medulloblastomas (MBs), though the classification has been a topic of much debate.[1,2] CNS-PNET and PBL have thus been treated as a single group using protocols designed for high-risk medulloblastomas.[3,4] In recent years, molecular profiling using genome-wide DNA methylation of histopathologically diagnosed CNS-PNETs has revealed a wide spectrum of distinct molecular entities,

Received April 8, 2019; accepted after revision August 21.

From the Department of Radiology (A.J.), Ann and Robert H Lurie Children's Hospital of Chicago, Chicago, Illinois; Northwestern University Feinberg School of Medicine (A.J.), Chicago, Illinois; Brain Tumor Institute (E.I.H., R.J.P.), Children's National Health System, Washington, DC; Department of Pediatric Neurooncology (M.K., S.B., S.M.P.), German Cancer Research Center, Heidelberg, Baden-Württemberg, Germany; Department of Pediatric Neuropathology (D.C.), University Hospital Heidelberg, Heidelberg, Baden-Württemberg, Germany; Department of Medicine (L.C.), University of California San Diego, La Jolla, California; Department of Biostatistics (C.B., Y.L.), St. Jude Children's Research Hospital, Memphis, Tennessee; Brain Tumor Center (M.F.), Cincinnati Children's Hospital, Cincinnati, Ohio; Fred Hurtchinson Cancer Research Center (J.M.O.), Seattle Children's Hospital, Seattle, Washington; and Department of Radiology (L.A.H.), New York Presbyterian Hospital, New York, New York.

This work was supported, in part, by National Institutes of Health grants No. U10-CA180886 (National Clinical Trials Network Operations Center Grant) and U10-CA180899 (National Clinical Trials Network Statistics and Data Center) and a grant from the St. Baldrick's Foundation.

Paper previously presented, in part, at: Annual Meeting of the American Society of Neuroradiology, May 18–23, 2019; Boston, Massachusetts.

Please address correspondence to Alok Jaju, MD, Ann and Robert H Lurie Children's Hospital of Chicago, Northwestern University Feinberg School of Medicine, 225 E. Chicago Ave, Box 9, Chicago, IL 60611; e-mail: ajaju@luriechildrens.org

Indicates open access to non-subscribers at www.ajnr.org

http://dx.doi.org/10.3174/ajnr.A6253

including high-grade gliomas (HGGs), atypical teratoid/rhabdoid tumors (ATRTs), ependymomas (EPs), and at least 4 new molecular entities.[5-7] The 2016 World Health Organization classification has removed CNS-PNET as a diagnostic category, in part substituting a broad group termed "CNS embryonal tumors, not otherwise specified" (NOS), in addition to more specific entities, such as embryonal tumor with multilayered rosettes (ETMR).[8]

Molecularly defined entities may more accurately predict clinical outcomes when compared with standard histopathologic diagnoses in CNS-PNET,[7] as well as in other pediatric CNS tumors such as medulloblastoma and ependymoma.[9,10] However, practical barriers such as cost, availability, timeliness of results, and assay certification can hamper use. In recent years, there has been growing interest in correlating imaging features with molecular markers in an attempt to identify imaging phenotypes that may serve as surrogates for molecular subtypes.[11,12] This radiogenomic approach has been applied with some success in CNS tumors such as glioblastomas,[13,14] medulloblastomas,[15] ATRT,[16] and non-CNS tumors.[17]

The Children's Oncology Group study, ACNS0332, a multicenter Phase III prospective trial, investigated 2 approaches for treatment intensification, the addition of carboplatin during irradiation and the addition of adjuvant isotretinoin, in patients diagnosed with either CNS-PNET/PBL or high-risk medulloblastoma in 2 parallel randomized strata. The results from the completed CNS-PNET/PBL portion of the trial, including an analysis of molecular profiles and patient outcomes, have been published.[7] These results have shown that the molecularly diagnosed HGG had significantly worse survival compared with supratentorial embryonal tumors and PBL.[7] Thus, the distinction between these 2 categories is critical to the management of these patients.

As a part of this trial, MR imaging of the brain and spine was performed at multiple time points and submitted for central review. The current report focuses on the MR imaging features of CNS-PNET/PBL and their correlation with molecular subtypes and outcomes. Identifying reliable correlations would facilitate imaging-guided clinical decision-making when molecular profiling is unavailable or delayed.

MATERIALS AND METHODS

Patient Cohort

For the strata included in this report, children from 3 to 22 years were eligible, who had newly diagnosed primary CNS-PNET or PBL by institutional pathologists per the 2007 World Health Organization classification system, defined as undifferentiated or poorly differentiated tumors with the capacity for divergent differentiation. Subjects had minimum functional scores (Karnofsky/Lansky) of 30 and adequate renal, marrow, and hepatic function and were staged with spinal CSF cytology and MR imaging of the brain and spine. Institutional review board approval and individual informed consent were obtained before enrollment, and the study was registered with clinicaltrials.gov (NCT00392327).

Molecular Analysis

DNA methylation profiling was performed for all cases with sufficient tumor DNA using the Infinium HumanMethylation450 (450k; https://www.illumina.com/products/by-type/microarray-kits/infinium-methylation-epic.html) or the EPIC BeadChip arrays (http://emea.support.illumina.com/array/array_kits/infinium-methylationepic-beadchip-kit/downloads.html), and the tumors were classified using the recently developed brain diagnostic classifier algorithm (www.molecularneuropathology.org).[18] The methods are described in more detail in earlier publications.[5,7,19]

Neuroimaging Guidelines and Central Review

MRIs of the brain without and with contrast were obtained at diagnosis and after definitive surgery (within 72 hours). For patients who underwent stereotactic biopsy only, a postoperative MR imaging was not required. MR imaging of the spine with contrast was obtained within 10 days of surgery if done preoperatively, and within 28 days of surgery if done postoperatively. Additional MRIs of the brain and spine were obtained at the end of radiation therapy, the end of maintenance chemotherapy, at relapse (if any), and at best response.

For this multi-institutional study, guidelines were provided for the technical parameters of MR imaging. The minimum recommended sequences for the brain included sagittal and axial T1-weighted, axial T2-weighted, axial T2 FLAIR, axial diffusion-weighted, and postcontrast axial and sagittal T1-weighted. The minimum recommended sequences for the spine included postcontrast sagittal and axial T1-weighted imaging. The studies were performed on a variety of scanners from different vendors, including both 1.5 and 3T field strengths, and with varying technical parameters.

The MR imaging studies were retrospectively reviewed after treatment completion by 2 experienced pediatric neuroradiologists by consensus (L.A.H. and A.J.), blinded to the histopathologic and molecular diagnoses. Only the MR imaging studies deemed technically acceptable by the central reviewers were included in this analysis, and there was no opportunity to obtain repeat or additional imaging because of the retrospective nature of the review. MR imaging features of the lesions were recorded including location, laterality, size, margins, surrounding edema, enhancement, cyst/necrosis, hemorrhage/calcification, and metastasis. The size was measured as the longest linear dimension in centimeters. The margins were described as well-defined or ill-defined (>50% margins were indistinct). The surrounding edema was assessed as absent, <2 cm from the tumor margin, or >2 cm from the tumor margin. The extent of enhancement of the solid portion of the tumor was categorized subjectively as none, <25%, 25%–75%, and >75%. The degree of enhancement was subjectively assessed as none, mild, moderate, or marked. The presence of cysts or necrosis and low signal on T2 or gradient recalled-echo sequences suspicious for calcification or hemorrhage was noted, and both of these findings were subjectively quantified as involving <25%, 25%–50%, or >50% of the tumor.

The radiographic presence of intracranial and spinal metastasis was assessed and, in conjunction with CSF cytology, was used to assign the M stage (modified Chang staging). Also, the postoperative MRIs were reviewed, and the extent of resection was

Table 1: Molecular diagnoses for tumors with both imaging and methylation profiles available ($n = 56$)[a]

PBL/ET	No.	Non-ET	No.
PBL	27	GBM_G34[d]	8
CNS_NB_FOXR2[b]	3	GBM_MYCN[d]	5
ETMR[b]	1	DMG_K27[d]	2
HGNET_MN1[b]	1	GBM_MID[d]	2
MB_WNT[b]	1	EP_RELA	2
CNS ET, NOS[b]	1		
ATRT_SHH[c]	2		
ATRT_MYC[c]	1		
Total	37		19

Note:—CNS_NB_FOXR2 indicates CNS neuroblastoma with *FOXR2* activation; HGNET_MN1, CNS high-grade neuroepithelial tumor with *MN1* alteration; MB_WNT: medulloblastoma with *wingless* (*Wnt*) activation; ATRT_SHH, atypical teratoid/rhabdoid tumor with *sonic hedgehog* (*shh*) activation; ATRT_MYC, atypical teratoid/rhabdoid tumor, subclass MYC; GBM_G34, glioblastoma, Isocitrate dehydrogenase (*IDH*) wild-type, H3.3 G34 mutant; GBM_MYCN, glioblastoma, *IDH* wild-type, subclass MYCN; DMG_K27, diffuse midline glioma H3K27M mutant; GBM-MID, glioblastoma, *IDH* wild-type, subclass midline; EP-RELA, ependymoma with positive *RELA* fusion.

[a] For further analysis, the following have been combined into single groups:
[b] As ET, other.
[c] As ATRT.
[d] As HGG.

classified as biopsy (<10%), partial (10%–49%), subtotal (50%–95%), radical subtotal (>95%), and gross total (no visible tumor on imaging).

Outcome Analysis

"Event-free survival" was defined as the time interval from the date of study enrollment to the date of first event (disease progression or recurrence, second malignant neoplasm, or death from any cause) or to the date of last follow-up for patients without events.

Statistical Analysis

The exact Wilcoxon rank sum test was used to compare continuous variables among patient groups. The Fisher exact test and the exact χ^2 test were used to compare distributions of categoric variables. Outcome estimates were obtained using the method of Kaplan and Meier. The log-rank test was used to compare outcome distributions. Cox regression was used to examine tumor size as a continuous predictor of outcome. Two-sided P values are reported. Note that patient numbers were quite small in some patient groups. Data frozen as of December 31, 2016, were used for this analysis.

RESULTS

Between March 2007 and August 2014, eighty-five patients with institutionally diagnosed CNS-PNET/PBL were enrolled and randomized among the 4 trial regimens. Of these, 56 patients met the inclusion criteria for the current analysis, including availability of molecular classification by DNA methylation and complete imaging datasets.

Methylation profiling revealed a spectrum of molecular diagnoses broader than those found by histopathology (see Table 1 for further elaboration of these diagnoses) and included PBL ($n = 27$); HGG ($n = 17$, including 8 glioblastoma multiforme [GBM]_G34s, 5 GBM_MYCNs, 2 DMG_K27s, 2 GBM_MIDs); ATRT ($n = 3$, including 2 ATRT_SHHs, 1 ATRT_MYC); CNS neuroblastoma with *FOXR2* activation ($n = 3$); ependymoma with positive *RELA* fusion (EP-RELA, $n = 2$); medulloblastoma with *Wnt* activation (MB_WNT, $n = 1$); ETMR ($n = 1$); and high-grade neuroepithelial tumor with *MN1* alteration (HGNET-MN1, $n = 1$). One tumor could not be classified and was designated as embryonal tumor, NOS (ET NOS, $n = 1$). The molecularly diagnosed supratentorial embryonal tumors were grouped together with PBLs, and the combined group is referred to as PBL/ET hereafter ($n = 37$, including the following: 27 PBLs, 3 CNS neuroblastomas, 3 ATRTs, 1 MB, 1 ETMR, 1 HGNET, and 1 ET NOS) (Table 1). The rest of the subgroups, including HGG and EP, neither of which were intended for inclusion in the trial, were combined into 1 group, hereafter referred to as nonembryonal tumors (non-ET; $n = 19$, including: 17 HGGs and 2 EPs). Of note, ATRT, although an embryonal tumor, has historically been considered a unique subset with specific treatment algorithms and was also not intended for trial inclusion. However, keeping with the embryonal tumor definition, we included these under PBL/ET.

Table 2: Molecular diagnoses for tumors by pineal and nonpineal locations

	Pineal	Nonpineal
PBL	26	1
ET, other	0	7
ATRT	1	2
HGG	1	16
EP	0	2
Total	28	28

For the included 56 patients, the median age at diagnosis was 9 years (range, 3–18 years). The median age for patients with molecularly diagnosed PBL/ET was 8.6 years (range, 3–18 years), and that for patients with non-ET was 11.0 years (range, 3.8–16.1 years), with no significant difference ($P = .21$). There were 22 males (39%) and 34 females (61%) overall. In the PBL/ET group, there were 11 males (30%) and 26 females (70%), while in the non-ET group, there were 11 males (58%) and 8 females (42%). The median age at diagnosis for pineoblastomas in our study was 8.7 years (range, 3–18 years).

Overall, 28 tumors involved the pineal region and 28 were extrapineal (Table 2 and Fig 1). Among the extrapineal tumors, 64% (18/28) belonged to the non-ET group, compared with only 7% (2/28) of the pineal region tumors ($P < .001$). Twenty-four of the extrapineal tumors were centered in the parenchyma, and 4, within the ventricles. For the parenchymal tumors, frontal lobe involvement was most common (56%), followed by parietal lobe involvement (36%), with temporal and occipital lobe involvement being rare (7% each) (Fig 1).

Considering the locations of individual tumor categories, almost all (26 of 27) pineoblastomas were centered in the pineal cistern, with variable involvement of the third ventricle. In 1 patient, the tumor was centered more anteriorly in the third ventricle, without pineal cistern involvement. Five PBLs had tail-like extensions into the cerebral aqueduct, and PBLs rarely demonstrated parenchymal invasion. There were 3 ATRTs, of which 2 were centered in the cerebral hemispheres, and 1, in the pineal cistern. Of the remaining 7 embryonal tumors, 5 were centered in

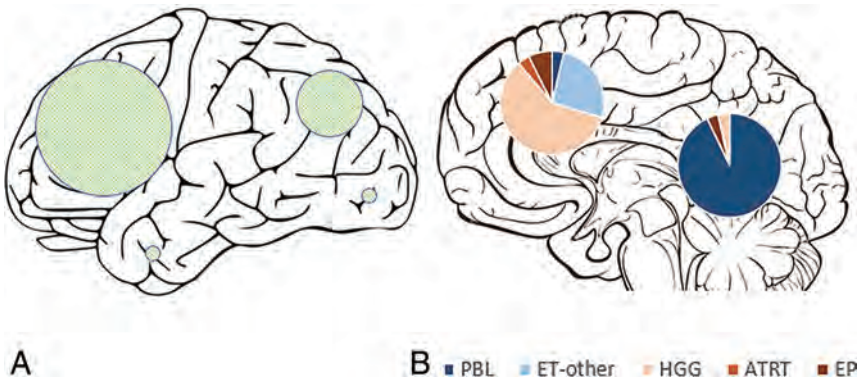

FIG 1. Schematic representation of the external surface of cerebral hemispheres (*A*) shows the locations of hemispheric tumors, with the sizes of the *shaded circles* proportional to the number of tumors in each lobe. A midline sagittal section of the brain (*B*) shows pineal and nonpineal tumors, with *pie diagrams* representing the subgroups.

Table 3: MR imaging features by tumor group (all patients $n = 56$)

	Group						
	PBL/ET		Non-ET			All Patients	
	No.	%	No.	%	*P* Value	No.	%
Size (cm)					<.001		
Median	3.6	–	6.2	–		4.3	–
Minimum	1.1	–	2.7	–		1.1	–
Maximum	9.1	–	9.3	–		9.3	–
% Enhancement					.17[a], .80[b]		
None	1	2.7	0	0		1	1.8
0–25	3	8.1	3	15.8		6	10.7
25–75	6	16.2	7	36.8		13	23.2
>75	27	73.0	9	47.4		36	64.3
Margins					<.001		
Well-defined	37	100.0	13	68.4		50	89.3
Ill-defined	0	0	6	31.6		6	10.7
Presence of edema					<.001[c]		
Absent	32	86.5	5	26.3		37	66.1
<2 cm from tumor margin	4	10.8	13	68.4		17	30.4
>2 cm from tumor margin	1	2.7	1	5.3		2	3.6
Presence of cyst/necrosis					.22		
Absent	12	32.4	3	15.8		15	26.8
Present	25	67.6	16	84.2		41	73.2
Presence of calcification or hemorrhage					.26		
Absent	16	43.2	5	26.3		21	37.5
Present	21	56.8	14	73.7		35	62.5
DWI					–		
Bright	28	75.7	15	78.9		43	76.8
Dark	1	2.7	0	0		1	1.8
Intermediate	5	13.5	3	15.8		8	14.3
Artifact or not available	3	8.1	1	5.3		4	7.1
Metastasis					–		
Intracranial	1	2.7	0	0		1	1.8
Spinal	5	13.5	0	0		5	8.9
Intracranial and spinal	6	16.2	0	0		6	10.7
None	25	67.6	19	100.0		44	78.6
All patients	37	100.0	19	100.0		56	100.0

Note:—– indicates no data available.
[a] Comparison of none versus 0%–25% versus 25%–75% versus >75%.
[b] Comparison of >75% versus ≤75%.
[c] Comparison of absent versus present.

the cerebral hemispheres and 2 were located within the lateral ventricles (Fig 1). The hemispheric embryonal tumors included 3 CNS_NBs, 1 HGNET_MN1, and 1 ET, NOS, while the 2 lateral ventricular embryonal tumors included 1 each of ETMR and MB_WNT subtypes.

In the HGG subgroup, 16 of 17 tumors primarily involved the cerebral hemispheres, and one was centered in the lateral ventricle. Both of the molecularly diagnosed EPs were centered in the cerebral hemispheres.

MR imaging features were compared between the 2 broad groups: PBL/ET and non-ET (Table 3). The median tumor size for the non-ET group was 6.2 cm (range, 2.7–9.3 cm), while that for PBL/ET group was 3.6 cm (range 1.1–9.1 cm), and the difference was statistically significant ($P < .001$). Thirty-two percent of tumors in the non-ET group (6/19) had ill-defined margins, compared with none in the PBL/ET group ($P < .001$). Of note, all 6 tumors with ill-defined margins were HGG. Perilesional edema was seen in 74% of the non-ET group (14/19) compared with 14% in the PBL/ET group (5/37), also statistically significant ($P < .001$). Enhancement was seen in nearly all tumors in both non-ET (19/19) and PBL/ET (36/37) groups, though 47% of tumors in the non-ET group had >75% enhancement, compared with 73% of tumors in the PBL/ET group ($P = .08$), suggesting a tendency for more homogeneous enhancement in PBL/ET. Most tumors in both groups demonstrated restricted diffusion, cysts/necrosis, and calcification/hemorrhage, with no significant differences for any of these parameters (Table 3).

None of the patients with non-ET had intracranial or intraspinal metastasis identified by MR imaging, while 32% of those with PBL/ET (12/37) had metastasis by MR imaging (1 intracranial, 5 intraspinal, and 6 both) (Table 3). One patient in each of the non-ET and PBL/ET groups had CSF cytology positive for malignant cells, but no detectable metastasis by MR imaging.

Table 4: MR imaging features by tumor group after excluding pineoblastomas ($n = 29$)

	Group						
	ET		Non-ET			All Patients	
	No.	%	No.	%	*P* Value	No.	%
Size (cm)					.95		
Median	5.7	–	6.2	–		6.1	–
Minimum	3.6	–	2.7	–		2.7	–
Maximum	9.1	–	9.3	–		9.3	–
% Enhancement					.68[a]		
None	0	0	0	0		0	0
0–25	2	20	3	15.8		5	17.2
25–75	5	50	7	36.8		12	41.4
>75	3	30	9	47.4		12	41.4
Margins					.068		
Well-defined	10	100.0	13	68.4		23	79.3
Ill-defined	0	0	6	31.6		6	20.7
Presence of edema					.24[b]		
Absent	5	50	5	26.3		10	34.5
<2 cm from tumor margin	4	40	13	68.4		17	58.6
>2 cm from tumor margin	1	10	1	5.3		2	6.9
Presence of cyst/necrosis					.53		
Absent	0	0	3	15.8		3	10.3
Present	10	100	16	84.2		26	89.7
Presence of calcification or hemorrhage					.11		
Absent	6	60	5	26.3		11	37.9
Present	4	40	14	73.7		18	62.1
DWI					–		
Bright	9	90	15	78.9		24	82.8
Dark	0	0	0	0		0	0
Intermediate	0	0	3	15.8		3	10.3
Artifact or not available	1	10	1	5.3		2	6.9
Metastasis							
Intracranial	0	0	0	0		0	0
Spinal	0	0	0	0		0	0
Intracranial and spinal	0	0	0	0		0	0
None	10	100	19	100.0		29	100
All patients	10	100.0	19	100.0		29	100.0

Note:— – indicates no data available.
[a] Comparison of none versus 0%–25% versus 25%–75% versus >75%.
[b] Comparison of absent versus present.

After excluding PBL, statistical asso-ciations were examined between the remaining ET ($n = 10$) and non-ET ($n = 19$) groups. The median age at diagnosis for this ET subgroup was slightly lower (8.4 years) compared with the non-ET group (11 years), though the difference was not statistically significant ($P = .10$). None of the studied MR imaging parameters showed any statistically significant differences, though we observed some trends (Table 4). Ill-defined margins were observed in 31.6% of the non-ET compared with none in the ET group. Calcification and hemorrhage were more commonly seen in the non-ET (73.7%) compared with ET (40%) group.

A univariable analysis of imaging parameters with event-free survival was performed (Fig 2). Larger tumor size and ill-defined margins were statistically significant predicators of worse outcomes ($P = .023$ and .006, respectively).

DISCUSSION

To our knowledge, this is the largest series describing the MR imaging findings of histologically diagnosed supratentorial PNET and PBL and the first to correlate MR imaging features with molecular diagnoses and patient outcomes.

The rapid advances in understanding of the genomic characteristics of tumor cells have led to reassessment of tumor classification and traditional risk factors.[19-21] In particular, both supra- and infratentorial embryonal tumors are moving from a traditional histology only–based ap-proach to molecular diagnoses for risk stratification and treatment planning.[7,16,22,23] In keeping with the new classification systems, there is a need to change the reference point of oncologic imaging from histopathology to molecularly integrated diagnoses.

The above numbers show that with histopathology only for diagnosis, 39% of all tumors (17 HGGs, 2 EPs, and 3 ATRTs of 56) and 71% of nonpineal tumors (16 HGGs, 2 EPs, 2 ATRTs of 28) in this study represented discrepant molecular diagnoses not intended for inclusion in this PNET trial. Our previously published results have shown markedly worse outcomes for these non-ETs[7] despite a much smaller incidence of CSF dissemination by imaging and CSF cytology (5% for non-ET versus 35% for PBL/ET).

Most pineal region tumors in our study were confirmed to be pineoblastomas (Figs 3 and 4). The pineal region ATRTs in our study could not be subjectively distinguished from PBL (Fig 3). Also, there was 1 HGG in the pineal region, which, interestingly, belonged to the methylation class of diffuse midline glioma H3K27M-mutant. Of the nonpineal tumors, which include both hemispheric and ventricular locations, only 43% belonged to the embryonal group, with the remainder being HGG and EP (Table 2), with substantial overlap in the imaging appearances (Figs 5 and 6).

The median age (9 years) in this study was higher than that previously reported for supratentorial PNETs (6.5 years).[4] The median age at diagnosis for pineoblastomas (8.7 years) in our study is also higher than that in a recent large series (5.5 years).[24]

With all locations included, the non-ETs were larger with more ill-defined margins and surrounding edema compared with the PBLs/ETs. This finding may be partly related to location, with pineal region tumors probably presenting earlier because of hydrocephalus, though tumor biology and rate of growth could be contributing factors. After we excluded pineoblastomas, none of the MR imaging parameters were statistically significant between the remaining ETs and non-ETs; however, the ETs had a

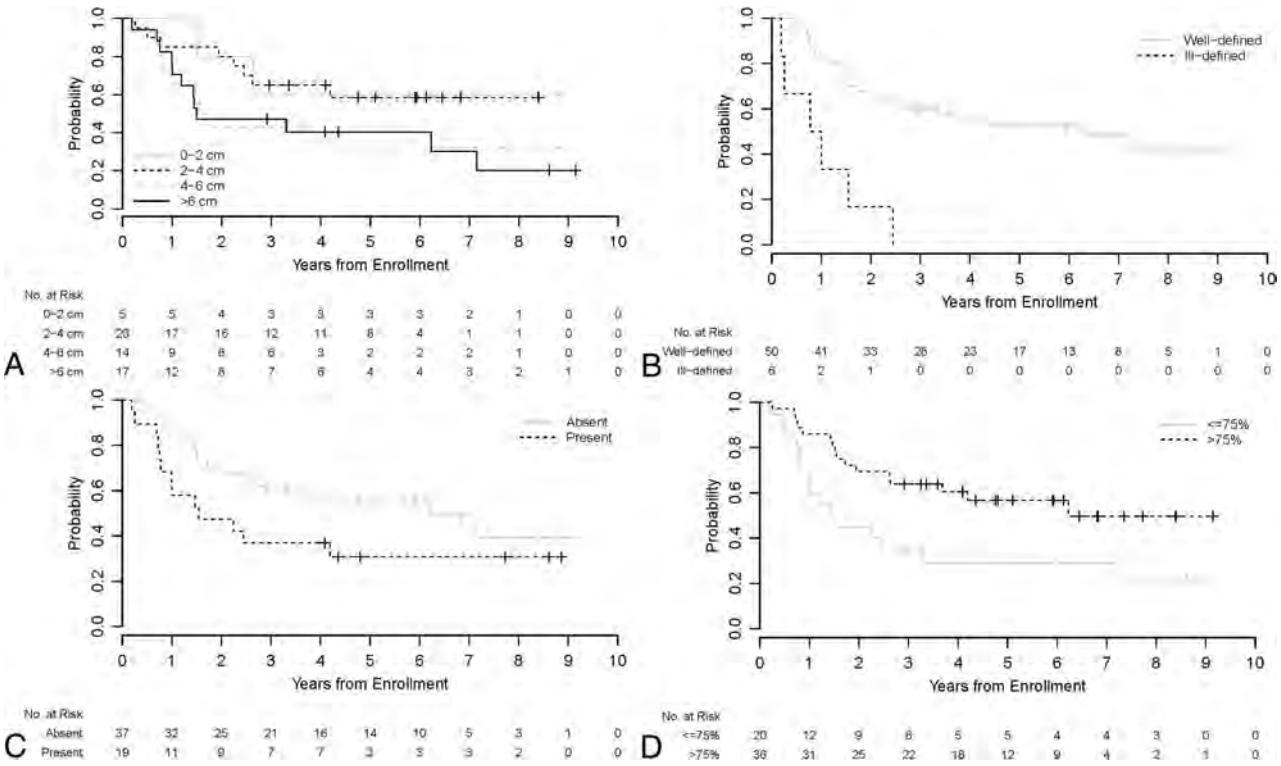

FIG 2. Kaplan-Meier curves show event-free survival distributions by tumor size (*A*), margins (*B*), presence of edema (*C*), and percentage enhancement (*D*) for all patients ($n = 56$).

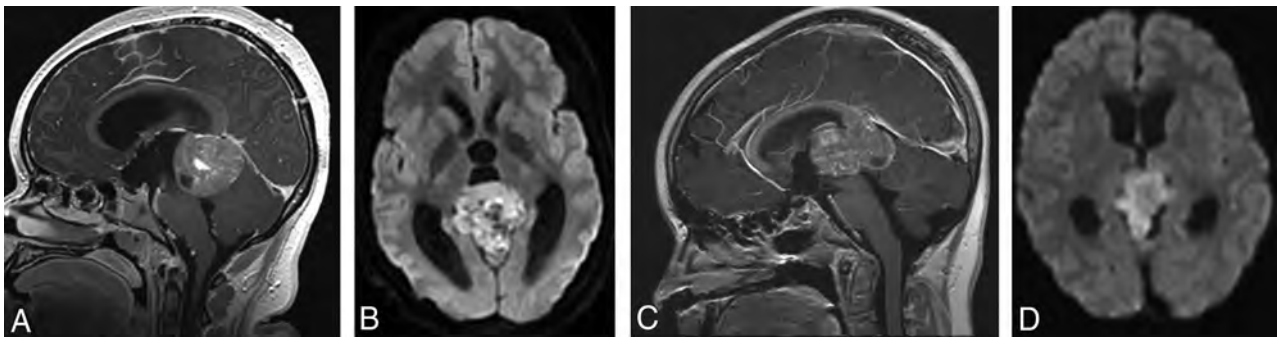

FIG 3. (*A* and *B*), A 15-year-old girl with a molecular diagnosis of pineoblastoma. Sagittal T1-weighted postcontrast (*A*) and axial diffusion-weighted (*B*) MR images demonstrate a mass centered in the pineal region with diffuse heterogeneous enhancement, small cystic foci, and diffusion restriction. (*C* and *D*), A 9-year-old girl with a molecular diagnosis of ATRT_MYC. Sagittal T1-weighted postcontrast (*C*) and axial diffusion-weighted (*D*) images demonstrate a similar mass centered in the pineal region with diffuse heterogeneous enhancement, small cystic foci, and diffusion restriction. Note the similarities in imaging appearance between the 2 examples.

tendency toward less heterogeneity and better-defined margins and occurred at a slightly younger age compared with non-ETs.

Because of the rarity of these tumors, there are only a few published reports on their imaging features.[25-28] The PBLs in our study demonstrated MR imaging features broadly similar to those in previous descriptions, including diffusion restriction, cystic/necrotic change, and variable enhancement. Parenchymal invasion, however, was rare in our study, which conflicts with one of the prior reports.[27] An "aqueductal tail" was seen in 19% of PBL (Figs 3 and 4). Other than a single case report on PBL,[29] this finding has not been mentioned in any of the previous descriptions of PBL or pineal region germ cell tumors. Although such a "plastic" tumor extension is well-described for infratentorial ependymomas,[30] neither of the 2 molecularly diagnosed EPs in our study were seen in the pineal region. This observation can be explored in future studies to potentially distinguish PBLs from other pineal region masses, an issue that has always been considered difficult by imaging.[31,32]

CNS-PNETs have typically been described on imaging as large, heterogeneous, diffusion-restricting hemispheric or ventricular masses in young children.[28] No studies have compared the imaging findings with other malignant supratentorial tumors like high-grade gliomas. A report from the German multicenter HIT trial compared the MR imaging findings of ependymoblastomas and ependymomas with CNS-PNET NOS. Although the authors found some differences by imaging, their overall conclusion was that precise distinction in individual cases may not be feasible.[33]

The study has several limitations that must be acknowledged. Methylation profiling was not available for all enrolled patients, and some additional patients were excluded because of inadequate imaging. The MR imaging techniques were not standardized, and quantitative assessments such as ADC measurements were not performed. The patients received different treatments based on the trial protocol, and that feature could potentially confound the correlation with outcomes, though there were no significant differences in the outcome among treatment groups in our primary analysis.[7] Radiologically, these supratentorial tumors can be viewed as 2 groups based on location, pineal and extrapineal; however, they were included together for analysis because of shared histopathology and their designation as a single entity by neuro-oncologists for treatment purposes. Because most of the pineal region tumors eventually were proved to be pineoblastomas and most of the nonpineal tumors were nonembryonal, including these together skewed the statistical results. We also did a separate statistical analysis of ET versus non-ET after excluding pineoblastomas, a distinction that is more of a diagnostic dilemma from a radiologic standpoint.

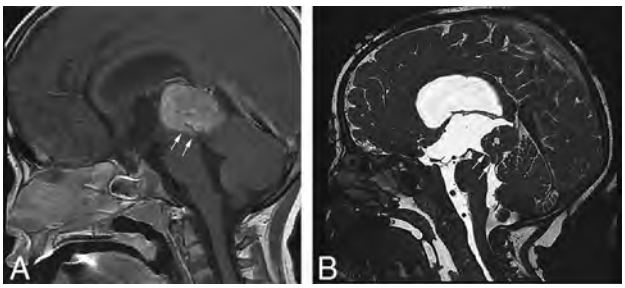

FIG 4. Sagittal T1-weighted postcontrast (*A*) and sagittal high-resolution balanced steady-state gradient-echo (*B*) images from 2 different patients with molecularly proved pineoblastomas demonstrating a tail-like aqueductal extension (*white arrows*).

CONCLUSIONS

We describe the imaging features of a large cohort of histologically diagnosed supratentorial PNETs, including pineoblastomas, in correlation with the molecular diagnoses and outcomes. Knowledge of current molecularly defined tumor entities and their relative frequencies and locations will help the radiologist make more accurate predictions of the tumor types. For

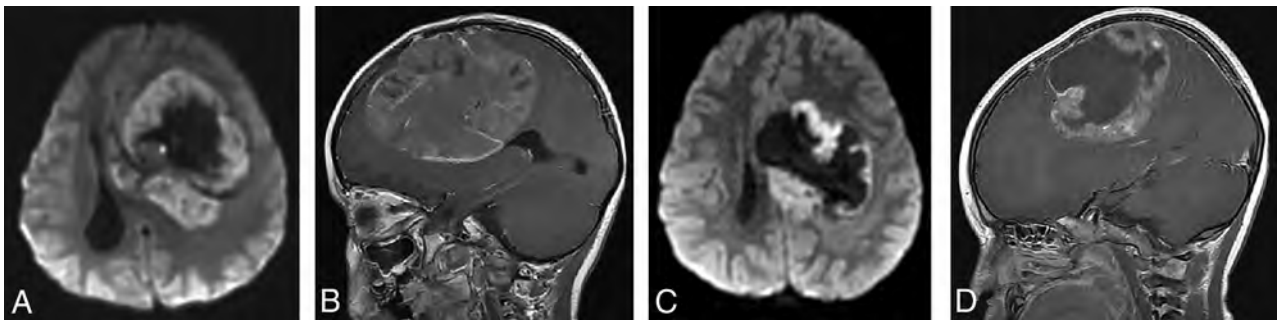

FIG 5. (*A* and *B*), A 4-year-old girl with a molecular diagnosis of high-grade glioma (GBM_MYCN). Axial DWI (*A*) and sagittal postcontrast T1-weighted (*B*) images demonstrate a large mass centered in the left frontal lobe with prominent necrotic/cystic areas centrally and diffusion restriction and moderate heterogeneous enhancement of the solid component. (*C* and *D*), A 4-year-old boy with a molecular diagnosis of ependymoma (EP_RELA). Axial DWI (*C*) and sagittal postcontrast T1-weighted (*D*) images demonstrate a large mass centered deep in the left hemisphere with prominent necrotic/cystic areas centrally and diffusion restriction and moderate heterogeneous enhancement of the solid component. Note the similarities in age and imaging appearance between these 2 patients with different molecular diagnoses.

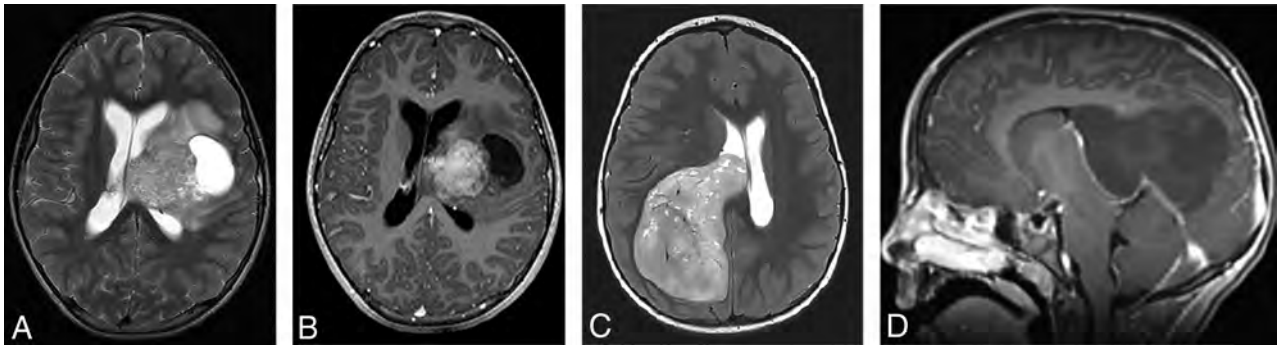

FIG 6. Two different patients with a molecular diagnosis of ET. (*A* and *B*), A 10-year-old girl with axial T2-weighted (*A*) and axial postcontrast T1-weighted (*B*) images has a large mass centered in the left deep nuclei with a prominent cystic component and moderate enhancement of the solid component. The tumor subclass was CNS_NB_FOXR2. Please note the similarities with high-grade glioma and ependymoma illustrated in Fig 5. (*C* and *D*), A 5-year-old girl with axial T2-weighted (*C*) and sagittal postcontrast T1-weighted (*D*) images has a large solid mass centered in the right lateral ventricle with minimal-to-no enhancement. The tumor subclass was ETMR. Of note, both of these tumors demonstrated diffusion restriction (not shown).

nonpineal tumors, a diagnosis of non-ET such as HGG or EP should be high on the list of a radiographic differential. Given the overlap of MR imaging findings, it may not be possible to offer a single diagnosis with certainty; thus, imaging does not substitute for obtaining molecular testing. However, a narrower differential diagnosis in conjunction with initial histopathology will be more helpful in guiding the surgery and radiation planning, and the criterion standard molecular testing should guide the eventual course of treatment. The current study provides a systematic description of conventional MR imaging findings in reference to the molecular diagnoses, and future studies in this direction using advanced imaging and radiomic techniques may be useful.

Disclosures: Alok Jaju—*RELATED*: *Grant:* Children's Oncology Group, *Comments*: National Institutes of Health (National Clinical Trials Network) grant U10 CA180886*; *Support for Travel to Meetings for the Study or Other Purposes*: Children's Oncology Group, *Comments*: National Institutes of Health (National Clinical Trials Network) grant U10 CA180886. David Capper—*UNRELATED*: *Patents (Planned, Pending or Issued)*: patent pending for a method to classify brain tumors by DNA methylation profiling. *Money paid to the institution.

REFERENCES

1. Rorke LB. **The cerebellar medulloblastoma and its relationship to primitive neuroectodermal tumors.** *J Neuropathol Exp Neurol* 1983; 42:1–15 CrossRef Medline
2. Rorke LB, Trojanowski JQ, Lee VMY, et al. **Primitive neuroectodermal tumors of the central nervous system.** *Brain Pathol* 1997;7:765–84 CrossRef Medline
3. Jakacki RI, Burger PC, Kocak M, et al. **Outcome and prognostic factors for children with supratentorial primitive neuroectodermal tumors treated with carboplatin during radiotherapy: a report from the Children's Oncology Group.** *Pediatr Blood Cancer* 2015; 62:776–83 CrossRef Medline
4. Pizer BL, Weston CL, Robinson KJ, et al. **Analysis of patients with supratentorial primitive neuro-ectodermal tumors entered into the SIOP/UKCCSG PNET 3 study.** *Eur J Cancer* 2006;42:1120–28 CrossRef Medline
5. Sturm D, Orr BA, Toprak UH, et al. **New brain tumor entities emerge from molecular classification of CNS-PNETs.** *Cell* 2016; 164:1060–72 CrossRef Medline
6. Schwalbe EC, Hayden JT, Rogers HA, et al. **Histologically defined central nervous system primitive neuro-ectodermal tumours (CNS-PNETs) display heterogeneous DNA methylation profiles and show relationships to other paediatric brain tumour types.** *Acta Neuropathol* 2013;126:943–46 CrossRef Medline
7. Hwang EI, Kool M, Burger PC, et al. **Extensive molecular and clinical heterogeneity in patients with histologically diagnosed CNS-PNET treated as a single entity: a report from the children's oncology group randomized ACNS0332 trial.** *J Clin Oncol* 2018;36:3388–95 CrossRef Medline
8. Louis DN, Perry A, Reifenberger G, et al. **The 2016 World Health Organization Classification of Tumors of the Central Nervous System: a summary.** *Acta Neuropathol* 2016;131:803–20 CrossRef Medline
9. Pajtler KW, Witt H, Sill M, et al. **Molecular classification of ependymal tumors across all CNS compartments, histopathological grades, and age groups.** *Cancer Cell* 2015;27:728–43 CrossRef Medline
10. Ramaswamy V, Remke M, Bouffet E, et al. **Risk stratification of childhood medulloblastoma in the molecular era: the current consensus.** *Acta Neuropathol* 2016;131:821–31 CrossRef Medline
11. Kuo MD, Yamamoto S. **Next generation radiologic-pathologic correlation in oncology: Rad-Path 2.0.** *AJR Am J Roentgenol* 2011; 197:990–97 CrossRef Medline
12. Kuo MD, Jamshidi N. **Behind the numbers: decoding molecular phenotypes with radiogenomics–guiding principles and technical considerations.** *Radiology* 2014;270:320–25 CrossRef Medline
13. Diehn M, Nardini C, Wang DS, et al. **Identification of noninvasive imaging surrogates for brain tumor gene-expression modules.** *Proc Natl Acad Sci U S A* 2008;105:5213–18 CrossRef Medline
14. Jamshidi N, Diehn M, Bredel M, et al. **Illuminating radiogenomic characteristics of glioblastoma multiforme through integration of MR imaging, messenger RNA expression, and DNA copy number variation.** *Radiology* 2014;270:1–2 CrossRef Medline
15. Perreault S, Ramaswamy V, Achrol AS, et al. **MRI surrogates for molecular subgroups of medulloblastoma.** *AJNR Am J Neuroradiol* 2014;35:1263–69 CrossRef Medline
16. Nowak J, Nemes K, Hohm A, et al. **Magnetic resonance imaging surrogates of molecular subgroups in atypical teratoid/rhabdoid tumor (ATRT).** *Neuro Oncol* 2018;20:1672–79 CrossRef Medline
17. Karlo CA, Di Paolo PL, Chaim J, et al. **Radiogenomics of clear cell renal cell carcinoma: associations between CT imaging features and mutations.** *Radiology* 2014;270:464–71 CrossRef Medline
18. Capper D, Jones DTW, Sill M, et al. **DNA methylation-based classification of central nervous system tumors.** *Nature* 2018;555:469–74 CrossRef Medline
19. Aryee MJ, Jaffe AE, Corrada-Bravo H, et al. **Minfi: a flexible and comprehensive bioconductor package for the analysis of Infinium DNA methylation microarrays.** *Bioinformatics* 2014;30:1363–69 CrossRef Medline
20. Gajjar A, Pfister SM, Taylor MD, et al. **Molecular insights into pediatric brain tumors have the potential to transform therapy.** *Clin Cancer Res* 2014;20:5630–40 CrossRef Medline
21. Zaky W. **Revisiting management of pediatric brain tumors with new molecular insights.** *Cell* 2016;164:844–46 CrossRef Medline
22. Leary SE, Olson JM. **The molecular classification of medulloblastoma: driving the next generation clinical trials.** *Curr Opin Pediatr* 2012;24:33–39 CrossRef Medline
23. Sin-Chan P, Li BK, Ho B, et al. **Molecular classification and management of rare pediatric embryonal brain tumors.** *Curr Oncol Rep* 2018;20:69 CrossRef Medline
24. Parikh KA, Venable GT, Orr BA, et al. **Pineoblastoma-the experience at St. Jude Children's Research Hospital.** *Neurosurgery* 2017; 81:120–28 CrossRef Medline
25. Chawla A, Emmanuel JV, Seow WT, et al. **Paediatric PNET: pre-surgical MRI features.** *Clin Radiol* 2007;62:43–52 CrossRef Medline
26. Klisch J, Husstedt H, Hennings S, et al. **Supratentorial primitive neuroectodermal tumours: diffusion-weighted MRI.** *Neuroradiology* 2000;42:393–98 CrossRef Medline
27. Nakamura M, Saeki N, Iwadate Y, et al. **Neuroradiological characteristics of pineocytoma and pineoblastoma.** *Neuroradiology* 2000; 42:509–14 CrossRef Medline
28. Dai AI, Backstrom JW, Burger PC, et al. **Supratentorial primitive neuroectodermal tumors of infancy: clinical and radiologic findings.** *Pediatr Neurol* 2003;29:430–34 CrossRef Medline
29. Fujita A, Asada M, Saitoh M, et al. **Pineoblastoma showing unusual ventricular extension in a young adult: case report.** *Neurol Med Chir(Tokyo)* 1999;39:612–16 CrossRef Medline
30. Yuh EL, Barkovich AJ, Gupta N. **Imaging of ependymomas: MRI and CT.** *Childs Nerv Syst* 2009;25:1203–13 CrossRef Medline
31. Dumrongpisutikul N, Intrapiromkul J, Yousem DM. **Distinguishing between germinomas and pineal cell tumors on MR imaging.** *AJNR Am J Neuroradiol* 2012;33:550–55 CrossRef Medline
32. Kakigi T, Okada T, Kanagaki M, et al. **Quantitative imaging values of CT, MR, and FDG-PET to differentiate pineal parenchymal tumors and germinomas: are they useful?.** *Neuroradiology* 2014; 56:297–303 CrossRef Medline
33. Nowak J, Seidel C, Pietsch T, et al. **Systematic comparison of MRI findings in pediatric ependymoblastoma with ependymoma and CNS primitive neuroectodermal tumor not otherwise specified.** *Neuro Oncol* 2015;17:1157–65 CrossRef Medline

Diffusion Characteristics of Pediatric Diffuse Midline Gliomas with Histone H3-K27M Mutation Using Apparent Diffusion Coefficient Histogram Analysis

M.S. Aboian, E. Tong, D.A. Solomon, C. Kline, A. Gautam, A. Vardapetyan, B. Tamrazi, Y. Li, C.D. Jordan, E. Felton, B. Weinberg, S. Braunstein, S. Mueller, and S. Cha

ABSTRACT

BACKGROUND AND PURPOSE: Diffuse midline gliomas with histone H3 K27M mutation are biologically aggressive tumors with poor prognosis defined as a new diagnostic entity in the 2016 World Health Organization Classification of Tumors of the Central Nervous System. There are no qualitative imaging differences (enhancement, border, or central necrosis) between histone H3 wild-type and H3 K27M-mutant diffuse midline gliomas. Herein, we evaluated the utility of diffusion-weighted imaging to distinguish H3 K27M-mutant from histone H3 wildtype diffuse midline gliomas.

MATERIALS AND METHODS: We identified 31 pediatric patients (younger than 21 years of age) with diffuse gliomas centered in midline structures that had undergone assessment for histone H3 K27M mutation. We measured ADC within these tumors using a voxel-based 3D whole-tumor measurement method.

RESULTS: Our cohort included 18 infratentorial and 13 supratentorial diffuse gliomas centered in midline structures. Twenty-three (74%) tumors carried H3-K27M mutations. There was no difference in ADC histogram parameters (mean, median, minimum, maximum, percentiles) between mutant and wild-type tumors. Subgroup analysis based on tumor location also did not identify a difference in histogram descriptive statistics. Patients who survived <1 year after diagnosis had lower median ADC (1.10×10^{-3} mm^2/s; 95% CI, 0.90–1.30) compared with patients who survived >1 year (1.46×10^{-3} mm^2/s; 95% CI, 1.19–1.67; $P < .06$). Average ADC values for diffuse midline gliomas were 1.28×10^{-3} mm^2/s (95% CI, 1.21–1.34) and 0.86×10^{-3} mm^2/s (95% CI, 0.69–1.01) for hemispheric glioblastomas with $P < .05$.

CONCLUSIONS: Although no statistically significant difference in diffusion characteristics was found between H3-K27M mutant and H3 wildtype diffuse midline gliomas, lower diffusivity corresponds to a lower survival rate at 1 year after diagnosis. These findings can have an impact on the anticipated clinical course for this patient population and offer providers and families guidance on clinical outcomes.

Diffuse midline glioma with histone H3-K27M mutation is a new class of gliomas that was defined by the 2016 World Health Organization Classification.[1,2] These tumors arise within the midline of the CNS, most commonly within the pons, thalamus, or spinal cord. Patients with histone H3-K27M mutant gliomas have worse survival compared with those with-wild type tumors,[3,4] but there are no currently known imaging markers that can distinguish tumors with histone H3-K27M mutations from wild-type tumors.[5] Tumor size, infiltrative appearance on

Received August 11, 2017; accepted after revision August 31, 2019.

From the Department of Radiology and Biomedical Imaging (M.S.A.), Yale School of Medicine, New Haven, Connecticut; Department of Radiology (E.T.), Stanford University, Stanford, California; Division of Neuropathology (D.A.S.), Department of Pathology, Departments of Radiology (Y.L., C.D.J., S.C.), Radiation Oncology (S.B.), Neurological Surgery (S.M.), and Neurology (S.M.), and Division of Pediatric Hematology/Oncology (C.K., E.F., S.M.), Department of Pediatrics, University of California, San Francisco, California; Johns Hopkins University (A.G.), Baltimore, Maryland; University of California Berkeley (A.V.), Berkeley, California; Department of Radiology (B.T.), Children's Hospital Los Angeles, Los Angeles, California; and Department of Neuroradiology (B.W.), Emory University, Atlanta, Georgia.

Mariam Aboian was funded by American Society of Neuroradiology Fellow Award 2018 and the National Institutes of Health T32 Grant 5T32EB001631-12. Elizabeth Tong was funded by National Institutes of Health T32 Grant 5T32EB001631-12. David A. Solomon is funded by the NIH Director's Early Independence Award from the National Institutes of Health, Office of the Director (DP5 OD021403). Cassie Kline was funded by National Institutes of Health National Center for Advancing Translational Sciences University of California, San Francisco–Clinical and Translational Science Grant KL2TR000143.

Paper previously presented as a podium presentation at: Annual Meeting of the American Society of Neuroradiology, April 22–27, 2017; Long Beach, California. We also presented it in abstract format at: Annual Meeting of the Society of NeuroOncology, November 16–19, 2017; San Francisco, California. American College of Radiology/Association of University Radiologists, Research Scholar Award, May 8-11, 2017; Hollywood, Florida.

Please address correspondence to Mariam Aboian, MD, PhD, Department of Radiology and Biomedical Imaging, Yale University School of Medicine, 789 Howard Avenue (CB30), PO Box 208042, New Haven, CT 06520; e-mail: mariam.aboian@yale.edu

Indicates open access to non-subscribers at www.ajnr.org
Indicates article with supplemental on-line tables.
http://dx.doi.org/10.3174/ajnr.A6302

FLAIR imaging, mass effect, enhancement characteristics, presence of necrosis, and pattern of disease recurrence have previously been shown to be no different between wild-type and histone H3-K27M mutant tumors.[5]

ADC histogram analysis is a technique that has been used to distinguish different pediatric tumor types, including histologically distinct posterior fossa tumors.[6,7] In pediatric diffuse intrinsic pontine gliomas, ADC histogram analysis identified lower ADC values correlated with worse patient outcomes.[6,7] In adult patients, ADC histogram analysis has been used to predict tumor response to antiangiogenic therapy.[8-10]

In the current study, we completed ADC histogram analysis using a cohort of patients with diffuse midline gliomas located within the pons, cerebellopontine angle/fourth ventricle, and thalamus who have been tested for the histone H3-K27M mutation via immunohistochemistry. We aimed to identify differences in imaging diffusion characteristics that can discriminate between wild-type diffuse midline gliomas and those carrying histone H3-K27M mutations.

MATERIALS AND METHODS

We completed retrospective chart review to identify a cohort of pediatric patients (younger than 21 years of age) with diffuse midline gliomas who were tested for histone H3-K27M mutation based on University of California San Francisco institutional tumor board review. This study was reviewed and approved by University of California San Francisco Institutional Review Board. Inclusion criteria required for consideration of statistical analysis were the following: 1) the presence of a diffuse midline glioma, 2) available pathologic testing for the presence of histone H3-K27M mutation, and 3) completion of prebiopsy MR imaging with DWI sequences of sufficient quality to perform independent ADC map calculation.

Independent ADC maps were generated for all patients with DWI sequences using Osirix/Horos software (https://horosproject.org) and an ADC plugin (http://web.stanford.edu/~bah/software/ADCmap/versions.html).

Histologic Review

Tumor tissue was fixed in formalin and embedded in paraffin for analysis by our institution's neuropathologists. The University of California, San Francisco Neuropathology BTRC Biomarkers Laboratory performed immunohistochemistry for the presence of histone H3-K27M mutant tails with the ABE419 antibody (EMB Milipore, Billerica, Massachusetts), as previously described.[2]

Imaging Protocol

MR imaging of the brain was performed on either 1.5T or 3T clinical scanners. Axial DWI sequences were generated at b-values of 0 and 1000 s/mm^2 at TR/TE = 7000/60 ms, 5-mm, gap = zero, 3–6 orthogonal diffusion gradient directions. ADC maps were generated independently using the Osirix/Horos ADC plugin. Tumor segmentation was performed manually by a neuroradiology fellow (M.S.A.) and generated 3D ROIs using FLAIR images. The ROI was coregistered with ADC maps, and borders were checked side by side with FLAIR images to ensure correct coregistration. Voxel-based ADC values were extracted, and a range of ADC values was generated for each patient.

Patient demographics

	All Patients (n = 31)	Histone H3-K27M (n = 23)	Histone H3 Wild-Type (n = 8)
Male	22	14	8
Age (mean) (range) (yr)	9.8 (0.45–21.7)	8.9 (0.45–19.3)	12.5 (0.68–21.7)
Tumor location			
Pons/vermis/ 4th ventricle	21	17	4
Thalamus	7	5	2
Tectum	2	0	2
Subcallosal	1	1	0

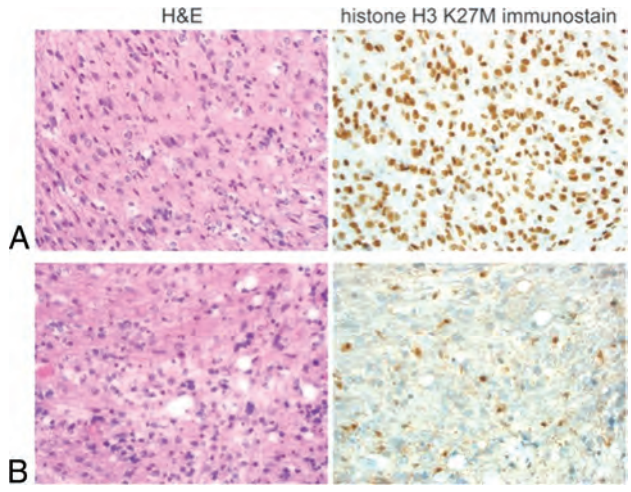

FIG 1. Histology of H3-K27M and wild-type diffuse midline gliomas. Hematoxylin and eosin (H&E) and antihistone H3-K27M immunohistochemistry of diffuse intrinsic pontine gliomas with H3-K27M mutation (*A*) and histone H3 wildtype (*B*). 400x magnification.

Data Analysis

Histogram descriptive statistics were calculated using STATA SE, 14.1 2016 (StataCorp, College Station, Texas) and included mean, median, minimum, maximum, and percentiles (5th to 95th in increments of 5, 1st percentile, and 99th percentile). Comparative analysis of histogram descriptive statistics between histone H3-K27M mutant and wild-type diffuse midline gliomas was performed using standardized Student t tests. Kaplan-Meier survival analysis was completed in patient subgroups on the basis of the presence of the histone H3-K27M mutation and an ADC below 1.1 $\times$ 10^{-3}mm^2/s.

RESULTS

Forty-four pediatric patients with diffuse gliomas were initially identified on retrospective chart review (Table). Thirty-one patients had diffuse midline gliomas and met all inclusion criteria necessary for analysis. Twenty-one patients (68%) had infratentorial tumors located within the pons, vermis, or fourth ventricle. Independent testing for the presence of the histone H3-K27M mutant protein by immunohistochemistry within these tumors was available in all patients. Twenty-three patients (73%) carried

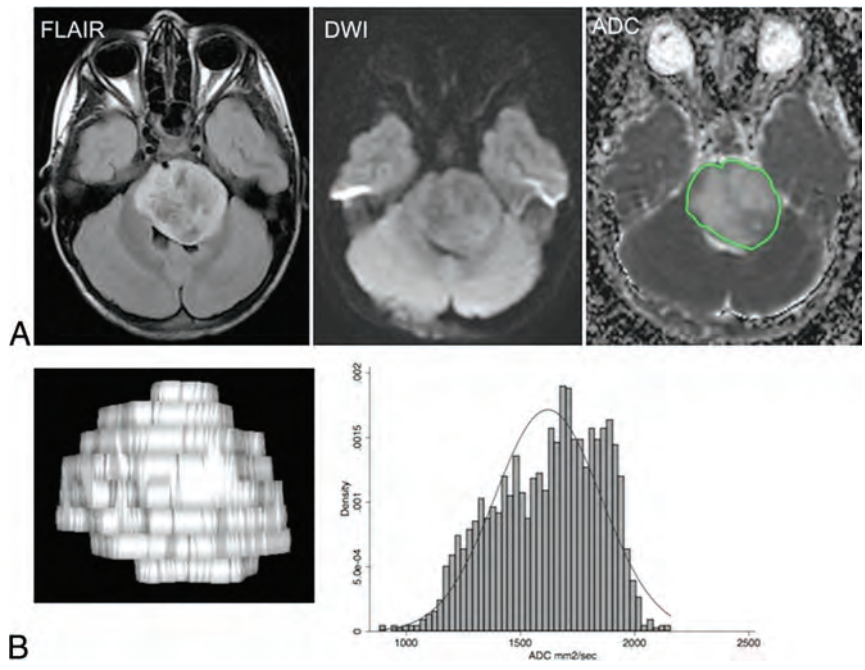

FIG 2. Diffusion characteristics of diffuse midline gliomas based on the presence of the H3-K27M mutation. Tumor 3D volume segmented from the FLAIR image (*A*) was coregistered onto the ADC map. Voxel-based histogram of tumor (*B*). Normal distribution curves are superimposed on the ADC histograms.

histone H3-K27M mutations. Tumors carrying histone H3-K27M mutations showed positive nuclear staining with the anti-H3-K27M antibody (Fig 1).

Tumor segmentation was performed, and an ROI was manually drawn (Fig 2). Distribution of ADC values per voxel within the segmented tumor was displayed as a histogram (Fig 2*B*) and descriptive statistics, including percentile values, variance, skewness, and kurtosis. There were no statistically significant differences in ADC mean, median, minimum, and percentile values between histone H3-K27M mutant and wild-type tumors (Fig 3 and On-line Table 1). There were also no statistically significant differences in variance, skewness, or kurtosis of the histograms between H3-K27M mutant and wild type tumors (Fig 4). Representative images of patients with positive and negative skewness and high and low kurtosis are demonstrated in Fig 4*B*.

ADC histogram characteristics of diffuse midline gliomas were compared with 5 hemispheric glioblastomas that were present within our cohort, which were all histone H3 wild-type. The midline gliomas had higher mean and median ADC values compared with hemispheric glioblastomas ($P < .05$; Fig 5). The ADC mean for diffuse midline gliomas was 1.28×10^{-3}mm^2/s (95% CI, 1.21–1.34) and 0.86×10^{-3}mm^2/s (95% CI, 0.69–1.01) for hemispheric glioblastomas ($P < .05$).

Clinical outcomes at 12 months after diagnostic biopsy were available in 19 patients. Thirteen patients were alive at 12 months after biopsy. Among patients with histone H3-K27M mutant tumors ($n = 15$), nine were alive at 12 months after diagnostic biopsy. Among patients with wild-type diffuse midline gliomas ($n = 6$), five had follow-up with only 2 patients alive at 12 months after biopsy.

Kaplan-Meier curves demonstrated that survival was worse in patients with histone H3-K27M mutated tumors (Fig 6*A*). Statistically significant higher mean and median ADC values were found in patients who survived longer than 12 months compared with those who died within 12 months of biopsy (On-line Table 2). Kaplan-Meier survival comparison of patients segregated on the basis of the ADC cutoff value of 1.1×10^{-3}mm^2/s demonstrated that patients with lower ADC values had worse survival. The ADC cutoff was determined using receiver operating characteristic curve analysis for prediction of survival after 12 months, which identified a cutoff of 1.18×10^{-3} mm^2/s. There were 8 patients with ADC values below 1.1×10^{-3} mm^2/s, 5 of whom had a mutation for histone H3-K27M and 3 of whom had wild-type tumors. There were 23 patients with elevated ADC values, with 18 patients having the histone H3-K27M mutation and 5 having wild-type tumors. For evaluating mutations beyond histone H3-K27M, gene panel testing of 500 cancer genes was available in only 1 patient from the decreased diffusivity group (ADC $< 1.1 \times 10^{-3}$mm^2/s), which revealed somatic mutations in histone H3-K27M, *PIK3CA*, and *PPM1D* genes, and gain of chromosome 1q. On the other hand, 2 of the patients with elevated ADC were tested with the cancer gene panel demonstrating mutations in *TP53*, *BCORL1*, *PDGFRA*, *PIK3CA*, and *ASXL1*, with both of the tumors carrying the *TP53* mutation.

DISCUSSION

Pediatric diffuse midline gliomas tend to be refractory to treatment and carry some of the poorest prognoses of all pediatric cancers. Yet, even within this group, there is some variability in outcome. Diffuse midline gliomas carrying histone H3-K27M mutations appear to represent the worst prognosis. It is challenging to identify these tumors on the basis of imaging, and to date, no reliable imaging characteristics have been found to delineate histone H3-K27M mutant gliomas from wild-type diffuse midline gliomas.[5] We previously described the qualitative characteristics of these diffuse midline gliomas with the histone H3-K27M mutation, including patterns of enhancement, necrosis, and infiltrative appearance. Unfortunately, none of these qualitative characteristics could distinguish the K27M mutant tumors from wild-type tumors. In the current article, we evaluated the diffusion characteristics of diffuse midline gliomas based on clinical DWI imaging and ADC histogram analysis.

In our study, ADC histogram analysis of diffuse midline gliomas did not demonstrate statistically significant differences in mean, median, minimum, maximum, and percentile ADC values between histone H3-K27M mutant and wild-type tumors, nor

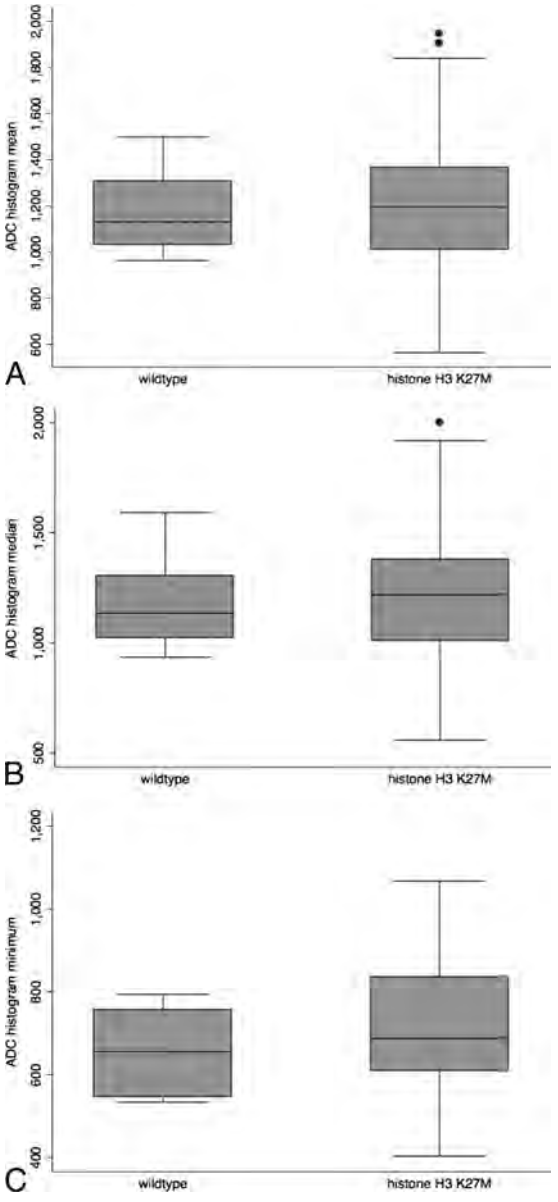

FIG 3. Voxel-based 3D whole-tumor ADC boxplots comparing histone H3-K27M and wild-type tumors without a difference in ADC_{mean} (*A*), ADC_{median} (*B*), and ADC_{min} ($10^{-6}mm^2/s$) (*C*).

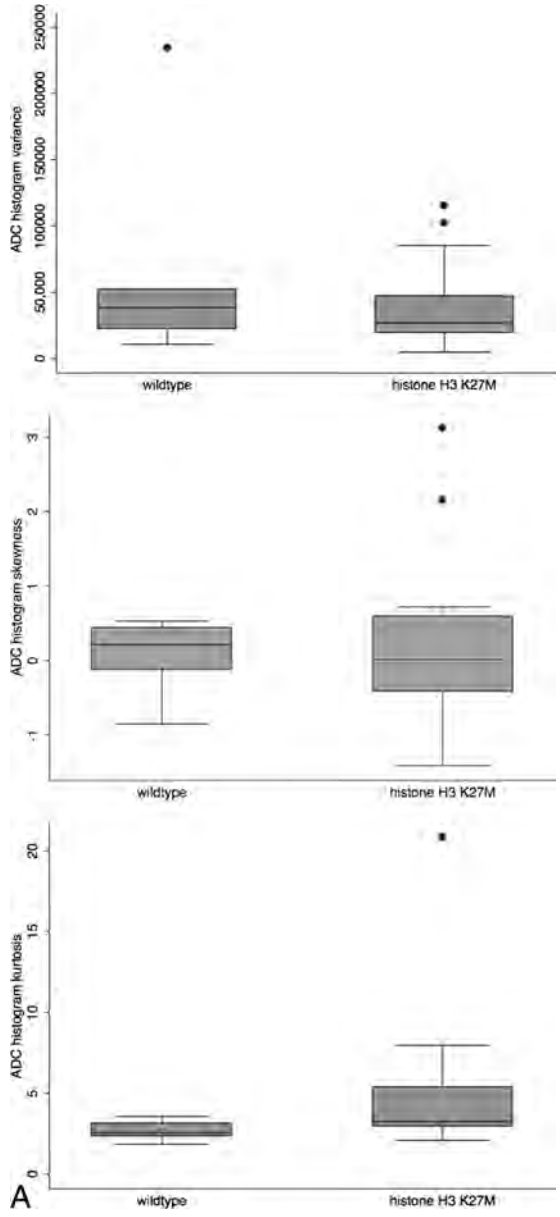

FIG 4. ADC histogram descriptive statistics of diffuse midline gliomas. No difference in skewness, kurtosis, and variance between wild-type and histone H3-K27M mutant tumors (*A*). Examples of histogram parameters of ADC ($10^{-6}mm^2/s$) (*B*). Normal distribution curves are superimposed on the ADC histograms. (*Continued on next page*)

did it demonstrate differences in variance, kurtosis, or skewness of the comparison histograms. These findings suggest that diffuse midline gliomas are architecturally very similar, despite molecular differences in the presence or absence of histone H3-K27M mutations. Given that tumors with histone H3-K27M mutations are known to carry worse outcomes than wild-type tumors,[4,11] we remain hopeful that there may be more advanced imaging markers that can help delineate these tumors on imaging such as advanced imaging postprocessing and metabolic imaging with MR spectroscopy.

Our study did reveal that pediatric diffuse midline gliomas have overall ADC values with a mean of $1.4 \times 10^{-3}mm^2/s$. This was statistically significantly higher than infiltrative glioblastomas located within the cerebral hemisphere, suggesting a different cellular architecture within these tumors. We anticipate that the infiltrative cellular organization in midline gliomas leads to increased diffusivity, while tight cellular architecture within hemispheric glioblastomas results in reduced diffusivity on DWI sequences. Further studies with larger patient numbers need to be performed.

One notable finding that our study demonstrated was that patients with lower ADC values had lower survival rates at 12 months than patients with ADC values higher than 1.1. This finding agrees with a previous report showing that lower ADC values in a group of diffuse intrinsic pontine glioma tumors correlated with worse patient outcomes.[12] The combination of these findings suggests that a lower ADC within diffuse midline gliomas is an independent imaging marker of

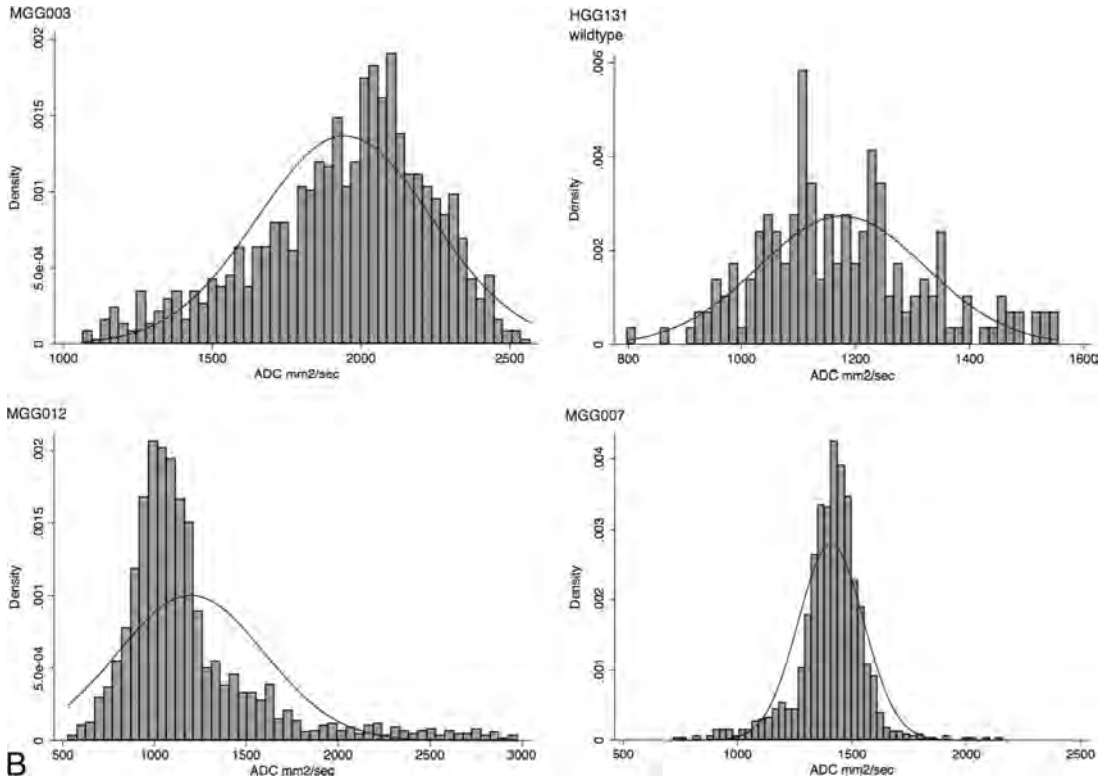

FIG 4. Continued.

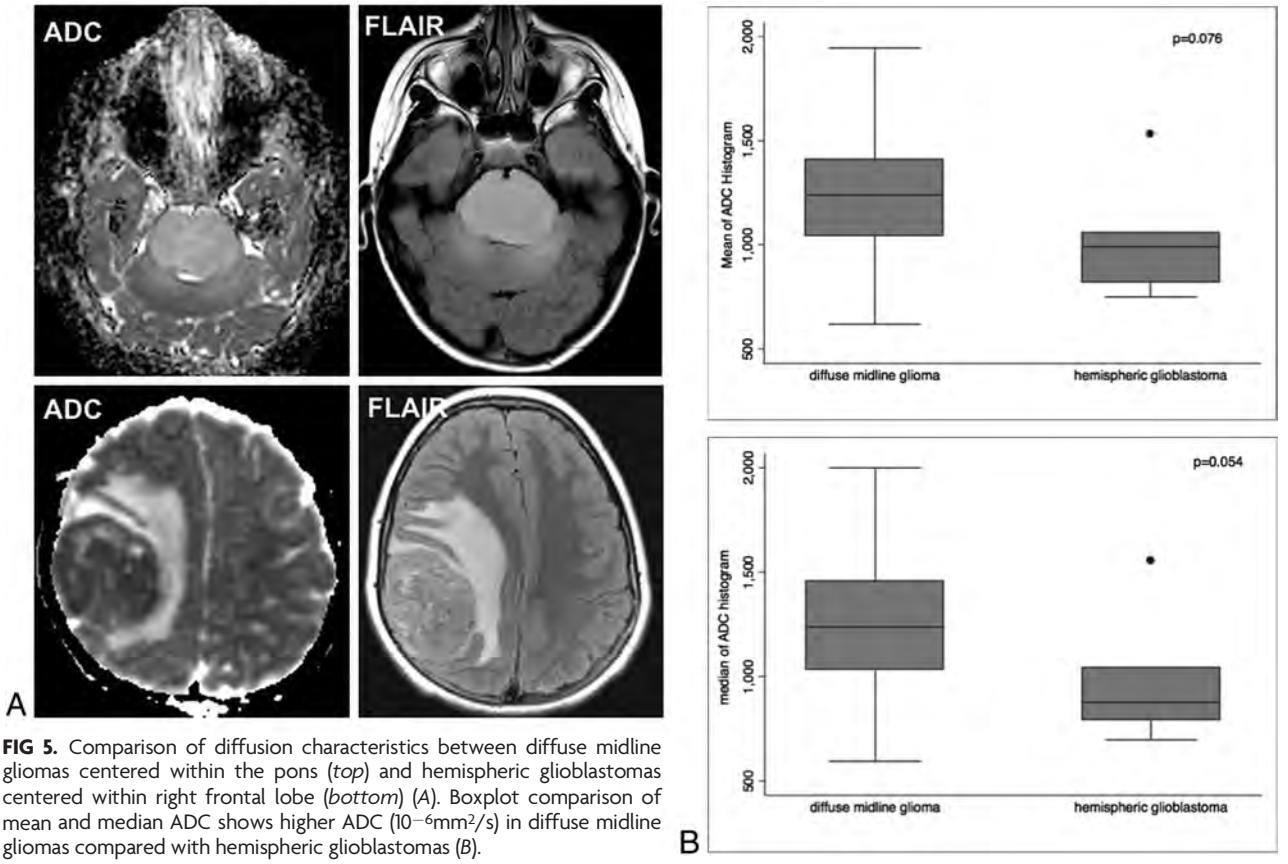

FIG 5. Comparison of diffusion characteristics between diffuse midline gliomas centered within the pons (*top*) and hemispheric glioblastomas centered within right frontal lobe (*bottom*) (*A*). Boxplot comparison of mean and median ADC shows higher ADC (10^{-6}mm^2/s) in diffuse midline gliomas compared with hemispheric glioblastomas (*B*).

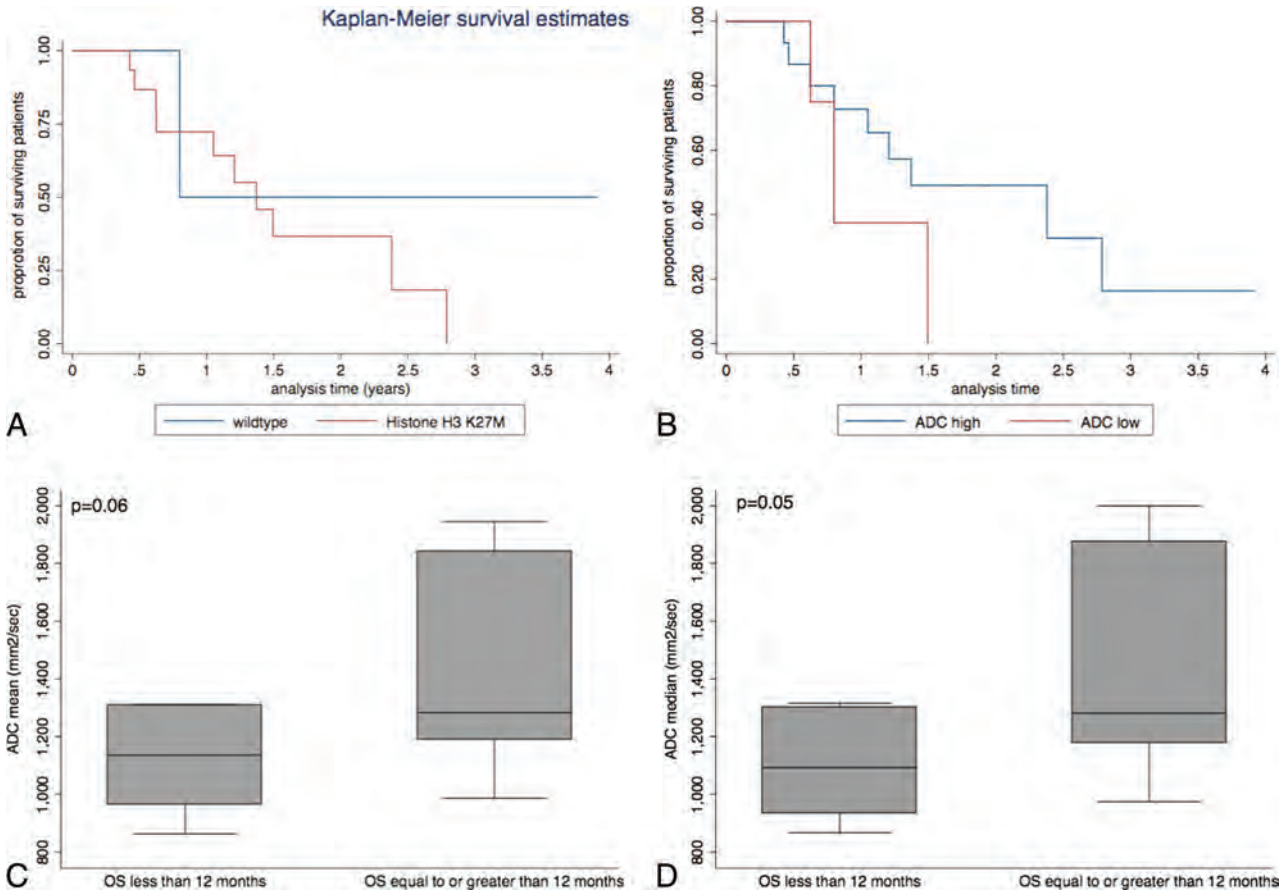

FIG 6. Kaplan-Meier survival curve based on histone H3-K27M mutation status (*A*) and ADC (10^{-6}mm^2/s) being below the 1.1 × 10^{-3}mm^2/s cut-off (*B*). Boxplots of ADC mean and median comparing patients with overall survival <12 months and ≥12 months (*C* and *D*).

worse outcomes, perhaps even independent of the H3-K27M mutation. This also suggests the need for differentiation of histone H3.1 and H3.3 K27M mutations in clinical samples because standard of care clinical evaluation of these tumors involves immunohistochemistry staining with an antibody that detects both H3.1 and H3.3 histone subtypes. Prior studies demonstrated that patients with histone H3.3 K27M mutant tumors had worse overall survival compared with those with H3.1 tumors; thus, it is important to evaluate the diffusivity in patients having histone H3.3 and H3.1 mutations.[3] In our study, we had a small subset of patients who had the 500 Cancer Gene Panel Test with 1 patient tested in the low-ADC group and 2 patients tested in the high-ADC group. Both patients in the high-ADC group had mutations in the *TP52* gene, while the patient in the low-ADC group had mutations previously described in diffuse midline gliomas, *PIK3CA* and *PPM1D*.[13] Further detailed genetic analysis of these subgroups based on tumor diffusion characteristics may identify the genes that influence patient outcomes and may identify new therapeutic targets.

CONCLUSIONS

Although no statistically significant difference in diffusion characteristics is found between histone H3-K27M mutant and wild-type midline tumors, lower diffusivity corresponds to a lower survival rate at 1 year after diagnosis. These findings can have an impact on the anticipated clinical course for this patient population and offer providers and families guidance on clinical outcomes.

Disclosures: Cassie Kline—*UNRELATED*: *Grant*: Cannonball Kids' Cancer Foundation, Frank A. Campini Foundation, University of California, San Francisco School of Medicine Dean's Diversity Award. Elizabeth Tong—*RELATED*: *Grant*: National Institutes of Health T32 Grant. Caroline Jordan—*RELATED: Grant*: National Institutes of Health. Steve Braunstein—*UNRELATED*: *Employment*: University of California, San Francisco, *Comments*: Faculty Radiation Oncologist. Sabine Mueller—*RELATED*: *Grant*: Clinical and Translational Science KL2 Award, *Comments*: The National Center for Advancing Translational Sciences, National Institutes of Health, through the University of California, San Francisco–Clinical and Translational Science Institute Grant No. KL2TR000143.

REFERENCES

1. Hoshide R, Jandial R. **2016 World Health Organization Classification of Central Nervous System Tumors: an era of molecular biology.** *World Neurosurg* 2016;94:561–62 CrossRef Medline
2. Solomon DA, Wood MD, Tihan T, et al. **Diffuse midline gliomas with H3-K27M mutation: a series of 47 cases assessing the spectrum of morphologic variation and associated genetic alterations.** *Brain Pathol* 2016;26:569–80 CrossRef Medline
3. Castel D, Philippe C, Calmon R, et al. **Histone H3F3A and HIST1H3B K27M mutations define two subgroups of diffuse intrinsic pontine gliomas with different prognosis and phenotypes.** *Acta Neuropathol* 2015;130:815–27 CrossRef Medline
4. Korshunov A, Ryzhova M, Hovestadt V, et al. **Integrated analysis of pediatric glioblastoma reveals a subset of biologically favorable**

tumors with associated molecular prognostic markers. *Acta Neuropathol* 2015;129:669–78 CrossRef Medline
5. Aboian MS, Solomon DA, Felton E, et al. **Imaging characteristics of pediatric diffuse midline gliomas with histone mutation.** *AJNR Am J Neuroradiol* 2017;38:795–800 CrossRef Medline
6. Rodriguez Gutierrez D, Awwad A, Meijer L, et al. **Metrics and textural features of MRI diffusion to improve classification of pediatric posterior fossa tumors.** *AJNR Am J Neuroradiol* 2014;35:1009–15 CrossRef Medline
7. Bull JG, Saunders DE, Clark CA, et al. **Discrimination of paediatric brain tumours using apparent diffusion coefficient histograms.** *Eur Radiol* 2012;22:447–57 CrossRef Medline
8. Nowosielski M, Recheis W, Goebel G, et al. **ADC histograms predict response to anti-angiogenic therapy in patients with recurrent high-grade glioma.** *Neuroradiology* 2011;53:291–302 CrossRef Medline
9. Pope WB, Lai A, Mehta R, et al. **Apparent diffusion coefficient histogram analysis stratifies progression-free survival in newly diagnosed bevacizumab-treated glioblastoma.** *AJNR Am J Neuroradiol* 2011;32:882–89 CrossRef Medline
10. Pope WB, Kim HJ, Huo J, et al. **Recurrent glioblastoma multiforme: ADC histogram analysis predicts response to bevacizumab treatment.** *Radiology* 2009;252:182–89 CrossRef Medline
11. Sturm D, Witt H, Hovestadt V, et al. **Hotspot mutations in H3F3A and IDH1 define distinct epigenetic and biological subgroups of glioblastoma.** *Cancer Cell* 2012;22:425–37 CrossRef Medline
12. Poussaint TY, Vajapeyam S, Ricci KI, et al. **Apparent diffusion coefficient histogram metrics correlate with survival in diffuse intrinsic pontine glioma: a report from the Pediatric Brain Tumor Consortium.** *Neuro Oncol* 2016;18:725–34 CrossRef Medline
13. Nikbakht H, Panditharatna E, Mikael LG, et al. **Spatial and temporal homogeneity of driver mutations in diffuse intrinsic pontine glioma.** *Nat Commun* 2016;7:11185 CrossRef Medline

Imaging Characteristics of Wingless Pathway Subgroup Medulloblastomas: Results from the German HIT/SIOP-Trial Cohort

A. Stock, M. Mynarek, T. Pietsch, S.M. Pfister, S.C. Clifford, T. Goschzik, D. Sturm, E.C. Schwalbe, D. Hicks, S. Rutkowski, B. Bison, M. Pham, and M. Warmuth-Metz

ABSTRACT

BACKGROUND AND PURPOSE: In addition to the 4 histopathologically defined entities of medulloblastoma, 4 distinct genetically defined subgroups have been included in the World Health Organization classification of 2016. The smallest subgroup is the medulloblastoma with activated wingless pathway. The goal of this study was to identify a typical MR imaging morphology in a larger number of pediatric patients with wingless pathway medulloblastoma.

MATERIALS AND METHODS: From January 2001 to October 2017, of 75 patients with histologically confirmed and molecularly subgrouped wingless pathway medulloblastomas recruited to the German Pediatric Brain Tumor (HIT) trials, 38 patients (median age, 12.8 ± 4.6 years at diagnosis; 24 [63.2%] female) had preoperative imaging that passed the entry criteria for this study. Images were rated by the local standardized imaging criteria of the National Reference Center of Neuroradiology. Additionally, a modified laterality score was used to determine tumor localization and extension.

RESULTS: Twenty-eight of 38 (73.7%) were primary midline tumors but with a lateral tendency in 39.3%. One extensively eccentric midline tumor was rated by the laterality score as in an off-midline position. Five tumors were found in the cerebellopontine angle; 3, in the deep white matter; and 2, in a cerebellar hemisphere. Leptomeningeal dissemination was rare (11.5%). In 60.5%, intratumoral blood-degradation products were found, and 26.3% showed cysts with blood contents.

CONCLUSIONS: According to our observations, wingless pathway medulloblastomas are not preferentially off-midline tumors as postulated in previous studies with smaller wingless pathway medulloblastoma cohorts. Dense intratumoral blood-degradation products and cysts with blood contents are frequently found and might help to differentiate wingless pathway medulloblastoma from other medulloblastoma subtypes.

ABBREVIATIONS: CMB = classic medulloblastoma; CPA = cerebellopontine angle; HIT = German abbreviation for brain tumor; LCMB = large-cell medulloblastoma (according to the World Health Organization classification of 2007); LS = laterality score; MB = medulloblastoma; SHH = sonic hedgehog pathway; WHO = World Health Organization; WNT = wingless-activated; WNT-MB = WNT-activated medulloblastoma

According to the revised *WHO Classification of Tumors of the Central Nervous System* of 2016,[1] medulloblastoma (MB) is not considered a single tumor entity but represents several entities with different cells of origin, location, biology, genetic or (epi-)genetic alterations, histology, and clinical behavior. According to the concept of an integrated diagnosis in the World Health Organization (WHO) classification of 2016, medulloblastoma (MB) entities are defined by both histologic and molecular/genetic features, allowing a precise assignment of patients for risk-adapted stratification in current therapeutic studies and the comparison with results of study cohorts in the past. All MB entities correspond to WHO grade IV. For a definition of the histologic diagnosis, the tumors should be assigned to 1 of the 4 entities: classic (CMB), desmoplastic nodular, extensive

Received May 14, 2019; accepted after revision September 3.

From the Department of Neuroradiology (A.S., B.B., M.P., M.W.-M.), University Hospital Wuerzburg, Wuerzburg, Germany; Department of Pediatric Hematology and Oncology (M.M., S.R.), University Medical Center Hamburg-Eppendorf, Hamburg, Germany; Institute of Neuropathology (T.P., T.G.), DGNN Brain Tumor Reference Center, University of Bonn Medical Center, Bonn, Germany; Department of Pediatric Hematology and Oncology (S.M.P.), Heidelberg University Hospital, Heidelberg, Germany; Division of Pediatric Neurooncology (S.M.P.), German Cancer Consortium, German Cancer Research Center, Heidelberg, Germany; Hopp Children's Cancer Heidelberg (S.M.P., D.S.), Heidelberg, Germany; Wolfson Childhood Cancer Research Centre (S.C.C., E.C.S., D.H.), Northern Institute for Cancer Research, Newcastle University, Newcastle upon Tyne, UK; and Department of Applied Sciences (E.C.S.), Northumbria University, Newcastle upon Tyne, UK.

This study was supported by grants from the German Children's Cancer Foundation and Cancer Research UK.

Paper previously presented, in part, as a scientific abstract at: Annual Meeting of the German Society of Neuroradiology, October 10, 2018; Frankfurt, Germany.

Please address correspondence to Annika Stock, MD, Department of Neuroradiology, University Hospital Wuerzburg, Josef-Schneider-Str 11, D-97080 Wuerzburg, Germany; e-mail: stock_a@ukw.de

http://dx.doi.org/10.3174/ajnr.A6286

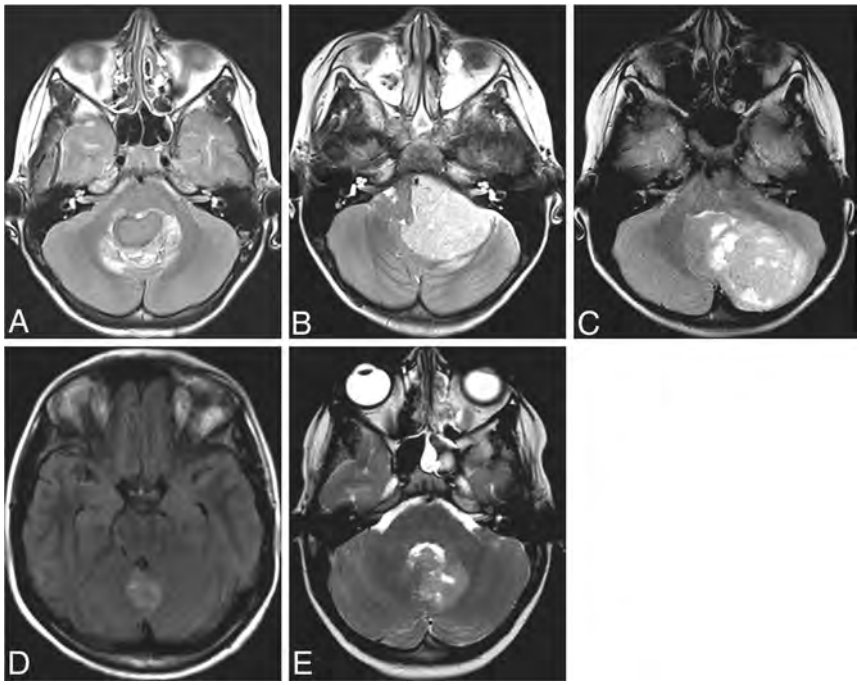

FIG 1. *A–C*, and *E*, T2WI. *D*, T2-FLAIR. Examples for primary tumor positions in WNT-MB. The midline fourth ventricle (*A*), cerebellopontine angle (*B*), cerebellar hemisphere (*C*), midline cerebellar vermis (*D*), and periventricular deep white matter (*E*).

nodularity, or large cell/anaplastic MB. Large-cell MB (LCMB) and anaplastic MB were separate histologic entities before 2016.[2] In addition to these histologic entities, 4 genetically defined subgroups have been introduced by the WHO classification of 2016.[1] Two subgroups are defined by their genetic pathway, wingless-activated (WNT) and sonic hedgehog–activated (SHH) MB, the latter with or without an accompanying *TP53* mutation. The non-WNT/non-SHH subgroup is provisionally subclassified into group 3 and 4 medulloblastomas, which seem to be overlapping variants. WNT-MBs are characterized by activating mutations of *CTNNB1*,[3,4] which encodes a central component of the WNT pathway or, alternatively, by inactivating mutations of *APC*,[3,5] *AXIN1*[6,7] or *AXIN2*,[8] leading to nuclear accumulation of β-catenin. Accounting for approximately 10%[9,10] of all MBs, WNT-MBs form a small-but-distinct MB entity. In children, they show a significantly better progression-free survival and overall survival compared with other subgroups.[4,9–11] In patients with WNT-MB younger than 16 years of age at diagnosis, a progression-free survival of 100% for 5 years has been observed.[11]

Current therapy studies, such as the SIOP-PNET5 (NCT02066220) medulloblastoma trial, have implemented upfront genetic evaluations so that patients with low-risk WNT-MBs are eligible for radiation therapy reduction aimed at reducing late effects, with the therapy increasingly being adapted to the specific risk profile of each patient. Additionally, radiologic imaging signatures have become apparent for certain brain tumors and their underlying genetic profiles. The term "radiomics" is increasingly applied to describe the association between imaging phenotype and tumor genotype. A priori knowledge of the radiologic imaging phenotype can become clinically meaningful, for example, when it offers the neurosurgeons and neuro-oncologists a better preoperative estimation of the prognosis and risk of relapse of the tumor. Based on the principle of radiomics, our aim was to evaluate specific imaging characteristics of WNT-MB. Due to the large number of participating study sites, automated techniques of radiomics image analyses including algorithms of machine learning, were not included in this study.

Besides standard imaging characteristics, radiologic studies have mainly focused on correlations of tumor position and genetic information. A first radiologic subgroup analysis showed a preferential tumor location for WNT-MB in the cerebellopontine angle (CPA) and for sonic hedgehog–activated medulloblastoma (SHH-MB) in the cerebellar hemisphere.[12] More recent studies with sample sizes of WNT-MB of $n = 15$,[13] $n = 16$,[14] and $n = 17$[15] yielded heterogeneous results with regard to tumor localization. The goal of the present study was to analyze structural MR imaging features according to defined MR imaging criteria in a large number of genetically determined WNT-MBs ($n = 38$) in children within the framework of the German Pediatric Brain Tumor (HIT) trials and the National Reference Center for Neuroradiology.

MATERIAL AND METHODS

Study Cohort

Cases were retrospectively collected from the data base of the National Reference Center for Neuroradiology (Department for Neuroradiology, Wuerzburg University Hospital) for the German Brain Tumor (HIT) trials, conducted in German-speaking countries of Europe. All patients were registered to the HIT-2000 trial (January 2001 to December 2011 [NCT00303810]), including participants of the German PNET 4 cohort from January 2001 to December 2007 [NCT01351870]), the HIT-2000 interim registry (recruiting January 2012 to December 2014 [NCT02238899]), the I-HIT-MED registry (recruiting since January 2015 [NCT02417324]), or the SIOP-PNET 5 MB trial (recruiting since June 2014 [NCT02066220]). Each patient or legal guardian signed an informed consent declaration when entering the study allowing the scientific evaluation of biologic and imaging data. All cases were centrally reviewed at the National Brain Tumor Reference Center of the German Society of Neuropathology and Neuroanatomy, Institute of Neuropathology, Bonn University. Patients were eligible if they had histopathologic and genetic classification data and preoperative cranial and spinal imaging

Table 1: Overview of absolute and relative (%) frequencies of MR imaging features

	Available Data	No.	%
Sex	38		
Male		14	36.8
Female		24	63.2
Histology	38		
CMB		36	94.7
AMB[a]		1	2.6
LCMB[a]		1	2.6
Hydrocephalus	38		
No		15	39.5
Slight		6	15.8
Moderate		15	39.5
Severe		2	5.3
Enhancement	38		
No		0	0
Light		4	10.5
Moderate		12	31.6
Strong		22	57.9
Enhancing area	38		
0%–25%		0	0
26%–50%		1	2.6
51%–75%		1	2.6
76%–100%		36	94.7
T2-weighted images	37		
Homogeneous		6	16.2
Inhomogeneous		31	83.8
Hyperintense		4	10.8
Isointense		20	54.1
Hypointense		13	35.1
T1-weighted images	36		
Homogeneous		15	41.7
Inhomogeneous		21	58.3
Hyperintense		1	2.8
Isointense		8	22.2
Hypointense		27	75
Cysts	38		
No		20	52.6
As bright as the CSF		3	7.9
Brighter than the CSF		5	13.2
Blood-fluid level		10	26.3
Blood-degradation products on T1WI, T2WI or T2*/SWI	38		
Yes		23	60.5
No		15	39.5
Mass of iron contents on T2*/SWI	18		
No		2	11.1
<50%		11	61.1
>50%		5	27.8
Dissemination	35		
No		31	88.6
M2		1	2.9
M3		1	2.9
M2 + 3		2	5.7

Note:—AMB indicates anaplastic medulloblastoma according to the WHO classification of 2007.

[a] According to the WHO classification of 2007.

data. Images on x-ray films and examinations with strong movement artifacts were excluded.

Molecular Analysis

Histological diagnosis was made at inclusion into the trial according to the WHO classification valid at the time. Patients were diagnosed by a combination of histologic examination by immunohistochemistry and Sanger sequencing of exon 3 of *CTNNB1*.[16,17] In case of negative *CTNNB1* mutation, *APC, AXIN1,* and *AXIN2* sequences were assessed additionally.[11] Neuropathologic evaluation and *CTNNB1* mutation analysis were supplemented by 450k DNA methylation microarray (Illumina, San Diego, California) if applicable.[18,19] Where tissue was too scarce for analysis by methylation microarray, subgroup was assigned using the mass spectrometry–minimal methylation classifier assay in addition to immunohistochemistry and *CTNNB1* mutation analysis.[11,20] Where the initial work-up did not include prospective assessment of WNT activation, this was done during retrospective work-up as previously described.[11,18] Patients were considered to have WNT-MB if molecular analysis confirmed a mutation in *CTNNB1* or *APC* and/or assignment to the WNT-subgroup by methylation profiling or mass spectrometry–minimal methylation classifier.

Imaging Analysis

All MR imaging datasets were assessed in consensus by 2 neuroradiologists dedicated to pediatric brain tumor imaging (M.W.-M. and A.S.).

Multicenter data acquisition resulted in nonuniform MR imaging protocols, sequence technique, parameters, and field strength. Inclusion was possible with T2WI or T2-FLAIR and contrast-enhanced T1WI. The primary tumor location was determined as: cerebellar hemisphere, deep white matter, CPA, cerebellar vermis, or fourth ventricle (Fig 1). Deep white matter, cerebellar hemisphere, and CPA were rated as primary lateral positions. When the CPA was involved, the status of the fourth ventricle and the foramen of magendie was recorded additionally. Fourth ventricle and cerebellar vermis were defined as primary midline positions. Additionally, laterality of primary midline tumors was assessed according to a modification of the laterality score (LS) by Patay et al.[14] Primary positions in the fourth ventricle or the cerebellar vermis were rated as midline (LS-0). Fourth ventricle or cerebellar vermis plus bilateral recess extension was rated as LS-0 as well. Midline tumors were rated as moderately lateralized in case of tumor extension into only the unilateral recess or bilateral recesses plus 1 CPA (LS-1). Extension into only the unilateral recess and further into the ipsilateral CPA was rated as heavily lateralized and off-midline (L-2).

Local standardized diagnostic parameters were supplemented and used for the imaging assessment. The tumor volume is calculated using the approximation of the ellipsoid volume formula $A \times B \times C$ ½, where A, B, and C are the maximum dimensions in the standard anterior-posterior, craniocaudal, and transverse planes. The largest diameter of the perifocal edema was measured in centimeters. Signal intensity and homogeneity of the tumor were assessed in comparison with gray matter on T2WI and T1WI without contrast enhancement. Intensity and percentage of enhancing volume after gadolinium application were estimated. The contrast-enhancing area of the tumor mass is mainly diffuse, whereas the rating was subjective in approximate percentages (0%–25%, 26%–50%, 51%–75%, 76%–100%).

Hydrocephalus was rated as slight, moderate, and severe (slight meaning only visible dilation of the ventricles, moderate showing CSF pressure caps, and severe showing pressure caps

Table 2: Overview of the tumor proposed epicenter and direction of extension

Primary Location (No. of WNT-MBs)	Extension		Further Extension		LS
Fourth ventricle (25) (66%)	Unilateral recess	$n = 7$	Plus uni CPA	$n = 1$	2
			No	$n = 6$	1
	Bilateral recesses	$n = 16$	Plus uni CPA	$n = 4$	1
			Plus bi CPA	$n = 0$	0
			No	$n = 12$	0
	No extension	$n = 2$			0
Cerebellar vermis (3) (8%)	Unilateral recess	$n = 1$			1
	Bilateral recesses	$n = 1$			0
	Fourth ventricle only	$n = 1$			0
	No extension	$n = 0$			0
CPA (5) (13%)	Unilateral recess	$n = 4$	Plus fourth ventricle	$n = 4$	2
	Bilateral recesses	$n = 0$			2
	No extension	$n = 1$			2
Deep WM (3) (8%)	Unilateral recess	$n = 1$	Plus uni CPA	$n = 1$	2
	Bilateral recesses	$n = 0$			2
	Fourth ventricle only	$n = 1$			2
	No extension	$n = 1$			
Cerebellar hemisphere (2) (5%)	Unilateral recess	$n = 2$	Plus uni CPA	$n = 1$	2
	Bilateral recesses	$n = 0$			2
	Fourth ventricle only	$n = 0$			2
	No extension	$n = 0$			2

Note:—uni indicates unilateral; bi, bilateral.

with compression of the sulci at the vertex). Fluid of intratumoral cysts was compared with the signal of CSF and defined as: as bright as CSF and brighter than CSF, presence of blood-degradation products like methemoglobin or hemosiderin was noted. Leptomeningeal dissemination was assessed only by MR imaging according to the classification of Chang et al.[21] Cranial dissemination was rated as M2; spinal dissemination, as M3; and cranial-plus-spinal dissemination, as M2 + 3. In addition to these standard diagnostic parameters, we rated the presence of blood-degradation products like methemoglobin and hemosiderin within the solid tumor mass as: no blood-degradation products, blood-degradation products in <50% of the tumor volume, and blood-degradation products in >50% of the tumor mass.

RESULTS

From January 2001 to October 2017, WNT activation was confirmed in 75 patients with MB. Preoperative cranial MR imaging and pre- or postoperative spinal MR imaging that passed entry criteria for this study were available in 38 patients with WNT-MB. In this MR imaging cohort, age ranged from 5 to 21.6 years (median, 12.8 ± 4.6 years) and a female predominance (1.71:1, female/male ratio) was found. According to traditional histopathologic criteria, most WNT-MB cases of this cohort were CMB (36/38; 94.7%) and further 2 large-cell/anaplastic MB (1 anaplastic MB and 1 LCMB diagnosed before 2016 [2.6% each] according to the WHO classification of 2007). Thirty-four tumors were diagnosed by a combination of immunohistochemistry and Sanger sequencing of exon 3 of *CTNNB1,* each with a detectable mutation of *CTNNB1.* In 15 of these patients, 450k methylation microarray was supplemented and classified all tumors as WNT. There were 2 cases without Sanger sequencing: One was categorized as WNT-activated by mass spectrometry–minimal methylation classifier assay and the other one by 450k methylation microarray. In 1 tumor, analysis was negative for the *CTNNB1* mutation but was classified as a WNT subgroup by 450k methylation microarray analysis, and additionally, a copy-neutral loss of heterozygosity within the chromosome arm 5q (*APC)* and a R213* mutation in the *APC* gene were identified. One patient was diagnosed as having WNT-MB based on tissue of tumor recurrence; here, *CTNNB1* mutation and WNT-activation in 450k methylation microarray were detectable.

An overview of the MR imaging features is shown in Table 1, and primary tumor localization and extension are presented in Table 2. Twenty-eight tumors were primarily located in the midline position. Fourteen of 25 (56%) WNT-MBs in the fourth ventricle and 2 of 3 in the cerebellar vermis were midline tumors without lateral tendency (LS-0). Eleven of 28 (39.3%) WNT-MBs showed extension into 1 recess only or into both recesses with further extension into only 1 CPA (LS-1). Only 1 WNT-MB located in the fourth ventricle extended into a unilateral recess and further into the ipsilateral CPA (LS-2). In summary, 74% of all WNT-MBs showed primarily a midline position, but only 42% represented "pure" midline tumors, with nearly half of the midline tumors showing a lateral tendency (39.3%). Only 1 (3.6%) primarily midline-located WNT-MB was rated as off-midline according to our LS score because of its strong eccentric position. Five of 38 (13%) WNT-MBs were positioned in the cerebellopontine angle; 2 of 38 (5%), in the cerebellar hemisphere; and 3 of 38 (8%), in the deep white matter. These positions were rated as off-midline. One CPA tumor showed some extension into the fourth ventricle. In both cerebellar hemisphere tumors, the ipsilateral recess was involved. One tumor with its epicenter in the deep white matter expanded into the fourth ventricle; and one, into the ipsilateral recess. In all deep white matter and cerebellar hemisphere tumors, WNT activation was confirmed by 450k DNA methylation microarray and a *CTNNB1* mutation was found as well.

Most WNT-MBs were moderately (39.5%) to very sharply (42.1%) delineated. Eighteen of 38 (47.4%) WNT-MBs contained cysts. In 10 of 18 (55.6%) partly cystic tumors, the cysts contained blood-degradation products, visible as blood-fluid levels (Fig 2). The cyst contents were brighter than CSF in 27.8% and similar to CSF in 16.7%. Twenty-three patients had hydrocephalus. Six (15.8%) patients showed slight, and 15 (39.5%) patients, moderate hydrocephalus; only 2 patients (5.3%) had severe

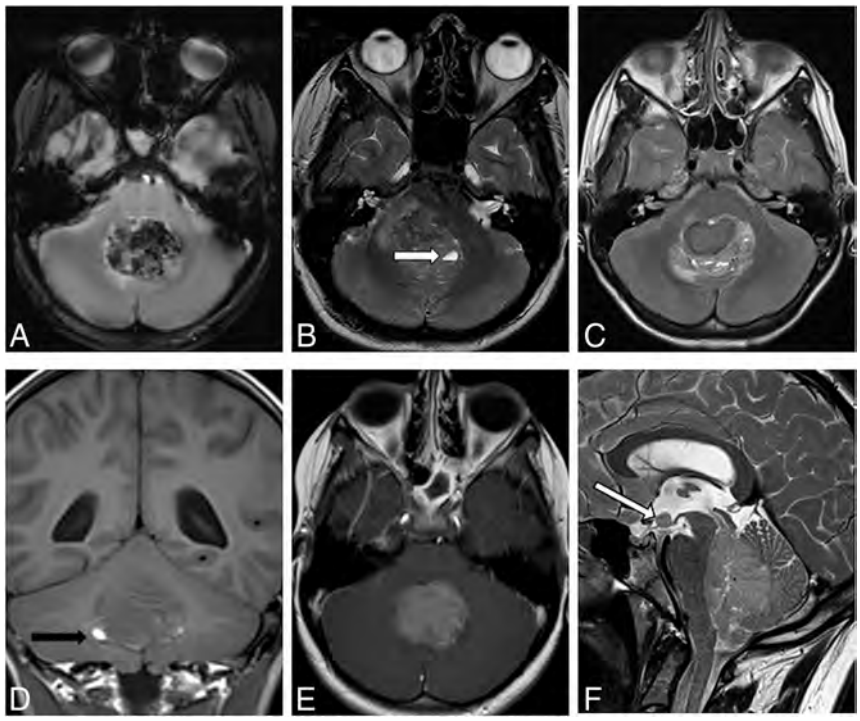

FIG 2. *A*, Deoxygenated blood in T2*WI. *B*, Intratumoral cyst with a blood-fluid level in T2WI (→). *C*, Inhomogeneous signal in T2WI. *D*, Hypointense signal in T1WI and small areas of methemoglobin (eg, →). *E*, One hundred percent contrast enhancement in T1WI. *F*, Leptomeningeal dissemination in T2WI, M2 on the floor of the third ventricle (→).

hydrocephalus. Fifteen (39.5%) patients had no hydrocephalus at diagnosis. Tumor signal intensity in T2WI compared with the supratentorial cortex was predominantly isointense (54.1%) to hypointense (35.1%). Only 4 tumors (10.8%) were hyperintense in comparison with the signal intensity of the cortex on T2WI. In 1 child, no standard T2 sequence but a FLAIR sequence was available for evaluation. Thirty-one (83.8%) tumors showed inhomogeneous signal on T2WI; only 6 of 37 (16.2%) showed homogeneous signal. On T1WI, the signal intensity was hypointense in 27 of 38 (75%) tumors. Eight (22.2%) tumors showed an isointense signal, and only 1 tumor (2.8%) showed a completely hyperintense signal. Two patients had no standard unenhanced T1WI at diagnosis. Signal on T1WI was homogeneous in 41.7% and inhomogeneous in 58.3%. Thirty-six of 38 (94.7%) WNT-MBs showed contrast enhancement in 76%–100% of the tumor volume; only 1 WNT-MB showed an enhancing volume of 26%–50%, and 1 WNT-MB, 26%–50%. Signs of bleeding in T1WI, T2WI, or susceptibility-weighted images were found in 23/38 (60.5%).

In 18 of those cases, susceptibility-weighted images such as SWI or T2* sequences had been acquired. Sixteen of 18 (88.9%) susceptibility-weighted images showed iron content. Five of 16 MBs showed iron deposition in >50% of the tumor mass. The extension of perifocal edema ranged from 0 to 2.6 cm (mean, 0.66 ± 0.62 cm). Twenty-seven of 38 (71.1%) MBs showed perifocal edema. Tumor volume ranged from 2.68 to 68.59 cm^3 (mean, 27.79 ± 16.87 cm^3). LCMBs are usually significantly smaller than other histologic MB types (mean, 15 cm^3) as described previously.[22] By means of this value from the literature as a cutoff between large and small tumor sizes, 10 of 40 WNT tumors were small (range, 2.68–12.77 cm^3); all of them presented with classic histology. The 2 large-cell/anaplastic MBs had volumes of 29.81 and 46.39 cm^3. Leptomeningeal dissemination at diagnosis was assessable in 35 patients and was positive in 11.5% (4 of 35). One patient showed cranial dissemination (M2), 2 had cranial and spinal dissemination (M2 + 3), and 1 patient showed isolated spinal dissemination (M3). All 4 disseminated WNT-MBs showed classic histology in the primary tumor.

DISCUSSION

To our knowledge, this series represents the largest cohort of WNT-MBs analyzed for characteristic MR imaging features thus far. Our results show that the preferred primary position of our WNT-MBs is the midline fourth ventricle or vermis in 28 of 38 (74%). Perreault et al[12] were the first to report that WNT-MBs are characterized by an off-midline position in 75% (3 of 4 were located in the CPA or cerebellar peduncle), leading to a positive predictive value of 100% for this tumor site. In our cohort, only 5 of 38 (13%) WNT-MBs had their epicenter in the CPA; altogether, only 26% were primarily located in an off-midline position. This is much lower compared with earlier study results.[12–14] Gibson et al[23] indicated that WNT-MBs arise in the lower rhombic limb from progenitor cells of nuclei in the dorsal brain stem and all 6 WNT-MBs in this publication were reported as midline tumors. Similarly, Łastowska et al[24] found 5/6 and Teo et al[25] described 5 WNT-MBs in a midline position. On the basis of the hypothesis of Gibson et al[23] on the individual tumor origin, the pathways of extension were evaluated in more detail. With a self-defined score, Patay et al[14] emphasized the lateralized position of WNT-MBs (50% off-midline position). We support the conclusion of Patay et al that WNT-MBs are paramedian midline tumors, describing a lateralized position in 22/38 tumors in our cohort. However, a purely CPA localization (5 of 38) seems to be much rarer than previously noted.[12] The primary midline position is in line with the hypothesis that WNT-MBs arise from the dorsal brain stem and grow within the CSF spaces. Notably, the fourth ventricle may be the preferred pathway of tumor growth because it offers the least resistance. With only 3 tumors having their epicenter in the deep white matter surrounding the fourth ventricle in our study, this localization was significantly less frequent compared with that in previous studies (8% versus 20%).[13]

While Perreault et al[12] and Mata-Mbemba et al[13] assigned a cerebellar hemispheric origin as highly predictive of SHH-activated MB, we found 2 WNT tumors located in the cerebellar

hemisphere. However, both tumors were large, rendering the definition of their origin in differentiation between hemisphere and paraventricular white matter to be challenging. These different tumor locations in our cohort and partially divergent results compared with the previous studies question whether the off-midline or midline position has any useful diagnostic predictive value. The 4 genetic subgroup model was refined by Taylor et al[26] in 2012 and has been updated recently.[27–29] Further refined definitions of substructures within the 4 WHO entities of MB may be expected. The existence of such substructures might be a possible cause for the heterogeneity of the epicenter of the tumor in our study and the divergent reports of the typical location of WNT-MBs in previous studies.

The children in our cohort were older than 4 years of age; this matches previous observations that WNT-MBs do not typically occur in early childhood.[9] Most WNT-MBs in our cohort were histologically CMBs, but there were single other histologic types (large-cell/anaplastic MB, $n = 2$) as well. The fact that WNT-MBs are not exclusively CMBs has been reported previously.[9,10,13] Our cohort contained 1 tumor corresponding to an LCMB (according to the WHO classification of 2007). This is in accordance with Ellison et al[9] and Kool et al[10] reporting 2% LCMBs among their group of WNT-MBs. With a mean tumor volume of 15 cm^3, LCMBs have been described as significantly smaller than other histologic types of MB.[22] Most interesting, 10 CMBs in our cohort had a tumor size of >15 cm^3, and the only LCMB showed double that size. In our cohort, 11.5% of patients showed a macroscopic leptomeningeal dissemination at diagnosis. This percentage is similar to the numbers reported in studies on neuropathology but higher than in previous radiologic studies.[9,13,15,30] We found a female predominance, which is contrary to that in the cohort of Patay et al.[14] The female predominance in our cohort should be considered with caution due to the small cohort size in comparison with publications that have recorded the demographic data of significantly more WNT-MBs and found no predominance of male or female.[9,10,26]

MBs are tumors of high cellularity for which a lower signal on T2WI can be expected. In our cohort, WNT-MBs were primarily iso- to hypointense on T2WI. The comparatively low T2 signal is useful to differentiate MBs from pilocytic astrocytomas and, to a lesser extent, also from ependymomas. Inhomogeneous signal on T2WI and the moderate-to-strong contrast enhancement do not seem to be specific criteria to separate WNT-MBs from other highly cellular tumors, for example, atypical teratoid/rhabdoid tumors. So far, the literature has been heterogeneous with regard to intratumoral blood-degradation products in MBs. Patay et al[14] reported blood-degradation products in only 31.25%, whereas Reisinger et al[31] found substantial intratumoral hemorrhage in 54% of assessed tumors. Still another group (Perreault et al[12]) did not find any subgroup-specific features on iron-sensitive images. However, as one of the major findings in our study, a high proportion of tumors showed large areas of methemoglobin or hemosiderin (60.5%) and cysts containing blood-degradation products with blood-fluid levels.

Limitations

We acknowledge as a limitation that in this work, we only examined the WNT subgroup for imaging characteristics and, thus, did not directly compare the results with those of other MB subgroups. Due to the multicenter principle, we assessed imaging data from MR imaging scanners at different magnetic field strengths and sequence techniques. Thus, heterogeneity of imaging data could not be completely controlled.

CONCLUSIONS

WNT-MBs are found predominately in the fourth ventricle. However, a certain laterality can be noted by their hypothetic point of origin and possible growth characteristics. However, hemispherically positioned WNT-MBs and leptomeningeal dissemination can occur and may not be used as a criterion to exclude WNT-MB. Dense intratumoral blood-degradation products and cysts with blood contents are frequently found and might help to differentiate WNT-MBs from other MB subtypes.

ACKNOWLEDGMENTS

We thank Dr D. Engel for her support in manuscript correction.

Disclosures: Annika Stock—*RELATED*: *Grant*: German Children's Cancer Foundation.* Torsten Pietsch—*RELATED*: *Grant*: German Children's Cancer Foundation, *Comments*: grant money for reference pathologic evaluation and retrospective reclassification according to revised World Health Organization classification.* Steven C. Clifford—*RELATED*: *Grant*: Cancer Research UK, *Comments*: research grant.* Stefan Rutkowski—*RELATED*: *Grant*: German Children's Cancer Foundation.* Brigitte Bison—*RELATED*: *Grant*: German Children's Cancer Foundation, *Comments*: The Neuroradiological Reference Center, as part of the HIT-network, is supported by the German Children's Cancer Foundation*; *Support for Travel to Meetings for the Study or Other Purposes*: Deutsche Kinderkrebsstiftung, *Comments*: Travel Support is to The Reference Center for the German Brain Tumor Studies by Deutsche Kinderkrebsstiftung.* Mirko Pham—*RELATED*: *Grant*: German Children's Cancer Foundation*; *UNRELATED*: *Grants/Grants Pending*: Deutsche Forschungsgemeinschaft (CRC TR 240 B02, CRC 1158/1 A03, CRC 1158/2 A10)*; *Payment for lectures/travel expenses from Bayer AG and Merck Serono GmbH*, *Comments*: speaker honoraria.* Monika Warmuth-Metz—*RELATED*: *Grant*: German Children's Cancer Foundation, *Comments*: The reference center is only possible with the permanent financial support of the German Children's Cancer Foundation, which is the association of parents of children with cancer*; *UNRELATED*: *Grants/Grants Pending*: German Children's Cancer Foundation, *Comments*: The reference center is only possible with the permanent financial support of the German Children's Cancer Foundation, which is the association of parents of children with cancer.* Martin Mynarek—*RELATED*: *Grant*: German Children's Cancer Foundation*; *UNRELATED*: *Grants/Grants Pending*: Riemser Pharma, Greifswald, Germany, *Comments*: for activities outside of this work.* *Money paid to the institution/personal.

REFERENCES

1. Louis DN, Ohgaki H, Wiestler OD, et al, eds. *WHO Classification of Tumours of the Central Nervous System*, 4th ed. Geneva: IARC Press; 2016
2. Louis DN, Wiestler OD, Cavenee WK, et al. *WHO Classification of Tumors of the Central Nervous System*. Geneva: IARC Press; 2007
3. Koch A, Waha A, Tonn JC, et al. **Somatic mutations of WNT/wingless signaling pathway components in primitive neuroectodermal tumors.** *Int J Cancer* 2001;93:445–49 CrossRef Medline
4. Ellison DW, Onilude OE, Lindsey JC, et al. **Beta-catenin status predicts a favorable outcome in childhood medulloblastoma: the United Kingdom Children's Cancer Study Group Brain Tumour Committee.** *J Clin Oncol* 2005;23:7951957 CrossRef Medline
5. Waszak SM, Northcott PA, Buchhalter I, et al. **Spectrum and prevalence of genetic predisposition in medulloblastoma: a retrospective genetic study and prospective validation in a clinical trial cohort.** *Lancet Oncol* 2018;19:785–98 CrossRef Medline

6. Baeza N, Masuoka J, Kleihues P, et al. **AXIN1 mutations but not deletions in cerebellar medulloblastomas.** *Oncogene* 2003;22:632–36 CrossRef Medline
7. Dahmen RP, Koch A, Denkhaus D, et al. **Deletions of AXIN1, a component of the WNT/wingless pathway, in sporadic medulloblastomas.** *Cancer Res* 2001;61:7039–43 Medline
8. Koch A, Hrychyk A, Hartmann W, et al. **Mutations of the Wnt antagonist AXIN2 (Conductin) result in TCF-dependent transcription in medulloblastomas.** *Int J Cancer* 2007;121:284–91 CrossRef Medline
9. Ellison DW, Dalton J, Kocak M, et al. **Medulloblastoma: clinicopathological correlates of SHH, WNT, and non-SHH/WNT molecular subgroups.** *Acta Neuropathol* 2011;121:381–96 CrossRef Medline
10. Kool M, Korshunov A, Remke M, et al. **Molecular subgroups of medulloblastoma. An international meta-analysis of transcriptome, genetic aberrations, and clinical data of WNT, SHH, group 3, and group 4 medulloblastomas.** *Acta Neuropathol* 2012;123:473–84 CrossRef Medline
11. Goschzik T, Schwalbe EC, Hicks D, et al. **Prognostic effect of whole chromosomal aberration signatures in standard-risk, non-WNT/non-SHH medulloblastoma: a retrospective, molecular analysis of the HIT-SIOP PNET 4 trial.** *Lancet Oncol* 2018;19:1602–16 CrossRef Medline
12. Perreault S, Ramaswamy V, Achrol AS, et al. **MRI surrogates for molecular subgroups of medulloblastoma.** *AJNR Am J Neuroradiol* 2014;35:1263–69 CrossRef Medline
13. Mata-Mbemba D, Zapotocky M, Laughlin S, et al. **MRI characteristics of primary tumors and metastatic lesions in molecular subgroups of pediatric medulloblastoma. a single-center study.** *AJNR Am J Neuroradiol* 2018;39:949–55 CrossRef Medline
14. Patay Z, DeSain LA, Hwang SN, et al. **MR imaging characteristics of wingless-type-subgroup pediatric medulloblastoma.** *AJNR Am J Neuroradiol* 2015;36:2386–93 CrossRef Medline
15. Dasgupta A, Gupta T, Pungavkar S, et al. **Nomograms based on preoperative multiparametric magnetic resonance imaging for prediction of molecular subgrouping in medulloblastoma: results from a radiogenomics study of 111 patients.** *Neuro Oncol* 2019;21:115–24 CrossRef Medline
16. Pietsch T, Haberler C. **Update on the integrated histopathological and genetic classification of medulloblastoma: a practical diagnostic guideline.** *Clin Neuropathol* 2016;35:344–52 CrossRef Medline
17. Goschzik T, Zur Mühlen A, Kristiansen G, et al. **Molecular stratification of medulloblastoma: comparison of histological and genetic methods to detect Wnt activated tumours.** *Neuropathol Appl Neurobiol* 2015;41:135–44 CrossRef Medline
18. Pietsch T, Schmidt R, Remke M, et al. **Prognostic significance of clinical, histopathological, and molecular characteristics of medulloblastomas in the prospective HIT2000 multicenter clinical trial cohort.** *Acta Neuropathol* 2014;128:137–49 CrossRef Medline
19. Capper D, Jones DT, Sill M, et al. **DNA methylation-based classification of central nervous system tumours.** *Nature* 2018;555:469–74 CrossRef Medline
20. Schwalbe EC, Hicks D, Rafiee G, et al. **Minimal methylation classifier (MIMIC). A novel method for derivation and rapid diagnostic detection of disease-associated DNA methylation signatures.** *Sci Rep* 2017;7:13421 CrossRef Medline
21. Chang CH, Housepian EM, Herbert C. **An operative staging system and a megavoltage radiotherapeutic technic for cerebellar medulloblastomas.** *Radiology* 1969;93:1351–59 CrossRef Medline
22. Warmuth-Metz M. *Imaging and Diagnosis in Pediatric Brain Tumor Studies*. Cham: Springer-Verlag International Publishing; 2017:8–12
23. Gibson P, Tong Y, Robinson G, et al. **Subtypes of medulloblastoma have distinct developmental origins.** *Nature* 2010;468:1095–99 CrossRef Medline
24. Łastowska M, Jurkiewicz E, Trubicka J, et al. **Contrast enhancement pattern predicts poor survival for patients with non-WNT/SHH medulloblastoma tumours.** *J Neurooncol* 2015;123:65–73 CrossRef Medline
25. Teo WY, Shen J, Su JM, et al. **Implications of tumor location on subtypes of medulloblastoma.** *Pediatr Blood Cancer* 2013;60:1408–10 CrossRef Medline
26. Taylor MD, Northcott PA, Korshunov A, et al. **Molecular subgroups of medulloblastoma: the current consensus.** *Acta Neuropathol* 2012;123:465–72 CrossRef Medline
27. Northcott PA, Buchhalter I, Morrissy AS, et al. **The whole-genome landscape of medulloblastoma subtypes.** *Nature* 2017;547:311–17 CrossRef Medline
28. Schwalbe EC, Lindsey JC, Nakjang S, et al. **Novel molecular subgroups for clinical classification and outcome prediction in childhood medulloblastoma: a cohort study.** *Lancet Oncol* 2017;18:958–71 CrossRef Medline
29. Cavalli FM, Remke M, Rampasek L, et al. **Intertumoral heterogeneity within medulloblastoma subgroups.** *Cancer Cell* 2017;31:737–54 e6 CrossRef Medline
30. Zapotocky M, Mata-Mbemba D, Sumerauer D, et al. **Differential patterns of metastatic dissemination across medulloblastoma subgroups.** *J Neurosurg Pediatr* 2018;21:145–52 CrossRef Medline
31. Reisinger D, Gojo J, Kasprian G, et al. **Predisposition of wingless subgroup medulloblastoma for primary tumor hemorrhage.** *Neurosurgery* 2019 May 7. [Epub ahead of print] CrossRef Medline

Incidental Brain MRI Findings in Children: A Systematic Review and Meta-Analysis

V. Dangouloff-Ros, C.-J. Roux, G. Boulouis, R. Levy, N. Nicolas, C. Lozach, D. Grevent, F. Brunelle, N. Boddaert, and O. Naggara

ABSTRACT

BACKGROUND: The detection of incidental findings on children's brain MR imaging poses various practical issues because the life-long implications of such findings may be profound.

PURPOSE: Our aim was to assess the prevalence and characteristics of incidental brain MR imaging findings in children.

DATA SOURCES: Electronic databases (PubMed, EMBASE, and Cochrane) were searched for articles published between 1985 to July 2018, with the following search terms: "incidental," "findings," "brain," "MR imaging."

STUDY SELECTION: Inclusion criteria were the following: 1) patients younger than 21 years of age, 2) healthy children without any clinical condition, 3) MR images obtained with at least a 1.5T magnet, 4) original articles, and 5) a methodologic quality score of ≥10.

DATA ANALYSIS: Two observers independently extracted data and assessed data quality and validity. The number and type of incidental findings were pooled. Heterogeneity was assessed using the Cochran *Q* statistic and the I^2 statistic.

DATA SYNTHESIS: Seven studies were included, reporting 5938 children (mean age, 11.3 ± 2.8 years). Incidental findings were present in 16.4% (99% CI, 9.8–26.2; Q = 117.5, I^2 = 94.9%) of healthy children, intracranial cysts being the most frequent (10.2%, 99% CI, 3.1–28.5; Q = 306.4, I^2 = 98.0%). Nonspecific white matter hyperintensities were reported in 1.9% (99% CI, 0.2–16.8; Q = 73.6, I^2 = 94.6%), Chiari 1 malformation was found in 0.8% (99% CI, 0.5–1.3; Q = 7.6, I^2 = 60.5%), and intracranial neoplasms were reported in 0.2% (99% CI, 0.1–0.6; Q = 3.4, I^2 = 12.3%). In total, the prevalence of incidental findings needing follow-up was 2.6% (99% CI, 0.5–11.7; Q = 131.2, I^2 = 95.4%). Incidental findings needing specific treatment were brain tumors (0.2%) and cavernomas (0.2%).

LIMITATIONS: Limitations were no age stratification or ethnicity data and variation in the design of included studies.

CONCLUSIONS: The prevalence of incidental findings is much more frequent in children than previously reported in adults, but clinically meaningfull incidental findings were present in <1 in 38 children.

ABBREVIATION: IF = incidental finding

MR imaging of the brain is increasingly used in both pediatric research and clinical routine, with constantly improving image quality due to advances in hardware and sequence development. Performing MR imaging at a higher resolution and/or field strength using more sensitive sequences may lead to the detection of subtle brain abnormalities that would not have been previously detected. Furthermore, with the steadily increasing number of brain MR imaging scans obtained each year,[1] these technical advances will result in more patients and physicians being confronted with and needing to manage incidental brain findings.[2] Incidental findings (IFs) are previously undetected abnormalities of potential clinical relevance that are unexpectedly discovered and, by definition, unrelated to the purpose of the examination. The detection of IFs poses various practical and ethical issues, particularly when the subjects/patients are children, in whom the life-long implications of such findings may be profound. Detection is potentially detrimental because the treatment

Received June 28, 2019; accepted after revision September 3.

From the Pediatric Radiology Department (V.D.-R., C.-J.R., G.B., R.L., N.N., C.L., D.G., F.B., N.B., O.N.), Hôpital Necker-Enfants Malades, Paris, France; Institut National de la Santé et de la Recherche Médicale U1000 (V.D.-R., C.-J.R., R.L., N.N., C.L., D.G., F.B., N.B.), Paris, France; Unité Mixte de Recherche 1163 (V.D.-R., C.-J.R., R.L., N.N., C.L., D.G., F.B., N.B.), Institut Imagine, Paris, France; University René Descartes (V.D.-R., C.-J.R., G.B., R.L., N.N., C.L., D.G., F.B., N.B., O.N.), PRES Sorbonne Paris Cité, Paris, France; and Neuroradiology Department (G.B., O.N.), Centre Hospitalier Sainte-Anne, Paris, France.

Please address correspondence to Volodia Dangouloff-Ros, MD, MSc, Assistance-Publique Hôpitaux de Paris, Hôpital Necker-Enfants Malades, Department of Pediatric Radiology, 149 rue de Sèvres, 75015 Paris, France; e-mail: Volodia.dangouloff-ros@aphp.fr; @Volodia_DR

Indicates article with supplemental on-line table.

http://dx.doi.org/10.3174/ajnr.A6281

can have harmful as well as beneficial consequences. Estimating the probability of discovering incidental brain findings is of importance to help clinicians inform patients of these risks and to guide researchers to adequately inform either healthy volunteers in imaging research or individuals being considered for screening by brain MR imaging.

The clinical relevance and natural course of these unexpected asymptomatic findings have been studied in adults but remain largely unexplored in the pediatric population. Previous studies have investigated pediatric IFs in healthy research volunteers and in populations of children who underwent MR imaging examinations for various reasons.[3-8] Recently, Jansen et al,[9] in a monocentric study of 3966 children, reported that at least 1 IF was present in 25.6% of the children (95% CI, 24.2–27.0), though the prevalence of findings requiring clinical follow-up was only 0.43% (95% CI, 0.26–0.70). A systematic review and meta-analysis of the published literature has been recommended[10] to provide more precise estimates of the range of IFs on brain MR imaging and explore the influence of study design, patient characteristics, and imaging parameters on the detection of incidental brain findings. In the present study, our aim was to assess the prevalence and characteristics of incidental brain MR imaging findings in children through a systematic review and meta-analysis of the current literature.

MATERIALS AND METHODS

Before conducting this review, we developed a detailed protocol, including objectives and plans for collecting and analyzing data. The manuscript was prepared in accordance with the Meta-Analysis of Observational Studies in Epidemiology (MOOSE) and Preferred Reporting Items for Systematic Review and Meta-Analysis Protocols (PRISMA) guidelines.[11,12] This study was designed, conducted, and analyzed, and the article was written independent of industry or any financial support.

Search Strategy and Selection Criteria

The medical literature on incidental brain MR imaging findings, published between1985 to July 2018, was reviewed using PubMed, EMBASE, and the Cochrane data bases. Candidate studies were searched using the following keywords/MeSH terms and Boolean logic operators: "incidental," "findings," "brain," "MR imaging." No age keyword was used in the data base search. The search was supplemented by hand searching the reference list of each selected article and each review article.

Inclusion criteria for study selection were the following: 1) pediatric patients younger than 21 years of age (according to the guidelines of the American Academy of Pediatrics[13]), 2) healthy children without any clinical condition (ie, research controls or research cohort), 3) MR images obtained with at least a 1.5T magnet, 4) original articles (ie, not a review), 5) published in English or French, and 6) a methodologic quality score of ≥10, as defined below. Studies were excluded if patients' ages were not specified.

Data Extraction

Data from the included studies were extracted by 2 pediatric neuroradiologists (V.D.-R. and C.-J.R.) using a standardized critical appraisal and data-extraction form, and any disagreements were resolved by consensus. The data-extraction form was subdivided into 4 sections: 1) study characteristics, 2) patients characteristics, 3) imaging methods, and 4) imaging findings.

Study Characteristics

We extracted the following data: single institution/multicenter, prospective/retrospective data collection, consecutive/sporadic cases, midyear of study (defined as median calendar year of the MR imaging acquisition period), and country.

Patient Characteristics

Children's baseline extracted data included sex, number, mean age of the eligible children, and inclusion criteria (research cohort versus research controls).

Imaging Methods

We recorded the MR imaging magnet field used (1.5T or 3T), available MR imaging sequences, and occupation of the imaging reviewer (radiologist or not). We distinguished between standard and high-resolution MR imaging protocols. High-resolution brain MR imaging protocols were defined as those performed on a 3T MR imaging unit with an effective voxel resolution of at best $2 \times 2 \times 2$ mm^3 and as standard protocols otherwise.

Imaging Findings

We recorded the presence and number of IFs per patient, the number of IFs needing follow-up or treatment, the number of IFs according to sex, and detailed IFs. Six categories were created to further analyze common IFs: 1) normal variation (except those included in the other categories, such as pineal cysts), 2) cysts, 3) vascular abnormalities (developmental venous anomaly, cavernoma, capillary telangiectasia), 4) developmental disorders (Chiari 1 malformation, corpus callosum anomaly), 5) white matter hyperintensities, and 6) neoplasms.

Intracranial cysts were recorded as a whole group and according to subtypes (pineal cyst, choroid plexus cyst, arachnoid cyst, and so forth). White matter hyperintensities were gathered in 1 group, regardless of their localization. Findings outside the cranial vault (ie, nasopharynx and sinus conditions) were not considered.

Quality of Reporting in Included Studies

We assessed the quality of reporting of all included studies based on the Strengthening the Reporting of Observational Studies in Epidemiology (STROBE) statement checklist,[14] used to build a quality score of 0–22.

Risk of Bias Assessment

After the selection of studies, quality and risk of biases when pooling in meta-analysis were critically appraised on the basis of the scheme suggested by the Cochrane Collaboration tool.[15]

Statistical Analysis

In all analyses, inconsistency of findings across studies was assessed using the Cochran Q statistic and the I^2 statistic.[15] We used a fixed-effects weighted model to calculate the pooled estimates, except with P (heterogeneity) $< .10$ or $I^2 > 30\%$, in which case a random-effects weighted model was used. We assessed

publication bias using visual inspection of scatterplots according to study size or precision (ie, funnel plot.)[16] Due to marked heterogeneity, uncontrolled nature of the data, and multiplicity of testing, a 2-sided *P* value of < .01 was prespecified to indicate a convincing statistical difference. All *P* values were 2-tailed. Analyses were performed using Comprehensive Meta-Analysis 2.0 for Windows (Biostat, Englewood, New Jersey).

RESULTS

The initial search identified 1216 publications, 55 of which were evaluated in full text (see the flow chart in Fig 1). Seven studies, with 5938 children (mean age, 11.3 ± 2.8 years) were included.[3-9] One study published as a short report[9] was fully evaluated (methodologic data) thanks to the related methodologic report.[17]

Study and Patient Characteristics

Table 1 and the On-line-Table describe the characteristics of the included studies.

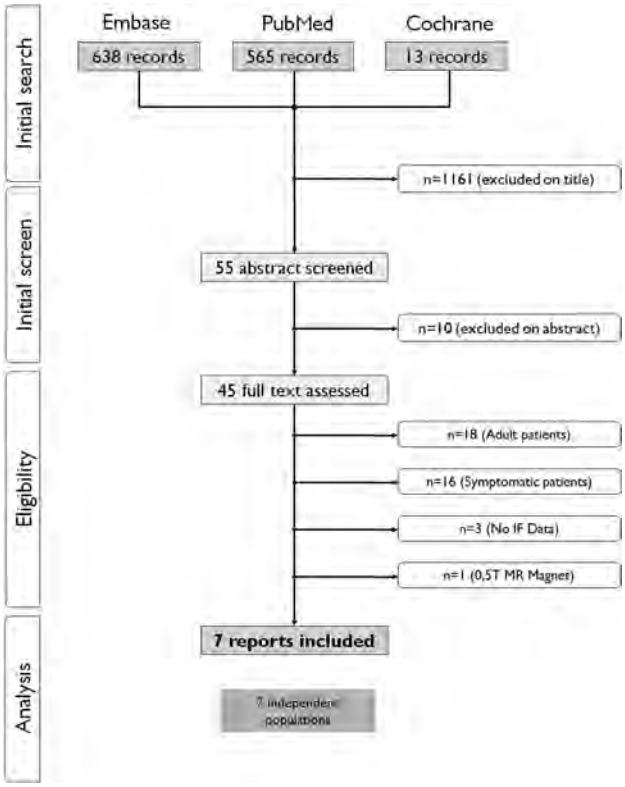

FIG 1. Flow chart of included studies.

The mean value of the methodologic quality scores was 15.3 ± 2.1/22. No study scored positively on all items, and all studies were monocentric. The case series were from the United States (*n* = 5), the Netherlands (*n* = 1), and Japan (*n* = 1). Table 2 details patient characteristics.

Imaging Methods

Imaging was performed using either a 1.5T (*n* = three; 395 children) or 3T magnet (*n* = four; 5543 children). All the imaging protocols included a T1-weighted sequence (6/7 studies using 3D, 1/7 using 2D or 3D images [53%/47%]), and 4 studies also reported 2D T2-weighted or FLAIR sequences. Four studies, including 5545 patients, were defined as high-resolution MRI.[6-9] Images were reviewed by neuroradiologists, except for 1 study in which the reviewer was a pediatric neurologist.[5]

Incidental Findings

A total of 1189 children (16.4%, 99% CI, 9.8–26.2) had at least 1 IF (Table 2), corresponding to a number needed to scan ~6 (99% CI, 3.8–10.2) to identify 1 IF. Publication bias is presented in the funnel plot analysis (Fig 2). A referral or a follow-up was needed in 67/5938 children (2.6%; 99% CI, 0.5–11.7; the number needed to scan ~38). There was no significant difference in IF prevalence between boys and girls (relative risk, 1.86; 99% CI, 0.70–4.94; *P* = .10).

IF prevalence appeared significantly higher (relative risk, 1.32; 99% CI, 1.04–1.67; *P* = .02) in studies with high-resolution MR imaging protocols (relative risk, 18.9%; 99% CI, 9.4–34.6) than in studies with standard-resolution MR imaging protocols (relative risk, 13.2%; 99% CI, 5.8–27.2).

Cysts were the most frequent IF (Table 3), found in 10.2% (1096) of children, with pineal cyst being the most frequently reported (2.3%, 704/5878), followed by arachnoid cyst (2.2%, 89/4256). The proportion of enlarged perivascular spaces was high (7.4%) but was reported in only 2 small cohorts (24/175 children). White matter hyperintensities were found in 1.9% (27/4428) (most being focal [19/27], the others being less clearly defined [8/27]); venous developmental anomaly, in 1.6% (66/4256); and Chiari I malformation, in 0.8% (32/4263). Corpus callosum anomalies were reported in 0.7% (7/4143), 5 with partial corpus callosum agenesis.

IFs that required therapeutic management were rare, with asymptomatic tumors reported in 9 children (0.2%, 9/4368). Eight were low-grade tumors (4 low-grade gliomas, 1 neuroepithelial dysembryoplastic tumor, 1 craniopharyngioma, 2 nonspecified lesions), and only 1 patient had a high-grade tumor, an

Table 1: Characteristics of included studies

Study	Country	Total Sample Size	Mean Age (Range) (yr)	% Male	MR Imaging Magnet	<2 mm³ Resolution	T2 or FLAIR WI	T2 or FLAIR 3D
Kim et al, 2002[3]	US	225	NA (1–18)	44	1.5	No	Yes	No
Kumra et al, 2006[4]	US	60	NA (10–21)	NA	1.5	No	Yes	Yes
Seki et al, 2010[5]	Japan	110	NA (5–8)	54	1.5	No	Yes	Yes
Gur et al, 2013[6]	US	1400	14.8 (8–21)	48	3	Yes	No	Yes
Kaiser et al, 2015[7]	US	114	8.3 (0.2–18)	41	3	Yes	Yes	Yes
Monterrey et al, 2017[8]	US	65	10.1 (NA)	71	3	Yes	No	Yes
Jansen et al, 2017[9]	Netherlands	3966	10.1 (8.6–11.9)	49	3	Yes	Yes	Yes

Note:—NA indicates not applicable; WI, weighted imaging.

Table 2: Population characteristics and incidental findings in pooled studies[a,3-9]

	No. Available (Studies)	Rate (%) (No.) or Mean Value ± SD	99% CI	*P* (Het)	I^2/Q Value
Patients	5938 (7)				
Sex (female)	5878 (6)	50.2 (2990)	45.0–55.4	.001	76.0/20.9
Age (mean) (SD) (yr)	5543 (4)	11.3 ± 2.8			
Incidental findings					
No IF	5938 (7)	79.9 (4648)	66.1–89.0	<.001	96.7/183.3
≥1 IF	5938 (7)	16.4 (1189)	9.8–26.2	<.001	94.9/117.6
≥1 IF, high resolution	5543 (4)	18.9 (1128)	9.4–34.6	<.001	97.1/104.6
≥1 IF, standard resolution	395 (3)	13.2 (61)	5.8–27.2	.016	75.7/8.2
≥1 IF, boys	816 (3)	17.6 (133)	14.1–21.7	<.001	97.5/81.0
≥1 IF, girls	874 (3)	16.3 (100)	9.2–19.9	.002	83.4/12.0
IF to follow	5938 (7)	2.6 (67)	0.5–11.7	<.001	95.4/131.2

Note:—Het indicates heterogeneity.
[a] Values are expressed as absolute number of patients (studies) or a percentage, unless otherwise specified.

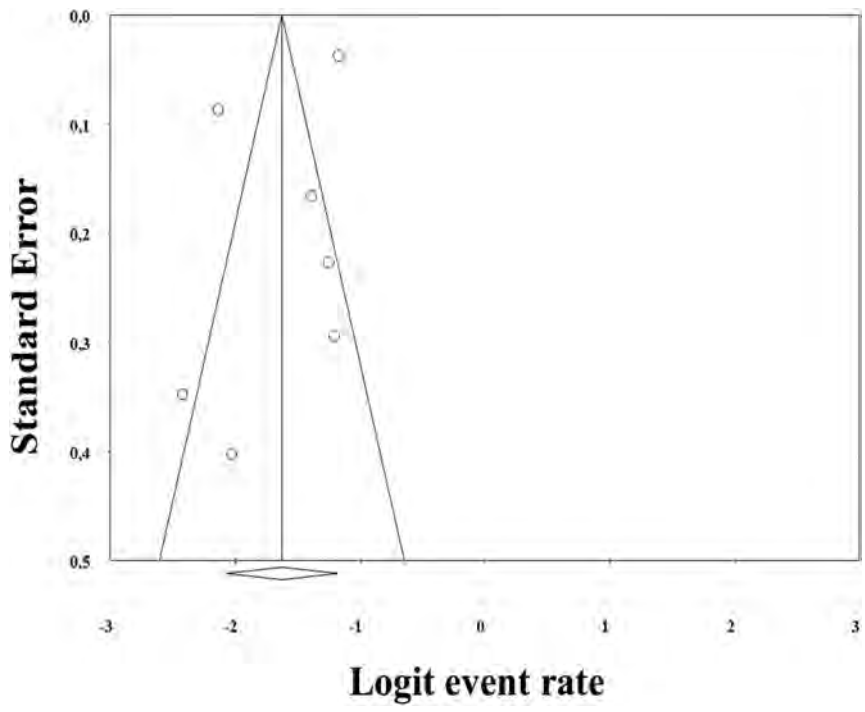

FIG 2. Funnel plot of incidental findings in brain MR imaging of healthy children. Each *dot* represents a study; the y-axis represents the size of the study (ie, number of subjects) and the x-axis shows the result of the study (ie, prevalence of incidental findings). Aysmmetric funnel plot suggests no relationship between IF prevalence and study size.

ependymoma.[9] Cavernomas were present in 7 children (0.2%, 7/3966).

DISCUSSION

In this systematic review and meta-analysis, we report a prevalence of 16.4% of IFs on brain MR imaging within a population of 5938 healthy children. Most of these IFs were benign and did not require routine or urgent referral, treatment, or follow-up.

Relatively few studies have examined incidental findings in healthy children, and prior studies have been limited by both the effective resolution of the imaging sequence used and small sample sizes. By synthesizing all the published data on incidental brain findings in children, we have increased the precision of existing estimates of their prevalence by showing that IFs were encountered in about 1 in every 6 children, whereas referral or follow-up was needed in about 1 in every 38 children. Given the increasingly common use of high-resolution brain MR imaging in pediatric populations, it is important to establish both a baseline rate for IFs and a framework for their evaluation.

A meta-analysis of 16 adult studies, including nearly 20,000 scans, found that the rate of IFs was related to image resolution.[18] In the case of sequences considered high-resolution by present standards, we found an IF prevalence that was significantly higher than with standard sequences. In such a situation (ie, with an imaging resolution $<2 \times 2 \times 2$ mm^3 on a 3T MR imaging unit), the prevalence of pediatric brain IFs is likely to be in the region of 1 in 5 children. However, the high-resolution studies were the most recent ones (2013–2017 versus 2002–2010 for low-resolution studies), which may suggest that the difference could be also due to the MR imaging scan generation, and not only to the magnet strength.

The rate of IFs was much higher in our study (16.4%) than in the adult meta-analysis[18] (2.7%), but direct comparison remains difficult. First, the nature of IFs strongly varies. In adults, Vernooij et al[19] demonstrated that asymptomatic brain infarcts were present in 7.2%, and cerebral aneurysms, in 1.8%, whereas they were not observed in pediatric studies. Second, the definition of incidental findings varies between adults and children. Hence, focal white matter abnormalities are considered "age-related modifications" in adults, but not in children. If we excluded these findings in our study, the IF rate changes from 16.4% to 9.6%. Third, imaging protocols strongly vary between adult and pediatric studies (resolution, duration, 3D) and may account for rate differences.

We did not encounter differences in IFs or subtype of IF according to sex, whereas a previous study[3] reported significant differences in IF prevalence between male and female subjects.

Pineal cysts were the most frequent IF, encountered in 2.3% of children. The prevalence of these cysts in clinical cohorts varies, from 1.8% when cysts are defined as having a diameter of >10 mm[20] up to 57%,[21] most likely due to differences in the

Table 3: Detailed incidental findings in pooled studies[3-9]

	No. Available (Studies)	Rate % (No.)	99% CI	*P* (Heterogeneity)	I^2/Q Value
Normal variations					
Mega cisterna magna	4428 (5)	2.5 (116)	0.8–7.4	<.001	78.0/22.7
Cavum septum pellucidum	5653 (5)	2.2 (105)	1.1–4.6	.007	71.4/14.0
Empty sella	3966 (1)	0.2 (7)	0.1–0.5	1	0/0
Cysts	5938 (7)	10.2 (1096)	3.1–28.5	<.001	98.0/306.4
Pineal	5878 (6)	2.3 (704)	0.4–12.4	<.001	97.1/175.4
Arachnoid	4256 (3)	2.2 (89)	1.7–2.9	.10	52.8/6.4
Choroid plexus	4031 (2)	0.4 (8)	0.1–6.4	.04	75.6/4.1
Porencephalic	4143 (3)	0.2 (4)	0.1–0.6	.05	69.7/5.8
Ventricular dilation	5656 (4)	1.1 (46)	0.1–12.4	<.001	95.5/65.9
Enlarged perivascular spaces	175 (2)	7.4 (24)	0.1–93.9	<.001	93.6/15.5
Vascular anomalies					
Developmental venous anomaly	4256 (3)	1.6 (66)	1.1–2.1	.72	0/0.66
Cavernoma	3966 (1)	0.2 (7)	0.1–0.5	1	0/0
Capillary telangiectasia	3966 (1)	0.1 (2)	0–0.3	1	0/0
Developmental disorders					
Gray matter heterotopia	4031 (2)	0.5 (19)	0.3–0.9	.75	0/0.1
Gray matter dysplasia	3966 (1)	0.1 (2)	0–0.3	1	0/0
Corpus callosum anomaly	4143 (3)	0.7 (7)	0.1–15.1	<.001	90.3/20.5
Chiari I malformation	4263 (4)	0.8 (32)	0.5–1.3	.06	60.5/7.6
White matter hyperintensities	4428 (5)	1.9 (27)	0.2–16.8	<.001	94.6/73.6
Neoplasm	4368 (4)	0.2 (9)	0.1–0.6	.33	12.3/3.4

definition of the cyst versus normal gland. The clinical meaning of these cysts may be challenging.[22] Jussila et al[20] recently reported that even above 10 mm in diameter, pineal cysts most often remain unchanged or display minimal growth. Consequently, size is probably less relevant than mass effect seen on the aqueduct. In the absence of such mass effect, pineal cysts may be overlooked and considered as a nonevolutive normal variant.

Our review found that Chiari I malformation was reported in 0.8% of these asymptomatic children. As in the case of pineal cysts, the clinical relevance of the tonsillar position remains problematic[22] because no definite morphologic criterion is predictive of symptomatology[23] and tonsillar position may be corrected with age.[24] Chiari I malformation, considered asymptomatic after careful specialized clinical evaluation, should not be systematically followed.

White matter FLAIR hyperintensities were observed in 1.9% of children, a finding that is far less frequent than in adults, in whom they are encountered in 8%–28% according to age.[25] Therefore, these anomalies imply the need for cautious evaluation by pediatric neuroradiologists. Eidlitz-Markus et al[26] reported that focal hyperintensities are more frequent (up to 10%) in children with migraine.

Corpus callosum anomalies were very rare (0.7%), with no complete agenesis reported and only 0.5% with partial agenesis. Nevertheless, the review by Sotiriadis and Makrydimas[27] showed that up to 75% of patients with isolated corpus callosum agenesis have normal development; caution is therefore needed when assessing these patients because this anomaly appears to be so rare in asymptomatic children.

Meaningful IFs (ie, implying the need for therapeutic management) were exceptionally reported, with neoplasms in 0.2% (99% CI, 0.1–0.6) of children and only 1 high-grade tumor. If this prevalence is lower than in adults[18,28,29] mainly because meningiomas are much rarer in children, it was higher than expected, according to estimates from cancer registries, which have shown a prevalence of 35 in 100 000 (0.04%).[30] Therefore, reviewing images from research pediatric protocols in healthy volunteers, readers should be aware of the possibility of discovering a brain tumor in about 1 in every 500 children.

Our study has several limitations. First, we do not have patient-level data allowing IFs to be stratified by age, which could be of interest because some of the IFs may appear or vanish with age (such as tonsillar ptosis). We may also have missed data included in published studies that did not detail the subjects' ages. Second, data according to ethnicity were not available, and this may be a potential confounding factor in the present meta-analysis. Third, the influence of variations in study design may have impacted the precision of IF rates and explain the substantial heterogeneity of studies assessed by Cochran statistics ($I^2 >$ 75%) for most IFs, in particular for IF s that could be considered normal variants (cysts, enlarged perivascular spaces). However, the prevalence of meaningful IFs, such as tumors, was more homogeneous ($I^2 = 12.3$). Fourth, in our systematic review, while the comprehensive search was designed to include as many pertinent studies as possible, some publications may have been missed. Finally, baseline characteristics were often limited to the entire series, without details by subgroups. Detailed data about IFs needing follow-up or specific treatment were not reported in the included studies, precluding any detailed subgroup or meta-regression analyses, and none of our results could be corrected for confounders.

CONCLUSIONS

Incidental findings in healthy children's brain MR imaging are frequent (16.4%), but rarely require referral, follow-up, or, even rarer, any treatment (0.4%), and parents and children should be informed accordingly before imaging examination for research purposes. Researchers must develop specific procedures, in a

cost-effective fashion, including management of brain MR imaging examinations, detection of IF, disclosure, and reporting to parents and appropriate follow-up by specialized clinicians.

REFERENCES

1. Trost MJ, Robison N, Coffey D, et al. **Changing trends in brain imaging technique for pediatric patients with ventriculoperitoneal shunts.** *Pediatr Neurosurg* 2018;53:116–20 CrossRef Medline
2. Shoemaker JM, Cole C, Petree LE, et al. **Evolution of universal review and disclosure of MRI reports to research participants.** *Brain Behav* 2016;6:e00428 CrossRef Medline
3. Kim BS, Illes J, Kaplan RT, et al. **Incidental findings on pediatric MR images of the brain.** *AJNR Am J Neuroradiol* 2002;23:1674–77 Medline
4. Kumra S, Ashtari M, Anderson B, et al. **Ethical and practical considerations in the management of incidental findings in pediatric MRI studies.** *J Am Acad Child Adolesc Psychiatry* 2006;45:1000–06 CrossRef Medline
5. Seki A, Uchiyama H, Fukushi T, et al. **Incidental findings of brain magnetic resonance imaging study in a pediatric cohort in Japan and recommendation for a model management protocol.** *J Epidemiol* 2010;20:S498–504 CrossRef Medline
6. Gur RE, Kaltman D, Melhem ER, et al. **Incidental findings in youths volunteering for brain MRI research.** *AJNR Am J Neuroradiol* 2013;34:2021–25 CrossRef Medline
7. Kaiser D, Leach J, Vannest J, et al. **Unanticipated findings in pediatric neuroimaging research: prevalence of abnormalities and process for reporting and clinical follow-up.** *Brain Imaging Behav* 2015;9:32–42 CrossRef Medline
8. Monterrey JC, Philips J, Cleveland S, et al. **Incidental brain MRI findings in an autism twin study.** *Autism Res* 2017;10:113–20 CrossRef Medline
9. Jansen PR, Dremmen M, van den Berg A, et al. **Incidental findings on brain imaging in the general pediatric population.** *N Engl J Med* 2017;377:1593–95 CrossRef Medline
10. Wolf SM, Lawrenz FP, Nelson CA, et al. **Managing incidental findings in human subjects research: analysis and recommendations.** *J Law Med Ethics* 2008;36:219–48 CrossRef Medline
11. Stroup DF, Berlin JA, Morton SC, et al. **Meta-analysis of observational studies in epidemiology: a proposal for reporting—Meta-analysis Of Observational Studies in Epidemiology (MOOSE) group.** *JAMA* 2000;283:2008–12 CrossRef Medline
12. Moher D, Shamseer L, Clarke M, et al. **Preferred reporting items for systematic review and meta-analysis protocols (PRISMA-P) 2015 statement.** *Syst Rev* 2015;4 CrossRef Medline
13. Hardin AP, Hackell JM, COMMITTEE ON PRACTICE AND AMBULATORY MEDICINE. **Age limit of pediatrics.** *Pediatrics* 2017;140:e20172151 CrossRef Medline
14. Vandenbroucke JP, von Elm E, Altman DG, et al. **Strengthening the Reporting of Observational Studies in Epidemiology (STROBE): explanation and elaboration.** *Int J Surg* 2014;12:1500–24 CrossRef Medline
15. Higgins JPT, Altman DG, Gøtzsche PC, et al. **The Cochrane Collaboration's tool for assessing risk of bias in randomised trials.** *BMJ* 2011;343:d5928 CrossRef Medline
16. Sterne JA, Egger M. **Funnel plots for detecting bias in meta-analysis: guidelines on choice of axis.** *J Clin Epidemiol* 2001;54:1046–55 CrossRef Medline
17. White T, Muetzel RL, El Marroun H, et al. **Paediatric population neuroimaging and the Generation R Study: the second wave.** *Eur J Epidemiol* 2018;33:99–125 CrossRef Medline
18. Morris Z, Whiteley WN, Longstreth WT, et al. **Incidental findings on brain magnetic resonance imaging: systematic review and meta-analysis.** *BMJ* 2009;339:b3016 CrossRef Medline
19. Vernooij MW, Ikram MA, Tanghe HL, et al. **Incidental findings on brain MRI in the general population.** *N Engl J Med* 2007;357:1821–28 CrossRef Medline
20. Jussila M-P, Olsén P, Salokorpi N, et al. **Follow-up of pineal cysts in children: is it necessary?** *Neuroradiology* 2017;59:1265–73 CrossRef Medline
21. Whitehead MT, Oh CC, Choudhri AF. **Incidental pineal cysts in children who undergo 3-T MRI.** *Pediatr Radiol* 2013;43:1577–83 CrossRef Medline
22. Maher CO, Piatt JH Jr, Section on Neurologic Surgery, American Academy of Pediatrics. **Incidental findings on brain and spine imaging in children.** *Pediatrics* 2015;135:e1084–96 CrossRef Medline
23. Khalsa SSS, Geh N, Martin BA, et al. **Morphometric and volumetric comparison of 102 children with symptomatic and asymptomatic Chiari malformation Type I.** *J Neurosurg Pediatr* 2018;21:65–71 CrossRef Medline
24. Whitson WJ, Lane JR, Bauer DF, et al. **A prospective natural history study of nonoperatively managed Chiari I malformation: does follow-up MRI surveillance alter surgical decision making?** *J Neurosurg Pediatr* 2015;16:159–66 CrossRef Medline
25. Vermeer SE, Longstreth WT, Koudstaal PJ. **Silent brain infarcts: a systematic review.** *Lancet Neurol* 2007;6:611–19 CrossRef Medline
26. Eidlitz-Markus T, Zeharia A, Haimi-Cohen Y, et al. **MRI white matter lesions in pediatric migraine.** *Cephalalgia* 2013;33:906–13 CrossRef Medline
27. Sotiriadis A, Makrydimas G. **Neurodevelopment after prenatal diagnosis of isolated agenesis of the corpus callosum: an integrative review.** *Am J Obstet Gynecol* 2012;206:337.e1–5 CrossRef Medline
28. Bos D, Poels MM, Adams HH, et al. **Prevalence, clinical management, and natural course of incidental findings on brain MR images: the population-based Rotterdam Scan Study.** *Radiology* 2016;281:507–15 CrossRef
29. Gibson LM, Paul L, Chappell FM, et al. **Potentially serious incidental findings on brain and body magnetic resonance imaging of apparently asymptomatic adults: systematic review and meta-analysis.** *BMJ* 2018;363:k4577 CrossRef Medline
30. Porter KR, McCarthy BJ, Freels S, et al. **Prevalence estimates for primary brain tumors in the United States by age, gender, behavior, and histology.** *Neuro Oncol* 2010;12:520–27 CrossRef Medline

Age-Dependent Signal Intensity Changes in the Structurally Normal Pediatric Brain on Unenhanced T1-Weighted MR Imaging

T.F. Flood, P.R. Bhatt, A. Jensen, J.A. Maloney, N.V. Stence, and D.M. Mirsky

ABSTRACT

BACKGROUND AND PURPOSE: Various pathologic and nonpathologic states result in brain parenchymal signal intensity changes on unenhanced T1-weighted MR imaging. However, the absence of quantitative data to characterize typical age-related signal intensity values limits evaluation. We sought to establish a range of age-dependent brain parenchymal signal intensity values on unenhanced T1WI in a sample of individuals (18 years of age or younger) with structurally normal brains.

MATERIALS AND METHODS: A single-center retrospective study was performed. Gadolinium-naïve pediatric patients with structurally normal MR brain imaging examination findings were analyzed ($n = 114$; 50% female; age range, 68 days to 18 years). ROI signal intensity measurements were obtained from the globus pallidus, thalamus, dentate nucleus, pons, and frontal lobe cortex and subcortical white matter. Multivariable linear regression was used to analyze the relationship between signal intensity values and age.

RESULTS: Results demonstrated a statistically significant association between signal intensity values and linear age in all neuroanatomic areas tested, except the frontal gray matter, ($P < .01$). There were no statistically significant differences attributable to patient sex.

CONCLUSIONS: Age-dependent signal intensity values were determined on unenhanced T1WI in structurally normal pediatric brains. Increased age correlated with increased signal intensity in all brain locations, except the frontal gray matter, irrespective of sex. The biologic mechanisms underlying our results remain unclear and may be related to chronologic changes in myelin density, synaptic density, and water content. Establishing age-dependent signal intensity parameters in the structurally normal pediatric brain will help clarify developmental aberrations and enhance gadolinium-deposition research by providing an improved understanding of the confounding effect of age.

The development of the human brain is a dynamic process, which continuously changes on both a macro- and microstructural level.[1] MR imaging has proved useful not only in characterizing normal morphologic brain maturation but in describing chronologic changes in cortical structure and myelination patterns.[2–20] Furthermore, various pathologic and nonpathologic states are now known to result in brain parenchymal signal intensity changes on unenhanced T1WI, including gadolinium deposition.[21–30] Chronologic signal intensity changes on T1WI and myelination patterns within the cortex and subcortical white matter, corpus collosum, and various white matter tracts within the supratentorial and infratentorial brain have been well-characterized in pediatric and adult populations.[2–17,19,20] However, age-dependent T1WI signal intensity alterations within the deep gray nuclei, cerebellar nuclei, and brain stem in pediatric subjects are less well-understood. Establishing signal intensity parameters on unenhanced T1WI in structurally normal pediatric brains, including within subcortical and deep cerebellar nuclei, will help clarify developmental aberrations, elucidate pathology, and enhance gadolinium-deposition research by providing an improved understanding of the confounding effect of age. Therefore, we sought to establish an expected range of age-dependent signal intensity values in specific anatomic regions in a sample of structurally normal pediatric brains on unenhanced T1WI.

MATERIALS AND METHODS

Participants

This single-center, retrospective study was approved by the local institutional review board of the University of Colorado

Received April 19, 2019; accepted after revision August 21.

From the Departments of Radiology (T.F.F., P.R.B.) and Biostatistics & Informatics (A.J.), University of Colorado, Aurora, Colorado; and Department of Radiology (J.A.M., N.V.S., D.M.M.), University of Colorado Children's Hospital, Aurora, Colorado.

Paper previously presented as a Turbo Talk at: Annual Meeting of the American Society of Neuroradiology, April 22–27, 2017; Long Beach, California.

Please address correspondence to David M. Mirsky, MD, Department of Radiology, University of Colorado Children's Hospital, 13123 East 16th Ave, Box B125, Aurora, CO 80045; e-mail: David.Mirsky@childrenscolorado.org

Indicates article with supplemental on-line tables.

Indicates article with supplemental on-line photos.

http://dx.doi.org/10.3174/ajnr.A6254

Table: Linear and quadratic age parameter estimates from the general linear model

ROI	Linear Age			Quadratic Age		
	Estimate	95% CI	*P* Value	Estimate	95% CI	*P* Value
Globus pallidus	0.00900	0.006–0.012	<.001	–0.00003	−0.000041 to −0.000015	<.001
Thalamus	0.006	0.003–0.008	<.001	–0.000017	−0.000029 to −0.000005	.005
Dentate	0.00500	0.002–0.008	.001	–0.000017	−0.00003 to −0.000003	.02
Frontal GM	0.003	0.001–0.005	.01	–0.000009	−0.000019 – 0.000001	.07
Frontal WM	0.011	0.008–0.014	<.001	–0.000038	−0.000053 – 0.000024	<.001

and was compliant with the Health Insurance Portability and Accountability Act. Informed consent was waived. Pediatric patients older than 31 days and younger than 18 years who underwent an unenhanced brain MR imaging examination between January 1, 2012, and December 31, 2012, were consecutively identified from our institution's electronic medical record data base. The first 3 male and the first 3 female patients per year of life encountered in the data base who met the following criteria were included for analysis: the presence of an interpretable 3D-MPRAGE sequence; structurally normal brain per the imaging report; no history of prior exposure to gadolinium-based contrast agents; and no brain radiation, neurofibromatosis type 1, impaired renal or hepatic function, and systemic or metabolic illness, as per review of the patient's electronic medical record (see On-line Table 1 for a complete list of MR imaging examination indications). The MPRAGE MR imaging sequence was chosen for analysis to limit variation secondary to analysis of differing imaging sequences.[28] One hundred fourteen pediatric brain MR imaging examinations were analyzed, which comprised 57 male and 57 female age-matched patients (age range, 68 days to 18 years). Patient data were used from no more than 1 examination.

Imaging Protocol

All brain MR imaging examinations were performed with a 1.5T whole-body MR imaging system within our institution (Avanto; Siemens, Erlangen, Germany) on 1 of 2 identical scanners. All ROI measurements were made on an unenhanced axial T1WI 3D-MPRAGE sequence created with uniform acquisition parameters (TR range = 1700–1800 ms, TE = 2.92 ms, section thickness = 1.0 mm, FOV = 250 mm, matrix = 250 × 250).

Data Collection

Measurements of signal intensity in a 5-mm circular ROI within the globus pallidus, thalamus, dentate nucleus, pons, frontal lobe cortical gray matter, and frontal lobe subcortical white matter were performed on unenhanced axial T1WI for all patients (see On-line Figs 1–9 for representative ROI measurements). Bilateral measurements were averaged from the globus pallidus, thalamus, dentate nucleus, and frontal lobes; single measurements were obtained from the pons. All parenchymal measurements were normalized to CSF signal intensity. The measurements were acquired by 2 radiology residents; investigators were not blinded to the patient's age. Measurement screenshots were saved and reviewed by 3 attending pediatric neuroradiologists to ensure appropriate measurement location by consensus agreement. No measurement disagreements were noted. The signal intensity measurements were transcribed into software (Excel, Version 2011; Microsoft, Redmond, Washington).

Statistical Analysis

To account for the effect of CSF, we normalized all ROI signal intensities to the CSF intensity scale. Signal intensity as a function of age (in months) was investigated for all ROIs using 2 general linear models to compare linear with quadratic fits. The linear fit used the covariates of subject sex and age, while the quadratic fit included the additional covariate of squared age. The Akaike information criteria were used to determine which model provided a higher quality fit. Additionally, to determine whether there was an acute period of signal intensity change, we conducted a piecewise linear spline analysis, and if significant, a knot corresponding to the significant change in linear slope was included in the model. Ninety-five percent confidence intervals were calculated in all figures to show the variability of the average normalized signal intensity across all ages. All analyses were performed using R statistical and computing software (Version 3.60; http://www.r-project.org/). A Bonferroni-corrected significance value of $P < .01$ was considered indicative of a statistically significant parameter estimate.

RESULTS

The general linear model, which included a variable for quadratic age, was found to have a better fit to the data than the model that only included subject sex and linear age across all ROIs. This model fit satisfied all modeling assumptions (linearity, homoscedasticity, normality, and independence) via examination of diagnostic plots and tests. Subject sex was not found to be significantly associated with normalized signal intensity for any of the ROIs ($P > .01$). For all ROIs, except the frontal gray matter using both models and the dentate nucleus using the quadratic model, both the linear and quadratic age parameters were statistically significant (Table). To assess whether there existed an acute period of signal intensity change in each ROI, we conducted independent piecewise linear spline analyses, with a grid search to determine the optimal placement of the knots. This analysis was conducted on the model with only subject sex and linear age. For all ROIs, the age parameter estimate was found to be significantly different at the 36-month mark; therefore, a knot, used to allow the parameter estimate to be different before and after 36 months, was included in each ROI model. A comparison of these estimates showed that for all ROIs except frontal gray matter and the dentate nucleus, the parameter estimate for age was significantly larger during the first 3 years of life (On-line Table 2), indicating an acute period of signal intensity change throughout the brain in these regions. Figures 1 and 2 illustrate the quadratic and linear

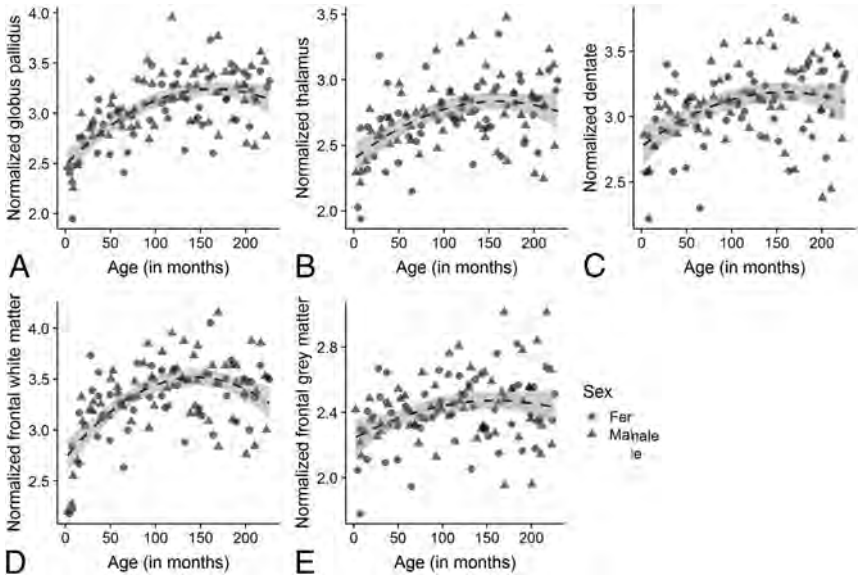

FIG 1. Multivariable linear regression with the quadratic age effect of signal intensity in the globus pallidus (*A*), thalamus (*B*), dentate (*C*), frontal white matter (*D*), and frontal gray matter (*E*). The *dashed line* represents the average predicted signal intensity at each age with the *gray shading* representing the 95% confidence band. Points on the scatterplots are differentiated by sex.

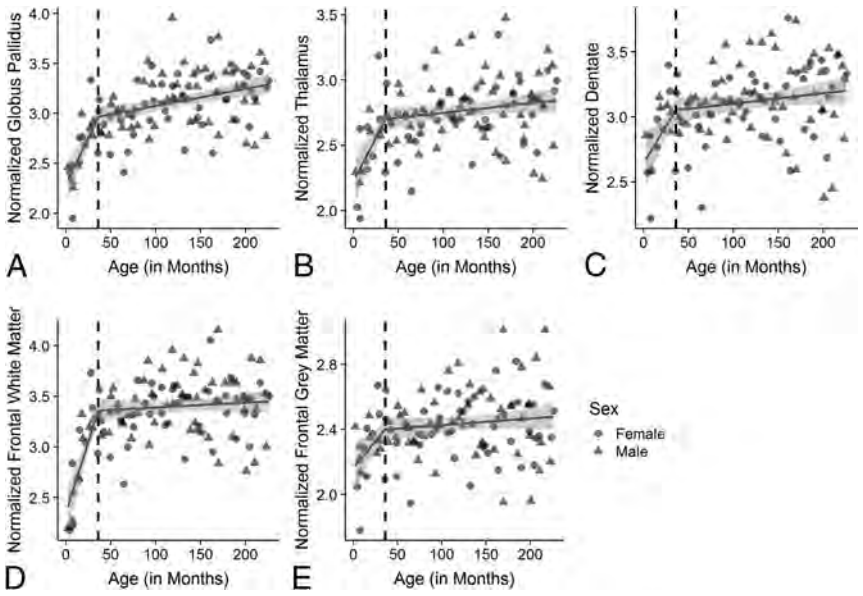

FIG 2. Multivariable linear regression of signal intensity in the globus pallidus (*A*), thalamus (*B*), dentate (*C*), frontal white matter (*D*), and frontal gray matter (*E*), The *solid line* represents the average predicted signal intensity at each age with the *gray shading* representing the 95% confidence band. The *vertical dashed line* shows the location of the spline, where the effect of age on signal intensity changes. Points on the scatterplots are differentiated by sex.

spline model fits of age (in months) to normalized signal intensity for each ROI, respectively.

DISCUSSION

This study establishes a range of age-dependent signal intensity values in the structurally normal pediatric brain on unenhanced T1WI in multiple neuroanatomic areas. Increased age was associated with increased signal intensity values in all brain locations tested, except the frontal gray matter, irrespective of sex. Furthermore, in all brain regions tested, except the frontal gray matter and the dentate nucleus, there was a statistically significant period of increased positive signal intensity change in the first 36 months of life relative to later time points. Although the frontal gray matter and dentate nucleus failed to achieve statistical significance, as above, both anatomic regions demonstrated a similar trend relative to the other regions tested. Overall, these results are in line with multiple published studies that demonstrated temporal changes in brain development on MR imaging.[2–20] Specifically, our results parallel those of multiple

published studies showing a nonlinear positive correlation between T1WI signal intensity and age in numerous cortical areas and white matter tracts within the brain, including a similar steeper slope at earlier time points.[10,12,16,20] Furthermore, our results correlate with known developmental changes in brain myelin content; however, additional less dominant factors, as listed below, likely also contributed.[8,20]

In the current study, by establishing age-dependent signal intensity values in the structurally normal pediatric brain on unenhanced T1WI throughout infancy to older adolescence, especially in deep gray and cerebellar nuclei, our results fill an existing gap in the literature. It is known that various pathologic and nonpathologic processes result in pediatric brain parenchymal signal intensity changes on MR imaging, such as hypoxic-ischemic injury, infection, mitochondrial or metabolic disorders, and, most recently, gadolinium deposition.[8–14] Establishing brain signal intensity parameters in the structurally normal pediatric brain on unenhanced T1WI will help clarify developmental aberrations, elucidate pathology, and enhance gadolinium-deposition research by providing an improved understanding of the confounding effect of age. Specifically, these results will aid in the recognition of deviations from the expected brain parenchymal signal intensity changes, which occur throughout development. The biologic mechanisms underlying our results remain unclear and may be related to chronologic changes in myelin density, synaptic density, physiologic mineral and metal deposition, water content, and/or the glymphatic system.

Study limitations include a small single-center retrospective design and reliance on signal intensity measurements, which limit generalization of the results. T1 mapping would be more accurate to characterize T1-weighted signal intensity values, but it is not currently performed on a routine clinical basis at our institution. An additional limitation is reliance on our institution's electronic medical record to exclude prior gadolinium-based contrast material exposure; it is possible that a prior exposure was not documented in our electronic medical record.

CONCLUSIONS

Age-dependent signal intensity values in the structurally normal pediatric brain were determined on unenhanced T1-weighted MR imaging. Increased age was associated with increased signal intensity values in all brain locations tested, except the frontal gray matter, irrespective of sex. Establishing signal intensity parameters in the structurally normal pediatric brain will help clarify developmental aberrations, elucidate pathology, and enhance gadolinium-deposition research by providing an improved understanding of the confounding effect of age.

Disclosures: Thomas F. Flood—*UNRELATED: Support for Travel to Meetings for the Study or Other Purposes*: University of Colorado Radiology Department, *Comments*: Turbo Talk at the American Society of Neuroradiology 2017 annual meeting with travel expenses funded by the University of Colorado Department of Radiology.

REFERENCES

1. Kandel ER, Mack S, eds. *Principles of Neural Science*. 5th ed. New York: McGraw-Hill Medical; 2013
2. Salat DH, Tuch DS, Hevelone ND, et al. **Age-related changes in prefrontal white matter measured by diffusion tensor imaging.** *Ann N Y Acad Sci* 2005;1064:37–49 CrossRef Medline
3. Welker KM, Patton A. **Assessment of normal myelination with magnetic resonance imaging.** *Semin Neurol* 2012;32:15–28 CrossRef Medline
4. Tamnes CK, Ostby Y, Fjell AM, et al. **Brain maturation in adolescence and young adulthood: regional age-related changes in cortical thickness and white matter volume and microstructure.** *Cereb Cortex* 2010;20:534–48 CrossRef
5. Westlye LT, Walhovd KB, Dale AM, et al. **Differentiating maturational and aging-related changes of the cerebral cortex by use of thickness and signal intensity.** *Neuroimage* 2010;52:172–85 CrossRef Medline
6. Sowell ER, Thompson PM, Toga AW. **Mapping changes in the human cortex throughout the span of life.** *Neuroscientist* 2004;10:372–92 CrossRef Medline
7. Paus T, Collins DL, Evans AC, et al. **Maturation of white matter in the human brain: a review of magnetic resonance studies.** *Brain Res Bull* 2001;54:255–66 CrossRef Medline
8. Barkovich AJ, Kjos BO, Jackson DE, et al. **Normal maturation of the neonatal and infant brain: MR imaging at 1.5 T.** *Radiology* 1988;166:173–80 CrossRef Medline
9. Cho S, Jones D, Reddick WE, et al. **Establishing norms for age-related changes in proton T1 of human brain tissue in vivo.** *Magn Reson Med* 1997;15:1133–43 CrossRef
10. Dean DC, O'Muircheartaigh J, Dirks H, et al. **Modeling healthy male white matter and myelin development: 3 through 60 months of age.** *Neuroimage* 2014;84:742–52 CrossRef Medline
11. Deoni SCL, Mercure E, Blasi A, et al. **Mapping infant brain myelination with magnetic resonance imaging.** *J Neurosci* 2011;31:784–91 CrossRef Medline
12. Deoni SCL, Dean DC, O'Muircheartaigh J, et al. **Investigating white matter development in infancy and early childhood using myelin water faction and relaxation time mapping.** *Neuroimage* 2012;63:1038–53 CrossRef Medline
13. Gilmore JH, Shi F, Woolson SL, et al. **Longitudinal development of cortical and subcortical gray matter from birth to 2 years.** *Cereb Cortex* 2012;22:2478–85 CrossRef Medline
14. Glasser MF, Van Essen DC. **Mapping human cortical areas in vivo based on myelin content as revealed by T1- and T2-weighted MRI.** *J Neurosci* 2011;31:11597–616 CrossRef Medline
15. Grydeland H, Walhovd KB, Tamnes CK, et al. **Intracortical myelin links with performance variability across the human lifespan: results from T1- and T2-weighted MRI myelin mapping and diffusion tensor imaging.** *J Neurosci* 2013;33:18618–30 CrossRef Medline
16. O'Muircheartaigh J, Dean DC, Ginestet CW, et al. **White matter development and early cognition in babies and toddlers.** *Hum Brain Mapp* 2014;35:4475–87 CrossRef Medline
17. Shafee R, Buckner RL, Fischl B. **Gray matter myelination of 1555 human brains using partial volume corrected MRI images.** *Neuroimage* 2015;105:473–85 CrossRef Medline
18. Sowell ER, Thompson PM, Leonard CM, et al. **Longitudinal mapping of cortical thickness and brain growth in normal children.** *J Neurosci* 2004;24:8223–31 CrossRef Medline
19. Travis KE, Curran MM, Torres C, et al. **Age-related changes in tissue signal properties within cortical areas important for word understanding in 12- to 19-month-old infants.** *Cereb Cortex* 2014;24:1948–55 CrossRef Medline
20. Deoni SC, Dean DC, Remer J, et al. **Cortical maturation and myelination in healthy toddlers and young children.** *Neurorimage* 2015;115:147–61 CrossRef
21. Finelli PF, Singh JU. **A syndrome of bilateral symmetrical basal ganglia lesions in diabetic dialysis patients.** *Am J Kidney Dis* 2014;63:286–88 CrossRef Medline
22. Hedge AN, Mohan S, Lath N, et al. **Differential diagnosis for bilateral abnormalities of the basal ganglia and thalamus.** *Radiographics* 2011;31:5–30 CrossRef Medline

23. Zuccoli G, Yannes MP, Nardone R, et al. **Bilateral symmetrical basal ganglia and thalamic lesions in children: an update (2015).** *Neuroradiology* 2015;57:973–89 CrossRef Medline
24. Kanda T, Ishii K, Kawaguchi H, et al. **High signal intensity in the dentate nucleus and globus pallidus on unenhanced T1-weighted MR images: relationship with increasing cumulative dose of a gadolinium-based contrast material.** *Radiology* 2014;270:834–41 CrossRef Medline
25. Kanda T, Matsuda M, Oba H, et al. **Gadolinium deposition after contrast-enhanced MR imaging.** *Radiology* 2015;277:924–25 CrossRef Medline
26. Flood TF, Stence NV, Maloney JA, et al. **Pediatric brain: repeated exposure to linear gadolinium-based contrast material is associated with increased signal intensity at unenhanced T1-weighted MR imaging.** *Radiology* 2017;282:222–28 CrossRef Medline
27. Radbruch A, Weberling LD, Kieslich PJ, et al. **Gadolinium retention in the dentate nucleus and globus pallidus is dependent on the class of contrast agent.** *Radiology* 2015;275:783–91 CrossRef Medline
28. Ramalho J, Ramalho M, AlObaidy M, et al. **T1 signal-intensity increase in the dentate nucleus after multiple exposures to gadodiamide: intraindividual comparison between 2 commonly used sequences.** *AJNR Am J Neuroradiol* 2016;37:1427–31 CrossRef Medline
29. Blumfield E, Swenson D, Ramesh I, et al. **Gadolinium-based contrast agents review of recent literature on magnetic resonance imaging signal intensity changes and tissue deposits, with emphasis on pediatric patients.** *Pediatr Radiol* 2019;49:448–57 CrossRef Medline
30. Deike-Hofman K, Reuter J, Haase R, et al. **Glymphatic pathway of gadolinium-based contrast agents through the brain overlooked and misinterpreted.** *Invest Radiol* 2019;54:229–37 CrossRef Medline

Signal Change in the Mammillary Bodies after Perinatal Asphyxia

M. Molavi, S.D. Vann, L.S. de Vries, F. Groenendaal, and M. Lequin

ABSTRACT

BACKGROUND AND PURPOSE: Research into memory deficits associated with hypoxic-ischemic encephalopathy has typically focused on the hippocampus, but there is emerging evidence that the medial diencephalon may also be compromised. We hypothesized that mammillary body damage occurs in perinatal asphyxia, potentially resulting in mammillary body atrophy and subsequent memory impairment.

MATERIALS AND METHODS: We retrospectively reviewed brain MRIs of 235 clinically confirmed full-term patients with hypoxic-ischemic encephalopathy acquired at a single center during 2004–2017. MRIs were performed within 10 days of birth (median, 6; interquartile range, 2). Two radiologists independently assessed the mammillary bodies for abnormal signal on T2-weighted and DWI sequences. Follow-up MRIs were available for 9 patients; these were examined for evidence of mammillary body and hippocampal atrophy.

RESULTS: In 31 neonates (13.2%), abnormal high mammillary body signal was seen on T2-weighted sequences, 4 with mild, 25 with moderate, and 2 with severe hypoxic-ischemic encephalopathy. In addition, restricted diffusion was seen in 6 neonates who had MR imaging between days 5 and 7. For these 31 neonates, the most common MR imaging pattern (41.9%) was abnormal signal restricted to the mammillary bodies with the rest of the brain appearing normal. Follow-up MRIs were available for 9 patients: 8 acquired between 3 and 19 months and 1 acquired at 7.5 years. There was mammillary body atrophy in 8 of the 9 follow-up MRIs.

CONCLUSIONS: Approximately 13% of full-term infants with hypoxic-ischemic encephalopathy showed abnormal high mammillary body signal on T2-weighted images during the acute phase, which progressed to mammillary body atrophy in all but 1 of the infants who had follow-up MR imaging. This mammillary body involvement does not appear to be related to the severity of encephalopathy, MR imaging patterns of hypoxic-ischemic encephalopathy, or pathology elsewhere in the brain.

ABBREVIATIONS: MB = mammillary body; HIE = hypoxic-ischemic encephalopathy; IQ = intelligent quotient

The mammillary bodies (MBs) are a pair of small projections situated at the posterior margin of the hypothalamus at the base of the brain, named "mammillary" because of their shape. They have repeatedly been implicated in mnemonic processes and are particularly important for episodic (ie, event) memory.[1-3] MB damage is typically associated with conditions linked to thiamine deficiency, in particular Korsakoff syndrome;[4] however, it appears that the MBs may be implicated in a greater number of neurologic conditions than previously appreciated.[5-7]

In infants, brain areas typically vulnerable to hypoxic-ischemic encephalopathy (HIE) include the deep gray nuclei, cortex, and white matter, depending on the severity and duration of the insult.[8] In addition, the limbic system is involved in some patients, showing diffusion restriction on DWI, particularly in the hippocampal region.[9,10] Full-term neonates with perinatal asphyxia can exhibit hippocampal volume loss from childhood onward as a consequence of possible cytotoxic injury at the time of hypoxia-ischemia.[11] Developmental amnesia, a disorder primarily affecting episodic memory, typically occurs as a result of early-onset hypoxia-induced damage to the hippocampus.[12] However, the extent of hippocampal pathology does not always predict the severity of subsequent memory impairment.[13] Consistent with this finding, a recent study by Dzieciol et al[14]

Received April 17, 2019; accepted after revision August 8.

From the Departments of Radiology and Neonatology (M.M., L.S.d.V., F.G., M.L.), Wilhelmina Children's Hospital, University Medical Center Utrecht and Utrecht University, Utrecht, the Netherlands; and School of Psychology (S.D.V.), Cardiff University, Cardiff, UK.

S.D. Vann is funded by a Wellcome Trust Senior Research Fellowship in Biomedical Sciences (WT 12273/Z/18/Z).

Please address correspondence to Maarten Lequin, MD, Department of Radiology, Wilhelmina Children's Hospital, University Medical Center Utrecht and Utrecht University, Lundlaan 6, 3584 EA Utrecht, the Netherlands; e-mail: M.H.Lequin@umcutrecht.nl

Indicates open access to non-subscribers at www.ajnr.org

Indicates article with supplemental on-line table.

http://dx.doi.org/10.3174/ajnr.A6232

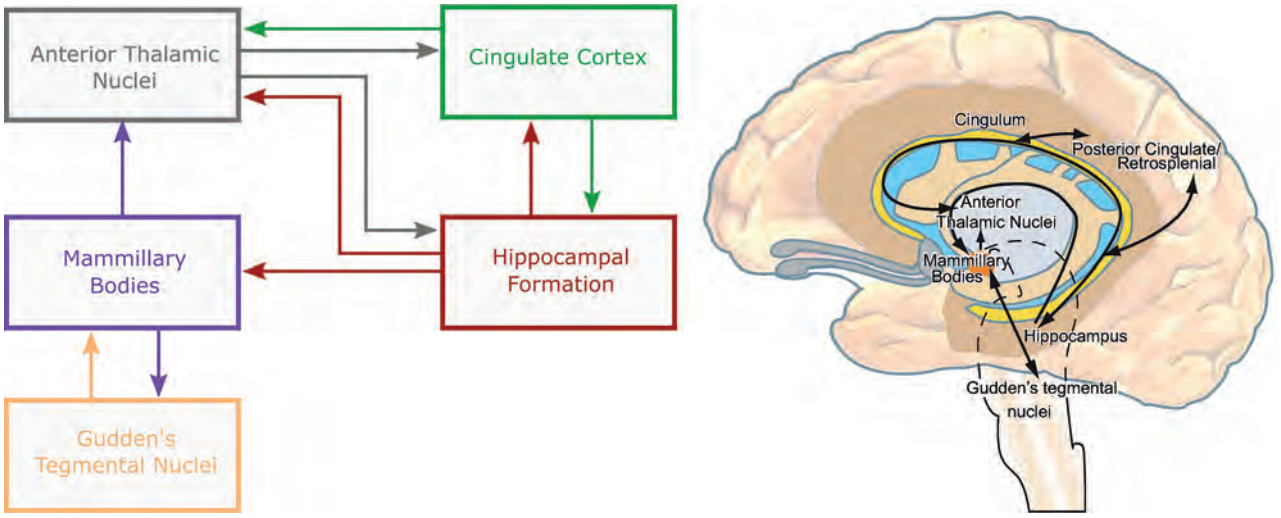

FIG 1. Schematic of the extended Papez system highlighting the principal connections of the mammillary bodies.

examined MR images of 18 patients with developmental amnesia (11–35 years of age) and uncovered a marked degree of atrophy in the MBs in two-thirds of the patients. However, because the MR images were acquired a number of years following the hypoxic-ischemic event, the authors were unable to conclude whether the MB atrophy was directly related to the hypoxic-ischemic episode or due to subsequent degeneration.[14,15]

The aim of the present study, therefore, was to examine whether the MBs are affected in infants with HIE. Given previous reports of MB sensitivity to hypoxia in adults,[16,17] we hypothesized that the MBs would be directly compromised in HIE in neonates with changes evident on MRIs acquired during the neonatal period. We assessed MR imaging signal change in the MBs of infants with perinatal asphyxia. The sample group included infants treated with therapeutic hypothermia and those who did not undergo hypothermia treatment. In infants with abnormal MB signal, the wider Papez circuit (eg, hippocampal formation, fornix, cingulate gyri, and the anterior thalamic nuclei; Fig 1) was also examined for abnormalities. When possible, follow-up MR images were evaluated to determine whether abnormal MB signal during the acute phase was associated with subsequent MB atrophy.

MATERIALS AND METHODS

Patients

In this retrospective, observational, single-center study, a total of 235 full-term neonates were enrolled, meeting the previously described clinical criteria of HIE[18] and having undergone brain MR imaging at the University Medical Center Utrecht, Wilhelmina Children's Hospital, during 2004–2017. The patients have been included in previous studies.[8,9,19-22] A waiver of informed consent was obtained, according to European regulations, because the present study involved the analysis of anonymized data.

The total group included 2 subsets. The first subset comprised 70 neonates, born between 2004 and January 2008, who did not receive therapeutic hypothermia. The second subset comprised 165 neonates, born between February 2008 and 2017, who were treated with whole-body hypothermia. Clinical data were retrieved from the patients' records.

MR Imaging Acquisition and Assessment

Cerebral MR imaging was performed within 3–10 days of birth (median, 6; interquartile range, 2), on days 3–9 (infants with normothermia), and days 5–10 (infants with hypothermia).[20,23] MR imaging protocols have been described previously.[19] Briefly, MR imaging was performed on a 1.5T or 3T MR imaging system (Achieva Philips Healthcare Best, the Netherlands). The scanning protocol included sagittal T1 before 2013 and sagittal T2-weighted imaging after 2013 (sagittal T2-weighted images were available for 64 patients). This was followed by axial T1-weighted and T2-weighted sequences with 2-mm section thickness. In addition, an echo-planar imaging technique was used for diffusion-weighted imaging, with axial 4-mm section thickness, 0-mm section gap, and b-values of 0 and 1000 s/mm^2 (1.5T) or b-values of 0 and 800 s/mm^2 (3T).

All MRIs were retrospectively screened, independently, by 2 radiologists (M.L. and M.M., with experience in reporting neonatal MRIs for 20 years and 3 years, respectively). The MBs were assessed for abnormal high signal on the T2-weighted images and/or abnormal signal on DWI (high signal on the trace maps and low signal on the ADC maps). Given the size and location of the MBs, it was important to reduce the likelihood of identifying artifactual signal due to partial volume effects. Therefore, an increased signal intensity had to be clearly visible over 2 consecutive T2-weighted slices. This increased signal intensity was then confirmed by subjectively assessing swelling in MBs and/or observing decreased signal intensity on T1-weighted images. All available sections and directions were evaluated. DWI was considered to have positive findings when signal changes (high signal on trace maps and low signal on ADC maps) were present over 2 consecutive slices. The section thickness in DWI sequences was 4 mm; therefore, they were more prone to artifactual signals. Thus, only infants with obvious signal changes on T2-weighted images were included (Fig 2). In addition to examining the MBs, images were examined for abnormal signal

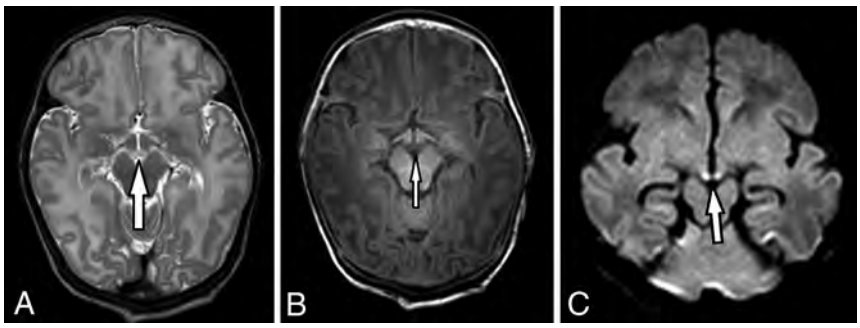

FIG 2. *Arrows* indicate the following: abnormally high-signal MBs on an axial T2-weighted image (*A*); abnormally low-signal MBs on an axial T1-weighted image (*B*); and abnormally high-signal MBs on DWI, b-value = 1000, accompanied by low ADC (not shown) (*C*).

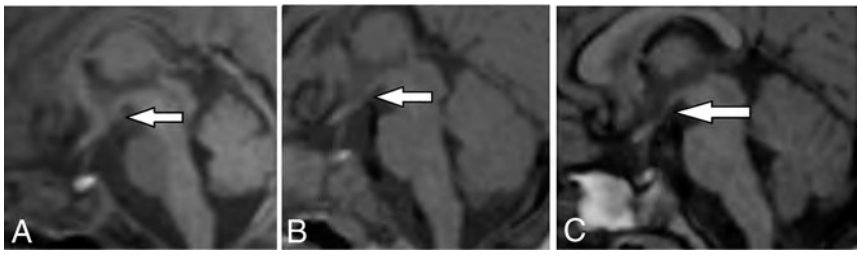

FIG 3. Sagittal T1-weighted MR imaging. The *arrows* indicate abnormal, low signal in MBs at 6 days (*A*) and MB atrophy at 3 (*B*) and 19 (*C*) months.

Table 1: General demographic and clinical findings of neonates with high MB signal on T2-weighted images

Cases with T2-Weighted High-Signal MB (*n* = 31)	
Sex, male/female	15:16
Gestational age (mean) (wk)	40 ± 2.0
Birth weight (mean) (kg)	3113 ± 556
Apgar 1 min (median) (IQR)	2 (3)
Apgar 5 min (median) (IQR)	5 (4)
Age at first MR imaging in days after birth (median) (IQR)	6 (2)
Field strength of MR imaging (1.5T/3T)	17/14
Grade of encephalopathy (Sarnat I/II/III)	4/25/2
Hypothermia (%)	18 (58)
Died (%)	4 (13)
Normal findings on clinical follow-up (%)	21 (68)
Abnormal findings on clinical follow-up (%)	5 (16)
Severe hyponatremia (<130 mEq/L) (%)	8 (26)
Systemic infection (%)	3 (10)

Note:—IQR indicates interquartile range.

intensity in other constituents of the extended Papez circuit (Fig 1):[24,25] hippocampi, fornices, anterior nuclei of the thalamus, and cingulate gyri. The tegmental nuclei in the brain stem were too small to assess due to a section thickness of 2 mm (T2) or more (DWI).

Nine patients underwent follow-up MR imaging: 8 at 3–19 months and 1 at 7.5 years. Two radiologists (M.L. and M.M.) independently assessed the scans for evidence of subjectively judged MB atrophy. The MBs were considered atrophic if there was a lack of protrusion clearly seen on sagittal sections (Fig 3). The hippocampi were also examined for signs of atrophy.

Neurodevelopmental Follow-Up

Clinical follow-up data were reviewed, when available, which focused on intelligence quotient (IQ) and motor and neurologic functions. The assessments provide a general evaluation of development but do not specifically measure memory. The tests administered were the following: Bayley Scales of Infant Development, Griffiths Mental Development Scales, Wechsler Preschool and Primary Scales of Intelligence, and Movement Assessment Battery for Children. Patients were tested with the Bayley Scales of Infant Development and Griffiths Mental Development Scales at 24 months and the Wechsler Preschool and Primary Scales of Intelligence and Movement Assessment Battery for Children test at 5 years.

Descriptive statistics were calculated using SPSS, Version 21 (IBM, Armonk, New York).

RESULTS

An increased T2-weighted signal was noted in the MBs in 31 of the 235 infants (13.2%) (Fig 2). Details of these patients are presented in Table 1. T2-weighted hyperintensity was observed in the MBs of 18 infants (10.9%) with therapeutic hypothermia and 13 infants (18.6%) without therapeutic hypothermia. Concomitant diffusion restriction was found in 6 of these infants (4 with therapeutic hypothermia and 2 without). The day of the MR imaging acquisition is shown in Fig 4; abnormal MB signal could be identified across imaging days 3–10.

In 13 (41.9%) of these 31 patients, the MR imaging findings appeared otherwise normal. The occurrence rates of common pathology patterns associated with hypoxia are summarized in Table 2. When additional damage was present, the watershed predominant pattern of damage occurred most commonly (in 29% of infants). Involvement of other structures within the Papez circuit is shown in Table 3; hippocampal involvement was the most common presentation, occurring in approximately one-third of infants.

Of the 31 patients, 8 patients had at least 1 follow-up MR scan ranging between 3 and 19 months after the first MR scan and 1 patient had follow-up MR imaging at 7.5 years. Clinical findings for patients with available follow-up MRIs are provided in Table 4. MB atrophy was observed in 8 of 9 infants with follow-up MR imaging (the On-line Table); hippocampal atrophy was present in 6 of these patients.

Clinical Follow-Up Results

Of the 31 identified neonates with abnormal MB signal, 4 died before discharge due to redirection of care because of severe brain injury or associated multiorgan failure. Most (n = 21) were assessed as "healthy" at early follow-up. Five patients had an

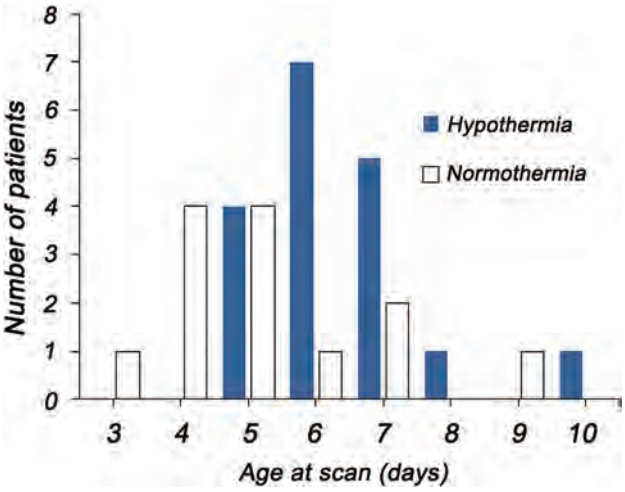

FIG 4. Day (postbirth) of initial MR imaging in patients with hypothermia treatment or without (normothermia). The day of scanning was typically days 5–7 for the hypothermia-treated patients, whereas there was a greater range of scanning days for patients with normothermia.

Table 2: MR imaging pattern of hypoxic-ischemic lesions

Pattern	
NL	13 (41.9%)
BGT	5 (16.1%)
WS	9 (29%)
NT	3 (9.7%)
Large subdural hematoma	1 (3.2%)
Total	31

Note:—NL indicates normal; BGT, basal ganglia and thalamus; WS, watershed; NT, near total.

Table 3: Involvement of additional structures within the Papez circuit

Additional Structures	
F	1
HC	4
AT	0
CG	1
AT/F	1
HC/F	7
More than 2 involved	4
None	13 (41.9%)
Total	31

Note:—F indicates fornix; HC, hippocampus; AT, anterior thalamus; CG, cingulate gyrus.

abnormal outcome. Three of these patients had a total IQ on the Wechsler Preschool and Primary Scales of Intelligence of <85 at 5 years. In one of these patients, this low IQ was associated with hearing loss and concentration problems. The fourth patient had cerebral visual impairment, though normal performance on IQ tests. One patient showed some behavioral problems but was otherwise healthy. The final patient was younger than 12 months, too young to be assessed.

DISCUSSION

Improvements in medical care have resulted in an increasing number of children surviving perinatal asphyxia. Therefore, there is a growing need to identify the sites of neuropathology following hypoxic-ischemic episodes in neonates and how this may contribute to subsequent cognitive impairments.

The present study focused on the MBs because atrophy in this region has been reported in an older group of patients who had a hypoxic-ischemic episode in childhood.[14] However, the suggestion from this earlier study was that MB atrophy was a result of degeneration following primary damage to the hippocampus or limbic cortex.[14] Contrary to this explanation, we found evidence of MR imaging signal change in the MBs of neonates with HIE with a T2 signal rise in 13% of patients with HIE. In 13/31 infants, the signal intensity abnormalities were seen only in the MBs, making them almost certain to be the site of primary injury. It is, therefore, possible to conclude that the MBs can be directly affected in HIE. Where signal change is observed in multiple regions, it is possible that the MB involvement is secondary. However, if this were the case, on the basis of known connectivity, the most likely site of primary pathology would be the hippocampal formation.[1] A study in rhesus monkeys found no abnormal MB signal 6 days following experimental hippocampal lesions,[26] again suggesting that in the timescale of the current study, the MB involvement is likely to be a primary effect. Together, the implication is that while secondary degeneration may cause additional pathology within the MBs at longer time periods, this structure is nonetheless sensitive to direct effects of hypoxic-ischemic episodes in neonates.

To the best of our knowledge, this is the first study to assess MB MR imaging signal changes in neonates with HIE. Therefore, the current findings add to the increasing body of literature from adult patients in whom there is antemortem and postmortem evidence of MB necrosis following severe HIE.[17,27] Reduced MB volume has also been reported in patients with obstructive sleep apnea[6] and those with heart failure,[28] again conditions linked to both acute and chronic hypoxia. The findings from both neonatal and adult patients further highlight the need to assess MB status in conditions with both acute and chronic low brain oxygen levels.

MB pathology is most commonly associated with, or exaggerated by, thiamine deficiency.[4,29-31] Thiamine is essential for intracellular metabolism and acts as a neuroprotective agent against oxidative stress. Reduced thiamine may exacerbate the effects of hypoxia on MBs and has been indicated as a possible contributing factor in a number of studies in which adult MB atrophy has been found following hypoxic-ischemic episodes.[6,17,27,28] However, thiamine deficiency is not a prerequisite for hypoxia-related MB atrophy in adults.[16] Furthermore, all patients in the present study were administered thiamine following birth; therefore, thiamine deficiency is unlikely to be a contributing factor to the increased signal intensity observed in the current cohort.

We also checked for signs of cerebritis, which may be a possible cause of MB signal rise and DWI restriction. No evidence of cerebral infection was found either on MR images or clinically, except in 3 patients with signs of a systemic infection. None of the 31 patients underwent a lumbar puncture, so a CNS infection cannot be ruled out completely. However, it seems unlikely, looking at the clinical outcome and, in some patients, follow-up MR imaging findings.

Surprisingly, we noticed MB involvement not only in patients with severe HIE but also in those with milder HIE. On the other hand, it was of interest that some infants with severe HIE did not show any MB abnormality on T2 or DWI series. These preliminary findings would suggest that MB involvement does not directly correspond to HIE severity. Furthermore, in some patients, the MB were the only structure that showed a signal change, again suggesting that this region has a different sensitivity to hypoxia than other brain structures. The duration and severity of the hypoxic-ischemic episode may be key determinants of the MBs sensitivity. For example, a short acute moment of hypoperfusion of the brain due to HIE-triggered cardiac malfunctioning may be sufficient to cause damage to the MBs. This could explain those patients with abnormal MB signal but otherwise normal MR imaging. The lack of MB pathology in some severely asphyxiated patients would, however, suggest some degree of neuroprotection in these patients, which needs to be investigated further.

Given the importance of the MBs for episodic memory,[32] it is likely that MB pathology in patients with HIE contributes to memory impairment that can be associated with this patient group. However, the concomitant hippocampal damage makes it difficult to attribute specific impairment to the MBs. In the current study, there were 13 patients (42%) in whom the initial scan showed MB signal rise without any visible signal changes of other structures within the Papez circuit. These patients would be of particular interest in terms of neuropsychological follow-up. While there are reports of localized MB infarcts causing amnesia in adults,[33,34] it is not known whether developmentally acquired MB damage would produce similar neuropsychological outcomes.

In 1 case, we noted an acute T2-weighted signal change in the MBs, but there was no observable atrophy on follow-up MR imaging. Unfortunately, long-term clinical follow-up was not available in this case. It is possible that the MBs were dysfunctional despite no obvious cell loss; alternatively, it is possible that there was some degree of neuroprotection against subsequent cell loss. Again, this case highlights the importance of assessing individual differences in response to HIE because this could prove critical in generating treatment that provides additional neuroprotection to those populations most at risk.

While 13% of examined cases were found to have signal change in the MBs, this is likely to be an underestimation of total occurrence. Given the size of the MBs, particularly in neonates, a 4-mm section thickness results in the MBs being poorly visualized.[3] Furthermore, the location of the MBs at the base of the brain can produce artifacts, which obscure imaging details. This problem was exacerbated further with the ADC maps, but in some patients, we noted low ADC signal at the MBs suggesting ischemia. This emphasizes the need to focus on the T2 sequence because in all 6 patients in whom the DWI was positive, the T2 imaging findings were also positive, but the reverse was not found to be true.

In summary, this study has shown that abnormal MB signal can be found in the acute period following HIE in neonates, and this abnormal signal appears an effective predictor of subsequent MB atrophy. The sensitivity for damage to the MBs does not seem to be directly related to the severity of hypoxia, as indicated by standard measures, and does not appear to be affected by treatment involving whole-body cooling. Given the importance of the MBs for memory, this further highlights the need to more closely examine this structure in patient groups with both HIE and other conditions associated with reduced brain oxygen levels.

Conclusions

This study highlights the need to carefully assess the MBs in neonates with HIE. For the most accurate assessment of the MBs, high-resolution images are needed using the thinnest slices possible (≤2 mm for the T2-weighted sequence). Furthermore, the use of a dedicated thin-section DWI sequence, adjusted for the skull base, would improve the accuracy of identifying MB involvement in this patient group. Repeated scanning for a range of days after birth could also be informative for identifying the time window most sensitive to MB signal change. With detailed clinical assessment and subsequent MR imaging and neurocognitive follow-up at school age, it may be possible to determine the consequences of early-onset MB pathology and identify those patients most at risk during the acute phase.

Disclosures: Seralynne D. Vann—*RELATED*: *Grant*: Wellcome Trust, *Comments*: My salary is supported by the Wellcome Trust by way of a Senior Research Fellowship*; *UNRELATED*: *Grants/Grants Pending*: Wellcome Trust, *Comments*: I am supported by a Wellcome Trust Fellowship.* *Money paid to the institution.

REFERENCES

1. Vann SD. **Re-evaluating the role of the mammillary bodies in memory.** *Neuropsychologia* 2010;48:2316–27 CrossRef Medline
2. Sziklas V, Petrides M. **Memory and the region of the mammillary bodies.** *Prog Neurobiol* 1998;54:55–70 CrossRef Medline
3. Vann SD, Aggleton JP. **The mammillary bodies: two memory systems in one?** *Nat Rev Neurosci* 2004;5:35–44 CrossRef Medline
4. Kopelman MD. **The Korsakoff syndrome.** *Br J Psychiatry* 1995; 166:154–73 CrossRef Medline
5. Tsivilis D, Vann SD, Denby C, et al. **A disproportionate role for the fornix and mammillary bodies in recall versus recognition memory.** *Nat Neurosci* 2008;11:834–42 CrossRef Medline
6. Kumar R, Birrer BVX, Macey PM, et al. **Reduced mammillary body volume in patients with obstructive sleep apnea.** *Neurosci Lett* 2008;438:330–34 CrossRef Medline
7. Bernstein HG, Krause S, Krell D, et al. **Strongly reduced number of parvalbumin-immunoreactive projection neurons in the mammillary bodies in schizophrenia: further evidence for limbic neuropathology.** *Ann N Y Acad Sci* 2007;1096:120–27 CrossRef Medline
8. de Vries LS, Groenendaal F. **Patterns of neonatal hypoxic-ischaemic brain injury.** *Neuroradiology* 2010;52:555–66 CrossRef Medline
9. Alderliesten T, Nikkels PG, Benders MJ, et al. **Antemortem cranial MRI compared with postmortem histopathologic examination of the brain in term infants with neonatal encephalopathy following perinatal asphyxia.** *Arch Dis Child Fetal Neonatal Ed* 2013;98:F304–09 CrossRef Medline
10. Kasdorf E, Engel M, Heier L, et al. **Therapeutic hypothermia in neonates and selective hippocampal injury on diffusion-weighted magnetic resonance imaging.** *Pediatr Neurol* 2014;51:104–08 CrossRef Medline
11. Maneru C, Serra-Grabulosa JM, Junque C, et al. **Residual hippocampal atrophy in asphyxiated term neonates.** *J Neuroimaging* 2003; 13:68–74 CrossRef Medline
12. Gadian DG, Aicardi J, Watkins KE, et al. **Developmental amnesia associated with early hypoxic-ischaemic injury.** *Brain* 2000;123(Pt 3):499–507 CrossRef Medline

13. Cooper JM, Gadian DG, Jentschke S, et al. **Neonatal hypoxia, hippocampal atrophy, and memory impairment: evidence of a causal sequence.** *Cereb Cortex* 2015;25:1469–76 CrossRef Medline
14. Dzieciol AM, Bachevalier J, Saleem KS, et al. **Hippocampal and diencephalic pathology in developmental amnesia.** *Cortex* 2017;86:33–44 CrossRef Medline
15. Loftus M, Knight RT, Amaral DG. **An analysis of atrophy in the medial mammillary nucleus following hippocampal and fornix lesions in humans and nonhuman primates.** *Exp Neurol* 2000;163:180–190 CrossRef Medline
16. Johkura K, Naito M. **Wernicke's encephalopathy-like lesions in global cerebral hypoxia.** *J Clin Neurosci* 2008;15:318–319 CrossRef Medline
17. Schmidtke K. **Wernicke-Korsakoff syndrome following attempted hanging.** *Rev Neurol (Paris)* 1993;149:213–16 Medline
18. Cowan F, Rutherford M, Groenendaal F, et al. **Origin and timing of brain lesions in term infants with neonatal encephalopathy.** *Lancet* 2003;361:736–42 CrossRef Medline
19. Alderliesten T, de Vries LS, Benders MJ, et al. **MR imaging and outcome of term neonates with perinatal asphyxia: value of diffusion-weighted MR imaging and ^{1}H MR spectroscopy.** *Radiology* 2011;261:235–42 CrossRef Medline
20. Alderliesten T, de Vries LS, Staats L, et al. **MRI and spectroscopy in (near) term neonates with perinatal asphyxia and therapeutic hypothermia.** *Arch Dis Child Fetal Neonatal Ed* 2017;102:F147–52 CrossRef Medline
21. Alderliesten T, de Vries LS, Khalil Y, et al. **Therapeutic hypothermia modifies perinatal asphyxia-induced changes of the corpus callosum and outcome in neonates.** *PLoS One* 2015;10:e0123230 CrossRef
22. Weeke LC, Groenendaal F, Mudigonda K, et al. **A novel magnetic resonance imaging score predicts neurodevelopmental outcome after perinatal asphyxia and therapeutic hypothermia.** *J Pediatrics* 2018;192:33–40.e2 CrossRef Medline
23. Bednarek N, Mathur A, Inder T, et al. **Impact of therapeutic hypothermia on MRI diffusion changes in neonatal encephalopathy.** *Neurology* 2012;78:1420–27 CrossRef Medline
24. Papez JW. **A proposed mechanism of emotion.** *Archives of Neurology and Psychiatry* 1937;38:725–43 CrossRef
25. Vann SD, Nelson AJ. **The mammillary bodies and memory: more than a hippocampal relay.** *Prog Brain Res* 2015;219:163–85 CrossRef Medline
26. Froudist-Walsh S, Browning PGF, Croxson PL, et al. **The rhesus monkey hippocampus critically contributes to scene memory retrieval, but not new learning.** *J Neurosci* 2018;38:7800–08 CrossRef Medline
27. Vortmeyer AO, Hagel C, Laas R. **Hypoxia-ischemia and thiamine deficiency.** *Clin Neuropathol* 1993;12:184–90 Medline
28. Kumar R, Woo MA, Birrer BVX, et al. **Mammillary bodies and fornix fibers are injured in heart failure.** *Neurobiol Dis* 2009;33:236–42 CrossRef Medline
29. Beh SC, Frohman TC, Frohman EM. **Isolated mammillary body involvement on MRI in Wernicke's encephalopathy.** *J Neurol Sci* 2013;334:172–75 CrossRef Medline
30. Kornreich L, Bron-Harlev E, Hoffmann C, et al. **Thiamine deficiency in infants: MR findings in the brain.** *AJNR Am J Neuroradiol* 2005;26:1668–74 Medline
31. Zuccoli G, Siddiqui N, Bailey A, et al. **Neuroimaging findings in pediatric Wernicke encephalopathy: a review.** *Neuroradiology* 2010;52:523–29 CrossRef Medline
32. Dillingham CM, Milczarek MM, Perry JC, et al. **Mammillothalamic disconnection alters hippocampo-cortical oscillatory activity and microstructure: implications for diencephalic amnesia.** *J Neurosci* 2019;39:6696–6713 CrossRef Medline
33. Amuluru K, Filippi CG, Lignelli A. **Acute amnesia due to isolated mammillary body infarct.** *J Stroke Cerebrovasc Dis* 2015;24:e303–05 CrossRef Medline
34. Male S, Zand R. **Isolated mammillary body infarct causing global amnesia: a case report.** *J Stroke Cerebrovasc Dis* 2017;26:e50–52 CrossRef Medline
35. Denby CE, Vann SD, Tsivilis D, et al. **The frequency and extent of mammillary body atrophy associated with surgical removal of a colloid cyst.** *AJNR Am J Neuroradiol* 2009;30:736–43 CrossRef Medline

Biometry of the Cerebellar Vermis and Brain Stem in Children: MR Imaging Reference Data from Measurements in 718 Children

C. Jandeaux, G. Kuchcinski, C. Ternynck, A. Riquet, X. Leclerc, J.-P. Pruvo, and G. Soto-Ares

ABSTRACT

BACKGROUND AND PURPOSE: Objective and quantitative data to define cerebellar vermis and/or brain stem hypoplasia in children are lacking. Our aim was to provide MR imaging biometric references for the cerebellar vermis and brain stem from a large cohort of children with normal cerebellums.

MATERIALS AND METHODS: The MR imaging data were retrospectively selected from our hospital data base from January 1, 2014, to December 31, 2017. All MR imaging examinations of children between 1 day and 15 years of age, including midline sagittal sections, were included. Children with a clinical history or MR imaging abnormalities that may affect the posterior fossa were excluded. We manually measured four 2D parameters: vermian height, anterior-posterior diameter of the vermis, anterior-posterior diameter of the midbrain-pons junction, and anterior-posterior midpons diameter. The inter- and intraobserver agreement was evaluated.

RESULTS: Seven hundred eighteen children were included (372 boys and 346 girls), from 1 day to 15 years of age. Normal values (third to 97th percentiles) were provided for each parameter. The vermis parameters showed a rapid growth phase during the first year, a slower growth until the fifth year, and finally a near-plateau phase. The brain stem parameters showed more progressive growth. The intra- and interobserver agreement was excellent for all parameters.

CONCLUSIONS: We provide reference biometric data of the vermis and the brain stem using simple and reproducible measurements that are easy to use in daily practice. The relevance of these 2D measurements should be further validated in diseases associated with cerebellar abnormalities.

ABBREVIATIONS: APD-MP = anterior-posterior diameter at the midbrain-pons junction; APD-P = anterior-posterior midpons diameter; APD-V = anterior-posterior diameter of vermis; H-V = vermian height; ICC = intraclass correlation coefficient

The important role of the cerebellum in nonmotor functions has been confirmed in recent studies performed in healthy subjects.[1,2] In this setting, the diagnosis of cerebellar hypoplasia is essential, particularly in children with mental retardation in whom impairment in cerebellar cognitive functions is frequently observed.[3] Cerebellar hypoplasia has been further associated with impairment in reasoning, spatial recognition, language, timing of the speech, and disorders of personality.[4-6]

Even if different methods of volumetry and segmentation have already been reported in the literature,[7-9] the interpretation of the vermis as normal or pathologic in daily routine is only based on subjective criteria. Because morphologic variations and changes occur throughout infancy, this subjective approach may be inappropriate to state the normality of the vermis or to claim the diagnosis of vermian hypoplasia, which is defined as a small, harmonious vermis with fissures of normal width.[10] Pons hypoplasia has been also described in association with vermis abnormalities in specific syndromes such as pontocerebellar hypoplasia.[11]

To our knowledge, no reference data have been published that can be easily used in daily practice to define vermis or pons hypoplasia. The aim of our study was to provide reference biometric data of the vermis and brain stem from a large cohort of children with normal cerebellums and brain stems to increase the accuracy of MR imaging for the diagnosis of vermis and/or pons hypoplasia.

Received June 4, 2019; accepted after revision August 21.

From the Departments of Neuroradiology (C.J., G.K., X.L., J.-P.P., G.S.-A.), Biostatistics and Epidemiology (C.T.), and Neuropediatrics (A.R.), Centre Hospitalier Universitaire Lille, Lille, France.

Please address correspondence to Gustavo Soto-Ares, MD, PhD, CHU Lille, Department of Neuroradiology, Rue Emile Laine, F-59000 Lille, France; e-mail: gustavo.sotoares@chru-lille.fr

Indicates article with supplemental on-line appendix and tables.

Indicates article with supplemental on-line photos.

http://dx.doi.org/10.3174/ajnr.A6257

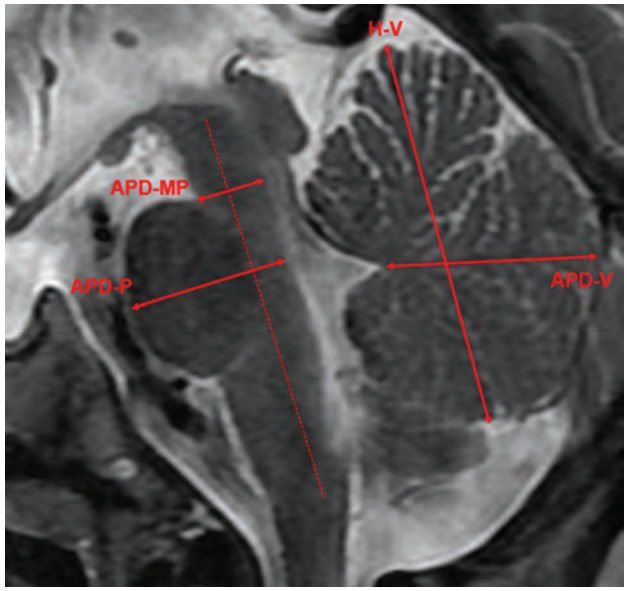

FIG 1. Illustration of the 2D measurements of the cerebellar vermis and the brain stem. H-V indicates the largest craniocaudal diameter of the vermis; APD-V, the largest anterior-posterior diameter of the vermis passing through the tip of the V4; APD-MP, perpendicular to the major axis of the brain stem passing through the midbrain-pons junction; APD-P, perpendicular to the major axis of the brain stem passing through the middle of the pons.

MATERIALS AND METHODS

Population

The protocol has been approved by our institutional review board. Given the retrospective nature of the study, informed consent from the parents was not required. The MR imaging data were nonconsecutive cases selected retrospectively from our hospital data base from January 1, 2014, to December 31, 2017.

MR imaging examinations of children between 1 day and 15 years of age, including midline sagittal sections from 2D or 3D T1- or T2-weighted sequences, were included. All children in the present study had no self- or parent-reported clinical history of cognitive disorders or mental illness that could have a potential impact on the cognitive status and cerebellum alteration. We also excluded all patients with a history or symptoms that may be responsible for or associated with cerebellar abnormalities: prematurity (birth at <37 weeks of amenorrhea according to the World Health Organization), metabolic disorder, neuropsychological disorder, hypoxic pathology, cerebellar syndrome, autistic syndrome, axial hypotonia, delayed acquisition, posterior fossa pathology, and posterior fossa or midline malformation. All MR images were reviewed by a board-certified pediatric neuroradiologist to ensure that there were no posterior fossa abnormalities. Mass effect, signal abnormalities, vermian or pons hypoplasia, atrophy, and other midline malformations were sought, and if present, the corresponding data were excluded. The MR imaging data that did not allow precise measurements because of unsatisfactory quality were also excluded.

MR Imaging Analysis

All acquisitions were performed on a 1.5T MR imaging scanner (Ingenia; Philips Healthcare, Best, the Netherlands). Midline sagittal sections were obtained from 2D sagittal T1- or T2-weighted sequences or reconstructed from 3D T1-weighted sequences (section thickness, ≤3 mm).

Table 1: Distribution of the study population by age and sex (*n* = 718)

Age Class (yr)	Boys (*n* = 372)	Girls (*n* = 346)	All (*n* = 718)
Younger than 1	58	56	114
1–2	37	32	69
2–3	39	28	67
3–4	31	22	53
4–5	27	23	50
5–6	20	21	41
6–7	30	18	48
7–8	17	17	34
8–9	9	16	25
9–10	16	12	28
10–11	10	12	22
11–12	11	14	25
12–13	11	18	29
13–14	13	20	33
14–15	17	19	36
15–16	26	18	44

All measurements were performed by a board-certified neuroradiologist. Simple 2D measurements were manually performed on a sagittal section passing through the midsagittal plane and were defined as follows: 1) The height of the vermis (H-V) was the largest craniocaudal diameter of the vermis; 2) the anterior-posterior diameter of the vermis (APD-V) was the largest anterior-posterior diameter of the vermis passing through the tip of the V4; 3) the anterior-posterior diameter of the midbrain-pons junction (APD-MP) was measured perpendicular to the major axis of the brain stem passing through the midbrain-pons junction; and 4) the anterior-posterior midpons diameter (APD-P) was measured perpendicular to the major axis of the brain stem passing through the middle of the pons (Fig 1).

To evaluate the interobserver reproducibility, a second senior neuroradiologist performed the measurements independently on a sample of 50 children randomly selected. Each radiologist was unaware of the results obtained by the other one. Moreover, to evaluate the intraobserver reproducibility, the first reader repeated the measurements on the same sample after 1 month.

Statistical Analysis

We first assessed the intra- and interobserver reproducibility of measurements of the cerebellar vermis by calculating the intraclass correlation coefficient (ICC) and using the Bland-Altman method on a random sample of 50 patients. The ICCs were estimated using a 2-way random-effects model (absolute agreement), and 95% confidence intervals were obtained using bootstrap methods (2000 bootstrap samples). ICC values <0.5, between 0.5 and 0.75, between 0.75 and 0.9, and >0.90 were interpreted as poor, moderate, good, and excellent reproducibility.[12] According to the Bland Altman method,[13] we calculated the mean bias as well as the limits of agreement between readers. The remaining data analyses were performed on the overall study sample to provide age-specific reference intervals ("normal ranges") for each

Table 2: Indications for brain MR imaging in the study population ($n = 718$)

Diseases	Prevalence
Epilepsy	123 (17.2%)
Supratentorial, suprasellar, or optic tumors	65 (9%)
Ocular globe pathology	56 (7.7%)
Suspicion of pituitary lesion (staturo-pondéral growth retardation, obesity, and so forth)	55 (7.6%)
Encephalitis, mastoiditis, meningitis, endocarditis, otitis, or empyema	52 (7.3%)
Extracerebral tumor or histiocytosis or blood disease	40 (5.6%)
Cranial trauma	37 (5.2%)
Spinal or medullary pathology, scoliosis, low back pain	36 (5%)
Supratentorial benign lesion (arachnoid cyst, pineal cyst, interhemispheric cyst, and so forth)	32 (4.4%)
Extracerebral or supratentorial vascular malformation	28 (3.9%)
Extracerebral venous-lymphatic malformation	26 (3.6%)
Isolated cervicofacial pathology (cervical mass, velar insufficiency, and so forth)	21 (2.9%)
Cyst or nasal root mass	19 (2.6%)
Headache	15 (2.1%)
Deafness	10 (1.4%)
Others	103 (14.5%)

Table 3: Equation for estimating reference values for the different parameters[a]

	Equations
H-V girls	$\mu = 443\ 574.11 - 97\ 540.24\sqrt{X} - 231\ 497.89X^3$ $\sigma = 104\ 925.72 - 37\ 776.52X$
H-V boys	$\mu = 707\ 969.47 - 45\ 502.94 \log X - 538\ 257.55X^3$ $\sigma = 200\ 387.18 - 82\ 416.42X$
APD-V girls	$\mu = 585.75 - 336.12X^3$ $\sigma = 121.27$
APD-V boys	$\mu = 1\,083.91 - 689.41X^3$ $\sigma = 226.61$
APD-P girls	$\mu = 38.13 - 2 \log X - 10.21X^3$ $\sigma = 4.09$
APD-P boys	$\mu = 83.63 - 6.40 \log X - 31.23X^3$ $\sigma = 12.09 - 4.71X$
APD-MP	$\mu = 5.98 + 0.053X^{-0.05} - 1.31X$ $\sigma = 0.48$

[a] With $X = \exp\left\{\frac{T-T_1}{T_n-T_1}\log\rho\right\}$, where T denotes the age, T_1 and T_n denote minimum and maximum ages, respectively, and ρ is a preselected constant for which a suitable value is .01. All measurements needed prior Box-Cox transformation. The values of APD-MP were similar in both sexes.

measurement of the cerebellar vermis. To appreciate the shape of the relationship between age and each measurement of interest and to investigate the necessity to provide age-specific reference intervals by sex, we used a nonparametric smoothing technique (LOESS regression). Age-specific reference intervals for each measurement of interest were constructed from the parametric method proposed by Royston and Wright,[14] providing smooth centile curves and explicit formulae for the centile estimates. This method has been previously applied to provide reference biometric data of the corpus callosum in MR imaging in children[15] and is one of the methods recommended by the World Health Organization Multicenter Growth Reference Study Group. Further details about this method are available in the On-line Appendix. All analyses were computed using R statistical and computing software, Version 3.4.3 (http://www.r-project.org/).

RESULTS

We included 718 children (372 boys and 346 girls), from 6 days to 15 years of age. The distribution of the number of children as a function of age and sex is described in Table 1. Table 2 shows the indications of MR imaging for the children included in the study. Measurements were performed on T2 images in 331 children and on T1 images in 387. The average time to complete the 4 measurements was 1 minute.

The 7 models built were normal, and the 7 measurements needed prior Box-Cox transformation. The equations for estimating the reference values for the different parameters are presented in Table 3. Smoothing curves of the different parameters are depicted in Fig 2. For each parameter, reference values (from the third, median, and 97th percentiles) are depicted in Fig 3 and summarized in On-line Table 1. Model adequacy was satisfied for all models (On-line Figs 1 and 2). The curves showed similar growth in girls and boys. Vermis parameters (H-V, APD-V) showed a very rapid growth phase during the first year, then a slower growth until the fourth year, and finally a near-plateau phase. Brain stem parameters showed a different growth pattern, more progressive, with relatively rapid growth during the first 4 years and then slower thereafter. The values of these parameters were higher in boys except for APD-MP, which demonstrated similar values in both sexes. As shown in Table 4, the intraobserver agreement was excellent for each parameter, with an ICC ranging from 0.916 to 0. 994. The interobserver agreement was good to excellent, with an ICC ranging from 0.846 for APD-P to 0.981 for H-V. Intra- and interobserver agreement did not significantly differ for measurements performed on T1 or T2 images (On-line Table 2).

DISCUSSION

Our study used a simple method, easily reproducible in daily practice in a large cohort of children with normal vermes and brain stems. Findings showed an important growth of the vermian parameters during the first year, while the brain stem

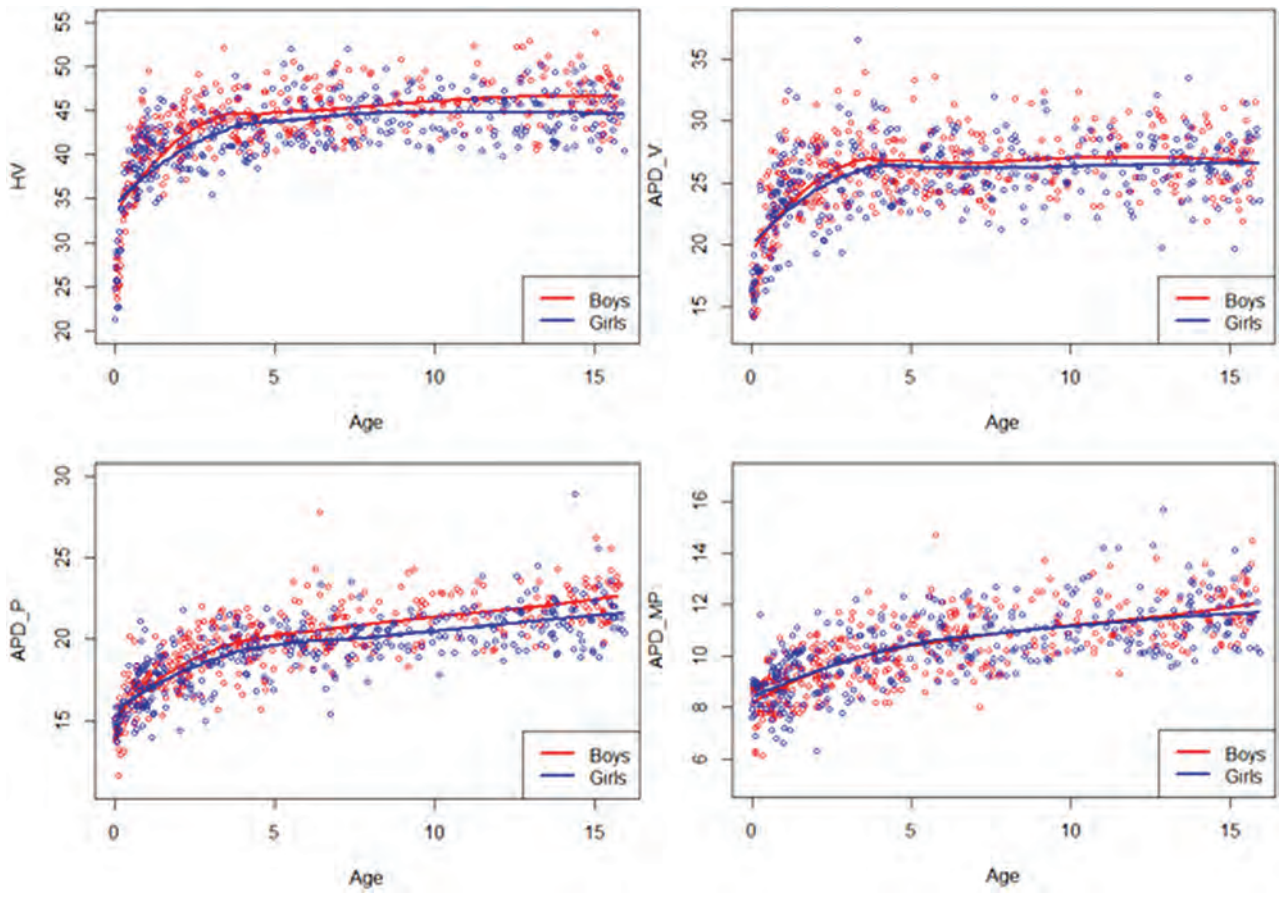

FIG 2. Smoothed curves of the different parameters (H-V, APD-V, APD-P, APD-MP) by age and sex.

parameters grew gradually. The values of these parameters were higher in boys except for APD-MP, for which the values were similar in both sexes.

To our knowledge, this is the first reference biometric data for the vermis and the brain stem in children. Previous studies assessed normal MR imaging biometric data of the posterior fossa in the fetus,[7,16-18] and quantitative methods have already been used to diagnose vermis hypoplasia, but no MR imaging biometric data of the normal cerebellum and brain stem have been reported before. Makris et al[9] described a surface-based parcellation of the human cerebellar cortex and provide cerebellar surface and volumetry from 10 volunteer subjects with a good-to-excellent reproducibility. This method integrated automated and semiautomated and manual procedures using postprocessing software. Joyal et al[19] suggested measuring the area of the vermis from a single midsagittal section, but reproducibility has not been studied. In addition, both studies were performed in the adult population, and their methodology is not easy to apply in daily practice. Our 2D measurements have the advantage of being highly reproducible, easy, and fast to perform. An interactive tool derived from the biometric models has been created and is available on-line (http://ci2c.fr/vermis.php) to facilitate its application.

Data about the growth of the cerebellum during childhood are scarce. During fetal life, the cerebellum has a long period of development that makes it particularly vulnerable to prenatal disorders, including genetic or metabolic diseases, toxins, or infections.[20-22] In early stages, perturbations of the expression of genes involved in cerebellar patterning or abnormal proliferation and migration produce a wide spectrum of abnormal phenotypes from agenesis to minor abnormalities such as hypoplasia or abnormal cerebellar foliation. The fastest development is observed for the vermis and the cerebellum in comparison with other brain structures in the third trimester of pregnancy.[17] Their growth is multiplied by 2 between the 20th and the 35th week of development.[23] As the proliferation and migration of granular cells continue during the first postnatal months, the last granular cell migration occurs in humans at about 18 months of age. In line with previous studies suggesting further proliferation and neuronal migration in the cerebellum during the postnatal period,[20,24,25] our data show the persistence of a rapid growth of the vermis during the first year of life.

Cerebellar hypoplasia has been described in many conditions associated with mental retardation.[3-5,26] In this setting, morphologic variations may disclose underlying structural and functional impairment of cerebellar structures potentially involved in cognitive functions. Advanced MR imaging techniques such as DTI-based tractography have emphasized the anatomic relationship between the cerebellum and the other structures of the central nervous system involved in nonmotor functions,[27] especially dentato-thalamo-cortical fibers and fibers connecting the cerebellum to visuospatial, cognitive, and memory-related areas, in healthy

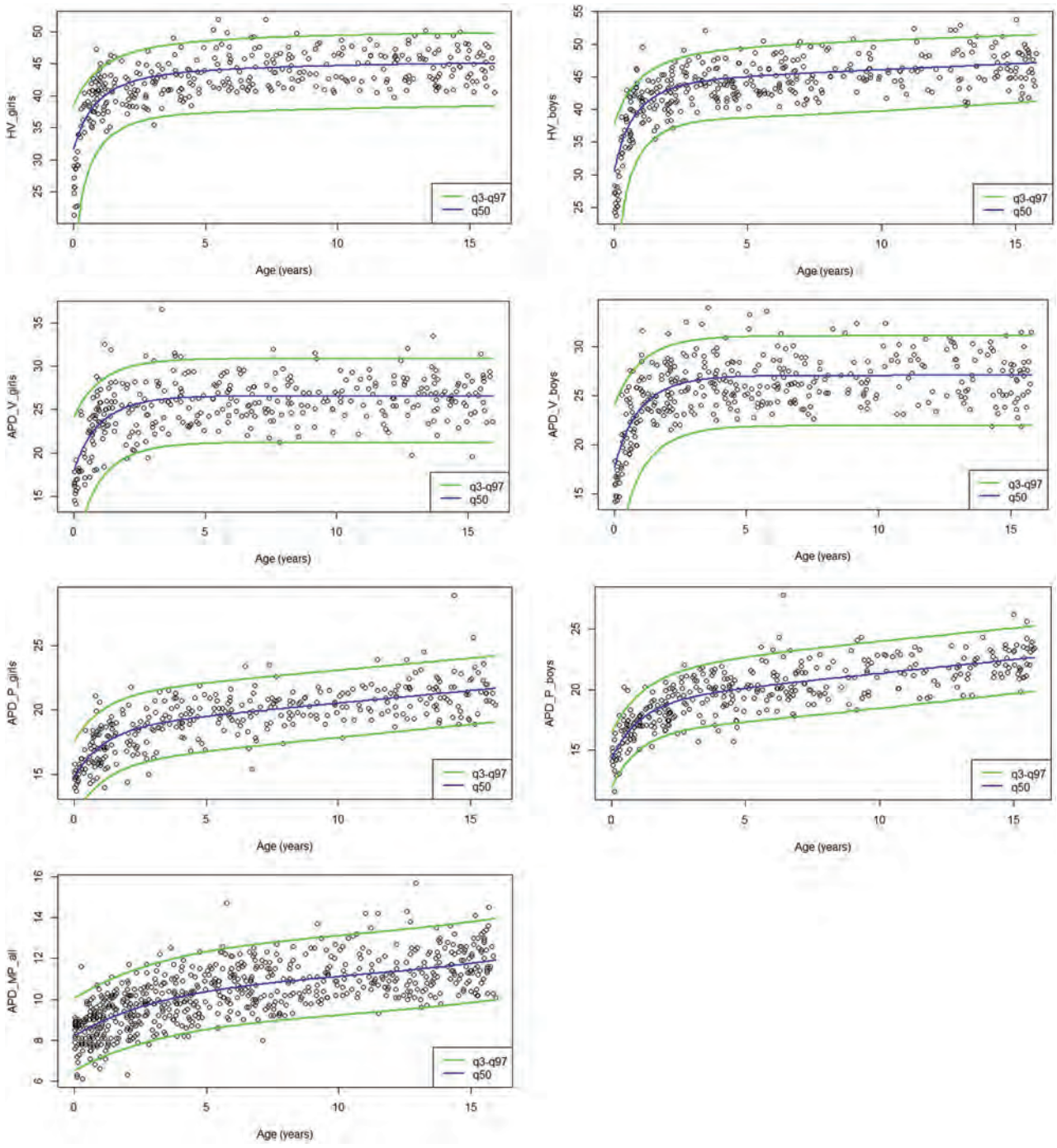

FIG 3. Reference intervals (third, 50th, 97th) for the different parameters (H-V, APD-V, APD-P, APD-MP). The values of APD-MP are similar in both sexes.

Table 4: Inter- and intraobserver agreement for cerebellar vermis and brain stem parameters

	Intraobserver Agreement			Interobserver Agreement		
Parameter	Mean Bias	95% Limits of Agreement	ICC (95% CI)	Mean Bias	95% Limits of Agreement	ICC (95% CI)
H-V	0.156	0.869, 1.181	0.994 (0.982–0.998)	–0.302	–2.129, 1.525	0.981 (0.948–0.991)
APD-V	0.332	1.831, 2.494	0.941 (0.878–0.970)	0.242	–2.851, 3.335	0.893 (0.799–0.948)
APD-P	0.100	–1.161, 1.361	0.916 (0.854–0.953)	0.088	1.704, 1.880	0.846 (0.674–0.944)
APD-MP	0.052	–0.729, 0.833	0.988 (0.978–0.994)	0.188	–1.238, 1.614	0.959 (0.918–0.978)

subjects.[27-29] Furthermore, in children with cerebellar hypoplasia, impairment of cerebellar white matter tracts has been observed in preliminary studies.[30] These structural data have been strengthened by functional MR imaging studies exploring the anatomofunctional segmentation of the cerebellum.[1] These studies highlighted a limbic area corresponding to lobules VI and VII,[31] left lateralization of the activation on visuospatial tasks, right activation in linguistic and working memory tasks,[2] and activation of the anterior lobes in language articulation, whereas the posterior lobules were activated in silent langage.[32]

Our study has some limitations. First, our study population consisted of nonconsecutive cases examined retrospectively. We acknowledge that while effort was made to exclude children with posterior fossa abnormalities, we included children with pathologies that could potentially affect the cerebellum despite a macroscopically normal appearance on MR imaging. For children older than 6 years of age, our results should be confirmed by larger trials imaging strictly healthy children. Although measurements have been performed on different MR images, this feature did not significantly affect their reliability. Finally, our global measurements do not allow detecting a focal cerebellar hypoplasia involving a single lobe or lobule. Further studies are necessary to confirm the accuracy of our biometric data when applied to the evaluation of children with vermian hypoplasia and other posterior fossa abnormalities.

CONCLUSIONS

We provide reference biometric data of the vermis and the brain stem using simple and reproducible measurements that are easy to use in daily practice. Our results show a more important growth of the vermian parameters during the first year of life, while the brain stem parameters grow gradually. The relevance of these 2D measurements should be further validated in diseases associated with cerebellar abnormalities responsible for developmental disorders of so-called higher cerebellar functions.

REFERENCES

1. Klein AP, Ulmer JL, Quinet SA, et al. **Nonmotor functions of the cerebellum: an introduction.** *AJNR Am J Neuroradiol* 2016;37:1005–09 CrossRef Medline
2. Timmann D, Drepper J, Frings M, et al. **The human cerebellum contributes to motor, emotional and cognitive associative learning: a review.** *Cortex* 2010;46:845–57 CrossRef Medline
3. Soto-Ares G, Joyes B, Lemaître MP, et al. **MRI in children with mental retardation.** *Pediatr Radiol* 2003;33:334–45 CrossRef Medline
4. Schmahmann JD, Sherman JC. **The cerebellar cognitive affective syndrome.** *Brain* 1998;121:561–79 CrossRef Medline
5. Cotes C, Bonfante E, Lazor J, et al. **Congenital basis of posterior fossa anomalies.** *Neuroradiol J* 2015;28:238–53 CrossRef Medline
6. Shevell MI, Majnemer A. **Clinical features of developmental disability associated with cerebellar hypoplasia.** *Pediatr Neurol* 1996; 15:224–29 CrossRef Medline
7. Kyriakopoulou V, Vatansever D, Davidson A, et al. **Normative biometry of the fetal brain using magnetic resonance imaging.** *Brain Struct Funct* 2017;222:2295–307 CrossRef Medline
8. Ber R, Hoffman D, Hoffman C, et al. **Volume of structures in the fetal brain measured with a new semiautomated method.** *AJNR Am J Neuroradiol* 2017;38:2193–98 CrossRef Medline
9. Makris N, Schlerf JE, Hodge SM, et al. **MRI-based surface-assisted parcellation of human cerebellar cortex: an anatomically specified method with estimate of reliability.** *Neuroimage* 2005;25:1146–60 CrossRef Medline
10. Adamsbaum C, Merzoug V, André C, et al. **Imaging of the pediatric cerebellum [in French].** *J Neuroradiol* 2003;30:158–71 Medline
11. Namavar Y, Barth PG, Poll-The BT, et al. **Classification, diagnosis and potential mechanisms in pontocerebellar hypoplasia.** *Orphanet J Rare Dis* 2011;6:50 CrossRef Medline
12. Koo TK, Li MY. **A guideline of selecting and reporting intraclass correlation coefficients for reliability research.** *J Chiropr Med* 2016;15:155–63 CrossRef Medline
13. Bland JM, Altman DG. **Statistical methods for assessing agreement between two methods of clinical measurement.** *Lancet* 1986;1:307–10 Medline
14. Royston P, Wright E. **A method for estimating age-specific reference intervals ('normal ranges') based on fractional polynomials and exponential transformation.** *Journal of the Royal Statistical Society Series A (Statistics in Society)* 2002;161:79–101 CrossRef
15. Garel C, Cont I, Alberti C, et al. **Biometry of the corpus callosum in children: MR imaging reference data.** *AJNR Am J Neuroradiol* 2011;32:1436–43 CrossRef Medline
16. Saleem SN. **Fetal magnetic resonance imaging (MRI): a tool for a better understanding of normal and abnormal brain development.** *J Child Neurol* 2013;28:890–908 CrossRef Medline
17. Chang CH, Chang FM, Yu CH, et al. **Assessment of fetal cerebellar volume using three-dimensional ultrasound.** *Ultrasound Med Biol* 2000;26:981–88 CrossRef Medline
18. Ber R, Bar-Yosef O, Hoffmann C, et al. **Normal fetal posterior fossa in MR imaging: new biometric data and possible clinical significance.** *AJNR Am J Neuroradiol* 2015;36:795–802 CrossRef Medline
19. Joyal CC, Pennanen C, Tiihonen E, et al. **MRI volumetry of the vermis and the cerebellar hemispheres in men with schizophrenia.** *Psychiatry Res* 2004;131:115–24 CrossRef Medline
20. Ten Donkelaar HJ, Lammens M. **Development of the human cerebellum and its disorders.** *Clin Perinatol* 2009;36:513–30 CrossRef Medline
21. Basson MA, Wingate RJ. **Congenital hypoplasia of the cerebellum: developmental causes and behavioral consequences.** *Front Neuroanat* 2013;7:29 CrossRef Medline
22. Bosemani T, Poretti A. **Cerebellar disruptions and neurodevelopmental disabilities.** *Semin Fetal Neonatal Med* 2016;21:339–48 CrossRef Medline
23. Cignini P, Giorlandino M, Brutti P, et al. **Reference charts for fetal cerebellar vermis height: a prospective cross-sectional study of 10605 fetuses.** *PLoS One* 2016;11:e0147528 CrossRef Medline
24. Garel C, Fallet-Bianco C, Guibaud L. **The fetal cerebellum: development and common malformations.** *J Child Neurol* 2011;26:1483–92 CrossRef Medline
25. Chédotal A. **Should I stay or should I go? Becoming a granule cell.** *Trends Neurosci* 2010;33:163–72 CrossRef Medline
26. Berthel-Tatray MC. **Le syndrome cognitivo-affectif du cervelet.** *Rev Neurol (Paris)* 2017;173:S184 CrossRef
27. Granziera C, Schmahmann JD, Hadjikhani N, et al. **Diffusion spectrum imaging shows the structural basis of functional cerebellar circuits in the human cerebellum in vivo.** *PLoS One* 2009;4:e510v CrossRef Medline
28. Habas C, Cabanis EA. **Cortical projection to the human red nucleus: complementary results with probabilistic tractography at 3 T.** *Neuroradiology* 2007;49:777–84 CrossRef Medline

29. Jissendi P, Baudry S, Balériaux D. **Diffusion tensor imaging (DTI) and tractography of the cerebellar projections to prefrontal and posterior parietal cortices: a study at 3T.** *J Neuroradiol* 2008;35:42–50 CrossRef Medline
30. Fiori S, Poretti A, Pannek K, et al. **Diffusion tractography biomarkers of pediatric cerebellar hypoplasia/atrophy: preliminary results using constrained spherical deconvolution.** *AJNR Am J Neuroradiol* 2016;37:917–23 CrossRef Medline
31. Baumann O, Mattingley JB. **Functional topography of primary emotion processing in the human cerebellum.** *Neuroimage* 2012; 61:805–11 CrossRef Medline
32. Méndez Orellana C, Visch-Brink E, Vernooij M, et al. **Crossed cerebrocerebellar language lateralization: an additional diagnostic feature for assessing atypical language representation in presurgical functional MR imaging.** *AJNR Am J Neuroradiol* 2015;36:518–24 CrossRef Medline

Comparison of CBF Measured with Combined Velocity-Selective Arterial Spin-Labeling and Pulsed Arterial Spin-Labeling to Blood Flow Patterns Assessed by Conventional Angiography in Pediatric Moyamoya

D.S. Bolar, B. Gagoski, D.B. Orbach, E. Smith, E. Adalsteinsson, B.R. Rosen, P.E. Grant, and R.L. Robertson

ABSTRACT

BACKGROUND AND PURPOSE: Imaging CBF is important for managing pediatric moyamoya. Traditional arterial spin-labeling MR imaging detects delayed transit thorough diseased arteries but is inaccurate for measuring perfusion because of these delays. Velocity-selective arterial spin-labeling is insensitive to transit delay and well-suited for imaging Moyamoya perfusion. This study assesses the accuracy of a combined velocity-selective arterial spin-labeling and traditional pulsed arterial spin-labeling CBF approach in pediatric moyamoya, with comparison to blood flow patterns on conventional angiography.

MATERIALS AND METHODS: Twenty-two neurologically stable pediatric patients with moyamoya and 5 asymptomatic siblings without frank moyamoya were imaged with velocity-selective arterial spin-labeling, pulsed arterial spin-labeling, and DSA (patients). Qualitative comparison was performed, followed by a systematic comparison using ASPECTS-based scoring. Quantitative pulsed arterial spin-labeling CBF and velocity-selective arterial spin-labeling CBF for the middle cerebral artery, anterior cerebral artery, and posterior cerebral artery territories were also compared.

RESULTS: Qualitatively, velocity-selective arterial spin-labeling perfusion maps reflect the DSA parenchymal phase, regardless of postinjection timing. Conversely, pulsed arterial spin-labeling maps reflect the DSA appearance at postinjection times closer to the arterial spin-labeling postlabeling delay, regardless of vascular phase. ASPECTS comparison showed excellent agreement (88%, $\kappa = 0.77$, $P < .001$) between arterial spin-labeling and DSA, suggesting velocity-selective arterial spin-labeling and pulsed arterial spin-labeling capture key perfusion and transit delay information, respectively. CBF coefficient of variation, a marker of perfusion variability, was similar for velocity-selective arterial spin-labeling in patient regions of delayed-but-preserved perfusion compared to healthy asymptomatic sibling regions (coefficient of variation = 0.30 versus 0.26, respectively, Δcoefficient of variation = 0.04), but it was significantly different for pulsed arterial spin-labeling (coefficient of variation = 0.64 versus 0.34, Δcoefficient of variation = 0.30, $P < .001$).

CONCLUSIONS: Velocity-selective arterial spin-labeling offers a powerful approach to image perfusion in pediatric moyamoya due to transit delay insensitivity. Coupled with pulsed arterial spin-labeling for transit delay information, a volumetric MR imaging approach capturing key DSA information is introduced.

ABBREVIATIONS: ACA = anterior cerebral artery; ASL = arterial spin-labeling; CV = coefficient of variation; PASL = pulsed arterial spin-labeling; PCA = posterior cerebral artery; pCASL = pseudocontinuous arterial spin-labeling; PLD = postlabeling delay; VSASL = velocity-selective arterial spin-labeling

Perfusion imaging plays an important role in the management of patients with moyamoya. Conventional catheter DSA is the criterion standard technique used to assess intracranial arteriopathy and blood flow patterns, but it is invasive, uses ionizing radiation, and introduces a small risk of neurologic

Received April 24, 2019; accepted after revision August 21.

From the Department of Radiology (D.S.B.) and Center for Functional Magnetic Resonance Imaging (D.S.B.), UC San Diego, La Jolla, California; Fetal Neonatal Neuroimaging and Developmental Science Center (B.G., P.E.G.), Department of Radiology (B.G., D.B.O., P.E.G., R.L.R.), Division of Neurointerventional Radiology (D.B.O.), Department of Neurosurgery (E.S.), and Division of Newborn Medicine (P.E.G.), Department of Medicine, Boston Children's Hospital, Boston, Massachusetts; Department of Electrical Engineering & Computer Science (E.A.), Massachusetts Institute of Technology, Cambridge, Massachusetts; and MGH/HST Athinoula A. Martinos Center for Biomedical Imaging (E.A., B.R.R.), Charlestown, Massachusetts.

Paper previously presented, in part, at: Annual Meeting of the International Society for Magnetic Resonance in Medicine, May 30 to June 5, 2015; Toronto, Ontario, Canada; and Annual Meeting of the Radiological Society of North America, November 29 to December 4, 2015; Chicago, Illinois.

Please address correspondence to Divya S. Bolar, MD, PhD, UCSD Center for Functional Magnetic Resonance Imaging, W.M. Keck Building, 9500 Gilman, 0677, La Jolla, CA 92037-0677; e-mail: dbolar@ucsd.edu

Indicates article with supplemental on-line photos.

http://dx.doi.org/10.3174/ajnr.A6262

Table 1: Patient demographics

Pt.	Moyamoya Etiology	Age (yr)	Sex	Laterality	Operative Status	Suzuki[37] (R/L), Preoperative	Treatment	Matsushima[38] (R/L)
1	Idiopathic	11	F	Left	Pre	IV		
		12			Post		Left synangiosis	C
2	NF1	6	M	Right	Post	IV–V	Right synangiosis	A
3	SCD	13	F	Bilateral	Post	NA	Bil synangiosis	A
4	Idiopathic	14	F	Bilateral	Post	III–IV/III–IV	Bil synangiosis	A/A
5	Idiopathic	19	F	Bilateral	Post	V–VI/III–IV	Bil synangiosis	A/C
6	NF1	17	F	Bilateral	Pre	I/III–IV		
7	SCD	11	M	Bilateral	Post	II/II	Bil synangiosis	A/B
8	Idiopathic	14	M	Bilateral	Post	IV/IV	Bil synangiosis	A/A
9	Idiopathic	13	F	Bilateral	Post	II/III	Bil synangiosis	B/C
10	Idiopathic	16	F	Bilateral	Pre	I/I		
11	Idiopathic	7	F	Bilateral	Pre	II/II		
12	NF1[a]	5	F	Right	Pre	I		
13	SCD	11	F	Right	Pre	II		
14	NF1	8	M	Left	Post	III	Left synangiosis	A
15	Idiopathic	7	F	Right	Post	III	Right synangiosis	A
16	Idiopathic	13	F	Left	Post	NA	Left synangiosis	B
17	Idiopathic	19	F	Bilateral	Pre	III/I–II		
18	Idiopathic	3	M	Bilateral	Post	II–III/II–III	Bil synangiosis	B/A–B
19	NF1	15	M	Left	Post	V	Left synangiosis	B
20	Idiopathic	12	M	Right	Post	III–IV	Right synangiosis	B–C
21	Idiopathic	15	M	Bilateral	Post	III/III	Bil synangiosis	B/B
22	Idiopathic	2	M	Bilateral	Post	IV/II	Bil synangiosis	A/A–B

Note:—NF1 indicates neurofibromatosis type 1; SCD, sickle cell disease; Pre, before; Post, after; R, right; L, left; NA, not applicable; Bil, bilateral.
[a] Patient with NF1 with radiated right masticator space tumor; arteriopathy possibly related to radiation.

complication.[1,2] Therefore, noninvasive imaging techniques remain attractive to reduce the necessity of DSA for evaluation of cerebral blood flow.

Standard MR perfusion approaches such as pulsed and pseudocontinuous arterial spin-labeling (PASL and pCASL) are limited in imaging moyamoya perfusion because they are affected by prolonged arterial arrival times secondary to the arteriopathy. Arrival of the arterial spin-labeling (ASL) magnetic label to the brain parenchyma is subsequently delayed, resulting in macrovascular signal (so-called arterial transit artifact) and artifactual areas of perfusion deficit.[3,4]

Velocity-selective ASL (VSASL) is a newer perfusion technique that relies on imaging principles not affected by variations in arterial arrival time. Using velocity-selective labeling modules, VSASL creates the magnetic label in small arteries within the imaging voxels themselves, allowing immediate delivery to target microvasculature, circumventing transit delay errors.[5] A recent study compares VSASL, pCASL, and xenon-enhanced CT CBF in adult patients with moyamoya[6] and supports these hypotheses but lacks comparison with DSA. Furthermore, xenon is not FDA-approved for pediatric use.[7]

The current study evaluates a combined VSASL and PASL protocol in pediatric moyamoya and adds a critical comparison with blood flow patterns assessed by DSA. We hypothesized the following: 1) VSASL is insensitive to arterial transit delays, allowing assessment of parenchymal perfusion; and 2) PASL is sensitive to arterial transit delays, facilitating identification of affected territories, but it is inaccurate for measuring perfusion within these territories. We believe that each ASL approach provides unique but complementary information about cerebral hemodynamics in moyamoya. To investigate these hypotheses, we performed a systematic comparison of PASL/VSASL to DSA and compared perfusion variability measured with VSASL and PASL in disease-affected regions.

MATERIALS AND METHODS

Subjects

The study was approved by the Boston Children's Hospital institutional review board; informed consent was not required. PASL and VSASL sequences were added to moyamoya MR imaging protocols in late 2014 after a short trial period, resulting in approximately 100 pediatric patients with moyamoya and 5 asymptomatic siblings scanned during 3 years. Of these, 23 patients were selected on the basis of the following inclusion criteria: stable appearance of stenoses and collaterals between the time of MRI/MRA and DSA (either pre- or postsynangiosis), closely matched slice position between VSASL and PASL, and lack of recent neurologic events. For studies >2 months apart, vascular stability was confirmed by comparing the MRA appearance before and after the DSA (in addition to direct comparison to DSA itself). Using these criteria, 22 patients were selected, after excluding 1 patient due to ASL artifacts (primarily related to motion and susceptibility from surgical hardware). For one of the patients, both preoperative and postoperative data were included. Data from 5 asymptomatic sibling screens thought not to have frank moyamoya were also included and consisted of ASL data only, except for 1 sibling who also underwent conventional angiography due to initially suspected disease by MRA. Subjects ranged from 2 to 19 years of age, 17 female and 9 male (patients listed in Table 1).

Data Acquisition

MRI/MRA scans were performed at 3T (Siemens Trio and Skyra, Erlangen, Germany) and included PASL, VSASL, and standard anatomic/angiographic sequences.

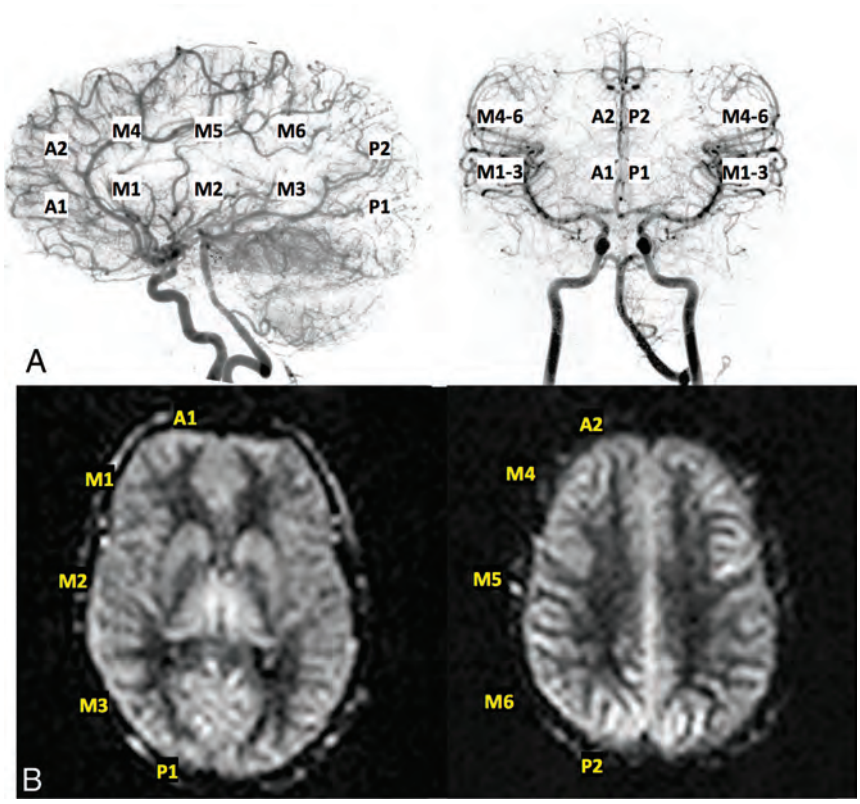

FIG 1. Representative ASPECTS regions used for scoring of both DSA (*A*) and ASL data (*B*); specifically, 2 ACA regions, 6 MCA regions, and 2 posterior cerebral artery regions per side were evaluated.

VSASL-specific parameters were V_{CUTOFF} = 2.1 cm/s and TI/postlabeling delay (PLD) = 1300 ms to the center slice (VSASL-PLD). PASL (quantitative imaging of perfusion using a single subtraction II [QUIPSS II] with thin-slice saturation) specific parameters were TI_1 = 700 ms, $TI_{1,stop}$ = 1400 ms, and TI/PLD = 2000 ms to the center slice (PASL-PLD), and PASL label width = 110 mm. VSASL parameters are similar to those used in initial studies previously found to target parenchymal perfusion,[5,8] and PASL parameters were adapted on the basis of ASL white paper recommendations.[9] The imaging module for both PASL and VSASL included an EPI readout with TE/TR = 13/3000 ms, voxel size = 3.5 × 3.5 × 5.0 mm^3, 20 slices, bandwidth = 2300 Hz/pixel, 90 measurements, and scan time = 4 minutes 30 seconds. A single EPI scan (<1 second) was acquired for absolute CBF quantification, the so-called M0 scan.[10]

DSA was performed using a biplane cerebral angiographic system (Axiom Artis dBA Twin; Siemens). Images of ICA, external carotid artery, and vertebral artery injections were obtained in lateral and frontal projections. Temporal resolution for DSA was typically 2 frames/s. Postinjection time is defined as the time between the frame in which contrast first appears and the frame of interest.

Data Analysis

Data processing for PASL and VSASL was identical except for the exact equations used for quantification. Generation of absolute CBF maps involved an analysis stream based on standard ASL approaches and equations described in detail elsewhere.[5,11]

PASL-CBF and VSASL-CBF maps were qualitatively compared to each other noting discrepant parenchymal signal and areas of PASL macrovascular artifacts. Coronal and sagittal multiplanar reformats of ASL perfusion maps were generated to facilitate comparison to frontal and lateral DSA projections. Attention was paid to whether the ASL-CBF maps resembled the DSA parenchymal phase or arterial phase.

Months later, a more rigorous, systematic comparison between ASL and DSA was performed by 2 independent graders, respectively, using a modified ASPECTS scoring system.[4,12] DSA and PASL/VSASL data were graded using a 4-point system that evaluates regions corresponding to 10 ASPECTS locations (2 anterior cerebral artery [ACA], 6 MCA, and 2 posterior cerebral artery [PCA]) over 2 standard ASPECTS levels (Fig 1). The DSA scale is the following: 0, absence of capillary blush; 1, incomplete capillary blush (ie, decreased parenchymal filling of the ASPECT region); 2, complete-but-delayed capillary blush (eg, due to proximal stenosis and/or collaterals); and 3, complete blush from anterograde flow, without delay. The analogous ASL scale is the following: 0, complete absence of parenchymal perfusion by VSASL; 1, incomplete parenchymal perfusion by VSASL (ie, partially absent or conspicuously decreased perfusion within the region); 2, delayed-but-complete parenchymal perfusion as assessed by PASL and VSASL (ie, VSASL demonstrates complete parenchymal perfusion, but PASL shows arterial transit artifact and/or perfusion deficits); and 3, complete/normal perfusion (ie, both VSASL and PASL show approximately matched, homogeneous parenchymal perfusion, without obvious deficit). On-line Figure 1 shows ASL scoring in further detail. An additional subscore of U could be granted, for "uncertain" regions whose score represents a best guess. DSA was scored by an attending pediatric neuroradiologist and former interventionalist (R.L.R.), and ASL was scored by a senior neuroradiology fellow (D.S.B.). Grading was performed in a randomized fashion, with the reviewers blinded to each other's scores. Agreement between the DSA and ASL scores was assessed using the Cohen κ coefficient (Matlab; MathWorks, Natick, Massachusetts).

A quantitative PASL-CBF and VSASL-CBF analysis was also performed on 19 patients and all asymptomatic siblings, but it could not be performed on 3 patients due to misalignment between the perfusion-weighted scan and the M0 calibration scan. CBF maps were normalized to a standard pediatric atlas (Montreal Neurological Institute, Montreal, Canada)[13] and overlaid with vascular territory masks based on microanatomic studies[14,15] to allow regional measurements. Mean CBF and SD were

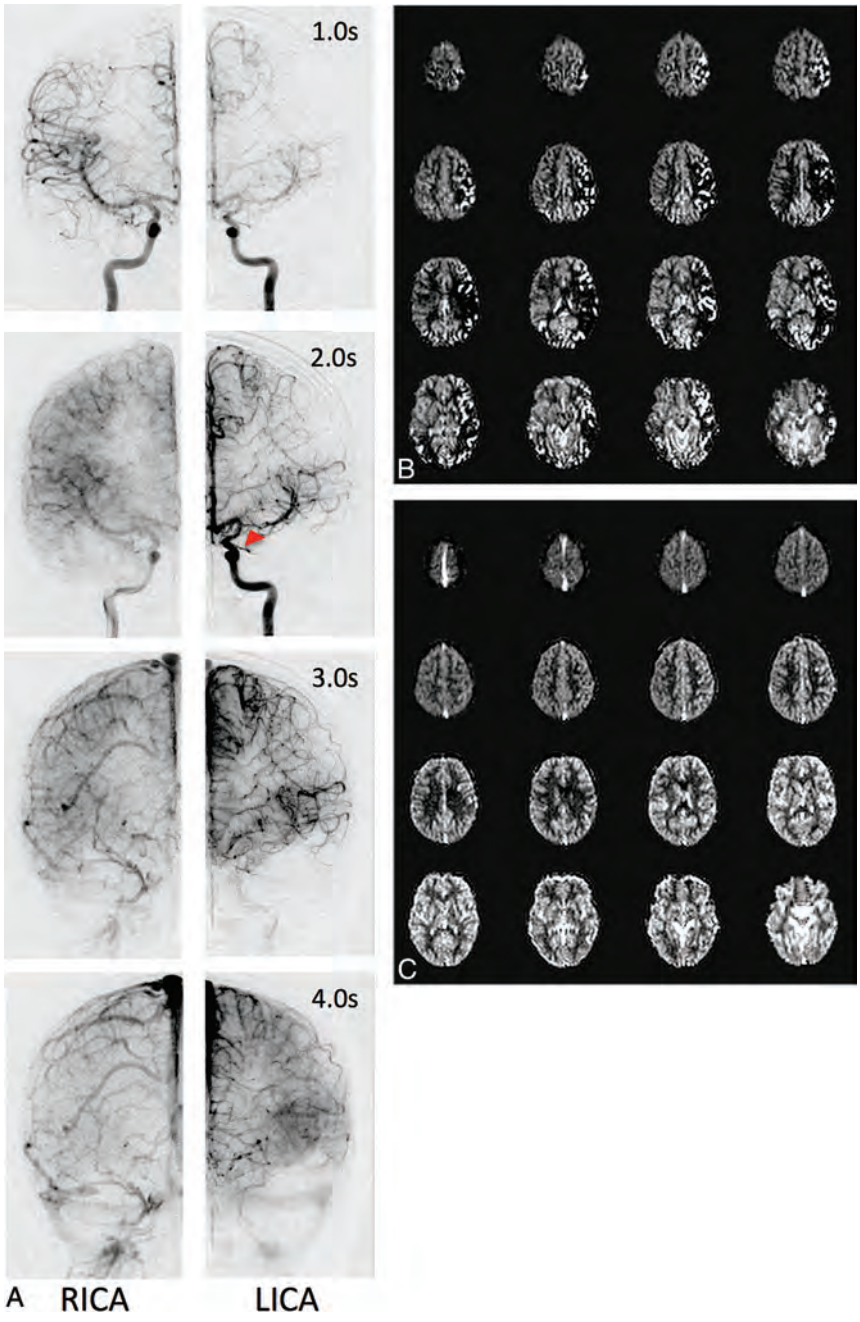

FIG 2. Representative DSA data (*A*), PASL CBF maps (*B*), and VSASL CBF maps (*C*) for a preoperative patient with left-sided moyamoya. *A*, Frontal DSA data from bilateral ICA injections at various postinjection times. The right side appears relatively normal, with early arterial filling and ACA/MCA parenchymal blush at 2.0 seconds. In contrast, the left side demonstrates delayed anterograde filling through a proximal M1 MCA stenosis (*red arrowhead*), retrograde filling via ACA-MCA collaterals, and delayed parenchymal perfusion of the MCA territory. Parenchymal perfusion of the left MCA territory is finally reached by 4.0 seconds. PASL maps (*B*) reflect the DSA appearance at 2.0 seconds bilaterally, including areas of curvilinear hyperintensity corresponding to macrovascular flow and perfusion deficit, while VSASL maps (*C*) reflect parenchymal DSA phases, despite these occurring at different times (2.0 seconds on the right, 4.0 seconds on the left). RICA indicates right ICA injection; LICA, left ICA injection.

measured for ACA, MCA, and PCA vascular territories. The coefficient of variation (CV), a marker of perfusion variability, was then calculated by dividing the mean by the SD. Due to frequent macrovascular artifacts seen on PASL-CBF maps, values of >115 mL/100g/min were excluded from mean, SD, and CV calculations because this threshold was thought to be above physiologic perfusion based on published pediatric CBF values.[16,17] PASL and VSASL-CBF were compared in a pair-wise fashion between patients and asymptomatic siblings on a territory-by-territory basis using a Wilcoxon signed rank test (Matlab). Additionally, patient PASL and VSASL CVs of territories with delayed-but-complete capillary blush by DSA (ie, ≥80% territory with a score of 2) were compared with asymptomatic sibling CVs using a Wilcoxon rank-sum test (Matlab).

RESULTS

Comparisons of DSA, PASL, and VSASL

For nearly all subjects with DSA and ASL data, PASL appearance is qualitatively similar to DSA appearance at postinjection times close to the PASL-PLD, regardless of vascular phase. Conversely, VSASL appearance closely matches the DSA parenchymal phase appearance, regardless of the postinjection time required to reach the parenchymal phase.

Figure 2 shows representative DSA, PASL-CBF, and VSASL-CBF data of a patient with unilateral disease. Frontal DSA from bilateral ICA injections is presented at multiple postinjection times, with excellent correlation to ASL.

On-line Figures 2 and 3 provide additional sets of DSA, PASL, and VSASL data, further highlighting ASL/DSA correlation. On-line Figure 2 provides data from subject 7, a patient who underwent bilateral pial synangiosis. On-line Figure 3 provides data from subject 9, a patient post-bilateral pial synangiosis with a chronic right MCA infarction.

ASPECTS Comparisons between DSA and PASL/VSASL

Table 2 summarizes ASPECTS-based scoring of DSA and ASL data for the 23 subjects with both DSA and ASL data (noting patient 1 with both preoperative and postoperative data). Excellent agreement between DSA and ASL was achieved, with 88% agreement and observed Cohen $\kappa = 0.77$, $P < .001$. Specifically, 420/480 ASPECTS regions

had identical scores, and 60/480 regions had discordant scores. U subscores were given to 51 DSA and 15 ASL regions. Notably, 35% of discordant regions had U subscores (19 DSAs, 2 ASLs), with 15 of these regions graded 1U on DSA and 2 or 3 on ASL.

Quantitative CBF with PASL and VSASL

Figure 3 provides a graphical representation of PASL and VSASL average CBF CV values in patient vascular territories (ie, ACA, MCA, and PCA) affected by transit delay, but ultimately with complete parenchymal perfusion by DSA (44/120), and all asymptomatic sibling vascular territories (30/30). High PASL-CBF variability for patients is highlighted (mean CV = 0.64 compared to 0.34 for asymptomatic sibling scans, statistically different at $P < .001$), which is discordant with the homogeneous parenchymal perfusion seen by DSA. Conversely, VSASL-CBF in the same regions demonstrated significantly less variability compared with PASL-CBF (mean VSASL-CBF CV = 0.30, statistically different from PASL-CBF CV = 0.64 at $P < .001$) and is similar to that of asymptomatic sibling scans (VSASL-CBF CV = 0.26, though still statistically different at $P < .005$) and concordant with homogeneous parenchymal perfusion on DSA.

Table 2: Contingency table of ASPECTS-based scoring for ASL and DSA data[a]

	ASL Score				
DSA Score	0	1	2	3	Totals
0	0	1	0	0	1 (<1%)
1	0	6	17	1	24 (5%)
2	0	7	192	21	220 (46%)
3	0	0	13	222	235 (49%)
Totals	0 (0%)	14 (3%)	222 (46%)	244 (51%)	480

[a] Agreement = 88%, Cohen κ = 0.77, $P < .0001$.

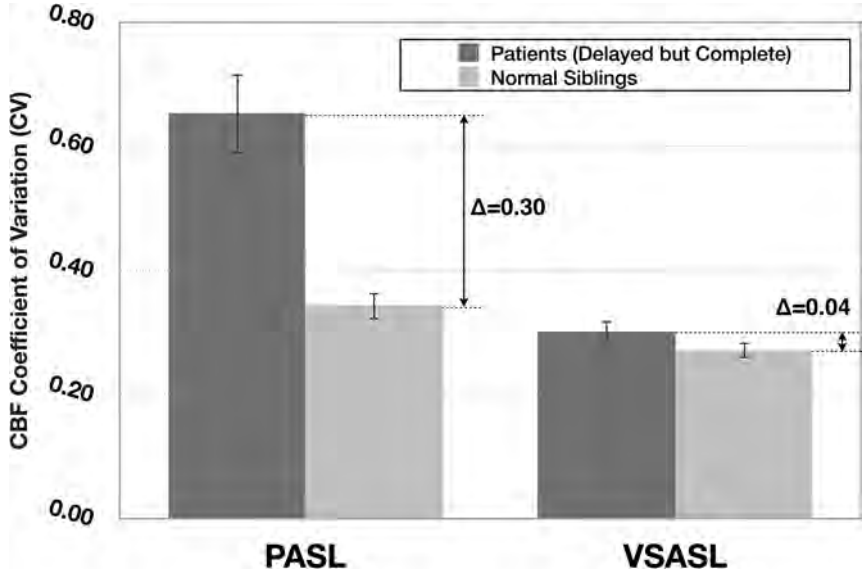

FIG 3. Average PASL and VSASL-CBF CV (a marker of perfusion variability) calculated for patient vascular territories demonstrating delayed-but-complete parenchymal perfusion by DSA, with normal sibling values provided for comparison. Patient VSASL values are similar to those of healthy siblings, consistent with the DSA appearance, but PASL values are markedly different. *Error bars* denote 95% CI.

CBF values themselves were statistically different between VSASL and PASL in patients, when compared on a pair-wise, territory-by-territory basis, yet they were not statistically different in the asymptomatic sibling group (both at $P < .05$).

DISCUSSION

VSASL offers a powerful approach to image perfusion in pediatric moyamoya due its transit delay insensitivity. Traditional PASL and pCASL are limited in moyamoya because they use a spatially defined magnetic label that flows from the proximal arteries and accumulates in distal microvasculature during the PLD, analogous to transit of contrast during DSA (Fig 4). Due to a spatial separation between the arterial label and microvascular imaging regions, a temporal delay arises between labeling and microvascular arrival, the so-called arterial transit delay.[10] As these the transit delays elongate in moyamoya due to stenoses and collateral pathways, PASL/pCASL techniques become increasingly inaccurate for measuring perfusion. This phenomenon results in the following: 1) visualization of larger arteries proximal to the microvasculature (ie, arterial transit artifact)[18,19], since the label fails to clear these arteries during the PLD, and 2) absence of microvascular signal and apparent perfusion deficits because the label fails to sufficiently accumulate in the microvasculature by the PLD.[4,10,20] These effects are depicted in Fig 4*B*, *-D*. Thus, PASL and pCASL do not always reflect parenchymal perfusion, rendering perfusion assessment in moyamoya by traditional ASL techniques difficult and, in many cases, impossible.[4,6,21]

Conversely, VSASL uses velocity-selective modules to create the magnetic label within small arteries in the imaging slice itself, allowing immediate delivery to the microvasculature during the PLD. VSASL is theoretically insensitive to transit delay and should not experience contamination from macrovascular artifacts or associated apparent perfusion deficits like those seen with PASL in Fig 4*D*. In situations without pronounced transit delays, VSASL performs comparably with PASL and can similarly identify regions of altered cerebral perfusion.[22]

Our results show that in moyamoya, 1) VSASL is largely insensitive to arterial transit delays, allowing accurate assessment of parenchymal perfusion, and 2) PASL is highly sensitive to arterial transit delays, facilitating identification of affected territories, but inaccurate for measuring perfusion within these territories. These assessments were made by comparing ASL data with the temporal and spatial characteristics of the intracranial circulation with DSA (whose dynamic acquisition captures both macrovascular and microvascular phases of circulation) and also by comparing ASL perfusion variability (CBF CV) in patients and asymptomatic siblings not thought to have frank moyamoya.

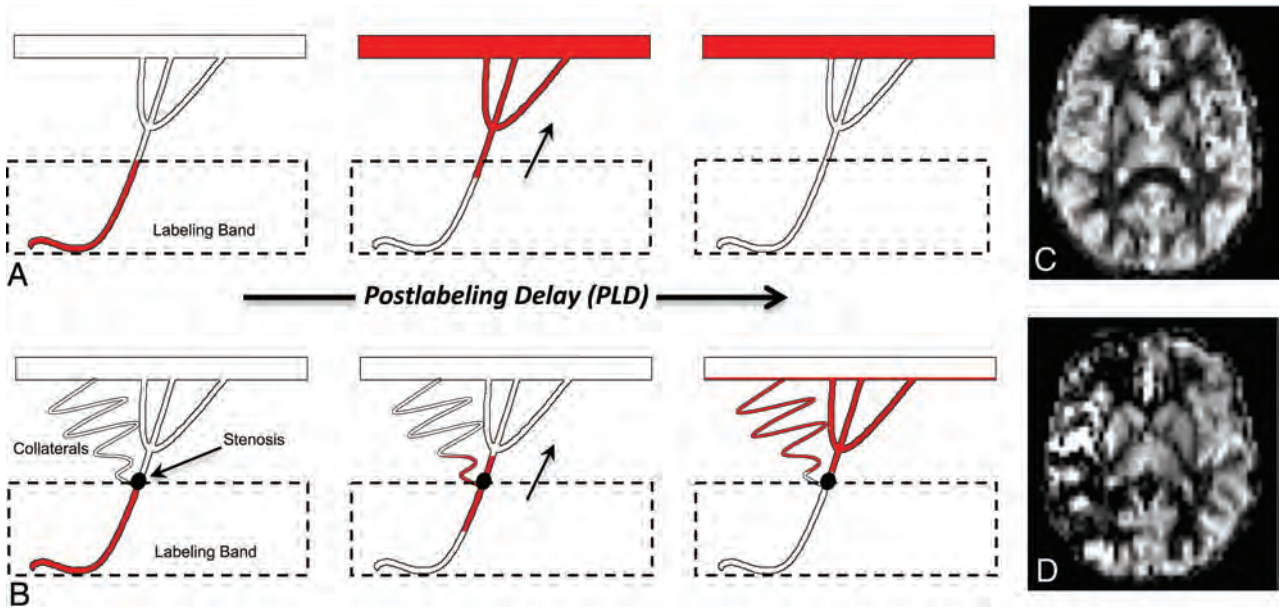

FIG 4. Standard ASL label propagation with patent proximal vessels (*A*) and steno-occlusive disease with secondary collateralization (*B*). *A*, The ASL label travels from the labeling band to the distant microvasculature during the standard PLD, resulting in symmetric, homogeneous gray matter perfusion (*C*). *B*, The label is delayed due to slow flow through the stenosis and circuitous collateral pathways. Consequently, the label does not fully reach the distal microvasculture during PLD and remains caught in the macrovasculature, resulting in areas of apparent perfusion deficit and hyperintense arterial transit artifacts (*D*).

Qualitatively, VSASL shows homogeneous and symmetric parenchymal perfusion in cortical gray matter for nearly all patients, consistent with robust compensation and known neurologic and conventional MR imaging stability. These regions consistently corresponded to areas of parenchymal blush seen on DSA, regardless of blush timing. PASL, on the other hand, shows areas of perfusion deficit and hyperintense macrovascular flow, both secondary to delayed arterial transit, corresponding to the DSA appearance at a fixed postinjection time closer to the PASL-PLD. It is clear that PASL can result in erroneous perfusion, resulting in perceived perfusion deficits that do not truly exist (best highlighted in Fig 2 and On-line Fig 2). In patients with real perfusion deficits, for example in a patient with a known infarct (On-line Fig 3), PASL transit errors can mask the true perfusion deficit on a background of artifactually deficient regions. In this example, VSASL easily identifies the truly deficient region, discriminating true hypoperfusion from apparent hypoperfusion.

Compared with a purely qualitative analysis, the newly introduced ASPECTS analysis offers a more rigorous and systematic approach for evaluating ASL and DSA data. Excellent agreement between ASL and DSA was observed (88%, $\kappa = 0.77$, $P < .001$), which would have been even higher if U regions were excluded. Interestingly, there were nearly 3-4 times as many uncertain regions for DSA ($n = 51$) compared to ASL ($n = 15$). This discrepancy was thought to reflect challenges in localizing perfusion in three dimensions using an inherently two dimensional DSA technique confounded by vessel overlap, cross-filling via contralateral hemispheric branches, and mental summation of multiple single-vessel injections. This limitation of DSA is highlighted by the fact that 79% of uncertain regions scored as incomplete perfusion by DSA ("1U") were unequivocally scored as delayed-but-complete ("2") or complete ("3") perfusion by ASL, suggesting that DSA analysis may underestimate compensation in certain situations. Thus, the ASPECTS analysis supports higher confidence and less equivocality of ASL data, likely due to its volumetric, 3D nature. Given the importance of accurate localization for properly delineating regions of hypoperfusion (and, for example, computing tissue volumes), the ASL approach may in fact surpass DSA in this area.

Another powerful advantage of ASL over DSA is its unique ability to quantify microvascular CBF in absolute units (milliliters/100g/min), which can reveal subtle CBF changes not obvious qualitatively. An approach to measure CBF in ACA, MCA, and PCA territories is introduced in this study, with a vascular territory mask offering a standardized means to enable interterritorial and interhemispheric comparisons.[16,17] Due to the known heterogeneity of normal CBF values in children of different ages,[16,23] an arguably more useful quantitative metric of perfusion for group comparison is the CBF CV, which provides a measure of perfusion variability within a vascular territory, with lower values suggesting more homogeneous perfusion. PASL-CBF values in regions of transit delay demonstrate high variability (particularly when compared to asymptomatic siblings), despite more homogeneous perfusion seen on DSA and VSASL. This is presumably due to averaging of erroneously high CBF voxels (due to the arterial transit artifact) with erroneously low CBF voxels (due to the apparent perfusion deficit).

In contrast to PASL, VSASL-CBF CV values in regions affected by transit delay in patients were similar to those of normal regions in the asymptomatic siblings (Fig. 3), corroborating the homogeneous (but delayed) territorial parenchymal phase demonstrated by DSA. However, while the absolute difference in VSASL-CBF CV between patients and asymptomatic siblings was small (0.04), this difference was still statistically significant at $P < .005$, suggesting that despite generally preserved perfusion in

these patients, there may be subtly increased variability due to the disease process/surgery itself. This may be interesting to investigate in future studies and suggests added value of VSASL over DSA alone. Notably, when using VSASL within a single individual (for example, to compare diseased with healthy regions or follow serially), accurate absolute CBF will be crucial.

Unlike in the patient group, no statistical difference was found between PASL and VSASL-CBF measurements in the asymptomatic siblings, supporting that both ASL methods give accurate results in the absence of significant stenoses and transit delays.

This study suggests that PASL and VSASL together provide a robust, noninvasive, cerebral hemodynamic assessment in childhood moyamoya, allowing evaluation of parenchymal perfusion by VSASL and regional transit delay via PASL. Cerebral perfusion is universally acknowledged as a critically important parameter related to clinical outcome[24-28] and may even be more predictive of outcome than angiographic state.[25] Such functional information may be used preoperatively to monitor progression and better inform future surgical needs, and postoperatively to measure the combined impact of surgical and native collaterals on regional CBF and also to monitor postsurgical progression. Given our findings, both PASL and VSASL have now become part of the moyamoya MR imaging protocol at our home institution of Boston Children's Hospital (a major moyamoya referral center) and are routinely performed on all patients with moyamoya for both initial assessment and periodic follow-up. VSASL has also been added to certain adult and pediatric protocols at a nearby institution (Massachusetts General Hospital), with preliminary results suggesting that VSASL-CBF may have greater predictive value relative to PASL in suspected ischemic stroke.[29]

Several limitations of this study must be mentioned. First, ASL is an inherently SNR-limited technique, necessitating large voxels and low resolution. Future studies will incorporate a background-suppressed, segmented 3D readout to improve SNR and resolution. PASL may also be replaced by pCASL, which is a higher SNR spatial-based ASL approach. An artifact unique to VSASL is CSF contamination, particularly within the basal cisterns/ventricles, due to velocity-based labeling. A CSF-suppressed approach is under development.

While bolus propagation is similar for both PASL and DSA, the PASL bolus travels at the velocity of inflowing arterial blood, whereas the DSA bolus may also be affected by the force/rate of injection. Combined with low DSA temporal resolution (500 ms), correspondence between DSA phase and PASL-PLD is an approximation and thus included in our qualitative assessment only.

One important limitation of our PASL/VSASL approach is that while it detects transit delay/collaterals and measures CBF, it does not make a distinction between surgical or native collaterals. This could be potentially addressed using new vessel-encoded ASL techniques to image collateral pathways.[30]

Other spatial-based ASL approaches to mitigate arterial transit delay effects in moyamoya have been attempted. A recent study evaluated pCASL with both long PLDs (>4 seconds) and multi-PLDs (0.7–3 seconds) for moyamoya CBF measurement.[31] This study found that even multi-PLD approaches underestimate CBF in the presence of long transit delays, whereas PLDs of >4 seconds result in stronger correlation with ^{15}O-PET CBF. Such long delays, however, will result in marked signal loss due to T1 decay and may also violate a fundamental ASL assumption: that the magnetic label remains within the microvascular tree during the experiment. At PLDs of >4 seconds, labeled spins will start clearing into the venous circulation in regions without significant transit delay, leading to CBF underestimation. This feature becomes especially relevant in patients with heterogeneous and/or unilateral disease. VSASL, on the other hand, will be accurate in all regions, insensitive to large variations in transit delay across the brain.

Acetazolamide challenge to measure cerebral vascular reserve (typically with SPECT/PET[32] and potentially ASL[33]) is performed in many moyamoya centers and can provide important information about hemodynamic status and postoperative clinical outcome.[32] Because this is not routinely performed at Boston Children's Hospital, we are unable to draw comparisons with cerebral vascular reserve metrics. We assert, however, that ASL methods presented here may complement cerebral vascular reserve and can be performed without administration of exogenous agents and on routine follow-up MRIs. Moreover, if cerebral vascular reserve measurement is desired using MR imaging, it should be more accurate using a VSASL-based approach since moyamoya transit delay will decrease accuracy in spatial-based ASL–cerebral vascular reserve approaches.[34,35] Of note, VSASL will accurately measure CBF even in the acetazolamide-increased CBF state; while higher CBF will shift the leading edge of the magnetic label downstream toward the capillary bed, the CBF measurement will not be adversely affected.[35,36]

Finally, lack of a quantitative criterion standard for comparison/validation, such as ^{15}O-PET or xenon-enhanced CT is another important limitation; these methods, however, require ionizing radiation and exogenous agents and are not generally feasible in children. We thus relied on DSA as a qualitative criterion standard because it was part of the clinical protocol at Boston Children's Hospital.

CONCLUSIONS

We present a combined VSASL and PASL approach for imaging perfusion and transit delay, respectively, in pediatric moyamoya, using the temporal and spatial vascular patterns on DSA as the criterion standard comparison. Due to its insensitivity to arterial transit delays, VSASL offers a powerful new way to accurately image perfusion in moyamoya and provides important spatial and quantitative CBF information unobtainable by DSA. Such an approach may further characterize disease progression and response to therapy. Additional studies to assess this potential by comparing pre- and postoperative data are necessary and underway.

Disclosures: Divya S. Bolar—*UNRELATED*: *Employment*: Massachusetts General Hospital, *Comments*: I was a resident, then fellow, in the Radiology Department at Massachusetts General Hospital from 2013 to 2018 and was paid as such; *Grants/Grants Pending*: Radiological Society of North America Resident Grant, *Comments*: I received a Radiological Society of North America Resident Grant in 2016; these funds were used for other related projects and not directly for this project (which started before I received the grant). Elfar Adalsteinsson—*UNRELATED*: *Grants/Grants Pending*: National Institutes of Health, *Comments*: National Institutes of Health 1U01HD087211-01 and 5R01EB017337-02, National Institutes of Health applications under review*; *Royalties*: Stanford Licensing Office, *Comments*: patents on MRI methods issued by Stanford University. Borjan Gagoski—*UNRELATED*: *Grants/Grants Pending*: National Institutes of Health 1U01HD087211-01 and 5R01EB017337-02.* Bruce R. Rosen—*UNRELATED*: *Grants/Grants*

Pending: National Institutes of Health P41-EB015896.* P. Ellen Grant—*UNRELATED*: *Grants/Grants Pending*: National Institutes of Health 1U01HD087211-01 and 5R01EB017337-02.* *Money paid to the institution.

REFERENCES

1. Lin N, Smith ER, Scott RM, et al. **Safety of neuroangiography and embolization in children: complication analysis of 697 consecutive procedures in 394 patients.** *J Neurosurg Pediatr* 2015;16:432–38 CrossRef Medline
2. Robertson RL, Chavali RV, Robson CD, et al. **Neurologic complications of cerebral angiography in childhood moyamoya syndrome.** *Pediatr Radiol* 1998;28:824–29 CrossRef Medline
3. Calamante F, Ganesan V, Kirkham FJ, et al. **MR perfusion imaging in moyamoya syndrome: potential implications for clinical evaluation of occlusive cerebrovascular disease.** *Stroke* 2001;32:2810–16 CrossRef Medline
4. Zaharchuk G, Do HM, Marks MP, et al. **Arterial spin-labeling MRI can identify the presence and intensity of collateral perfusion in patients with moyamoya.** *Stroke* 2011;42:2485–91 CrossRef Medline
5. Wong EC, Cronin M, Wu WC, et al. **Velocity-selective arterial spin labeling.** *Magn Reson Med* 2006;55:1334–41 Medline
6. Qiu D, Straka M, Zun Z, et al. **CBF measurements using multidelay pseudocontinuous and velocity-selective arterial spin labeling in patients with long arterial transit delays: comparison with xenon CT CBF.** *J Magn Reson Imaging* 2012;36:110–19 CrossRef Medline
7. US Food and Drug Administration. *Xenon Xe 133 Gas*. Washington, DC: US Food and Drug Administration; 2016 https://www.accessdata.fda.gov/drugsatfda_docs/label/2016/018327s005lbl.pdf. Accessed December 26, 2016
8. Wu W, Wong E. **Intravascular effect in velocity-selective arterial spin labeling.** *Conf Proc IEEE Eng Med Biol Soc* 2005;6:5790–93 Medline
9. Alsop DC, Detre JA, Golay X, et al. **Recommended implementation of arterial spin-labeled perfusion MRI for clinical applications: a consensus of the ISMRM perfusion study group and the European consortium for ASL in dementia.** *Magn Reson Med* 2015;73:102–16 CrossRef Medline
10. Buxton RB, Frank LR, Wong EC, et al. **A general kinetic model for quantitative perfusion imaging with arterial spin labeling.** *Magn Reson Med* 1998;40:383–96 CrossRef Medline
11. Cavusoglu M, Pfeuffer J, Uğurbil K, et al. **Comparison of pulsed arterial spin labeling encoding schemes and absolute perfusion quantification.** *Magn Reson Imaging* 2009;27:1039–45 CrossRef Medline
12. Kim JJ, Fischbein NJ, Lu Y, et al. **Regional angiographic grading system for collateral flow: correlation with cerebral infarction in patients with middle cerebral artery occlusion.** *Stroke* 2004;35:1340–44 CrossRef Medline
13. Fonov V, Evans AC, Botteron K, et al. **Unbiased average age-appropriate atlases for pediatric studies.** *Neuroimage* 2011;54:313–27 CrossRef Medline
14. Mutsaerts HJ, van Dalen JW, Heijtel DF, et al. **Cerebral perfusion measurements in elderly with hypertension using arterial spin labeling.** *PLoS One* 2015;10:e0133717 CrossRef Medline
15. Tatu L, Moulin T, Bogousslavsky J, et al. **Arterial territories of the human brain: cerebral hemispheres.** *Neurology* 1998;50:1699–1708 CrossRef Medline
16. Biagi L, Abbruzzese A, Bianchi MC, et al. **Age dependence of cerebral perfusion assessed by magnetic resonance continuous arterial spin labeling.** *J Magn Reson Imaging* 2007;25:696–702 CrossRef Medline
17. Wang J, Licht DJ. **Pediatric perfusion MR imaging using arterial spin labeling.** *Neuroimaging Clin N Am* 2006;16:149–67, ix CrossRef Medline
18. Detre JA, Samuels OB, Alsop DC, et al. **Noninvasive magnetic resonance imaging evaluation of cerebral blood flow with acetazolamide challenge in patients with cerebrovascular stenosis.** *J Magn Reson Imaging* 1999;10:870–75 CrossRef Medline
19. Zaharchuk G. **Arterial spin label imaging of acute ischemic stroke and transient ischemic attack.** *Neuroimaging Clin N Am* 2011;21:285–301, x CrossRef Medline
20. Deibler AR, Pollock JM, Kraft RA, et al. **Arterial spin-labeling in routine clinical practice, part 1: technique and artifacts.** *AJNR Am J Neuroradiol* 2008;29:1228–34 CrossRef Medline
21. Mutke MA, Madai VI, von Samson-Himmelstjerna FC, et al. **Clinical evaluation of an arterial-spin-labeling product sequence in steno-occlusive disease of the brain.** *PLoS One* 2014;9:e87143 CrossRef Medline
22. Schmid S, Heijtel DF, Mutsaerts HJ, et al. **Comparison of velocity- and acceleration-selective arterial spin labeling with [15O]H2O positron emission tomography.** *J Cereb Blood Flow Metab* 2015;35:1296–1303 CrossRef Medline
23. Wang J, Licht DJ, Jahng G-H, et al. **Pediatric perfusion imaging using pulsed arterial spin labeling.** *J Magn Reson Imaging* 2003;18:404–13 CrossRef Medline
24. Ishii R, Takeuchi S, Ibayashi K, et al. **Intelligence in children with moyamoya: evaluation after surgical treatments with special reference to changes in cerebral blood flow.** *Stroke* 1984;15:873–77 CrossRef Medline
25. McAuley DJ, Poskitt K, Steinbok P. **Predicting stroke risk in pediatric moyamoya with xenon-enhanced computed tomography.** *Neurosurgery* 2004;55:327–32; discussion 332–33 CrossRef Medline
26. Touho H, Karasawa J, Ohnishi H. **Preoperative and postoperative evaluation of cerebral perfusion and vasodilatory capacity with 99mTc-HMPAO SPECT and acetazolamide in childhood moyamoya.** *Stroke* 1996;27:282–289 CrossRef Medline
27. Lee M, Zaharchuk G, Guzman R, et al. **Quantitative hemodynamic studies in moyamoya: a review.** *Neurosurg Focus* 2009;26:E5 CrossRef Medline
28. Ikezaki K, Matsushima T, Kuwabara Y, et al. **Cerebral circulation and oxygen metabolism in childhood moyamoya: a perioperative positron emission tomography study.** *J Neurosurg* 1994;81:843–50 CrossRef Medline
29. Bolar DS, Rosen BR, Schaefer PW. **Comparison of Velocity-selective and Pulsed ASL Perfusion MRI in Patients with Suspected Cerebral Cortical Ischemia.** In: *Proceedings of the Annual Meeting of American Society of Neuroradiology*, Vancouver, BC. June 6, 2018:1–4
30. Wu B, Wang X, Guo J, et al. **Collateral circulation imaging: MR perfusion territory arterial spin-labeling at 3T.** *AJNR Am J Neuroradiol* 2008;29:1855–60 CrossRef Medline
31. Fan AP, Guo J, Khalighi MM, et al. **Long-delay arterial spin labeling provides more accurate cerebral blood flow measurements in moyamoya patients: a simultaneous positron emission tomography/MRI study.** *Stroke* 2017;48:2441–49 CrossRef Medline
32. So Y, Lee H-Y, Kim SK, et al. **Prediction of the clinical outcome of pediatric moyamoya with postoperative basal/acetazolamide stress brain perfusion SPECT after revascularization surgery.** *Stroke* 2005;36:1485–89 CrossRef Medline
33. Yun TJ, Paeng JC, Sohn C-H, et al. **Monitoring cerebrovascular reactivity through the use of arterial spin labeling in patients with moyamoya.** *Radiology* 2016;278:205–13 CrossRef Medline
34. Blauwblomme T, Lemaitre H, Naggara O, et al. **Cerebral blood flow improvement after indirect revascularization for pediatric moyamoya: a statistical analysis of arterial spin-labeling MRI.** *AJNR Am J Neuroradiol* 2016;37:706–12 CrossRef Medline
35. Wu WC, Wong EC. **Feasibility of velocity selective arterial spin labeling in functional MRI.** *J Cereb Blood Flow Metab* 2007;27:831–38 CrossRef Medline
36. Wu WC, Wong EC. **Intravascular effect in velocity-selective arterial spin labeling: the choice of inflow time and cutoff velocity.** *Neuroimage* 2006;32:122–28 CrossRef Medline
37. Suzuki J, Takaku A. **Cerebrovascular "moyamoya" disease: disease showing abnormal net-like vessels in base of brain.** *Arch Neurol* 1969;20:288–99 CrossRef Medline
38. Matsushima T, Inoue T, Suzuki SO, et al. **Surgical treatment of moyamoya disease in pediatric patients: comparison between the results of indirect and direct revascularization procedures.** *Neurosurgery* 1992;31:401–05 CrossRef Medline

Susceptibility-Weighted Imaging Findings in Aspartylglucosaminuria

A. Tokola, M. Laine, R. Tikkanen, and T. Autti

ABSTRACT

BACKGROUND AND PURPOSE: Aspartylglucosaminuria is a rare lysosomal storage disorder that causes slowly progressive, childhood-onset intellectual disability and motor deterioration. Previous studies have shown, for example, hypointensity in the thalami in patients with aspartylglucosaminuria on T2WI, especially in the pulvinar nuclei. Susceptibility-weighted imaging is a neuroimaging technique that uses tissue magnetic susceptibility to generate contrast and is able to visualize iron and other mineral deposits in the brain. SWI findings in aspartylglucosaminuria have not been reported previously.

MATERIALS AND METHODS: Twenty-one patients with aspartylglucosaminuria (10 girls; 7.4–15.0 years of age) underwent 3T MR imaging. The protocol included an SWI sequence, and the images were visually evaluated. Thirteen patients (6 girls, 7.4–15.0 years of age) had good-quality SWI. Eight patients had motion artifacts and were excluded from the visual analysis. Thirteen healthy children (8 girls, 7.3–14.1 years of age) were imaged as controls.

RESULTS: We found a considerably uniform distribution of decreased signal intensity in SWI in the thalamic nuclei in 13 patients with aspartylglucosaminuria. The most evident hypointensity was found in the pulvinar nuclei. Patchy hypointensities were also found especially in the medial and anterior thalamic nuclei. Moreover, some hypointensity was noted in globi pallidi and substantia nigra in older patients. The filtered-phase images indicated accumulation of paramagnetic compounds in these areas. No abnormal findings were seen in the SWI of the healthy controls.

CONCLUSIONS: SWI indicates accumulation of paramagnetic compounds in the thalamic nuclei in patients with aspartylglucosaminuria. The finding may raise the suspicion of this rare disease in clinical practice.

ABBREVIATIONS: *AGA* = *aspartylglucosaminidase*; AGU = aspartylglucosaminuria; SI = signal intensity

Aspartylglucosaminuria (AGU) is a rare lysosomal storage disorder causing progressive decline in intellectual and motor functions. It is a generalized disease affecting the whole body. The clinical picture was comprehensively described in a previously published review article,[1] but we have recently also published new data on cognitive profiles of school-aged patients with AGU.[2] Children with AGU appear healthy at birth. An infantile growth spurt and respiratory infections and hernias are among the first signs of the disease. Delayed speech development and clumsiness are noted in early childhood. Typical facial features including a short and broad nose with periorbital fullness developing during the first years.[3] An abnormally slow-but-positive intellectual and motor development up to teenage years is typical. After a relatively stable period of about 10 years up to 15 years of age, there is first a slow decline in intellectual and motor functions up to the age of 25–28 years, followed by a more rapid decline, finally resulting in severe mental impairment.[2] There are notable individual differences, but the disease leads to death usually before 50 years of age.

AGU is an inherited, autosomal recessive disorder caused by a mutation in the *aspartylglucosaminidase* (*AGA*) gene located on 4q34.3.[4] The disease is enriched in the Finnish population, and about 98% of the Finnish patients with AGU are homozygous for a specific point mutation, AGUFIN major.[5] The data from the

Received June 12, 2019; accepted after revision September 3.

From the HUS Medical Imaging Center, Radiology (A.T., T.A.), University of Helsinki and Helsinki University Hospital, Helsinki, Finland; Department of Child Neurology (M.L.), Helsinki University Hospital, Helsinki, Finland; and Institute of Biochemistry, Medical Faculty (R.T.), University of Giessen, Giessen, Germany.

This study was supported by the Jane and Aatos Erkko Foundation, the Finnish patient organization Suomen AGU ry, the Rare Trait Hope Fund (R.T.), the Scientific Fund of HUS Medical Imaging Center of Helsinki University Hospital (A.T.), the Pediatric Research Center (M.L.) and the Lastenlinna Foundation (M.L.).

Paper previously presented, in part, at: Annual Meeting of European Society of Neuroradiologists, September 19–23, 2018; Rotterdam, the Netherlands.

Please address correspondence to Anna Tokola, HUS Medical Imaging Center, PO Box 340, 00029 HUS, Finland; e-mail: anna.tokola@hus.fi

Indicates article with supplemental on-line table.

http://dx.doi.org/10.3174/ajnr.A6288

Human Gene Mutation Database lists >30 different AGU disease-causing mutations in the *AGA* gene.[6] In Finland, the prevalence is approximately 1.7–5/100,000 live births. Sporadic cases have been reported globally, but the worldwide incidence is unknown.

The AGUFIN major mutation causes local misfolding and deficient activity of the aspartylglucosaminidase enzyme, which catalyzes the hydrolysis of aspartylglucosamine and other glycoasparagines.[7] This results in accumulation of undegraded aspartylglucosamine and other glycoasparagines in body fluids and tissues of patients with AGU. Hypertrophied storage lysosomes are present in all tissues and organs.

Therapies for many lysosomal storage disorders have improved during the past decades, but no approved treatment is currently available to cure or slow down the progression of AGU. Recently, a chaperone treatment trial in patients with AGU was initiated, and the patients in our study are currently participating in the trial. The treatment exploits a small chemical compound that functions as a pharmacologic chaperone for the mutated *AGA*.[8] Small molecules known as pharmacologic chaperones bind to their protein targets and stabilize their native structures, helping mutated proteins to regain their biologic function. In preclinical studies, treatment of patient fibroblasts with these compounds resulted in increased *AGA* activity and improved lysosomal morphology in patient fibroblasts with 2 different AGU mutations.[8]

Previously, mouse-model studies investigating virus-mediated gene therapy and enzyme replacement therapy in AGU have shown some metabolic correction and decreased storage in the brain.[9,10] So far, gene therapy or enzyme replacement therapy trials have not been reported in human patients with AGU. Bone marrow transplantation was investigated on a small group of patients with AGU, with no long-term benefit.[11]

Previous MR imaging studies in patients with AGU have shown, for example, a T2 signal intensity decrease in the thalami and cerebral and/or cerebellar atrophy at later stages of the disease. SWI is a velocity-corrected gradient-echo MR imaging sequence with a high spatial resolution. It uses tissue magnetic susceptibility differences to generate contrast,[12,13] providing information about tissues that have a different susceptibility than the surrounding tissues. The susceptibility difference can be caused by substances such as deoxygenated blood, hemosiderin, ferritin, and calcium. Filtered-phase images can be used to differentiate between paramagnetic substances (ie, iron) and diamagnetic substances (calcium).[14] The paramagnetic and diamagnetic substances have opposite signal intensities on filtered-phase images, but the particular signal intensity depends on the scanner and the manufacturer. If the scanner is so-called "left-handed," the paramagnetic substances appear bright in the filtered-phase images, whereas if the scanner is "right-handed," the paramagnetic substances appear dark.

SWI has several clinical applications in the neuroimaging field. The method has been used to monitor the amount of iron in the brain in various diseases and conditions, including aging, Alzheimer disease, stroke, trauma, tumors, and multiple sclerosis.[13,15,16] To our knowledge, SWI findings in AGU have not been previously described in the literature, and our aim was to evaluate whether SWI is able to depict mineral deposits and their distribution in patients with AGU.

MATERIALS AND METHODS

We imaged 21 patients (10 girls, 7.4–15.0 years of age; mean, 10.9 ± 2.4 years) and 13 healthy controls (8 girls, 7.3–14.1 years of age; mean, 10.2 ± 2.3 years) with MR imaging (3T Magnetom Skyra; Siemens, Erlangen, Germany). The patients are participants of a recently initiated chaperone treatment trial, and they were imaged before the onset of treatment. The protocol included the following sequences: T1-weighted 3D-MPRAGE (TR = 2000 ms, TE = 2.74 ms, flip angle = 10°, thickness = 1 mm, matrix = 256 × 256), FLAIR 3D (TR = 5000 ms, TE = 386 ms, TI = 1800 ms, flip angle = 120°, thickness = 1 mm, matrix = 244 × 244), T2-weighted TSE axial (TR = 4000 ms, TE = 82 ms, flip angle = 150°, thickness = 3 mm, matrix = 448 × 448), diffusion-weighted imaging (TR = 10 160 ms, TE = 64 ms, flip angle = 180°, thickness = 3 mm, matrix = 160 × 160), diffusion tensor imaging (TR = 3700 ms, TE = 108 ms, flip angle = 90°, thickness = 2.4 mm, matrix = 98 × 96), and susceptibility-weighted imaging (TR = 27 ms, TE = 20 ms, flip angle = 15°, thickness = 2 mm, matrix = 256 × 232). The scanner manufacturer uses a so-called "left-handed" reference scheme in the SWI filtered-phase images.

Twelve patients were sedated for the MR imaging examination, whereas 9 patients were imaged without sedation. Eight of these unsedated patients had motion artifacts and were excluded from the SWI analysis, so images of altogether 13 patients (6 girls, 7.4–15.0 year of age; mean, 11.2 ± 2.5 years) were analyzed by 2 radiologists (A.T. and T.A.).

The study was approved by the local ethical committee. Written informed consent was obtained from the parents of the participants because the participants were minors and intellectually disabled.

RESULTS

Interestingly, all 13 patients with good-quality SWI showed a highly similar distribution of hypointensity in the thalamic nuclei (Fig 1). The most evident hypointensity was found in the pulvinar nuclei. Patchy hypointensities were also found, especially in the medial and anterior nuclei. Moreover, some hypointensity was noted in the globi pallidi in 6 of the patients, especially in the medial aspect. In 5 patients between 11.5 and 15.0 years of age, hypointensity was also evident in the substantia nigra. The filtered-phase images indicated accumulation of paramagnetic compounds in these areas (Fig 2). No microhemorrhages, lobar hemorrhages, or signs of subarachnoid hemorrhage were seen.

In T2WI, a signal intensity (SI) decrease was seen in all patients in the thalami, with a more intense decrease in the pulvinar nuclei, which is a previously described typical finding in AGU.[17] The SI in the thalami was normal on T1WI in all patients. Mild T2 hyperintensity in the WM was found in all patients, especially in the periventricular and deep white matter. A more intense thin lining of periventricular hyperintensity was seen in the FLAIR images in nearly all patients. Deficiencies of differentiation between gray and white matter

in the frontal and temporal lobes were common findings. Mild atrophy in the form of a thin corpus callosum, mildly dilated ventricles or cortical sulci, or cerebellar atrophy was also common in the patient group. The findings in T1- and T2-weighted sequences correspond to previously reported typical MR imaging findings in AGU.[17,18] The MR imaging findings are described in the On-line Table, and images of one patient are presented in Fig 3.

In those patients with AGU who were excluded from the SWI visual analysis due to motion artifacts, it was possible to see some SI decrease in SWI in the thalami, but more precise evaluation was not possible. In the healthy control group, no abnormal SI decrease was seen in the deep gray matter, and no other clinically relevant findings were noted in SWI or other sequences.

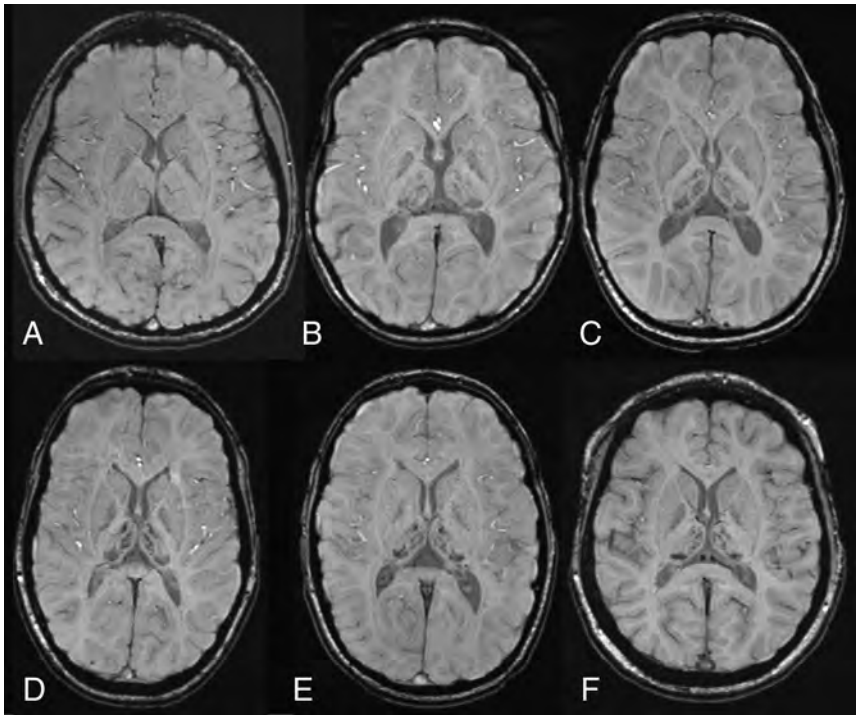

FIG 1. Susceptibility-weighted axial images at the level of basal ganglia and thalami. *A*, A healthy control, an 11-year-old girl with normal findings. *B–F*, Five patients with AGU at different ages (7.9, 9.5, 11.4, 13.8, and 14.2 years) show a strikingly similar distribution of hypointensity in deep gray matter structures, with a maximum-intensity decrease in the pulvinar nuclei. Patchy decrease is also noted in the medial and anterior thalamic nuclei. Some signal intensity decrease is also seen in the globi pallidi.

DISCUSSION

Histopathology, Cell Biology, and Role of Iron in AGU and Some Other Lysosomal Storage Disorders

In a study investigating the cerebral histopathology in patients with AGU, the basic cortical cytoarchitecture was generally preserved, but most neurons contained vacuoles that were also found in the neurons of the deep gray matter, including the thalami. In 2 of the 4 postmortem cases, the white matter showed a diffuse pallor of myelin staining and some gliosis.[19] Mouse model studies have shown similar histopathologic findings.[20]

The identity of the paramagnetic compounds causing the SWI hypointensity in the thalamic nuclei in patients

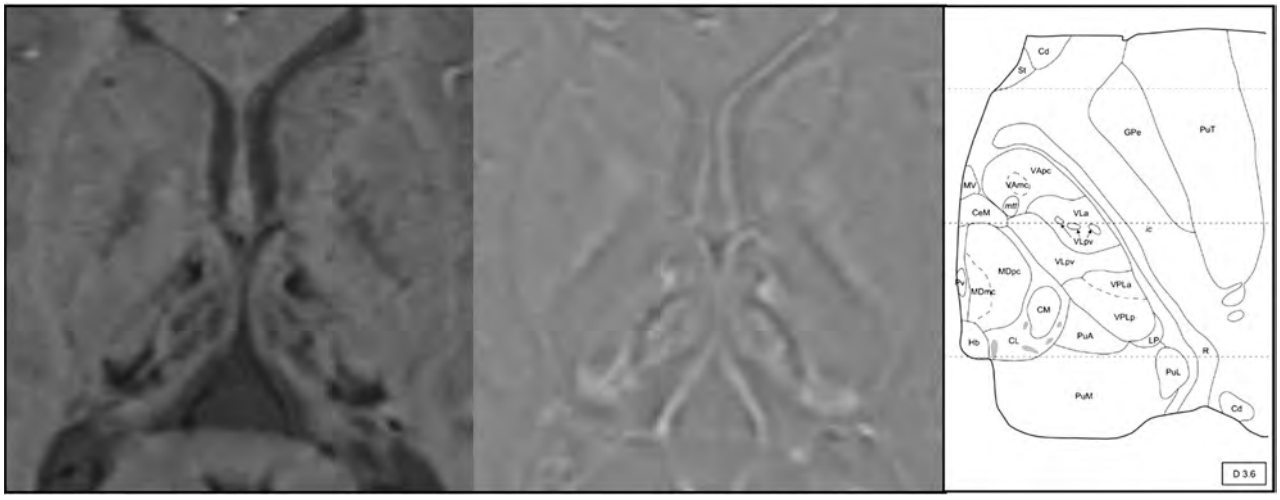

FIG 2. On the left, susceptibility-weighted axial image and magnification of the thalami in a 13-year-old boy with AGU showing the distribution of decreased signal intensity in the thalamic nuclei. The most evident decrease is seen in the pulvinar nuclei, but a patchy signal intensity decrease is also seen in the medial and anterior nuclei. In the middle, a filtered-phase image indicates accumulation of paramagnetic compounds in these areas. On the right, a schematic illustration of the nuclei of the left thalamus (figure from the atlas by Morel used with permission[29]).

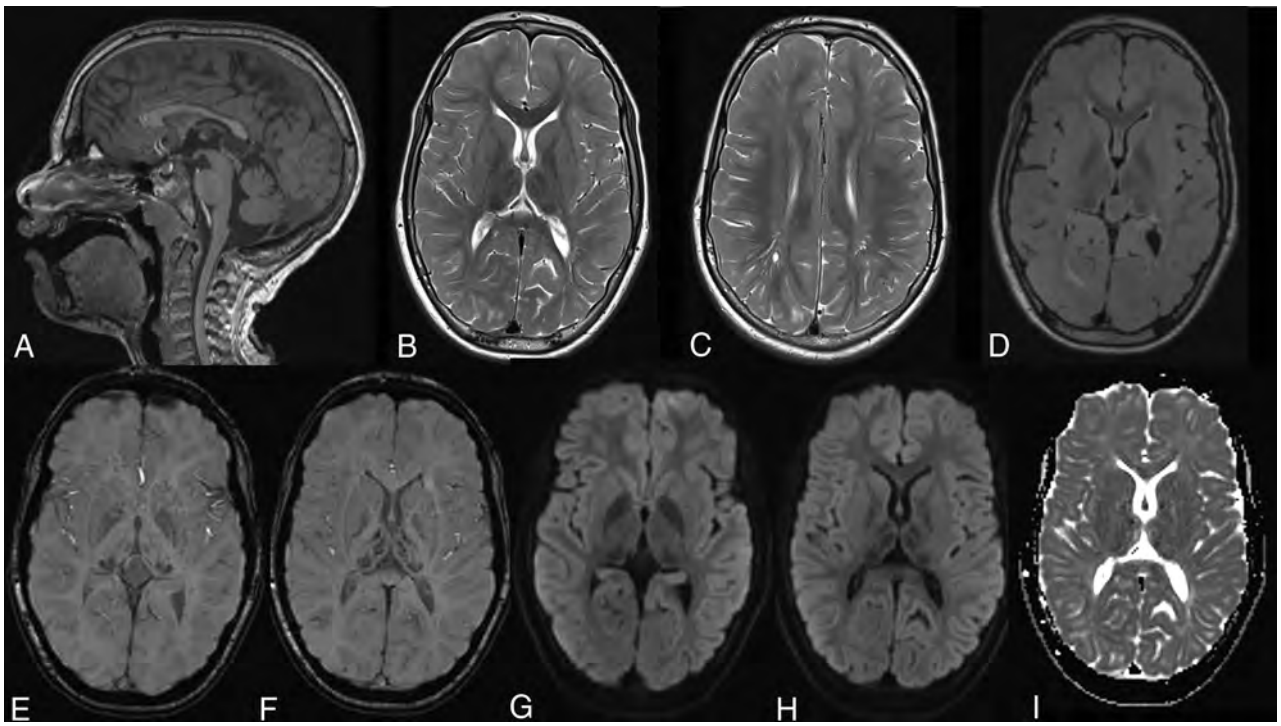

FIG 3. Typical MR imaging findings in an 11-year-old girl with AGU. *A*, Sagittal T1WI shows a relatively thin corpus callosum and a pineal cyst. *B*, Axial T2WI with typical hypointensity in the thalami and especially in the pulvinar nuclei. *C*, Axial T2WI shows hyperintensity in the white matter, poor differentiation between gray and white matter especially in frontal lobe, and some mildly dilated perivascular spaces. *D*, Axial FLAIR image also shows the hypointensity in the pulvinar nuclei and hyperintensity in the white matter. *E* and *F*, Axial SWI with hypointensity in the pulvinar and medial and anterior nuclei in the thalami. *G–I*, Axial DWI and ADC images show no signs of restricted diffusion.

with AGU remains unclear. For example, free radicals, iron, manganese ion, or deoxyhemoglobin, each of which contain unpaired electrons, may cause such an effect. On the basis of studies of cell biology and iron deposition mechanisms in other lysosomal storage disorders, it may be assumed that the finding in SWI is caused by iron in some form.

There are potential explanations for iron deposition seen especially in the thalami and other deep gray matter structures. In the brain, most of the iron is found in the oligodendrocytes and their processes, and there is a high oligodendrocyte density in the deep gray matter.[21] The SWI SI decrease may also be a result of iron accumulation of the microglia. It has been proposed that neuroinflammation is a factor in many lysosomal storage disorders, and it may negatively impact neuronal survival and contribute to neurodegeneration.[22] Microglia and astrocyte activation and influx of highly iron-laden microglia in the thalami and other structures are also possible mechanisms for iron deposition visualized by SWI. In lysosomal storage disorders, substrate accumulation disrupts the normal homeostatic function, including iron homeostasis. The accumulation of iron and its toxic effects, related to the increased cellular oxidative stress, may also have an important role in the downstream cellular pathways, resulting in cell and tissue dysfunction.[23,24]

In AGU, as the disease progresses, there are widespread changes in the brain parenchyma, for example, delayed or deficient myelination and, at later stages, also demyelination, neuronal loss, and atrophy. It is, therefore, not possible to evaluate the role of thalamic iron deposition and possible thalamic dysfunction in the various neuropsychiatric symptoms. However, thalamic pathology has been shown to correlate with cognitive dysfunction, and it may also play a role in the clinical picture of AGU. The functions of the thalamus include relaying sensory signals as well as motor signals to the cerebral cortex, but also regulation of consciousness, sleep, and alertness. Thalamocortical connectivity is associated with diverse functions of higher level cognitive processes, such as working and episodic memory, attention, and speed of information processing,[21,25] which are impaired in AGU as the disease progresses.

In a previous report of adolescent twins, one of whom had AGU, the volume of the thalami was about 30% smaller in the twin with AGU than in the healthy twin brother,[26] and the difference in volume progressed during the 4-year follow-up. This may be due to demyelination and neuronal loss. The observed SI decrease in the T2WI and SWI seen in the present study might, in part, be due to condensation of iron in the tissue, but there is apparently also an increased amount of iron due to disturbed function of lysosomes and disrupted iron homeostasis.

Iron deposition in the brain is a common finding in elderly individuals, but in healthy children and adolescents, the deep GM nuclei do not show signs of iron or other mineral deposits on SWI. In our study, the SI decrease in the pulvinar nuclei was noted even in the youngest participants with AGU, who were 7 years of age. It is possible that this finding could be observed even in younger children with AGU.

Limitations and Future Aspects

The limitation of the study is the relatively small number of patients, which is due to the rarity of the disease. In the future, it will be interesting to see whether the emerging treatments have

an effect on the MR imaging findings in AGU, including the deposition of paramagnetic compounds seen in SWI. Quantitative susceptibility mapping, which is a novel technique for the assessment of magnetic tissue susceptibility differences,[27,28] might also be used to determine disease-related iron concentration in AGU.

CONCLUSIONS

SWI showed a recognizable distribution of SI decrease in the thalamic nuclei in children and adolescents with AGU, and some of the patients also had an SI decrease in the globi pallidi and substantia nigra. The described pattern, together with other previously described MR imaging findings, may raise the suspicion of this rare disease when observed in patients with an unknown diagnosis in clinical practice. This will be increasingly important when, hopefully, there is an efficient treatment available for this disease in the near future.

ACKNOWLEDGMENTS

The authors would like to thank the participants and their families and also the Finnish patient organization Suomen AGU ry for their valuable help with the recruitment.

Disclosures: Anna Tokola—*RELATED*: *Grant*: Scientific Fund of HUS Medical Imaging Center of Helsinki University Hospital, *Comments*: Grant was used for writing this article. Minna Laine—*RELATED*: *Grant*: Jane and Aatos Erkko Foundation, Lastenlinna Foundation, Pediatric Research Center; *UNRELATED*: *Travel/Accommodations/Meeting Expenses Unrelated to Activities Listed*: Shire/Takeda, Orion, Taylor's Tale. Ritva Tikkanen—*RELATED*: *Grant*: Jane and Aatos Erkko Foundation, *Comments*: grant for research; *Support for Travel to Meetings for the Study or Other Purposes*: Suomen AGU ry, *Comments*: travel grants for meetings due to the study; *UNRELATED*: *Grants/Grants Pending*: Deutsche Forschungsgesellschaft, Succinic Semialdehyde Dehydrogenase Deficiency Association, NCL-Stiftung, *Comments:* all research grants.

REFERENCES

1. Arvio M, Mononen I. **Aspartylglycosaminuria: a review.** *Orphanet J Rare Dis* 2016;11:162 CrossRef Medline
2. Harjunen E, Laine M, Tikkanen R, et al. **Detailed profile of cognitive dysfunction in children with aspartylglucosaminuria.** *J Inherit Metab Dis* 2019 Aug 15. [Epub ahead of print] CrossRef Medline
3. Arvio P, Arvio M. **Progressive nature of aspartylglucosaminuria**. *Acta Paediatr* 2002;91:255–57 CrossRef Medline
4. Saarela J, Laine M, Oinonen C, et al. **Molecular pathogenesis of a disease: structural consequences of aspartylglucosaminuria mutations**. *Hum Mol Genet* 2001;10:983–95 CrossRef Medline
5. Syvänen AC, Ikonen E, Manninen T, et al. **Convenient and quantitative determination of the frequency of a mutant allele using solid-phase minisequencing: application to aspartylglucosaminuria in Finland**. *Genomics* 1992;12:590–95 CrossRef Medline
6. Stenson PD, Mort M, Ball EV, et al. **The Human Gene Mutation Database: building a comprehensive mutation repository for clinical and molecular genetics, diagnostic testing and personalized genomic medicine**. *Hum Genet* 2014;133:1–9 CrossRef Medline
7. Mononen I, Fisher KJ, Kaartinen V, et al. **Aspartylglycosaminuria: protein chemistry and molecular biology of the most common lysosomal storage disorder of glycoprotein degradation**. *FASEB J* 1993;7:1247–56 CrossRef Medline
8. Banning A, Gülec C, Rouvinen J, et al. **Identification of small molecule compounds for pharmacological chaperone therapy of aspartylglucosaminuria**. *Sci Rep* 2016;6:37583 CrossRef Medline
9. Dunder U, Valtonen P, Kelo E, et al. **Early initiation of enzyme replacement therapy improves metabolic correction in the brain tissue of aspartylglycosaminuria mice**. *J Inherit Metab Dis* 2010;33:611–17 CrossRef Medline
10. Virta S, Rapola J, Jalanko A, et al. **Use of nonviral promoters in adenovirus-mediated gene therapy: reduction of lysosomal storage in the aspartylglucosaminuria mouse**. *J Gene Med* 2006;8:699–706 CrossRef Medline
11. Arvio M, Sauna-Aho O, Peippo M. **Bone marrow transplantation for aspartylglucosaminuria: follow-up study of transplanted and non-transplanted patients**. *J Pediatr* 2001;138:288–90 CrossRef Medline
12. Haacke EM, Xu Y, Cheng Y-C, et al. **Susceptibility weighted imaging (SWI)**. *Magn Reson Med* 2004;52:612–18 CrossRef Medline
13. Haacke EM, Mittal S, Wu Z, et al. **Susceptibility-weighted imaging: technical aspects and clinical applications, Part 1**. *AJNR Am J Neuroradiol* 2009;30:19–30 CrossRef Medline
14. Schweser F, Deistung A, Lehr BW, et al. **Differentiation between diamagnetic and paramagnetic cerebral lesions based on magnetic susceptibility mapping**. *Med Phys* 2010;37:5165–78 CrossRef Medline
15. Ropele S, Enzinger C, Fazekas F. **Iron mapping in multiple sclerosis**. *Neuroimaging Clin N Am* 2017;27:335–42 CrossRef Medline
16. Sehgal V, Delproposto Z, Haacke EM, et al. **Clinical applications of neuroimaging with susceptibility-weighted imaging**. *J Magn Reson Imaging* 2005;22:439–50 CrossRef Medline
17. Tokola AM, Åberg LE, Autti TH. **Brain MRI findings in aspartylglucosaminuria**. *J Neuroradiol* 2015;42:345–57 CrossRef Medline
18. Autti T, Lonnqvist T, Joensuu R. **Bilateral pulvinar signal intensity decrease on T2-weighted images in patients with aspartylglucosaminuria**. *Acta Radiol* 2008;49:687–92 CrossRef Medline
19. Autti T, Raininko R, Haltia M, et al. **Aspartylglucosaminuria: radiologic course of the disease with histopathologic correlation**. *J Child Neurol* 1997;12:36 CrossRef Medline
20. Jalanko A, Tenhunen K, McKinney CE, et al. **Mice with an aspartylglucosaminuria mutation similar to humans replicate the pathophysiology in patients**. *Hum Mol Genet* 1998;7:265–72 CrossRef Medline
21. Schweser F, Raffaini Duarte Martins AL, Hagemeier J, et al. **Mapping of thalamic magnetic susceptibility in multiple sclerosis indicates decreasing iron with disease duration: a proposed mechanistic relationship between inflammation and oligodendrocyte vitality**. *Neuroimage* 2018;167:438–52 CrossRef Medline
22. Bosch ME, Kielian T. **Neuroinflammatory paradigms in lysosomal storage diseases**. *Front Neurosci* 2015;9:417 CrossRef Medline
23. Futerman AH, Van Meer G. **The cell biology of lysosomal storage disorders**. *Nat Rev Mol Cell Biol* 2004;5:554–65 CrossRef Medline
24. Bras JM. **Lysosomal storage disorders and iron**. *Int Rev Neurobiol* 2013;110:251–75 CrossRef Medline
25. Mitchell AS, Sherman SM, Sommer MA, et al. **Advances in understanding mechanisms of thalamic relays in cognition and behavior**. *J Neurosci* 2014;34:15340–46 CrossRef Medline
26. Tokola A, Brandstack N, Hakkarainen A, et al. **Erratum: White matter microstructure and subcortical gray matter structure volumes in aspartylglucosaminuria; a 5-year follow-up brain MRI study of an adolescent with aspartylglucosaminuria and his healthy twin brother.** *JIMD Rep* 2017;35:117 CrossRef Medline
27. Wang Y, Liu T. **Quantitative susceptibility mapping (QSM): decoding MRI data for a tissue magnetic biomarker**. *Magn Reson Med* 2015;73:82–101 CrossRef Medline
28. Schweser F, Deistung A, Lehr BW, et al. **Quantitative imaging of intrinsic magnetic tissue properties using MRI signal phase: an approach to in vivo brain iron metabolism?** *Neuroimage* 2011;54:2789–807 CrossRef Medline
29. Morel A. *Stereotactic Atlas of the Human Thalamus and Basal Ganglia*. Boca Raton; CRC Press; 2007

Evaluation of Lower-Dose Spiral Head CT for Detection of Intracranial Findings Causing Neurologic Deficits

J.G. Fletcher, D.R. DeLone, A.L. Kotsenas, N.G. Campeau, V.T. Lehman, L. Yu, S. Leng, D.R. Holmes III, P.K. Edwards, M.P. Johnson, G.J. Michalak, R.E. Carter, and C.H. McCollough

ABSTRACT

BACKGROUND AND PURPOSE: Despite the frequent use of unenhanced head CT for the detection of acute neurologic deficit, the radiation dose for this exam varies widely. Our aim was to evaluate the performance of lower-dose head CT for detection of intracranial findings resulting in acute neurologic deficit.

MATERIALS AND METHODS: Projection data from 83 patients undergoing unenhanced spiral head CT for suspected neurologic deficits were collected. Cases positive for infarction, intra-axial hemorrhage, mass, or extra-axial hemorrhage required confirmation by histopathology, surgery, progression of findings, or corresponding neurologic deficit; cases negative for these target diagnoses required negative assessments by two neuroradiologists and a clinical neurologist. A routine dose head CT was obtained using 250 effective mAs and iterative reconstruction. Lower-dose configurations were reconstructed (25-effective mAs iterative reconstruction, 50-effective mAs filtered back-projection and iterative reconstruction, 100-effective mAs filtered back-projection and iterative reconstruction, 200-effective mAs filtered back-projection). Three neuroradiologists circled findings, indicating diagnosis, confidence (0–100), and image quality. The difference between the jackknife alternative free-response receiver operating characteristic figure of merit at routine and lower-dose configurations was estimated. A lower 95% CI estimate of the difference greater than −0.10 indicated noninferiority.

RESULTS: Forty-two of 83 patients had 70 intracranial findings (29 infarcts, 25 masses, 10 extra- and 6 intra-axial hemorrhages) at routine head CT (CT dose index = 38.3 mGy). The routine-dose jackknife alternative free-response receiver operating characteristic figure of merit was 0.87 (95% CI, 0.81–0.93). Noninferiority was shown for 100-effective mAs iterative reconstruction (figure of merit difference, −0.04; 95% CI, −0.08 to 0.004) and 200-effective mAs filtered back-projection (−0.02; 95% CI, −0.06 to 0.02) but not for 100-effective mAs filtered back-projection (−0.06; 95% CI, −0.10 to −0.02) or lower-dose levels. Image quality was better at higher-dose levels and with iterative reconstruction ($P < .05$).

CONCLUSIONS: Observer performance for dose levels using 100–200 eff mAs was noninferior to that observed at 250 effective mAs with iterative reconstruction, with iterative reconstruction preserving noninferiority at a mean CT dose index of 15.2 mGy.

ABBREVIATIONS: $CTDI_{vol}$ = volume CT dose index; eff. mAs = effective mAs; FBP = filtered back-projection; GEE = generalized estimating equation; IR = iterative reconstruction; JAFROC FOM = jackknife alternative free-response receiver operating characteristic figure of merit

Unenhanced head CT is frequently requested in the emergency department or inpatient setting to examine patients with suspected neurologic deficit as well as those having undergone recent trauma. Surprisingly, the technique is not standardized, and the radiation dose varies substantially among institutions.[1] Radiologists strive to acquire CT examinations at the lowest dose that will answer the diagnostic question in accordance with the as low as reasonably achievable principle[2] and the justification that the diagnostic benefit to the patient

Received March 29, 2019; accepted after revision August 21.

From the Departments of Radiology (J.G.F., D.R.D., A.L.K., N.G.C., V.T.L., L.Y., S.L., G.J.M., C.H.M.), Biomedical Imaging Resource (D.R.H., P.E.), and Biomedical Statistics and Informatics (M.P.J.), Mayo Clinic, Rochester, Minnesota; and Health Sciences Research (R.E.C.), Mayo Clinic, Jacksonville, Florida.

The project described was supported by the National Institutes of Health grant No. U01 EB17185.

The content is solely the responsibility of the authors and does not necessarily represent the official views of the National Institutes of Health.

Paper previously presented, in part, at: Scientific Assembly and Annual Meeting of the Radiological Society of North America, November 27 to December 2, 2016; Chicago, Illinois.

Please address correspondence to Joel G. Fletcher, MD, Mayo Clinic, Department of Radiology, 200 First St SW, Rochester, MN 55905; e-mail: fletcher.joel@mayo.edu

Indicates open access to non-subscribers at www.ajnr.org

Indicates article with supplemental on-line appendix.

http://dx.doi.org/10.3174/ajnr.A6251

outweighs the small theoretic risk[3,4] of associated radiation injury. Unfortunately, trade-offs between observer performance and radiation dose are not well-delineated, even for most common CT tasks, and this dearth of information likely contributes to the differences in doses among institutions.

When one uses CT to answer very specific clinical questions, dramatic dose reduction for high-contrast detection tasks using unenhanced head CT can be undertaken (eg, to rule out craniosynostosis or shunt check).[5-7] However, there are scarce scientific data or an established consensus for the lowest acceptable dose for head CT for the general evaluation of suspected neurologic deficit. CT detection of early acute cerebral infarction, subtle intracranial hemorrhage, or intracranial masses is a more challenging and demanding diagnostic task because these pathologies result in only subtle low-contrast differences in the involved structures. Iterative reconstruction (IR) can provide noninferior performance for high-contrast detection tasks at lower doses; however, recent data in phantoms and abdominal CT suggest that the improvement in observer performance compared with filtered back-projection (FBP) may be limited.[8-11]

Most studies examining lower-dose head CT with iterative reconstruction have relied on subjective comparisons of image quality or contrast-to-noise ratios rather than observer (ie, radiologist) performance. Practical considerations such as collecting cases with proven imaging findings, obtaining CT images at multiple doses, and correlating imaging findings between dose levels and reference standards make such research challenging.

We have recently studied a small number of patients ($n = 43$) with suspected neurologic deficit.[12,13] This preliminary study defined lower-dose levels that were unable to preserve observer performance but included a mix of both subtle and very obvious cases, which may have affected our ability to discriminate observer performance among varying dose levels. The current study builds on these initial results to compare observer performance between routine and lower-dose levels for the detection of visually challenging intracranial findings causing acute neurologic deficit in a larger number of patients and addresses the ability of iterative reconstruction to assist with dose reduction.

MATERIALS AND METHODS

Patients and Cases

The primary diagnostic task for this study was to identify imaging findings that may require further treatment or evaluation or that may potentially explain patient signs or symptoms in patients with suspected acute neurologic deficit. After approval by the institutional review board of Mayo Clinic, we archived CT image and projection data of patients who underwent clinically indicated spiral head CT examinations for suspected acute neurologic deficit and who provided consent for the use of medical records for research purposes. CT image and projection data were collected between August 20, 2013, and May 3, 2014. Archived CT images were then reviewed by a board-certified reference neuroradiologist (D.R.D., with 19 years of experience as an attending neuroradiologist) to ensure that inclusion and exclusion criteria were met for this retrospective, case-control study.

All patients underwent CT for suspected acute neurologic deficit. Inclusion criteria were different for positive and negative cases but required reference criteria to be met. Positive cases were additionally required to have sufficient clinical evidence to meet reference standard criteria for at least 1 of 4 target conditions causing acute neurologic deficit: 1) infarction (acute, subacute, chronic, or indeterminate age), 2) intra-axial hemorrhage (eg, contusion), 3) mass, or 4) extra-axial hemorrhage (eg, subdural, subarachnoid, epidural, intraventricular). Reference standard criteria for accepting positive cases into the study required confirmation of an imaging abnormality on the CT examination by the reference radiologist, in addition to the following: 1) clinical physician confirmation of neurologic deficits at physical examination corresponding to abnormal imaging findings on the index CT examination, 2) progression or confirmation of imaging findings on another imaging examination (eg, subsequent MR imaging, CT perfusion), or 3) confirmation of imaging findings at an operation. The reference neuroradiologist, unblinded to all clinical information and all subsequent imaging and surgical reports, then marked CT images for all CT findings relating to the target diagnosis that were present within the imaged volume that met inclusion criteria using a specially designed computer workstation, tightly circumscribing each CT imaging finding relating to each diagnosis and documenting correlative reference information using standard menus. An ROI was also placed within white or gray matter (as appropriate) to reflect the background CT number in which the target lesion was located.

Negative cases were required to have sufficient evidence that a suspected acute neurologic deficit was not present. Reference standard criteria for accepting negative cases into the study included both the clinical neuroradiologist interpreting the head CT at the time of imaging as well as the unblinded reference neuroradiologist indicating that no imaging findings associated with the 4 target conditions were present, and lack of focal neurologic findings on physical examination by the clinical attending neurologist. Imaging findings of small vessel ischemic change associated with aging (leukoaraiosis) were noted in all included CT exams whether or not one of the four target diagnoses were present.

To determine the lowest radiation dose at which observer performance was noninferior to routine dose, we constructed the study cohort to display visually challenging imaging findings that might affect a radiologist's ability to detect the target diagnoses at different radiation dose levels. Obvious CT findings such as a large intracranial hemorrhage can be detected at even the 10%–20% dose levels,[12] and inclusion of such obvious cases does not help discriminate the diagnostic differences among dose levels. The nonreader reference neuroradiologist visually evaluated 857 CT examinations (620 negative and 237 positive) that met all reference and inclusion criteria and graded the conspicuity of abnormal imaging findings associated with the target diagnoses along a 4-point scale: 1) minimally evident (eg, minimal obscuration of the lentiform nucleus and insular cortex in new infarcts that might be easily missed), 2) subtle (eg, more definite acute infarct or small metastases on noncontrast spiral head CT), 3) distinct abnormality with well-defined borders (eg, small chronic infarct, small intraparenchymal hematoma), or 4) obvious

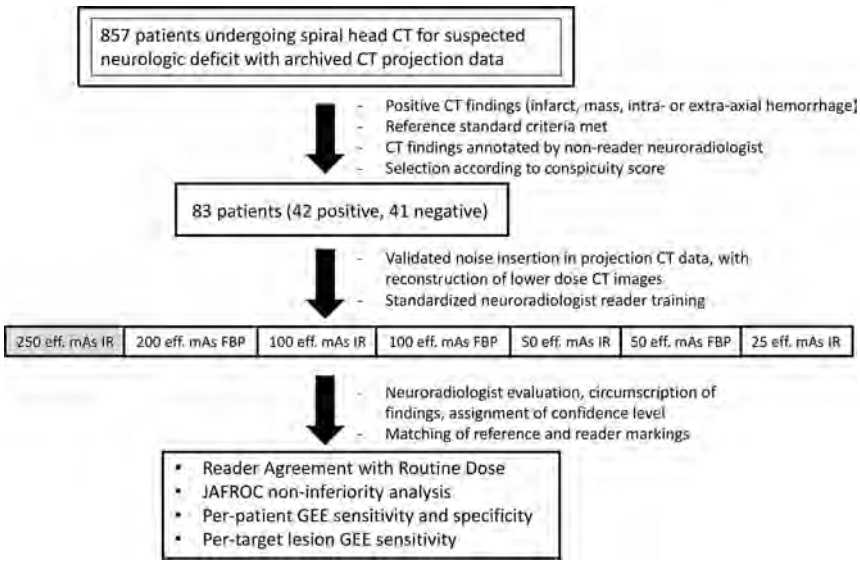

FIG 1. Study schema.

Table 1: Dose levels and reconstruction kernels for unenhanced CT examinations used in this study

Tube Current Setting	$CTDI_{vol}$ (mGy)	Reconstruction Kernel (Type, Strength)
250 eff. mAs	38.1	J40 (IR 2)
200 eff. mAs	30.5	H40 (FBP)
100 eff. mAs	15.2	J40 (IR 2)
100 eff. mAs	15.2	H40 (FBP)
50 eff. mAs	7.6	J40 (IR 2)
50 eff. mAs	7.6	H40 (FBP)
25 eff. mAs	3.8	J40 (IR 2)

finding (eg, chronic territorial infarct, large acute intraparenchymal hematoma, or diffuse subarachnoid hemorrhage). Thus, cases with obvious imaging findings that would have no discriminatory value in selecting the appropriate radiation dose level would not be included. On the basis of this subjective conspicuity score, visually challenging positive cases that met reference criteria were selected from among the collected positive cases meeting inclusion criteria (Fig 1).

The target population for this study was constructed as previously described, with a population of 83 patients, approximately half of whom would have 1 of the 4 target lesions causing acute neurologic deficit.[12]

Image Acquisition and Reconstruction

Unenhanced spiral head CT examinations were acquired using nearly identical CT platforms (Definition FLASH or Definition AS+; Siemens, Erlangen, Germany) using a single x-ray tube, a detector configuration of 64 × 0.6 mm with a z-flying focal spot yielding 128 detector rows, 1-second tube rotation time, 120 kV (peak), and either 250 effective mAs (eff. mAs) or 340 eff. mAs. The higher tube current was obtained if the examination was part of a trauma scan in our emergency department. Routine-dose CT images were reconstructed using a J40 head kernel using iterative reconstruction with a strength of 2 (sinogram-affirmed iterative reconstruction [SAFIRE]; Siemens), with 5-mm-thick images reconstructed every 5 mm in the axial plane and 2-mm-thick images reconstructed every 2 mm in the coronal plane. CT images corresponding to lower-dose levels were created by inserting image noise in CT projection data using a highly accurate and validated noise-insertion tool.[5,6,13,14] For projection data obtained using 120 kV and 340 eff. mAs, noise was inserted to obtain images corresponding to 250 eff. mAs so that all patient "routine" dose examinations corresponded to the same dose level. On the basis of the prior results, CT projection data dose levels corresponding to 100, 50, and 25 eff. mAs were then also created using iterative reconstruction at these dose levels, and additionally with FBP at 50, 100, and 200 eff. mAs (Table 1). Noise-inserted CT projection data for each case were subsequently loaded back onto the CT system to reconstruct corresponding axial and coronal images with the appropriate reconstruction kernel.

Image Evaluation by Neuroradiologists

Three neuroradiologists with 18, 18, and 5 years of experience as clinical neuroradiologists at our institution were selected as blinded radiologist readers. Because of the unique features of head CT (complicated anatomy, variety of normal aging processes not representing pathology), a standardized reader training manual that defined pathologies to be detected and instructions for reporting reader confidence scores (with anchors) was developed and reviewed by each participating neuroradiologist (On-line Appendix). Confidence scores ranged from 0 (indicating certainty that the circumscribed finding is not one of the target lesions) to 100 (indicating the highest degree of certainty that can be achieved with CT for one of the target findings).[15,16] Neuroradiologists were instructed not to mark frequently seen aging processes such as small-vessel ischemic change (leukoaraiosis), benign intraparenchymal calcification, chronic lacunar infarctions, or arachnoid cysts. Formal one-on-one reader training with the principal investigator was completed, with each reader interpreting 20 training cases selected to match the case mix, pathologies, and dose-reconstruction configurations in the subsequent reader study, discussing reader confidence ratings and any questions.[17]

Readers evaluated routine-dose–reconstruction and 6 lower-dose–reconstruction configurations using a specialized computer workstation viewing images using at least 2 window settings (80/40 and 33/40) in multiple sessions. Once a CT finding corresponding to a target diagnosis was identified, readers were instructed to tightly circumscribe all imaging abnormalities

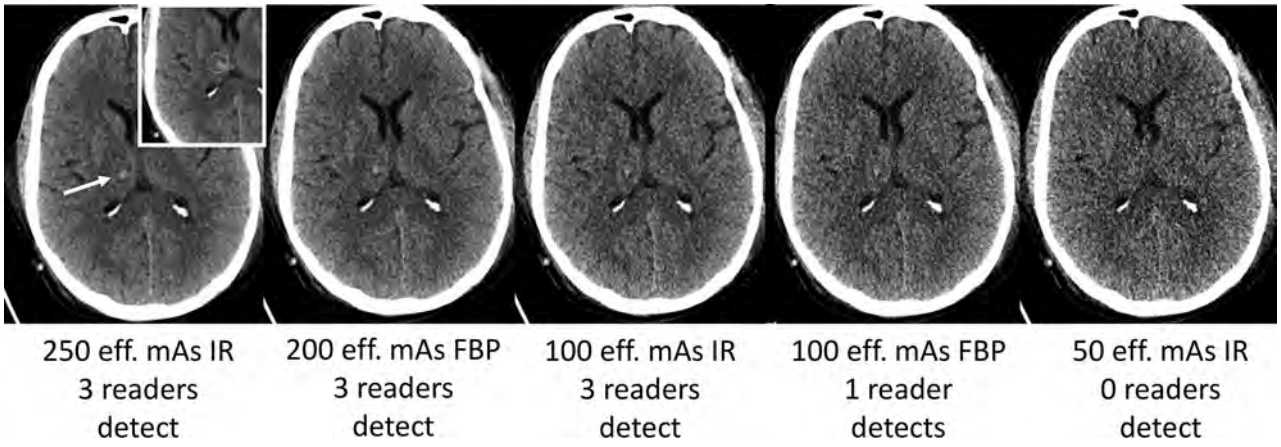

FIG 2. Small right thalamic hemorrhage (*white arrow*) shown on routine-dose CT image (250-eff. mAs IR) along with lower-dose configurations. The small left inset shows reference neuroradiologist markings of the target lesion (*green circle*). This CT examination was performed after trauma, with hemorrhage confirmed surgically, and the final diagnosis was recorded as right thalamic hemorrhage consistent with shear injury.

corresponding to one of the target diagnoses using a spline tool. Readers rated their level of confidence that one of the target diagnoses was present. Subsequently, readers answered 4 image-quality questions related to overall quality, image sharpness, image noise, and noise texture based on the modified European Quality Criteria, with overall image quality rated along a 5-point scale (1, nondiagnostic due to excessive noise or artifacts; 2, diagnosis questionable due to excessive noise or artifacts, moderate decrease in confidence; 3, diagnostic with moderate-but-acceptable noise or artifacts; 4, mild noise, no change in confidence; and 5, routine diagnostic image quality).[14,18] Examinations were interpreted in random order, with only 1 dose-reconstruction configuration per patient interpreted during each session.

Statistical Analysis

The sample size for this study was determined as a part of a 3-stage study design with the objective in this stage to screen and prioritize imaging strategies for evaluation in a large, future 10-reader, multicase study (stage 3). Stage 1, which consisted of 43 independent cases, has been previously published.[12] The original sample size calculations determined that 83 cases were needed for this second stage of the study.

Matching of colocalized reference and reader detections was performed by the reference neuroradiologist (Fig 2). Comparison of reader performance between routine-dose head CT (at 250 eff. mAs) using a head IR kernel (J40 strength 2) with lower-dose reconstruction configurations was performed using reader agreement rules and jackknife alternative free-response receiver operating characteristic figure of merit (JAFROC FOM) noninferiority analysis. Reader agreement rules compared reader localizations on the routine dose with the lower-dose configurations. For positive cases (i.e., one of the four target diagnoses was present), readers had to localize all target lesions, which were identified by 2 of 3 neuroradiologist readers at routine-dose configurations (denoted as "essential lesions"). For negative cases without imaging findings corresponding to a focal neurologic deficit, no false-positive localizations could be made by $\geq$2 of the neuroradiologist readers. Preset criteria for prioritization of a lower-dose configuration were agreement with routine dose interpretation in 71 of the 83 cases (86% of examinations).[8]

JAFROC FOM analysis used the reader confidence scores input by the readers as well as their circumscribed imaging findings. A full description of JAFROC FOM for a mixed population as in this study has been provided previously.[19,20] When $>$1 imaging finding was present in positive cases, findings were weighted according to the reciprocal of the number of findings. FOMs were calculated for every dose level and every reader. The contrasts (comparisons) of FOMs were estimated using the Hillis improvement (Dorfman, Berbaum, and Metz method under the modeling assumption of fixed readers, random cases using the Rjafroc package, Version 1.0.1 [https://cran.r-project.org/]). Noninferiority of lower-dose configurations was represented by calculating the estimated difference between routine and lower-dose configurations, with the limit of noninferiority set at -0.10, a value determined a priori on the basis of investigator consensus. This limit means that when the lower limit of the 95% confidence interval is greater than -0.10, noninferiority with observer performance at a routine dose is achieved.

In addition to these analyses, typical measures of diagnostic accuracy such as per-patient sensitivity and specificity and per-lesion sensitivity were performed. For the purposes of this calculation, a cutoff reader confidence of 10 (of 100) for one of the target findings was used. For per-patient specificity, there could be no reader circumscriptions with a confidence level of $>$10 in negative cases. For these measures of diagnostic performance, generalized estimating equations (GEEs) were used to estimate the pooled estimate across the 3 readers for each imaging strategy.

For the image quality ratings (eg, overall impression of diagnostic image quality), a summary score was computed for each of the datasets. The summary score was the mean of the 3 readers. Tests for differences in image quality across dose and reconstruction were facilitated by a mixed model consisting of a random patient factor to account for the correlation of image qualities across the doses and assumed Gaussian errors. Post hoc

Table 2: Reference documentation and conspicuity of proved lesions in positive CT examinations with imaging findings corresponding to cause of acute neurologic deficit ($n = 42$)

Target Diagnosis	No. of Imaging Findings with Target Diagnosis	No. with Reference Criterion (Nonexclusive List)	Ranking of Conspicuity Scores[a] (Mean) (SD)
Infarct	29	Clinical confirmation of corresponding deficit = 29 Progression/confirmation on another imaging study = 23 Confirmation at surgery = 0	2.10 (0.76)
Mass	25	Clinical confirmation of corresponding deficit = 22 Progression/confirmation on another imaging study = 21 Confirmation at surgery = 2	2.80 (0.70)
Extra-axial hemorrhage	10	Clinical confirmation of corresponding deficit = 10 Progression/confirmation on another imaging study = 3 Confirmation at surgery = 0	2.60 (0.66)
Intra-axial hemorrhage	6	Clinical confirmation of corresponding deficit = 6 Progression/confirmation on another imaging study = 2 Confirmation at surgery = 0	2.67 (0.47)

[a] Please see Materials and Methods. In brief, conspicuity scores: 1, minimally evident; 2, subtle; 3, distinct focal abnormality; 4, obvious.

Table 3: Reader agreement of lower-dose reconstruction configurations compared with routine-dose unenhanced head CT examinations, along with JAFROC FOMs[a]

Lower-Dose–Reconstruction Configuration	% of the 47 Essential Lesions[b] Detected by Readers at Lower-Dose Configurations		No. of Successful Interpretations per Lower-Dose–Reconstruction Configuration			
	2 of 3	3 of 3	Cases with at Least 1 Essential Lesion ($n = 34$)	Cases without Any Essential Lesions ($n = 49$)	No. Successful Interpretations (≥71 Required per Design)	JAFROC FOM (95% CI)
200 eff. mAs FBP	44 (94%)	39 (83%)	30	48	78	0.846 (0.78–0.912)
100 eff. mAs IR	43 (92%)	37 (79%)	29	46	75	0.831 (0.764–0.898)
100 eff. mAs FBP	42 (89%)	36 (77%)	28	45	73	0.805 (0.732–0.878)
50 eff. mAs IR	41 (87%)	32 (68%)	26	47	73	0.795 (0.727–0.864)
50 eff. mAs FBP	38 (81%)	31 (66%)	25	47	72	0.789 (0.717–0.861)
25 eff. mAs IR	34 (72%)	25 (53%)	22	45	67[c]	0.754 (0.681–0.827)

[a] The JAFROC FOM for routine unenhanced head CT (250 eff. mAs with IR) was 0.867 (0.805–0.929).
[b] Essential lesions are described in the Materials and Methods. Briefly, they represent lesions correctly localized and classified at the routine dose (250 eff. mAs with IR) by majority of readers.
[c] Dose-reconstruction configuration did not meet preset criteria for agreement with routine-dose interpretation, which was defined as agreement in 71 of the 83 examinations.

comparisons of the quality summary score were considered descriptive and were not adjusted for multiple testing across doses. We evaluated the effect of certain CT lesion characteristics such as size, CT number difference, and contrast-to-noise ratio compared with adjacent normal-appearing brain parenchyma on observer performance using Spearman rank coefficients comparing these parameters with mean reader confidence for correctly detected lesions. For false-negative examinations, a confidence score of zero was assigned.

RESULTS

Eighty-three CT examinations in patients with suspected neurologic deficit had a mean volume CT dose index ($CTDI_{vol}$) of 38.1 ± 1.3 mGy. Forty-two positive cases had 70 proven target lesions (ie, mean, 1.6 ± 1.2 target imaging findings causing suspected neurologic deficit per patient). There were 29 infarcts, 25 masses, 10 extra-axial hemorrhages, and 6 intra-axial hemorrhages (Table 2). The mean area for the imaging findings was 6.9 ± 8.2 cm^2, with the longest and shortest linear dimensions being 3.9 ± 3.0 cm and 2.2 ± 1.1 cm, respectively. Thirty patients (36%) had leukoaraiosis (17 with proven target lesions, 13 without lesions).

Table 3 shows reader agreement for lower-dose configurations along with JAFROC FOMs. The 25-eff. mAs IR configuration failed to meet preset criteria for reader agreement rules. For lower-dose configurations, a greater proportion of nonagreement with the routine dose comes from missed lesions (false-negative interpretations) rather than false-positive interpretations (or localizations) in negative examinations (Figs 2 and 3). At least 2 of 3 of the neuroradiologists identified 94% of the target lesions at 200-eff. mAs FBP, and this declined to 87% at 50-eff. mAs IR and 81% at 50-eff. mAs FBP, while the number of correctly interpreted negative cases remained virtually identical.

Table 4 shows the GEE per-patient sensitivity and specificity, as well as the target lesion sensitivity for CT findings accounting for neurologic deficits in our patient

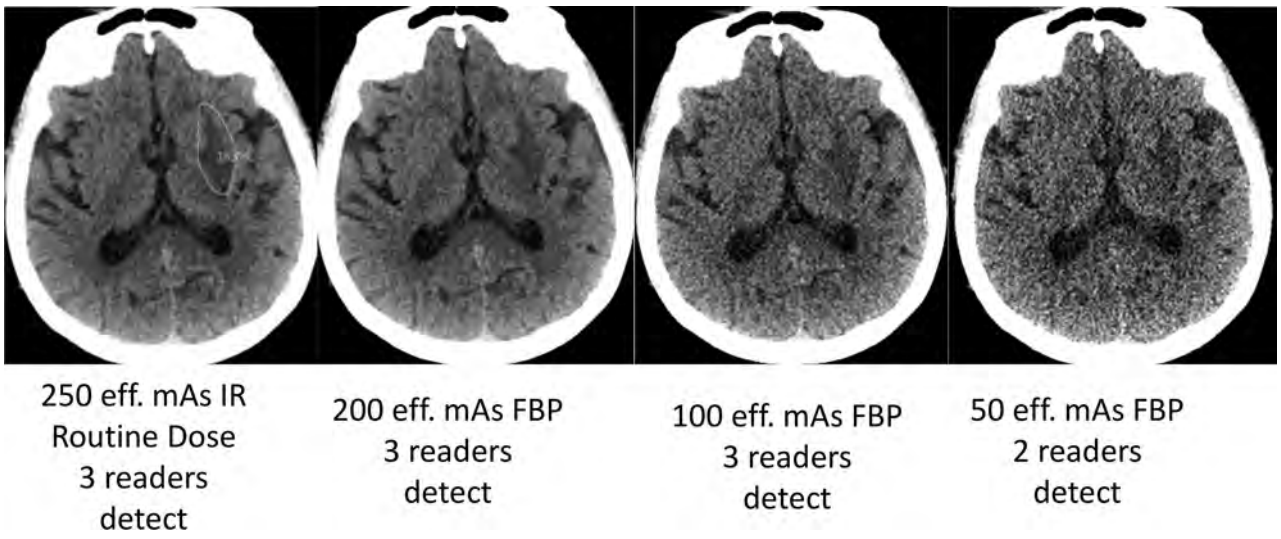

FIG 3. Acute left lentiform nucleus infarct (*green circle* indicates reference neuroradiologist markings at routine dose) with corresponding lower-dose FBP CT images along with reader results. The imaging finding on this CT examination evolved with time, with corresponding clinical confirmation of corresponding neurologic deficit by a staff neurologist, and the final diagnosis was recorded as acute left striatal infarct.

Table 4: Per-patient and per-lesion sensitivity and specificity using GEEs for target neurologic findings accounting for acute neurologic deficits

Dose-Kernel Configuration	Per-Patient Sensitivity for CT Findings Accounting for Acute Neurologic Deficits (GEE) (%) (95% CI) (Range) (%)	Per-Patient Specificity for CT Findings Accounting for Acute Neurologic Deficits (GEE) (%) (95% CI) (Range) (%)	Target Lesion Sensitivity for CT Findings Accounting for Acute Neurologic Deficits (GEE) (%) (95% CI) (Range) (%)
250-eff. mAs IR	81.7 (71.1–92.3) (78.6–83.3)	93.5 (88.9–98.1) (85.4–100.0)	
200-eff. mAs FBP	79.4 (68.2–90.6) (76.2–83.3)	91.9 (87.5–96.3) (80.5–100.0)	68.6 (62.3–74.9) (61.4–72.9)
100-eff. mAs IR	77.0 (65.5–88.5) (73.8–81.0)	88.6 (82.8–94.4) (73.2–95.1)	68.1 (61.8–74.4) (64.3–71.4)
100-eff. mAs FBP	74.6 (62.4–86.8) (69.0–78.6)	87.0 (81.1–92.9) (75.6–95.1)	62.9 (56.3–69.4) (57.1–65.7)
50-eff. mAs IR	73.8 (62.3–85.4) (66.7–78.6)	88.6 (82.8–94.4) (75.6–97.6)	60.5 (53.9–67.1) (52.9–65.7)
50-eff. mAs FBP	72.2 (60.6–83.8) (71.4–73.8)	83.7 (77.7–89.8) (69.8–86.0)	61.0 (54.4–67.6) (60.0–62.9)
25-eff. mAs IR	65.9 (53.3–78.4) (61.9–71.4)	88.6 (82.4–94.8) (85.4–92.7)	53.3 (46.6–60.1 (45.7–62.9)[a]

[a] The 95% confidence interval does not overlap the routine dose, so the dose-reconstruction configuration is significantly worse.

population. Per-target lesion GEE sensitivity was significantly decreased compared with routine-dose unenhanced head CT for a 25-eff. mAs IR configuration (Figs 4 and 5). Per-patient GEE sensitivity was not significantly different from the reference dose at any lower configurations. GEEs per patient specificity declined only slightly at lower doses.

Figure 4 is the forest plot demonstrating the difference between routine-dose and the lower-dose configurations. Only the 100-eff. mAs IR and 200-eff. mAs FBP lower-dose configurations demonstrated noninferiority compared with the routine dose, with noninferiority not demonstrated for 100-eff. mAs FBP and lower-dose configurations.

Figure 5 demonstrates the overall image-quality ratings for routine and lower-dose configurations. Each lower-dose configuration had significantly inferior image quality ($P < .05$). At 100-eff. mAs and 50-eff. mAs dose levels, configurations with iterative reconstruction had significantly higher image quality ($P < .001$).

Mean reader confidence was moderately affected by lesion size (Spearman correlation coefficients for lower-dose configurations: $p = 0.23$, $P = .053$ for FBP 200 eff. mAs and $p = 0.35$–0.39, $P < .05$ for lower doses). Mean reader confidence had a somewhat weaker relationship with both the contrast-to-noise ratio ($p = 0.16$, $P = .18$ for FBP 200 eff. mAs and $p = 0.24$–0.32, $P < .05$ for lower doses) and the CT number difference ($p = 0.11$, $P = .35$ at FBP 200 eff. mAs and $p = 0.2$–0.29 for lower doses with $P < .05$ at FBP 100 eff. mAs, FBP 50 eff. mAs, and IR 25 eff. mAs).

DISCUSSION

In keeping with the as low as reasonably achievable principle, radiologists strive to perform diagnostically useful imaging at the lowest possible radiation exposure dose to the patient. In this work, we systematically evaluated the ability to reduce the radiation dose for spiral unenhanced head CT for acute neurologic deficit without compromising neuroradiologist observer performance. Our study cohort included patients with suspected neurologic deficit with either proven CT findings positive for infarction, intra-axial hemorrhage, mass, or extra-axial hemorrhage by the reference criteria or CT examinations negative for imaging findings correlating to these target diagnoses accompanied by lack of focal neurologic findings on physical

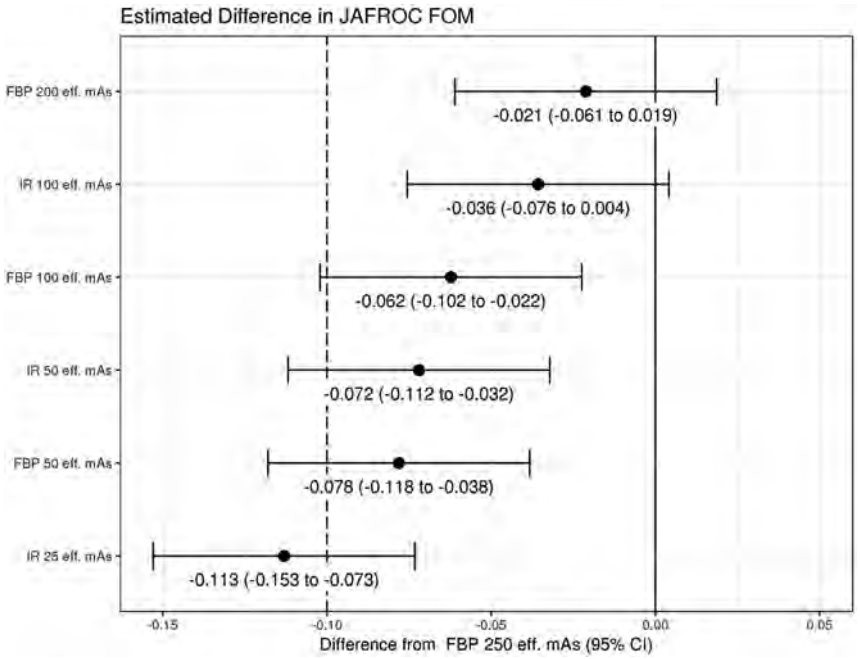

FIG 4. Noninferiority analysis showing the difference between JAFROC FOM at a routine dose and the lower-dose configurations for CT findings causing acute neurologic deficit. The limit of noninferiority was established a priori to be −0.10, meaning that if the lower limit of the 95% confidence interval is greater than −0.10, then noninferiority was shown.

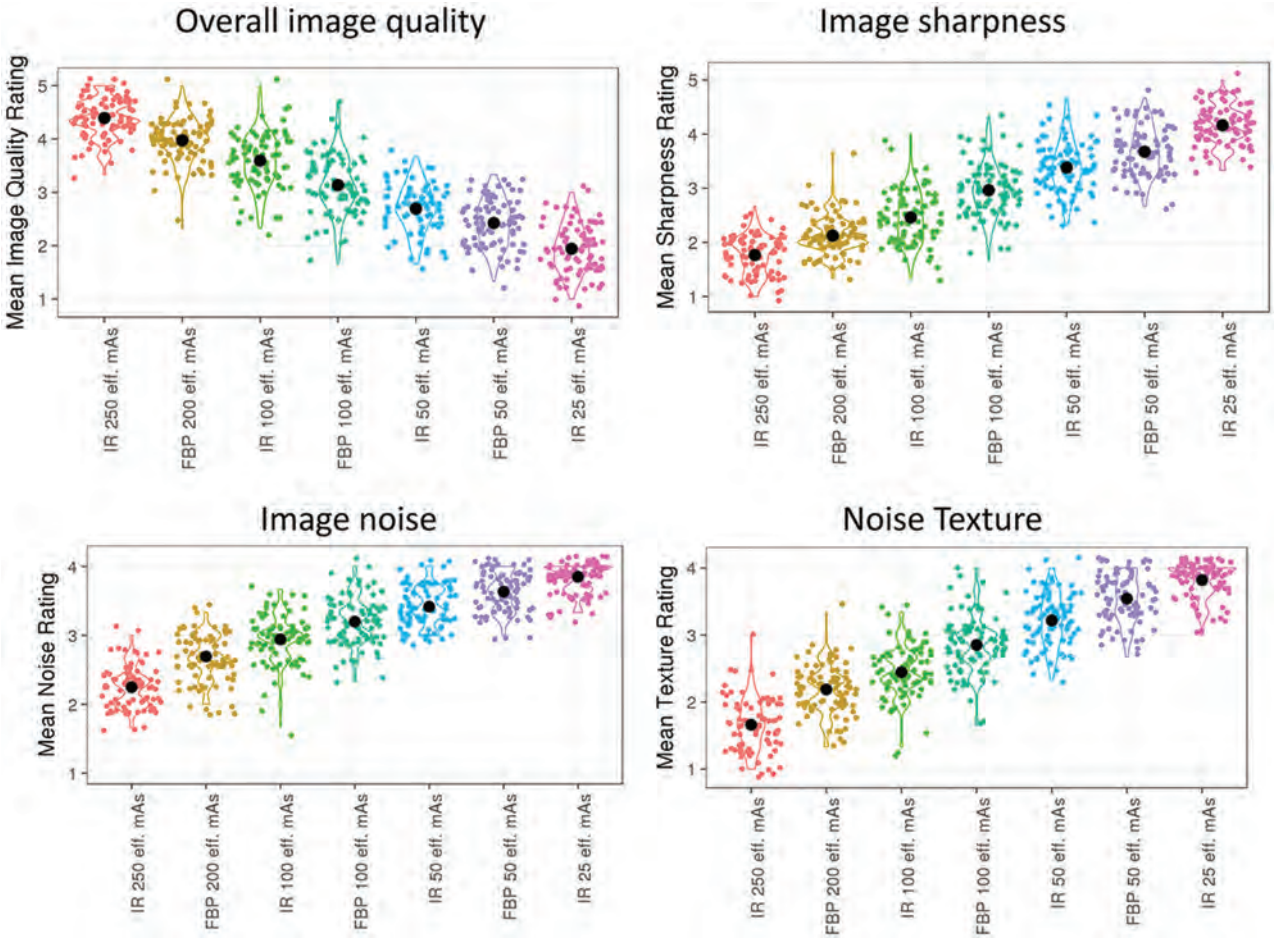

FIG 5. Image-quality metrics for routine and lower-dose configurations in this study. Optimal ratings were 5 for image quality and 1 for individual image metrics (i.e. image sharpness, noise, and texture).

examination by the clinical attending neurologist. We found that there were small, nonsignificant decreases in sensitivity for CT findings accounting for neurologic deficits at all lower-dose configurations but that there was substantial opportunity for dose reduction if small decreases in performance were acceptable. Specifically, we found that observer performance was noninferior down to 40% of our routine dose level (ie, a tube current setting of 100 effective mAs, corresponding to a $CTDI_{vol}$ of 15.2 mGy; Table 4) when iterative reconstruction was used. At the same dose level with images reconstructed with weighted FBP, sensitivity for target lesions accounting for neurologic deficits declined by about 2%–3% and specificity declined by 1.5%–5%.

Prior work examining the ability to lower the radiation dose at unenhanced head CT has been largely focused on the ability to improve image quality,[21-23] because this may be a barrier to radiologists examining noisier, lower-dose images. Wu et al[24] examined image quality and diagnostic accuracy using iterative reconstruction with a case-control design and lowering the rotation dose by 43% with either tube current or tube voltage reduction. They found that dose reduction achieved with tube current reduction and IR preserved image quality, but their study did not report observer performance for pathologic entities, relying instead on detection of subcortical arteriosclerotic encephalopathy and the number of infarcts as a surrogate marker. Additionally, several studies evaluating unenhanced head CT have not used spiral head CT, which can facilitate a lower radiation dose compared with sequential scanning.[25] Without observer performance data to ensure that lower doses do not result in inferior performance, routine diagnostic levels are often set by subjective image-quality perceptions of individuals or by benchmarking to other institutions. Having observer performance data on which to facilitate dose reduction is needed for making objective decisions and may assist in overcoming differences among institutions.

Recent clinical and phantom studies in abdominal CT have highlighted the limitations of iterative reconstruction and its ability to facilitate radiation-dose reduction for low-contrast objects such as hepatic metastases. Mileto et al[9] recently had 16 radiologists examine a low-contrast detectability phantom and found that radiation doses resulted in similar declines in observer performance for FBP and IR and that differences among radiologists were larger than across reconstruction algorithms. Jensen et al[11] found that an approximately 50% dose reduction with one iterative reconstruction approach did not preserve observer performance for the detection of hepatic metastases. Fletcher et al[8,12] found that FBP and IR performed similarly at lower doses in detecting hepatic metastases and that IR might only be needed to maintain observer performance at a certain threshold dose. Similar to these studies, we found that performance for the detection of intracranial findings causing acute neurologic deficits declined slightly at lower doses using JAFROC FOM as a metric of observer performance but that iterative reconstruction was helpful in preserving noninferiority at 100 eff. mAs. On the basis of this work, we plan to refine the results with a multireader, multcase study with 10 neuroradiologists to better predict the lowest dose that can preserve performance.

Our study has limitations. Because of the concern for missing subtle findings in patients with acute neurologic deficits, we used a retrospective case-control study design using an enriched cohort of visually challenging CT findings to discriminate radiation dose levels, with these findings proven on the basis of surgical assessment, follow-up imaging, or corresponding neurologic deficits. From a radiation exposure standpoint, it is not possible to re-image patients directly at multiple differing exposures during the same imaging session. Therefore, we relied on a validated noise-insertion method to reconstruct CT images corresponding to multiple dose levels; however, we have found that this method is highly accurate and has allowed our clinical practice to readily adopt research findings obtained using this method.[5,6] CT interpretation at reduced radiation dose levels is subjectively more demanding and fatiguing than at standard doses, and the potential effects of radiologist fatigue could not be measured in our study because neuoradiologists interpreted cases with different dose levels in each interpretation session. Finally, our results relied on interpretations by only 3 neuroradiologists, and extrapolation of their interpretations to a larger number of neuroradiologists or general radiologists may be limited.

CONCLUSIONS

This study helps to better define the potential dose reduction that can be achieved with conventional spiral CT and IR that will maintain diagnostic performance for evaluation of suspected neurologic deficit. Our study demonstrates that substantial opportunity exists for dose reduction using spiral nonenhanced head CT and that the dose level might potentially be reduced to 40% of routine dose levels or a $CTDI_{vol}$ of approximately 15 mGy if slight decreases in performance are acceptable (eg, in follow-up and surveillance). Furthermore, the beneficial effect of IR was most pronounced at this 15-mGy dose level. Above this dose level, observer performance might be preserved with filtered back-projection alone.

ACKNOWLEDGMENTS

We acknowledge Maria Shiung, Adam Bartley, and Kris Nunez for their dedicated assistance in carrying out this study and preparing the manuscript. We appreciate the support of Dr Kent Thielen, Chair of the Department of Radiology at Mayo Clinic Rochester, for his commitment to ensure that a large number of staff could participate in this endeavor over a long period of time.

Disclosures: Joel G. Fletcher—*UNRELATED*: *Grants/Grants Pending*: Siemens.* David R. Holmes—*RELATED*: *Grant*: National Institutes of Health.* Cynthia H. McCollough—*UNRELATED*: *Grants/Grants Pending*: Siemens, *Comments*: Industry Research Grant.* *Money paid to the institution.

REFERENCES

1. Smith-Bindman R, Wang Y, Yellen-Nelson TR, et al. **Predictors of CT radiation dose and their effect on patient care: a comprehensive analysis using automated data.** *Radiology* 2017;282:182–93 CrossRef Medline

2. Centers for Disease Control and Prevention. **ALARA: As Low As Reasonably Achievable.** https://www.cdc.gov/nceh/radiation/alara.html. Accessed February 22, 2019
3. McCollough CH, Bushberg JT, Fletcher JG, et al. **Answers to common questions about the use and safety of CT scans.** *Mayo Clin Proc* 2015;90:1380–92 CrossRef Medline
4. McCollough CH, Guimaraes L, Fletcher JG. **In defense of body CT.** *AJR Am J Roentgenol* 2009;193:28–39 CrossRef Medline
5. Gabriel S, Eckel LJ, DeLone DR, et al. **Pilot study of radiation dose reduction for pediatric head CT in evaluation of ventricular size.** *AJNR Am J Neuroradiol* 2014;35:2237–42 CrossRef Medline
6. Montoya JC, Eckel LJ, DeLone DR, et al. **Low-dose CT for craniosynostosis: preserving diagnostic benefit with substantial radiation dose reduction.** *AJNR Am J Neuroradiol* 2017;38:672–77 CrossRef Medline
7. Widmann G, Schullian P, Gassner EM, et al. **Ultralow-dose CT of the craniofacial bone for navigated surgery using adaptive statistical iterative reconstruction and model-based iterative reconstruction: 2D and 3D image quality.** *AJR Am J Roentgenol* 2015;204:563–69 CrossRef Medline
8. Fletcher JG, Fidler JL, Venkatesh SK, et al. **Observer performance with varying radiation dose and reconstruction methods for detection of hepatic metastases.** *Radiology* 2018;289:455–64 CrossRef Medline
9. Mileto A, Zamora DA, Alessio AM, et al. **CT detectability of small low-contrast hypoattenuating focal lesions: iterative reconstructions versus filtered back projection.** *Radiology* 2018;289:443–54 CrossRef Medline
10. Goenka AH, Herts BR, Obuchowski NA, et al. **Effect of reduced radiation exposure and iterative reconstruction on detection of low-contrast low-attenuation lesions in an anthropomorphic liver phantom: an 18-reader study.** *Radiology* 2014;272:154–63 CrossRef Medline
11. Jensen CT, Wagner-Bartak NA, Vu LN, et al. **Detection of colorectal hepatic metastases is superior at standard radiation dose CT versus reduced dose CT.** *Radiology* 2019;290:400–09 CrossRef Medline
12. Fletcher JG, Yu L, Fidler JL, et al. **Estimation of observer performance for reduced radiation dose levels in CT: eliminating reduced dose levels that are too low is the first step.** *Acad Radiology* 2017;24:876–90 CrossRef Medline
13. Yu L, Shiung MM, Jondal D, et al. **Development and validation of a practical lower-dose-simulation tool for optimizing CT scan protocols.** *J Comput Assist Tomogr* 2012;36:477–87 CrossRef Medline
14. Fletcher JG, Yu L, Li Z, et al. **Observer performance in the detection and classification of malignant hepatic nodules and masses with CT image-space denoising and iterative reconstruction.** *Radiology* 2015;276:465–78 CrossRef Medline
15. Briggs M, Closs JS. **A descriptive study of the use of visual analogue scales and verbal rating scales for the assessment of postoperative pain in orthopedic patients.** *J Pain Symptom Manage* 1999;18:438–46 CrossRef Medline
16. Hadjiiski L, Chan HP, Sahiner B, et al. **Quasi-continuous and discrete confidence rating scales for observer performance studies: effects on ROC analysis.** *Acad Radiol* 2007;14:38–48 CrossRef Medline
17. Dendumrongsup T, Plumb AA, Halligan S, et al. **Multi-reader multicase studies using the area under the receiver operator characteristic curve as a measure of diagnostic accuracy: systematic review with a focus on quality of data reporting.** *PLoS One* 2014;9:e116018 CrossRef Medline
18. Froemming AT, Kawashima A, Takahashi N, et al. **Individualized kV selection and tube current reduction in excretory phase computed tomography urography: potential for radiation dose reduction and the contribution of iterative reconstruction to image quality.** *J Comput Assist Tomogr* 2013;37:551–59 CrossRef
19. Chakraborty D, Yoon H. **JAFROC analysis revisited: figure-of-merit considerations for human observer studies.** *Proceedings of SPIE* 2009;7263:72630T CrossRef Medline
20. Chakraborty D, Philips P, Zhai X, et al. **RJafroc: Analyzing Diagnostic Observer Performance Studies.** https://CRAN.R-project.org/package=RJafroc. Accessed January 14, 2019
21. Harris M, Huckle J, Anthony D, et al. **The acceptability of iterative reconstruction algorithms in head CT: an assessment of sinogram affirmed iterative reconstruction (SAFIRE) vs. filtered back projection (FBP) using phantoms.** *J Med IMag Rad Sci* 2017;48:259–69 CrossRef Medline
22. Korn A, Fenchel M, Bender B, et al. **Iterative reconstruction in head CT: image quality of routine and low-dose protocols in comparison with standard filtered back-projection.** *AJNR Am J Neuroradiol* 2012;33:218–24 CrossRef Medline
23. Love A, Olsson ML, Siemund R, et al. **Six iterative reconstruction algorithms in brain CT: a phantom study on image quality at different radiation dose levels.** *Br J Radiol* 2013;86:20130388 CrossRef Medline
24. Wu TH, Hung SC, Sun JY, et al. **How far can the radiation dose be lowered in head CT with iterative reconstruction? Analysis of imaging quality and diagnostic accuracy.** *Eur Radiol* 2013;23:2612–21 CrossRef Medline
25. Pace I, Zarb F. **A comparison of sequential and spiral scanning techniques in brain CT.** *Radiol Technol* 2015;86:373–78 Medline

Dose Reduction While Preserving Diagnostic Quality in Head CT: Advancing the Application of Iterative Reconstruction Using a Live Animal Model

F.D. Raslau, E.J. Escott, J. Smiley, C. Adams, D. Feigal, H. Ganesh, C. Wang, and J. Zhang

ABSTRACT

BACKGROUND AND PURPOSE: Iterative reconstruction has promise in lowering the radiation dose without compromising image quality, but its full potential has not yet been realized. While phantom studies cannot fully approximate the subjective effects on image quality, live animal models afford this assessment. We characterize dose reduction in head CT by applying advanced modeled iterative reconstruction (ADMIRE) in a live ovine model while evaluating preservation of gray-white matter detectability and image texture compared with filtered back-projection.

MATERIALS AND METHODS: A live sheep was scanned on a Force CT scanner (Siemens) at 12 dose levels (82–982 effective mAs). Images were reconstructed with filtered back-projection and ADMIRE (strengths, 1–5). A total of 72 combinations (12 doses × 6 reconstructions) were evaluated qualitatively for resemblance to the reference image (highest dose with filtered back-projection) using 2 metrics: detectability of gray-white matter differentiation and noise-versus-smoothness in image texture. Quantitative analysis for noise, SNR, and contrast-to-noise was also performed across all dose-strength combinations.

RESULTS: Both qualitative and quantitative results confirm that gray-white matter differentiation suffers at a lower dose but recovers when complemented by higher iterative reconstruction strength, and image texture acquires excessive smoothness with a higher iterative reconstruction strength but recovers when complemented by dose reduction. Image quality equivalent to the reference image is achieved by a 58% dose reduction with ADMIRE-5.

CONCLUSIONS: An approximately 60% dose reduction may be possible while preserving diagnostic quality with the appropriate dose-strength combination. This in vivo study can serve as a useful guide for translating the full implementation of iterative reconstruction in clinical practice.

ABBREVIATIONS: ADMIRE = advanced modeled iterative reconstruction; CNR = contrast-to-noise ratio; FBP = filtered back-projection; IR = iterative reconstruction

Iterative reconstruction (IR), in requiring less radiation to produce diagnostic images, plays a central role in dose reduction while maintaining image quality.[1,2] Although IR has been widely adopted, its full implementation is yet to be realized. It is our observation that hesitation in using the highest IR strengths is mainly due to overly "smooth" or "plastic" image texture that is deemed undesirable by radiologists. Image noise and texture characteristics reconstructed in a statistically optimal fashion could be rather different from those of filtered back-projection (FBP). The traditional FBP reconstruction algorithm is analytic in nature. The relationship between radiation dose and perceived image quality is well known—that is, image noise is inversely proportionate to the square root of the radiation dose. However, IR algorithms are nonlinear in nature, so the use of low radiation does not necessarily translate into high image noise. In addition, the application of IR may push noise texture toward the lower frequency of the Fourier spectrum, resulting in a plastic appearance in the presented images.[3] It is our contention that further dose reduction can be achieved without sacrificing image quality, but optimal imaging parameters must be established because various combinations influence the balance of image quality and radiation dose.[4]

Protocol optimization has traditionally turned to anthropomorphic phantoms[4-13] and clinical patients.[10-21] However, they have advantages and limitations. Phantoms (and cadavers) allow

Received July 5, 2019; accepted after revision August 21.

From the Departments of Radiology (F.D.R., E.J.E., C.A., D.F., H.G., J.Z.), Neurology (F.D.R.), Neurosurgery (F.D.R.), Otolaryngology-Head and Neck Surgery (E.J.E.), Laboratory Animal Resources (J.S.), and Biostatistics (C.W.), University of Kentucky, Lexington, Kentucky.

Paper previously presented as an electronic scientific poster at: Annual Meeting of the American Society of Neuroradiology, May 18–23, 2019; Boston, Massachusetts.

Please address correspondence to Flavius D. Raslau, MD, University of Kentucky, 800 Rose St, Lexington, KY 40536; e-mail: flavius.raslau@uky.edu

http://dx.doi.org/10.3174/ajnr.A6258

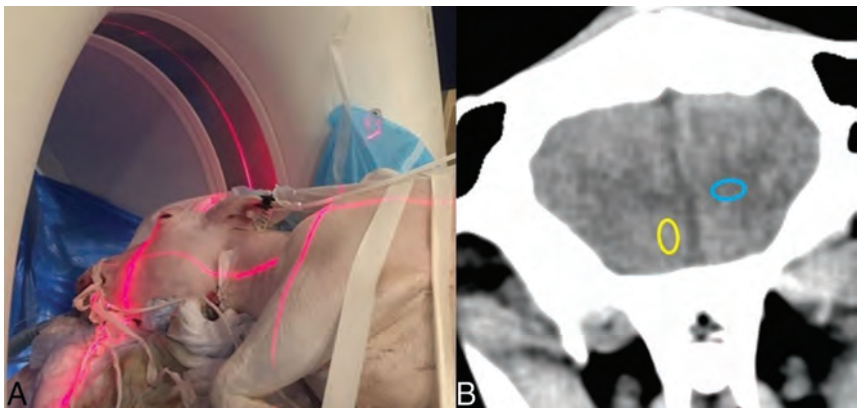

FIG 1. *A*, Positioning of the sheep, a 4-year-old 72-kg hornless white Dorper ewe, in the CT scanner. *B*, Sample coronal head CT images with ROIs marking the cortical gray matter (yellow) and deep white matter (blue) for quantitative analysis.

convenient repeatable testing under controlled conditions and additionally provide an objective metric for lesion detectability, which has emerged as an important metric in IR optimization.[5-9] Even so, phantom studies are limited in that they fail to adequately reproduce the complexities of living tissue (eg, gray-white matter differentiation). Clinical trials are indispensably valuable, but this approach fails to control for many potential variables. Unwarranted radiation exposure should be avoided; therefore, only a narrow range of parameters can be tested and usually between follow-up scans separated by time.

Live animal studies provide a crucial bridge that can leverage advantages from both sides. Despite the virtues of such a middle-of-the-road approach, it is a path rarely trodden. Sparse studies have used pig[22] brain with IR as well as dog[23] and pig[24] brains unrelated to IR, yet these animals were euthanized at the time of scanning, which alters physiology and calls into question their adequacy. Only in vivo models can adequately simulate the real-life concerns of practicing radiologists. Thus, live animal studies can help close the gap between the knowledge learned from anthropomorphic phantoms and its translation into clinical practice.

Advanced modeled iterative reconstruction (ADMIRE), which is made available by Siemens on their high-end CT scanners, is a model-based iterative reconstruction algorithm with more advanced noise-reduction methods. Our preliminary observations suggest that higher IR strengths require an appropriate choice of radiation exposure to mitigate the unwanted smoothing texture.[25] Moreover, the fact that image-quality assessment must scrutinize image texture is another point often neglected, which we wish to bring to the forefront. The purpose of this study was to characterize dose reduction in head CT by applying ADMIRE in a live ovine model, while evaluating preservation of gray-white matter detectability and image texture compared with the FBP reference.

MATERIALS AND METHODS

Animal Subject

This study was reviewed and approved by the University of Kentucky Institutional Animal Care and Use Committee and conducted in accordance with principles in the National Research Council, 2011, *Guide for the Care and Use of Laboratory Animals*. 8th ed. Washington DC: National Academic Press.

The animal used for the study was a 4-year-old, 72-kg, hornless, white Dorper ewe procured from the University of Kentucky Research Sheep Center, Department of Food and Animal Sciences. The ewe was a cull breeding animal scheduled to be removed from the flock due to the loss of an udder to mastitis (condition resolved at time of the study).

Before transfer to the University of Kentucky Division of Laboratory Animal Resources facilities, negative pregnancy and Q fever statuses were confirmed. The Division of Laboratory Animal Resources Experimental Surgery staff and a veterinarian oversaw anesthesia induction, monitoring, and animal transport. The animal fasted overnight and was induced with a mixture of midazolam (0.4 mg/kg, IV) + ketamine (5.5 mg/kg, IV) and orotracheal intubated and maintained on isoflurane (1.75%–2.0%) in 100% O_2 with breathing self-regulated. Isotonic crystalloid (0.9% NaCl, 5–10 mL/kg/h) was administered for the duration of the study. At the conclusion of imaging, the animal was euthanized by sodium pentobarbital overdose while remaining under anesthesia.

Scanning Protocol

Images were obtained on a Force CT scanner (Siemens, Erlangen, Germany). The sheep was in a lateral decubitus position in the gantry for the acquisition of coronal sections of the head (Fig 1*A*). Considering the morphology of the animal brain, the coronal section was chosen for optimal presentation and discrimination of cortical gray matter versus subcortical white matter. The FOV was 142 × 142 mm, and the matrix was 512 × 512, yielding 0.28 × 0.28 in-plane spatial resolution and a 5-mm section thickness. Tube voltage was fixed at 120 kV, pitch at 0.55, and row collimation at 0.6 mm. Tube current was varied from 982 to 82 effective mAs in 12 levels, with approximately 8% dose reduction between each level. Automated exposure control was turned off to control tube current in each run.

A standard protocol does not exist for scanning a small brain, weighing just 10% of the weight of a normal adult human brain. The application of automated exposure control to establish the starting reference dose did not produce adequate gray-white matter differentiation by the judgment of 2 neuroradiologists. The algorithm, which relies on a topogram-based calculation, likely failed due to the animal's disproportionately large face. Thus, the tube current for the reference protocol was identified by raising the tube current until the 2 neuroradiologists were satisfied with the diagnostic image quality and gray-white differentiation. Reconstruction algorithms performed at each dose level included FBP and ADMIRE IR strengths 1–5. A total of 72 combinations were generated by 12 dose levels × 6 reconstruction levels.

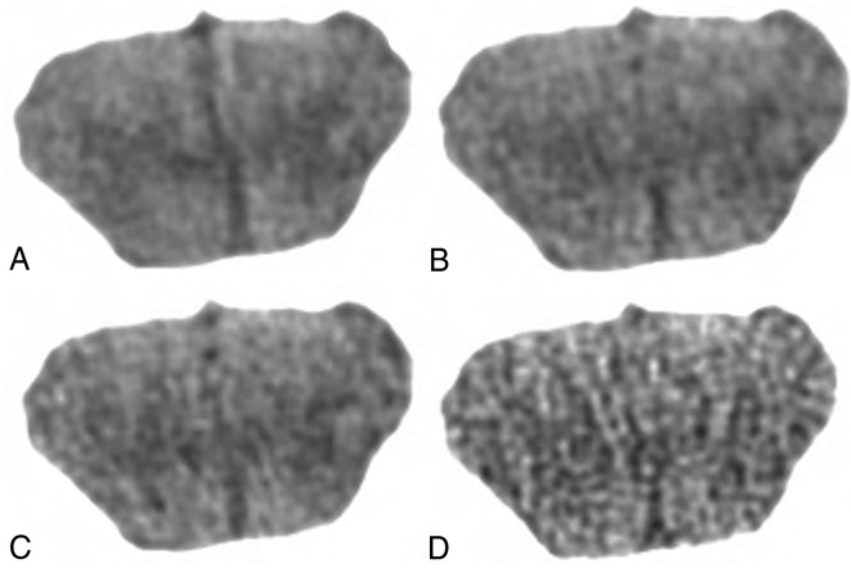

FIG 2. Benchmark coronal head CT images for rating scales of gray-white differentiation: 982 mAs with FBP for score = 4 (*A*), 573 mAs with FBP for score = 3 (*B*), 327 mAs with FBP for score = 2 (*C*), and 82 mAs with FBP for score = 1 (*D*).

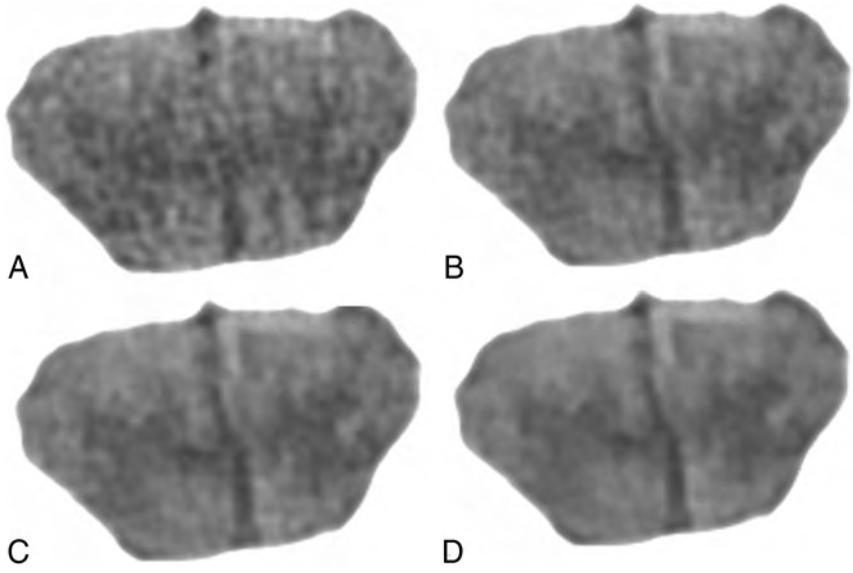

FIG 3. Benchmark coronal head CT images for rating scales of image texture: 409 mAs with FBP for score = 4 (*A*), 982 mAs with FBP for score = 3 (*B*), 982 mAs with ADMIRE-3 for score = 2 (*C*), and 982 with ADMIRE-5 for score = 1 (*D*).

Image Evaluation

One coronal section was chosen for evaluation on the basis of the criterion of maximizing the display of gray-white matter differentiation. All 72 images were anonymized in terms of technical and reconstruction factors and randomized and then evaluated on a standard PACS station. Both qualitative and quantitative measures were performed.

Qualitative ratings were made by 2 neuroradiologists (with 24 and 7 years' experience), who were blinded to all imaging parameters. They rated two 4-point metrics of image quality, gray-white matter differentiation and image texture: in the case of gray-white matter differentiation, 4 = distinct, 3 = regionally decreased, 2 = globally decreased, 1 = indistinguishable; in the case of image texture: 4 = excessive pixilation (ie, noisy), 3 = balanced pixilation and smoothing, 2 = increased smoothing, 1 = excessive smoothing. Benchmark sample images were assigned to each score of the rating scale to restrict subjectivity on the part of the qualitative assessment; for the gray-white rating scale: 982 effective mAs with FBP for score = four, 573 effective mAs with FBP for score = three, 327 effective mAs with FBP for score = two, and 82 effective mAs with FBP for score = 1 (Fig 2). For the texture-rating scale, the scores were the following: 409 effective mAs with FBP for score = four, 982 effective mAs with FBP for score = three, 982 effective mAs with ADMIRE-3 for score = two, 982 effective mAs with ADMIRE-5 for score = 1 (Fig 3). The default score of the reference image (highest dose with FBP) was 4 for gray-white and 3 for texture, yielding a maximum combined score of 7 (Note that a rating of 4 in texture is suboptimal; therefore, it had to be reclassified as 2, thereby allowing the optimal middle-of-the-road texture to contribute to the highest score in simple algebraic combined scoring). All 72 randomized images were evaluated by matching the closest image on the rating scales. The scores by the 2 neuroradiologists were averaged. Heat maps were generated for gray-white, texture, and combined scores.

Quantitative analysis was also performed. Using a self-developed Matlab script (MathWorks, Natick, Massachusetts), an ROI was marked on 1 image and automatically reproduced on all other images of the same size and in the same location. Two samples were taken, one centered in the cerebral cortical gray matter and another in the deep white matter (Fig 1*B*). Mean and SD values were recorded for each ROI. From these values, we calculated the noise and SNR of the white matter as well as contrast-to-noise ratio (CNR) of the cortex:

$$\text{Noise}_{\text{wm}} = \text{SD}_{\text{wm}}$$

$$\text{SNR}_{\text{wm}} = \text{mean}_{\text{wm}}/\text{SD}_{\text{wm}}$$

$$\text{CNR}_{\text{cortex}} = (\text{mean}_{\text{cortex}} - \text{mean}_{\text{wm}})/\text{SD}_{\text{wm}}.$$

Graphs were plotted to demonstrate the relationship among image quality, radiation dose, and reconstruction algorithm.

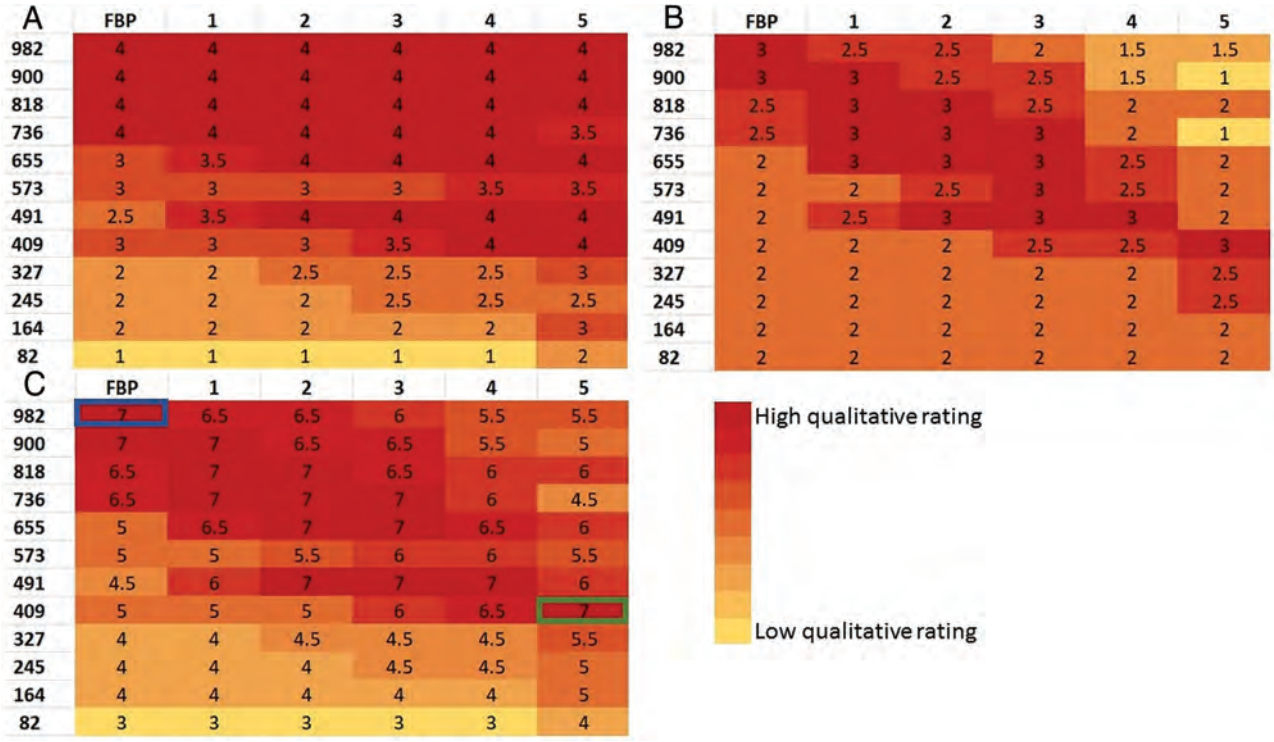

FIG 4. Heat maps of qualitative ratings of gray-white differentiation (*A*), image texture (*B*), and combined scores (*C*). Note that scores of 2 in the bottom left corner of the texture heat map were reclassified from original scores of 4 as explained in the Materials and Methods section. Most important, the low scores in the top right corner of texture heat map reveal the inadequacy of the high-dose and high-strength combination. The greatest dose reduction (58%) that preserves comparable gray-white differentiation and texture to the reference FBP (*blue outline*) is achieved at 409 mAs with ADMIRE-5 (*green outline*).

Statistical Analysis

Interneuroradiologist agreement was assessed using the weighted κ, which quantifies the agreement between the 2 neuroradiologists, adjusting for random chance and weighting by the degree of disagreement.

RESULTS

Heat maps of the qualitative rating of gray-white matter differentiation, image texture, and combined score reveal a distinct pattern. The highest score for gray-white matter differentiation (Fig 4*A*) is found with higher radiation doses across every reconstruction algorithm. Distinct gray-white matter differentiation was preserved at low radiation doses but only when using higher IR strengths.

The image texture heat map (Fig 4*B*) confirms that the combination of high radiation dose and high IR strength creates the smoothing texture. However, at lower radiation doses, with which noisy images would have been generated with FBP, higher IR strengths recover the normal image texture.

The heat map of the combined scores (Fig 4*C*) reveals optimal image quality along a diagonal, so that high dose levels with FBP, mid-dose levels with mid-IR strengths, and low-dose levels with high IR strengths produce images with gray-white matter differentiation and texture comparable with the reference image. According to this qualitative assessment, a 58% dose reduction can be achieved with ADMIRE-5 without compromising gray-white matter differentiation or image texture (see Fig 5 for sample images).

The quantitative analysis also reveals the effects of radiation dose and iterative strength on the noise of the white matter, SNR of the white matter, and CNR of the cortex (Fig 6). Noise, SNR, and CNR all improve with higher IR strength but worsen with dose reduction. Noise, SNR, and CNR equivalent to the reference image (ie, highest dose with FBP) can be maintained with a maximum of 67% dose reduction if the highest IR strength is used. Figure 6*D* further demonstrates the relationship between radiation dose and iterative strength. For any given reconstruction technique, CNR will drop when lowering the radiation dose, but it can be recovered by switching to higher iterative strengths. Therefore, the correct combination of dose reduction and higher iterative strength can preserve image quality. According to the quantitative analysis, 67% dose reduction can be achieved with ADMIRE-5, which is comparable with the independent results of the qualitative analysis.

Qualitative ratings made by 2 neuroradiologists showed very good agreement on both gray-white differentiation (weighted κ = 0.91) and image texture (weighted κ = 0.84).

DISCUSSION

While CT is indispensable for patient management, its contribution to radiation exposure and its potential for cancer induction has come under scrutiny.[26-28] There are dueling incentives to both produce high quality imaging and reduce radiation exposure. Toward this end, our application of an in vivo model simultaneously achieves 2 critical experimental approaches: 1) to explore the full range of tube current and IR strengths, thus

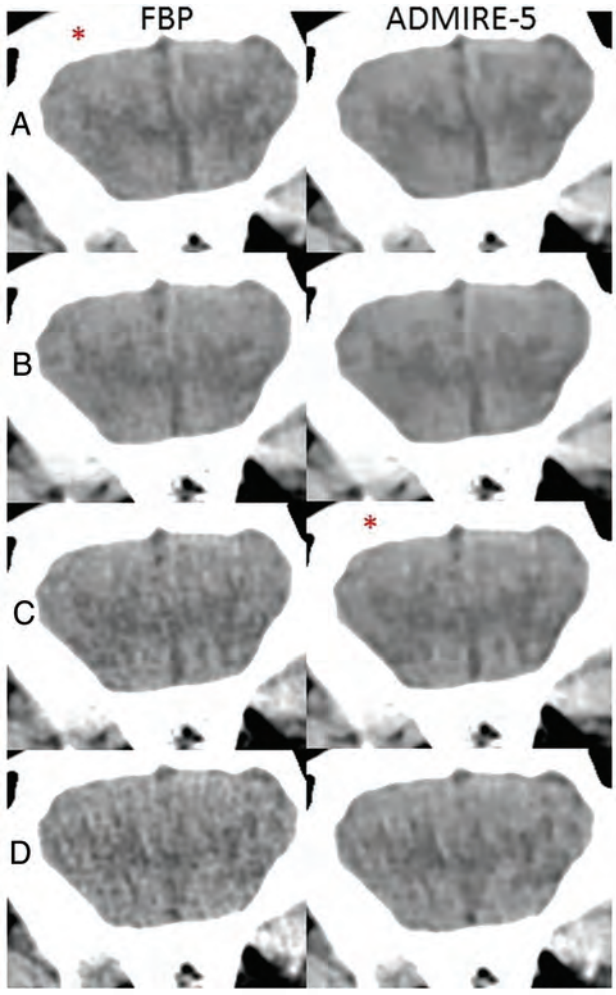

FIG 5. Sample coronal head CT images comparing FBP (*left column*) and ADMIRE-5 (*right column*) at the reference dose (*A*), 8% dose reduction (*B*), 58% dose reduction (*C*), and 75% dose reduction (*D*). Gray-white detectability and image texture were subjectively scored as equivalent between the reference dose with FBP (*left, A*) and a 58% dose reduction with ADMIRE-5 (*right, C*) as marked with an *asterisk*.

leveraging the advantage of phantom studies; and 2) to reproduce realistic gray-white matter differentiation, thus leveraging the advantage of clinical studies.

The search for an appropriate animal proxy faced several challenges. First, although apes would have offered the most comparable brains, the National Institutes of Health no longer supports biomedical research on apes for ethical considerations. Other animals with relatively large brains have prohibitively large bodies (eg, horse) or require specialized housing facilities (eg, California sea lion), and most other available animals have brains that are much too small (eg, macaque monkey). The sheep can serve as a suitable research subject for several reasons: Its body weight (72 kg in our subject) is acceptable for handling while anesthetized, it is widely available in agricultural centers, and its acceptability for human consumption renders the choice less ethically controversial. The ovine brain has garnered research interest in several areas, including functional cortical mapping,[29] modeling Huntington disease[30] and other neurodegenerative diseases,[31] and evaluating surgical techniques.[32] Calvarial thickness is 6 mm,[32] which is comparable with that of the human skull, whereas the pig skull is much thicker.[33] Even so, the sheep brain is modest in size, weighing only 120–140g,[29] which is a mere 10% of an adult human brain and even less than half of that of a neonate.[34] In addition, the animal has a disproportionately large snout and masticator apparatus, which may be expected to attenuate x-rays and potentially interfere with image reconstruction of the brain. Despite these caveats, the sheep is a suitable animal model.

The present study advances our understanding of the application of IR technology. Early studies, including of the brain, tended to conclude, in glowing terms, that IR successfully achieves dose reduction while preserving image quality.[10-18] Despite these bullish pronouncements, practicing radiologists have remained resistant to the full implementation of this technology. The facts of decreased noise, increased CNR, and qualitative ratings of noise and diagnostic acceptability were not capturing the whole story because it is well-known that radiologists hesitate to use high IR strengths due to a dissatisfaction with the generated images. A factor that merits more attention is that higher IR strengths introduce textural changes, which have been called blotchy, plastic, or smoothing in the literature. These textural effects are unfamiliar to radiologists and are perceived to cause decreased image quality and therefore are thought to produce inferior diagnostic quality. We created a 4-point rating scale that recognizes too noisy as being problematic on one end but also too smooth as being undesirable on the other end. We believe this noise-versus-smoothness metric will be sensitive to a principal reason that practicing radiologists are reticent to adopt the full implementation of IR technology.

While quantitative analysis suggested that a 67% dose reduction should be achievable without compromising image quality, qualitative evaluation concluded that only a 58% dose reduction is possible. If the degree of dose reduction were based on quantitative factors alone using SNR and CNR criteria, radiologists may not be comfortable with the generated image quality. These differential results advise caution and argue for the added value of qualitative metrics such as gray-white detectability and textural smoothness.

A second design feature that was specifically aimed at the concerns of practicing radiologists is to use resemblance to the reference FBP image as a pragmatic metric for assessing IR-rendered quality. Radiologists are already accustomed to the overall appearance and texture of FBP images; therefore, any replacement that might be rated subjectively equivalent would need to most resemble what is currently already widely in use. Therefore, the rating scale was benchmarked to preselected images and viewed at the time of qualitative assessment for the goal of identifying gray-white differentiation for low-contrast detectability and image texture that most closely resembled the reference image.

Our study surveyed a range of dose-strength combinations and found that lower doses and higher IR strengths must be properly paired for the preservation of image quality. If the dose is not low enough for the chosen IR strength or the IR strength is not high enough for the desired dose reduction, image quality may suffer. Below a certain dose, no level of IR strength can recover image quality. Our study suggests that up to 60% dose

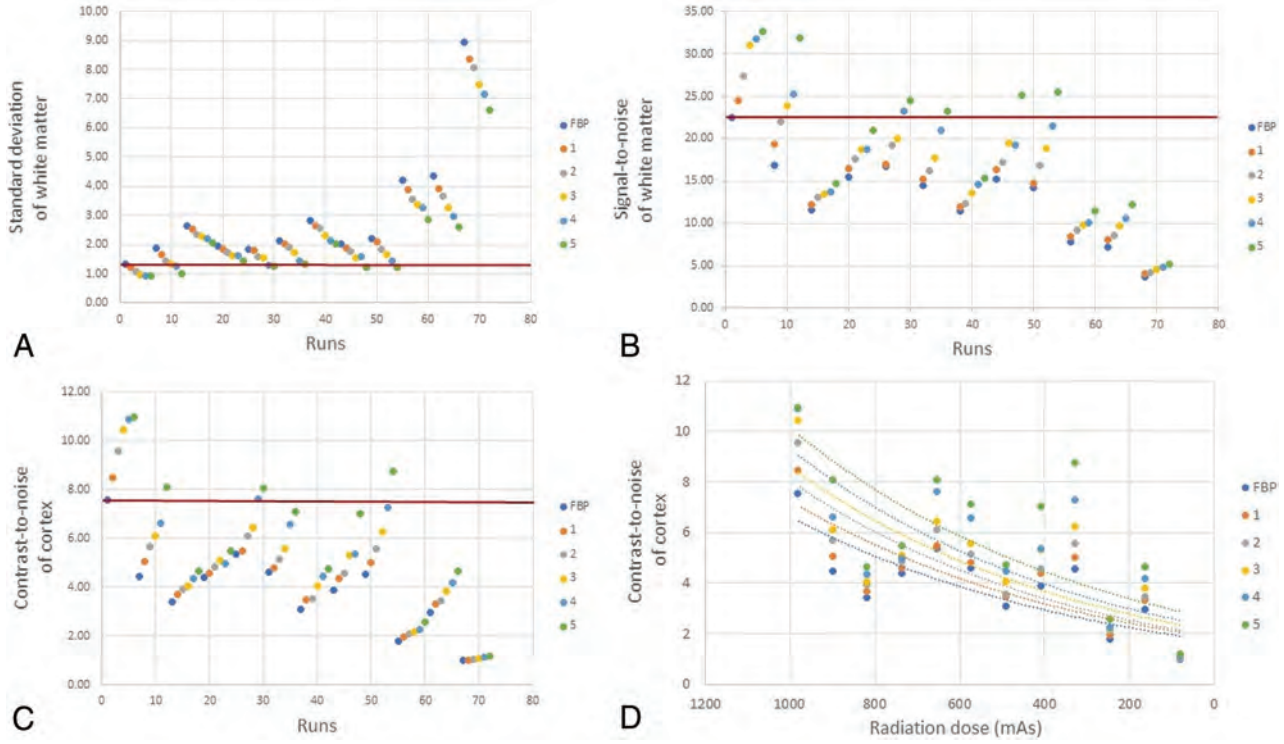

FIG 6. SD (ie, noise) of the white matter (*A*), signal-to-noise of the white matter (*B*), and contrast-to-noise of the cortex (*C*) for each run, from the highest (982 mAs) to lowest (82 mAs) effective dose; FBP followed by ADMIRE 1–5 for each dose level. Noise, SNR, and CNR all improve with higher IR strength but worsen with dose reduction. Noise, SNR, and CNR equivalent to the reference image (ie, highest dose with FBP) as illustrated by *red horizontal line* can be maintained with a 67% dose reduction at the highest IR strengths. Equivalent noise, SNR, and CNR cannot be preserved at further dose reductions regardless of IR strength. The last graph (*D*) relates CNR of the cortex to the radiation dose for each reconstruction technique. In each case, the CNR decreases with progressive dose reduction. However, for any given radiation dose, higher IR strengths improve the CNR. If the CNR is to be preserved, dose reduction must be complemented by higher IR strength.

reduction may be achieved in brain imaging with appropriate dose-strength combinations.

A limitation of our study is that results apply only to ADMIRE, which is Siemens' most advanced IR algorithm available on their newest scanners. Because IR algorithms work differently and possess different profiles of advantages and disadvantages,[6-8,35] how these results translate to other techniques is not well-understood. This study also did not evaluate the impact of varying spatial resolution. Different from FBP, IR does not have the sharpness-noise trade-off limitation. In other words, an equivalent noise profile could be produced at a higher spatial resolution setting.[36] Another concern is that only 1 subject was included in this study. A limitation of this (and every) study is that dose reduction is dependent on the starting reference FBP dose. It is not entirely clear how our starting reference dose in the sheep (though appropriately chosen for its small brain and disproportionately large face) might translate to the proportions of the human brain. These preliminary results require additional larger trials using multiple vendors, and clinical validation is necessary.

CONCLUSIONS

IR has promise in lowering radiation exposure without compromising image quality, but its full implementation has not yet been reached. The present study uses an in vivo animal model, which affords assessment of the full range of tube current and ADMIRE strengths in the living brain. Qualitative assessment of low-contrast detectability and image texture for resemblance to the reference FBP image suggests that an approximately 60% dose reduction is achievable with ADMIRE-5.

Disclosures: Jeffrey Smiley—*UNRELATED*: *Employment*: University of Kentucky. Jie Zhang—*UNRELATED*: *Grants*: National Institutes of Health, R21, *Comments*: This is a research grant from the National Institutes of Health, R21, and I am a coinvestigator with 4% effort*; *Payment for Development of Educational Presentations*: Radiological Society of North America physics module revision, *Comments*: We are revising the Radiological Society of North America physics module gamma camera.* *Money paid to the Institution.

REFERENCES

1. Geyer LL, Schoepf UJ, Meinel FG, et al. **State of the art: iterative CT reconstruction techniques.** *Radiology* 2015;276:339–57 CrossRef Medline
2. Padole A, Khawaja RDA, Kalra MK, et al. **CT radiation dose and iterative reconstruction techniques.** *AJR Am J Roentgenol* 2015;204:W384–92 CrossRef Medline
3. Ghetti C, Palleri F, Serreli G, et al. **Physical characterization of a new CT iterative reconstruction method operating in sinogram space.** *J Appl Clin Med Phys* 2013;14:434 CrossRef Medline
4. Solomon J, Mileto A, Ramirez-Giraldo JC, et al. **Diagnostic performance of an advanced modeled iterative reconstruction algorithm for low-contrast detectability with a third-generation dual-source multidetector CT scanner: potential for radiation dose reduction in a multireader study.** *Radiology* 2015;275:735–45 CrossRef Medline

5. Schindera ST, Odedra D, Raza SA, et al. **Iterative reconstruction algorithm for CT: can radiation dose be decreased while low-contrast detectability is preserved?** *Radiology* 2013;269:511–18 CrossRef Medline
6. Mieville FA, Gudinchet F, Brunelle F, et al. **Iterative reconstruction methods in two different MDCT scanners: physical metrics and 4-alternative forced-choice detectability experiments: a phantom approach.** *Phys Med* 2013;29:99–110 CrossRef Medline
7. Jensen K, Martinsen ACT, Tingberg A, et al. **Comparing five different iterative reconstruction algorithms for computed tomography in an ROC study.** *Eur Radiol* 2014;24:2989–3002 CrossRef Medline
8. Love A, Olsson ML, Siemund R, et al. **Six iterative reconstruction algorithms in brain CT: a phantom study on image quality at different radiation dose levels.** *Br J Radiol* 2013;86:20130388 CrossRef Medline
9. Dobeli KL, Lewis SJ, Meikle SR, et al. **Noise-reducing algorithms do not necessarily provide superior dose optimisation for hepatic lesion detection with multidetector CT.** *Br J Radiol* 2013;86: 20120500 CrossRef Medline
10. Vorona GA, Zuccoli T, Sutcavage T, et al. **The use of adaptive statistical iterative reconstruction in pediatric head CT: a feasibility study.** *AJNR Am J Neuroradiol* 2013;34:205–211 CrossRef Medline
11. Baskan O, Erol C, Ozbek H, et al. **Effect of radiation dose reduction on image quality in adult head CT with noise-suppressing reconstruction system with a 256 slice MDCT.** *J Appl Clin Med Phys* 2015;16:285 CrossRef Medline
12. Singh S, Kalra MK, Hsieh J, et al. **Abdominal CT: comparison of adaptive statistical iterative and filtered back projection reconstruction techniques.** *Radiology* 2010;257:373–83 CrossRef Medline
13. Baker ME, Dong F, Primak A, et al. **Contrast-to-noise ratio and low-contrast object resolution on full- and low-dose MDCT: SAFIRE versus filtered back projection in a low-contrast object phantom and in the liver.** *AJR Am J Roentgenol* 2012;199:8–18 CrossRef Medline
14. Kilic K, Erbas G, Guryildirim M, et al. **Lowering the dose in head CT using adaptive statistical iterative reconstruction.** *AJNR Am J Neuroradiol* 2011;32:1578–82 CrossRef Medline
15. Korn A, Fenchel M, Bender B, et al. **Iterative reconstruction in head CT: image quality of routine and low-dose protocol in comparison with standard filtered back-projection.** *AJNR Am J Neuroradiol* 2012;33:218–24 CrossRef Medline
16. Alper S, Mohan P, Chaves I, et al. **Image quality and radiation dose comparison between filtered back projection and adaptive statistical iterative reconstruction in non-contrast head CT studies.** *OMICS J Radiol* 2013;2:7 CrossRef
17. Rapalino O, Kamalian S, Kamalian S, et al. **Cranial CT with adaptive statistical iterative reconstruction: improved image quality with concomitant radiation dose reduction.** *AJNR Am J Neuroradiol* 2012;33:609–15 CrossRef Medline
18. Brodoefel H, Bender B, Schabel C, et al. **Potential of combining iterative reconstruction with noise efficient detector design: aggressive dose reduction in head CT.** *Br J Radiol* 2015;88:20140404 CrossRef Medline
19. Iyama Y, Nakaura T, Oda S, et al. **Iterative reconstruction designed for brain CT: a correlative study with filtered back projection for the diagnosis of acute ischemic stroke.** *J Comput Assist Tomogr* 2017;41:884–90 CrossRef Medline
20. Kataria B, Althen JN, Smedby O, et al. **Assessment of image quality in abdominal CT: potential dose reduction with model-based iterative reconstruction.** *Eur Radiol* 2018;28:2464–73 CrossRef Medline
21. Pickhardt PJ, Lubner MG, Kim DH, et al. **Abdominal CT with model-based iterative reconstruction (MBIR): initial results of a prospective trial comparing ultralow-dose with standard-dose imaging.** *AJR Am J Roentgenol* 2012;199:1266–74 CrossRef Medline
22. Kim HJ, Lee HK, Song H, et al. **Reduction in radiation dose with reconstruction technique in the brain perfusion CT.** *Radiation Effects and Defects in Solids* 2011;166:918–26 CrossRef
23. Zarelli M, Schwarz T, Puggioni A, et al. **An optimized protocol for multislice computed tomography of the canine brain.** *Vet Radiol Ultrasound* 2014;55:387–92 CrossRef Medline
24. Zarb F, McEntee MF, Rainford L. **CT radiation dose and image quality optimization using a porcine model.** *Radiol Technol* 2013;85:127–36 Medline
25. Ge G, Zhang J. **Noise and texture properties for the optimization of CT protocols with iterative reconstruction algorithms.** *In: Proceedings of the Annual Meeting of American Association of Physicists in Medicine*, Nashville, Tennessee. July 29 to August 2, 2018
26. Pearce MS, Salotti JA, Little MP, et al. **Radiation exposure from CT scans in childhood and subsequent risk of leukaemia and brain tumours: a retrospective cohort study.** *Lancet* 2012;380:499–505 CrossRef Medline
27. Brenner DJ, Hall EJ. **Cancer risks from CT scans: now we have data, what next?** *Radiology* 2012;265:330–31 CrossRef Medline
28. Miglioretti DL, Johnson E, Williams A, et al. **Pediatric computed tomography and associated radiation exposure and estimated cancer risk.** *JAMA Pediatr* 2013;167:700–07 CrossRef Medline
29. John SE, Lovell TJH, Opie NL, et al. **The ovine motor cortex: a review of functional mapping and cytoarchitecture.** *Neurosci Biobehav Rev* 2017;80:306–15 CrossRef Medline
30. Handley RR, Reid SJ, Patassini S, et al. **Metabolic disruption identified in the Huntington's disease transgenic sheep model.** *Sci Rep* 2016;6:20681 CrossRef Medline
31. Oswald MJ, Palmer DN, Kay GW, et al. **Glial activation spreads from specific cerebral foci and precedes neurodegeneration in presymptomatic ovine neuronal ceroid lipofuscinosis (CLN6).** *Neurobiol Dis* 2005;20:49–63 CrossRef Medline
32. Laure B, Petraud A, Sury F, et al. **Resistance of the sheep skull after a monocortical cranial graft harvest.** *J Craniomaxillofac Surg* 2012;40:261–65 CrossRef Medline
33. Shridharani JK, Wood GW, Panzer MB, et al. **Porcine head response to blast.** *Front Neurol* 2012;3:70 CrossRef Medline
34. Dekaban AS. **Changes in brain weights during the span of human life: relation of brain weights to body heights and body weights.** *Ann Neurol* 1978;4:345–56 CrossRef Medline
35. Stiller W. **Basics of iterative reconstruction methods in computed tomography: a vendor-independent overview.** *Eur J Radiol* 2018; 109:147–54 CrossRef Medline
36. Mehta D, Bayraktar B. **Iterative reconstruction techniques for spatial resolution improvements: phantom study.** In: *Proceedings of the Annual Meeting of European Society of Radiology*. Vienna, Austria. March 3–7, 2011

Imaging G-Ratio in Multiple Sclerosis Using High-Gradient Diffusion MRI and Macromolecular Tissue Volume

F. Yu, Q. Fan, Q. Tian, C. Ngamsombat, N. Machado, J.D. Bireley, A.W. Russo, A. Nummenmaa, T. Witzel, L.L. Wald, E.C. Klawiter, and S.Y. Huang

ABSTRACT

BACKGROUND AND PURPOSE: Remyelination represents an area of great therapeutic interest in multiple sclerosis but currently lacks a robust imaging marker. The purpose of this study was to use high-gradient diffusion MRI and macromolecular tissue volume imaging to obtain estimates of axonal volume fraction, myelin volume fraction, and the imaging g-ratio in patients with MS and healthy controls and to explore their relationship to neurologic disability in MS.

MATERIALS AND METHODS: Thirty individuals with MS (23 relapsing-remitting MS, 7 progressive MS) and 19 age-matched healthy controls were scanned on a 3T MRI scanner equipped with 300 mT/m maximum gradient strength using a comprehensive multishell diffusion MRI protocol. Macromolecular tissue volume imaging was performed to quantify the myelin volume fraction. Diffusion data were fitted to a 3-compartment model of white matter using a spheric mean approach to yield estimates of axonal volume fraction. The imaging g-ratio was calculated from the ratio of myelin volume fraction and axonal volume fraction. Imaging metrics were compared between groups using 2-sided *t* tests with a Bonferroni correction.

RESULTS: The mean g-ratio was significantly elevated in lesions compared with normal-appearing WM (0.74 vs 0.67, $P < .001$). Axonal volume fraction (0.17 vs 0.23, $P < .001$) and myelin volume fraction (0.17 vs 0.25, $P < .001$) were significantly lower in lesions than normal-appearing WM. Myelin volume fraction was lower in normal-appearing WM compared with that in healthy controls (0.25 vs 0.27, $P = .009$). Disability, as measured by the Expanded Disability Status Scale, was significantly associated with myelin volume fraction ($\beta = -40.5$, $P = .001$) and axonal volume fraction ($\beta = -41.0$, $P = .016$) in normal-appearing WM.

CONCLUSIONS: The imaging g-ratio may serve as a biomarker for the relative degree of axonal and myelin loss in MS.

ABBREVIATIONS: AVF = axonal volume fraction; EDSS = Expanded Disability Status Scale; HC = healthy controls; MSFC = multiple sclerosis functional composite; MTV = macromolecular tissue volume; MVF = myelin volume fraction; NAWM = normal-appearing white matter; NODDI = neurite orientation dispersion and density imaging; PMS = progressive MS; qMT = quantitative magnetization transfer; RRMS = relapsing-remitting MS

Multiple sclerosis is a disease of the CNS characterized by inflammatory demyelination and axonal loss. Demyelination predisposes axons to immune-mediated injury, resulting in axonal loss that is thought to be the substrate of permanent disability.[1] Myelin repair occurs to a variable extent, and promoting remyelination represents an area of great therapeutic interest.[2,3] Unfortunately, conventional MRI is unable to distinguish remyelination from myelin loss and axonal damage. This lack of sensitivity and specificity highlights the need for more specific imaging approaches.

Received July 27, 2019; accepted after revision August 12.

From the Division of Neuroradiology (F.Y.), Department of Radiology, University of Texas Southwestern Medical Center, Dallas, Texas; Athinoula A. Martinos Center for Biomedical Imaging (Q.F., Q.T., C.N., A.N., T.W., L.L.W., S.Y.H.), Department of Radiology, Massachusetts General Hospital, Charlestown, Massachusetts; Department of Neurology (N.M., J.D.B., A.W.R., E.C.K., S.Y.H.) and Division of Neuroradiology (S.Y.H.), Department of Radiology, Massachusetts General Hospital, Boston, Massachusetts; and Harvard-MIT Division of Health Sciences and Technology (L.L.W., S.Y.H.), Massachusetts Institute of Technology, Cambridge, Massachusetts.

Research reported in this publication was supported by the National Institute of Neurological Disorders and Stroke of the National Institutes of Health under award Nos. K23NS096056 (S.Y.H.) and K23NS078044 (E.C.K.), by the National Institute of Biomedical Imaging and Bioengineering of the National Institutes of Health under award No. R00EB015445 (A.N.), the National Multiple Sclerosis Society (PR-1412-02194 to E.C.K.), the Radiological Society of North America (F.Y., S.Y.H.), the Conrad N. Hilton Foundation (S.Y.H.), the Altschul Foundation (E.C.K.), and an American Heart Association Postdoctoral Fellowship (Q.F.).

Paper previously presented, in part, at: Annual Meeting of the American Society of Neuroradiology, April 22–27, 2017; Long Beach, California; and Annual Meeting of the Eastern Neuroradiological Society, August 24–27, 2017; Toronto, Ontario, Canada, where it was awarded the Norman E. Leeds Award for Best Scientific Paper.

Please address correspondence to Fang Frank Yu, MD, UT Southwestern Medical Center, 5323 Harry Hines Blvd, Dallas, TX 75390; e-mail: Frank.yu@utsouthwestern.edu; @FrankFYuMD1

Indicates open access to non-subscribers at www.ajnr.org
Indicates article with supplemental on-line table.

http://dx.doi.org/10.3174/ajnr.A6283

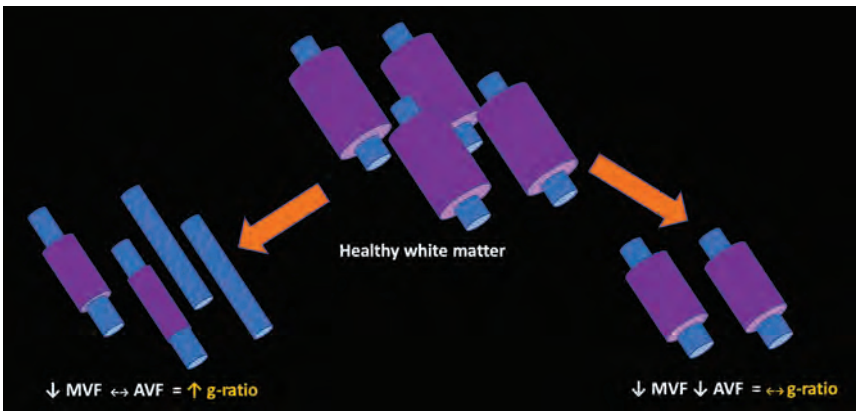

FIG 1. Schematic diagram outlining different possible outcomes for the g-ratio based on alterations in myelination and axonal integrity relative to healthy white matter. *Left*, When demyelination predominates and axonal integrity is preserved, the g-ratio is elevated. *Right*, When axonal loss occurs with concordant loss of myelin, the g-ratio may be relatively conserved.

Advanced diffusion MRI methods such as diffusional kurtosis imaging,[4] neurite orientation dispersion and density imaging (NODDI),[5] and AxCaliber,[6] provide metrics such as the axonal volume fraction (AVF) that may be more specific to axonal microstructure than DTI metrics in white matter disease[7] and neurodegeneration.[8] The availability of higher gradient strengths on clinical and research MRI scanners also offers improved sensitivity to intra-axonal water diffusion compared with measurements at conventional gradient strengths.[9-11] Quantitative MRI markers sensitive to myelin volume fraction (MVF) include quantitative magnetization transfer (qMT),[12] myelin water imaging,[13] and macromolecular tissue volume (MTV) imaging.[14]

Combining myelin and axonal metrics has the potential to offer a richer in vivo characterization of white matter integrity than either metric alone. The synergistic combination of MVF and AVF can be used to estimate an aggregate myelin g-ratio, which is defined as the ratio of the inner-to-outer diameter of the myelin sheath.[15] The g-ratio could be used to extract the degree of axonal myelination, illuminating disease evolution that might otherwise be challenging to interpret. For example, lesions with demyelination as the predominant pathology would demonstrate an increased g-ratio (Fig 1). On the other hand, in lesions with concomitant myelin and axonal loss, the g-ratio would remain unchanged.

Several studies have used MR imaging to interrogate the g-ratio in the brain[15-18] and spinal cord,[19,20] referred to here as the imaging g-ratio. Previous imaging studies in MS demonstrated an increase in g-ratio within lesions compared with the normal-appearing white matter (NAWM) using NODDI for estimation of AVF, and qMT and synthetic MRI for estimation of MVF, respectively.[15,17] We postulate that the use of high-gradient diffusion MRI imaging should provide consistent estimates of AVF compared with those reported in previous studies and, when combined with measurements of MVF, should yield consistent trends in the imaging g-ratio between lesions and NAWM.

The purpose of this study was to use high-gradient diffusion MRI and MTV imaging to obtain estimates of AVF, MVF, and imaging g-ratio in patients with MS and healthy controls (HC) and to explore the relationship of these imaging markers with neurologic disability in MS. We hypothesized that lesions would show evidence of demyelination and axonal loss manifesting as decreased MVF, decreased AVF, and increased g-ratio relative to NAWM and white matter of HC.

MATERIALS AND METHODS

This prospective study was approved by the Massachusetts General Hospital institutional review board and is compliant with the Health Insurance Portability and Accountability Act guidelines. All participants provided written informed consent.

Subjects

Thirty patients with a clinical diagnosis of MS and 19 age-matched healthy volunteers were prospectively recruited from March 2016 through March 2018 (On-line Table). Of the 30 patients with MS, 23 had relapsing-remitting MS (RRMS), while 7 had progressive MS (PMS; consisting of 2 primary-progressive and 5 secondary-progressive MS patients. Inclusion criteria for subjects with MS were a diagnosis of clinically definite MS, absence of clinical relapse within 3 months, and being on stable disease-modifying treatment or no treatment for at least 6 months. Exclusion criteria for all subjects were evidence of other structural brain diseases, severe claustrophobia, or other contraindications to MR imaging.

Neurologic disability in the patients with MS was assessed using the Expanded Disability Status Scale (EDSS) and Multiple Sclerosis Functional Composite (MSFC). A board-certified neurologist blinded to the imaging results conducted a standard clinical examination, which was used in the calculation of the EDSS. A trained examiner administered the MSFC-3, and the *z* score was calculated using the Symbol Digit Modalities Test, Timed 25-Foot Walk, and Timed Nine-Hole Peg Test.

MRI Acquisition

All subjects were imaged on a 3T MRI scanner (Magnetom Connectom; Siemens, Erlangen, Germany) with a maximum gradient strength of 300 mT/m and a maximum slew rate of 200 T/m/s. A custom-built 64-channel phased array head coil was used for signal reception.[21] Diffusion data were acquired using a diffusion-weighted spin-echo single-shot EPI sequence in the sagittal plane with 2-mm isotropic voxel size, TE/TR = 77/3600 ms, parallel imaging acceleration factor R = 2, simultaneous multislice imaging with a slice acceleration factor of 2, and anterior-to-posterior phase encoding. Interspersed b=0 images were acquired every 16 images. A multishell diffusion imaging protocol was performed using a diffusion gradient pulse duration of 8 ms, diffusion times of 19 and 49 ms, and 8 diffusion gradient increments linearly spaced from 30 to 290 mT/m per diffusion time, for a total of 16 b-values. The diffusion gradients were applied in 32 directions for b-values of $<$2300 s/mm^2 and 64 directions for b-

values of >2300 s/mm^2, uniformly distributed on a sphere. The maximum b-value was 17,800 s/mm^2. A set of 5 *b*=0 images with a reversed-phase encoding direction was acquired to correct for susceptibility-induced distortions. The diffusion MRI protocol was designed to include the minimum number of diffusion-weighted imaging volumes to obtain reproducible estimates of apparent axon diameter and density compared with a more extensive acquisition,[22] while keeping the scan time within an acceptable duration for imaging patients (<1 hour). The total acquisition time was 51 minutes.

MTV data for myelin quantification were acquired using a multiple flip angle spoiled gradient-echo 3D-FLASH sequence at 1-mm isotropic resolution with TE/TR = 2.74/20 ms and flip angle = 4°, 10°, 20°. The duration of each 3D-FLASH sequence was 5 minutes 6 seconds, resulting in a total acquisition time of 15 minutes 18 seconds. Structural images were acquired including a T1-weighted multiecho MPRAGE sequence at 1-mm isotropic resolution with TE/TR = 1.15, 3.03, 4.89, 6.75 ms/2530 ms, TI = 1100 ms, R = 3, and flip angle = 7° (acquisition time of 3 minutes 58 seconds), and a 3D-FLAIR sequence at 0.9-mm isotropic resolution with TE/TR/TI = 389/5000/1800 ms and R = 2 (acquisition time of 5 minutes 47 seconds).

Data Processing and Analysis

Diffusion Imaging. All data were corrected for gradient nonlinearity using in-house software.[23] Susceptibility- and eddy current–induced distortions and motion in the diffusion-weighted images were corrected using topup (https://fsl.fmrib.ox.ac.uk/fsl/fslwiki/topup) and eddy (https://fsl.fmrib.ox.ac.uk/fsl/fslwiki/eddy) in FSL (https://fsl.fmrib.ox.ac.uk).[24-26]

A recently developed approach for inferring axonal compartment size and volume fraction from a multicompartment spherical mean signal model of white matter was used to quantify the axonal volume fraction.[27] A 3-compartment model of restricted diffusion within impermeable cylindric axons, hindered Gaussian diffusion in the extra-axonal space, and free diffusion in CSF was used to model water diffusion in white matter. The spherically averaged form of the signal model was fitted using Markov chain Monte Carlo sampling to yield orientation-independent estimates of restricted volume fraction (f_r), hindered diffusion coefficient, and CSF volume fraction (f_{csf}).[28] The longitudinal diffusion coefficient was assumed to be 1.7×10^{-3} mm^2/s within axons, and the free diffusivity coefficient was assumed to be 3 mm^2/s (diffusivity of free water at 37° C).

Macromolecular Tissue Volume. The 3D-FLASH magnitude images were corrected for B_1 inhomogeneity.[20] The FLASH images with flip angle = 4°, 10° were then registered to the FLASH image with flip angle = 20° using the FSL Linear Registration Tool (FLIRT; http://www.fmrib.ox.ac.uk/fsl/fslwiki/FLIRT). The equilibrium magnetization M_0 (product of the coil reception profile and proton density) and T1 values were estimated on a voxel-wise basis.[20] The macromolecular tissue volume was computed as[14]

1)
$$MTV = 1 - \left(\frac{Proton\ Density}{Proton\ Density\ of\ Free\ Water}\right).$$

Registration and Segmentation

Cortical surface reconstruction and volumetric segmentation were performed on T1-weighted images using FreeSurfer (Version 5.3.0; http://surfer.nmr.mgh.harvard.edu).[29,30] The FLASH images at flip angle = 20° and *b*=0 diffusion images were coregistered to each subject's T1-weighted image using the boundary-based registration tool in FreeSurfer with 6 *df*. The resultant transformations were applied to the MTV, f_r, and f_{csf} maps for alignment with the T1-weighted images.

Binary lesion masks were generated from the T1 MPRAGE and 3D-FLAIR images using an in-house automated segmentation procedure developed within the FreeSurfer image analysis suite, described in detail in Lindemer et al[31] and adapted for use in patients with MS by the authors of that work. In brief, this segmentation tool performs intensity normalization of a subject's T1- and FLAIR-weighted images using a multimodal atlas and segments white matter lesions from NAWM using a multimodal Gaussian classifier array as well as individual-based heuristics. The lesion masks generated by the automated tool tended to overestimate the lesion size and were manually edited by 2 experienced neuroradiologists, who overlaid the lesion masks generated by automated segmentation on the 3D-FLAIR images and removed voxels that did not clearly contain T2/FLAIR hyperintensity in the perilesional white matter. In cases in which there were incongruences between the lesion masks generated by the 2 raters, the decisions on which voxels to include in the lesion mask were made by consensus. Whole-brain cerebral white matter masks were created by combining the FreeSurfer segmentations of right and left hemispheric white matter and the corpus callosum. Masks of NAWM in the patients with MS were generated by subtracting the lesion masks from the cerebral white matter masks.

Comparisons to prior clinical MR imaging were performed for the subjects with MS. Of these, 22 (16 RRMS) subjects had clinical contrast-enhanced MRI of the brain completed within one year before the study scan.

G-Ratio Calculation

The g-ratio-weighted maps were generated assuming that MTV reflects the MVF.[20] The AVF was calculated by combining f_r, f_{csf}, and MTV:[15,20]

2)
$$AVF = (1 - MTV) \times \left(1 - f_{csf}\right) \times f_r.$$

The g-ratio (g) was then computed as[15]

3)
$$g = \sqrt{\frac{1}{1 + \frac{MTV}{AVF}}}.$$

Statistical Analysis

Statistical analysis was performed in STATA 12.1 (StataCorp, College Station, Texas). Comparisons of MVF, AVF, and the g-ratio among lesions, NAWM, and white matter in HC (HCWM) were performed using a 2-sided *t* test, following the 1-sample Kolmogorov-Smirnov test for normality. The Mann-Whitney *U* test was used to compare subsets of patients with MS (RRMS versus PMS). Bonferroni correction was performed to account for multiple comparisons (uncorrected $P < .05$, corrected $P < .0167$)

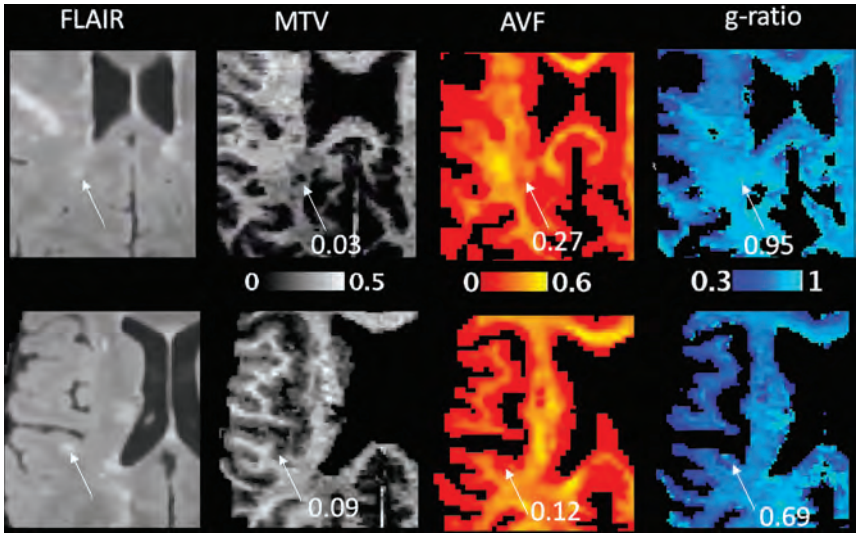

FIG 2. Representative axial T2-FLAIR image and maps of macromolecular tissue volume reflecting myelin content, axonal volume fraction, and g-ratio in a patient with RRMS. The *upper row* shows a lesion with an elevated g-ratio (0.95), indicating a greater degree of demyelination relative to axonal loss. The *lower row* shows a lesion with concordant axonal and myelin loss, which is reflected by a g-ratio similar to that of NAWM (0.69). For comparison, the conventional T2-FLAIR images do not demonstrate a discernible difference in contrast between the 2 lesions.

for each set of tissue contrasts. Raw uncorrected *P* values surviving Bonferroni correction are reported throughout this work.

Correlations between disability scores and imaging metrics averaged in each subject were assessed using linear regression, adjusting for age and sex.

RESULTS

Demographic and clinical characteristics of the MS and HC groups are shown in the On-line Table. The MS group did not differ significantly from the HC group in age or sex ratio. Furthermore, the RRMS subgroup did not differ significantly from the combined PMS subgroups in age, sex, disease duration, or use of disease-modifying therapy. Among all subjects with MS, there were 1418 supratentorial lesions. The mean number of lesions per subject was 48.9 ± 51 (range, 4–212). Based on comparison with clinical scans, 10 subjects with MS had lesions (total of 17 lesions) that developed within 1 year before the study scan.

Figure 2 highlights the variability in the g-ratio as exemplified in a patient with RRMS, including a lesion with an elevated g-ratio reflecting myelin loss but preserved AVF, in comparison with a lesion with a g-ratio similar to that of NAWM. This example demonstrates the potential of the imaging g-ratio to distinguish lesions affected predominantly by demyelination from those with concordant axonal and myelin loss.

Among all patients with MS, lesion AVF and MVF were significantly lower than in NAWM, (0.17 versus 0.23 for AVF, $P < .001$, and 0.17 versus 0.25 for MVF, $P < .001$) (Table 1). The mean g-ratio was significantly elevated in lesions compared with NAWM (0.74 versus 0.67, $P < .001$). The MVF was lower in NAWM compared with HCWM (0.25 versus 0.27, $P < .009$). No significant difference was observed in the g-ratio and AVF of NAWM and HCWM.

When we compared imaging metrics in RRMS and PMS subgroups (Table 2), the average lesion AVF (0.14 versus 0.18, $P < .006$) and MVF (0.13 versus 0.18, $P < .001$) were significantly lower in PMS. The average lesion g-ratio was not significantly different between RRMS and PMS. NAWM MVF was significantly lower in PMS compared with RRMS (0.22 versus 0.26, $P < .01$). No significant difference in AVF or g-ratio was observed for NAWM in subjects with RRMS and PMS.

Disability, measured by the EDSS, was significantly associated with MVF ($\beta = -40.5$, $P < .001$) and AVF ($\beta = -41.0$, $P < .02$) in NAWM, with lower MVF and AVF observed with higher EDSS scores. No significant relationship was observed between the EDSS and the g-ratio in NAWM averaged in each subject ($\beta = 16.5$, $P = .20$). Higher EDSS scores were significantly associated with lower MVF ($\beta = -21.9$, $P = .03$) and higher g-ratios ($\beta = 11.9$, $P = .04$) in lesions. Disability, measured by the MSFC-3, was significantly associated with MVF in NAWM ($\beta = 45.9$, $P = .001$), with lower MVF observed with lower MSFC-3 *z* scores. Lower AVF ($\beta = 35.8$, $P = .06$) and a higher g-ratio in NAWM ($\beta = -25.6$, $P = .07$) were associated with worse performance on the MSFC-3, though the correlations did not meet statistical significance. Lower MSFC-3 *z*-scores correlated with lower MVF ($\beta = 31.4$, $P = .003$) and higher g-ratios ($\beta = -18.5$, $P = .003$) in lesions.

DISCUSSION

In this study, we estimated AVF using a spheric mean analysis of high-gradient diffusion MRI data and quantified myelin content using MTV imaging. We examined the imaging metrics of AVF and MVF separately and combined them to probe alterations in the imaging g-ratio within lesions and NAWM in patients with MS. We found evidence of myelin and axonal loss within lesions compared with NAWM, as well as myelin loss in NAWM compared with HCWM. Lower AVF and MVF in NAWM were significant predictors of neurologic disability as measured by the EDSS and the MSFC-3 in the case of MVF. A trend toward a higher g-ratio was observed in patients who performed worse on the EDSS and MSFC-3, though the correlations did not meet statistical significance.

MVF and AVF were significantly lower in lesions relative to NAWM, consistent with prior g-ratio imaging studies that reported both myelin and axonal loss within focal lesions in MS.[15,17] The finding of an elevated g-ratio in lesions compared with NAWM suggested that myelin loss was the predominant

Table 1: Comparison of imaging metrics in patients with multiple sclerosis and healthy controls

	HC	NAWM	Lesions	HC vs NAWM (*P* Value)	NAWM vs Lesions (*P* Value)
AVF	0.24 ± 0.02	0.23 ± 0.02	0.17 ± 0.04	.15[a]	<.001[a,b]
MVF	0.27 ± 0.02	0.25 ± 0.03	0.17 ± 0.04	.009[b,c]	<.001[a,b]
G-ratio	0.66 ± 0.02	0.67 ± 0.03	0.74 ± 0.06	.17[a]	<.001[b,d]

[a] Student *t* test.
[b] Significance following Bonferroni correction.
[c] Mann-Whitney *U* test.
[d] Wilcoxon signed rank test.

pathology and the resulting myelin sheaths were thinner. Examining the relative change in MVF and AVF as estimated through these advanced MRI metrics may help to distinguish among acute demyelinating, remyelinating, and chronic lesions, which is not possible with conventional T2/FLAIR sequences.[32] Following the initial demyelinating event, MVF would be expected to decrease while AVF would be relatively preserved, resulting in an elevation of the g-ratio. The g-ratio would be expected to normalize with more complete remyelination. Alternatively, chronic lesions with complete loss of the axolemma would also be expected to demonstrate g-ratio values approaching those of NAWM.

Lesions in patients with MS demonstrated significantly lower MVF and AVF compared with those in patients witb RRMS, consistent with more profound myelin and axonal loss. The g-ratio did not differ significantly, indicating a similar degree of relative lesion demyelination in PMS and RRMS. The NAWM of patients with PMS also showed lower MVF and AVF compared with patients with RRMS, but to a lesser degree than in lesions.

The estimated MVF and AVF were lower in NAWM compared with HCWM, though not to the same degree as in lesions. The g-ratio in NAWM also did not differ significantly from HCWM. One possible explanation is that there may be relatively concordant myelin and axonal loss in NAWM. This hypothesis is supported by previous studies of clinically progressive MS that showed that the underlying pathology shifts from one of inflammatory attacks to neurodegeneration of the NAWM.[34]

In evaluating the correlation between neurologic disability and MVF, AVF, and g-ratio in the NAWM, we found significant negative correlations between EDSS and MVF and AVF, indicating that clinical disability worsens as NAWM loses myelin and axonal integrity. The trend toward an elevated g-ratio with more profound disability suggests that more pronounced relative demyelination, or incomplete remyelination, may contribute to greater clinical disability.

To date, most in vivo studies of g-ratios within the CNS have been performed using NODDI to estimate AVF[16,20,22,34] and qMT[15,16,19,20,34] to estimate MVF. Our estimates for the mean g-ratio within lesions and NAWM were similar to those previously reported using qMT and NODDI.[15] Hagiwara et al[17] found higher lesion g-ratios, likely due to differences in their approach to myelin quantification using synthetic MRI. Specifically, their estimates for MVF were considerably lower within lesions than prior qMT estimates[35] as well as our MTV results, possibly due to not including a partial volume pool to account for magnetization transfer effects, which could result in a downward bias in the MVF estimates.[17] Accordingly, the estimated g-ratio in lesions was also higher.

Our estimates for AVF were generally lower than those of previous studies using NODDI, a finding we attribute to differences in the assumptions of the 2 diffusion models. The NODDI approach assumes fixed and equal parallel diffusivities in the intra- and extra-axonal space, which has been shown to produce substantial overestimation of the AVF on the order of 30%–50%.[5,36] By comparison, in our spheric mean model, we explicitly estimated the extra-axonal hindered diffusivity, constraining it to be less than the intra-axonal parallel diffusivity, as suggested by independent validation of the compartment parallel diffusivities.[37] In our work, we also took advantage of the 300-mT/m maximum gradient strength accessible on the Connectom scanner. Higher gradient strengths have been shown to increase the sensitivity of diffusion MRI experiments to intra-axonal water diffusion.[9-11] The accuracy of the AVF values obtained in our study is supported by systematic numeric simulations and validation experiments on a biomimetic brain phantom composed of textile hollow fibers with restricted volume fractions ranging from 0.1 to 0.7.[38] The estimates of AVF using the spheric mean approach and related techniques are in line with those obtained from histology,[39] with estimates of AVF in human white matter from electron microscopy being on the order of 0.2–0.3, which is consistent with the AVF values estimated in healthy controls and NAWM in our study.

If substantiated in larger studies, the imaging g-ratio may be used as a biomarker to aid in patient selection for disease-modifying therapy. In particular, early-phase clinical trials for remyelinating therapies have yielded inconsistent results to date,[33] possibly due to suboptimal patient selection.[32] MS is a heterogeneous disease with specific phenotypes that may be more

Table 2: Comparison of imaging metrics in patients with relapsing-remitting and progressive multiple sclerosis

	RRMS Lesions	PMS Lesions	RRMS NAWM	PMS NAWM	RRMS vs PMS Lesions (*P* Value)	RRMS vs PMS NAWM (*P* Value)
AVF	0.18 ± 0.04	0.14 ± 0.02	0.24 ± 0.02	0.22 ± 0.02	.006[a]	.06
MVF	0.18 ± 0.03	0.13 ± 0.03	0.26 ± 0.02	0.22 ± 0.03	.001[a]	.01[a]
G-ratio	0.72 ± 0.05	0.78 ± 0.07	0.67 ± 0.02	0.68 ± 0.04	.13	.39

[a] Significance following Bonferroni correction.

responsive to remyelinating therapy, which could vary within the same patient at different time points.[40] The incorporation of g-ratio-weighted imaging with myelin and axonal metrics may offer additional tools to help address this issue. Specifically, patients with acute lesions who show elevated g-ratios consistent with more profound demyelination may be more likely to respond to remyelinating therapies, whereas patients with near-normal g-ratios reflecting more complete remyelination, or axonal loss, may be less likely to derive a benefit.

CONCLUSIONS

In this study, we imaged the g-ratio in patients with MS using AVF derived from high-gradient diffusion MRI and MVF quantified through MTV. We found evidence of disproportionately greater myelin loss resulting in elevated g-ratios within lesions compared with NAWM. NAWM showed a lesser degree of axonal and myelin loss that was relatively concordant compared with white matter in healthy controls. Clinical disability as measured by the EDSS and MSFC-3 correlated with MVF, AVF, and, to a lesser degree, with the g-ratio in patients with MS. Longitudinal studies are needed to determine the potential role that these imaging metrics could play as outcome measures or in aiding patient selection for clinical trials of remyelinating therapies.

Disclosures: Fang Yu—*RELATED*: *Grant*: Radiological Society of North America Research Resident Grant, *Comments*: funds to support the purchase of research-related equipment and software, such as Matlab and SPSS.* Aapo Nummenmaa—*RELATED*: *Grant*: National Institutes of Health, *Comments*: Work was partially supported by the National Institutes of Health under award No. R00EB015445.* Lawrence L. Wald—*RELATED*: *Grant*: National Institutes of Health*; *UNRELATED*: *Employment*: Massachusetts General Hospital. Eric C. Klawiter—*RELATED*: *Grant*: National Institutes of Health, National MS Society, Altschul Foundation, *Comments*: National Institutes of Health K23NS078044, NMSS PR-1412-02194*; *UNRELATED*: *Consultancy*: Acorda, Alexion Pharmaceuticals, Atlas5D, Biogen, Celgene, EMD Serono, Genentech, MedDay; *Grants/Grants Pending*: AbbVie, Atlas5D, Biogen, EMD Serono, Genentech, Genzyme.* Susie Y. Huang—*RELATED*: *Grant*: Conrad N. Hilton Foundation, *Comments*: research grant.* *Money paid to institution.

REFERENCES

1. Dutta R, Trapp BD. **Mechanisms of neuronal dysfunction and degeneration in multiple sclerosis.** *Prog Neurobiol* 2011;93:1–12 CrossRef Medline
2. Kremer D, Akkermann R, Kury P, et al. **Current advancements in promoting remyelination in multiple sclerosis.** *Mult Scler* 2019;25:7–14 CrossRef Medline
3. Mallik S, Samson RS, Wheeler-Kingshott CA, et al. **Imaging outcomes for trials of remyelination in multiple sclerosis.** *J Neurol, Neurosurg, Psychiatry* 2014;85:1396–1404 CrossRef Medline
4. Jensen JH, Helpern JA, Ramani A, et al. **Diffusional kurtosis imaging: the quantification of non-gaussian water diffusion by means of magnetic resonance imaging.** *Magn Reson Med* 2005;53:1432–40 CrossRef Medline
5. Zhang H, Schneider T, Wheeler-Kingshott CA, et al. **NODDI: practical in vivo neurite orientation dispersion and density imaging of the human brain.** *Neuroimage* 2012;61:1000–16 CrossRef Medline
6. Assaf Y, Blumenfeld-Katzir T, Yovel Y, et al. **AxCaliber: a method for measuring axon diameter distribution from diffusion MRI.** *Magn Reson Med* 2008;59:1347–54 CrossRef Medline
7. Huang SY, Tobyne SM, Nummenmaa A, et al. **Characterization of axonal disease in patients with multiple sclerosis using high-gradient-diffusion MR imaging.** *Radiology* 2016:280:244–51 CrossRef Medline
8. Fu X, Shrestha S, Sun M, et al. **Microstructural white matter alterations in mild cognitive impairment and Alzheimer's disease: study based on neurite orientation dispersion and density imaging (NODDI).** *Clin Neuroradiol* 2019 June 7. [Epub ahead of print] CrossRef Medline
9. Huang SY, Nummenmaa A, Witzel T, et al. **The impact of gradient strength on in vivo diffusion MRI estimates of axon diameter.** *Neuroimage* 2015;106:464–72 CrossRef Medline
10. Veraart J, Fieremans E, Rudrapatna U, et al. **Breaking the power law scaling of the dMRI signal on the Connectom scanner reveals its sensitivity to axon diameters.** In: *Proceedings of the Annual Meeting of the International Society for Magnetic Resonance in Medicine*. Paris, France; June 16–21, 2018: 252
11. Veraart J, Fieremans E, Novikov DS. **On the scaling behavior of water diffusion in human brain white matter.** *Neuroimage* 2019;185:379–87 CrossRef Medline
12. Henkelman RM, Huang X, Xiang QS, et al. **Quantitative interpretation of magnetization transfer.** *Magn Reson Med* 1993;29:759–66 CrossRef Medline
13. MacKay A, Whittall K, Adler J, et al. **In vivo visualization of myelin water in brain by magnetic resonance.** *Magn Reson Med* 1994;31:673–77 CrossRef Medline
14. Mezer A, Yeatman JD, Stikov N, et al. **Quantifying the local tissue volume and composition in individual brains with magnetic resonance imaging.** *Nat Med* 2013;19:1667–72 CrossRef Medline
15. Stikov N, Campbell JS, Stroh T, et al. **In vivo histology of the myelin g-ratio with magnetic resonance imaging.** *Neuroimage* 2015;118:397–405 CrossRef Medline
16. Cercignani M, Giulietti G, Dowell NG, et al. **Characterizing axonal myelination within the healthy population: a tract-by-tract mapping of effects of age and gender on the fiber g-ratio.** *Neurobiol Aging* 2017;49:109–18 CrossRef Medline
17. Hagiwara A, Hori M, Yokoyama K, et al. **Analysis of white matter damage in patients with multiple sclerosis via a novel in vivo MR method for measuring myelin, axons, and g-ratio.** *AJNR Am J Neuroradiol* 2017;38:1934–40 CrossRef Medline
18. Berman S, West KL, Does MD, et al. **Evaluating g-ratio weighted changes in the corpus callosum as a function of age and sex.** *Neuroimage* 2018;182:304–13 CrossRef Medline
19. Campbell JSW, Leppert IR, Narayanan S, et al. **Promise and pitfalls of g-ratio estimation with MRI.** *Neuroimage* 2018;182:80–96 CrossRef Medline
20. Duval T, Le Vy S, Stikov N, et al. **G-ratio weighted imaging of the human spinal cord in vivo.** *Neuroimage* 2017;145:11–23 CrossRef Medline
21. Keil B, Blau JN, Biber S, et al. **A 64-channel 3T array coil for accelerated brain MRI.** *Magn Reson Med* 2013;70:248–58 CrossRef Medline
22. Huang SY, Witzel T, Fan Q, et al. **TractCaliber: axon diameter estimation across white matter tracts in the in vivo human brain using 300 mT/m gradients.** In: *Proceedings of the Annual Meeting of the International Society for Magnetic Resonance in Medicine*. Toronto, Ontario, Canada; May 20 to June 5, 2015
23. Fan Q, Witzel T, Nummenmaa A, et al. **MGH-USC Human Connectome Project datasets with ultra-high b-value diffusion MRI.** *Neuroimage* 2016;124:1108–14 CrossRef Medline
24. Andersson JL, Skare S, Ashburner J. **How to correct susceptibility distortions in spin-echo echo-planar images: application to diffusion tensor imaging.** *Neuroimage* 2003;20:870–88 CrossRef Medline
25. Smith SM, Jenkinson M, Woolrich MW, et al. **Advances in functional and structural MR image analysis and implementation as FSL.** *Neuroimage* 2004;23(Suppl 10):S208–19 Medline
26. Andersson JLR, Sotiropoulos SN. **An integrated approach to correction for off-resonance effects and subject movement in diffusion MR imaging.** *Neuroimage* 2016;125:1063–78 CrossRef Medline
27. Fan Q, Nummenmaa A, Witzel T, et al. **Axon diameter mapping independent of crossing structures using spherical mean technique.**

In: *Proceedings of the Annual Meeting of the International Society for Magnetic Resonance in Medicine*. Paris, France; June 16–21, 2018
28. Huang SY, Tobyne SM, Nummenmaa A, et al. **Characterization of axonal pathology independent of fiber crossings in multiple sclerosis using high-gradient diffusion MRI.** *Radiology* 2016;280:244–51 CrossRef Medline
29. Dale AM, Fischl B, Sereno MI. **Cortical surface-based analysis, I: segmentation and surface reconstruction.** *Neuroimage* 1999;9:179–94 CrossRef Medline
30. Fischl B, van der Kouwe A, Destrieux C, et al. **Automatically parcellating the human cerebral cortex.** *Cereb Cortex* 2004;14:11–22 CrossRef Medline
31. Lindemer ER, Salat DH, Smith EE, et al. **White matter signal abnormality quality differentiates mild cognitive impairment that converts to Alzheimer's disease from nonconverters.** *Neurobiol Aging* 2015;36:2447–57 CrossRef Medline
32. Plemel JR, Liu W-Q, Yong VW. **Remyelination therapies: a new direction and challenge in multiple sclerosis.** *Nat Rev Drug Discov* 2017;16:617–34 CrossRef Medline
33. Stangel M, Kuhlmann T, Matthews PM, et al. **Achievements and obstacles of remyelinating therapies in multiple sclerosis.** *Nat Rev Neurol* 2017;13:742–54 CrossRef Medline
34. Berman S, West KL, Does MD, et al. **Evaluating g-ratio weighted changes in the corpus callosum as a function of age and sex.** *Neuroimage* 2018;182:1304–13 CrossRef Medline
35. Levesque IR, Giacomini PS, Narayanan S, et al. **Quantitative magnetization transfer and myelin water imaging of the evolution of acute multiple sclerosis lesions.** *Magn Reson Med* 2010;63:633–40 CrossRef Medline
36. Jelescu IO, Veraart J, Adisetiyo V, et al. **One diffusion acquisition and different white matter models: how does microstructure change in human early development based on WMTI and NODDI?** *Neuroimage* 2015;107:242–56 CrossRef Medline
37. Kunz N, da Silva AR, Jelescu IO. **Intra- and extra-axonal axial diffusivities in the white matter: which one is faster?** *Neuroimage* 2018;181:314–22 CrossRef Medline
38. Fan Q, Nummenmaa A, Wichtmann B, et al. **Validation of diffusion MRI estimates of compartment size and volume fraction in a biomimetic brain phantom using a human MRI scanner with 300mT/m maximum gradient strength.** *Neuroimage* 2018;182:469–78 CrossRef Medline
39. Duval T, Saliani A, Nami H, et al. **Axons morphometry in the human spinal cord.** *Neuroimage* 2019;185:119–28 CrossRef Medline
40. Frischer JM, Weigand SD, Guo Y, et al. **Clinical and pathological insights into the dynamic nature of the white matter multiple sclerosis plaque.** *Ann Neurol* 2015;78:710–21 CrossRef Medline
41. Abelev B, Adam J, Adamova D, et al; ALICE Collaboration. **A measurement of quarkonium production at forward rapidity in [Formula: see text] collisions at [Formula: see text]TeV.** *Eur Phys J C Part Fields* 2014;74:2974 CrossRef Medline

Prolonged Microgravity Affects Human Brain Structure and Function

D.R. Roberts, D. Asemani, P.J. Nietert, M.A. Eckert, D.C. Inglesby, J.J. Bloomberg, M.S. George, and T.R. Brown

ABSTRACT

BACKGROUND AND PURPOSE: Widespread brain structural changes are seen following extended spaceflight missions. The purpose of this study was to investigate whether these structural changes are associated with alterations in motor or cognitive function.

MATERIALS AND METHODS: Brain MR imaging scans of National Aeronautics and Space Administration astronauts were retrospectively analyzed to quantify pre- to postflight changes in brain structure. Local structural changes were assessed using the Jacobian determinant. Structural changes were compared with clinical findings and cognitive and motor function.

RESULTS: Long-duration spaceflights aboard the International Space Station, but not short-duration Space Shuttle flights, resulted in a significant increase in total ventricular volume (10.7% versus 0%, $P < .001$, $n = 12$ versus $n = 7$). Total ventricular volume change was significantly associated with mission duration ($r = 0.72$, $P = .001$, $n = 19$) but negatively associated with age ($r = -0.48$, $P = .048$, $n = 19$). Long-duration spaceflights resulted in significant crowding of brain parenchyma at the vertex. Pre- to postflight structural changes of the left caudate correlated significantly with poor postural control; and the right primary motor area/midcingulate correlated significantly with a complex motor task completion time. Change in volume of 3 white matter regions significantly correlated with altered reaction times on a cognitive performance task (bilateral optic radiations, splenium of the corpus callosum). In a post hoc finding, astronauts who developed spaceflight-associated neuro-ocular syndrome demonstrated smaller changes in total ventricular volume than those who did not (12.8% versus 6.5%, $n = 8$ versus $n = 4$).

CONCLUSIONS: While cautious interpretation is appropriate given the small sample size and number of comparisons, these findings suggest that brain structural changes are associated with changes in cognitive and motor test scores and with the development of spaceflight-associated neuro-optic syndrome.

ABBREVIATIONS: CDS = code substitution; CPT = continuous performance; %ΔVV = percentage total ventricular volume change; FTT Functional Task Test; ISS = International Space Station; LSAH = Lifetime Surveillance of Astronaut Health; NASA = National Aeronautics and Space Administration; PVE = partial volume estimation; SANS = spaceflight-associated neuro-ocular syndrome; WinSCAT = Spaceflight Cognitive Assessment Tool for Windows

The effects of spaceflight on the human brain must be understood to ensure the safety of astronauts who participate in long-duration missions aboard the International Space Station (ISS) and to support future space-exploration missions. We have previously shown an upward shift of the brain, crowding of eloquent brain tissue at the vertex, and enlargement of the ventricular system in astronauts following long-duration missions aboard the ISS.[1] Similarly, other investigators have described local

Received June 2, 2019; accepted after revision August 19.

From the Departments of Radiology and Radiological Science (D.R.R., D.A., D.I., T.R.B.), Department of Neurosciences (D.R.R.), Public Health Sciences (P.J.N.), Otolaryngology–Head and Neck Surgery (M.A.E.), and Psychiatry and Behavioral Sciences (M.S.G.), Medical University of South Carolina, Charleston, South Carolina; Neurosciences Laboratory (J.J.B.), NASA Johnson Space Center, Houston, Texas; and Ralph H. Johnson VA Medical Center (M.S.G.), Charleston, South Carolina.

This study was funded by a grant from the National Aeronautics and Space Administration (NNX13AJ92G). Dr Nietert's time on this project was funded, in part, by the National Institutes of Health National Center for Advancing Translational Science (grant No. UL1-TR001450) and the National Institute of General Medical Sciences (grant No. U54-GM104941). Dr Inglesby's time on this project was funded by a Minorities in STEM Student Scholarship from the South Carolina Space Grant Consortium (grant No. NNX15AL49H).

All study data were provided by the NASA Lifetime Surveillance of Astronaut Health office. The study was approved by the NASA Johnson Spaceflight Center and the Medical University of South Carolina institutional review boards. All participants provided written informed consent for use and publication of their data. NASA has reviewed the manuscript and figures, which preserve astronaut anonymity and are compliant with NASA Astronaut Office privacy standards. To obtain access to the data, one should make application to the NASA Lifetime Surveillance of Astronaut Health Office. Any release of data must be approved by NASA.

Dr. Asemani made significant contributions to this paper as co-first author.

Please address correspondence to Donna R. Roberts, MD, Departments of Radiology and Radiological Science and Neurosciences, Medical University of South Carolina, 96 Jonathan Lucas Street, MSC 323, CSB Suite 210, Charleston, SC 29425; e-mail: robertdr@musc.edu; @BrainsOnMars

Indicates open access to non-subscribers at www.ajnr.org

Indicates article with supplemental on-line appendix and tables.

http://dx.doi.org/10.3174/ajnr.A6249

nonlinear deformations in astronaut brain structure postflight.[2-4] While clinically relevant functional decrements in essentially every other body system have been documented following spaceflight,[5] the etiology and functional significance of these brain structural changes remain unclear. Here, we sought to determine the extent to which pre- to postflight structural brain changes may be associated with changes in astronauts' cognitive or motor performances postflight.

A subset of astronauts develop a constellation of clinical findings, including altered visual acuity, ophthalmologic changes such as cotton wool spots, choroidal folds, and optic disc edema.[6] The National Aeronautics and Space Administration (NASA) has termed this constellation of clinical findings "spaceflight-associated neuro-ocular syndrome" (SANS).[7] Therefore, we also examined post hoc the extent to which pre- to postflight structural brain changes were associated with the development of SANS.

We hypothesized that regional brain changes of astronauts identified on postflight MR imaging are progressive on the basis of mission duration, may affect cognitive and motor performance, and may provide insight into the pathophysiology of SANS.

MATERIALS AND METHODS

Experimental Design

The study was approved by the Institutional Review Boards of the NASA Johnson Spaceflight Center and the Medical University of South Carolina. After the nature and possible consequences of the study, including potential loss of privacy, were explained to the astronauts, informed consent was obtained.

For this study, we retrospectively analyzed data obtained from the NASA Lifetime Surveillance of Astronaut Health (LSAH) Program. Due to the retrospective nature of the study, data for some of the tests were not available for all astronauts in the study. This article was reviewed by NASA to ensure astronaut anonymity.

Participants

The participants in this study represent a subset of astronauts from a previously described NASA astronaut cohort.[1] The inclusion criterion was any astronaut to date at the time of the study who had undergone both pre- and postflight brain MR imaging. The exclusion criterion was the lack of 3D high-resolution imaging on pre- or postflight brain MR imaging, which was required to perform the quantitative analysis. Of a cohort of 34 astronauts, the necessary pre- and postflight high-resolution imaging was available for 19 astronauts: 7 astronauts (1 woman; mean age, 46.7 ± 2.1 years) who underwent short-duration flights aboard the Space Shuttle (14.7 ± 1.6 days) and 12 astronauts (2 women; mean age, 47.5 ± 4.8 years) who underwent long-duration missions aboard the ISS (162.7 ± 21.8 days).

Brain MR Imaging Analysis

For each astronaut, 3D high-resolution MR imaging was performed on a 3T Verio system (Siemens, Erlangen, Germany) before and within 3 weeks following spaceflight using the following parameters: T1-weighted magnetization-prepared rapid acquistion of gradient-echo sequence; 176 sagittal slices; TR = 2300 ms; TE = 2.98 ms; TI = 90 ms; flip angle = 7°; FOV = 240 × 256 mm^2; matrix = 240 × 256; 1 × 0.9 × 0.9 mm^3 voxels. Details of the MR imaging analysis are provided in the On-line Appendix. Briefly, the images of the outer skull were used to coregister the pre- and postflight images to correct for head positioning within the MR imaging scanner. Volumetric analysis was performed using publicly available software (FSL, Version 5.0; http://www.fmrib.ox.ac.uk/fsl). Local crowding or displacement of brain tissue along the brain-CSF interface was assessed by subtracting the affine-transformed preflight brain parenchyma image from the skull-aligned postflight brain parenchyma image. Finally, regional deformation of the brain parenchyma was assessed on the basis of the extent of nonlinear warping of the preflight whole brain to the postflight whole brain, as defined by the Jacobian determinant.

Cognitive Performance: Changes in the Spaceflight Cognitive Assessment Tool for Windows Scores

Cognitive testing was available for the 12 long-duration astronauts who participated in ISS missions, which we obtained from the LSAH. Per NASA protocol, all astronauts on ISS missions participate in the Spaceflight Cognitive Assessment Tool for Windows (WinSCAT) battery, which was developed by NASA as a sensitive screening tool for astronauts to monitor their neurocognitive status while in space and to alert NASA flight surgeons to any alterations in astronaut performance.[8,9] Because WinSCAT testing was not NASA protocol for Shuttle flights, no data were available for Shuttle astronauts. The WinSCAT is composed of 5 subtests that characterize visual search, processing speed/efficiency, and learning (Code Substitution, CDS); memory (Code Substitution Delayed Recognition, CCD); working memory (Delayed Matching to Sample, MSP); arithmetic (Mathematical Processing, MTH); and sustained attention (Continuous Performance, CPT). Accuracy and reaction time were obtained for each subtest.[8,9] The WinSCAT has been validated in various patient populations and has proved useful in identifying alterations in cognitive performance with high sensitivity and specificity.[8] The standard NASA procedure is for ISS astronauts to take the WinSCAT 6 times before flight to allow familiarization with testing. Per the NASA standard, the performances on the last 3 WinSCAT tests taken before flight were averaged and considered baseline for each astronaut.[9] During the mission onboard the ISS, astronauts took the WinSCAT every 30 days; therefore, depending on the mission length, the number of inflight tests varied among astronauts. Finally, approximately 1 month following return to Earth (mean, 35.2 ± 4.8 days), astronauts underwent a postflight WinSCAT. We chose the postflight examination as the comparator study to be consistent with the MR imaging data. The percentage change in WinSCAT scores was calculated as

$$\%\ \text{Change Postflight to Preflight} = \frac{Score_{\text{Post}} - \text{Score}_{\text{Pre}}}{\text{Score}_{\text{Pre}}} \times 100,$$

where $Score_{\text{Pre}}$ and $\text{Score}_{\text{Post}}$ represent the pre- and postflight accuracy and reaction time scores for each of the WinSCAT subtests.

Motor Performance: Changes in Functional Task Performance and Postural Equilibrium Control

Eight astronauts (7 long-duration and 1 short-duration) in this study had participated in a separate Functional Task Test (FTT) study. The FTT is a separate NASA-sponsored research study designed to assess the impact of spaceflight on the astronauts' performance of mission-critical tasks required after landing on a planetary surface, for example, hatch opening or egress from a space capsule.[10] The study protocol had 11 subtests relevant to motor control: Activity Board, Dynamic Postural Stability, Recovery from Fall/Stand, Supine Egress and Walk, Pegboard Test, Seated Egress and Walk, Object Translation, Ladder Climb, Hatch Opening, Jump Down, and Tandem Walk.[10] More complete descriptions of each subtest are provided elsewhere[10] and in the On-line Appendix. We obtained the FTT data from the LSAH.

Each ISS astronaut underwent FTT approximately 100 and 60 days before launch and within 24–48 days following return from spaceflight. The average score from the 2 testing sessions before spaceflight was used as the preflight baseline. We calculated the percentage change in scores for each test as

$$\%\ \text{Change Postflight to Preflight} = \frac{Score_{\text{Post}} - \text{Score}_{\text{Pre}}}{\text{Score}_{\text{Pre}}} \times 100,$$

where $Score_{\text{Pre}}$ and $Score_{\text{Post}}$ represent the pre- and postflight scores for each of the 11 FTT subtests.

Clinical Findings of SANS

The current diagnostic criteria for SANS have been defined by NASA to include ocular disc edema of variable Frisén grades, globe flattening, choroidal folds, hyperopic refractive error shifts, and cotton wool spots.[11] Using this definition of SANS, we obtained the ophthalmologic records for each ISS astronaut from the LSAH and screened for any documented clinical signs of SANS.

Statistical Analyses

Several analytic approaches were used to assess changes in brain MR imaging metrics, and cognitive and motor function scores, and to quantify correlations among relevant study variables. All analyses were conducted using SAS, Version 9.4 (SAS Institute, Cary, North Carolina). Given the relatively small number of cases composing this sample, nonparametric statistical approaches were used throughout. Within-group, pre- to postflight changes in brain MR imaging metrics (ie, volume metrics) were calculated using Wilcoxon signed rank tests, while between-group differences of these changes were calculated using Wilcoxon rank sum tests. Unadjusted and adjusted (partial) Spearman rank–based correlations were calculated using data from all 19 astronauts to quantify the associations between changes in brain MR imaging metrics with age at launch and flight duration.

To estimate local crowding or displacement of brain tissue along the brain-CSF interface within the Shuttle and ISS astronaut groups from the Jacobian modulated pre- to postflight difference image, we used the FSL Randomise function (https://fsl.fmrib.ox.ac.uk/fsl/fslwiki/Randomise) to correct for multiple comparisons across the whole brain, assuming an overall threshold of $P < .05$ based on 5000 random permutations and threshold-free cluster enhancement.[12]

To estimate voxelwise associations between brain volume change and each of the cognitive and motor test scores separately, we obtained nonparametric correlations between the normalized Jacobian determinant and each cognitive and motor test score as a covariate. Again, the FSL Randomise function was used to correct for multiple comparisons across the whole brain.[12]

Spearman correlations were also used to quantify associations between changes in the 12 ISS astronauts' WinSCAT scores, flight duration, and changes in brain MR imaging metrics. Spearman correlations were also used to quantify associations between changes in the 8 astronauts' FTT scores and changes in brain MR imaging metrics. A correlation of >0.5 was considered large on the basis of Cohen, 1992.[13]

To correct for multiple comparisons, we used an adaptive linear step-up procedure as suggested by Benjamini et al.[14] Using this method, we corrected the P value for 21 tests (5 WinSCAT subtests, each with accuracy and reaction time, and 11 FTT subtests) to control the false discovery rate at 5%. The false discovery rate is the expected percentage of "discoveries" (ie, significant findings) that are, in fact, spurious. Instead of the nominal P value = .05, we used smaller P value thresholds for flagging significant results. For the comparison between pre- and postflight test scores, a corrected P value of .0476 was used. For the correlations between the percentage total ventricular volume change (%ΔVV) and percentage changes in cognitive/motor testing, a corrected P value of .00238 was used.

In a post hoc analysis, we used a Wilcoxon rank sum test to compare %ΔVV among astronauts who developed SANS versus those who did not; because this particular comparison was deemed secondary, the resulting P value was not accounted for when adjusting for multiple comparisons.

RESULTS

Volumetric Analysis by Brain Tissue Segment

No significant change was seen pre- to postflight in the total volume of gray matter or white matter for either the Shuttle or ISS astronauts (On-line Table 1). In accordance with our prior study,[1] there was a significant increase in the total ventricular volume postflight compared with preflight in the ISS astronauts but not in the Shuttle astronauts (+10.7% versus 0%, respectively, $P < .001$, Fig 1*A*). For the ISS astronauts, the percentage change in ventricular volume for the left lateral, right lateral, third, and fourth ventricles was respectively 17.1% ± 7.3% ($P = .005$), 15.2% ± 8.4% ($P = .005$), 15.4% ± 4.9% ($P = .005$), and −0.83% ± 4.57% ($P = .68$). The %ΔVV pre- to postflight was significantly associated with the flight duration across astronauts ($r = 0.72$, $P = .001$, $n = 19$, Fig 1*B*), which remained significant after adjusting for astronauts' ages at time of launch. There was a significant negative association between astronauts' ages and %ΔVV when adjusted for flight duration ($r = -0.48$, $P = .048$, $n = 19$, Fig 1*C*), with the younger astronauts experiencing larger %ΔVV.

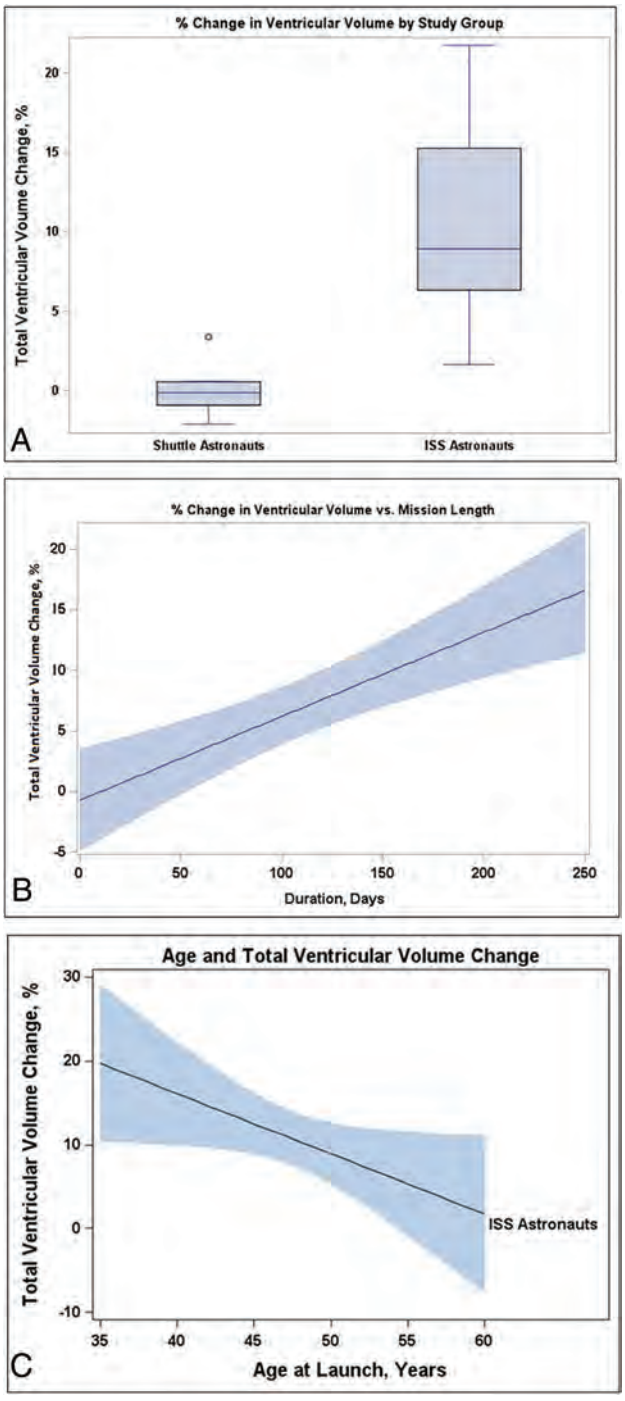

FIG 1. Ventricular volume increases depended on duration in flight, type of space flight, and astronaut age (*A*–*C*). Note that the following modifications were made to the figures to protect astronaut anonymity: Individual data points for mission duration and ISS astronaut ages are not plotted. Instead, the regression line and 95% confidence bands are shown. *A*, Boxplot showing %ΔVV versus mission duration. *B*, %ΔVV versus mission duration, including Shuttle and ISS astronauts. *C*, %ΔVV versus ISS astronaut age at launch.

Local Brain Boundary Change Estimation

After accounting for global shift of the brain, we quantified local crowding or displacement of brain tissue along the brain-CSF interface (the boundary of the brain). In the astronauts who had undergone long-duration spaceflights, significant local changes in brain structure were noted (Fig 2). There was significant crowding of brain parenchyma at the vertex involving supplementary motor, premotor, and primary sensorimotor regions, consistent with our previously reported radiographic findings of central sulcus narrowing.[1] There was also displacement of brain tissue along the ventricular margins, consistent with enlargement of the ventricular system. No significant local changes in brain boundary were observed in the Shuttle astronauts following short-duration spaceflight.

Associations between Structural Brain Changes and Motor Function

On-line Table 2 shows the descriptive statistics (corrected for multiple comparisons) for the pre- and postflight scores for each of the functional task-testing domains, including the pronounced change in postural control as measured by sway speed on the Recovery from Fall/Stand Test and equilibrium score on the Dynamic Postural Stability Test.

To test for any voxelwise associations between brain volume change and motor function, we obtained nonparametric correlations between the normalized Jacobian determinant and each motor test score as a covariate. Local changes in brain structure were assessed using the Jacobian determinant, and several areas emerged as significant predictors of altered motor performance on postflight testing ($P < .05$, $n = 8$, permutation-corrected) (Fig 3). Local structural change of the left caudate nucleus predicted a decrement in postural control as measured by the Recovery from Fall/Stand Test and the Dynamic Postural Stability Test. Prolonged completion time on the Seated Egress and Walk Test was predicted by local structural change of the right lower extremity primary motor area/midcingulate. No other brain areas demonstrated local changes in structure that correlated significantly with changes in postflight performance on the other FTT subtests.

We also tested for any association between %ΔVV and changes in motor test scores (On-line Table 3). There was a large correlation between %ΔVV and the sway speed on the Recovery from Fall/Stand Test ($r = 0.74$, $n = 8$), indicating that those astronauts with the largest increases in %ΔVV had a greater loss of postural control postflight; however, this correlation did not survive correction for multiple comparisons.

Associations between Structural Brain Changes and Cognitive Function

Because of various mission lengths, individual astronauts had taken the WinSCAT between 9 and 12 times before the postflight examination; however, no significant association was seen between mission length and performance on any of the subtests of the WinSCAT. Given the small sample size and the repeated design at baseline, we did not attempt to correct for further potential learning effects among the astronauts.

On-line Table 4 shows the descriptive statistics for the pre- and postflight scores for each of the WinSCAT domains. Postflight, the astronauts demonstrated a significant (corrected for multiple comparisons) decrement in accuracy on the CDS

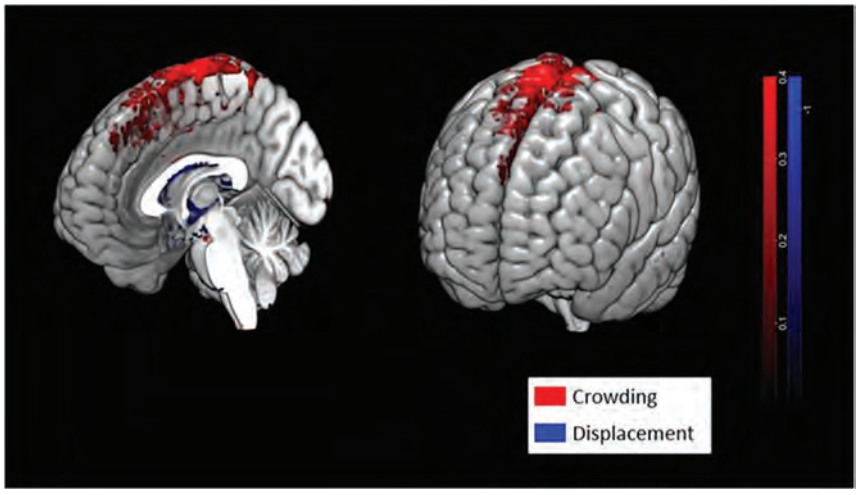

FIG 2. Spaceflight results in crowding of brain tissue at the vertex. *Red voxels* indicate regions along the brain surface where there was an increase in brain parenchyma pre- to postflight due to crowding of the brain tissue as the brain shifted upwards. *Blue voxels* indicate displaced brain tissue that occurred predominantly along the margins of the lateral and third ventricles due to enlargement of the ventricles postflight.

processing speed and learning subtest (−0.8% ± 1.1%, $P = .02$, $n = 12$) but faster reaction times for CDS and the CPT sustained attention subtest as indicated by negative percentage changes in reaction time (−9.1% ± 10.8%, $P = .02$ and −9.4% ± 8.2%, $P = .001$, respectively; $n = 12$).

To test for any voxelwise associations between brain volume change and cognitive function, we obtained nonparametric correlations between the normalized Jacobian determinant and each cognitive test score as a covariate. Three white matter regions emerged as significant predictors of altered reaction time on the CPT (bilateral optic radiations and splenium of the corpus callosum; $P < .05$, $n = 12$, permutation-corrected) (Fig 4). Those astronauts with the least reduction in reaction time postflight showed the greatest change in local volume in these 3 white matter regions. No area of the brain demonstrated local structural change that correlated significantly with postflight performance changes on any other WinSCAT subtests in this relatively small sample.

We also tested for any association between %ΔVV and changes in cognitive test scores (On-line Table 5). While there was a large negative correlation between accuracy on the CDS subtest and the %ΔVV ($r = -0.60$, $n = 12$), indicating a decrement in accuracy in astronauts with the greatest increases in %ΔVV, and a large negative correlation between %ΔVV and reaction time on the CPT subtest ($r = -0.62$, $n = 12$), indicating that those astronauts with smaller increases in %ΔVV exhibited slower reaction times postflight, neither of these correlations survived correction for multiple comparisons.

Associations between Structural Brain Changes and Clinical Findings of SANS

Of the 12 long-duration astronauts, 1 astronaut had optic disc edema and increased intracranial pressure (21.5 cm H_2O) at lumbar puncture following the spaceflight. Three additional astronauts demonstrated choroidal folds but did not undergo lumbar puncture. These 4 astronauts (all men) were classified as SANS cases. Compared with the 8 long-duration astronauts who did not develop findings of SANS, there was a smaller change in %ΔVV postflight in the 4 astronauts with SANS (12.8% versus 6.5%, $P = .02$). Because this was a post hoc comparison between 2 relatively small groups of people, we believe the findings should be considered preliminary rather than confirmatory.

DISCUSSION

Here we show that alteration of brain structure during spaceflight is likely progressive on the basis of mission duration, affects the younger astronauts, and correlates with postflight changes in motor and cognitive performance. These findings suggest that the brain changes seen with microgravity have measurable behavioral consequences. While observed in a relatively small sample, with some variation based on astronaut demographics, these results may have major health significance that should be considered in spaceflight policy and planning.

The results suggest that long-duration spaceflight causes both global and local changes in brain structure. There is a redistribution of CSF, which occurs with ventricular enlargement, a global upward brain shift, and narrowing of the CSF spaces at the vertex along the inner table of the skull.[1] As a result, significant local changes include crowding of brain parenchyma along the superior-medial aspects of the frontal and parietal lobes and displacement of brain parenchyma along the margins of the lateral and third ventricles as the ventricles expand (Fig 2).

For the 2 FTT tasks requiring the greatest demand for dynamic control of postural equilibrium, we found a significant association between altered postural control postflight and local structural changes of the left caudate nucleus, an important structure in postural and locomotion control.[15-17] For example, the caudate nucleus has been proposed to play a role in the pathophysiology of idiopathic normal pressure hydrocephalus, in which patients commonly present with abnormal gait and enlarged ventricles on brain imaging and have been found to have reduced volume[18] and hypometablism[19] of the caudate nuclei compared with healthy controls. Restoration of normal perfusion of the caudate nuclei after shunt placement has been shown to correlate with improved gait in patients with idiopathic normal pressure hydrocephalus.[20] Similarly, in astronauts, our current findings suggest that structural changes of the caudate nucleus may contribute to the substantial deficits in postural control experienced by astronauts postflight.[10] We hypothesize that unilateral association with the left caudate nucleus is due to the

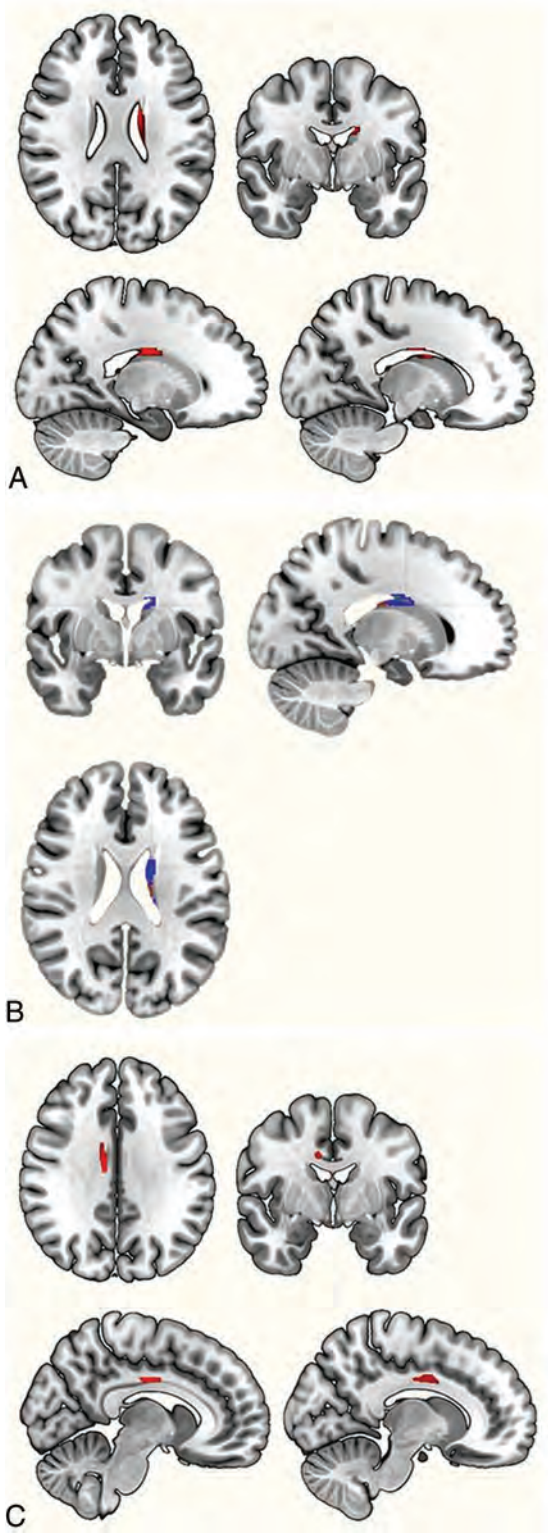

FIG 3. Regional deformation of brain parenchyma that significantly predicted performance on motor function tests. *A*, Regional deformation of brain parenchyma that significantly predicted performance on the Recovery from Fall/Stand Test ($P < .05$). *B*, Regional deformation of brain parenchyma that significantly predicted performance on the Dynamic Postural Stability Test ($P < .05$). *C*, Regional deformation of brain parenchyma that significantly predicted performance on the Seated Egress and Walk Test ($P < .05$).

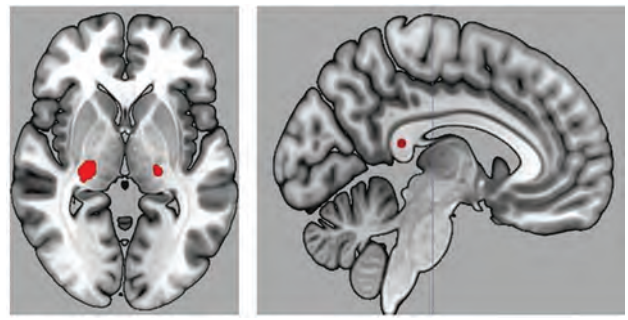

FIG 4. Regional deformation of brain parenchyma that significantly predicted performance on the Continuous Performance Test ($P < .05$).

larger increase in left-versus-right ventricular volume (17.1% versus 15.2%), resulting in a large change in the volume of the left caudate nucleus.

Alternatively, for the Seated Egress and Walk Test, we found a significant association between task-completion time and local structural changes of the right lower extremity primary motor area/midcingulate. The Seated Egress and Walk Test is a complex task that involves completing an obstacle course and therefore would be expected to engage higher order cortical areas. Unilateral association with the right motor area is consistent with previous results in which exposure to simulated microgravity caused a decrease in the activity of the left prefrontal and parietal cortices involved in preparation and realization of motor responses with a compensatory increase in right hemispheric activation.[21] Pechenkova et al[22] have also demonstrated several asymmetric alterations in motor system connectivity following spaceflight in a group of cosmonauts.

Postflight, the astronauts demonstrated reduced accuracy on the CDS subtest and faster reaction times for CDS and CPT. The change in reaction time could indicate ongoing learning effects during spaceflight on cognitive tasks as has been previously suggested.[23] For example, Basner et al[24] performed a normative study in astronauts, astronaut candidates, and NASA mission controllers using a test battery known as Cognition, which includes 2 subtests comparable with the CDS and CPT of the WinSCAT. Each participant performed the Cognition battery repeatedly to document the trajectory of speed and accuracy measures, and during 15 administrations of Cognition, the response times continued to decrease, suggesting ongoing learning. Alternatively, a change in reaction time and decreased accuracy on the CDS subtest may reflect a trade-off of accuracy for faster reaction times. A similar effect was also documented in the study of Basner et al[24] for the CDS subtest. Faster reaction times were also seen at cognitive testing in a spaceflight analog study in which participants underwent long-term head-down-tilt bed rest simulating the headward fluid shifts of spaceflight while exposed to elevated carbon dioxide levels similar to those on the ISS. The authors suggested that the chronic exposure to elevated carbon dioxide experienced on the ISS may lead to altered cerebrovascular reactivity favoring the visual cortex and improved visual performance.[25] Indeed, many factors affect individual astronaut performance, including hypercapnia, sleep, stress levels, noise, medications, and other psychosocial factors; therefore, further

studies with larger sample sizes are needed to characterize cognitive performance in astronauts. Our current findings suggest individual brain structural adaption during spaceflight may also be an important factor affecting astronaut cognitive performance.

Local volume change of the right greater than left optic radiations and splenium of the corpus callosum was associated with relatively unaltered reaction times on the CPT compared with those astronauts who displayed faster reaction times on postflight testing. This finding is consistent with the known role of the splenium of the corpus callosum in mediating fast visuomotor responses.[26] In astronauts, abnormal diffusion metrics involving multiple white matter tracts indicative of disrupted white matter connectivity have been identified postflight,[27] and in particular, a recent study found focally reduced fractional anisotropy within the right posterior thalamic radiation in astronauts postflight, a physiologic correlate to the local volume change we identify here.[28]

Initially, we had hypothesized that ventricular enlargement postflight would correlate with the development of SANS; however, the 4 astronauts with ophthalmologic changes had a smaller change in %ΔVV than those without SANS (12.8% versus 6.5%, $P = .02$, $n = 8$ versus $n = 4$). While the etiology of SANS remains unclear, this preliminary result suggests that ventricular enlargement, as seen in astronauts without SANS, may not be a characteristic feature of SANS.

While there was a large correlation between %ΔVV and postflight sway speed (Recovery from Fall/Stand Test) and a large negative correlation with accuracy (CDS cognitive subtest), indicating that ventricular enlargement was associated with a loss of postflight postural control and a decrement in accuracy, these did not survive correction for multiple comparisons. There was also a large negative correlation between %ΔVV and reaction time on the CPT subtest, indicating that those astronauts with smaller increases in %ΔVV exhibited slower reaction times postflight. While this finding is consistent with the smaller change in %ΔVV experienced by astronauts with SANS whose visual changes may have affected visuomotor performance, this finding also did not survive correction for multiple comparisons. Therefore, any association between %ΔVV and altered cognitive or motor performance will need to be studied in a larger group of astronauts.

The opportunity for individuals to experience spaceflight is limited; thus, the unique sample described here is important for guiding decision-making about future spaceflight. However, this uniqueness also limits the strength of inference that can be made from results involving a relatively small sample size, particularly for female astronauts who were under-represented in the current sample. Another limitation is the lack of uniform testing across all astronauts due to the retrospective nature of this study.

CONCLUSIONS

In the context of cautious interpretation, we found clear evidence of changes in brain structure that appear to occur with changes in behavior involving postural adjustment and reaction time during a cognitive task. The importance of these results is to highlight the need to prioritize further studies of human brain adaptation to spaceflight to ensure the safety of ISS astronauts and to prepare for long-duration exploration missions to the Moon and ultimately to Mars. Our findings support the need for advanced neuroimaging protocols and long-term follow-up imaging of the astronaut population. Most important, understanding the influences of gravity on CSF homeostasis and brain health may provide insights into abnormalities of CSF homeostasis such as idiopathic normal pressure hydrocephalus.

ACKNOWLEDGMENTS

We thank Emily Kreibich, Kaylen Bradley, and Brandon Dixon for assistance in data analysis. We thank Drs James Picano and Kimberly Seaton for assistance with interpretation of the WinSCAT data. We also thank Wafa Taiym and Sara Mason of the Lifetime Surveillance of Astronaut Health program and NASA Johnson Space Center, who provided the astronaut WinSCAT scores and imaging data. We thank members of the Functional Task Test study team at NASA Johnson Space Center for the FTT and balance data.

Disclosures: Donna R. Roberts—*RELATED*: *Grant*: National Aeronautics and Space Administration*; *Support for Travel to Meetings for the Study or Other Purposes*: National Aeronautics and Space Administration.* Truman R. Brown—*UNRELATED*: *Employment*: Medical University of South Carolina. Paul J. Nietert—*RELATED*: *Grant*: National Institutes of Health, *Comments*: grant No. UL1TR001450.* Dani Inglesby—*RELATED*: *Grant*: South Carolina Space Grant Minorities in STEM Student Scholarship. Mark S. George—*RELATED*: *Grant*: National Aeronautics and Space Administration.* Davud Asemani—*RELATED*: *Grant*: National Aeronautics and Space Administration. *Money paid to the institution.

REFERENCES

1. Roberts DR, Albrecht MH, Collins HR, et al. **Effects of spaceflight on astronaut brain structure as indicated on MRI.** *N Engl J Med* 2017;377;1746–53 CrossRef Medline
2. Alperin N, Bagci AM, Lee SH. **Spaceflight-induced changes in white matter hyperintensity burden in astronauts.** *Neurology* 2017;89:2187–91 CrossRef Medline
3. Koppelmans V, Bloomberg JJ, Mulavara AP, et al. **Brain structural plasticity with spaceflight.** *NPJ Microgravity* 2016;2:2 CrossRef Medline
4. Van Ombergen A, Jillings S, Jeurissen B, et al. **Brain tissue-volume changes in cosmonauts.** *N Engl J Med* 2018;379:1678–80 CrossRef Medline
5. Nicogossian AE, Huntoon CL, Pool SL. In: Nicogossian AE, Huntoon CL, Pool SL, eds.. *Space Physiology and Medicine*. 2nd ed. Philadelphia: Lea & Febiger; 1989
6. Mader TH, Gibson CR, Pass AF, et al. **Optic disc edema, globe flattening, choroidal folds, and hyperopic shifts observed in astronauts after long-duration space flight.** *Ophthalmology* 2011;118:2058–69 CrossRef Medline
7. Lee AG, Mader TH, Gibson CR, et al. **Space flight-associated neuro-ocular syndrome (SANS).** *Eye (Lond)* 2018;32;1164–67 CrossRef Medline
8. Kane RL, Short P, Sipes W, et al. **Development and validation of the spaceflight cognitive assessment tool for Windows (WinSCAT).** *Aviat Space Environ Med* 2005;76(6 Suppl):B183–91 Medline
9. Seaton KA, Slack KJ, Sipes WA, et al. **Cognitive functioning in long-duration head-down bed rest.** *Aviat Space Environ Med* 2009;80(5 Suppl);A62–65 CrossRef Medline
10. Mulavara AP, Peters BT, Miller CA, et al. **Physiological and functional alterations after spaceflight and bed rest.** *Med Sci Sports Exerc* 2018;50:1961–80 CrossRef Medline
11. Lee AG, Tarver WJ, Mader TH, et al. **Neuro-ophthalmology of space flight.** *J Neuroophthalmol* 2016;36:85–91 CrossRef Medline

12. Winkler AM, Ridgway GR, Webster MA, et al. **Permutation inference for the general linear model.** *Neuroimage* 2014:92:381–97 CrossRef Medline
13. Cohen J. **A power primer.** Psychological Bulletin [PsycARTICLES] 1992;112:1 http://www.bwgriffin.com/workshop/Sampling%20A%20Cohen%20tables.pdf. Accessed May 22, 2019
14. Benjamini Y, Keiger AM, Yekutieli D. **Adaptive linear step-up procedures that control the false discovery rate.** *Biometrika* 2006;93:491–507 CrossRef
15. Takakusaki K, Oohinata-Sugimoto J, Saitoh K, et al. **Role of basal ganglia-brainstem systems in the control of postural muscle tone and locomotion.** *Prog Brain Res* 2004;143:231–37 CrossRef Medline
16. Takakusaki K, Tomita N, Yano M. **Substrates for normal gait and pathophysiology of gait disturbances with respect to the basal ganglia dysfunction.** *J Neurol* 2008;255(Suppl 4);19–29 CrossRef Medline
17. Villablanca JR. **Why do we have a caudate nucleus?** *Acta Neurobiol Exp (Wars)* 2010;70:95–105 Medline
18. DeVito EE, Salmond CH, Owler BK, et al. **Caudate structural abnormalities in idiopathic normal pressure hydrocephalus.** *Acta Neurol Scand* 2007;116:328–32 CrossRef Medline
19. Townley RA, Botha H, Graff-Radford J, et al. **(18)F-FDG PET-CT pattern in idiopathic normal pressure hydrocephalus.** *Neuroimage Clin* 2018;18:897–902 CrossRef Medline
20. Ziegelitz D, Arvidsson J, Hellström P, et al. **In patients with idiopathic normal pressure hydrocephalus postoperative cerebral perfusion changes measured by dynamic susceptibility contrast magnetic resonance imaging correlate with clinical improvement.** *J Comput Assist Tomogr* 2015;39:531–40 CrossRef Medline
21. Kirenskaya AV, Tomilovskaya ES, Novototskii-Vlasov VY, et al. **The effects of simulated microgravity on characteristics of slow presaccadic potentials [in Russian].** *Fiziol Cheloveka* 2006;32:131–39 Medline
22. Pechenkova E, Nosikova I, Rumshiskaya A, et al. **Alterations of functional brain connectivity after long-duration spaceflight as revealed by fMRI.** *Front Physiol* 2019;10:761 CrossRef Medline
23. Strangman GE, Sipes W, Beven G. **Human cognitive performance in spaceflight and analogue environments.** *Aviat Space Environ Med* 2014;85:1033–48 CrossRef Medline
24. Basner M, Savitt A, Moore TM, et al. **Development and validation of the cognition test battery for spaceflight.** *Aerosp Med Hum Perform* 2015;86:942–52 CrossRef Medline
25. Lee J, De Dios YE, Gadd NE,et al. **The effects of 30 days of bed rest with elevated carbon dioxide on cognitive performance.** In: *Proceedings of the Annual Meeting of the Society for Neuroscience*, San Diego, California**.** November 3–7, 2018
26. Peru A, Beltramello A, Moro V, et al. **Temporary and permanent signs of interhemispheric disconnection after traumatic brain injury.** *Neuropsychologia* 2003;41:634–43 CrossRef Medline
27. Lee JK, Koppelmans V, Riascos RF, et al. **Spaceflight-associated brain white matter microstructural changes and intracranial fluid redistribution.** *JAMA Neurol* 2019;76:412–19 CrossRef Medline
28. Riascos RF, Kamali A, Hakimelahi R, et al. **Longitudinal analysis of quantitative brain MRI in astronauts following microgravity exposure.** *J Neuroimaging* 2019;29:323–30 CrossRef Medline

Middle Cerebral Artery Plaque Hyperintensity on T2-Weighted Vessel Wall Imaging Is Associated with Ischemic Stroke

Y.-N. Yu, M.-W. Liu, J.P. Villablanca, M.-L. Li, Y.-Y. Xu, S. Gao, F. Feng, D.S. Liebeskind, F. Scalzo, and W.-H. Xu

ABSTRACT

BACKGROUND AND PURPOSE: Vessel wall imaging can identify intracranial atherosclerotic plaque and give clues about its components. We aimed to investigate whether the plaque hyperintensity in the middle cerebral artery on T2-weighted vessel wall imaging is associated with ischemic stroke.

MATERIALS AND METHODS: We retrospectively reviewed our institutional vessel wall MR imaging data base. Patients with an acute ischemic stroke within 7-day onset in the MCA territory were enrolled. Patients with stroke and stenotic MCA plaque (stenosis degree, ≥50%) were included for analysis. Ipsilateral MCA plaque was defined as symptomatic, and contralateral plaque, as asymptomatic. Plaque was manually delineated on T2-weighted vessel wall imaging. The plaque signal was normalized to the ipsilateral muscle signal. The thresholds and volume of normalized plaque signal were investigated using logistic regression and receiver operating characteristic analysis to determine the association between normalized plaque signal and stroke.

RESULTS: One hundred eight stenotic MCAs were analyzed (from 88 patients, 66 men; mean age, 58 ± 15 years), including 72 symptomatic and 36 asymptomatic MCA plaques. Symptomatic MCA plaque showed larger plaque hyperintensity volume compared with asymptomatic MCA plaque. The logistic regression model incorporating stenosis degree, remodeling ratio, and normalized plaque signal 1.3–1.4 (OR, 6.25; 95% CI, 1.90–20.57) had a higher area under curve in differentiating symptomatic/asymptomatic MCA plaque, compared with a model with only stenosis degree and remodeling ratio (area under curve, 0.884 versus 0.806; $P = .008$).

CONCLUSIONS: The MCA plaque hyperintensity on T2-weighted vessel wall imaging is independently associated with ischemic stroke and adds value to symptomatic MCA plaque classification. Measuring the normalized signal intensity may serve as a practical and integrative approach to the analysis of intracranial atherosclerotic plaque.

ABBREVIATIONS: AUC = area under curve; NPS = normalized plaque signal; MCA = middle cerebral artery

Intracranial atherosclerotic disease is a common cause of ischemic stroke, especially in Asian populations.[1,2] Atherosclerotic plaque rupture is one of the major mechanisms leading to ischemic events.[3] Plaque components such as a thin fibrous cap, a large lipid core, the presence of neoangiogenesis, intraplaque hemorrhage, and juxtaluminal thrombus are associated with an elevated risk of plaque rupture in extracranial artery atherosclerosis.[3,4] However, the association between intracranial plaque components and the risk of ischemic stroke has not been well-studied.

Recently, the development of vessel wall imaging has provided a repeatable and reliable tool for observing intracranial plaque in vivo,[5] which is demonstrated as an eccentric arterial wall thickening.[6] Although noncontrast and postcontrast T1-weighted vessel wall MR imaging has been used to study intracranial atherosclerotic disease,[7,8] the clinical utility of T2-weighted vessel wall imaging has not been well-established. Thin fibrous cap,[6,9] intraplaque hemorrhage, and juxtaluminal thrombus were associated with hyperintensity of atherosclerotic plaque on T2-weighted imaging,[4,10] while calcification[11,12] and hemosiderin were associated

Received March 23, 2019; accepted after revision August 27.

From the Departments of Neurology (Y.-N.Y., Y.-Y.X., S.G., W.-H.X.) and Radiology (M.-L.L., F.F.), Peking Union Medical College Hospital, Chinese Academy of Medical Sciences, Beijing, China; and Department of Radiology (J.P.V.) and Neurovascular Imaging Research Core and UCLA Stroke Center (M.-W.L., D.S.L., F.S.), Los Angeles, California.

This work was supported by the Ministry of Science and Technology of the People's Republic of China (2017YFC1307900 and 2017YFC1307902), the National Natural Science Foundation of China (81471207 and 81671370), and the 2016 Peking Union Medical College Hospital science fund for junior faculty.

Please address correspondence to Wei-Hai Xu, MD, Departments of Neurology, Peking Union Medical College Hospital, Shuaifuyuan 1, Beijing, China; e-mail: xuwh@pumch.cn

Indicates open access to non-subscribers at www.ajnr.org
Indicates article with supplemental on-line tables.
Indicates article with supplemental on-line photos.

http://dx.doi.org/10.3174/ajnr.A6260

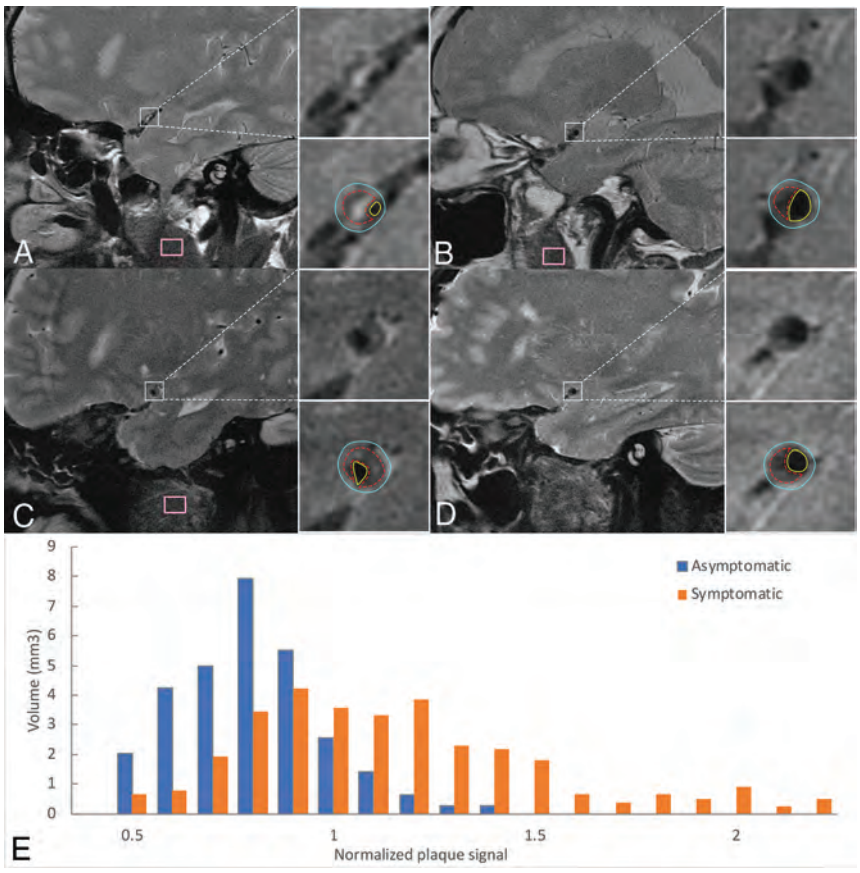

FIG 1. Example of plaque from 4 patients with symptomatic MCA plaque (*A* and *C*) and asymptomatic MCA plaque (*B* and *D*) and a histogram of 2 individual plaques (*E*). *A* and *B*, Scanned with a non-fat-suppressed T2 sequence. *C* and *D*, Scanned with a fat-suppressed T2 sequence. *A* and *B*, Plaque has a similar total volume but different signal features. *E*, *Orange bars* represents the signal distribution of *A*, which has more hyperintense signals seen as larger volume within high normalized plaque signal; *blue bars* represent the signal distribution of *B*, which has fewer hyperintense signals seen as larger volume within low normalized plaque signal. The plaque area (*red dotted contour lines*), vessel outer wall area (*blue contour lines*), and luminal area (*yellow contour lines*) are manually delineated on every cross-section containing plaque. Facial muscle signals are sampled by the *pink box*. The muscle signal of *D* was sampled in adjacent slices. Note the consistent image quality.

with hypointensity on T2-weighted imaging. The purpose of the study was to investigate whether symptomatic middle cerebral artery (MCA) plaque is associated with a characteristic signal distribution on T2-weighted imaging.

MATERIALS AND METHODS

Patients

We retrospectively reviewed our vessel wall MR imaging data base starting from January 2007 to December 2016. Patients with acute stroke (within 7-day onset) in the MCA territory with confirmed infarct lesions on DWI were included in this study. Patients were excluded if they had evidence of the following: 1) cardioembolism, such as a history of atrial fibrillation or recent myocardial infarction within 1 month, atrial fibrillation identified by electrocardiography or Holter monitor, or left atrial/ventricular thrombus identified by echocardiography; 2) extracranial atherosclerosis with stenosis degree of >50%; and 3) nonatherosclerotic vasculopathy such as Moyamoya disease, vasculitis, and arterial dissection. Symptomatic MCA plaque was defined as MCA plaque ipsilateral to the infarct lesions with stenosis degree exceeding 50%, mea-sured on vessel wall MR imaging (see Imaging Analysis). Asymptomatic MCA plaque was defined as present if the MCA was contralateral to the infarct lesions with stenosis exceeding 50% and no history of ischemic stroke or transient ischemic attack in that territory. Occluded MCAs and motion- or artifact-degraded studies were excluded. The study protocol was approved by the ethics committee of the Peking Union Medical College Hospital. All patients or their families gave written consent before participation.

Imaging Protocol

MR imaging was performed on 3T systems (Signa VH/I; GE Healthcare, Milwaukee, Wisconsin) from January 2007 to June 2013 and Discovery MR750 (GE Healthcare) from June 2013 to November 2016, equipped with an 8-channel head coil. The protocol included conventional 3D TOF-MRA, DWI, and a fat-suppressed (June 2013 to November 2016) or non-fat-suppressed (January 2007 to June 2013) sequence of the MCA. Vessel wall imaging was performed perpendicular to the MCA M1 segment after TOF-MRA. A non-fat-suppressed T2-weighted fast spin-echo sequence was obtained using the following parameters: TR/TE, 3200/45 ms; FOV, 13 × 13 cm; matrix size, 256 × 256; section thickness, 2 mm; 4 signal averages; pixel band width, 97.6. The total scan time was 3 minutes 20 seconds. A fat-suppressed T2-weighted fast spin-echo sequence was performed with the following parameters: TR/TE, 4200/60 ms; FOV, 13 × 13 cm; matrix size, 256 × 256; section thickness, 2 mm; 4 signal averages; pixel band width, 162.7. Total scan time was 3 minutes 20 seconds, and total study protocol time was approximately 10 minutes. The parameters of the other imaging series were described in our previous studies.[7,13]

Imaging Analysis

Image quality was graded as poor if the MCA lumen was poorly visible with moderate-to-substantial blurring or artifacts and good if the MCA lumen was clearly identified with minimal or no blurring or artifacts.[14] Only patients with good image quality were included in the analysis (Fig 1).

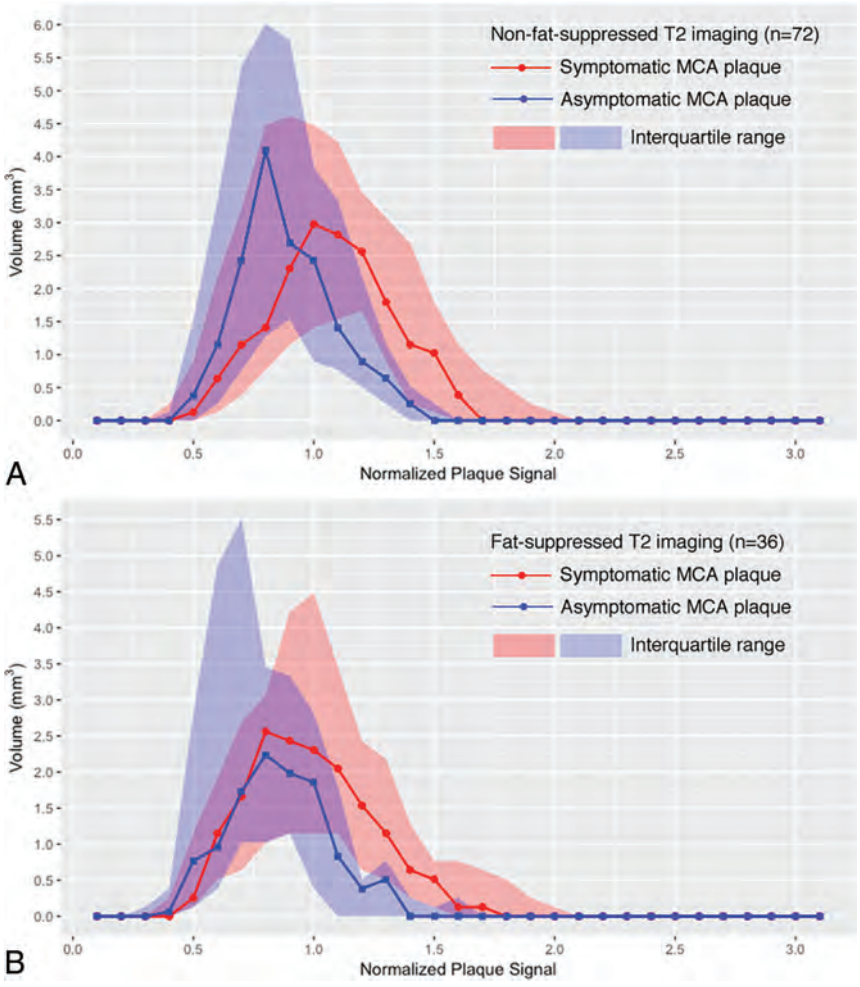

FIG 2. The summary of the median volume of normalized plaque signal in non-fat-suppressed and fat-suppressed T2 imaging. *A*, The median volume of symptomatic and asymptomatic MCA plaque in patients with non-fat-suppressed T2-weighted imaging. The difference between the 2 groups becomes more significant when normalized plaque signal is high. *B*, The median volume of symptomatic and asymptomatic MCA plaque in patients with fat-suppressed T2-weighted imaging. The difference between the 2 groups also becomes more significant when normalized plaque signal is high.

Atherosclerotic plaque was defined as eccentric vessel wall thickening in which the thickest wall was twice the size of the thinnest wall by visual inspection[15] on T2-weighted images. The region of plaque in an MCA M1 segment was manually delineated along all involved cross-sectional images using ROI tools in Osirix MD (https://download.cnet.com/OsiriX-MD/3000-2054_4-75705449.html) by a neurologist with 5-years' experience (Y.-N.Y.) blinded to all clinical information (Fig 1). For evaluation of interobserver and intraobserver agreement of area and volume, J.P.V. (with 10-years' experience) and Y.-N.Y., respectively, repeated the identification of the target ROIs and confirmed the plaque contours of each ROI in 18 randomly selected MCA segments. Consensus interpretations were used in case of disagreements. The interobserver and intraobserver agreement of luminal area and outer wall area measurements was also performed using the intraclass correlation coefficient.

To convert MR imaging signals to a comparable value among subjects, we used muscle signal as the reference to normalize the plaque signal.[7] Instead of using 1 summarized value such as mean, we used a histogram that contains the normalized plaque signal (NPS) of each pixel within the ROIs to represent the detailed signal distribution of MCA plaque. The plaque hyperintensity was quantitatively eva-luated as the volume of tissue within a certain NPS threshold. The NPS was defined as the ratio of the signal of each pixel in MCA plaque to the mean muscle signal. The mean muscle signal is calculated from the reference ROI delineated in the masseter or buccinator muscle in the same section containing the plaque or the section adjacent to the plaque (Fig 1). We chose those large facial muscles because larger ROIs can obtain an unbiased mean value of the muscle signal and the signal is not affected by any intracranial lesions. An automated tool programmed using Python (Version 2.7; https://www.python.org/download/releases/2.7/) extracted the pixels inside the plaque and calculated NPS according to the manually delineated ROIs.

Stenosis degree and remodeling ratio have both been reported to be important characteristics of symptomatic plaque.[16] Therefore, they were also measured in this study to adjust the logistic regression models. The luminal and outer wall areas were manually measured on the maximal lumen narrowing section of the M1 segment. Reference slices were defined as the plaque-free section that was proximal and distal to the maximal narrowing section (the averaged area was calculated); when plaque involved the entire M1 segment, the plaque-free counterpart of the contralateral artery was used as the reference section:[17] Stenosis Degree = 100% × (1 – Luminal Area at the Maximal Lumen Narrowing Site/Reference Luminal Area); Remodeling Ratio = Outer Wall Area at the Maximal Lumen Narrowing Site/Reference Outer Wall Area.[17,18]

Statistical Analysis

Statistical analysis was performed using STATA 14.0 (StataCorp, College Station, Texas) and R 3.4.0 statistical and computing software (http://www.r-project.org). Patients with and without fat-suppression imaging were analyzed separately. According to the data distribution shown in Fig 2, thresholds of the NPS were

Table 1: Volume of NPS threshold, stenosis degree, and remodeling ratio in non-fat-suppressed imaging[a]

Non-Fat-Suppressed T2-Weighted Vessel Wall MR Imaging	Symptomatic MCA Plaque ($n = 47$)	Asymptomatic MCA Plaque ($n = 26$)	AUC
Stenosis degree (%)	72 ± 14	62 ± 12	0.692
Remodeling ratio	1.10 ± 0.20	1.03 ± 0.18	0.608
Volume of each NPS threshold, mm^3			
0.4∼0.5	0.1 (0–0.9)	0.4 (0–1.5)	0.408
0.5∼0.6	0.6 (0.1–2.2)	1.3 (0.3–3.3)	0.394
0.6∼0.7	1.2 (0.4–3.2)	2.5 (0.8–5.0)	0.415
0.7∼0.8	1.4 (0.9–4.2)	3.4 (1.3–6)	0.398
0.8∼0.9	2.4 (1.2–4.6)	2.4 (1.5–5.5)	0.482
0.9∼1.0	3.1 (1.4–4.6)	2.2 (0.8–3.3)	0.592
1.0∼1.1	2.8 (1.5–4.2)	1.9 (0.8–3.3)	0.615
1.1∼1.2	2.6 (1.7–3.8)	0.8 (0.5–2.2)	0.740
1.2∼1.3	1.9 (0.9–3.2)	0.5 (0.1–1.2)	0.797
1.3∼1.4	1.2 (0.3–2.8)	0.1 (0–0.5)	0.837
1.4∼1.5	1.2 (0.1–1.9)	0 (0–0.3)	0.798
1.5∼1.6	0.5 (0–1.2)	0 (0–0)	0.764
1.6∼1.7	0.1 (0–0.9)	0 (0–0)	0.731
1.7∼1.8	0 (0–0.6)	0 (0–0)	0.667
≥0.9	15.1 (9.2–22.7)	7.0 (2.9–12.3)	0.760
≥1.0	11.1 (6.3–18.8)	3.8 (1.5–8.2)	0.772
≥1.1	8.8 (3.8–14.0)	2.2 (0.6–4.6)	0.795
≥1.2	6.8 (1.5–10.8)	0.8 (0.1–2.2)	0.795
≥1.3	4.0 (0.5–7.8)	0.3 (0–0.9)	0.815
≥1.4	1.9 (0.1–5.2)	0 (0–0.4)	0.795
≥1.5	0.6 (0–3.2)	0 (0–0)	0.772

[a] Data are mean ± SD or median (interquartile range).

investigated with an increment of 0.1. Receiver operating characteristic analysis and logistic regression analysis were used to determine the diagnostic value of plaque hyperintensity (the volume of a given NPS threshold) associated with symptomatic MCA plaque after being adjusted for stenosis degree and remodeling ratio and whether fat suppressed imaging was used for analysis. The optimal NPS thresholds for patients with and without fat-suppression were then determined by selecting the largest average area under curve (AUC). Patients with bilateral MCAs included in this study were studied as a subgroup using paired-samples Wilcoxon test analysis to test whether the plaque hyperintensity was associated with symptomatic MCA plaque within a single individual. $P < .01$ was considered statistically significant after adjustment by the Benjamini-Hochberg method. All the statistical tests were 2-sided.

RESULTS

In total, 150 patients were enrolled. Of their 300 MCAs, 192 MCAs were excluded due to occlusion ($n = 17$), poor image quality or unavailability of vessel wall MR imaging ($n = 33$), and stenosis degree of <50% ($n = 142$), leaving a total of 72 symptomatic MCA plaques and 36 asymptomatic MCA plaques from 88 patients for analysis (20 patients had bilateral MCA plaques but only unilateral stroke). Thirty-five MCAs from 30 patients had fat-suppressed T2-weighted vessel wall imaging, and 73 MCAs from 58 patients underwent non-fat-suppressed T2-weighted vessel wall imaging. Of the 88 patients, 66 (75.0%) were men, and the mean age was 58 ± 15 years. Fifty-five patients (65%) had a history of hypertension, 22 (26%) had diabetes mellitus, 36 (43%) had dyslipidemia, and 9 (11%) had coronary artery disease.

Intraobserver agreement for plaque ROI analysis was 94%. The 6% discordance was for slices that were at the very edge (the beginning or ending) of a plaque and contained plaque that was thin and not T2-weighted hyperintense. In the 94% of concordant slices, agreement of visual plaque spatial location and contour reached 100%. The intraclass correlation coefficient for ROI volume reached 0.965 (95% CI, 0.905–0.987). For interobserver agreement, 95% of slices of the first reading were confirmed as containing plaque by a second reader, with agreement of plaque spatial location and contour reaching 100%. The intra- and interobserver agreement for luminal area measurement was 0.78 (95% CI, 0.54–0.91) and 0.78 (95% CI, 0.53–0.90); for outer wall area measurement, it was 0.92 (95% CI, 0.80–0.97) and 0.84 (95% CI, 0.65–0.93).

The average volume of symptomatic MCA plaque was 26.1 ± 16.0 mm^3, and 20.0 ± 13.3 mm^3 for asymptomatic MCA plaque. There was no statistical difference in plaque hyperintensity between non-fat-suppressed and fat-suppressed T2-weighted imaging.

Symptomatic MCA plaque demonstrated larger hyperintensity areas (volume of high NPS thresholds) than asymptomatic MCA plaque in both fat-suppressed and non-fat-suppressed T2-weighted imaging (Fig 2). For non-fat-suppressed T2-weighted imaging, the volume of areas with NPS 1.3–1.4 and no less than 1.3 had the highest AUCs in differentiating symptomatic and asymptomatic MCA plaque (Table 1). For fat-suppressed T2-weighted imaging, NPS 1.3–1.4 and not less than 1.0 had the highest AUCs (Table 2). The thresholds to differentiate symptomatic and asymptomatic MCA plaque were similar in both imaging sequences.

T2-weighted hyperintensity was independently associated with symptomatic MCA plaque, adjusted by stenosis degree and remodeling ratio in non-fat-suppressed imaging (On-line Table 1). Logistic regression was not performed separately within fat-suppressed data due to its small sample size. The NPS thresholds were similar in the separate analysis of fat-suppressed and non-fat-suppressed imaging. There was no interaction of fat-suppressed/non-fat-suppressed imaging on the association of plaque hyperintensity and symptomatic MCA plaque. Therefore, logistic regression models were also performed using the combined dataset. Two logistic regression models incorporating NPS thresholds, stenosis degree, and remodeling ratio with the highest AUCs among all the thresholds and one model incorporating only the stenosis degree and remodeling ratio were compared in Table 3 (see On-line Table 2 and On-line Fig 1 for all tested thresholds). NPS 1.3–1.4 (OR, 6.25 per 1-mm^3 increase; 95% CI, 1.90–20.57) was independently associated with symptomatic MCA plaque

Table 2: Volume of NPS threshold, stenosis degree, and remodeling ratio in fat-suppressed imaging[a]

Fat-Suppressed T2-Weighted Vessel Wall MR Imaging	Symptomatic MCA Plaque (n = 25)	Asymptomatic MCA Plaque (n = 10)	AUC
Stenosis degree (%)	66 ± 13	56 ± 4	0.768
Remodeling ratio	1.16 ± 0.27	0.93 ± 0.09	0.800
Volume of each NPS threshold (mm^3)			
0.4∼0.5	0.3 (0.1–1.2)	0.8 (0.1–2.8)	0.412
0.5∼0.6	1.2 (0.5–1.9)	1.0 (0.4–4.9)	0.466
0.6∼0.7	1.7 (0.6–2.7)	1.7 (1.0–5.5)	0.426
0.7∼0.8	2.6 (1–3.1)	2.2 (1.0–3.5)	0.508
0.8∼0.9	2.4 (1.2–4.2)	2.0 (1.2–3.3)	0.578
0.9∼1.0	2.3 (1.2–4.5)	1.9 (0.4–2.8)	0.656
1.0∼1.1	2.0 (1.2–3.5)	0.8 (0–1.8)	0.748
1.1∼1.2	1.5 (0.6–2.4)	0.4 (0–0.5)	0.738
1.2∼1.3	1.2 (0.5–2.2)	0.5 (0–0.8)	0.750
1.3∼1.4	0.6 (0.3–1.3)	0 (0–0.3)	0.774
1.4∼1.5	0.5 (0.1–0.8)	0 (0–0.1)	0.752
1.5∼1.6	0.1 (0–0.8)	0 (0–0.3)	0.616
1.6∼1.7	0.1 (0–0.6)	0 (0–0)	0.676
1.7∼1.8	0 (0–0.5)	0 (0–0)	0.680
≥0.9	10.0 (4.9–15.1)	3.1 (1.4–5.9)	0.764
≥1.0	7.7 (3.6–12.2)	1.8 (0.3–3.6)	0.794
≥1.1	3.8 (2.6–8.7)	1.2 (0–1.8)	0.770
≥1.2	2.3 (1.3–6.3)	0.9 (0–1.4)	0.772
≥1.3	1.4 (0.4–4.5)	0.3 (0–0.6)	0.764
≥1.4	0.8 (0.1–3.2)	0 (0–0.4)	0.746
≥1.5	0.3 (0–2.8)	0 (0–0.3)	0.650

[a] Data are mean ± SD or median (interquartile range).

Table 3: The logistic regression models of optimal NPS thresholds

Factors Included in Logistic Regression Model	OR (95% CI)	AUC (95% CI)
Model 1		
Volume of NPS 1.3–1.4, per 1-mm^3 increase	6.25 (1.90–20.57)	0.884 (0.822–0.945)
Stenosis degree, per 10% increase	1.99 (1.24–3.19)	
Remodeling ratio, per 0.1 increase	1.50 (1.08–2.10)	
Fat-suppressed imaging	2.88 (0.93–8.94)	
Model 2		
Volumetric summation of NPS no less than 1.2, per 1-mm^3 increase	1.30 (1.06–1.58)	0.863 (0.791–0.935)
Stenosis degree, per 10% increase	1.98 (1.26–3.10)	
Remodeling ratio, per 0.1 increase	1.45 (1.05–2.00)	
Fat-suppressed imaging	2.63 (0.89–7.81)	
Model 3[a]		
Stenosis degree, per 10% increase	2.43 (1.61–3.67)	0.806 (0.725–0.887)
Remodeling ratio, per 0.1 increase	1.51 (1.11–2.06)	
Fat-suppressed imaging	2.03 (0.73–5.69)	

[a] The AUC of model 3 is significantly lower than those of model 1 (P = .008) and model 2 (P = .027).

after adjusting for stenosis degree and remodeling ratio, and it had the highest AUC of 0.884 (95% CI, 0.822–0.945) among all models. NPS no less than 1.2 also demonstrated considerable diagnostic value with a model AUC of 0.863 (95% CI, 0.791–0.935). However, a logistic regression model with only stenosis degree and remodeling ratio yielded the AUC of 0.806 (95% CI, 0.725–0.887), which was lower than that in the best model (P = .008). The optimal cutoff for NPS no less than 1.2 was 3.2 mm^3, with a sensitivity of 61% and specificity of 94%.

In subgroup analysis of 20 patients with bilateral MCA plaque but only unilateral symptoms, the paired-samples Wilcoxon test showed that symptomatic MCA plaque had a larger volume of hyperintensity (NPS = 1.3–1.4) than asymptomatic MCA plaque, 1.7 (interquartile range, 0.4–3.1 mm^3) versus 0.3 (interquartile range, 0.0–0.5 mm^3) P = .0007; see On-line Fig 2 for the paired plot).

DISCUSSION

It is a critical-but-challenging task to identify the vulnerability of intracranial plaque. Fat-suppressed T1-weighted sequences with and without gadolinium are currently the most commonly used imaging sequences for evaluating intracranial plaque vulnerability. The plaque hyperintensity on the nonenhanced T1-weighted sequence is associated with intraplaque hemorrhage,[7,19] while hypointensity is associated with lipid core.[8] Gadolinium enhancement within intracranial plaque demonstrated a strong association with ischemic stroke.[20] However, the association between ischemic stroke and T2-weighted plaque signal was not well-studied.

The primary finding of this study was that MCA plaque hyperintensity on T2-weighted images with >50% stenosis was associated with symptomatic MCA plaque. We also generated optimal thresholds for identifying the plaque hyperintensity, which could be a reference for future research. The NPS of 1.3–1.4 provided the highest diagnostic value for symptomatic MCA plaque. The NPS of ≥1.2 also provided a clinically practical threshold for evaluating MCA plaque. In addition, the models with NPS performed better than the model with stenosis degree and remodeling ratio only, which are known factors associated with symptomatic plaque.[16]

There are several components in plaque that may produce a T2 hyperintense signal. These include the fibrous cap, collagen-rich plaque content, and hemorrhage. The fibrous cap of vulnerable plaque and collagen-rich content may demonstrate hyperintensity[12,21,22] or sometimes isointensity[11] on T2-weighted imaging. Intraplaque hemorrhage and juxtaluminal thrombus are also distinguishing features of vulnerable plaque[4,7,10,23] and may appear hyperintense on T2-weighted sequences if the blood products are in the extracellular methemoglobin state. Hyperacute (<12 hours, oxyhemoglobin) and late subacute (1 week to 2 months, extracellular methemoglobin) hemorrhage both demonstrate hyperintensity on T2-weighted imaging. Because the time window for hyperacute hemorrhage is too short to capture, most of the hemorrhage identified as T2-weighted hyperintensity is generally in the late subacute phase.

Our previous study found that intraplaque hemorrhage occurs in about 20% of symptomatic MCA stenoses and 3% of asymptomatic MCA stenoses,[7] which may contribute to the larger volume of hyperintensity in symptomatic MCA plaque. The variable T2 signal and heterogeneous distribution of specific commonly encountered plaque elements emphasize the challenge of attempting to parse individual plaque elements on a pixel-by-pixel basis and suggest that an integrative signal-intensity-based approach to plaque composition may be clinically useful.

Lipid core is an important element of progressive and vulnerable plaque,[5,24] which may influence plaque intensity in T2-weighted images. Although lipid may present as hyperintensity in non-fat-suppressed T2 imaging, the lipid in atherosclerotic plaque mainly consists of liquid cholesteryl esters, which produce hypointensity in non-fat-suppressed T2-weighted images,[25-27] while another form of lipid, cholesterol crystals, causes signal voids on T2-weighted images.[28] Previous studies were inconsistent in reporting the signal features of lipid in atherosclerotic plaque, partly due to inconsistent imaging sequences across the studies and the plaque heterogeneity.[27,29-31] This phenomenon mitigates potential differences between fat-suppressed and non-fat-suppressed T2-weighted imaging and justifies our combined modeling approach. A source of spurious T2 hyperintensity may occur with chemical shift artifacts. However, this was not observed in our image datasets.

The intraplaque T2 hyperintensity we observed may reflect primarily the overall load of intraplaque hemorrhage and juxtaluminal thrombus. These components have been associated with plaque vulnerability.[4,7] The optimal cutoff points of NPS in our study had a relatively low sensitivity (61%) but a high specificity (94%). Possible false-negative cases could have been caused by the following: 1) plaque component heterogeneity, in which the T2 signal may have been averaged or washed out if various plaque components existed in a microdistribution rather than as pure pools of specific components; and 2) intraplaque hemorrhage and lipid cores that are isointense or hypointense on T2-weighted imaging.

Nevertheless, our results suggest that by using signal intensity–based thresholding on T2-weighted vessel wall imaging in conjunction with stenosis degree and remodeling ratio, one may be able to classify symptomatic MCA plaque with a high level of specificity. That the results obtained from the subgroup of 20 patients with bilateral MCA plaque but unilateral symptoms were comparable with the conclusions derived from the entire dataset suggests that bilateral disease also comports to our identified NPS thresholds.

Symptomatic intracranial atherosclerotic stenosis has a higher risk for stroke recurrence compared with asymptomatic stenosis.[32,33] It is particularly challenging but important in clinical practice to predict the prognosis of an intracranial atherosclerotic disease lesion before symptoms occur. An increasing number of high-risk patients are incidentally discovered to have intracranial artery stenosis before an ischemic stroke or transient ischemic attack occurs, enabling researchers to study those lesions. Previous work suggested that stenosis degree,[34] remodeling ratio,[16,34] plaque size,[16,18,35] plaque surface irregularity,[34] MCA geometric features,[18] and hyperintensity on noncontrast or postcontrast T1-weighted sequences are indicators of vulnerable plaque.[6,7,20,36] Our results suggest that plaque hyperintensity on T2-weighted sequences, in addition to the stenosis degree and remodeling ratio, improves the classification of symptomatic MCA plaque. Further studies with larger sample sizes are required to validate our results and to determine whether intraplaque T2 hyperintensity is a marker comparable with other more commonly used plaque features such as T1-weighted hyperintensity and postcontrast enhancement.

Our study has several limitations. This was a retrospective study, and our conclusions establish associations and not a causal or predictive relationship. The study had a small sample size, and the case number with fat-suppressed imaging was limited, reducing the power of our conclusions. Although we did not use a 3D black-blood sequence and the sensitivity to detect small plaque is therefore limited, the 2D fast spin-echo sequence has blood signal suppressed and can identify most plaque clearly. We did not have patients who underwent both fat-suppressed and non-fat-suppressed imaging at the same time, limiting our ability to determine the signal change due to the fat suppression. However, this limitation is mitigated by the fact that lipid is mostly T2-weighted hypointense even in non-fat-suppressed imaging, and we found no difference between the 2 sequences. It may be interesting to further investigate whether fat-suppressed imaging adds any value in differentiating symptomatic and asymptomatic plaque. Because no histopathologic analysis was performed, we are unable to determine what proportion of our T2 signal was due to specific plaque components. Multicontrast MRIs such as susceptibility-weighted imaging[37] and T1-weighted imaging[7,8] may help differentiate the plaque components. However, this was not our objective, and we note that our integrative method simplifies the analysis of plaque vulnerability. In the future, we propose to use a multiple-parametric approach, including T1-weighted imaging in a similar patient population in an effort to increase the sensitivity of our approach while maintaining specificity. Finally, the results may not be generalizable to asymptomatic patients because only patients with acute stroke were analyzed in this study. It could be meaningful to design a prospective study including both symptomatic and asymptomatic patients to facilitate this comparison.

CONCLUSIONS

Plaque hyperintensity on fat-suppressed and non-fat-suppressed T2-weighted vessel wall imaging may be a potential imaging marker for identifying symptomatic MCA plaque. The plaque hyperintensity added diagnostic value to the symptomatic MCA plaque classification compared with a model that contains only stenosis degree and remodeling ratio. Therefore, the T2 plaque hyperintensity and its thresholds could provide a clinically practical evaluation method for MCA plaque.

Disclosures: Yunnan Yu—*UNRELATED*: *Employment*: Stanford University, *Comments*: currently a postdoctoral student at Stanford; submitted work was completed at the University of California, Los Angeles; *Travel/Accommodations/Meeting Expenses Unrelated to Activities Listed*: travel expense reimbursement from the radiology department at Stanford. Feng Feng—*UNRELATED*: *Board Membership*: *Journal of Magnetic Resonance Imaging* editorial board member, deputy editor stipend; *Consultancy*: GE Healthcare Medical Advisory Board for MRI 2017; *Grants/Grants Pending*: National Natural Sciences Foundation*; *Payment for Lectures Including Service on Speakers Bureaus*: GE Healthcare, Bracco; *Travel/Accommodations/Meeting Expenses Unrelated to Activities Listed*: Chinese Medical Foundation to attend academic conferences,* David S. Liebeskind—*UNRELATED*: *Consultancy*:

Cerenovus, Stryker, Medtronic, *Comments*: Consultant for Imaging Core Lab. Wei-Hai Xu—*RELATED*: *Grant*: National Natural Science Foundation of China (81471207 and 81671370)*; *UNRELATED*: *Employment*: Peking Union Medical College Hospital; *Travel/Accommodations/Meeting Expenses Unrelated to Activities Listed*: travel expense reimbursement from the hospital. *Money paid to the institution.

ACKNOWLEDGMENT

We appreciate the statistical consultation provided by Nicholas J. Jackson, PhD, MPH, Department of Medicine Statistics Core, University of California, Los Angeles.

REFERENCES

1. Gorelick PB, Wong KS, Bae HJ, et al. **Large artery intracranial occlusive disease: a large worldwide burden but a relatively neglected frontier.** *Stroke* 2008;39:2396–99 CrossRef Medline
2. Wang YJ, Zhao XQ, Liu LP, et al. **Prevalence and outcomes of symptomatic intracranial large artery stenoses and occlusions in China: the Chinese Intracranial Atherosclerosis (CICAS) study.** *Stroke* 2014;45:663–69 CrossRef Medline
3. Bentzon JF, Otsuka F, Virmani R, et al. **Mechanisms of plaque formation and rupture.** *Circ Res* 2014;114:1852–66 CrossRef Medline
4. Chu B, Ferguson MS, Underhill H, et al. **Images in cardiovascular medicine: detection of carotid atherosclerotic plaque ulceration, calcification, and thrombosis by multicontrast weighted magnetic resonance imaging.** *Circulation* 2005;112:e3–e4 CrossRef Medline
5. Yang WJ, Wong KS, Chen XY. **Intracranial atherosclerosis: from microscopy to high-resolution magnetic resonance imaging.** *J Stroke* 2017;19:249–60 CrossRef Medline
6. Mandell DM, Mossa-Basha M, Qiao Y, et al. **Intracranial Vessel Wall MRI: Principles and Expert Consensus Recommendations of the American Society of Neuroradiology.** *AJNR Am J Neuroradiol* 2017;38:218–29 CrossRef Medline
7. Xu WH, Li ML, Gao S, et al. **Middle cerebral artery intraplaque hemorrhage: prevalence and clinical relevance.** *Ann Neurol* 2012; 71:195–98 CrossRef Medline
8. Yang WJ, Chen XY, Zhao HL, et al. **Postmortem study of validation of low signal on fat-suppressed T1-weighted magnetic resonance imaging as marker of lipid core in middle cerebral artery atherosclerosis.** *Stroke* 2016;47:2299–2304 CrossRef Medline
9. Holmstedt CA, Turan TN, Chimowitz MI. **Atherosclerotic intracranial arterial stenosis: risk factors, diagnosis, and treatment.** *Lancet Neurol* 2013;12:1106–14 CrossRef Medline
10. Kampschulte A, Ferguson MS, Kerwin WS, et al. **Differentiation of intraplaque versus juxtaluminal hemorrhage/thrombus in advanced human carotid atherosclerotic lesions by in vivo magnetic resonance imaging.** *Circulation* 2004;110:3239–44 CrossRef Medline
11. Turan TN, Rumboldt Z, Granholm AC, et al. **Intracranial atherosclerosis: correlation between in-vivo 3T high resolution MRI and pathology.** *Atherosclerosis* 2014;237:460–63 CrossRef Medline
12. Toussaint JF, LaMuraglia GM, Southern JF, et al. **Magnetic resonance images lipid, fibrous, calcified, hemorrhagic, and thrombotic components of human atherosclerosis in vivo.** *Circulation* 1996;94:932–38 CrossRef Medline
13. Li ML, Xu WH, Song L, et al. **Atherosclerosis of middle cerebral artery: evaluation with high-resolution MR imaging at 3T.** *Atherosclerosis* 2009;204:447–52 CrossRef Medline
14. Nael K, Villablanca JP, Pope WB, et al. **Supraaortic arteries: contrast-enhanced MR angiography at 3.0 T–highly accelerated parallel acquisition for improved spatial resolution over an extended field of view.** *Radiology* 2007;242:600–09 CrossRef Medline
15. Xu WH, Li ML, Gao S, et al. **Plaque distribution of stenotic middle cerebral artery and its clinical relevance.** *Stroke* 2011;42:2957–59 CrossRef Medline
16. Xu WH, Li ML, Gao S, et al. **In vivo high-resolution MR imaging of symptomatic and asymptomatic middle cerebral artery atherosclerotic stenosis.** *Atherosclerosis* 2010;212:507–11 CrossRef Medline
17. Xu YY, Li ML, Gao S, et al. **Non-moyamoya vessel network formation along steno-occlusive middle cerebral artery.** *Neurology* 2016; 86:1957–63 CrossRef Medline
18. Yu YN, Li ML, Xu YY, et al. **Middle cerebral artery geometric features are associated with plaque distribution and stroke.** *Neurology* 2018;91:e1760–69 CrossRef Medline
19. Chen XY, Wong KS, Lam WW, et al. **High signal on T1 sequence of magnetic resonance imaging confirmed to be intraplaque haemorrhage by histology in middle cerebral artery.** *Int J Stroke* 2014;9:E19 CrossRef Medline
20. Gupta A, Baradaran H, Al-Dasuqi K, et al. **Gadolinium enhancement in intracranial atherosclerotic plaque and ischemic stroke: a systematic review and meta-analysis.** *J Am Heart Assoc* 2016;5:pii: e003816 CrossRef Medline
21. Chung GH, Kwak HS, Hwang SB, et al. **Magnetic resonance imaging of intracranial atherosclerosis: comparison of ex vivo 3T MRI and histologic findings.** *Eur J Radiol* 2017;97:110–14 CrossRef Medline
22. van der Kolk AG, Zwanenburg JJM, Denswil NP, et al. **Imaging the intracranial atherosclerotic vessel wall using 7T MRI: initial comparison with histopathology.** *AJNR Am J Neuroradiol* 2015;36:694–701 CrossRef Medline
23. Altaf N, MacSweeney ST, Gladman J, et al. **Carotid intraplaque hemorrhage predicts recurrent symptoms in patients with high-grade carotid stenosis.** *Stroke* 2007;38:1633–35 CrossRef Medline
24. Stefanadis C, Antoniou CK, Tsiachris D, et al. **Coronary atherosclerotic vulnerable plaque: current perspectives.** *J Am Heart Assoc* 2017;6:pii:e005543 CrossRef Medline
25. Qiao Y, Ronen I, Viereck J, et al. **Identification of atherosclerotic lipid deposits by diffusion-weighted imaging.** *Arterioscler Thromb Vasc Biol* 2007;27:1440–46 CrossRef Medline
26. Toussaint JF, Southern JF, Fuster V, et al. **T2-weighted contrast for NMR characterization of human atherosclerosis.** *Arterioscler Thromb Vasc Biol* 1995;15:1533–42 CrossRef Medline
27. Jiang YL, Zhu CC, Peng WJ, et al. **Ex-vivo imaging and plaque type classification of intracranial atherosclerotic plaque using high resolution MRI.** *Atherosclerosis* 2016;249:10–16 CrossRef Medline
28. Hallock KJ, Hamilton JA. **Ex vivo identification of atherosclerotic plaque calcification by a 31P solid-state magnetic resonance imaging technique.** *Magn Reson Med* 2006;56:1380–83 CrossRef Medline
29. Yuan C, Mitsumori LM, Ferguson MS, et al. **In vivo accuracy of multispectral magnetic resonance imaging for identifying lipid-rich necrotic cores and intraplaque hemorrhage in advanced human carotid plaques.** *Circulation* 2001;104:2051–56 CrossRef Medline
30. Clarke SE, Hammond RR, Mitchell JR, et al. **Quantitative assessment of carotid plaque composition using multicontrast MRI and registered histology.** *Magn Reson Med* 2003;50:1199–1208 CrossRef Medline
31. Harteveld AA, Denswil NP, Siero JCW, et al. **Quantitative intracranial atherosclerotic plaque characterization at 7T MRI: an ex vivo study with histologic validation.** *AJNR Am J Neuroradiol* 2016; 37:802–10 CrossRef Medline
32. Kern R, Steinke W, Daffertshofer M, et al. **Stroke recurrences in patients with symptomatic vs asymptomatic middle cerebral artery disease.** *Neurology* 2005;65:859–64 CrossRef Medline
33. Kang BS, Kwon HM, Ryu WS, et al. **Prognosis of symptomatic and asymptomatic middle cerebral artery occlusion.** *Cerebrovasc Dis* 2008;26:489–93 CrossRef Medline
34. Chung GH, Kwak HS, Hwang SB, et al. **High resolution MR imaging in patients with symptomatic middle cerebral artery stenosis.** *Eur J Radiol* 2012;81:4069–74 CrossRef Medline
35. Ryu CW, Jahng GH, Kim EJ, et al. **High resolution wall and lumen MRI of the middle cerebral arteries at 3 Tesla.** *Cerebrovasc Dis* 2009;27:433–42 CrossRef Medline
36. Yang WQ, Huang B, Liu XT, et al. **Reproducibility of high-resolution MRI for the middle cerebral artery plaque at 3 T.** *Eur J Radiol* 2014;83:E49–55 CrossRef Medline
37. Yang Q, Liu J, Barnes SR, et al. **Imaging the vessel wall in major peripheral arteries using susceptibility-weighted imaging.** *J Magn Reson Imaging* 2009;30:357–65 CrossRef Medline

Time to Discontinue Use of the Term "Hemorrhagic Stroke"

M. Aftab and M. Salman

Medicine advances with time, and so does our understanding of disease processes and therapy. Stroke has been the subject of intense research and study during the past few decades and tremendous advances have been made. These include a better understanding of the mechanism of stroke and the advent of endovascular clot-retrieval therapy. The literature backing these therapies has been quite impressive, and the recent trials have changed the current treatment guidelines. On the basis of clinical presentation, NIHSS, modified Rankin Scale score, and advanced imaging, patients may be eligible for thrombectomy up to 24 hours after the onset of symptoms.

One of the effects of our study of stroke has been a better understanding of what we mean by the term "stroke." In the past, a stroke had been defined as an acute neurologic deficit. Two primary processes had been identified as etiologies of such deficits: hemorrhagic and ischemic events. Thus, the terminology of hemorrhagic or ischemic stroke entered the medical lexicon. Today, however, the word "stroke" is much more closely aligned with the term "ischemia" than anything else. Stroke in the emergency setting is now understood to be an acute ischemic event.

Ischemic events are caused by hypoperfusion to a brain region, either secondary to vascular occlusion or hypoxia. In the setting of contemporary stroke research and therapy, a vascular occlusion is the most common and important etiology. In fact, identifying the location of the vascular occlusion becomes a critical diagnostic question in triaging these patients for appropriate stroke therapy in the emergency setting.

In this setting, using the term "hemorrhagic stroke" is ambiguous. Neither does it refer to any specific etiology of stroke, nor does it define any particular manifestation of stroke. Intracranial hemorrhages do exist and can be caused by a number of different factors. Neuroradiologists have long recognized this. A recent systematic review of literature presented at the American Society of Neuroradiology found that the term "hemorrhagic stroke" is almost never used in the neuroradiologic literature.[1]

On the contrary, the term is often used in the neurology literature and is still taught in medical school curriculum, influencing the lexicon of emergency medicine trainees. The problem with the term "hemorrhagic stroke" is that it is both scientifically inaccurate and creates unnecessary confusion in the emergent setting in which critical decisions regarding stroke care need to be made.

It is not uncommon for the radiologist to be asked, "Is the stroke ischemic or hemorrhagic?" The latter carries almost no meaning for the radiologist. There are a number of reasons (tumor, trauma, hypertension, and so forth) and several different manifestations (subarachnoid, intraparenchymal, intraventricular, extra-axial, and so forth) of intracranial hemorrhage, and most have nothing to do with stroke as we understand it. Although it is true that an area of brain ischemia can bleed (ie, hemorrhagic transformation of stroke), this is a complication of stroke, not an etiology.

In some cases, an emergent endovascular intervention may be required for intracranial hemorrhage, such as aneurysmal subarachnoid hemorrhage. Despite the similarity in treatment, hemorrhage should not be conflated with ischemia. The disease processes, including the mechanism of disease and specifics of therapy, are distinctly different.

It is time, therefore, to do away with this unnecessary and superfluous term of "hemorrhagic stroke." The new guidelines from the American Heart Association/American Stroke Association have made progress toward this goal. The term has been removed and replaced with more descriptive definitions of stroke.[2] It does not, however, go far enough. Given our current state of understanding of the mechanism of stroke, and perhaps, more important, the development of emergent thrombectomy, it is time to adopt simple and clear language to communicate the disease process. In the emergent setting, our understanding of stroke is brain ischemia, which is most commonly caused by a vascular occlusion. Intracranial hemorrhages are not "strokes." Therefore, it is time to permanently do away with the outdated term of "hemorrhagic stroke."

http://dx.doi.org/10.3174/ajnr.A6240

REFERENCES

1. Salman M, Iordanou J, Aftab M. ***Usage of the term "hemorrhagic stroke" in neuroradiology and neurology literature: a systematic review.*** In: *Proceedings of the Annual Meeting of the American Society of Neuroradiology*, Boston, Massachusetts. May 18–23, 2019
2. Sacco RL, Kasner SE, Broderick JP, et al; American Heart Association Stroke Council, Council on Cardiovascular Surgery and Anesthesia; Council on Cardiovascular Radiology and Intervention; Council on Cardiovascular and Stroke Nursing; Council on Epidemiology and Prevention; Council on Peripheral Vascular Disease; Council on Nutrition, Physical Activity and Metabolism. **An updated definition of stroke for the 21st century: a statement for healthcare professionals from the American Heart Association/American Stroke Association**. *Stroke* 2013;44:2064–89 CrossRef Medline

Bayesian Estimation of CBF Measured by DSC-MRI in Patients with Moyamoya Disease: Comparison with ^{15}O-Gas PET and Singular Value Decomposition

S. Hara, Y. Tanaka, S. Hayashi, M. Inaji, T. Maehara, M. Hori, S. Aoki, K. Ishii, and T. Nariai

ABSTRACT

BACKGROUND AND PURPOSE: CBF analysis of DSC perfusion using the singular value decomposition algorithm is not accurate in patients with Moyamoya disease. This study compared the Bayesian estimation of CBF against the criterion standard PET and singular value decomposition methods in patients with Moyamoya disease.

MATERIALS AND METHODS: Nineteen patients with Moyamoya disease (10 women; 22–52 years of age) were evaluated with both DSC and ^{15}O-gas PET within 60 days. DSC-CBF maps were created using Bayesian analysis and 3 singular value decomposition analyses (standard singular value decomposition, a block-circulant deconvolution method with a fixed noise cutoff, and a block-circulant deconvolution method that adopts an oscillating noise cutoff for each voxel according to the strength of noise). Qualitative and quantitative analyses of the Bayesian-CBF and singular value decomposition–CBF methods were performed against ^{15}O-gas PET and compared with each other.

RESULTS: In qualitative assessments of DSC-CBF maps, Bayesian-CBF maps showed better visualization of decreased CBF on PET (sensitivity = 62.5%, specificity = 100%, positive predictive value = 100%, negative predictive value = 78.6%) than a block-circulant deconvolution method with a fixed noise cutoff and a block-circulant deconvolution method that adopts an oscillating noise cutoff for each voxel according to the strength of noise ($P < .03$ for all except for specificity). Quantitative analysis of CBF showed that the correlation between Bayesian-CBF and PET-CBF values ($\rho = 0.46$, $P < .001$) was similar among the 3 singular value decomposition methods, and Bayesian analysis overestimated true CBF (mean difference, 47.28 mL/min/100 g). However, the correlation between CBF values normalized to the cerebellum was better in Bayesian analysis ($\rho = 0.56$, $P < .001$) than in the 3 singular value decomposition methods ($P < .02$).

CONCLUSIONS: Compared with previously reported singular value decomposition algorithms, Bayesian analysis of DSC perfusion enabled better qualitative and quantitative assessments of CBF in patients with Moyamoya disease.

ABBREVIATIONS: CBF% = CBF values normalized to the cerebellum; cSVD = block-circulant deconvolution method with a fixed noise cutoff; oSVD = block-circulant deconvolution method that adopts an oscillating noise cutoff for each voxel according to the strength of noise; SVD = singular value decomposition; sSVD = standard SVD

DSC-PWI is an MR imaging–based perfusion measurement that relies on the measurement of T2* decrease during the first pass of an exogenous endovascular tracer through the capillary bed.[1,2] It obtains multiple hemodynamic parameters, including CBV, MTT, and CBF, by a single scan within a clinically feasible scanning duration.[3] Because of the better clinical availability and lower invasiveness of MR imaging compared with the criterion standard PET method, DSC is widely used for the assessment of cerebrovascular diseases.[3] There are many variations in the postprocessing of DSC, such as first-pass and singular value decomposition (SVD).[1,2] Although time-based perfusion parameters, such as the time of maximum concentration and MTT, are clinically useful in acute stroke[4] or chronic cerebrovascular disease such as Moyamoya disease,[5] the correlation between the CBF values obtained by SVD methods and by the criterion standard PET method is not sufficient, especially in patients with Moyamoya disease.[3,5-10]

Received April 4, 2019; accepted after revision August 19.

From the Department of Neurosurgery (S. Hara, Y.T., S. Hayashi, M.I., T.M., T.N.), Tokyo Medical and Dental University, Tokyo, Japan; Department of Radiology (S. Hara. M.H., S.A.), Juntendo University, Tokyo, Japan; and Research Team for Neuroimaging (S. Hayashi, M.I., K.I., T.N.), Tokyo Metropolitan Institute of Gerontology, Tokyo, Japan.

This work was supported by Grants-in-Aid for Scientific Research "KAKENHI", the Japan Society for the Promotion of Science (Grant Nos. 26305031 and 16H06280).

Please address correspondence to Shoko Hara, MD, PhD, Department of Neurosurgery, Tokyo Medical and Dental University, 1-5-45 Yushima, Bunkyo-ku, Tokyo 113-8519, Japan; e-mail: shara.nsrg@tmd.ac.jp

Indicates open access to non-subscribers at www.ajnr.org
Indicates article with supplemental on-line tables.
Indicates article with supplemental on-line photos.
http://dx.doi.org/10.3174/ajnr.A6248

Recently, Bayesian probabilistic analysis, which uses the Bayes theorem for parameter estimation, has emerged as a novel method to analyze DSC.[11] Bayesian analysis of DSC is more robust to noise and errors such as tracer delay and offers more accurate estimation of hemodynamic parameters such as CBF and MTT than SVD methods.[12] To date, the clinical feasibility of Bayesian perfusion analysis has been widely reported in acute stroke,[13,14] reduced contrast-dose protocols,[15] and the separation of tissue types of glioma.[16] It is possible that DSC-CBF obtained by Bayesian analysis reflects true CBF much better than SVD methods. However, to the best of our knowledge, no study has investigated the CBF accuracy of Bayesian analysis using PET as the criterion standard.

The purpose of this study was to investigate the accuracy of DSC-CBF obtained from Bayesian analysis in patients with Moyamoya disease—that is, chronic occlusive cerebrovascular disease with strong transit delay and increased CBV—compared with the criterion standard ^{15}O-gas PET and the SVD analysis of DSC.

MATERIALS AND METHODS

Patient Selection Protocol

This retrospective study was approved by the ethics committee of Tokyo Medical and Dental University (M2000-1331). We reviewed medical records from January 2014 to October 2015 and found 19 patients (10 women, 22–52 years of age) who were diagnosed with Moyamoya disease according to the diagnostic guidelines[17] and were evaluated with DSC and ^{15}O-gas PET within an interval of <60 days. Of 19 patients, 13 patients had an ischemic presentation (TIA and/or infarction) and 6 patients had a hemorrhagic event. The infarction and hemorrhage occurred >3 weeks before the imaging studies. Three patients received surgical treatment >200 days before the imaging period. The full details of the patient characteristics are described in On-line Table 1. All patients except 1 were evaluated with DSC before ^{15}O-gas PET, and no new lesions or symptoms occurred between the evaluations. None of the patients with TIA experienced TIA during or immediately before the DSC and PET studies.

DSC Acquisition and CBF Analysis

We used a 3T MR imaging scanner (Signa HDxt; GE Healthcare, Milwaukee, Wisconsin) with an 8-channel head coil and acquired gradient recalled-echo single-shot multislice EPI with a TR of 1000 ms, a TE of 40 ms, an FOV of 22 cm, a voxel size of 1.78 × 1.78 mm, and a matrix size of 128 × 128. A series of seven 5-mm-thick slices separated by 7.5-mm gaps was acquired after a bolus injection of gadodiamide (0.2 mmol/kg body weight, Omniscan 32%; GE Healthcare, Piscataway, New Jersey) via an antecubital vein using a power injector (Sonic Shot GX; Nemoto Kyorindo, Tokyo, Japan) at a rate of 3 mL/s, followed by a 15-mL saline flush.[5] The acquisition time was 3 minutes.

Acquired data were transferred to a personal computer with commercially available software, Olea Sphere, Version 3.0 (Olea Medical Solutions, La Ciotat, France) implemented with 4 DSC analyses: standard SVD (sSVD);[1] a block-circulant deconvolution method with a fixed noise cutoff (cSVD);[18] a block-circulant deconvolution method with an oscillating noise cutoff for each voxel according to the strength of noise (oSVD);[9,18] and Bayesian probabilistic analysis (Bayesian).[11,19] The motion correction (rigid coregistration) was automatically performed to fit all acquired images to a single reference image selected by the software algorithm. The arterial input function was automatically selected using a cluster analysis algorithm that reduces bias due to delay and dispersion,[20] and the same arterial input function was applied to all 4 analytic methods in each patient.

PET Data Acquisition

The PET data were acquired using a Discovery 710 PET/CT scanner (GE Healthcare).[21] The 3.5-minute acquisition of the scans was initiated simultaneously with a 1.5-minute inhalation of $C^{15}O_2$ (2000 MBq/min) and $C^{15}O$ (2000 MBq/min) using a neck shield.[22] The amount of radioactivity in the arterial whole blood was manually collected at 0, 2, and 4 minutes, and images of inhaled $C^{15}O_2$ were also acquired.[23] The images were reconstructed under the following conditions: a 3D-ordered-subset expectation-maximization algorithm, 128 × 128 matrix, 47 slices, 2.0 mm/pixel, 3.27-mm/section, 4 iterations, 16 subsets, and a Gaussian filter of 3.0 mm. The amount of radioactivity in the arterial blood was used to create CBF and CBV images using the PET autoradiographic method with Xeleris software (GE Healthcare).[25]

Visual Assessment of CBF Maps

Three neurosurgeons who specialized in cerebral perfusion (S. Hara, Y.T., and T.N., with 10, 23, and 34 years of clinical experience, respectively) assessed the presence of decreased CBF in each hemisphere of each absolute CBF map. The assessments were performed on separate occasions. Each surgeon was blinded to the patient information, except for the location of brain lesions (infarctions and hemorrhages) that should not be included in the visual assessments and the type of CBF analytic method, and each was without access to the conclusions of the other surgeons. During the assessment, each map was shown in the visually appropriate color scales to show similar contrasts; in the software we used (Dr. View R2.5; Infocom, Tokyo, Japan), the upper and lower thresholds of the color ranges were set to exclude the top 10% and the bottom 30% of the voxels of the histogram of each map. If necessary, the upper threshold was sometimes changed to produce similar contrasts. The median answer of the 3 evaluators was recorded as a consensus.

Calculation of Regional Values

PET and MR images were spatially coregistered using the image-registration function of Dr. View R2.5. Because our DSC is not 3D data, we reconstructed the PET-CBF and PET-CBV maps into 7 slices matched to the DSC maps using the raw DSC image of each patient as a reference. The ROIs were manually drawn on the raw DSC images over 10 cortical areas (bilateral frontal, parietal, rolandic, temporal, and occipital lobes) and the cerebellum,[5,26,27] as shown in On-line Fig 1, by a single neurosurgeon (S. Hara) who was blinded to the clinical information of the patients. The brain lesions visible on the raw DSC images (infarctions and hemorrhages) were omitted from the ROIs. To evaluate

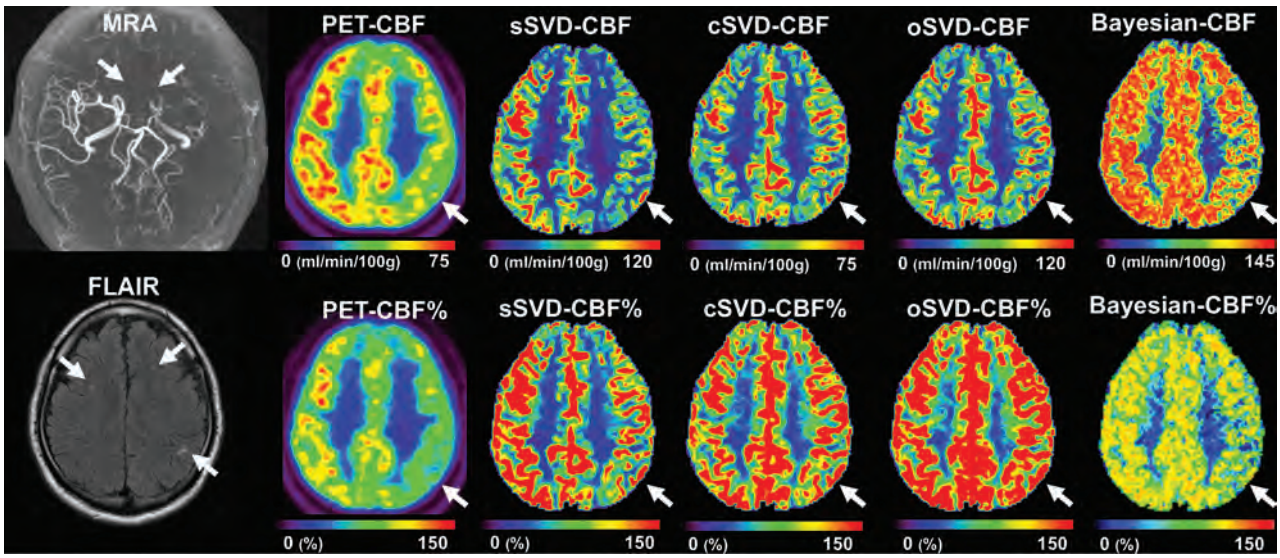

FIG 1. A representative case. A 48-year-old man was incidentally diagnosed with Moyamoya disease by nonspecific symptoms. MRA reveals occlusion of the terminal portion of the left ICA (*arrows*), bilateral anterior cerebral arteries, and the left MCA. FLAIR shows bilateral white matter hyperintensities. CBF maps obtained by PET, sSVD and Bayesian analysis shows clearly reduced CBF on the left sides (*arrows*). However, the CBF maps obtained by cSVD and oSVD do not show the laterality of the CBF that is evident on PET (*arrows*). The CBF% map of Bayesian analysis shows values close to the CBF% of PET. Please note that the color scale used in the raw CBF maps was the same as that used during the visual assessments and that the color scales of the CBF% maps were unified.

intrareader variability, ROIs were drawn twice for 40 randomly selected regions.

Statistical Analysis

Qualitative Analysis. We counted the number of hemispheres that were considered to exhibit a decrease in CBF on PET-CBF maps and the number of hemispheres in which the DSC-derived CBF maps were correctly correlated with the PET maps. Then, we calculated the sensitivity, specificity, positive predictive value, and negative predictive value of the visual assessment of CBF maps acquired by 4 DSC analytic methods using the decreased CBF on PET maps as the true-positive finding. The sensitivity and specificity were compared using the McNemar test, and weighted generalized score statistics were used to compare positive and negative predictive values.

Quantitative Analysis. The interclass correlation coefficient was calculated from 40 randomly selected areas where ROIs were drawn twice. The distribution of the CBF values of each technique was evaluated with the Shapiro-Wilk test for normality.

The correlation coefficients between the regional CBF values of 10 cortical areas (not including the cerebellum) in all patients obtained by the 4 analyses and PET were calculated and tested for significance using the Fisher Z transformation. By means of the Bland-Altman analysis, the average, 95% confidence intervals, and limits of agreement (average $\pm$ 1.96 $\times$ SDs) of the difference between DSC-CBF and PET-CBF and the correlation coefficients between the average and the difference between DSC-CBF and PET-CBF values were calculated. Because the software we used reported the DSC-CBF values in "arbitrary units (milliliters/minute/100 g)," the relationship among the CBF values normalized to the cerebellum (CBF%) was evaluated in addition to the relationship among the raw values. We also compared the correlation between the DSC-CBF and PET-CBF values in hemispheres with visually decreased CBF and in hemispheres with visually normal CBF determined by the qualitative analysis described above. The relationship between PET-CBV and DSC-CBV in each method was also evaluated.

All statistical analyses were performed using R, Version 3.2.2 (https://cran.r-project.org), and $P < .05$ was regarded as significant.

RESULTS

Qualitative Analysis

A representative case is shown in Fig 1. Of 38 hemispheres of 19 patients, 16 (42%) hemispheres were considered to have decreased CBF. The number of hemispheres that DSC-derived CBF maps correctly correlated with PET (ie, true-positive/true-negative) was 10/19 in sSVD, 3/19 in cSVD, 5/20 in oSVD, and 10/22 in Bayesian analysis. Overall, visual assessments of Bayesian-CBF maps offered higher sensitivity, specificity, positive predictive values, and negative predictive values than cSVD and oSVD, but these values did not significantly differ from those obtained by sSVD (Table and On-line Table 2).

Quantitative Analysis

The interclass correlation coefficients of each technique were 0.95–0.99. Because many CBF values were not normally distributed ($P = <.0001–.35$), we used Spearman correlation coefficients (ρ) to evaluate the CBF correlations between each technique.

The correlation between the absolute cerebral CBF values of PET and those of DSC analyses were moderate (Fig 2). The correlation strength of the Bayesian analysis was significantly better than that of sSVD but not better than that of oSVD and cSVD

(On-line Table 3). Bland-Altman analysis revealed that the Bayesian method overestimates CBF compared with PET, with strong constant bias and small proportional bias.

Among the correlation analyses of CBF% values, Bayesian-CBF% showed the best correlation with PET-CBF% (Fig 3), significantly better than those of the 3 SVD methods (On-line Table 3). The 3 SVD methods overestimated the CBF% values compared with PET, with significant proportional bias that was not observed in the Bayesian method.

When comparing the relationship between DSC-CBF and PET-CBF values in decreased CBF hemispheres and in normal CBF hemispheres, the difference between DSC-CBF% and PET-CBF% was larger and the proportional bias stronger in decreased CBF hemispheres than in normal CBF hemispheres in the sSVD, cSVD, and oSVD methods (On-line Table 4). In contrast, in the Bayesian method, the difference between DSC-CBF% and PET-CBF% was not higher in decreased CBF hemispheres than in normal CBF hemispheres.

The correlation between PET-CBV and DSC-CBV in each method did not differ significantly (On-line Fig 2 and On-line Table 5).

DISCUSSION

We demonstrated that Bayesian analysis depicted true CBF qualitatively and quantitatively compared with SVD methods in patients with Moyamoya disease. Although a good correlation between SVD-measured CBF and PET-CBF has been reported in analyses of pig stroke and a small number of healthy volunteers,[9,28-30] the SVD-CBF values did not correlate well with true CBF in patients with cerebrovascular diseases, especially in patients with Moyamoya disease.[5,26] The effect of global perfusion delay on arterial input function values and increased tissue signals caused by increased CBV are thought to negatively affect the accuracy of DSC-CBF values in these patients. In the Bayesian analysis of DSC, instead of simply fitting the observed tissue signal to the deconvolution formula, as in SVD analysis, the observed tissue signal was reconvoluted to create the CBF map, considering the accurate movement of the residue fraction of the injected tracer and the probability distribution of CBF values. This algorithm enables better assumptions for CBF, unaffected by tracer delay effects and increased noise signals from increased CBV, which are both prominent in patients with Moyamoya disease.[31]

Interestingly, the oldest SVD method (sSVD) was superior in qualitative analysis to the newer SVD methods (cSVD and oSVD) in terms of sensitivity to decreased regional CBF. The linear deconvolution used in sSVD is sensitive to the tracer-arrival delay effect that leads to the underestimation of CBF in regions with perfusion delay. The circular deconvolution used in cSVD and oSVD is proposed to eliminate the effect of tracer-arrival delay; cSVD

Sensitivity, specificity, positive predictive value, and negative predictive value of the visual assessment of the 4 DSC-CBF maps[a]

(%)	sSVD	cSVD	oSVD	Bayesian
Sensitivity	62.5 (35.4–84.8)[b]	18.8 (4.0–45.6)	31.3 (11.0–58.7)[c]	62.5 (35.4–84.8)[b]
Specificity	86.4 (65.1–97.1)	86.4 (65.1–97.1)	90.9 (70.8–98.9)	100 (78.1–100)
Positive predictive value	76.9 (46.2–95.0)	50.0 (11.8–88.2)	71.4 (29.0–96.3)	100 (58.7–100)[c]
Negative predictive value	76.0 (54.9–90.6)	59.4 (40.6–76.3)	64.5 (45.4–80.8)	78.6 (59.0–91.7)[b]

[a] Data are averages and 95% CI.
[b] $P < .05$ compared with cSVD and oSVD.
[c] $P < .05$ compared with cSVD.

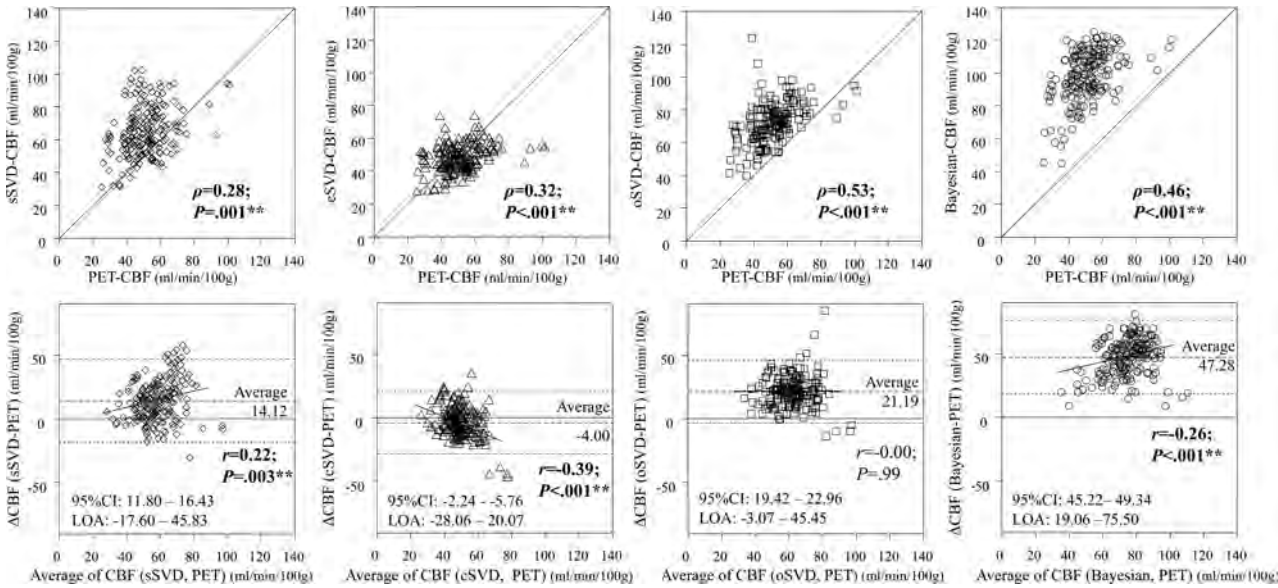

FIG 2. The Bland-Altmann analysis between the regional raw CBF values of PET and each of the 4 DSC analyses. All methods showed moderate correlation between DSC and PET, and there was no significant difference between Bayesian analysis and the other SVD methods except for sSVD (versus cSVD, $P = .11$; versus oSVD, $P = .37$; versus sSVD, $P = .04$). sSVD overestimates PET-CBF with a small proportional bias; cSVD underestimates PET-CBF with moderate negative proportional bias; oSVD overestimates PET-CBF without proportional bias; and Bayesian-CBF strongly overestimates PET-CBF with a small proportional bias. LOA, limits of agreement defined as average $\pm$ 1.96 $\times$ SD. *$P < .05$ and **$P < .005$.

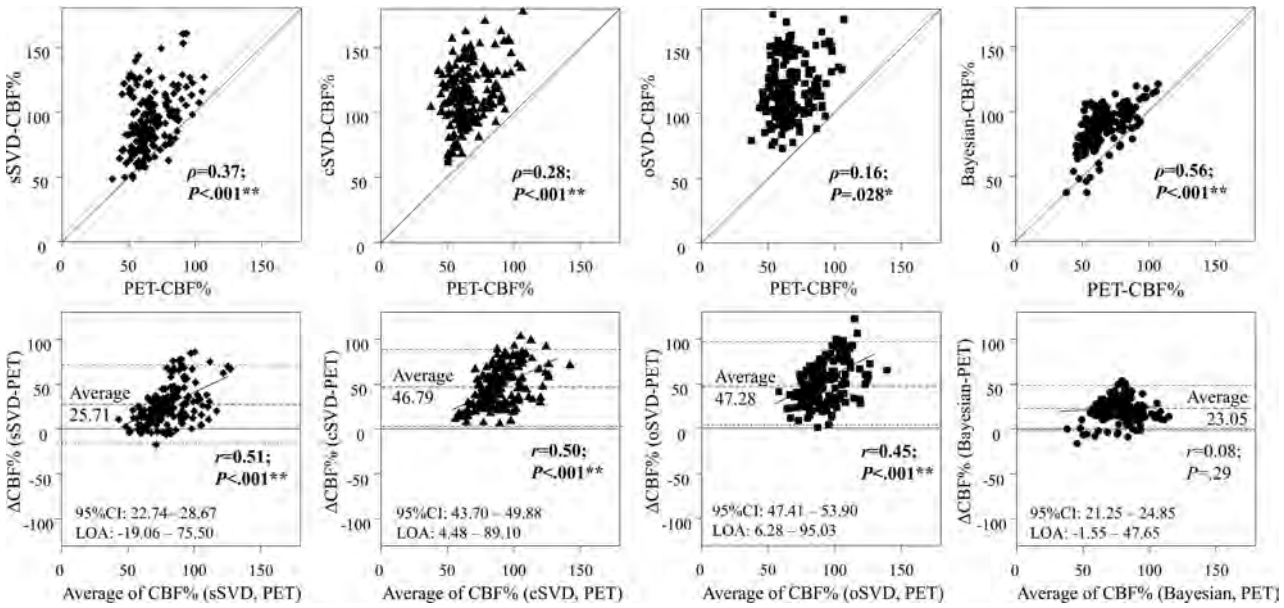

FIG 3. The Bland-Altmann analysis between the regional CBF values normalized to cerebellum (CBF%) of PET and the 4 DSC analyses. The correlation of the Bayesian analysis was significantly better than those of the 3 SVD methods (versus sSVD, $P = .02$; versus cSVD, $P < .001$; versus oSVD, $P < .001$). The limit of agreement (LOA, defined as average ±1.96 x SD) of the Bayesian method was also smaller than those of the 3 SVD methods. *$P < .05$ and **$P < .005$.

uses a global fixed threshold to eliminate noise, while the oSVD uses a different threshold in every voxel according to the strength of noise and is less sensitive to the effect of CBV than cSVD.[18] Therefore, in theory, oSVD-CBF should be the best method to depict CBF in patients with Moyamoya disease who exhibit increased CBV and prominent perfusion delay,[31,32] which was the opposite of what was actually observed. We also found that when SVD methods were used, the difference between DSC-CBF% and PET-CBF% was larger in hemispheres with decreased CBF than in normal CBF hemispheres, as indicated by the significant proportional bias. We speculated that the strongly increased CBV in our patients with Moyamoya overwhelmed the correction ability of the block-circulant methods and led to the improperly increased CBF signal in the affected regions. On the other hand, tracer arrival delay, which is strong in Moyamoya disease, might overwhelm the effect of increased signals resulting from increased CBV and lead to the proper depiction of decreased CBF in the sSVD method. It may be better to choose sSVD instead of cSVD or oSVD to qualitatively depict the decrease in CBF in patients with Moyamoya disease if Bayesian analysis is unavailable.

We found that Bayesian analysis was superior for the quantitative evaluation of CBF values normalized to the cerebellum but not the raw CBF values; all methods except oSVD overestimated the CBF values, and the overestimation was particularly prominent in the Bayesian method. Considering the completely different mechanisms of DSC using an intravascular tracer and PET using a diffusible tracer, it is not surprising that the raw CBF values of PET and DSC do not correlate well. The correlation of CBF values in the cerebellum, where CBF is unaffected and is used as a control in patients with Moyamoya disease, is also not perfect in any method (On-line Fig 3). In addition to the different tracer mechanisms, we speculated that the Bayesian analytic method essentially overestimates CBF values, possibly due to the higher values of the CBF distribution used in this software compared with the CBF distribution of ^{15}O-gas PET. However, the qualitative assessments using CBF values in reference to the cerebellum were better in Bayesian analysis than in the SVD methods. Additionally, the difference between the Bayesian-CBF% and PET-CBF% values was smaller than the differences obtained by the SVD methods, regardless of the presence of decreased CBF, suggesting that the Bayesian analytic method is more robust than the SVD methods to the errors resulting from increased CBV and transit time in patients with Moyamoya disease. In addition to the better CBF depiction ability we showed, the MTT values from the Bayesian method are shown to be superior to those from SVD methods,[19] and the correlation between DSC-CBV and PET-CBV was not different among the DSC methods. Considering that MTT values are biomarkers of clinical presentation,[32] increased oxygen extraction fraction,[5] and surgical outcome[33,34] in patients with Moyamoya disease, Bayesian analysis would be a better choice than SVD methods to analyze DSC in these patients.

The limitations of our study include the small sample size and the relatively long DSC-PET intervals, which were inevitable due to the limited availability of PET examinations. We did not perform first-pass method analysis, which was not implemented in our software. Considering the software-dependent nature of DSC analysis,[12] different analysis software must produce different results; however, to the best of our knowledge, the software we used is the only commercially available software that implements Bayesian analysis. Although several limitations exist, our results suggest that Bayesian analysis might be the current best method to analyze DSC-PWI in patients with Moyamoya disease.

CONCLUSIONS

Bayesian analysis of DSC perfusion enabled better qualitative and quantitative assessments of CBF in patients with Moyamoya disease than previously reported SVD algorithms.

ACKNOWLEDGMENTS

We thank Professor Kohsuke Kudo for suggestions regarding the interpretation of the results and Dr Masako Akiyama for statistical guidance.

Disclosures: Shoko Hara—*UNRELATED*: *Grants/Grants Pending*: Grants-in-Aid for Scientific Research "KAKENHI", the Japan Society for the Promotion of Science (Grant Nos. 16K19995 and 19K18406)/ Research Grant from the Japanese Society for Neuroradiology. Shigeki Aoki—*RELATED*: Grants-in-Aid for Scientific Research "KAKENHI", the Japan Society for the Promotion of Science (Grant No. 16H06280), *UNRELATED*: *Grants/Grants Pending*: Nihon Medi-physics, Toshiba, Bayer Yakuhin, Daiichi Sankyo, Eisai, Fujiyakuhin, FUJIFILM RI Pharma, *Comments*: grant for diagnostic radiology from Nihon Medi-physics, Toshiba, Bayer Yakuhin, Daiichi Sankyo, Eisai, Fujiyakuhin, FUJIFILM RI Pharma*; *Payment for Lectures Including Service on Speakers Bureaus*: Nihon Medi-physics, Toshiba, Bayer Yakuhin, Daiichi Sankyo, Eisai, Fujiyakuhin, FUJIFILM RI Pharma, *Comments*: honorarium for lectures/chair from GE Healthcare, Toshiba/Canon, Hitachi, Siemens, Bayer Yakuhin, Daiichi Sankyo, Eisai, Fujiyakuhin, FUJIFILM RI Pharma, Nihon Medi-physics, Novartis, Takeda Pharmaceutical Company, Biogen, Chugai Pharmaceutical Co. Tadashi Nariai—*RELATED*: Grants-in-Aid for Scientific Research "KAKENHI", the Japan Society for the Promotion of Science (Grant No. 26305031). *Money paid to the institution.

REFERENCES

1. Ostergaard L, Weisskoff RM, Chesler DA, et al. **High-resolution measurement of cerebral blood flow using intravascular tracer bolus passages, part I: mathematical approach and statistical analysis.** *Magn Reson Med* 1996;36:715–75 CrossRef Medline
2. Ostergaard LW, Chesler DA, Gyldensted C, et al. **High resolution measurement of cerebral blood flow using intravascular tracer bolus passages, part II: experimental comparison and preliminary results.** *Magn Reson Med* 1996;36:726–36 CrossRef Medline
3. Wintermark M, Sesay M, Barbier E, et al. **Comparative overview of brain perfusion imaging techniques.** *Stroke* 2005;36:e83–99 CrossRef Medline
4. Lansberg MG, Lee J, Christensen S, et al. **RAPID automated patient selection for reperfusion therapy: a pooled analysis of the Echoplanar Imaging Thrombolytic Evaluation Trial (EPITHET) and the Diffusion and Perfusion Imaging Evaluation for Understanding Stroke Evolution (DEFUSE) Study.** *Stroke* 2011;42:1608–14 CrossRef Medline
5. Tanaka Y, Nariai T, Nagaoka T, et al. **Quantitative evaluation of cerebral hemodynamics in patients with Moyamoya disease by dynamic susceptibility contrast magnetic resonance imaging: comparison with positron emission tomography.** *J Cereb Blood Flow Metab* 2006;26:291–300 CrossRef Medline
6. Ibaraki M, Shimosegawa E, Toyoshima H, et al. **Effect of regional tracer delay on CBF in healthy subjects measured with dynamic susceptibility contrast-enhanced MRI: comparison with 15O-PET.** *Magn Reson Med Sci* 2005;4:27–34 CrossRef Medline
7. Lin W, Celik A, Derdeyn C, et al. **Quantitative measurements of cerebral blood flow in patients with unilateral carotid artery occlusion: a PET and MR study.** *J Magn Reson Imaging* 2001;14:659–67 CrossRef Medline
8. Mukherjee P, Kang HC, Videen TO, et al. **Measurement of cerebral blood flow in chronic carotid occlusive disease: comparison of dynamic susceptibility contrast perfusion MR imaging with positron emission tomography.** *AJNR Am J Neuroradiol* 2003;24:862–71 Medline
9. Ostergaard L, Johannsen P, Host-Poulsen P, et al. **Cerebral blood flow measurements by magnetic resonance imaging bolus tracking: comparison with [(15)O]H2O positron emission tomography in humans.** *J Cereb Blood Flow Metab* 1998;18:935–40 CrossRef Medline
10. Vakil P, Lee JJ, Mouannes-Srour JJ, et al. **Cerebrovascular occlusive disease: quantitative cerebral blood flow using dynamic susceptibility contrast MR imaging correlates with quantitative H2[15O] PET.** *Radiology* 2013;266:879–86 CrossRef Medline
11. Boutelier T, Kudo K, Pautot F, et al. **Bayesian hemodynamic parameter estimation by bolus tracking perfusion weighted imaging.** *IEEE Trans Med Imaging* 2012;31:1381–95 CrossRef Medline
12. Kudo K, Christensen S, Sasaki M, et al. **Accuracy and reliability assessment of CT and MR perfusion analysis software using a digital phantom.** *Radiology* 2013;267:201–11 CrossRef Medline
13. Kudo K, Boutelier T, Pautot F, et al. **Bayesian analysis of perfusion-weighted imaging to predict infarct volume: comparison with singular value decomposition.** *Magn Reson Med Sci* 2014;13:45–50 CrossRef Medline
14. Nicoli F, Scalzo F, Saver JL, et al. **The combination of baseline magnetic resonance perfusion-weighted imaging-derived tissue volume with severely prolonged arterial-tissue delay and diffusion-weighted imaging lesion volume is predictive of MCA-M1 recanalization in patients treated with endovascular thrombectomy.** *Neuroradiology* 2014;56:117–27 CrossRef Medline
15. Nael K, Mossadeghi B, Boutelier T, et al. **Bayesian estimation of cerebral perfusion using reduced-contrast-dose dynamic susceptibility contrast perfusion at 3T.** *AJNR Am J Neuroradiol* 2015;36:710–18 CrossRef Medline
16. Hansen MB, Tietze A, Kalpathy-Cramer J, et al. **Reliable estimation of microvascular flow patterns in patients with disrupted blood-brain barrier using dynamic susceptibility contrast MRI.** *J Magn Reson Imaging* 2017;46:537–49 CrossRef Medline
17. Research Committee on the Pathology and Treatment of Spontaneous Occlusion of the Circle of Willis; Health Labour Sciences Research Grant for Research on Measures for Infractable Diseases. **Guidelines for diagnosis and treatment of Moyamoya disease (spontaneous occlusion of the circle of Willis).** *Neurol Med Chir (Tokyo)* 2012;52:245–66 CrossRef Medline
18. Wu O, Ostergaard L, Weisskoff RM, et al. **Tracer arrival timing-insensitive technique for estimating flow in MR perfusion-weighted imaging using singular value decomposition with a block-circulant deconvolution matrix.** *Magn Reson Med* 2003; 50:164–74 CrossRef Medline
19. Sasaki M, Kudo K, Boutelier T, et al. **Assessment of the accuracy of a Bayesian estimation algorithm for perfusion CT by using a digital phantom.** *Neuroradiology* 2013;55:1197–1203 CrossRef Medline
20. Mouridsen K, Christensen S, Gyldensted L, et al. **Automatic selection of arterial input function using cluster analysis.** *Magn Reson Med* 2006;55:524–31 CrossRef Medline
21. Bettinardi V, Presotto L, Rapisarda E, et al. **Physical performance of the new hybrid PETCT Discovery-690.** *Med Phys* 2011;38:5394–5411 CrossRef Medline
22. Shidahara M, Watabe H, Kim KM, et al. **Optimal scan time of oxygen-15-labeled gas inhalation autoradiographic method for measurement of cerebral oxygen extraction fraction and cerebral oxygen metabolic rate.** *Ann Nucl Med* 2008;22:667–75 CrossRef Medline
23. Kudomi N, Choi E, Yamamoto S, et al. **Development of a GSO detector assembly for a continuous blood sampling system.** *IEEE Trans Nucl Sci* 2003;50:70–73 CrossRef
24. Miwa K, Umeda T, Murata T, et al. **Evaluation of scatter limitation correction: a new method of correcting photopenic artifacts caused by patient motion during whole-body PET/CT imaging.** *Nucl Med Commun* 2016;37:147–54 CrossRef Medline
25. Shidahara M, Watabe H, Kim KM, et al. **Evaluation of a commercial PET tomograph-based system for the quantitative assessment of rCBF, rOEF and rCMRO2 by using sequential administration of 15O-labeled compounds.** *Ann Nucl Med* 2002;16:317–27 CrossRef Medline

26. Hara S, Tanaka Y, Ueda Y, et al. **Noninvasive evaluation of CBF and perfusion delay of Moyamoya disease using arterial spin-labeling MRI with multiple postlabeling delays: comparison with ^{15}O-gas PET and DSC-MRI.** *AJNR Am J Neuroradiol* 2017;38:696–702 CrossRef Medline
27. Kimura H, Kado H, Koshimoto Y, et al. **Multislice continuous arterial spin-labeled perfusion MRI in patients with chronic occlusive cerebrovascular disease: a correlative study with CO2 PET validation.** *J Magn Reson Imaging* 2005;22:189–98 CrossRef Medline
28. Grandin CB, Bol A, Smith AM, et al. **Absolute CBF and CBV measurements by MRI bolus tracking before and after acetazolamide challenge: repeatabilily and comparison with PET in humans.** *Neuroimage* 2005;26:525–35 CrossRef Medline
29. Takasawa M, Jones PS, Guadagno JV, et al. **How reliable is perfusion MR in acute stroke? Validation and determination of the penumbra threshold against quantitative PET.** *Stroke* 2008;39:870–77 CrossRef Medline
30. Sakoh M, Rohl L, Gyldensted C, et al. **Cerebral blood flow and blood volume measured by magnetic resonance imaging bolus tracking after acute stroke in pigs: comparison with [(15)O]H(2)O positron emission tomography.** *Stroke* 2000;31:1958–64 CrossRef Medline
31. Nariai T, Matsushima Y, Imae S, et al. **Severe haemodynamic stress in selected subtypes of patients with Moyamoya disease: a positron emission tomography study.** *J Neurol Neurosurg Psychiatry* 2005; 76:663–69 CrossRef Medline
32. Hirai S, Inaji M, Tanaka Y, et al. **Correlation between clinical presentations and hemodynamic parameters measured by dynamic susceptibility contrast magnetic resonance imaging in adult patients with Moyamoya disease.** *J Stroke Cerebrovasc Dis* 2017; 26:2814–20 CrossRef Medline
33. Ishii Y, Nariai T, Tanaka Y, et al. **Practical clinical use of dynamic susceptibility contrast magnetic resonance imaging for the surgical treatment of Moyamoya disease.** *Neurosurgery* 2014;74:302–09 CrossRef Medline
34. Ishii Y, Tanaka Y, Momose T, et al. **Chronologic evaluation of cerebral hemodynamics by dynamic susceptibility contrast magnetic resonance imaging after indirect bypass surgery for Moyamoya disease.** *World Neurosurg* 2017;108:427–35 CrossRef Medline

Role of 3D Pseudocontinuous Arterial Spin-Labeling Perfusion in the Diagnosis and Follow-Up in Patients with Herpes Simplex Encephalitis

R. Li, P.-A. Shi, T.-F. Liu, Y. Li, Y. Wang, K. Wu, X.-J. Chen, H.-F. Xiao, Y.-L. Wang, L. Ma, and X. Lou

ABSTRACT

BACKGROUND AND PURPOSE: Early diagnosis and treatment of herpes simplex encephalitis are crucial to reduce morbidity and mortality. Our aim was to investigate the role of 3D pseudocontinuous arterial spin-labeling in herpes simplex encephalitis.

MATERIALS AND METHODS: From 2014 to 2019, seventeen consecutive patients with herpes simplex encephalitis and 15 healthy volunteers were recruited in the study. Conventional MR imaging and 3D pseudocontinuous arterial spin-labeling were performed in all subjects. According to the disease duration, the lesions were classified into 3 groups, including acute, subacute, and chronic stages, respectively. Clinical, neuroradiologic, and follow-up features were studied. The normalized lesion/normal tissue CBF values of lesions at different stages were measured and compared with those in the control group, respectively.

RESULTS: Compared with the control group, herpes simplex encephalitis demonstrated hyperperfusion in 11 acute cases and 6 subacute cases and hypoperfusion in 6 chronic cases. The mean normalized lesion/normal tissue CBF values of the lesions were 2.68 ± 0.54 in the acute stage, 2.42 ± 0.52 in the subacute stage, and 0.87 ± 0.30 in the chronic stage, respectively. The mean normalized lesion/normal tissue CBF values of acute and subacute lesions were significantly higher than those of the control group (1.33 ± 0.08; $P < .001$, respectively), while the mean normalized lesion/normal tissue CBF values of chronic lesions were lower than those of the control group ($P < .05$). Gradual perfusion reduction on serial 3D pseudocontinuous arterial spin-labeling was observed in herpes simplex encephalitis after effective therapy.

CONCLUSIONS: Conventional MR imaging remains most helpful in the diagnosis of herpes simplex encephalitis, while 3D pseudocontinuous arterial spin-labeling could be an adjunctive technique by providing dynamic CBF features at different stages in herpes simplex encephalitis.

ABBREVIATIONS: ASL = arterial spin-labeling; 3D-pCASL = 3D pseudocontinuous ASL; HSE = herpes simplex encephalitis; HSV = herpes simplex virus; MELAS = mitochondrial encephalopathy with lactic acidosis and stroke-like episodes; nCBF = normalized lesion/normal tissue CBF

Viral encephalitis is a life-threatening infectious disease that can occur at any age.[1] More than 100 different viruses can result in acute encephalitis;[2] however, herpes simplex encephalitis (HSE) caused by the herpes simplex virus (HSV) is the most frequent and serious sporadic form of acute viral encephalitis all over the world, accounting for about 20% of all viral encephalitis cases.[3] Of all HSE cases, nearly 90% are caused by herpes simplex virus type 1 (HSV-1) and 10% by herpes simplex virus type 2 (HSV-2).[4] The death rate has dropped dramatically since antiviral drugs have been widely used; however, some patients survive with severe neurologic sequelae like epilepsy, cognitive impairment, or memory deterioration, and so forth.[5] Thus, early diagnosis and treatment are of great importance for patients with HSE to potentially decrease mortality.

In recent years, CT and MR imaging have been widely used in the early diagnosis of HSE. MR imaging has been reported to be superior to CT in revealing the characteristics of lesions, especially sequences such as T2 FLAIR and DWI.[6-8] Typically, HSE lesions are readily identified on such images (especially T2 FLAIR sequences). However, the conventional MR imaging appearance of HSE sometimes mimics other diseases, such as acute ischemic stroke,[9] mitochondrial encephalopathy with lactic acidosis and stroke-like episodes (MELAS),[10] or even diffuse low-grade glioma,[11] when the clinical presentations overlapping with other more common diseases are atypical.

Received June 25, 2019; accepted after revision August 26.

From the School of Medicine (R.L., L.M.), Nankai University, Tianjin, China; Department of Radiology (R.L., T.-F.L., Y.L., Y.W., K.W., X.-J.C., H.-F.X., Y.-L.W., L.M., X.L.), Chinese People's Liberation Army General Hospital, Beijing, China; and Department of Endocrinology (P.-A.S.), Cangzhou Central Hospital, Cangzhou, Hebei, China.

Please address correspondence to Lin Ma, MD, PhD, Department of Radiology, Chinese PLA General Hospital, 28 Fuxing Rd, Beijing 100853, China; e-mail: cjr.malin@vip.163.com

http://dx.doi.org/10.3174/ajnr.A6279

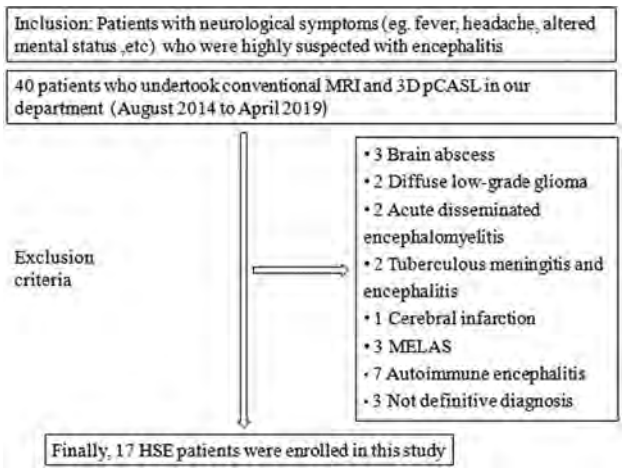

FIG 1. Flow chart showing the selection of the final study population. A total of 40 patients who underwent both conventional MR imaging and 3D-pCASL were clinically suspected of having encephalitis. Finally, 17 cases with HSE were included in this study.

Arterial spin-labeling (ASL) perfusion imaging is a completely noninvasive MR imaging technique for quantitative evaluation of CBF without exogenous injection of contrast agent.[12,13] The advantages and benefits of ASL have made it widely applied in evaluating brain perfusion in healthy populations (even in children and pregnant women), patients with renal insufficiency, and those who need repeat follow-up examinations.[13,14] Previous studies have shown that ASL has been widely applied in the diagnosis and differential diagnosis of many diseases, such as brain tumors,[15] stroke,[16] MELAS,[17] and so forth. Moreover, 3D pseudocontinuous ASL (pCASL) has combined the advantages of continuous ASL and pulsed ASL and has been recommended as standardized implementation for clinical applications.[12] However, few studies have yet been reported on the investigation of the perfusion appearance of HSE using 3D-pCASL.

Thus, the aim of this study was to retrospectively investigate the potential role of 3D-pCASL perfusion in HSE.

MATERIALS AND METHODS

Study Population

From August 2014 to April 2019, a total of 17 consecutive patients (12 males and 5 females; from 17 to 64 years of age; mean, 37.4 years) with a definite diagnosis of HSE were enrolled. A detailed flow chart of the study is shown in Fig 1. HSE was diagnosed according to the following criteria:[18,19] 1) acute or subacute onset of neurologic symptoms (eg, fever, disturbance of consciousness, seizure, and so forth); 2) abnormal findings on MR imaging; 3) CSF white blood cell count of $\geq 5/mm^3$; 4) virologic examination (including HSV DNA or increased HSV antibody level in CSF/serum or viral culture); 5) abnormal findings on an electroencephalogram; 6) empiric acyclovir and/or corticosteroid treatment being effective; and 7) exclusion of other encephalitis or other CNS diseases mimicking HSE.

The control group included 15 healthy volunteers (9 men and 6 women; age range, 20–60 years; mean, 36.8 years) imaged during the same period. The inclusion criteria were as follows: 1) roughly matched for age and sex with HSE subjects ($P > .05$); 2) no history of headache, epilepsy, head trauma, and other medical conditions affecting cerebral blood perfusion; and 3) normal findings on routine neurologic and conventional MR imaging examinations.

This study was approved by the PLA General Hospital ethics committee, and informed consent was also obtained. The healthy subject and patient information were anonymized during image analyses to protect privacy.

Inclusion/Exclusion Criteria for Study Patients

Patients were included in our study if they conformed to the above diagnostic criteria for HSE and had no history of other encephalitis, were admitted and treated at PLA General Hospital and underwent MR imaging, including conventional MR imaging and 3D-pCASL. On the contrary, patients were excluded from our study if HSE was suspected clinically without a final definite diagnosis; HSE was diagnosed on the basis of clinical criteria, but without abnormal findings on MR imaging; MR imaging had obvious motion artifacts or unusable images; and 3D-pCASL perfusion was not performed.

Conventional MR Imaging and 3D-pCASL

MR images were acquired on a 3T MR imaging system (Discovery 750; GE Healthcare, Milwaukee, Wisconsin) using a receive-only 32-channel phased-array head coil. Conventional MR imaging included T2WI (TR/TE = 4252/103.7 ms, FOV = 24 × 24 cm, matrix = 192 × 192, NEX = 1.5), T1WI (TR/TE/TI = 1750/24/780 ms, FOV = 24 × 24 cm, matrix = 320 × 320, NEX = 1), DWI (TR/TE = 6000/65.7 ms, FOV = 24 × 24 cm, matrix = 192 × 192, NEX = 2), and coronal and axial T2 FLAIR (TR/TE/TI = 8500/163/2100 ms, FOV = 24 × 24 cm, matrix = 288 × 224, NEX = 1). These images were obtained with identical section thickness (5 mm) and section space (1.5 mm). Postcontrast T1WI included axial, coronal, and sagittal planes (Magnevist, 0.1 mmol/kg, Bayer HealthCare Pharmaceuticals, Wayne, New Jersey).

3D-pCASL was acquired using a background-suppressed 3D spiral FSE technique. The parameters were as follows: TR/TE = 4844/10.5 ms, postlabeling delay = 2025 ms, FOV = 24 × 24 cm, section thickness = 4.0 mm, number of sections = 36, NEX = 3. In addition, a 3D T1-weighted fast-spoiled gradient recalled sequence was also obtained after contrast injection as an anatomic reference with TR/TE = 6.4/3.0 ms, FOV = 24 × 24 cm, section thickness = 4.0 mm, number of sections = 36, NEX = 1. Follow-up 3D-pCASL examinations were performed in patients 1, 2, 3, and 4 (Table 1).

Quantitative CBF Measurement and Normalized CBF

In this study, the lesions were classified into 3 categories according to the time from neurologic symptom onset to MR imaging evaluation. The acute stage of the lesion was up to 14 days from onset of symptoms; the subacute stage, from 15 to 25 days; and any duration beyond 26 days, the chronic stage.

ASL was postprocessed by functional software on a ADW4.5 workstation (GE Healthcare) to automatically generate CBF maps for every patient and all control individuals. For each patient, ROIs (28–40 mm^2) were manually and carefully placed within the lesions on CBF maps. The postcontrast 3D T1 fast-spoiled gradient recalled sequence, for accurate anatomic reference, was used

Table 1: Summary of the demographic and clinical features of consecutive patients with HSE

Case No.	Age (yr)	Sex	Clinical Presentation	Time (Days)[a]
1	17	M	Headache, fever, sudden unconscious attack, seizure	11/24/30
2	58	M	Headache, left lower extremity weakness and involuntary movement	4/14/20
3	35	M	Headache, nausea, vomiting, and memory deterioration	6/42
4	49	F	Headache and fever with irrelevant answer	2/17/29
5	21	F	Headache, fever, slow response, and memory deterioration	14
6	27	M	Persistent vertigo with sudden onset of left lower extremity weakness	26
7	32	M	Headache, fever, and seizure	7
8	28	M	Headache, dizziness, and memory deterioration	2
9	44	F	Memory deterioration, slow response	7
10	50	M	Headache, fever, dizziness, paroxysmal loss of consciousness, seizure	3
11	20	F	Fever, disturbance of consciousness with limb seizure	5
12	47	F	Headache, fever, behavioral and psychological disorder	15
13	47	M	Headache, fever, dizziness	20
14	26	M	Headache and fever with paroxysmal limb seizure	15
15	25	M	Recurrent fever, paraphasia, memory deterioration, and limb seizure	85
16	46	M	Headache, fever, convulsion with psychological and behavioral disorder	60
17	64	M	Headache, dizziness, memory deterioration, paroxysmal loss of consciousness, and seizure	6

[a] The time from symptom onset to 3D-pCASL evaluation.

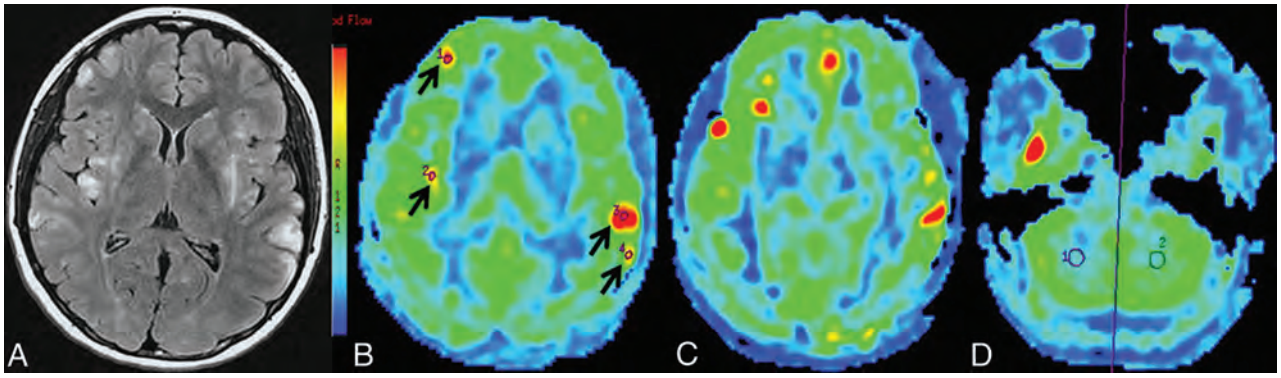

FIG 2. Case 11, a 20-year-old female patient at the acute stage (5 days after the onset of symptoms). *A*, Axial T2 FLAIR shows multiple lesions located in right frontal and bilateral insular lobes, as well as the bilateral temporal lobes. *B*, 3D-pCASL demonstrates increased CBF, consistent with involved regions on axial T2 FLAIR (*black arrows*). *C*, Other lesions also show hyperperfusion in different affected areas. *D*, ROI site selection for bilateral cerebellum CBF on the pCASL CBF color map.

for image registration with 3D-pCASL. Then 3D T1 fast-spoiled gradient recalled and T2 FLAIR images were cross-referenced for the lesion location. For each healthy individual, 3–5 round ROIs were placed in the temporal cortex as control group. To minimize individual differences, we applied the normalized CBF in this study. Previous studies have shown that cerebellar perfusion is relatively stable;[15,20] in addition, HSE rarely involves the cerebellum. Thus, the intraindividual normalization with the cerebellum was used. The nCBF value was defined as the CBF value of the lesions or the normal cortex in the temporal lobe divided by the mean CBF value in the cerebellum (nCBF = CBF lesion or temporal cortex/mean CBF cerebellum). The ROIs (approximately 100 mm^2) were positioned in the bilateral cerebellar hemispheres (Fig 2*D*), and the mean value was regarded as the final reference.

The ROIs were drawn by 2 neuroradiologists with >10 years' experience who were unaware of the clinical information and blinded to scan time points of the patients.

Statistical Analysis

Statistical analyses were performed with SPSS for Windows (Version 20.0; IBM, Armonk, New York). For each patient, the mean CBF value was acquired and calculated from all lesion foci. We compared the mean nCBF values of different stages with those of the control group. If 2 independent continuous variables complied with a normal distribution, the Student *t* test was used; otherwise, the Mann–Whitney *U* test was performed. Comparison among acute, subacute, and chronic stages was not performed. Interobserver variability assessments were evaluated with the intraclass correlation coefficient. The intraclass correlation coefficient was interpreted as follows: poor (<0.4), fair (0.4–0.59), good (0.6–0.74), and excellent (>0.74). $P < .05$ was considered statistically significant.

RESULTS

Patient Population

Demographic and clinical features of 17 consecutive patients with HSE are summarized in Table 1. On the basis of the laboratory tests, the causative agent was HSV-1 in all cases. Clinical manifestations were mainly such symptoms as headache ($n = 13$, 76.5%), fever ($n = 11$, 64.7%), seizure ($n = 8$, 47.1%), memory deterioration ($n = 6$, 35.3%), altered level of consciousness ($n = 4$, 23.5%),

Table 2: Initial conventional MR imaging and ASL findings after admission in patients with HSE

Case No.	Lesion Location[a]	T2WI	T1WI	CE	Perfusion[b]
1	L. T	Slight hyper/hypo	Slight hypo/hyper	NA	Obvious hyper
2	L. T, I	Slight hyper	Slight hypo/hyper	Gyriform enhancement	Obvious hyper
3	L. T, I	Slight hyper	Slight hypo/hyper	Patchy enhancement	Obvious hyper
4	R. F, T	Slight hyper	Slight hypo	None	Obvious hyper
5	L. F, I, and Bil. T	Slight hyper/hyper	Slight hypo/hyper	Gyriform enhancement	Obvious hyper
6	Bil. T, and R. P	Slight hyper/hyper	Slight hypo/hyper	None	Slight hypo
7	L. F, P, O, and Bil. I, T	Slight hyper	Iso	Patchy enhancement	Slight hyper/hyper
8	Bil. T, and L. I	Slight hyper	Slight hypo	None	Obvious hyper
9	Bil. F, T, I	Slight hyper	Slight hypo	None	Obvious hyper
10	Bil. F and cingulate gyrus	Slight hyper	Iso	None	Obvious hyper
11	R. F, and Bil. T, I	Slight hyper	Iso	None	Obvious hyper (multiple lesions)
12	Bil. F, T, I, and cingulate gyrus	Slight hyper	Slight hypo	Patchy enhancement	Obvious hyper
13	R. T, and Bil. I	Slight hyper	Slight hypo	Slight meningeal enhancement	Regional hyper
14	L. T, I	Slight hypo/hyper	Slight hypo/hyper	Gyriform enhancement	Regional hyper
15	L. T, I	Slight hyper/hyper	Slight hypo/hypo	Slight gyriform enhancement	Obvious hypo
16	R. T, I	Slight hyper/hyper	Slight hypo/hypo	Slight enhancement	Obvious hypo
17	R. T, I	Slight hyper	Slight hypo	None	Obvious hyper

Note:— R indicates right; L, left; Bil., bilateral; F, frontal lobe; T, temporal lobe; P, parietal lobe; O, occipital lobe; I, insular lobe; hyper, hyperintensity or hyperperfusion; hypo, hypointensity or hyperperfusion; Iso, isointensity; CE, contrast enhancement; NA, not applicable.

[a] Abnormal signals on T2 FLAIR.

[b] Perfusion performance on the first ASL examination.

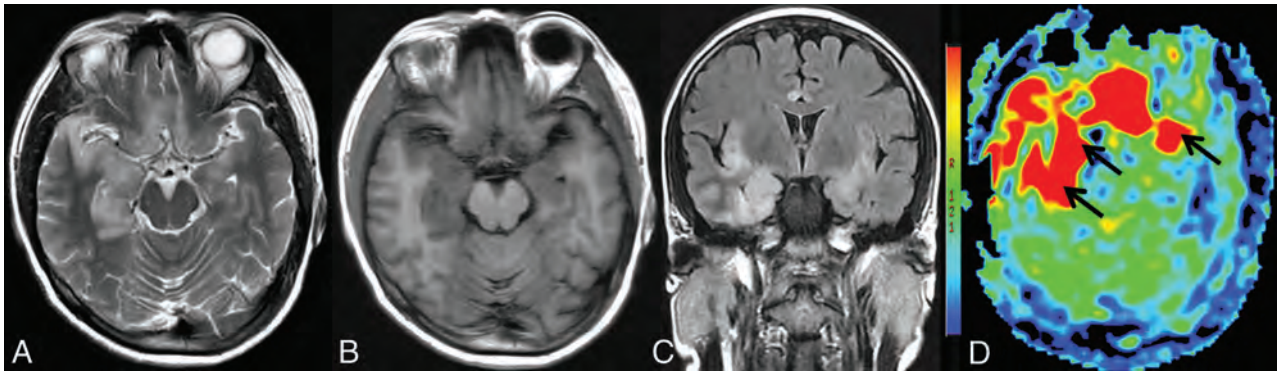

FIG 3. Case 12, a 47 -year-old female patient at the subacute stage (15 days after the onset of symptoms). *A*, Axial T2WI shows hyperintensities in bilateral frontal, temporal, and insular lobes and the cingulate gyrus. *B*, Axial T1WI demonstrates slight hypointensities. *C*, Slight hyperintensities are observed on coronal T2 FLAIR. *D*, 3D-pCASL shows high perfusion (*black arrows*) in the corresponding involved areas.

vertigo/dizziness ($n = 4$, 23.5%), behavioral and psychological disorder ($n = 2$, 11.8%), and nausea/vomiting ($n = 1$, 5.9%). The time from the onset of symptoms to the first 3D-pCASL scan ranged from 2 to 85 days (median time, 7 days) (Table 1).

Conventional MR Imaging Features

Table 2 summarizes the location of lesions and conventional MR imaging findings. The lesions were asymmetrically distributed bilaterally (52.9%) in 9 patients (patients 5, 6, 7, 8, 9, 10, 11, 12, and 13) and unilaterally (47.1%) in 8 patients (patients 1, 2, 3, 4, 14, 15, 16, and 17). The involved locations mainly included the temporal, frontal, and insular lobes; hippocampal region; and cingulate gyrus. The basal ganglia and cerebellum were spared in all cases.

ASL–MR Imaging Evaluation

By empiric visual inspection, 14 of 17 patients with HSE showed increased CBF in the affected regions on the initial 3D-pCASL scan, except for patients 6, 15, and 16 with hypoperfusion (Table 2). On the basis of the duration between the onset of symptoms and brain MR imaging, 11 cases were judged to be at the acute stage; 6 cases, at the subacute stage; and 6 cases, at the chronic stage. HSE demonstrated hyperperfusion in the acute (Fig 2) and subacute (Fig 3) stages, whereas it showed hypoperfusion in the chronic stage on 3D-pCASL (Fig 4*L*).

Interobserver reproducibility of CBF values was performed, and intraclass correlation coefficients were 0.92 at the acute stage, 0.90 at the subacute stage, 0.79 at the chronic stage, and 0.81 in the control group, respectively.

The mean CBF values of lesions in HSE were 121.5 ± 33.8 mL/100g/min (range, 59.5–162.3 mL/100g/min) in the acute stage, 98.3 ± 22.8 mL/100g/min (range, 66.1–126.5 mL/100g/min) in the subacute stage, and 33.9 ± 15.0 mL/100g/min (range, 23.0–63.1 mL/100g/min) in the chronic stage, respectively (Table 3). The mean nCBF values of lesions for different stages were 2.68 ± 0.54, 2.42 ± 0.52, and 0.87 ± 0.30 mL/100g/min at acute, subacute, and chronic stages, respectively (Table 3).

The mean nCBF values of acute and subacute lesions were significantly higher than those for the control group (both, $P < .001$), whereas the mean nCBF values of chronic lesions were lower than those of the control group ($P < .05$) (Fig 5*A*).

Serial 3D-pCASL was performed in 4 patients (patients 1–4), showing the time course of mean CBF changes of the lesions at different time points (Fig 5*B*) and dynamic perfusion reduction with time after treatment (Fig 4).

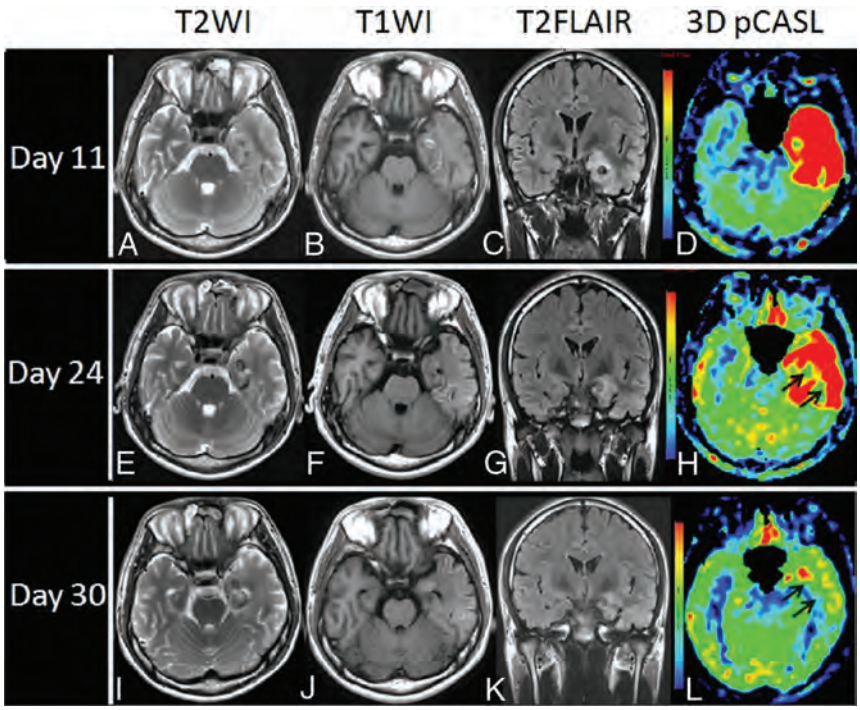

FIG 4. Case 1, a 17-year-old male patient. Serial T2WI (*A*, *E*, and *I*), T1WI (*B*, *F*, and *J*), and coronal T2 FLAIR (*C*, *G*, and *K*) demonstrate abnormal signals on the left temporal lobe and hippocampus. Serial follow-up 3D-pCASL perfusion imaging was performed, which reveals dynamic changes in the involved area on the 11th (*D*), 24th (*H*), and 30th day (*L*), respectively (*black arrows*). Meanwhile, the patient's condition markedly improved with effective therapeutic intervention.

Table 3: Mean CBF and mean nCBF values in the lesions at different stages and control group findings

Stage (Days)	No. of Cases	Range of CBF Values (mL/100g/min)	Mean CBF Values (mL/100g/min)	Mean nCBF Values
Acute stage (≤14)	11	59.5–162.3	121.5 ± 33.8	2.68 ± 0.54
Subacute stage (15–25)	6	66.1–126.5	98.3 ± 22.8	2.42 ± 0.52
Chronic stage (≥26)	6	23.0–63.1	33.9 ± 15.0	0.87 ± 0.30
Control group[a]	15	47.9–71.9	58.8 ± 7.0	1.33 ± 0.08

[a] The temporal cortex perfusion as a control reference.

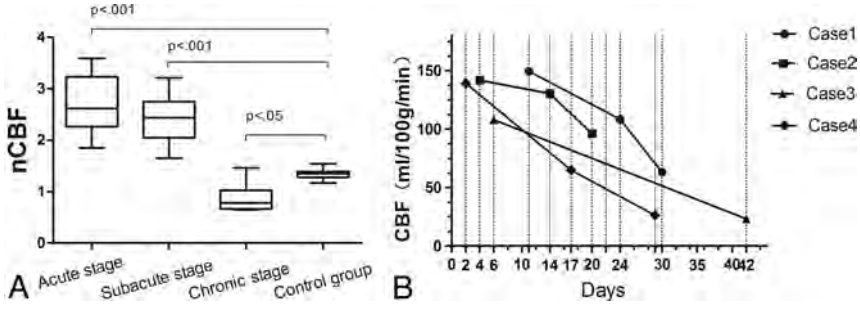

FIG 5. *A*, The boxplot of nCBF values in acute-, subacute-, and chronic-stage lesions and the control group, respectively. *B*, Time course of mean CBF changes for lesions at different time points in 4 follow-up HSE cases. The mean CBF value of the lesions gradually decreased after treatment in 4 case series.

DISCUSSION

In the present study, we explored the potential characteristics of 3D-pCASL perfusion in HSE. Our principal findings can be summarized as follows: 1) By visual assessment, patients with HSE demonstrated increased CBF in the affected area in the acute and subacute lesions, while CBF decreased in chronic lesions on 3D-pCASL; 2) quantitative analysis indicated that the nCBF values of acute and subacute lesions were obviously higher, whereas the nCBF values of chronic lesions were lower compared with the control group; and 3) follow-up 3D-pCASL examinations in 4 patients showed dynamic perfusion alterations with decreased perfusion after therapy.

HSE is a serious brain infection with high rates of mortality and morbidity, without timely and effective treatment.[21,22] The most important evidence in the diagnosis of HSE includes neurologic signs and symptoms and electroencephalogram and laboratory examinations. In clinical practice, once HSE is strongly suspected, the work-up must be initiated immediately and empiric antiviral therapy should be adopted promptly. However, the diagnosis is often delayed, and the main reason for the delay in the initiation of treatment is that the differential diagnosis should be made while waiting for the results of CSF polymerase chain reaction analysis.[23] Although virologic tests and pathologic biopsy are considered the criterion standard for the diagnosis of HSE, the former is relatively slow and has high false-negative rates within the initial few days[21] and the latter needs an invasive neurosurgical procedure, which is not widely accepted and applied in clinical practice.

Neuroimaging examinations may demonstrate characteristic findings of HSE and are of great importance in the differential diagnosis. As reported

in the literature,[5,11,24] our results also demonstrated that the lesions on conventional MR imaging manifest as an asymmetric involvement of the temporal lobes. Other brain regions, such as frontal lobes, insular lobes, hippocampus region, and cingulate cortex, might also be affected, while the basal ganglia region and cerebellum are rarely involved.[24] Routine MR images including T1WI, T2WI, T2 FLAIR, DWI, and postcontrast images are most important in identifying brain abnormalities in HSE.

Perfusion imaging has been widely applied in research and clinical practice to provide more information in various neurologic disorders.[25] Previous perfusion studies, either CTP[26] or SPECT,[27,28] have been reported for HSE, showing focal CBF abnormalities in the affected regions, but they are less often used in routine clinical practice because of contrast agent administration and radiation exposure. So far, 3D-pCASL perfusion alterations in HSE have not been well-described. Noguchi et al[29] have reported the application of ASL-MR imaging in central nervous system infections (including only 3 patients with HSE), with the results indicating that HSE showed high perfusion on ASL only by visual assessment without quantitative analysis. In this study, we found that the hyperintense lesions on T2 FLAIR demonstrated hyperperfusion in acute and subacute stages and hypoperfusion in the chronic stage.

The exact mechanism of increased CBF in the affected region of HSE has not been elucidated. We speculated that in the acute and subacute stages, angiitis due to direct invasion of HSV might cause blood vessel dilation,[30] resulting in increased metabolism and increased regional CBF. In the chronic stage, however, focal hypoperfusion in the involved areas was found possibly due to neuronal excessive damage and loss of brain parenchyma caused by a series of direct virus-mediated and indirect immune-mediated responses.[31] In addition, we also observed the quantitative perfusion alterations after appropriate therapy in 4 longitudinal HSE cases (Fig 5*B*). We found that high-perfusion lesions at the acute stage gradually evolved to low-perfusion areas with time, indicating that treatment may be effective (Fig 4).

Previous research has shown that perfusion alterations in patients with acute and subacute encephalitis have been correlated with clinical status, including seizure and clinical outcome.[30] Normal CBF in the subacute phase usually indicates a good neurologic outcome 1 year after the acute illness.[32] Moreover, we think 3D-pCASL perfusion can be helpful in the differential diagnosis among HSE, infarct, MELAS, and low- and high-grade gliomas, especially at the acute stage. Most important, acute infarct demonstrates hypoperfusion, which can be reliably differentiated from early HSE. MELAS initially misdiagnosed as HSE has been reported,[10] and both show hyperperfusion, while hyperperfusion is mainly located in the cortical region in MELAS.[17] MELAS and high-grade glioma, mimicking early HSE, present with hyperperfusion on 3D-pCASL, but differentiation can be made by combining the clinical manifestation, history, lesion location, and so forth.

According to the current guidelines,[21] it is generally recommended that the antiviral treatment be implemented in highly suspected HSE without the results of the CSF test. Our study found that hyperperfusion was observed in the affected area in the acute and subacute lesions in patients with HSE. If radiologists suggest the HSE diagnosis based on the ASL perfusion feature in the appropriate clinical setting, clinicians could be afforded the chance to start an immediate intervention before the results of laboratory tests are confirmed, which may give the patient a better prognosis. Therefore, we would expect that the initial 3D-pCASL after admission be performed as early as possible to diagnose and differentiate HSE from other neurologic disorders.

Besides its retrospective nature, some limitations of our study merit consideration. First, the sample size was relatively small, and serial 3D-pCASL was performed in only 4 patients, though the trends in perfusion changes were shown, with potential implications for follow-up evaluation and therapy monitoring. Second, other types of encephalitis and infectious diseases were not included in this study. Further investigation is required to establish the perfusion differences among different types of encephalitis.

CONCLUSIONS

Conventional MR imaging remains the optimal technique in the early diagnosis of HSE; however, we believe that 3D-pCASL can be used as an important adjunctive technique and that high perfusion in the lesion does add valuable information in diagnosing HSE, especially at the acute stage. Serial 3D-pCASL has a potential value in the evaluation of the therapeutic effect of HSE.

REFERENCES

1. Kiroğlu Y, Calli C, Yunten N, et al. **Diffusion-weighted MR imaging of viral encephalitis.** *Neuroradiology* 2006;48:875–80 CrossRef Medline
2. Choradia M, Rastogi H. **Viral encephalitis: imaging features.** *Apollo Medicine* 2008;5:111–17 CrossRef
3. Granerod J, Ambrose HE, Davies NW, et al. **Causes of encephalitis and differences in their clinical presentations in England: a multicentre, population-based prospective study.** *Lancet Infect Dis* 2010; 10:835–44 CrossRef Medline
4. Solomon T, Hart IJ, Beeching NJ. **Viral encephalitis: a clinician's guide.** *Pract Neurol* 2007;7:288–305 CrossRef Medline
5. Sili U, Kaya A, Mert A; HSV Encephalitis Study Group. **Herpes simplex virus encephalitis: clinical manifestations, diagnosis and outcome in 106 adult patients.** *Clin Virol* 2014;60:112–18 CrossRef Medline
6. Noguchi T, Yoshiura T, Hiwatashi A, et al. **CT and MRI findings of human herpesvirus 6-associated encephalopathy: comparison with findings of herpes simplex virus encephalitis.** *AJR Am J Roentgenol* 2010;194:754–60 CrossRef Medline
7. Sawlani V. **Diffusion-weighted imaging and apparent diffusion coefficient evaluation of herpes simplex encephalitis and Japanese encephalitis.** *J Neurol Sci* 2009;287:221–26 CrossRef Medline
8. Misra UK, Kalita J, Phadke RV, et al. **Usefulness of various MRI sequences in the diagnosis of viral encephalitis.** *Acta Tropica* 2010;116:206–11 CrossRef Medline
9. Hara Y, Ishii N, Sakai K, et al. **Herpes simplex encephalitis initially presented with parietal cortex lesions mimicking acute ischemic stroke: a case report [in Japanese].** *Rinsho Shinkeigaku* 2016;56:104–07 CrossRef Medline
10. Gooriah R, Dafalla BE, Venugopalan TC. **Led astray: MELAS initially misdiagnosed as herpes simplex encephalitis.** *Acta Neurol Belg* 2015;115:789–92 CrossRef Medline

11. Eran A, Hodes A, Izbudak I. **Bilateral temporal lobe disease: looking beyond herpes encephalitis.** *Insights Imaging* 2016;7:265–74 CrossRef Medline
12. Alsop DC, Detre JA, Golay X, et al. **Recommended implementation of arterial spin-labeled perfusion MRI for clinical applications: a consensus of the ISMRM perfusion study group and the European consortium for ASL in dementia.** *Magn Reson Med* 2015;73:102–16 CrossRef Medline
13. Petcharunpaisan S, Ramalho J, Castillo M. **Arterial spin labeling in neuroimaging.** *World J Radiol* 2010;2:384–98 CrossRef Medline
14. Detre JA, Rao H, Wang DJ, et al. **Applications of arterial spin labeled MRI in the brain.** *J Magn Reson Imaging* 2012;35:1026–37 CrossRef Medline
15. Xiao HF, Chen ZY, Lou X, et al. **Astrocytic tumour grading: a comparative study of three-dimensional pseudocontinuous arterial spin labelling, dynamic susceptibility contrast-enhanced perfusion-weighted imaging, and diffusion-weighted imaging.** *Eur Radiol* 2015;25:3423–30 CrossRef Medline
16. Bokkers RP, Hernandez DA, Merino JG, et al. **Whole-brain arterial spin labeling perfusion MRI in patients with acute stroke.** *Stroke* 2012;43:1290–94 CrossRef Medline
17. Li R, Xiao HF, Lyu JH, et al. **Differential diagnosis of mitochondrial encephalopathy with lactic acidosis and stroke-like episodes (MELAS) and ischemic stroke using 3D pseudocontinuous arterial spin labeling.** *J Magn Reson Imaging* 2017;45:199–206 CrossRef Medline
18. Venkatesan A, Tunkel AR, Bloch KC, et al; International Encephalitis Consortium. **Case definitions, diagnostic algorithms, and priorities in encephalitis: consensus statement of the international encephalitis consortium.** *Clin Infect Dis* 2013;57:1114–28 CrossRef Medline
19. Singh TD, Fugate JE, Hocker S, et al. **Predictors of outcome in HSV encephalitis.** *J Neurol* 2016;263:277–89 CrossRef Medline
20. Arbab AS, Aoki S, Toyama K, et al. **Brain perfusion measured by flow-sensitive alternating inversion recovery (FAIR) and dynamic susceptibility contrast-enhanced magnetic resonance imaging: comparison with nuclear medicine technique.** *Eur Radiol* 2001; 11:635–41 CrossRef Medline
21. Kennedy PG, Steiner P. **Recent issues in herpes simplex encephalitis.** *J Neurovirol* 2013;19:346–50 CrossRef Medline
22. Jha S, Patel R, Yadav RK, et al. **Clinical spectrum, pitfalls in diagnosis and therapeutic implications in herpes simplex encephalitis.** *J Assoc Physicians India* 2004;52:24–26 Medline
23. Hughes PS, Jackson AC. **Delays in initiation of acyclovir therapy in herpes simplex encephalitis.** *Can J Neurol Sci* 2012;39:644–48 CrossRef Medline
24. Adam G, Ferrier M, Patsoura S, et al. **Magnetic resonance imaging of arterial stroke mimics: a pictorial review.** *Insights Imaging* 2018; 9:815–31 CrossRef Medline
25. Essig M, Nguyen TB, Shiroishi MS, et al. **Perfusion MRI: the five most frequently asked clinical questions.** *AJR Am J Roentgenol* 2013;201:W495–510 CrossRef Medline
26. Marco de Lucas E, G, Mandly A, Gutierrez A, et al. **Computed tomography perfusion usefulness in early imaging diagnosis of herpes simplex virus encephalitis.** *Acta Radiol* 2006;47:878–81 CrossRef Medline
27. Launes J, Nikkinen P, Lindroth L, et al. **Diagnosis of acute herpes simplex encephalitis by brain perfusion single photon emission computed tomography.** *Lancet* 1988;1:1188–91 Medline
28. De Deyn PP, Van den Broucke PW, Pickut BA, et al. **Perfusion and thallium single photon emission computed tomography in herpes simplex encephalitis.** *J Neurol Sci* 1998;157:96–99 CrossRef Medline
29. Noguchi T, Yakushiji Y, Nishihara M, et al. **Arterial spin-labeling in central nervous system infection.** *Magn Reson Med Sci* 2016;15:386–94 CrossRef Medline
30. Wong AM, Yeh CH, Lin JJ, et al. **Arterial spin-labeling perfusion imaging of childhood encephalitis: correlation with seizure and clinical outcome.** *Neuroradiology* 2018;60:961–70 CrossRef Medline
31. Chucair-Elliott AJ, Conrady C, Zheng M, et al. **Microglia-induced IL-6 protects against neuronal loss following HSV-1 infection of neural progenitor cells.** *Glia* 2014;62:1418–34 CrossRef Medline
32. Kao CH, Wang SJ, Mak SC, et al. **Viral encephalitis in children: detection with technetium-99m HMPAO brain single-photon emission CT and its value in prediction of outcome.** *AJNR Am J Neuroradiol* 1994;15:1369–73 Medline

Cerebral Ketones Detected by 3T MR Spectroscopy in Patients with High-Grade Glioma on an Atkins-Based Diet

A. Berrington, K.C. Schreck, B.J. Barron, L. Blair, D.D.M. Lin, A.L. Hartman, E. Kossoff, L. Easter, C.T. Whitlow, Y. Jung, F.-C. Hsu, M.C. Cervenka, J.O. Blakeley, P.B. Barker, and R.E. Strowd

ABSTRACT

BACKGROUND AND PURPOSE: Ketogenic diets are being explored as a possible treatment for several neurological diseases, but the physiologic impact on the brain is unknown. The objective of this study was to evaluate the feasibility of 3T MR spectroscopy to monitor brain ketone levels in patients with high-grade gliomas who were on a ketogenic diet (a modified Atkins diet) for 8 weeks.

MATERIALS AND METHODS: Paired pre- and post-ketogenic diet MR spectroscopy data from both the lesion and contralateral hemisphere were analyzed using LCModel software in 10 patients.

RESULTS: At baseline, the ketone bodies acetone and β-hydroxybutyrate were nearly undetectable, but by week 8, they increased in the lesion for both acetone ($0.06 \pm 0.03 \geq 0.27 \pm 0.06$ IU, $P = .005$) and β-hydroxybutyrate ($0.07 \pm 0.07 \geq 0.79 \pm 0.32$ IU, $P = .046$). In the contralateral brain, acetone was also significantly increased ($0.041 \pm 0.01 \geq 0.16 \pm 0.04$ IU, $P = .004$), but not β-hydroxybutyrate. Acetone was detected in 9/10 patients at week 8, and β-hydroxybutyrate, in 5/10. Acetone concentrations in the contralateral brain correlated strongly with higher urine ketones ($r = 0.87$, $P = .001$) and lower fasting glucose ($r = -0.67$, $P = .03$). Acetoacetate was largely undetectable. Small-but-statistically significant decreases in NAA were also observed in the contralateral hemisphere at 8 weeks.

CONCLUSIONS: This study suggests that 3T MR spectroscopy is feasible for detecting small cerebral metabolic changes associated with a ketogenic diet, provided that appropriate methodology is used.

ABBREVIATIONS: AcAc = acetoacetate; Ace = acetone; bHB = β-hydroxybutyrate; IU institutional units; Lac = lactate; KD = ketogenic diet; WHO = World Health Organization

Ketogenic diets (KDs) have been used to treat epilepsy for almost 100 years[1] and recently have been explored for many other neurological conditions, including multiple sclerosis, Parkinson disease, Alzheimer disease, amyotrophic lateral sclerosis, migraine, autism, and glioma.[2–8] The physiologic effects of these diets are incompletely understood, but it is clear that they modify the body's energy metabolism, leading to lower systemic glucose levels and increased levels of ketone bodies. The ketone bodies β-hydroxybutyrate (bHB) and acetoacetate (AcAc) are produced in the liver from fatty acids under carbohydrate-restricted diets, and a third ketone body, acetone (Ace), is produced as the result of the breakdown of AcAc. The ketones are water soluble and transported to other parts of the body, including the brain. However, a challenge in the application of the ketogenic diet is measuring its effect

Received June 17, 2019; accepted after revision September 04.

From the Russell H. Morgan Departments of Radiology and Radiological Science (A.B., D.D.M.L., P.B.B.), Neurology (K.C.S., L.B., A.L.H., E.K., M.C.C., J.O.B., R.E.S.), Pediatrics (L.B., A.L.H.), and Institute of Clinical and Translational Research (B.J.B.), Johns Hopkins University School of Medicine, Baltimore, Maryland; Clinical and Translational Science Institute (L.E., R.E.S.), Departments of Radiology (C.T.W., Y.J.), Biostatistics and Data Science (F.-C.H.), Division of Public Health Sciences, and Departments of Neurology, Hematology and Oncology (R.E.S.), Wake Forest School of Medicine, Winston-Salem, North Carolina; and F. M. Kirby Research Center for Functional Brain Imaging (P.B.B., R.E.S.), Kennedy Krieger Institute, Baltimore, Maryland.

A. Berrington and K.C. Schreck contributed equally to this work.

This work was undertaken while A.L. Hartman was a full-time employee of Johns Hopkins University.

This work was supported by the National Center for Advancing Translational Sciences, National Institutes of Health KL2TR001421 and CTSA grant UL1TR001420, and the National Cancer Institute's Cancer Center Support Grant award number P30CA012197 issued to the Wake Forest Baptist Comprehensive Cancer Center. It was also supported, in part, by the National Institutes of Health P41EB015909.

The content is solely the responsibility of the authors and does not necessarily represent the official views of the National Cancer Institute or the National Institute of Neurological Disorders and Stroke or the National Institutes of Health.

Dr Berrington is now with the Sir Peter Mansfield Imaging Centre, School of Physics and Astronomy, University of Nottingham, Nottingham, UK.

Please address correspondence to Peter B. Barker, PhD, Department of Radiology, Johns Hopkins University School of Medicine, 600 N Wolfe St, Park 367B, Baltimore, MD 21287; e-mail: pbarker2@jhmi.edu

Indicates open access to non-subscribers at www.ajnr.org

Indicates article with supplemental on-line photos.

http://dx.doi.org/10.3174/ajnr.A6287

on cerebral metabolism. While dietary compliance may be estimated from measurements of urine ketones, weight, and dietary food records as well as measurement of serum ketone and glucose (and other) levels,[9–12] these measures provide a picture of the body's ketogenic state but may not reflect the level of cerebral ketosis.[13]

Because ketone bodies are known to accumulate in the brain in low millimolar concentrations during ketosis, they should be detectable using the noninvasive technique of proton MR spectroscopy. The earliest demonstration of this was in patients recovering from diabetic ketoacidosis, in whom it was shown that short-TE STEAM MR spectroscopy at 1.5T was able to detect elevated levels of brain Ace.[14] Subsequently both bHB and AcAc (as well as lactate [Lac]) were reported to be detected in children recovering from diabetic ketoacidosis by using a long-TE point-resolved spectroscopic sequence at 1.5T.[15] Increases in bHB and Lac using edited 4T MR spectroscopy have also been observed during fasting in healthy subjects,[16] and increased Ace (and possibly AcAc) was observed during ketogenic diet treatment for epilepsy using 1.5T MR spectroscopy.[17,18] Increases in Ace and AcAc levels were reported using short-TE 3T MR spectroscopy in patients with primary brain tumors undergoing the ketogenic diet.[19]

Overall, these prior studies indicate that ketone bodies are detectable by MR spectroscopy in some cases but that the results are often equivocal because of their low concentrations. In addition, it can be difficult to distinguish Ace from AcAc because their chemical shifts are very similar (2.22 versus 2.27 ppm, respectively), and the bHB doublet (at 1.20 ppm) is potentially obscured by overlap with lipids or lactate as well as signal losses due to chemical shift displacement effects at intermediate TE values.[20] Therefore, there is no general concordance in the literature as to which ketone bodies can be most reliably detected in the brain using MR spectroscopy or which acquisition methodology is optimal.

The purpose of this study was to evaluate the utility of short-TE 3T MR spectroscopy to quantify cerebral ketone body and metabolite levels in patients with high-grade glioma enrolled in an ongoing open-label, single-arm, Phase II clinical trial of the KD for 8 weeks. Note that this is an interim analysis that focuses only on the MR spectroscopy data. The primary objective of the main study is to investigate the feasibility of the dietary intervention as measured by dietary compliance. Here, the results of an interim analysis assessing the feasibility of MR spectroscopy for measuring cerebral ketones and the ability to detect KD-related changes are reported; the full clinical trial is still ongoing, and the results of the primary objective will be reported at a later date.

MATERIALS AND METHODS

Study Design and Participants

The study was conducted at Johns Hopkins and the Wake Forest Baptist Medical Center with the approval of both institutional review boards. Written informed consent was obtained from all patients. The trial design was a single-arm Phase II study designed to assess the feasibility, safety, and activity of a modified Atkins-based diet to prevent tumor recurrence in patients with glioma following the completion of adjuvant chemotherapy. Eligible patients were at least 18 years of age and had a Karnofsky Performance Scale status of ≥60 and a diagnosis of high-grade astrocytoma (World Health Organization [WHO] grade III or IV) and had completed ≥80% of prescribed radiation therapy with concurrent temozolomide and adjuvant temozolomide without Common Terminology Criteria for Adverse Events (CTCAE) grade 4 leukopenia, neutropenia, or thrombocytopenia. Patients were excluded if they had a history of a metabolic disorder, a body mass index >35.0 or <20.0 kg/m^2, or a milk allergy.

Treatment

The study intervention consisted of an 8-week diet, which included 2 days of fasting and 5 days on a modified Atkins diet each week. The nonconsecutive fasting days had strict caloric restriction of up to 20% of the recommended daily caloric intake of the patient provided via a 4:1 ratio ketogenic liquid (eg, KetoCal drink; Nutricia, Gaithersburg, Maryland). Modified Atkins diet days required net carbohydrate restriction to 20 g per day with no caloric restriction. All diets were customized with the guidance of a registered dietitian.

MR Imaging

Patients underwent MR spectroscopy at the beginning and end of the diet (8-week interval) on a 3T MR imaging scanner at either Johns Hopkins (12 patients) on a 3T Achieva MR imaging system (Philips Healthcare; Best, the Netherlands) or Wake Forest (2 patients) on a 3T Magnetom Skyra MR imaging system (Siemens, Erlangen, Germany) using 32-channel head coils. Conventional MR imaging included a 1-mm isotropic T1-weighted MPRAGE scan and axial FLAIR images. A $2 \times 2 \times 2$ cm^3 voxel was placed in a region maximally occupied by the lesion, while avoiding structures that might degrade spectral quality such as fluid-filled spaces, regions of high magnetic susceptibility variation (eg, due to hemorrhage, surgical clips, or air-tissue interfaces), and lipid signals from the scalp. In patients with a gross total resection, the lesion voxel was placed adjacent to the resection cavity, often in perilesional regions of T2 hyperintensity. A second voxel was placed in the contralateral hemisphere mirroring the location of the lesion voxel.

MR spectroscopy was performed using a semi localization by adiabatic selective refocusing (semi-LASER) sequence[21,22] (TR = 2.2 seconds, TE = 34 ms/40 ms at Johns Hopkins/Wake Forest). The semi-LASER sequence used broadband adiabatic refocusing pulses (3 kHz/5 kHz for Johns Hopkins/Wake Forest), which have excellent slice profiles. In addition to acquiring water-suppressed data (NEX = 128), 4 excitations were recorded without water suppression. Scan time per voxel was 4 minutes 54 seconds, including 2 dummy excitations to establish the steady-state. Before acquisition, field homogeneity was optimized up to second order using either a FASTMAP-based technique[23] or gradient-echo-based shimming at Johns Hopkins and Wake Forest, respectively.

The LCModel program (http://www.lcmodel.com/)[24] was used to fit spectra, with basis sets for each site containing 3 ketone bodies (Ace, bHB, and AcAc) (On-line Fig 1) as well as standard

MR spectroscopy metabolites: alanine, ascorbate, aspartate, creatine, γ-aminobutyric-acid, glutamine, glutamate, glycine, myo-inositol, Lac, glycerophosphocholine, phosphocreatine, phosphorylethanolamine, scyllo-inositol, taurine, glucose, glutathione, NAA, *N*-acetylaspartylglutamate, and 2-hydroxyglutarate. Literature values for chemical shifts and coupling constants were taken from de Graaf,[25] Govindaraju et al,[26] and Tkac.[27]Basis spectra were generated using density matrix simulations, which incorporated real refocusing pulse information and 2D localization (Matlab; MathWorks, Natick, Massachusetts). Macromolecular contributions in the spectra were modeled using simulated components available in LCModel. Metabolite concentrations were estimated relative to an internal water reference (assuming a bulk water concentration of 55.5 mol/L), which were corrected for water T2 decay differences in tumors[28] and healthy brain.[29] Given the low concentrations of cerebral ketones in this study population, a rejection threshold using Cramér-Rao lower bounds of a metabolite fitting of >80% was applied to avoid statistical biasing of results when comparing increases of very low-concentration metabolites.[30] Additionally, no correction for either tissue water or CSF content of the voxel was applied; thus, reported concentrations are given in institutional units (IU), which are approximately equivalent to millimolar.

Statistical Analysis

Means and standard errors of the mean are presented for normally distributed continuous measures, and medians and ranges are presented for non-normally distributed continuous measures. Percentages and counts are presented for discrete measures. Approximate 95% confidence intervals on individual metabolite fits are calculated as 2× Cramér-Rao as indicated by Provencher.[24] After fitting spectral data with the LCModel, we performed statistical analysis using STATA 15 2017 (StataCorp, College Station, Texas). For this analysis of feasibility, the primary outcome was the change in cerebral ketone concentrations from baseline to week 8. The primary analysis focused on the 3 ketone bodies Ace, bHB, and AcAc. Differences among groups at each time point were assessed by paired *t* tests for normally distributed continuous measures. After we corrected for multiple comparisons using a Bonferroni correction, an acceptance threshold of $P < .008$ (= .05/6 corrected for the 3 primary ketone metabolites of interest at 2 time points) was considered significant. The Spearman rank correlation coefficient was calculated to evaluate the association among continuous measures.

RESULTS

Patient Characteristics

At the time of analysis, 14 subjects were enrolled. Two participants were excluded from the MR spectroscopy analysis due to either scanner error or a large spectral line width arising from magnetic susceptibility gradients in the temporal lobe, respectively. Only baseline MR spectroscopy data were available for 2 patients who did not complete the 8-week dietary intervention. Demographics of the 10 patients with evaluable pre- and postintervention MR spectroscopy are given in Table 1: Seven (70%) had WHO grade III anaplastic astrocytomas, and 3 (30%) had glioblastomas (Table 1). Two patients (20%) had previously undergone biopsy; 3 (30%), a subtotal resection; and 5 (50%), a gross total resection.

Table 1: Demographic features of participants

Demographics	(No.) (%)
Age (mean) (SD) (yr)	49.2 (10.6)
Male sex	6 (60%)
WHO grade	
III	7 (70%)
IV	3 (30%)
Extent of resection	
Biopsy	2 (20%)
Subtotal	3 (30%)
Gross total	5 (50%)
IDH1/2 mutational status	
IDH wild-type	4 (40%)
IDH mutant	6 (60%)
MGMT promoter methylation status	
Unmethylated	4 (40%)
Methylated	4 (40%)
Unknown	2 (20%)
Concurrent TMZ (median) (range) (% completed)	100% (80%–100%)
Adjuvant TMZ (median) (range) (No. of cycles)	6 (6–12)

Note:—*IDH* indicates *isocitrate dehydrogenase*; MGMT, O^6-methylguanine-DNA methyltransferase; TMZ, temozolomide.

With regard to biomarkers of dietary compliance, no participants had detectable urine ketones at baseline, and 9 of the 10 patients who completed the study achieved some level of ketosis, measured as trace (5 mg/dL) or greater, during the study. Eight (80%) achieved moderate (40 mg/dL) or greater urinary ketosis. Average fasting glucose levels in participants decreased modestly from 91 mg/dL at baseline to 84 mg/dL at 8 weeks.

Cerebral Ketone Levels

Figure 1 shows representative spectra from a single patient together with results of the LCModel fitting. Spectra and fitting results from each patient are provided in On-line Fig 2. Quantitative MR spectroscopy results for ketone bodies are summarized in Table 2; and for both ketones and other brain metabolites, in Fig 2. Mean water line widths from contralateral and lesion voxels were 6.7 ± 0.9 and 6.1 ± 1.9 Hz, respectively, indicating good shimming in quantified spectra.

In the lesion spectra, the ketone bodies Ace and bHB were detectable in a greater number of patient spectra following the dietary intervention according to the defined criteria. AcAc was only measured in 1 spectrum at baseline and week 8. Ketone bodies were largely undetectable in the lesion at baseline and increased significantly at week 8 for both Ace (baseline: 0.06 ± 0.03; week eight: 0.27 ± 0.06 IU; $P = .005$) and bHB (baseline: 0.07 ± 0.07; week eight: 0.79 ± 0.32 IU; $P = .046$, not significant after Bonferroni correction; Table 2). Overall, Ace was detected in 90%, and bHB, in 50% of lesion scans at week 8. The mean Cramér-Rao lower bounds of ketone fitting after KD in the lesion were 29% for Ace and 34% for bHB, which were considerably lower than the rejection threshold.

Changes in the contralateral brain largely mirrored those seen in the lesion. Ace measures increased significantly from baseline (0.04 ± 0.01 IU, mean Cramér-Rao = 64%) to (0.16 ± 0.04 IU, mean Cramér-Rao = 39%) ($P = .004$) at week 8. bHB in the

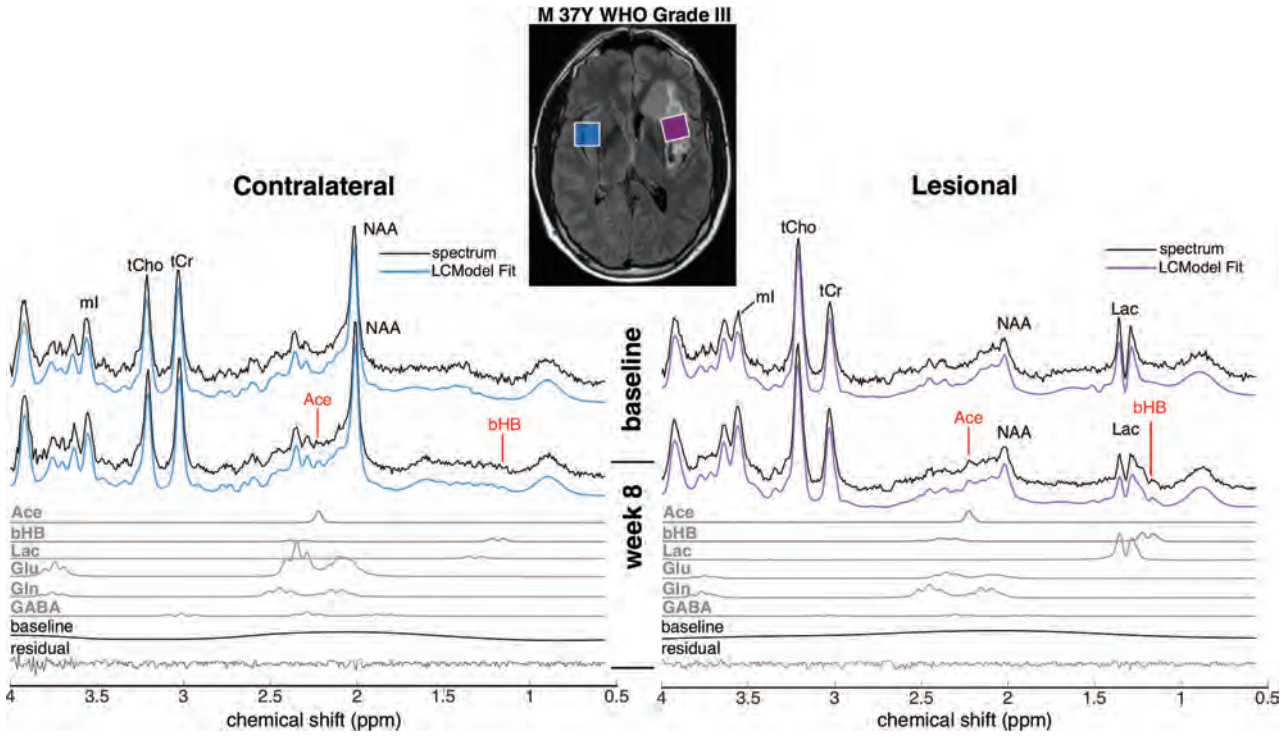

FIG 1. Representative MR spectra from 1 patient, together with spectral fitting results from the LCModel, at baseline and week 8. FLAIR MR imaging shows the voxel placement in the lesion in the left insular cortex and the corresponding voxel in the contralateral hemisphere. Individual fits of Ace and bHB at week 8 are also shown below the spectra, as well as those from Lac, glutamate (Glu), glutamine (Gln), and γ-aminobutyric acid (GABA). tCho indicates total Cho; tCr, total creatine; mI, myo-inositol.

Table 2: Ketone body concentrations as measured by MR spectroscopy before and after treatment with a ketogenic diet in both the lesion and contralateral brain[a]

	Baseline (IU)	No.	Week 8 (IU)	No.	*P* Value
Ace					
Contralateral brain	0.04 ± 0.01	5	0.16 ± 0.04	9	.004[b]
Lesion	0.06 ± 0.03	4	0.27 ± 0.06	9	.005[b]
bHB					
Contralateral brain	0.09 ± 0.06	2	0.28 ± 0.08	6	.12
Lesion	0.07 ± 0.07	1	0.79 ± 0.32	5	.046[c]
AcAc					
Contralateral brain	0.07 ± 0.04	3	0.06 ± 0.03	3	.76
Lesion	0.03 ± 0.03	1	0.02 ± 0.02	1	.72

[a] *P* value was computed using paired *t* tests; No. indicates number of spectra in which the metabolite was fitted according to defined criteria. Errors are provided as standard error of the mean. Data are means unless otherwise indicated.
[b] $P \leq .008$ (Bonferroni-adjusted threshold).
[c] $P \leq .05$.

contralateral brain also increased from 0.09 ± 0.06 to 0.28 ± 0.08 IU; however, there was wider variability in bHB, and this increase was not statistically significant ($P = .12$). Ace was detected in 90% and bHB in 60% of 8-week scans in the contralateral brain region.

Most interesting, there was significantly more Ace in the lesion than in the contralateral brain at week 8 (0.27 ± 0.06 versus 0.16 ± 0.04 IU, $P = .012$). A similar pattern was noted with bHB, though this difference was not statistically significant (0.79 ± 0.32 versus 0.28 ± 0.08 IU, $P = .17$).

Other Brain Metabolites

As expected, total NAA was lower in the lesion than in the contralateral brain both at baseline ($P = .02$) and at 8 weeks. Lac was significantly higher in the lesion compared with contralateral brain both at baseline and week 8 (2.5 ± 0.74 versus 0.25 ± 0.09 IU, $P = .004$). Otherwise, no significant differences in indigenous cerebral metabolites were observed between the lesion and contralateral side, including total choline ($P = .14$) and total creatine ($P = .09$).

Contralateral total NAA concentrations decreased by a small-but-significant amount from 7.9 ± 0.2 to 7.7 ± 0.2 IU ($P = .02$) during the 8-week treatment period, while lesion total NAA levels were stable. There were no detectable changes in the concentrations of any other reported metabolite in either the lesion or contralateral brain, including lactate ($P = 0.8$ for lesion, $P = .3$ for contralateral), during the 8-week period.

Correlation of Brain Ketone Levels with Peripheral Markers of Ketosis

Overall, patients with greater systemic measures of dietary compliance (as evidenced by urine ketones and fasting blood glucose at week 8) showed higher cerebral ketone concentrations. At week 8 MR spectroscopy, higher contralateral brain Ace levels were significantly associated with greater urine ketones (Fig 3*A*, $r = 0.87$, $P = .001$) and lower week 8 fasting glucose (Fig 3*B*, $r = -0.67$, $P = .03$). A similar trend was also seen for lesion Ace

concentrations and both urine ketones ($r = 0.54$, $P = .11$) and fasting glucose ($r = -0.54$, $P = .10$), but it did not reach significance. No significant correlations were seen between bHB levels in either the lesion or contralateral brain and urine ketones or fasting glucose levels.

DISCUSSION

The main finding of this study is that short-TE single-voxel brain MR spectroscopy performed at 3T using 32-channel receive head coils, in combination with LCModel analysis, was able to measure concentrations of ketone body Ace (90% of spectra) and, to a lesser extent, bHB (50%–60% of spectra) in patients with glioma who were on a modified Atkins diet for 8 weeks. Furthermore, the brain Ace concentrations were found to correlate with concurrent urine ketone level measurements. These results suggest that localized MR spectroscopy may provide a useful measure of brain ketosis and a possible noninvasive pharmacodynamic marker in clinical trials of ketogenic diets in glioma or other neurologic conditions.

However, the amplitudes of the ketone body signals in the spectrum are very small in this dietary treatment, so robust acquisition and analysis methods are required to estimate their concentrations. In the current study, spectral quality was maximized through the combined use of a semi-LASER localization sequence, high-order shimming, and 32-channel receiver coils. In addition, a carefully simulated and constructed LCModel basis set for the specific acquisition and quantitative criteria for considering a peak detectable or not were used for spectral analysis.

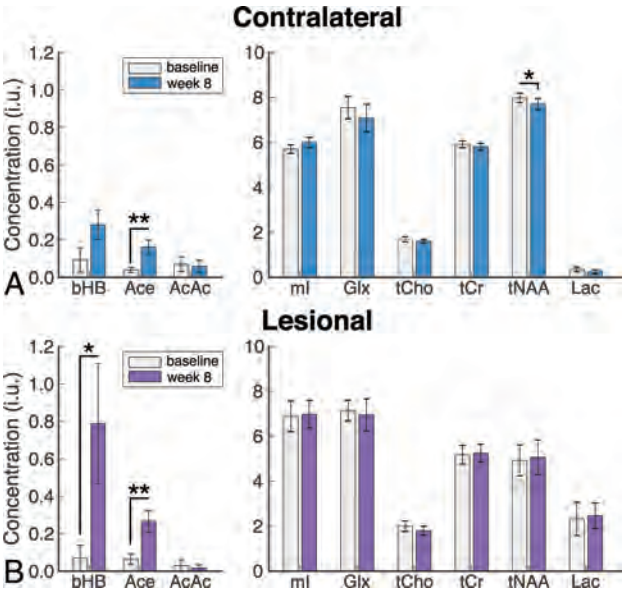

FIG 2. Ketone body (*left panel*) and metabolite (*right panel*) concentrations as measured by MR spectroscopy at baseline and week 8 in the contralateral brain (*A*) and lesion (*B*) for all subjects. The *asterisk* indicates $P \leq .05$; *double asterisks*, $P \leq .008$ (Bonferroni-adjusted threshold for ketone bodies). Glx indicates glucose; tCho, total choline; tCr, total creatine; tNAA, total NAA; mI, myo-inositol.

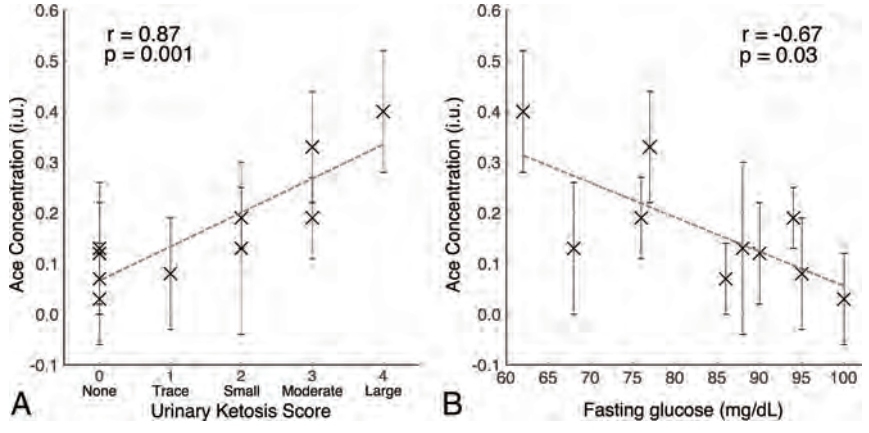

FIG 3. Association between contralateral brain acetone levels estimated by MR spectroscopy and systemic measures of ketosis at week 8. Spearman rank correlation between acetone concentrations (*IU error bars* represent the ±95% confidence interval based on the LCModel Cramér-Rao values) in the contralateral brain at week 8 plotted against the urinary ketosis score (*A*) and fasting serum glucose levels (*B*). Urine ketones are defined as 1, trace (~5 mg/dL); 2, small (~15 mg/dL); 3, moderate (~40 mg/dL); and 4, large (≥80 mg/dL).

Sensitivity of Detection of Ace, AcAc, and bHB

The ketone body most reliably detected in this study was Ace, which is consistent with prior KD studies in patients with epilepsy[18] and also in patients recovering from diabetic ketoacidosis.[14] However, other studies during fasting or ketogenic diet have also reported increases in bHB, AcAc, or Lac.[16,17,19] The MR spectroscopy detectability of these compounds is not uniform; Ace signal is a singlet at 2.22 ppm, which arises from 6 equivalent protons, whereas AcAc (a singlet at 2.27 ppm) arises from 3 equivalent protons and, therefore, is half the amplitude for the same molecular concentration. The 1.2-ppm bHB signal also arises from 3 protons but is a doublet due to J-coupling, so the peak height is further reduced by a factor of 2. The lack of correlation of bHB with systemic measures is likely the result of its lower sensitivity of detection by MR spectroscopy, resulting in fewer available data points and greater variability, and is not necessarily indicative of a true lack of a relationship between cerebral bHB and urine ketones or fasting glucose levels. The detectability of bHB may also be partially compromised by overlap with lipid resonances or reduced signal intensity due to J-modulation effects if intermediate or long TE values are used. Therefore, from a technical viewpoint, Ace is the ketone body most favorable for detection by MR spectroscopy.

The detectability of the 1.19-ppm resonance of bHB might be improved by using an optimized long-TE sequence (eg, $1/J = 160$ ms, $J = 6.3$ Hz) to discriminate it from other resonances such as lipid; however, this would also result in appreciable signal loss due to T2 decay and likely worsen detection of the small concentration singlet resonances of Ace and AcAc. Because lactate and bHB have similar coupling constants, the evolution of their signals as a function of

TE is also very similar (On-line Fig 3), so altering the TE is unlikely to improve separation of bHB and Lac. However, at 3T, the methyl doublets of bHB and Lac at 1.19 and 1.31 ppm are usually sufficiently well-resolved to be individually quantified by the LCModel, except perhaps in regions of poor B_0 field homogeneity.

Assignment of the singlet resonance at 2.2 ppm to either Ace or AcAc is quite challenging at typical in vivo line widths; the 0.05-ppm chemical shift difference between Ace and AcAc corresponds to approximately 6 Hz at 3T, which is comparable with the spectral line widths observed in this study (6.1 ± 1.9 Hz in lesions). However, LCModel fitting also makes use of the 3.43-ppm methylene (CH_2) peak of AcAc, which is not present in Ace, and in the current study, few of the LCModel analyses could identify this resonance (however, this peak may also be difficult to detect because it potentially overlaps with other peaks such as scyllo-inositol, taurine, and myo-inositol). Therefore, it seems likely that the 2.2-ppm peak arises from Ace, not AcAc; this finding is consistent with a previous study in patients with diabetic ketoacidosis that reported that bHB or AcAc can be converted to Ace quite rapidly.[15]

Choice of Cramér-Rao Thresholds for Detection of Metabolites

Traditionally, a Cramér-Rao lower bound (CRLB) threshold of 20% has been suggested for determining whether a metabolite concentration reported by the LCModel should be considered reliable or not.[24] However, recently it has been shown that using a low-threshold value such as this may lead to bias and non-normal distributions of metabolite concentrations, particularly for changes in low-concentration compounds.[30] Reported sensitivities of detection will vary according to the threshold chosen; the 80% value chosen here represents a reasonable compromise between under- and overfitting the data and avoiding bias for the low-concentrations ketone bodies. Hence, although Ace was measured in 5/10 contralateral spectra at baseline with these criteria, the mean concentration was over 2× lower compared with week 8 spectra ($n = 9/10$), and the associated error in fitting this low concentration was higher (64% versus 39%). In addition, the Ace measurements correlated well with peripheral measures of ketosis, suggesting that the 80% cutoff chosen did not result in erroneous values being reported.

Comparison of Ketone Bodies in Lesion and Contralateral Brain

One of the findings of this study was that lesion ketone levels were higher than in the contralateral brain; this is consistent with a KD study using ^{13}C MR spectroscopy in preclinical brain tumor models,[31] which found that the ketone body monocarboxylate transporter was upregulated, facilitating uptake and oxidation of ketone bodies in the tumors. Other underlying causes for this observation might be increased delivery of ketones (increased blood volume) and/or increased blood-brain barrier permeability in the lesions. One previous MR spectroscopic imaging[32] study also found that Ace was more detectable in fluid-filled spaces (such as ventricular CSF) compared with normal brain, perhaps due to longer T2 in these regions. It is therefore also possible that the lesion spectra in the current study (usually placed in regions of T2 hyperintensity on MR imaging) may also show increases in Ace signal for this reason.

Comparison of Other Brain Metabolites in Lesions and Contralateral Brain

The lesion spectra observed in this study are very consistent with those previously reported in the literature.[33] NAA was significantly lower in the lesion, consistent with neuroaxonal loss either in the tumor or peritumor regions, while Lac was significantly elevated due to nonoxidative glycolysis often seen in brain tumors. While it may seem surprising that Cho levels were not significantly elevated in the lesion, it should be remembered that all cases were scanned postsurgery and chemoradiation and that in 5 of 10 cases, a gross total resection was performed. In these cases, the lesion voxel placed adjacent to the surgical cavity may or may not contain any tumor tissue.

Effects of KD on Other Brain Metabolites and Brain MR Imaging

Overall, most brain metabolites and anatomic MR imaging findings were stable during the relatively short 8-week period of KD. In particular, no changes in the lesion Cho and NAA levels suggest that there was minimal tumor progression during this time. There were also no changes in Lac, the end product of nonoxidative glycolysis, despite lowering of systemic glucose levels. Further study will be required to determine whether baseline tumor lactate levels have any predictive value in determining a response to KD.

Interestingly, there was a small-but-statistically significant decrease in total NAA in the contralateral hemisphere at 8 weeks. Because NAA synthesis occurs in mitochondria and is dependent on tricarboxylic acid cycle metabolism, it is possible that decreased blood glucose levels during ketosis lead to reduced tricarboxylic acid cycle flux and NAA synthesis. Progressive total NAA reductions were previously reported in a teenager experiencing repeat episodes of diabetic ketoacidosis,[34] and reduced total NAA compared with healthy controls was reported in patients with epilepsy on the KD.[18]

Alternatively, the decrease in NAA seen in the contralateral hemisphere may represent delayed, ongoing changes in systemic brain metabolism as the result of the prior chemotherapy and radiation. Further studies will be required to investigate the origin of this effect.

This study has a number of limitations, including the small number of subjects, which precluded analysis of subgroups of patients (segregated, for example, by tumor grade or genetic mutation status). Another limitation is that no attempt was made to correct metabolite concentrations for voxel water (or CSF) content. However, we think that this did not significantly affect the results because voxels were carefully placed in either the solid part of the lesion or in the contralateral hemisphere, avoiding fluid-filled spaces. Voxel locations were also carefully matched between initial and follow-up scans, and brain MR images were stable during the 8-week duration of the diet, so it is unlikely that voxel water content changed during this period. Finally, the small ketone signals are of similar magnitude to

the noise in the spectra and thus difficult to ascertain visually. Increased numbers of signal averages (and associated scan time) may have resulted in improved detection of ketones; however, this was not possible in the current study because the MR spectroscopy was just one part of a lengthy clinical research protocol containing multiple other sequences. Future studies might use longer acquisition times and larger voxel sizes to increase the conspicuity of the ketone signals.

CONCLUSIONS

This study suggests that 3T MR spectroscopy is feasible for detecting small cerebral metabolic changes associated with a ketogenic diet, provided that appropriate methodology is used.

ACKNOWLEDGMENTS

We acknowledge use of the services and facilities of the Clinical Research Unit of the Wake Forest Clinical and Translational Sciences Institute, which is supported by National Center for Advancing Translational Sciences UL1TR001420. We also acknowledge philanthropy in memory of John Freeman.

Disclosures: Bobbie J. Barron—*UNRELATED*: *Board Membership*: Nutricia, *Comments*: I have taken part in 1 Advisory Board meeting. The nutrition supplements Nutricia makes were offered as part of a compliance strategy during the fasting part of the intervention but were not required and were not critical to the study; *Payment for Lectures Including Service on Speakers Bureaus*: Nutricia, *Comments*: I have been a speaker at a Nutricia conference; *Royalties*: Springer Publishing Company/Demos Health, *Comments*: for coauthoring *The Ketogenic and Modified Atkins Diets*, 6th ed; *Other*: BioMarin and Therachon, *Comments*: I have been a consultant for pediatric anthropometry for BioMarin and Therachon, neither of which has any conflict with the current study. Eric Kossoff—*UNRELATED*: *Board Membership*: Atkins Nutritionals; Nutricia *Royalties*: Springer Publishing Company/Demos Health, *Comments*: for coauthoring The Ketogenic and Modified Atkins Diets, 6th ed. Linda Easter—*RELATED*: *Grant*: Wake Forest Baptist Health Clinical and Translational Sciences Institute, *Comments*: CTSA grant UL1TR001420*; *UNRELATED*: *Consultancy*: Allena Pharmaceuticals. Mackenzie C. Cervenka—*RELATED*: *Grant*: Elaine Freeman Charitable donation, *Comments*: The money was paid to Johns Hopkins and not to me personally*; *UNRELATED*: *Consultancy*: Nutricia, Sage Therapeutics, *Comments*: I am a consultant for Nutricia, which produces KetoCal (4:1 ratio ketogenic liquid used in patients on the GLAD protocol referenced in the study). I was not paid directly by Nutricia for participation in the study. I was also a prior consultant for Sage Therapeutics (unrelated to this study); *Grants/Grants Pending*: Nutricia, Vitaflo, the William and Ella Owens Medical Research Foundation, the BrightFocus Foundation, *Payment for Lectures Including Service on Speakers Bureaus*: Nutricia, Epigenix, LivaNova, *Royalties*: Demos, *Comments*: I receive royalties for the book *The Ketogenic and Modified Atkins Diets: Treatments for Epilepsy and Other Disorders*. Peter B. Barker—*RELATED*: I was supported, in part, by the National Institutes of Health P41EB015909. Jaishri O. Blakeley—*RELATED*: *Comments*: philanthropic gift to the institution to support nutritional interventions for brain tumors*; *UNRELATED*: *Consultancy*: SpringWorks Therapeutics, *Comments*: agreement in place, no payments made*; *Grants/Grants Pending*: Sanofi, Lily, Bristol-Myers Squibb*; *Travel/Accommodations/Meeting Expenses Unrelated to Activities Listed*: AstraZeneca, SpringWorks Therapeutics, Exelixis. Roy E. Strowd—*RELATED*: *Grant*: National Institutes of Health, *Comments*: I was supported by the National Center for Advancing Translational Sciences National Institutes of Health KL2TR001421 and the National Cancer Institute's Cancer Center Support Grant award No. P30CA012197 issued to the Wake Forest Baptist Comprehensive Cancer Center. *UNRELATED*: *Consultancy*: Monteris Medical, Novocure. *Grants*: Southeastern Brain Tumor Foundation, American Society of Clinical Oncology, Conquer Cancer. *Money paid to the institution.

REFERENCES

1. Wilder RM. **The effect of ketonemia on the course of epilepsy.** *Mayo Clin Bull* 1921;2:307
2. Di Lorenzo C, Coppola G, Sirianni G, et al. **Migraine improvement during short lasting ketogenesis: a proof-of-concept study.** *Eur J Neurol* 2015;22:170–77 CrossRef Medline
3. El-Rashidy O, El-Baz F, El-Gendy Y, et al. **Ketogenic diet versus gluten free casein free diet in autistic children: a case-control study.** *Metab Brain Dis* 2017;32:1935–41 CrossRef Medline
4. Henderson ST, Vogel JL, Barr LJ, et al. **Study of the ketogenic agent AC-1202 in mild to moderate Alzheimer's disease: a randomized, double-blind, placebo-controlled, multicenter trial.** *Nutr Metab (Lond)* 2009;6:31 CrossRef Medline
5. Kim DY, Hao J, Liu R, et al. **Inflammation-mediated memory dysfunction and effects of a ketogenic diet in a murine model of multiple sclerosis.** *PLoS One* 2012;7:e35476 CrossRef Medline
6. Strowd RE, Cervenka MC, Henry BJ, et al. **Glycemic modulation in neuro-oncology: experience and future directions using a modified Atkins diet for high-grade brain tumors.** *Neurooncol Pract* 2015;2:127–36 CrossRef Medline
7. Vanitallie TB, Nonas C, Di Rocco A, et al. **Treatment of Parkinson disease with diet-induced hyperketonemia: a feasibility study.** *Neurology* 2005;64:728–30 CrossRef Medline
8. Wills AM, Hubbard J, Macklin EA, et al. **Hypercaloric enteral nutrition in patients with amyotrophic lateral sclerosis: a randomised, double-blind, placebo-controlled phase 2 trial.** *Lancet* 2014;383:2065–72 CrossRef Medline
9. Kesl SL, Poff AM, Ward NP, et al. **Effects of exogenous ketone supplementation on blood ketone, glucose, triglyceride, and lipoprotein levels in Sprague-Dawley rats.** *Nutr Metab (Lond)* 2016;13:9 CrossRef Medline
10. Urbain P, Bertz H. **Monitoring for compliance with a ketogenic diet: what is the best time of day to test for urinary ketosis?** *Nutr Metab (Lond)* 2016;13:77 CrossRef Medline
11. Urbain P, Strom L, Morawski L, et al. **Impact of a 6-week non-energy-restricted ketogenic diet on physical fitness, body composition and biochemical parameters in healthy adults.** *Nutr Metab (Lond)* 2017;14:17 CrossRef Medline
12. van Delft R, Lambrechts D, Verschuure P, et al. **Blood beta-hydroxybutyrate correlates better with seizure reduction due to ketogenic diet than do ketones in the urine.** *Seizure* 2010;19:36–39 CrossRef Medline
13. Hartman AL, Gasior M, Vining EP, et al. **The neuropharmacology of the ketogenic diet.** *Pediatr Neurol* 2007;36:281–92 CrossRef Medline
14. Kreis R, Ross BD. **Cerebral metabolic disturbances in patients with subacute and chronic diabetes mellitus: detection with proton MR spectroscopy.** *Radiology* 1992;184:123–30 CrossRef Medline
15. Wootton-Gorges SL, Buonocore MH, Kuppermann N, et al. **Detection of cerebral {beta}-hydroxy butyrate, acetoacetate, and lactate on proton MR spectroscopy in children with diabetic ketoacidosis.** *AJNR Am J Neuroradiol* 2005;26:1286–91 Medline
16. Pan JW, Rothman TL, Behar KL, et al. **Human brain beta-hydroxybutyrate and lactate increase in fasting-induced ketosis.** *J Cereb Blood Flow Metab* 2000;20:1502–07 CrossRef Medline
17. Cecil KM, Mulkey SB, Ou X, et al. **Brain ketones detected by proton magnetic resonance spectroscopy in an infant with Ohtahara syndrome treated with ketogenic diet.** *Pediatr Radiol* 2015;45:133–37 CrossRef Medline
18. Seymour KJ, Bluml S, Sutherling J, et al. **Identification of cerebral acetone by 1H-MRS in patients with epilepsy controlled by ketogenic diet.** *MAGMA* 1999;8:33–42
19. Artzi M, Liberman G, Vaisman N, et al. **Changes in cerebral metabolism during ketogenic diet in patients with primary brain tumors: (1)H-MRS study.** *J Neurooncol* 2017;132:267–75 CrossRef Medline
20. Edden RA, Schar M, Hillis AE, et al. **Optimized detection of lactate at high fields using inner volume saturation.** *Magn Reson Med* 2006;56:912–17 CrossRef Medline
21. Oz G, Tkac I. **Short-echo, single-shot, full-intensity proton magnetic resonance spectroscopy for neurochemical profiling at 4 T:**

validation in the cerebellum and brainstem. *Magn Reson Med* 2011;65:901–10 CrossRef Medline
22. Scheenen TW, Klomp DW, Wijnen JP, et al. **Short echo time 1H-MRSI of the human brain at 3T with minimal chemical shift displacement errors using adiabatic refocusing pulses.** *Magn Reson Med* 2008;59:1–6 CrossRef Medline
23. Gruetter R. **Automatic, localized in vivo adjustment of all first- and second-order shim coils.** *Magn Reson Med* 1993;29:804–11 CrossRef Medline
24. Provencher SW. **Automatic quantitation of localized in vivo 1H spectra with LCModel.** *NMR Biomed* 2001;14:260–64 CrossRef Medline
25. de Graaf RA. *In Vivo NMR Spectroscopy: Principles and Techniques.* New York: John Wiley and Sons; 2007:592
26. Govindaraju V, Young K, Maudsley AA. **Proton NMR chemical shifts and coupling constants for brain metabolites.** *NMR Biomed* 2000;13:129–53 CrossRef Medline
27. Tkac I. Refinement of simulated basis set for LCModel analysis. In: *Proceedings of the Scientific Meeting and Exhibition of the International Society for Magnetic Resonance in Medicine*. Toronto, Ontario, Canada. May 3–9, 2008: 1624
28. Madan A, Ganji SK, An Z, et al. **Proton T2 measurement and quantification of lactate in brain tumors by MRS at 3 Tesla in vivo.** *Magn Reson Med* 2015;73:2094–99 CrossRef Medline
29. Ganji SK, Banerjee A, Patel AM, et al. **T2 measurement of J-coupled metabolites in the human brain at 3T.** *NMR Biomed* 2012;25:523–29 CrossRef Medline
30. Kreis R. **The trouble with quality filtering based on relative Cramer-Rao lower bounds.** *Magn Reson Med* 2016;75:15–18 CrossRef Medline
31. De Feyter HM, Behar KL, Rao JU, et al. **A ketogenic diet increases transport and oxidation of ketone bodies in RG2 and 9L gliomas without affecting tumor growth.** *Neuro Oncol* 2016;18:1079–87 CrossRef Medline
32. Nagae-Poetscher LM, McMahon M, Braverman N, et al. **Metabolites in ventricular cerebrospinal fluid detected by proton magnetic resonance spectroscopic imaging.** *J Magn Reson Imaging* 2004;20:496–500 CrossRef Medline
33. Horska A, Barker PB. **Imaging of brain tumors: MR spectroscopy and metabolic imaging.** *Neuroimaging Clin N Am* 2010;20:293–310 CrossRef Medline
34. Wootton-Gorges SL, Buonocore MH, Caltagirone RA, et al. **Progressive decrease in N-acetylaspartate/creatine ratio in a teenager with type 1 diabetes and repeated episodes of ketoacidosis without clinically apparent cerebral edema: evidence for permanent brain injury.** *AJNR Am J Neuroradiol* 2010;31:780–81 CrossRef Medline

Hemodynamic Analysis of Postoperative Rupture of Unruptured Intracranial Aneurysms after Placement of Flow-Diverting Stents: A Matched Case-Control Study

W. Li, Z. Tian, W. Zhu, Y.S. Zhang, K. Wang, Y. Zhang, Y. Wang, X. Yang, and J. Liu

ABSTRACT

BACKGROUND AND PURPOSE: Postoperative rupture of intracranial aneurysm has been reported as a fatal complication after flow-diverter placement. We assessed several hemodynamic variables to explore risk factors in the postoperative rupture process.

MATERIALS AND METHODS: We enrolled 10 patients with intracranial aneurysms, treated with flow diverters between September 2014 and December 2018, who experienced postoperative aneurysm rupture (postoperative aneurysm rupture group). We matched these subjects 1:2 with 20 patients with postoperative unruptured (postoperative unruptured group) intracranial aneurysms based on clinical and morphologic factors. Using computational fluid dynamics, we assessed hemodynamic changes pre- and posttreatment between the 2 groups on a number of qualitative and quantitative parameters.

RESULTS: In the postoperative aneurysm rupture group, the proportion of patients with aneurysms with an unstable flow pattern increased to 60.0% after treatment, while the proportion in the postoperative unruptured group decreased to 20.0%, a significant difference between the 2 groups ($P = .028$). Energy loss in the postoperative unruptured group decreased after treatment but increased in the postoperative aneurysm rupture group. The reduction ratio of energy loss showed a significant difference between the 2 groups (22.73% ± 53.59% for postoperative unruptured versus −158.81% ± 183.95% for postoperative aneurysm rupture, $P = .02$). Other parameters and changes of pre- and posttreatment hemodynamic parameters showed no significant difference between 2 groups.

CONCLUSIONS: Compared with pretreatment, unstable flow pattern and higher energy loss after Pipeline Embolization Device placement for intracranial aneurysm may be the important hemodynamic risk factors related to delayed aneurysm rupture.

ABBREVIATIONS: CFD = computational fluid dynamics; EL = energy loss; IA = intracranial aneurysm; LSA = low wall shear stress area; OG = occlusion grade; OSI = oscillatory shear index; POR = postoperative ruptured; POU = postoperative unruptured; RRT = relative residual time; TAWSS = time-averaged wall shear stress; WSS = wall shear stress

Endoluminal reconstruction with the Pipeline Embolization Device (PED; Covidien, Irvine, California) has been widely used in large and giant intracranial aneurysms (IAs). The complete occlusion rate reported in the literature is encouraging;[1-4] however, postoperative delayed rupture of IAs has been reported as a fatal complication.[5-8] A meta-analysis showed that the incidence of subarachnoid hemorrhage after flow-diverter placement was 4.0%, with a higher incidence in patients with large or giant IAs.[9] The potential mechanisms of postoperative delayed rupture are still unclear, however.

Treatment of IAs with flow diverters and coils is thought to promote thrombosis and treat the aneurysm. Another hypothesis is that thrombosis and inflammation make the aneurysm wall more vulnerable.[7,10,11] With flow diverters and coils designed to cure the aneurysm by modifying the flow, hemodynamic changes are also thought to play an important role in the postoperative rupture process. However, hemodynamic research of

Received June 5, 2019; accepted after revision August 23.

From the Department of Interventional Neuroradiology (W.L., Z.T., W.Z., Y.S.Z., K.W., Y.Z., X.Y., J.L.), Beijing Neurosurgical Institute and Beijing Tiantan Hospital, Capital Medical University, Beijing, China; and Department of Neurosurgery (Y.W.), The First Affiliated Hospital of Nanchang University, Nanchang University, Nanchang, China.

W. Li and Z. Tian contributed equally to this work.

This work was supported by the National Key Research and Development Plan of China (grant No. 2016YFC1300800), the National Natural Science Foundation of China (grant Nos. 81220108007, 81801156, 81801158, 81471167, and 81671139), and the Special Research Project for Capital Health Development (grant No. 2018-4-1077).

Please address correspondence to Jian Liu, MD, Department of Interventional Neuroradiology, Beijing Neurosurgical Institute and Beijing Tiantan Hospital, Capital Medical University, NansanhuanXilu 119, Fengtai District, Beijing, China, 100070; e-mail: jianliu_ns@163.com

Indicates open access to non-subscribers at www.ajnr.org
Indicates article with supplemental on-line tables.
Indicates article with supplemental on-line photos.
http://dx.doi.org/10.3174/ajnr.A6256

postoperative rupture is limited.[5,12] In this study, we used the computational fluid dynamics (CFD) method and advanced virtual stent placement technique to explore the hemodynamic factors associated with postoperative delayed rupture. We compared unruptured IAs that ruptured after PED treatment with matched aneurysms that did not rupture during the observation period. We investigated whether hemodynamic parameters could predict postoperative aneurysm rupture.

MATERIALS AND METHODS

Patient Selection

This retrospective, matched case-control study was approved by the ethics committee of Beijing Tiantan hospital. We reviewed the medical records and image data in our aneurysm data base of patients diagnosed with unruptured IAs between September 2014 and December 2018. We identified 388 patients with 426 unruptured IAs treated with PEDs. From the CT scans, we identified patients who had a delayed aneurysmal subarachnoid hemorrhage after PED placement; intraparenchymal hemorrhages were excluded. Twelve patients experienced an unexpected aneurysmal subarachnoid hemorrhage complication after PED treatment, an incidence of 3.1% in our center (3.0% for PED with coils and 3.3% for PED alone). Two of these were excluded because of inadequate image quality for the computational simulation, so 10 patients with 10 PEDs were ultimately included in this study in the postoperative rupture (POR) group. For each case in the POR group, we enrolled 2 matched controls who did not have postoperative rupture and were analyzed as the postoperative unruptured (POU) group. The aneurysms in the control group should have had satisfactory angiographic results at follow-up, indicating a low probability of further rupture.

Aneurysms were graded on the degree of occlusion after PED placement as follows: complete occlusion (OG1), neck remnant (OG2), and residual sac filling (OG3).[13] A satisfactory angiographic result was defined as OG1, OG2, or progressive occlusion. The primary basis for the matched controls was treatment method: PED alone or PED-assisted coil embolization. Additional matching was performed in the following order: aneurysm location, aneurysm size, patient sex, and age. To find the matched control cases, we retrospectively reviewed all unruptured aneurysms with PED placement seen in our clinic during the specified timeframe. We excluded the following patients: 1) those for whom the treatment method, location, and size of aneurysm could not be matched; 2) those without angiographic follow-up or 3D images with sufficient resolution for computational simulation; and 3) those having previous endovascular or surgical treatment of the aneurysm.

Twenty matched patients were included as the POU group. The patient characteristics of both groups are summarized (On-line Table 1). Clinical and morphologic factors for all 30 patients (age, sex, smoking history, hypertension, symptomatic aneurysm, aneurysm size, aneurysm neck, size ratio, and aspect ratio) were collected and calculated. The treatment method, coil packing density, and initial angiographic results were also collected.

For the Pipeline Embolization Device, the patients were treated with aspirin, 100 mg, and clopidogrel, 75 mg, for a minimum of 5 days before the endovascular treatment. The antiplatelet sensitivity test was performed routinely, and a booster dose of 300 mg of clopidogrel was used if the patient was not sensitive to clopidogrel. After we achieved groin access, all patients received an initial heparin bolus administration (70–100 UI/kg) maintaining the activated clotting time between 250 and 300 seconds during the procedure. Dual-antiplatelet therapy (aspirin, 100 mg, and clopidogrel, 75 mg) will be maintained for 3 months after the procedure; then, aspirin monotherapy will be followed indefinitely.

Computational Modeling and Hemodynamic Simulations

Patient-specific 3D digital subtraction angiography data of all aneurysms were obtained and imported into Geomagic Studio, Version 12.0 software (Geomagic, Research Triangle Park, North Carolina). Images were displayed, segmented, and smoothed, and the surface geometries were saved as a Standard Tessellation Language format. We used a novel virtual stent placement technique[14] and porous media method[15] to simulate the in vivo stent and coil mass in the aneurysm dome region. The virtual stent placement consisted of 3 steps—1) preprocessing: the parent vessel was isolated from the aneurysm and trimmed down to the deployable region; 2) simplex mesh expansion: we obtained the centerline within the parent vessel and radial expansion to initialize a uniform small-diameter initial mesh (the expansion was stopped when the initialized simplex mesh was expanded inside the parent vessel with good apposition); and 3) postprocessing: the PED stent pattern was determined on the basis of the simplex mesh, and the wires were swept into the 3D structures using Computer Aided Design software (Creo Parametric 2.0; PTC, Needham, Massachusetts).[14]

The aneurysmal dome with coils was modeled as a porous medium described by Mitsos et al.[15] The virtual stent was merged with the aneurysm geometry using ICEM CFD software (ANSYS, Canonsburg, Pennsylvania) to create >1,000,000 finite-volume tetrahedral elements. The maximum element size of the vessel was set at 0.2 mm, and the element size of stents was approximately one-third the width of the strut of these stents. CFX 14.0 software (ANSYS) was used to simulate the hemodynamics of the aneurysm after meshing.

We treated blood as a Newtonian fluid. The blood vessel wall was assumed to be rigid with no-slip boundary conditions. The density was specified as $\rho = 1060\,kg/m^3$, and the dynamic viscosity of blood was $\mu = 0.004\,Pa \times s$. The governing equations underlying the calculation were based on the Navier-Stokes formula, with the assumption of homogeneous, laminar, incompressible blood flow. The inflow boundary condition was obtained using transcranial Doppler imaging as a representative pulsatile period velocity profile. The outlet pressure conditions at outlet arteries in our study were imposed to $P = 0\,Pa$. The flow waveforms were scaled to achieve a mean inlet wall shear stress (WSS) of 15 dyne/cm under pulsatile conditions.[14] To confirm the stability, we selected the third of 3 cardiac cycle simulations as the output for the final analyses.

Table 1: Univariate analysis results for hemodynamic parameters between POR and POU groups[a]

Parameters	POR Group ($n = 10$)	POU Group ($n = 20$)	*P* Value
Unstable flow (pre) (No.) (%)	3 (30.0)	10 (50.0)	.297
Unstable flow (post) (No.) (%)	6 (60.0)	4 (20.0)	.028[b]
Inflow jet (pre) (No.) (%)	8 (80.0)	15 (75.0)	.760
Inflow jet (post) (No.) (%)	2 (20.0)	9 (45.0)	.180
Flow complex (pre) (No.) (%)	4 (40.0)	9 (45.0)	.439
Flow complex (post) (No.) (%)	4 (40.0)	6 (30.0)	.584
Velocity (post) (m/s)	0.03 ± 0.04	0.04 ± 0.05	.286
WSS (post) (Pa)	1.42 ± 2.55	1.07 ± 1.36	.792
Pressure (post) (Pa)	1487.31 ± 799.68	4127.68 ± 5613.52	.930
Velocity at neck (post) (m/s)	0.30 ± 0.33	0.20 ± 0.37	.567
EL (post) (W/m^3)	906.32 ± 707.56	9871.75 ± 22215.52	.628
LSA (post) (mm^2)	0.56 ± 0.32	0.74 ± 0.26	.147
OSI (post)	0.02 ± 0.06	0.00 ± 0.00	.428
TAWSS (post) (Pa)	0.39 ± 0.68	0.23 ± 0.29	.965
RRT (post) (sec)	1.46 ± 2.54	1.07 ± 1.36	.725

Note:—Pre indicates before; post, after.
[a] Continuous variables are expressed as mean ± SD. Categoric variables are expressed as (No.) (%).
[b] $P < .05$. The Mann–Whitney *U* test was used, with $P < .05$ considered statistically significant.

Hemodynamic Analysis

We then postprocessed and visualized the results of these simulations using the CFD-Post (ANSYS). The hemodynamic results at peak systole were carefully examined.

We calculated 7 hemodynamic variables:

1) Flow pattern. Flow complexity (simple/complex), flow stability (stable/unstable), and inflow jet were defined as Cebral et al[16] reported. It was considered an improvement when the complex flow pattern turned to simple flow or the unstable flow pattern turned to stable flow. In flow complexity, a simple flow pattern consists of a single recirculation zone or vortex structure in the aneurysm, and a complex flow pattern contains >1 recirculation zone or vortex structure. With respect to flow stability, a stable flow pattern indicates that flow in an aneurysm is persistent during the cardiac cycle (does not move or change), and an unstable flow pattern is one in which the vortex structures are moved, created, or destroyed during the cardiac cycle.

2) WSS-related variables. The average WSS on the aneurysm sac was recorded. The time-averaged WSS (TAWSS) was calculated by integrating the WSS magnitude over the cardiac cycle and was normalized by the parent artery–averaged TAWSS in the same patient to allow comparison among different cases.[17]

3) Velocity. The average velocity in the aneurysm and the pressure on the aneurysm wall were recorded. The average flow velocity at the aneurysm neck plane was also recorded. The aneurysm neck plane was determined by a plane between the aneurysm sac and the parent artery.

4) Oscillatory shear index (OSI). The OSI was calculated using the method described by He and Ku[18] and defined as the spatially averaged OSI on the aneurysm.

5) Low WSS area (LSA). LSA is the proportion of the low WSS area (<10% of the mean vessel WSS at the parent artery) to the whole area of the aneurysm.[19]

6) Energy loss (EL). EL represents the expenditure of flow energy in the aneurysm region and was considered associated with aneurysm rupture.[20]

7) Relative residual time (RRT). RRT was defined as the inverse of the magnitude of the time-averaged WSS, which combined with WSS and oscillatory shear index. It quantifies the state of disturbed flow and reflects the duration of residence near the wall.[21]

To standardize the results, we used the reduction ratios of each of these parameters, and they were defined as (pretreatment parameter – posttreatment parameter)/pretreatment parameter.

Statistical Analysis

We performed matched case-control analysis using conditional logistic regression. For categoric parameters, the χ^2 test or the Fisher exact test was used to compare the differences between the POR and POU groups. For continuous parameters, the Mann-Whitney *U* test was used to compare the 2 groups. Statistical analyses were performed using statistical software (SPSS, Version 21.0; IBM, Armonk, New York). The level of statistical significance was established at $P < .05$.

RESULTS

Case Matching, Clinical Factors, and Aneurysm Morphology

In our study, 10 patients, each with an aneurysm, were included in POR group. After the primary matching and additional matching variables, each of the subjects with aneurysms was successfully matched with 2 control subjects with aneurysms. No PED malapposition was found in our included cases. For patients treated by PED and coils, the coiling and PED were performed in the same treatment session. The comparison of clinical and morphologic characteristics is shown in On-line Table 2. None of the clinical factors were statistically different between the 2 groups.

Hemodynamic Analyses Associated with Postoperative Rupture

We compared the pre- and postoperative flow patterns in each group and hemodynamic parameters between the 2 groups (Table 1).

Qualitative Analyses

Before treatment, the proportion of aneurysms with unstable flow patterns was 30% in the POR group and 50% in the POU group. The proportion of aneurysms with complex flow patterns was also lower in POR group than in the POU group, 40% versus 45%, respectively. The proportion of aneurysms with an inflow jet was higher in the POR group (80% versus 75%). There was no statistically significant difference between the 2 groups for these pretreatment measures.

After treatment, the proportion of the aneurysmal inflow jet decreased to 20.0% in the POR group and to 45.0% in the POU group. For complex flow patterns, there was no change in the

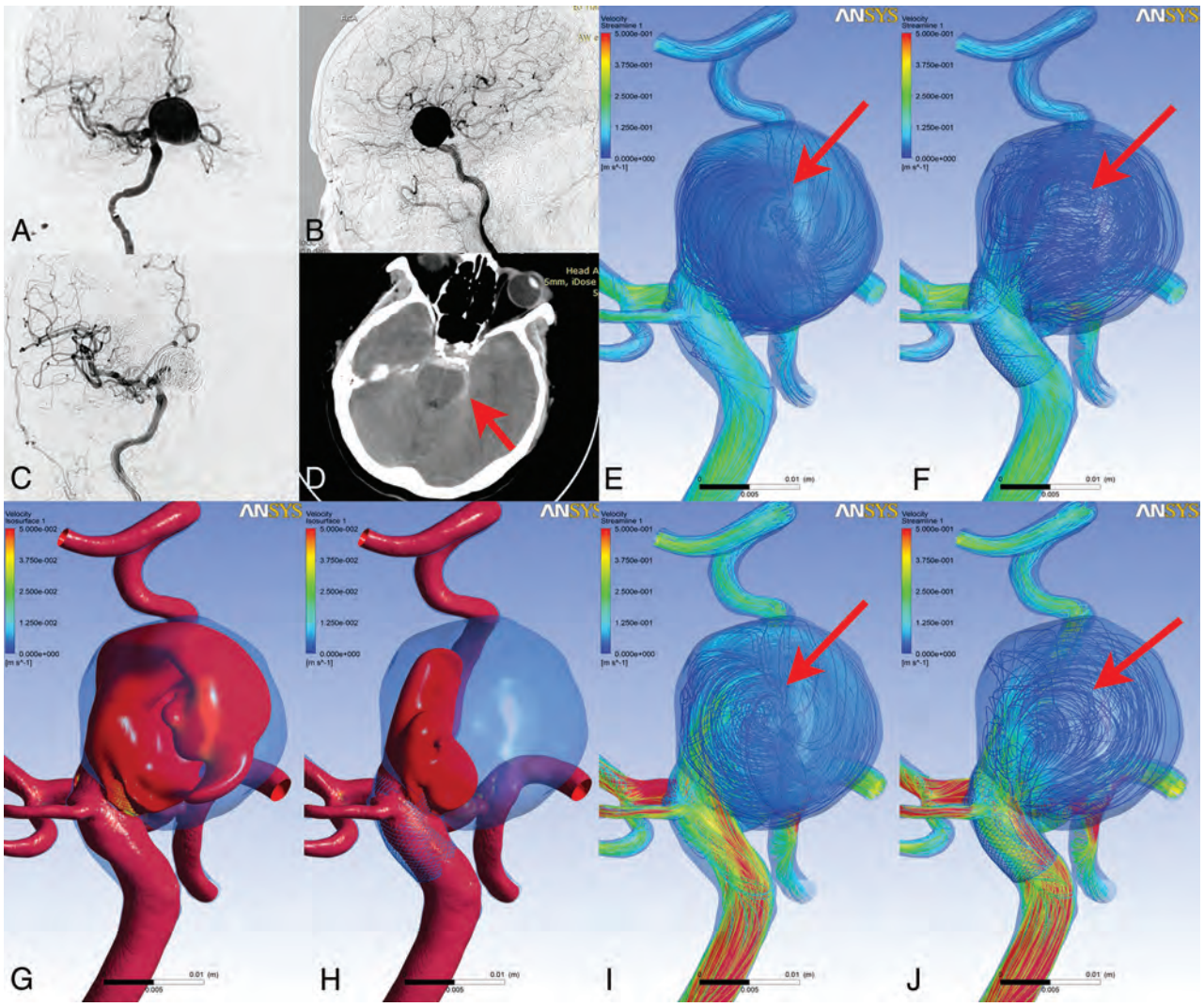

FIG 1. A female patient with a right internal carotid aneurysm was treated with PED-assisted coil embolization. Compared with the anteroposterior and lateral position of preoperative angiography (*A* and *B*), the aneurysm is embolized completely (*C*). Unfortunately, the aneurysm ruptured 3 days postoperatively (*D*, *arrow*). After CFD analysis, we found that an unstable flow pattern appeared after treatment. Compared with the streamlines at end diastole, the vortex structure in the preoperative streamlines (*E*, *arrow*) is not changed at peak systole (*I*, *arrow*). However, after treatment, the vortex structure is moved at peak systole (*F* and *J*, *arrows*). Isovelocity surfaces show that the velocity in the aneurysm lumen decreased between the preoperative (*G*) and postoperative (*H*) periods.

POR group, while in the POU group, it decreased to 30%. These differences showed no statistical significance. However, the proportion of aneurysms with unstable flow patterns did show a statistically significant difference between the 2 groups after treatment ($P = .028$). The proportion of unstable flow patterns in the POR group increased to 60.0%, while the proportion decreased to 20.0% in the POU group (Table 1). Figs 1 and 2 show the stable and unstable flow patterns of 2 cases, including a delayed-ruptured aneurysm with PED-assisted coils and a successfully cured aneurysm with PED-assisted coils. Moreover, 2 cases, including a delayed-ruptured aneurysm and a successfully cured aneurysm with PED-assisted coils, were also shown (Online Figs 1 and 2).

Quantitative Analyses

For the hemodynamic parameters after PED treatment, the flow velocity in the aneurysms was lower in the POR group compared with the POU group. The pressure, EL, and LSA of aneurysms were also lower for the POR group, while the WSS on the aneurysms, the velocity at the neck plane, OSI, TAWSS, and RRT of the aneurysms were higher. However, these differences were not statistically significant (Table 1).

We also compared the reduction ratio of these hemodynamic parameters before and after treatment (Fig 3). By means of the Mann–Whitney test, the reduction ratio of EL showed a significant difference between 2 groups ($P = .02$). EL was decreased after treatment in the POU group (reduction ratio = 22.73% ± 53.59%) and increased in the POR group (reduction ratio = −158.81% ± 183.95%). The OSI and pressure of the aneurysms increased after treatment, while other parameters decreased after treatment. The reduction of lumen velocity (Figs 1–3), TAWSS, velocity at the neck plane, and WSS was lower in the POR group, while the reduction ratio of RRT and LSA in the POR group was

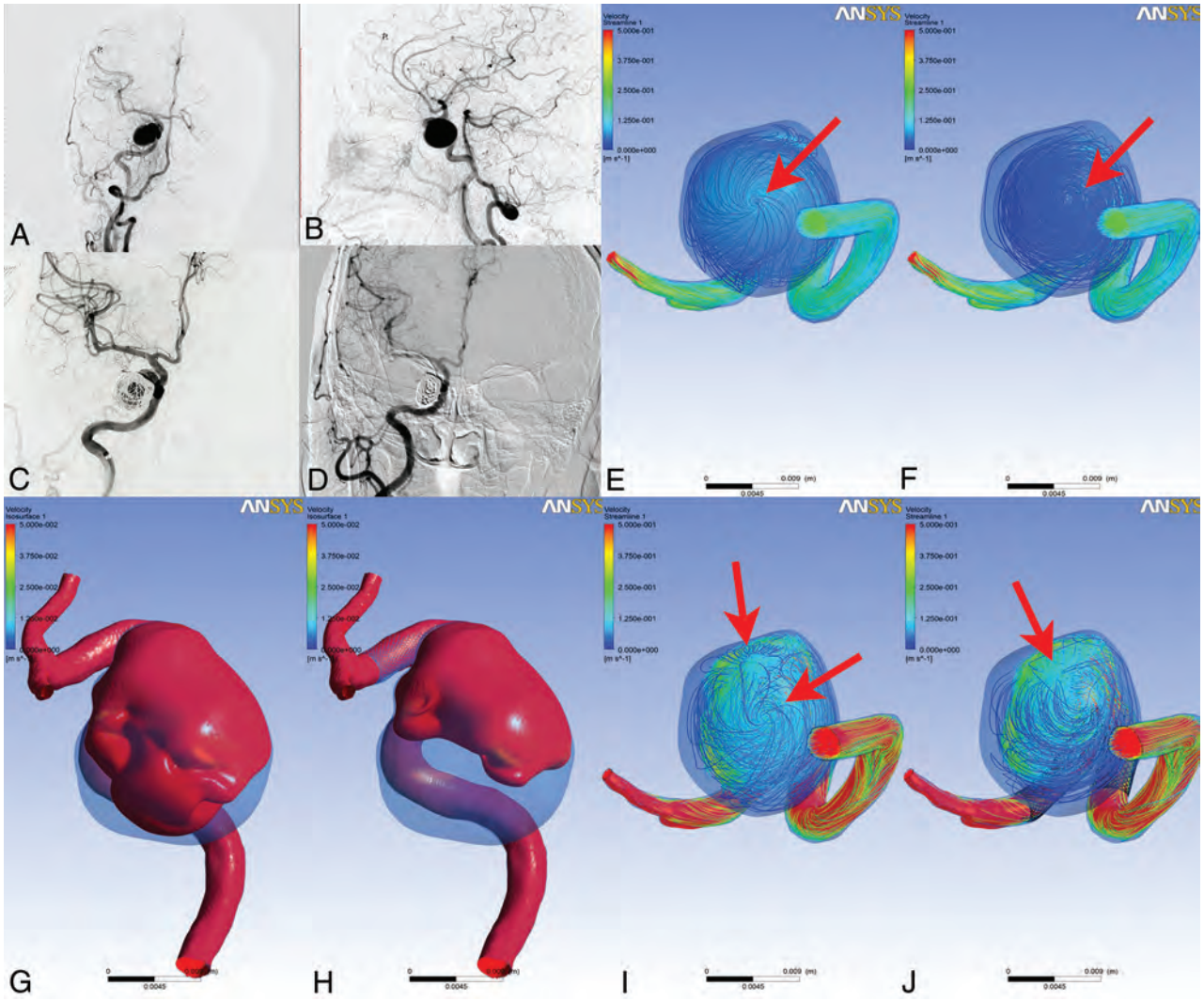

FIG 2. A female patient with a right internal carotid aneurysm treated with a PED-assisted coil embolization. Compared with the anteroposterior and lateral position of preoperative angiography (*A* and *B*), the aneurysm is embolized (*C*). At follow-up, the aneurysm is successfully embolized (*D*). After CFD analysis, we found that the unstable flow pattern disappeared after treatment. Compared with the streamlines at end diastole, 1 vortex structure in the preoperative streamlines (*E*, *arrow*) was found, and a created vortex appears at peak systole (*I*, *arrow*). However, after treatment, the amount of vortex structure is not changed at peak systole (*F* and *J*, *arrows*). Isovelocity surfaces show that the velocity in the aneurysm lumen decreased between the preoperative (*G*) and postoperative (*H*) periods.

higher. The difference in the reduction ratios between the 2 groups showed no statistical significance.

DISCUSSION

The mechanisms of postoperative rupture of IAs following flow-diversion treatment have been explored on the basis of clinical, morphologic, clinicopathologic, and hemodynamic characteristics.[5,8,22,23] However, most studies were case reports or included many confounding factors, such as differing locations and sizes of aneurysms. In the present study, we adjusted for and matched these confounding factors with an aim of investigating the hemodynamic risk factors for postoperative rupture. We found that the unstable flow patterns were significantly increased in postoperative ruptured aneurysms. We also found higher EL in postoperative ruptured aneurysms after PED treatment, with the reduction ratio of EL showing a significant difference between the 2 groups ($P = 0.02$).

Potential Delayed Ruptured Mechanism of Aneurysm after Flow Diverter

Initial experience with flow-diverter technology was encouraging. However, some reports indicated that PED placement might lead to later aneurysm rupture, which raises concerns about the safety of this device. The incidence of subarachnoid hemorrhage after flow-diverter placement has been reported as high as 4.0%.[5-9,22-24] Kulcsar et al[8] analyzed risk factors of delayed-ruptured aneurysms before and after flow-diversion treatment to understand the mechanisms leading to delayed rupture during the healing process. They proposed 4 clinical risk factors for delayed rupture: large and giant aneurysms, symptomatic aneurysms, saccular aneurysms with an aspect ratio of >1.6, and inertia-driven inflow. However, this study mainly evaluated the clinical characteristics, and no hemodynamics were included. Treatment of large or giant aneurysms with flow diverters, which are considered at high risk of postoperative rupture, is still

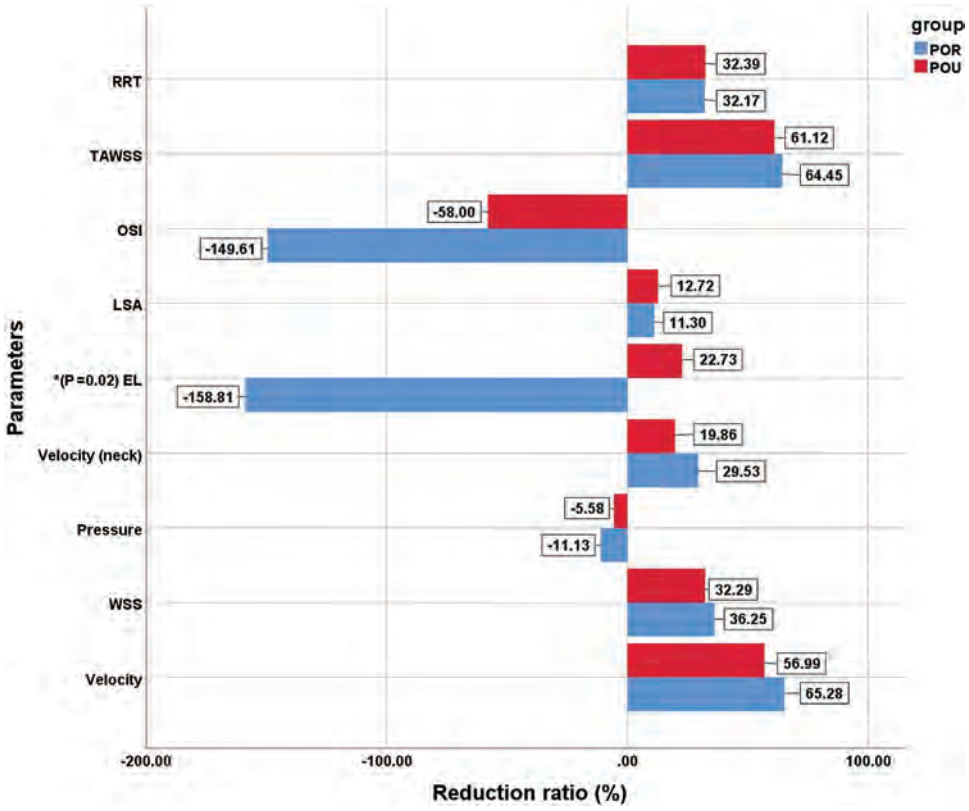

FIG 3. Comparisons of reduction ratios of hemodynamic parameters between the 2 groups. The *asterisk* indicates $P < .05$.

necessary, and the flow diverter is still a better choice than traditional stents. In our study, we primarily focused on hemodynamics because the flow diverter was designed to modify the aneurysmal flow. We strictly matched the control cases on the basis of clinical and morphologic factors and found that the hemodynamic risk factors indeed play a role in the postoperative rupture process.

A histologic study[25] found that a fresh and organizing aneurysm lumen thrombus can induce degeneration of the aneurysm wall and was a risk factor for aneurysms predisposed to rupture. Inflammatory infiltration in the aneurysm wall was an independent risk factor associated with aneurysm rupture. However, it is not clear whether the mechanism of a postoperative ruptured aneurysm with PED treatment is related to intraluminal thrombus and inflammation. Similarly, several studies reported that unstable and nonorganized red thrombi can be the result of immediate stagnation of blood flow after flow-diverter placement. Red thrombi have a high content of proteolytic enzymes that can weaken the wall of the aneurysm. The subsequent thrombus organization within the aneurysm can result in inflammatory changes in the aneurysm wall, leading to delayed rupture of the aneurysm.[7,10,11]

Our hemodynamic results also supported this "thrombus and inflammatory" mechanism. We found that the flow velocity in aneurysms after PED placement was lower in the POR group and that the reduction ratio of aneurysmal velocity was higher, while the difference was not significant. Lower flow velocity in aneurysms after treatment and a higher reduction ratio of aneurysmal flow velocity could lead to rapid thrombosis in the aneurysm lumen and inflammatory infiltration of the aneurysm wall, which could trigger the aneurysm rupture. In addition, an unstable flow pattern increased after PED placement in the POR group, and such an unstable flow pattern might also result in rapid thrombosis in the aneurysm lumen. With the rapid intra-aneurysmal thrombus volume enlargement soon after flow-diverter placement, the aneurysm wall might tear from the mechanical stretching force on it.

In clinical practice, use of coils in conjunction with the PED is preferred to prevent delayed aneurysm rupture.[26] Loose packing is usually performed in this circumstance, which is different from the dense packing in the conventional coil embolization. However, there is no guideline for the packing density in flow-diverter treatment, and there is also no solid evidence that coiling is the panacea. Shown in On-line Table 2 in our study, the difference in packing density was not significant between the 2 groups. The packing density may be too low to prevent delayed rupture in our data. Moreover, aneurysm rupture following flow-diverter therapy is a complex, multifactorial problem and needs to be further evaluated.

The Hemodynamic Factors Related to Delayed Rupture of Aneurysms Treated with Flow Diverters

Some computational fluid dynamics studies have tried to explain the mechanism of delayed rupture of aneurysms. Research has found that continued inflow and higher pressure in the aneurysm after flow-diverter stent placement might be potential mechanisms for delayed rupture.[5,24] There are some limitations that might introduce bias to this conclusion. Hassan et al[24] aimed to

demonstrate possible adverse effects of deployment of flow-diverter stents. They found that a slow blood flow jet still exists inside the aneurysm at the end of the procedure, which might be related to delayed aneurysm rupture after treatment. However, the study was based on the flow characteristics of artificial saccular aneurysm models and did not relate the results to the clinical outcomes.

Cebral et al[5] reported a computational fluid dynamics study in 3 patients who experienced postoperative rupture. They compared the hemodynamic factors with 4 successfully treated aneurysms and found that PED placement can increase intraaneurysmal pressure, which may potentially lead to rupture. However, the control cases were not strictly matched. Three of the 4 aneurysms were small- or medium-sized, so the flow pattern and hemodynamics may be different from those of giant aneurysms, and the small cases also have a low risk of postoperative rupture according to Kulcsar et al.[8]

In our study, we rigorously matched the control patients on the basis of clinical and morphologic factors. We found that the pressure in the aneurysm lumen increased after PED treatment, while the increasing ratio of pressure showed no significant difference between the POU and POR groups. Tateshima et al[12] and Schneiders et al[27] found similar results. These studies measured intrasaccular pressure before and after flow-diverter placement using pressure measurement wires and found no significant difference in intrasaccular pressures after flow-diverter placement.

Energy loss was introduced as a hemodynamic parameter, which is a more accurate estimate of the pressure variation and kinetic energy.[28] Energy should be lost when the blood flow passes through the aneurysm. Part of this attenuated energy was quantified to EL as a hemodynamic parameter to judge whether an aneurysm had ruptured. Some studies have reported that EL was a useful parameter for the quantitative estimation of the rupture risk for IAs. Higher EL might be correlated to aneurysm rupture if the lost energy caused expansion of the aneurysm, leading to aneurysm rupture.[20,28,29] However, until our study, there were no studies evaluating the role of EL in the process of postoperative rupture.

In this study, our results showed that EL was associated with postoperative aneurysm rupture. Higher energy loss after PED placement, then, might lead to delayed aneurysm rupture. As described by Takao et al,[20] EL is a hemodynamic parameter combining velocity and pressure. Our results showed that the flow velocity of the aneurysm lumen was decreased, while the pressure was increased. Although individually these parameters did not show a statistically significant difference between the 2 groups, the combined parameters, expressed as EL, did show a significant difference. Thus, EL might be a better hemodynamic parameter than pressure and velocity to predict aneurysmal delayed rupture after PED treatment.

Limitations

This study had some limitations. First, it was a retrospective analysis at a single center and lacked variety in the kind of flow-diverter device used; all cases were treated with a PED. Second, the study mainly aimed to investigate the hemodynamic factors and found that hemodynamic effects might play an important role in the causes of delayed rupture. However, the mechanism of aneurysm rupture following flow diversion is probably multifactorial and may include such things as antiplatelet regimen, thrombus formation, and inflammation. Last, several limitations of CFD hemodynamic analysis should be considered. Several assumptions, such as a rigid wall, laminar flow, and Newtonian blood, may affect the hemodynamic results, and the accuracy of the virtual stent placement technique still needs to be improved.

CONCLUSIONS

After PED treatment, an unstable flow pattern and higher energy loss compared with pretreatment might be the important hemodynamic factors related to delayed rupture of aneurysms. These analyses highlight the potential for CFD to play an important role in the clinical determination of POU IA risks.

REFERENCES

1. Walcott BP, Stapleton CJ, Choudhri O, et al. **Flow diversion for the treatment of intracranial aneurysms.** *JAMA Neurol* 2016;73:1002–08 CrossRef Medline
2. Kallmes DF, Brinjikji W, Cekirge S, et al. **Safety and efficacy of the Pipeline Embolization Device for treatment of intracranial aneurysms: a pooled analysis of 3 large studies.** *J Neurosurg* 2017;127:775–80 CrossRef Medline
3. Becske T, Kallmes DF, Saatci I, et al. **Pipeline for uncoilable or failed aneurysms: results from a multicenter clinical trial.** *Radiology* 2013;267:858–68 CrossRef Medline
4. Becske T, Brinjikji W, Potts MB, et al. **Long-term clinical and angiographic outcomes following Pipeline embolization device treatment of complex internal carotid artery aneurysms: five-year results of the Pipeline for Uncoilable or Failed Aneurysms Trial.** *Neurosurgery* 2017;80:40–48 CrossRef Medline
5. Cebral JR, Mut F, Raschi M, et al. **Aneurysm rupture following treatment with flow-diverting stents: computational hemodynamics analysis of treatment.** *AJNR Am J Neuroradiol* 2011;32:27–33 CrossRef Medline
6. Siddiqui AH, Kan P, Abla AA, et al. **Complications after treatment with Pipeline embolization for giant distal intracranial aneurysms with or without coil embolization.** *Neurosurgery* 2012;71:E509–13; discussion E513 CrossRef Medline
7. Chow M, McDougall C, O'Kelly C, et al. **Delayed spontaneous rupture of a posterior inferior cerebellar artery aneurysm following treatment with flow diversion: a clinicopathologic study.** *AJNR Am J Neuroradiol* 2012;33:E46–51 CrossRef Medline
8. Kulcsar Z, Houdart E, Bonafe A, et al. **Intra-aneurysmal thrombosis as a possible cause of delayed aneurysm rupture after flow-diversion treatment.** *AJNR Am J Neuroradiol* 2011;32:20–25 CrossRef Medline
9. Brinjikji W, Murad MH, Lanzino G, et al. **Endovascular treatment of intracranial aneurysms with flow diverters: a meta-analysis.** *Stroke* 2013;44:442–47 CrossRef Medline
10. Turowski B, Macht S, Kulcsar Z, et al. **Early fatal hemorrhage after endovascular cerebral aneurysm treatment with a flow diverter (SILK-Stent): do we need to rethink our concepts?** *Neuroradiology* 2011;53:37–41 CrossRef Medline
11. Hampton T, Walsh D, Tolias C, et al. **Mural destabilization after aneurysm treatment with a flow-diverting device: a report of two cases.** *J Neurointerv Surg* 2018;10:i51–55 CrossRef Medline
12. Tateshima S, Jones JG, Mayor BF, et al. **Aneurysm pressure measurement before and after placement of a Pipeline stent: feasibility study using a 0.014 inch pressure wire for coronary intervention.** *J Neurointervent Surg* 2016;8:603–07 CrossRef Medline

13. Byrne JV, Beltechi R, Yarnold JA, et al. **Early experience in the treatment of intra-cranial aneurysms by endovascular flow diversion: a multicentre prospective study.** *PLoS One* 2010;5:e12492 CrossRef Medline
14. Wang C, Tian Z, Liu J, et al. **Flow diverter effect of LVIS stent on cerebral aneurysm hemodynamics: a comparison with Enterprise stents and the Pipeline device.** *J Transl Med* 2016;14:199 CrossRef Medline
15. Mitsos AP, Kakalis NM, Ventikos YP, et al. **Haemodynamic simulation of aneurysm coiling in an anatomically accurate computational fluid dynamics model: technical note.** *Neuroradiology* 2008;50:341–47 CrossRef Medline
16. Cebral JR, Mut F, Weir J, et al. **Association of hemodynamic characteristics and cerebral aneurysm rupture.** *AJNR Am J Neuroradiol* 2011;32:264–70 CrossRef Medline
17. Liu J, Fan J, Xiang J, et al. **Hemodynamic characteristics of large unruptured internal carotid artery aneurysms prior to rupture: a case control study.** *J Neurointerv Surg* 2016;8:367–72 CrossRef Medline
18. He X, Ku DN. **Pulsatile flow in the human left coronary artery bifurcation: average conditions.** *J Biomech Eng* 1996;118:74–82 CrossRef Medline
19. Zhang Y, Jing L, Liu J, et al. **Clinical, morphological, and hemodynamic independent characteristic factors for rupture of posterior communicating artery aneurysms.** *J Neurointerv Surg* 2016;8:808–12 CrossRef Medline
20. Takao H, Murayama Y, Otsuka S, et al. **Hemodynamic differences between unruptured and ruptured intracranial aneurysms during observation.** *Stroke* 2012;43:1436–39 CrossRef Medline
21. Huang Q, Xu J, Cheng J, et al. **Hemodynamic changes by flow diverters in rabbit aneurysm models: a computational fluid dynamic study based on micro-computed tomography reconstruction.** *Stroke* 2013;44:1936–41 CrossRef Medline
22. Ikeda H, Ishii A, Kikuchi T, et al. **Delayed aneurysm rupture due to residual blood flow at the inflow zone of the intracranial paraclinoid internal carotid aneurysm treated with the Pipeline Embolization Device: histopathological investigation.** *Interv Neuroradiol* 2015;21:674–83 CrossRef Medline
23. Fox B, Humphries WE, Doss VT, et al. **Rupture of giant vertebrobasilar aneurysm following flow diversion: mechanical stretch as a potential mechanism for early aneurysm rupture.** *J Neurointerv Surg* 2015;7:e37 CrossRef Medline
24. Hassan T, Ahmed YM, Hassan AA. **The adverse effects of flow-diverter stent-like devices on the flow pattern of saccular intracranial aneurysm models: computational fluid dynamics study.** *Acta Neurochir (Wien)* 2011;153:1633–40 CrossRef Medline
25. Frosen J, Piippo A, Paetau A, et al. **Remodeling of saccular cerebral artery aneurysm wall is associated with rupture: histological analysis of 24 unruptured and 42 ruptured cases.** *Stroke* 2004;35:2287–93 CrossRef Medline
26. Rouchaud A, Brinjikji W, Lanzino G, et al. **Delayed hemorrhagic complications after flow diversion for intracranial aneurysms: a literature overview.** *Neuroradiology* 2016;58:171–77 CrossRef Medline
27. Schneiders JJ, VanBavel E, Majoie CB, et al. **A flow-diverting stent is not a pressure-diverting stent.** *AJNR Am J Neuroradiol* 2013;34:E1–4 CrossRef Medline
28. Qian Y, Takao H, Umezu M, et al. **Risk analysis of unruptured aneurysms using computational fluid dynamics technology: preliminary results.** *AJNR Am J Neuroradiol* 2011;32:1948–55 CrossRef Medline
29. Liu J, Xiang J, Zhang Y, et al. **Morphologic and hemodynamic analysis of paraclinoid aneurysms: ruptured versus unruptured.** *J Neurointerv Surg* 2014;6:658–63 CrossRef Medline

The Fate of Unruptured Intracranial Vertebrobasilar Dissecting Aneurysm with Brain Stem Compression According to Different Treatment Modalities

D.Y. Cho, B.-S. Kim, J.H. Choi, Y.K. Park, and Y.S. Shin

ABSTRACT

BACKGROUND AND PURPOSE: Unruptured intracranial vertebrobasilar dissecting aneurysms with brain stem compression are difficult to treat. In the present study, the clinical and radiologic outcomes of unruptured intracranial vertebrobasilar dissecting aneurysms with brain stem compression based on different treatment modalities were evaluated.

MATERIALS AND METHODS: This study included 28 patients with unruptured intracranial vertebrobasilar dissecting aneurysms with brain stem compression treated from January 2009 to December 2017. Treatment methods were observation ($n = 6$), stent-assisted coil embolization ($n = 9$), parent artery occlusion ($n = 6$), and flow diversion ($n = 7$). The data of baseline characteristics, change of aneurysm size, retreatment rate, stroke occurrence, and alteration of the mRS score were obtained from retrospective chart review.

RESULTS: The initial size of dissecting aneurysms was largest in the flow diversion group (22.5 ± 7.7 mm), followed by parent artery occlusion (20.3 ± 8.4 mm), stent-assisted coil embolization (11.7 ± 2.2 mm), and observation (17.8 ± 5.5 mm; $P = .01$) groups. The reduction rate of aneurysm size was highest in the parent artery occlusion group (26.7 ± 32.1%), followed by flow diversion (14.1% ± 28.7%), stent-assisted coil embolization (−17.9 ± 30.3%), and observation (−31.5 ± 30.8%; $P = .007$) groups. Additional treatment was needed in the observation (4/6, 66.7%) and stent-assisted coil embolization (3/9, 33.3%; $P = .017$) groups. Improvement of the mRS score on follow-up was observed in the flow diversion (6/7, 85.7%) and parent artery occlusion (4/6, 66.7%) groups but not in the stent-assisted coil embolization and observation groups. A worsened mRS score was most common in the observation group (4/6, 66.7%), followed by stent-assisted coil embolization (3/9, 33.3%), parent artery occlusion (2/6, 33.3%), and flow diversion (0/7, 0%) groups.

CONCLUSIONS: When treating intracranial vertebrobasilar dissecting aneurysms with brain stem compression, parent artery occlusion and flow diversion should be considered to reduce aneurysm size and improve the mRS score.

ABBREVIATIONS: FD = flow diversion; IVBDA = intracranial vertebrobasilar dissecting aneurysm; PAO = parent artery occlusion; SACE = stent-assisted coil embolization

Intracranial vertebrobasilar dissecting aneurysm (IVBDA) is one of the most common intracranial arterial dissections. On initiation of a sudden disruption of the internal elastic lamina and media, circulating blood invades the disrupted layer, resulting in formation of an intramural hematoma.[1] When the intramural hematoma extends toward the outer layer, the dissection presents as aneurysmal dilation due to hemodynamic stress to separated adventitia from invading circulating blood.[2] The aneurysmal dilation of intracranial arterial dissection may progress to subarachnoid hemorrhage with adventitial tearing. Moreover, a large IVBDA may induce brain stem compression due to the position adjacent to the brain stem, which might result in a neurologic deficit. Thus, treatment for unruptured large IVBDAs with brain stem compression should target the prevention of aneurysm rupture and relief of mass effect on the brain stem. Various treatment modalities, such as conservative, endovascular, and surgical treatments are available for IVBDAs. Possible surgical treatment options for IVBDA are reconstruction with direct clipping or proximal ligation; however, when the aneurysm is large, these options are commonly limited due to

Received May 17, 2019; accepted after revision August 20.

From the Department of Neurosurgery (D.Y.C.), Ewha Womans University Seoul Hospital, College of Medicine, Ewha Womans University, Seoul, Republic of Korea; Departments of Radiology (B.-S.K.) and Neurosurgery (J.H.C., Y.S.S.), Seoul St. Mary's Hospital, College of Medicine, The Catholic University of Korea, Seoul, Republic of Korea; and Department of Neurosurgery (Y.K.P.), Ilsan Paik Hospital, College of Medicine, Inje University, Goyang, Republic of Korea.

Please address correspondence to Yong Sam Shin, MD, PhD, Department of Neurosurgery, Seoul St. Mary's Hospital, The Catholic University of Korea, 222 Banpo-daero, Seocho-gu, Seoul 137-701, Republic of Korea; e-mail: nsshin@gmail.com

http://dx.doi.org/10.3174/ajnr.A6252

Table 1: Baseline characteristics of patients in the 4 different treatment technique groups[a]

Variables	Observation ($n = 6$)	SACE ($n = 9$)	PAO ($n = 6$)	FD ($n = 7$)	*P* Value
Age (yr)	58.2 ± 8.3	54.3 ± 14.7	45.3 ± 15.7	47.6 ± 22.1	.47[b]
Sex, male	3 (50)	3 (33.3)	2 (33.3)	2 (28.6)	.87[c]
DM	0 (0)	1 (11.1)	0 (0)	0 (0)	.51[c]
Hypertension	3 (50)	4 (44.4)	3 (50)	1 (14.3)	.47[c]
Dyslipidemia	2 (33.3)	0 (0)	0 (0)	2 (28.6)	.14[c]
Current smoker	1 (16.7)	0 (0)	0 (0)	2 (28.6)	.23[c]
Symptoms					.04[c]
Incidental	1 (16.7)	5 (55.6)	0 (0)	0 (0)	
Headache	3 (50)	2 (22.2)	2 (33.3)	1 (14.3)	
Neurologic deficit	2 (33.3)	2 (22.2)	4 (66.7)	6 (85.7)	
Location					.65[c]
Right VA	2 (33.3)	4 (44.4)	1 (16.7)	2 (28.6)	
Left VA	2 (33.3)	5 (55.6)	3 (50)	3 (42.9)	
BA	2 (33.3)	0 (0)	2 (33.3)	2 (28.6)	

Note:—DM indicates diabetes mellitus; VA, vertebral artery; BA, basilar artery.
[a] Values are presented as mean ± SD or number (%).
[b] ANOVA.
[c] Fisher exact test.

difficult access and postoperative complications. Because of these surgical limitations, diverse endovascular treatments for large vertebrobasilar dissecting aneurysms are currently performed, such as stent-assisted coil embolization (SACE), parent artery occlusion (PAO), and, recently, flow diversion (FD).[3-6] In the present study, clinical and radiologic outcomes of unruptured IVBDAs with brain stem compression based on different treatment modalities were evaluated.

MATERIALS AND METHODS

All patient data from a single institution (Seoul St. Mary's Hospital) were retrospectively reviewed, and data collection was approved by the institutional review board.

Patients

From January 2009 to December 2017, two hundred seventy-two IVBDAs were diagnosed in a single institution. Large IVBDAs with brain stem compression were diagnosed on the basis of the following criteria: 1) angiographic evidence of IVBDA (ie, aneurysmal dilation or a pearl-and-string sign of the vertebrobasilar artery on 3D-reconstruction digital subtraction angiography); 2) radiologic evidence of IVBDA on MR imaging (ie, intramural hematoma, double lumen sign, intimal flap); and 3) mass effect of an aneurysm compressing the brain stem, with distortion of boundary shape on MR imaging. Exclusion criteria were the following: 1) a ruptured IVBDA; 2) traumatic IVBDA; 3) iatrogenic IVBDA; 4) laboratory or radiologic findings suggestive of vasculopathy, fibromuscular dysplasia, or Bechet disease; and 5) patients lost to follow-up. All clinical and radiologic data, including age, sex distribution, risk factors (diabetes mellitus, hypertension, dyslipidemia, current smoker), location of the IVBDA, and follow-up period were collected retrospectively.

Treatment Modalities

Patients included in this study underwent 4 different treatment modalities: 1) observation, 2) SACE, 3) PAO, or 4) FD. Patients who refused endovascular treatment due to procedure-related complications underwent observation and were closely followed up in the outpatient clinic. These patients were counseled regarding a 30% risk of mortality and morbidity based on previous studies.[7-9] IVBDAs with minimal brain stem compression due to the relatively small size were typically treated with SACE. PAO and FD were performed when the IVBDA was large and the lesion was symptomatic. PAO was considered first when the branching arteries were not incorporated and enough collateral flow was expected after occlusion of the parent artery. FD was considered when postoperative ischemia was expected after PAO due to poor collateral flow and branching artery involvement. All endovascular treatments were performed with the patient under general anesthesia with right femoral artery puncture; aspirin (100 mg) and clopidogrel (75 mg) were given daily for 7 days before treatment. Intravenous heparin was administered during the procedure.

An Enterprise 2 self-expanding stent (Codman & Shurtleff, Raynham, Massachusetts) or a LVIS Blue or Jr (MicroVention, Tustin, California) with detachable coils was used for SACE, and PAO was performed with detachable coils. All SACE cases were treated with a conventional stent-assisted coiling using a single stent. The Pipeline Embolization Device (PED; Covidien, Irvine, California) or the Flow-Redirection Endoluminal Device (FRED; MicroVention) was used for FD. In the endovascular treatment groups, dual-antiplatelet medication with 100 mg of aspirin and 75 mg of clopidogrel was maintained for at least 6 months and was gradually reduced in the outpatient clinic. After 6 months of dual-antiplatelet medication, the SACE and PAO groups maintained a single antiplatelet regimen with 100 mg of aspirin for 18 more months, and the FD group maintained a single antiplatelet regimen with 100 mg of aspirin life-long.

Radiologic and Clinical Follow-Up

The patients in SACE, PAO, and FD groups underwent diffusion-weighted MR imaging on postoperative day 1 for evaluation of postprocedural infarction. Follow-up MR imaging was performed in all patients after 6, 12, and 24 months to evaluate changes in aneurysm size. Additional MR imaging was performed at 2-year intervals or if new neurologic symptoms developed. The preprocedural and postprocedural sizes of aneurysms were measured on axial sections of T2 sequence MR imaging, which presents the largest IVBDA diameter. The size of the IVBDA on the initial and last MR imaging examination was recorded, and the percentage of size reduction was calculated. Associated infarction on the initial clinical diagnosis of IVBDA and occurrence of newly developed infarctions during the follow-up period were recorded. The mRS score on the initial and last follow-up was recorded, and improvement or deterioration of the mRS was analyzed.

Table 2: Radiologic and clinical outcomes of patients in the 4 different treatment technique groups[a]

Variables	Observation ($n=6$)	SACE ($n=9$)	PAO ($n=6$)	FD ($n=7$)	*P* Value
Follow-up (mo)	28.3±14.2	27 ± 23.4	40.2 ± 37.4	16.3 ± 13.1	.37[b]
Initial aneurysm size (mm)	17.8 ± 5.5	11.7 ± 2.2	20.3 ± 8.4	22.5 ± 7.7	.01[b]
Aneurysm size on follow-up (mm)	23.4 ± 9.8	13.9 ± 5.2	14.4 ± 9.7	19.9 ± 10.1	.1[b]
Change of aneurysm size (%)	129.3 ± 29.5	117.8 ± 30.0	73.2 ± 32.2	85.9 ± 28.7	.008[b]
Retreatment	4 (66.7)	3 (33.3)	0 (0)	0 (0)	.017[c]
SACE	0 (0)	1 (33.3)	0 (0)	0 (0)	
PAO	1 (25)	0 (0)	0 (0)	0 (0)	
FD	3 (75)	2 (66.6)	0 (0)	0 (0)	
Initial ischemic stroke	0 (0)	1 (11.1)	1 (16.7)	1 (14.3)	.79[c]
Ischemic stroke on follow-up	1 (16.7)	1 (11.1)	1 (16.7)	0 (0)	.73[c]
Subarachnoid hemorrhage on follow-up	0 (0)	0 (0)	0 (0)	0 (0)	
Improvement of mRS score	0 (0)	0 (0)	4 (66.7)	6 (85.7)	<.001[c]
Worsening of mRS score	4 (66.7)	3 (33.3)	2 (33.3)	0 (0)	.086[c]

[a] Values are presented as mean ± SD or number (%).
[b] ANOVA test.
[c] Fisher exact test.

Statistical Analysis

Statistical analysis was performed using SPSS, Version 24 (IBM, Armonk, New York). Baseline characteristics and radiologic and clinical outcomes between different treatment technique groups were analyzed. One-way ANOVA with post hoc Bonferroni corrections and the Kruskal-Wallis test were used for numeric variables, and the Fisher exact test was used for nominal variables. *P* values < .05 were considered statistically significant.

RESULTS

Baseline Characteristics of Patients in the 4 Different Treatment Technique Groups

Among the 272 IVBDAs, 40 IVBDAs met the inclusion criteria. Twelve IVBDAs were excluded due to ruptured lesions ($n=6$), history of trauma ($n=1$), suggestive vasculopathy ($n=1$), and loss to follow-up ($n=4$). Finally, 28 patients with IVABADs were identified and enrolled in the study. Among the 28 patients with IVBDAs with brain stem compression, 6 patients underwent observation, 9 patients underwent SACE, 6 patients underwent PAO, and 7 patients underwent FD. Table 1 shows baseline characteristics of patients in each treatment technique group. Significant differences in age, male sex distribution, risk factors, and follow-up period were not observed. None of the basilar artery lesions were treated with SACE, and no significant difference was observed in the location of IVBDAs. Initial presenting symptoms were significantly different between the groups. The proportion of IVBDAs without symptoms was highest in the SACE group, and all IVBDAs treated with PAO and FD were symptomatic. The proportion of headache as an initial symptom was highest in the observation group, and the proportion of neurologic deficits was highest in the FD group ($P=.04$).

Radiologic and Clinical Outcomes of Patients in the 4 Different Treatment Technique Groups

The mean age of patients was 51.5 ± 16 years (range, 12–71 years), and the mean follow-up period was 27.4 ± 23.8 months. Table 2 shows radiologic and clinical outcomes of patients in the 4 different treatment-technique groups. The initial IVBDA size was significantly different between the groups. The initial size was largest in the FD group (22.5 ± 7.7 mm), followed by PAO (20.3 ± 8.4 mm), observation (17.8 ± 5.5 mm), and SACE (11.7 ± 2.2 mm; $P<.01$) groups. The change of IVBDA size was significantly different among the groups ($P=.008$). The reduction of IVBDA size on follow-up compared with initial size was observed in the PAO (73.2% ± 32.2%) and FD (85.9 ± 28.7%) groups. Conversely, increased IVBDA size was observed in the SACE (117.8% ± 30%) and observation (129.3% ± 29.5%) groups. The comparison of the reduction rate of aneurysm size is shown in Fig 1. The PAO group showed the highest rate of size reduction (73.2% ± 32.2%), followed by FD (14.1% ± 28.7%), SACE (−17.9% ± 30.3%), and observation (−31.5% ± 30.8%) groups. The PAO group showed a significantly large rate of size reduction compared with the SACE ($P=.047$) and observation ($P=.014$) groups. The size-reduction rate in the FD group was significantly different compared with the observation group ($P=.05$).

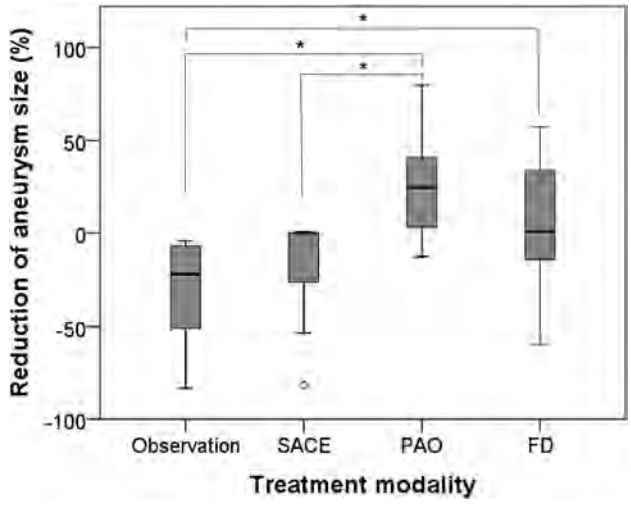

FIG 1. Reduction of vertebrobasilar dissecting aneurysm size based on treatment technique. The PAO group showed the greatest amount of aneurysm reduction followed by FD, SACE, and observation groups. The *asterisk* indicates $P<.05$.

The outlier in the SACE group in Fig 1 is shown in Fig 2. A 20-year-old man presented with headache, and MR imaging and

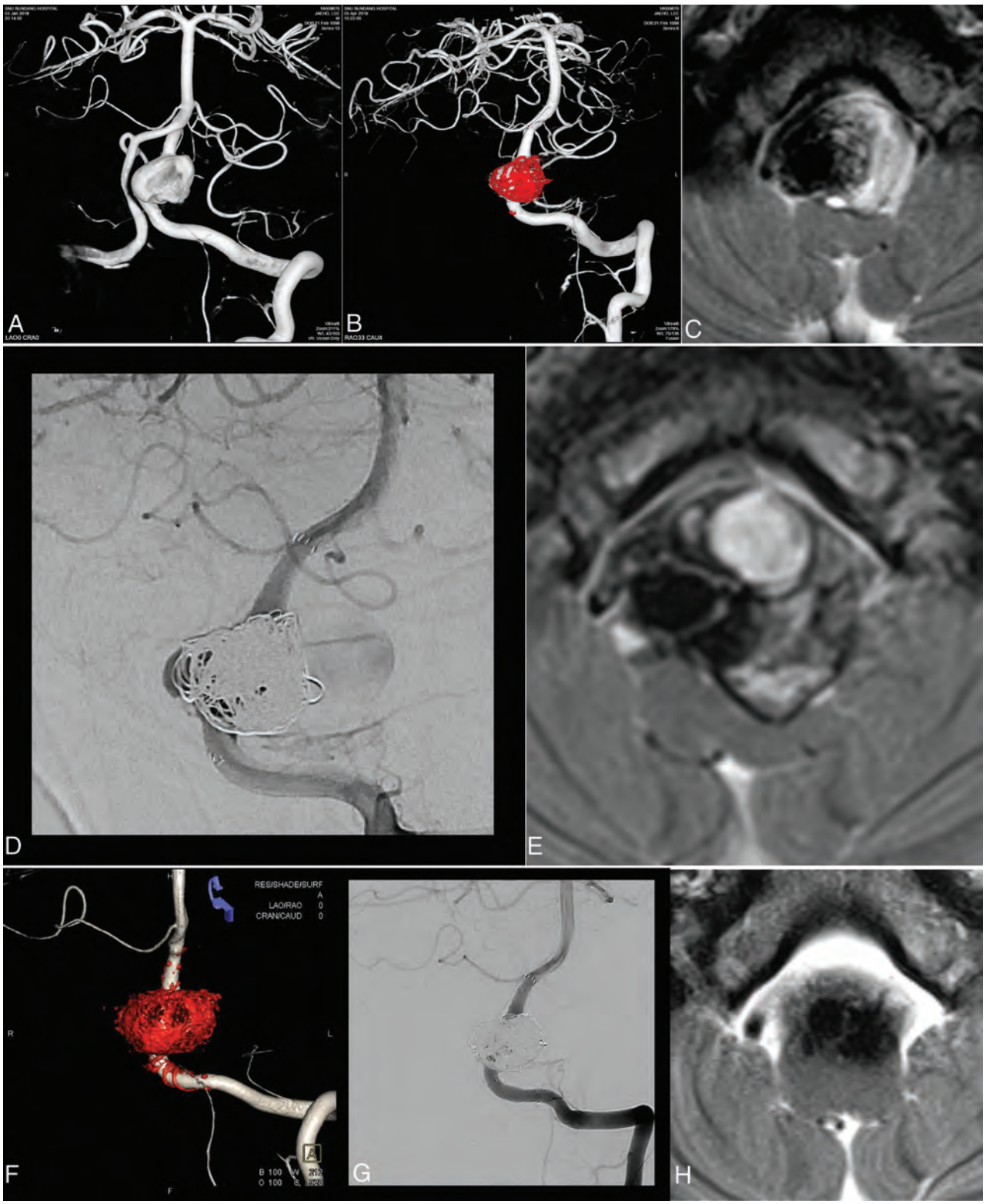

FIG 2. Treatment of large vertebral artery dissecting aneurysm with brain stem compression in a 20-year-old man. *A*, 3D rotational angiography shows a large dissecting aneurysm on the fourth segment of the right vertebral artery. *B*, Stent-assisted coil embolization was performed. *C*, T2 axial MR image on postoperative day 12 shows coil meshes with extended thrombus in the aneurysm sac. *D*, Angiography after 3 months shows a jet flow into aneurysm sac. *E*, T2 axial MR image shows enlargement of aneurysm diameter with aggravation of brain stem compression. *F*, FD was performed using the FRED. *G*, Angiography 5 months after FD shows complete regression of jet inflow. *H*, T2 axial MR imaging shows a markedly decreased aneurysm sac diameter with diminished brain stem compression.

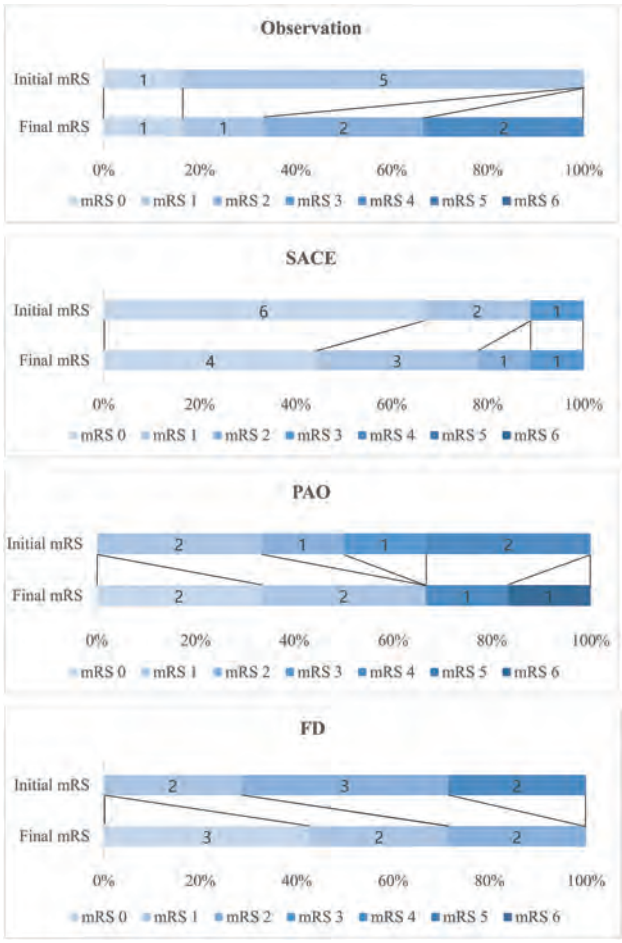

FIG 3. Alteration of mRS based on the treatment technique.

angiography showed a fusiform dissecting aneurysm on the left V4. SACE was initially performed but resulted in an 82% increase of aneurysm size after 3 months with development of a neurologic deficit. The patient was retreated with FD with excellent outcome. Among the 28 IVBDAs with brain stem compression, 4 of 6 (66.7%) observation patients and 3 of 9 (33.3%) patients treated with SACE underwent retreatment due to aggravation of brain stem mass effect and a worsened mRS score. Conversely, no patient needed additional treatment in the PAO and FD groups. These values were statistically significant ($P = .017$). Among the 4 retreated patients in the observation group, 1 underwent PAO and 3 underwent FD. Among the 3 patients treated with SACE, 1 underwent additional coil embolization and 2 underwent FD. Patients additionally treated with PAO or FD showed good outcomes with cessation of aneurysm growth; however, the aggravation of mass effect due to aneurysm growth was evident in patients who underwent additional coil embolization.

Among the 28 IVBDAs with brain stem compression, 3 associated ischemic strokes were observed on initial diagnosis: 1 transient ischemic attack in the SACE (1/9, 11.1%) and PAO (1/6, 16.7%) groups and 1 cerebellar infarction in the FD (1/7, 14.3%) group. On follow-up, there were 3 infarctions: 1 cerebellar infarction in the observation group (1/6, 16.7%), 1 medullary infarction in the SACE group on postoperative day 7 (1/9, 11.1%), and 1 cerebellar infarction in the PAO group on postoperative day 1 (1/6, 16.7%); no ischemic stroke occurred in the FD group. Initial and follow-up stroke rates were not statistically different among treatment modalities ($p = 0.79$, $p = 0.73$).

Ten patients showed improved mRS scores. The improvement rate of mRS scores was highest in the FD group (6/7, 85.7%) followed by the PAO group (4/6, 66.7%). The observation and SACE groups showed no mRS improvement. These values were statistically significant ($P < .001$). Lower mRS scores were observed in 9 patients. The rate of worsened mRS scores was highest in the observation group (4/6, 66.7%), followed by the SACE (3/9, 33.3%) and PAO (2/6, 33.3%) groups. A worsened mRS score was not observed in the FD group. However, the difference between the worsened rates of mRS scores was not statistically significant ($P = .086$). The changes in mRS scores based on treatment technique is shown in Fig 3. mRS scores in the observation and SACE groups showed a tendency to improve, whereas the mRS scores in the PAO and FD groups tended to decrease. Among the 28 patients, 1 patient in the PAO group died. The 47-year-old man with hypertension and end-stage renal disease was diagnosed with a large thrombosed dissecting aneurysm on the basilar artery. The patient was treated with PAO; however, the aneurysm continued to grow, and the patient progressed to a vegetative state due to brain stem compression and obstructive hydrocephalus after 5 months. The patient died after 8 months due to complications from pneumonia and sepsis caused by multiorgan failure.

DISCUSSION

Large IVBDAs typically have a poor prognosis due to the high risk of rupture and growth characteristics. Still, there is a question about the treatment technique as to whether such patients should undergo reconstructive or destructive treatment. A systematic review and meta-analysis showed higher angiographic occlusion rates for a destructive technique and lower morbidity rates for a reconstruction technique, but long-term neurologic outcomes and retreatment rates were not statistically different.[10] In the present study, we compared clinical and radiologic outcomes of various destructive and reconstructive treatments and compared them with each other and with an observation group.

The baseline characteristics of 4 different treatment-technique groups did not show a significant difference except for initial symptoms and the initial size of the IVBDAs. In our treatment strategy, IVBDAs with relatively small sizes and no symptoms were mostly treated with SACE to prevent ischemic complications and obtain immediate aneurysm occlusion. Large IVBDAs inducing a neurologic deficit were mostly treated with PAO or FD to avoid a mass effect caused by the coil mesh and to decrease the aneurysm size to relieve the neurologic deficit caused by brain stem compression. The initial size of IVBDAs in the observation group was higher than that in the SACE group. This finding might be due to patients who refused to undergo treatment or untreatable lesions due to large size with prominent brain stem perforators and incorporation of cerebellar arteries before approval of the FD device.

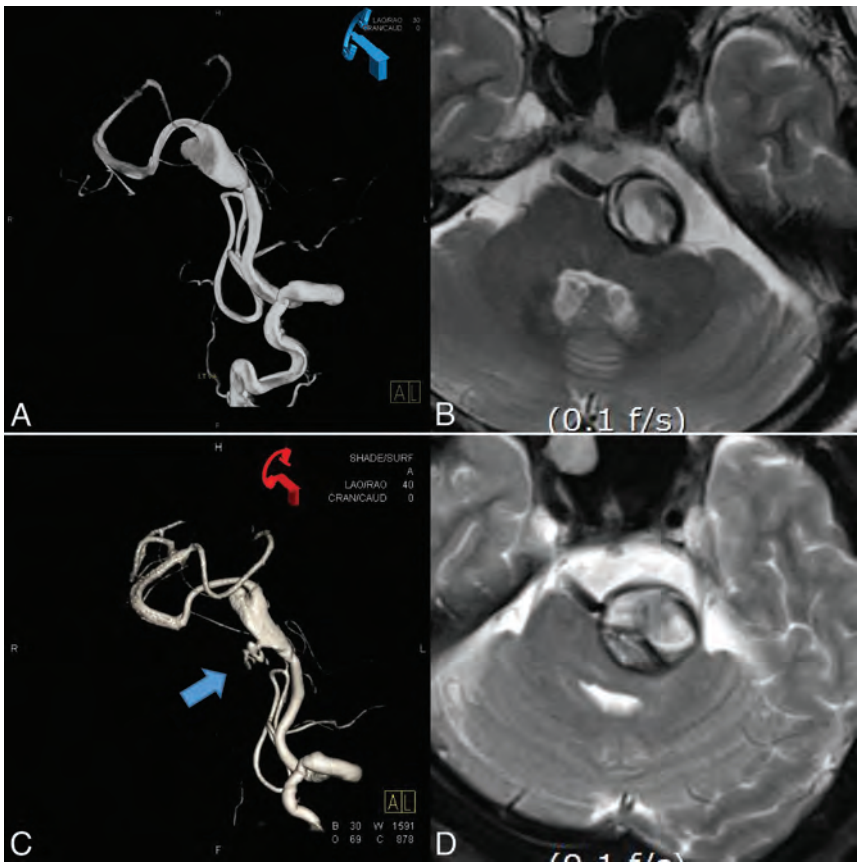

FIG 4. Growth of an observed vertebral artery dissecting aneurysm in a 67-year-old woman. *A*, 3D rotational angiography shows a fusiform-type vertebral artery dissecting aneurysm on the fourth segment of left vertebral artery. *B*, T2 axial MR image shows formation of intra-aneurysmal thrombus with brain stem compression. The patient underwent observation, and right-sided weakness developed after 5 years. *C*, 3D rotational angiography after 5 years shows contrast extension into the thrombosed aneurysm sac (*arrow*). *D*, T2 axial MR image shows enlargement of aneurysm diameter with aggravation of brain stem compression.

The natural course of vertebrobasilar dissection is benign.[2,11,12] The nature of an unruptured IVBDA is also not highly aggressive. Kai et al[13] reported that only 9 of 100 unruptured IVBDAs needed surgical or endovascular treatment due to progression of symptoms or change of angiographic shape during 24 months of follow-up. However, the prognosis of large IVBDAs is worse than that of stenotic-type dissections or small IVBDAs. Kobayashi et al[14] reported the need for treatment of IVBDAs larger than 10 mm due to aneurysm growth and clinical deterioration caused by a mass effect. Our study showed similar results, with the largest size increase and highest rate of mRS deterioration in the observation group. In addition to aggravation of a mass effect to the brain stem in growing IVBDAs, the high risk of rupture should also be considered. Naito et al[15] reported a higher-than-expected risk of bleeding in large or growing vertebral artery dissections (3/21), and Flemming et al[16] reported enlargement of a dissecting aneurysm as a risk factor of rupture. In our study, 4 of 6 patients in the observation group eventually underwent endovascular treatment due to aneurysm enlargement and clinical deterioration caused by a mass effect to the brain stem. One of the progressed cases of a large IVBDA with brain stem compression is described in Fig 4.

Surgical treatment of IVBDAs with brain stem compression was a unique option before approval of endovascular devices. Drake and Peerless[17] reported outcomes of 120 giant fusiform intracranial aneurysms with surgical treatment: Fifty-six were located in basilar trunk, vertebrobasilar junction, and vertebral artery. They were treated with surgical clipping, wrapping, or proximal ligation with or without bypass surgery. Four patients showed severe neurologic deficits, and 13 patients died. Due to the high mortality and morbidity of surgical treatment, endovascular treatments have emerged as treatments of choice. In our study, all IVBDAs with brain stem compression were treated endovascularly.

Although endovascular treatment of the IVBDAs shows lower mortality and morbidity rates compared with surgical treatment, various perioperative complications can occur. Destructive treatment might induce perioperative ischemic stroke due to occlusion of perforators or branching arteries. Reconstructive treatment also might cause ischemic and hemorrhagic stroke. SACE has the possibility of perioperative aneurysm rupture during aneurysm selection or coil deployment and thromboembolic infarction due to the deployment of stent. FD might cause delayed rupture of aneurysms and perforator infarction. The recent meta-analysis comparing the destructive technique with the reconstructive technique in treating IVBDAs showed similar perioperative mortality and morbidity.[10] In our study, the ischemic stroke rate during follow-up was higher in the deconstructive group (1/6, 16.7%) than in the reconstructive group (1/16, 6.3%), but it was not statistically significant due to small variables. No perioperative hemorrhagic stroke occurred in any treatment modality.

Stent-assisted coil embolization has been widely performed to treat vertebrobasilar dissecting aneurysms because of immediate aneurysm occlusion with preservation of parent artery flow. Jeon et al[18] reported the feasibility and safety of SACE in IVBDAs, with acceptable long-term follow-up results despite a high rate of incomplete immediate occlusion. In addition, 25 of 47 lesions (53.2%) showed no immediate contrast filling; during a mean follow-up of 20.2 months, 37 of 47 lesions (78.7%) appeared completely occluded. However, a high rate of immediate incomplete occlusion can be problematic in treating large IVBDAs with SACE. Because most large IVBDAs have a wide neck, it is difficult to achieve complete packing of the aneurysm, leading to coil

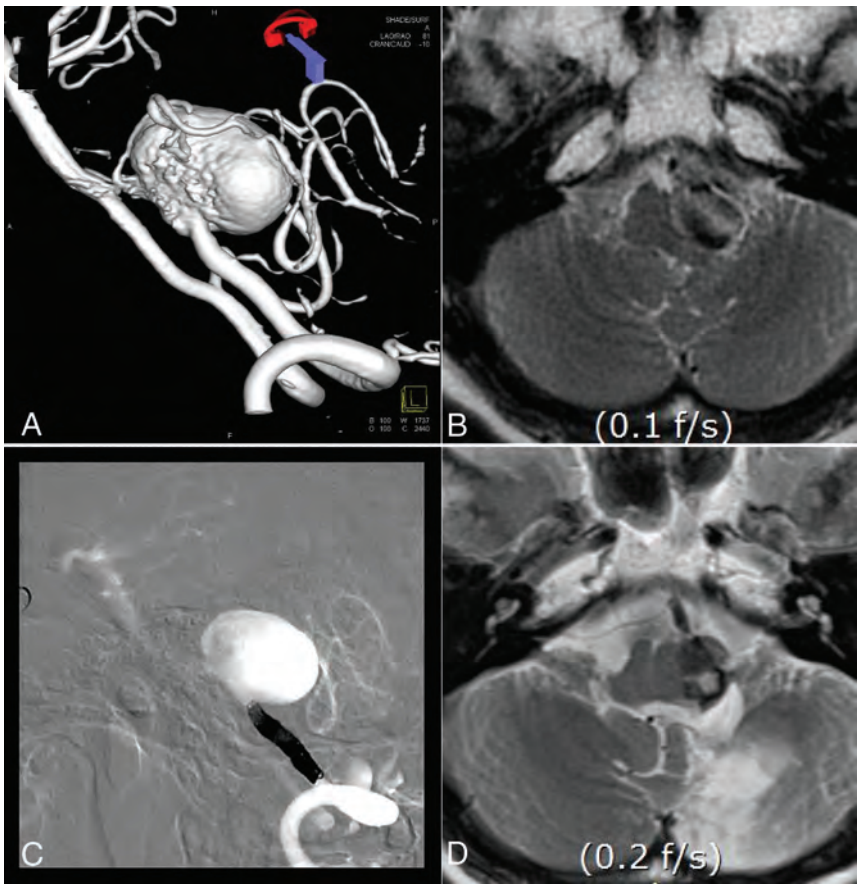

FIG 5. Reduction of vertebral artery dissecting aneurysm size using PAO in 58-year-old woman. *A*, Rotational 3D angiography shows a large vertebral artery dissecting aneurysm in the fourth segment of the left vertebral artery. *B*, T2 axial MR image shows thrombus formation with brain stem compression. *C*, PAO was performed. *D*, T2 axial MR imaging after 12 months shows a decreased diameter of the aneurysm with diminished brain stem compression.

compaction and reopening of the aneurysm. Furthermore, intra-aneurysmal thrombus is common in large IVBDAs and results in coil migration and loosening into the thrombosed portion.[19,20] These failures result in growth of the IVBDA with aggravating brain stem compression. In our study, the initial mean aneurysm size of the SACE group was 11.7 mm, which increased to 13.9 mm on follow-up. Three of 9 patients (33.3%) treated with SACE showed mRS deterioration or no mRS improvement.

Parent artery occlusion might be a good treatment option in large IVBDAs with brain stem compression if branching arteries are not incorporated. There are numerous studies of PAO in the treatment of IVBDAs. Aymard et al[21] reported a good outcome of PAO in unclippable vertebrobasilar aneurysms, and 13 of 21 IVBDAs showed good clinical and angiographic outcomes. Leibowitz et al[22] reported a high rate of aneurysm occlusion with PAO when complete thrombosis of the aneurysm was achieved. IVBDAs involving bilateral vertebral arteries or the basilar artery showed poor prognosis compared with unilateral vertebral artery involvement due to difficulties in thrombus formation caused by abundant collateral flow. In our study, 2 of 6 patients (33.3%) in the PAO group showed mRS deterioration: 1 of 4 patients with a unilateral vertebral artery lesion (25%) and 1 of 2 patients with a basilar artery lesion (50%). Both basilar aneurysms were thrombosed holobasilar aneurysms. The rest of the 4 patients in the PAO group showed mRS improvement. The risk of postoperative infarction in the PAO group was not significantly higher than in the other treatment groups. The mean reduction of aneurysm size was 73.2%, which is the largest among the treatment groups. One of the cases with reduction of IVBDA size using parent artery occlusion is described in Fig 5.

The efficacy of FD for anterior circulation aneurysms has been demonstrated in numerous studies,[23-25] but pessimism remains regarding FD for posterior circulation aneurysms because of concern for perforator infarction and delayed rupture. Siddiqui et al reported unfavorable outcome in 7 patients with symptomatic large or giant fusiform vertebrobasilar aneurysms treated with flow diverters. Of these, 4 patients died (2 with delayed rupture and 2 with brain stem infarction), and 1 patient had an mRS score of 5. Preoperative stroke and multiple uses of an FD device were risk factors for postoperative perforator infarction.[26] On the other hand, there are some reports presenting favorable outcomes. Natarajan et al[27] reported that 11 of 12 fusiform vertebrobasilar aneurysms treated with FD showed recovery of neurologic deficits, and all showed aneurysm occlusion at the final follow-up. This study suggests the importance of patient selection because they did not include patients with holobasilar aneurysms. We treated 2 basilar trunk aneurysms with flow diversion, both of which were midbasilar, not holobasilar aneurysms. Both patients with basilar aneurysms treated with FD showed improvement of the mRS and aneurysm size reduction. One case showing recurrent IVBDA after SACE is presented in Fig 2, and the other was a 10-year-old girl without intra-aneurysmal thrombus and with initial brain stem infarction. We achieved total occlusion with a single FD device without ischemic stroke on follow-up in both cases.

The limitations of this study are that it was retrospective and performed in a single center with a small number of patients with discordant initial variables, which may lead to statistical bias. Second, the prognoses of vertebral artery dissecting aneurysm and basilar artery aneurysm were not separately analyzed, despite their different disease natures. Third, there is lack of evidence to prove the superiority of PAO or FD in treating IVBDAs with brain stem compression. The rate of aneurysm size reduction was higher in the PAO group, and the proportion of patients with mRS improvement was higher in the FD group. The PAO group showed 2 of 6 with mRS worsening, and the FD group did not

show any mRS worsening. However, these differences between the 2 groups were not statistically significant due to a small number of variables. Moreover, FD sometimes causes unexpected postoperative aneurysm rupture due to a change of hemodynamics, which is fatal. Fortunately, our FD group did not show any postoperative delayed rupture of aneurysm, but the risk remains. Further study with a larger population is needed.

CONCLUSIONS

Unruptured IVBDAs with brain stem compression aggravate neurologic deficits and increase in size when untreated, indicating the need for active treatment. The SACE technique does not prevent aneurysm growth or neurologic deterioration in many cases. Thus, PAO and FD should be considered to obtain consistent reduction of aneurysm size and improvement of mRS.

REFERENCE

1. Park KW, Park JS, Hwang SC, et al. **Vertebral artery dissection: natural history, clinical features and therapeutic considerations.** *J Korean Neurosurg Soc* 2008;44:109–15 CrossRef Medline
2. Mizutani T. **Natural course of intracranial arterial dissections.** *J Neurosurg* 2011;114:1037–44 CrossRef Medline
3. Jin SC, Kwon DH, Choi CG, et al. **Endovascular strategies for vertebrobasilar dissecting aneurysms.** *AJNR Am J Neuroradiol* 2009; 30:1518–23 CrossRef Medline
4. Guerrero WR, Ortega-Gutierrez S, Hayakawa M, et al. **Endovascular treatment of ruptured vertebrobasilar dissecting aneurysms using flow diversion embolization devices: single-institution experience.** *World Neurosurg* 2018;109:e164–69 CrossRef Medline
5. Leibowitz R, Do HM, Marcellus ML, et al. **Parent vessel occlusion for vertebrobasilar fusiform and dissecting aneurysms.** *AJNR Am J Neuroradiol* 2003;24:902–07 Medline
6. Lylyk P, Ceratto R, Hurvitz D, et al. **Treatment of a vertebral dissecting aneurysm with stents and coils: technical case report.** *Neurosurgery* 1998;43:385–88 CrossRef Medline
7. Mu S, Li C, Yang X, et al. **Reconstructive endovascular treatment of spontaneous symptomatic large or giant vertebrobasilar dissecting aneurysms: clinical and angiographic outcomes.** *Clin Neuroradiol* 2016;26:291–300 CrossRef Medline
8. Steinberg GK, Drake CG, Peerless SJ. **Deliberate basilar or vertebral artery occlusion in the treatment of intracranial aneurysms: immediate results and long-term outcome in 201 patients.** *J Neurosurg* 1993;79:161–73 CrossRef Medline
9. van Oel LI, van Rooij WJ, Sluzewski M, et al. **Reconstructive endovascular treatment of fusiform and dissecting basilar trunk aneurysms with flow diverters, stents, and coils.** *AJNR Am J Neuroradiol* 2013;34:589–95 CrossRef Medline
10. Sönmez Ö, Brinjikji W, Murad MH, et al. **Deconstructive and reconstructive techniques in treatment of vertebrobasilar dissecting aneurysms: a systematic review and meta-analysis.** *AJNR Am J Neuroradiol* 2015;36:1293–98 CrossRef Medline
11. Kitanaka C, Tanaka J, Kuwahara M, et al. **Nonsurgical treatment of unruptured intracranial vertebral artery dissection with serial follow-up angiography.** *J Neurosurg* 1994;80:667–74 CrossRef Medline
12. Nakagawa K, Touho H, Morisako T, et al. **Long-term follow-up study of unruptured vertebral artery dissection: clinical outcomes and serial angiographic findings.** *J Neurosurg* 2000;93:19–25 CrossRef Medline
13. Kai Y, Nishi T, Watanabe M, et al. **Strategy for treating unruptured vertebral artery dissecting aneurysms.** *Neurosurgery* 2011;69:1085–91; discussion 1091–92 CrossRef Medline
14. Kobayashi N, Murayama Y, Yuki I, et al. **Natural course of dissecting vertebrobasilar artery aneurysms without stroke.** *AJNR Am J Neuroradiol* 2014;35:1371–75 CrossRef Medline
15. Naito I, Iwai T, Sasaki T. **Management of intracranial vertebral artery dissections initially presenting without subarachnoid hemorrhage.** *Neurosurgery* 2002;51:930–37; discussion 937–38 CrossRef Medline
16. Flemming KD, Wiebers DO, Brown RD Jr, et al. **Prospective risk of hemorrhage in patients with vertebrobasilar nonsaccular intracranial aneurysm.** *J Neurosurg* 2004;101:82–87 CrossRef Medline
17. Drake CG, Peerless SJ. **Giant fusiform intracranial aneurysms: review of 120 patients treated surgically from 1965 to 1992.** *J Neurosurg* 1997;87:141–62 CrossRef Medline
18. Jeon JP, Cho YD, Rhim JK, et al. **Stent-assisted coil embolization of vertebrobasilar dissecting aneurysms: procedural outcomes and factors for recanalization.** *Korean J Radiol* 2016;17:801–10 CrossRef Medline
19. van Rooij WJ, Sluzewski M. **Endovascular treatment of large and giant aneurysms.** *AJNR Am J Neuroradiol* 2009;30:12–18 CrossRef Medline
20. Sluzewski M, Menovsky T, van Rooij WJ, et al. **Coiling of very large or giant cerebral aneurysms: long-term clinical and serial angiographic results.** *AJNR Am J Neuroradiol* 2003;24:257–62 CrossRef Medline
21. Aymard A, Gobin YP, Hodes JE, et al. **Endovascular occlusion of vertebral arteries in the treatment of unclippable vertebrobasilar aneurysms.** *J Neurosurg* 1991;74:393–98 CrossRef Medline
22. Leibowitz R, Do HM, Marcellus ML, et al. **Parent vessel occlusion for vertebrobasilar fusiform and dissecting aneurysms.** *AJNR Am J Neuroradiol* 2003;24:902–07 Medline
23. Fischer S, Vajda Z, Aguilar Perez M, et al. **Pipeline embolization device (PED) for neurovascular reconstruction: initial experience in the treatment of 101 intracranial aneurysms and dissections.** *Neuroradiology* 2012;54:369–82 CrossRef Medline
24. Lylyk P, Miranda C, Ceratto R, et al. **Curative endovascular reconstruction of cerebral aneurysms with the Pipeline embolization device: the Buenos Aires experience.** *Neurosurgery* 2009;64:632–43 CrossRef Medline
25. Nelson P, Lylyk P, Szikora I, et al. **The Pipeline embolization device for the intracranial treatment of aneurysms trial.** *AJNR Am J Neuroradiol* 2011;32:34–40 CrossRef Medline
26. Siddiqui AH, Abla AA, Kan P, et al. **Panacea or problem: flow diverters in the treatment of symptomatic large or giant fusiform vertebrobasilar aneurysms.** *J Neurosurg* 2012;116:1258 CrossRef Medline
27. Natarajan SK, Lin N, Sonig A, et al. **The safety of Pipeline flow diversion in fusiform vertebrobasilar aneurysms: a consecutive case series with longer-term follow-up from a single US center.** *J Neurosurg* 2016;125:111–19 CrossRef Medline

Placement of a Stent within a Flow Diverter Improves Aneurysm Occlusion Rates

O. Ocal, A. Peker, S. Balci, and A. Arat

ABSTRACT

BACKGROUND AND PURPOSE: Placement of a stent within a flow diverter has been described previously but its consequences have not been analyzed. We evaluated the clinical and angiographic results of stent placement within a flow diverter during the same treatment session.

MATERIALS AND METHODS: All patients treated with a Surpass flow diverter were retrospectively evaluated. Patients with previously deployed stents and procedures in which scaffolding stents, a second flow diverter, or intrasaccular devices were used were excluded. Patient and aneurysm characteristics and clinical and imaging follow-up results were compared between stented and nonstented Surpass flow-diverter groups and stent assisted coiling.

RESULTS: Thirty-five patients (41 aneurysms) were treated with a Surpass flow diverter only (monotherapy group), and in 33 patients (35 aneurysms), a stent was placed within the Surpass flow diverter (stented group). Stents were placed inside the Surpass flow diverter for a variety of reasons at the operator's discretion. No statistical difference was noted between the 2 groups in age, body weight, sex, history of thromboembolic events, smoking, platelet inhibition levels, hypertension, hyperlipidemia, diabetes mellitus, malignancy, and aneurysm location. Aneurysms in the stented group were larger than those in the monotherapy group (14.8 versus 9.1 mm, $P < .001$). The rate of clinically significant adverse events and complete aneurysm occlusion rates at 0–3 and 3–6 months (73.3% versus 61.3%, $P = .31$, and 84.8% versus 70.2%, $P = .14$) were similar. At 9–12 months, a significantly higher proportion of aneurysms in the stented group achieved complete occlusion (93.9% versus 73.2%, $P = .019$). There was a trend toward a higher obliteration rate on final follow-up in the stented group (93.9% versus 82.9%, $P = .14$).

CONCLUSIONS: Placement of a stent within a flow diverter increases the rate of aneurysm occlusion. We propose that these results are from improved flow-diverter apposition due to the higher radial force of intracranial stents.

ABBREVIATIONS: FD = flow diverter; Mtg = monotherapy group; SAC = stent-assisted coiling; Stg = stented group; RR = Raymond-Roy

Flow diverters (FDs) are effective in the treatment of intracranial aneurysms, and they cause gradual thrombosis of the aneurysm sac by redirecting flow and causing stagnation. Aneurysm occlusion rates after flow diversion at 6 months are around 75%, and there is a rupture risk until complete occlusion occurs.[1,2] Several adjunctive techniques have been described to increase the safety and efficacy of the flow diversion, including coiling or placement of other intrasaccular devices such as flow diverters or the Medina embolization device (Covidien/eV3/Medtronic, Dublin, Ireland) or stent placement.[3-5] Among these techniques, stent placement has been proposed as a technique that enhances apposition and prevents device migration.[5-8] However, this proposal remains speculative and has not been validated. Indeed, to date, there are only 17 patients in the literature in whom placement of a stent inside a flow diverter has been documented[5-8]—that is, there is no comparative study assessing the safety of stent placement within a flow diverter and its effect on the outcome of aneurysms treated by flow diversion. We studied the safety and efficacy of stent placement within a single type of flow diverter during the same treatment session and discuss the rationale and results of this technique.

Received June 17, 2019; accepted after revision August 13.

From the Department of Radiology, Faculty of Medicine, Hacettepe University, Ankara, Turkey.

Please address correspondence to Anıl Arat, MD, Department of Radiology, School of Medicine, Hacettepe University, Sihhiye, 06100, Ankara, Turkey; e-mail: anilarat@hotmail.com

http://dx.doi.org/10.3174/ajnr.A6237

MATERIALS AND METHODS

Study Population

All patients treated with a single type of flow diverter (Surpass; Stryker Neurovascular, Kalamazoo, Michigan) for an intracranial

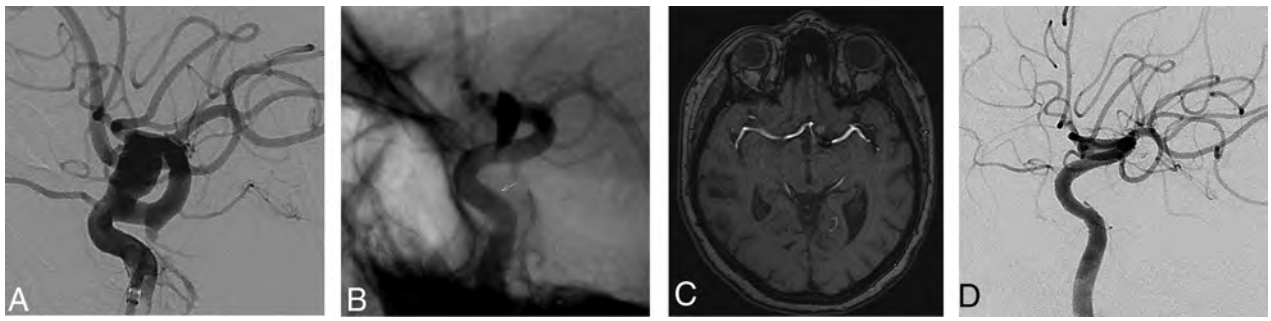

FIG 1. *A*, Left ICA angiogram shows a supraclinoid aneurysm. *B*, Angiogram after the deployment of the flow diverter shows good apposition of the device at the neck of the aneurysm but slight malapposition at the proximal landing zone (*arrow*). *C*, TOF-MRA image 3 months after the procedure shows residual filling in the aneurysm. *D*, Follow-up angiogram obtained 6 months after the procedure shows complete occlusion of the aneurysm. A filling defect is noted where the flow diverter was malapposed.

aneurysm in a single institution by a single operator between May 2013 and September 2017 were identified and evaluated retrospectively. Patients treated by placement of a flow diverter inside a scaffolding stent, adjunctive use of a second flow diverter (telescopic flow diverters), treatment with a flow diverter other than the Surpass device; those with ruptured aneurysms in the acute phase, patients previously treated by stent-assisted coiling, or those treated endosaccularly during the same session were excluded from the study, whereas tandem aneurysms were included and evaluated as separate aneurysms. Additionally, patients treated with a stent-assisted coiling technique in the same institution and by the same operator during the same period were identified. The included patients were evaluated for age, sex, weight, history of previous thromboembolic events, smoking, hypertension, diabetes, hyperlipidemia and malignancy, platelet inhibition levels on the day of treatment (percentage inhibition, VerifyNow P2Y12 assay; Accumetrics, San Diego, California), aneurysm location, maximum diameter and morphology (saccular versus fusiform/dissecting) of the aneurysm, follow-up imaging results (based on the Raymond-Roy [RR] scale), and clinically relevant adverse events (death or TIA/stroke or hemorrhage or any event resulting in change of the mRS). A proximal circulation aneurysm was defined as any aneurysm located on the arteries below the superior cerebellar arteries in the posterior circulation and below the dural ring in the anterior circulation. The remaining aneurysms were classified as distal. An anterior circulation aneurysm was defined as an aneurysm originating from arteries of the carotid circulation, including aneurysms of the posterior communicating artery.

General Description of the Procedure and Follow-Up

The specifications and technical properties of the Surpass flow diverter have been previously described.[9] Patients were pretreated with acetylsalicylic acid and clopidogrel (or prasugrel) on the basis of the previously described regimen in the literature.[10] They were treated under general anesthesia and heparinization using biplane angiographic equipment (Artis zee; Siemens, Erlangen, Germany). Using a triaxial system, we deployed a single Surpass device across the aneurysm neck (or the aneurysmal segment in fusiform cases). An intracranial stent was placed within the freshly deployed Surpass device in the following situations: wide-neck or fusiform aneurysms where the operator wanted to exclude the risk of device prolapse/migration after removal of the deployment system (to pin the flow diverter), cases in which the landing zone was shorter than ideal (to prevent delayed migration due to foreshortening), the landing zone of the device being at an arterial bend (to enable better apposition), the flow diverter partially covering a major branch at the distal or proximal landing zone (to enable further shortening of the device and unjail the branch), and discrepancy of $\geq$2 mm between the diameters of the parent artery at the proximal and distal landing zones (Figs 1 and 2). After the procedure, the patients were advised to come back in 1–3 months for noninvasive angiographic imaging, in 3–6 months for DSA, later at 9–12 months, and annually after that for noninvasive angiographic imaging. Patients were kept on dual-antiplatelet therapy for 6 months, and clopidogrel (or prasugrel) was discontinued after the 6-month DSA.

Statistical Analysis

Continuous variables were reported as mean $\pm$ SD. Categoric variables were compared by χ^2 or Fisher exact tests, as appropriate. Student *t* and Mann Whitney U tests were used for comparison of continuous variables as appropriate. Significance was set as $P < .05$.

Propensity score matching was performed to compare the monotherapy group (Mtg) and stented group (Stg) separately with those patients treated by stent-assisted coiling (SAC) during the same period. SPSS Statistics, Version 22.0 (IBM, Armonk, New York) was used for calculations. Matching was performed using a MatchIt package in R statistical and computing software, Version 3.5.0 (http://www.r-project.org/). Matching covariates were size and aneurysm location (anterior versus posterior and proximal versus distal). SAC and Mtg groups and SAC and Stg groups were matched in a 1:1 ratio, with the nearest calculated propensity logit, with a caliper width of $\leq$0.20 of the SD of the propensity score logit. Subsequently, aneurysm occlusion rates were compared by a χ^2 or Fisher exact test as appropriate.

We dichotomized the aneurysm size at 13 mm to see how aneurysm occlusion rates in larger-versus-smaller aneurysms were affected in a cohort in which stent placement within a FD was also used. We made a comparison for occlusion in the whole cohort at 0–3, 3–6, 9–12 and, >12 months. Occlusion rates were compared by a χ^2 or Fisher exact test as appropriate.

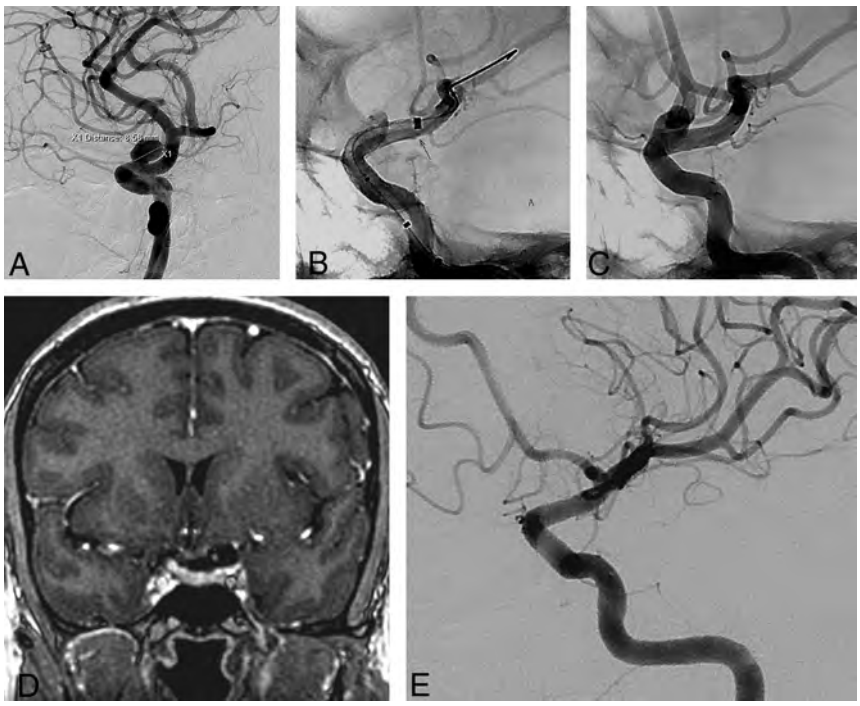

FIG 2. *A*, Left ICA angiogram shows a supraclinoid aneurysm similar to the aneurysm of the patient in Fig 1. *B*, Angiogram after deployment of the flow diverter shows malapposition at the distal end of the device (*arrow*). *C*, Angiogram at the end of the procedure shows good apposition of the device and a stent inside the device. *D*, Contrast-enhanced coronal MR image 3 months after the procedure shows no residual filling. *E*, Follow-up angiogram obtained 6 months after the procedure shows complete occlusion of the aneurysm.

Table 1: Comparison of categoric clinical variables in monotherapy and stented groups

	Monotherapy Group ($n = 35$)		Stented Group ($n = 33$)		
	No.	%	No.	%	*P*
Sex					
Male	14	40	11	33.3	.561
Female	21	60	22	66.7	
Prior thromboembolic event					
Negative	31	88.6	32	97	.357
Positive	4	11.4	1	3	
Smoking					
Negative	24	68.6	27	81.8	.267
Positive	11	31.4	6	18.2	
Hypertension					
Negative	24	68.6	23	69.6	.920
Positive	11	31.4	10	30.4	
Diabetes mellitus					
Negative	32	91.4	32	97	.614
Positive	3	8.6	1	3	
Hyperlipidemia					
Negative	33	94.2	30	90.9	.668
Positive	2	5.8	3	9.1	
Malignancy					
Negative	33	94.2	30	90.9	.668
Positive	2	5.8	3	9.1	

RESULTS

A total of 68 patients with 76 aneurysms were identified. Thirty-five patients with 41 aneurysms were in the Mtg, and 33 patients with 35 aneurysms, in the Stg. Twenty-five patients were male and 43 were female; and the mean age was 49.9 ± 14.8 years (range, 12–86 years).

The mean patient age did not differ between the monotherapy group (49.0 ± 15 years) and the stented group (51.0 ± 14.7 years, $P = .56$). Body weight; the proportion of female patients; prior history of thromboembolic events; and a history of smoking, hypertension, hyperlipidemia, diabetes mellitus, and malignancy were similar between the 2 groups. Results of point-of-care platelet inhibition tests were similar (79.8% versus 78.7%, $P = .92$). The demographics of the 2 groups are summarized in Tables 1 and 2.

Aneurysms of the stented group were statistically significantly larger than in the monotherapy group (14.8 versus 9.1 mm, $P < .001$). There was no difference between the 2 groups with respect to aneurysm location (anterior-versus-posterior circulation, $P = .32$, and proximal versus distal to the circle of Willis, $P = .28$). The ratio of saccular and fusiform aneurysms in both groups was also similar (saccular/fusiform, 32/9 versus 21/14, $P = .08$). There were 2 recurrent aneurysms in both groups, and all of them had been treated with coils in previous sessions. Two aneurysms had a previous history of rupture in the stented group. There was no difference in the rate of bifurcation aneurysms in each group (2 patients in the Mtg versus 1 patient in the Stg, $P = .65$).

The types of adjunctive stents were Atlas (Stryker) in 22 cases; coronary stents in 8 cases; and Neuroform (Stryker), Enterprise (Codman & Shurtleff, Raynham, Massachusetts), and LEO (Balt Extrusion, Montmorency, France) stents in 1 case each. Although there was a trend toward earlier complete occlusion (100%) of aneurysms in the stented group, the difference in complete aneurysm occlusion rates was not statistically significant at 0–3 and 3–6 months of follow-up (73.3% versus 61.3%, $P = .31$, and 84.8% versus 70.2%, $P = .14$). Nine- to 12-month follow-up showed a significantly higher proportion of aneurysms that achieved complete occlusion in the stented group compared with the monotherapy group (93.9% versus 73.1%, $P = .019$). There was no significant difference in complete

Table 2: Comparison of continuous clinical variables in monotherapy and stented groups

Variable	Monotherapy Group		Stented Group		P
	Mean	Median (Range)	Mean	Median (Range)	
Age	49.0 ± 15.0	50 (12–86)	51.0 ± 14.7	52 (22–84)	.561
Weight	73.7 ± 15.2	78 (41–101)	68.7 ± 11.5	66 (47–96)	.115
Platelet inhibition level (%)[a]	79.8 ± 16.2	78 (44–100)	78.7 ± 20.4	81 (33–100)	.925
Aneurysm diameter (mm)	9.1 ± 10.8	5.0 (2–56)	14.8 ± 9.0	13 (3–40)	<.001[b]

[a] VerifyNow P2Y12 assay.
[b] Statistical significance.

Table 3: Comparison of angiographic variables in monotherapy and stented groups

	Monotherapy Group		Stented Group		P
	No.	%	No.	%	
Aneurysm location[a]					
Proximal	36	87.8	34	97.1	.281
Distal	5	12.2	1	2.9	
Aneurysm location[a]					
Anterior	34	82.9	32	91.4	.326
Posterior	7	17.1	3	8.6	
Aneurysm morphology					
Saccular	32	78.0	21	60.0	.087
Fusiform	9	22.0	14	40.0	
0- to 3-mo follow-up					
Total occlusion	19	61.3	22	73.3	.316
Residual filling	12	38.7	8	26.7	
3- to 6-mo follow-up					
Total occlusion	26	70.2	28	84.8	.147
Residual filling	11	29.8	5	15.2	
9- to 12-mo follow-up					
Total occlusion	30	73.2	31	93.9	.019[b]
Residual filling	11	26.8	2	6.1	
>12-mo follow-up					
Total occlusion	34	82.9	31	93.9	.149
Residual filling	7	17.1	2	6.1	

[a] Please see the Materials and Methods section for the description of each of these variables.
[b] Statistical significance.

aneurysm obliteration rates on the final follow-up after 1 year (93.9% versus 82.9%, $P = .14$). Aneurysm characteristics and follow-up results are summarized in Table 3.

There was no clinically relevant adverse event in either group and no mortality. One parent artery occlusion occurred in each group during the follow-up period. In the monotherapy group, there were 2 patients with severe in-stent stenosis. One of these patients developed transient ischemic attacks and was managed with adjustment of the dual-antiplatelet treatment. The second patient was treated with balloon angioplasty and stent placement without an adverse event, and the residual aneurysm was treated with placement of another flow diverter during the same procedure. This was the only patient who needed retreatment in the whole cohort.

When the SAC group and either the Mtg and Stg were compared, there were significant differences in terms of location, size, and morphology of the aneurysms because we frequently reserve SAC for distal bifurcation aneurysms and FDs for sidewall or fusiform aneurysms. Thus, we decided to perform propensity score analysis to adjust for the selection bias between groups inherent in an analysis of aneurysm occlusion. After we performed a 1:1 match, 30 patients were selected in each of the monotherapy and SAC groups and 21 patients remained in each of the Stg and SAC groups. Statistical analysis after propensity score matching revealed that the total occlusion rate based on the last DSA follow-up available in each group was similar in SAC versus Mtg (mean DSA follow-up duration, 8.1 versus 6.8 months; occlusion rate, 65.3% versus 73.3%) and SAC versus Stg (mean DSA follow-up duration, 9.9 versus 7.4 months; occlusion rate, 70.5% versus 94.7%). When an "acceptable occlusion" criterion (based on the Raymond-Roy classification) of RR1 + RR2 instead of only RR1 was considered, the acceptable occlusion rates were 88.4 versus 93.3 in the SAC-versus-Mtg group and 88.2 versus 94.7 in the Stg group. The differences were not significant among any of the comparison groups.

There was no significant difference in the aneurysm occlusion rate (RR1) during any of the follow-up periods ($P = .49$, $P = .66$, $P = .22$, $P = .68$, respectively) in aneurysms of ≥13 mm versus those that were smaller. We noted that of the 26 aneurysms that were ≥13 mm, 18 actually belonged to the Stg. The evaluation of the available follow-up imaging in these 18 patients yielded a total occlusion rate of 62.5%, increasing to 82.4% and then to 94.1% and then becoming stable for the follow-up periods.

Of the 9 patients who had a cerebral DSA beyond 12 months (range, 13–46 months; mean, 28.5 months; median, 24 months), only 1 patient who was treated with FD placement-only had residual filling of her aneurysm.

DISCUSSION

The combined use of a stent and flow diverter has been thought to decrease the success rate of flow diverters.[11] However, this possibility refers to previously placed stents, and the consequences of placing a stent within a flow diverter have not been studied. Although there are 4 reports in the literature mentioning a total of 17 stents placed within flow diverters for better wall apposition, the safety or efficacy of this technique is unknown.[5-8]

We wanted to evaluate the safety and utility of stent placement within a freshly deployed flow diverter by comparing the aneurysms treated by flow diverters only (Mtg) with those treated by flow diverters followed by stents during the same procedure

(Stg). We included only aneurysms treated by a single type of flow diverter without adjunctive intrasaccular treatment so that the study population would be uniform as to the efficacy of the device used (Surpass device)—that is, we wanted to eliminate the variables of device type and adjunctive treatments. Both groups of patients were also similar for all variables (age, sex, history of a prior thromboembolic event, smoking, hypertension, diabetes mellitus, hyperlipidemia, malignancy, and platelet inhibition level) except for the size of the aneurysm. The mean size of aneurysms was 14.8 mm in the Stg and significantly higher than the Mtg (9.1 mm). Because a cutoff point of 13 mm was suggested for lower occlusion and higher complication rates[12] in flow diversion, we would actually expect a lower occlusion and a higher complication rate for the Stg. This was not the case for our cohort. Despite a larger aneurysm size in the Stg, the occlusion rates were higher. Additionally, there was no difference in the occurrence of significant adverse events between the 2 groups.

An earlier occlusion was noted in the Stg with statistical significance at 9–12 months. As the aneurysms in the Mtg progressed to occlusion after 1 year, the difference between occlusion rates of the groups decreased, yet there was still a trend in the Stg toward better occlusion rates at or after 1 year.

These findings suggest that stent placement within flow diverters does not significantly increase the risk of flow diversion and is associated with increased efficacy. Indeed, adverse events without clinical symptoms, namely fish mouthing and/or in-stent stenosis, were only observed in the Mtg, hinting at enhancement of safety with stent placement, which is an outcome that remains to be definitely demonstrated.

Braided stents and especially flow diverters have a lower radial force compared with laser-cut stents.[5-7] Consequently, flow diverters may not appose the arterial wall, especially in arterial segments with tight bends.[11] Hence, stents have been used only rarely for the apposition or anchoring of flow diverters in several patients as noted above.[5-7] The latest clinical and preclinical data suggest that incomplete wall apposition causes inhomogeneous and delayed endothelial coverage of stent struts and aneurysm neck,[13,14] and suboptimal apposition at the aneurysm neck causes persistent filling of the aneurysm.[15] Treatment failure rates (Raymond-Roy grade III) in malapposed flow diverters were 41.2% and significantly higher than in fully apposed devices (9.6%) in a study with 213 patients.[16] In our study, there were several reasons for stent placement within the flow diverter and not all stents were deployed for better apposition. Nevertheless, the better angiographic outcome in the Stg was presumably due to better wall apposition regardless of the presence of an angiographically visible overt malapposition. Incomplete apposition is not only a handicap in the periprocedural period, it also leads to delayed stent occlusions in the coronary arteries[17] and after flow diversion,[18] which may occur as late as 3 years after device placement.[19-21] Improvement of apposition by stents may help maintain flow-diverter patency in the long term.

Several strategies exist to enhance flow-diverter apposition to the arterial wall. Among these, the most commonly used ones are loading the device during delivery and recrossing it with the delivery microcatheter after deployment. Angioplasty is another technique that is adopted by some authors. However, angioplasty may paradoxically worsen device apposition, and this may be detected only by advanced imaging methods such as optical coherence tomography.[15] Balloon angioplasty can also result in thrombus formation inside the flow diverter[15] or, in case of a short landing zone, foreshortening and device prolapse into the aneurysm.[22]

It may be argued that placement of a stent inside the flow diverter will increase the metal coverage and consequently result in both an enhanced flow diversion and also an increased rate of perforator injury in vulnerable segments like the M1 segment of the MCA or the posterior circulation. Wall coverage of the current intracranial stents is very low, in the range of 10%–15% at most, and the cumulative coverage of overlapping devices is much less than the numeric sum of the coverage of telescoped devices.[23] The minimal increase of coverage by the intracranial stent is likely neither to cause an increase in the rate of perforator injury nor to result in an appreciable increase in flow diversion.

After propensity score matching, there was no statistically significant difference in the occlusion rates of cerebral aneurysms between SAC and either of the FD groups (Mtg and Stg). However, there was a clear trend in both the Stg and Mtg for an increased rate of total occlusion compared with the patients with stent-assisted coiling. This finding is concordant with those previously reported in the literature using similar methodology for comparison of SAC and flow diversion.[24,25] We believe that the absence of a statistically significant difference results largely from the low number of patients remaining in the study when propensity score matching was performed. Thus, our findings can only suggest that increased aneurysmal occlusion is the result of the use of a flow diverter rather than placement of a regular stent for SAC when flow diversion is compared with SAC. Although per our results, a statistical difference in favor of Stg compared with Mtg exists during early follow-up, larger cohorts are needed to validate this finding. It is conceivable that such larger cohorts may reveal differences in mid- or late-term follow-up periods as well.

One other unexpected result was the diminution of the gap between the occlusion rates of large-versus-small aneurysms as previously reported in the literature.[12,26] In our whole cohort of patients treated with flow diversion in this study, there was no difference in the occlusion rates of aneurysms of $\geq$13 mm in diameter versus those aneurysms $<$13 mm in diameter. Because 18 of the 26 aneurysms were treated with additional stent placement in the $\geq$13 mm subgroup (reaching 94% occlusion at 1 year in those that were stented), it is possible that the absence of a significant difference arises from the higher obliteration rates in the Stg. Nevertheless, the absence of such significance should be appraised with caution in studies like ours that have a limited number of patients.

There are 2 major disadvantages of stent placement within the flow diverter. The first one is the risk of flow-diverter migration during recrossing of the device or during the microcatheter exchange maneuver through the flow diverter. The second is cost. Fortunately, there is a matching intracranial stent for each flow diverter in terms of a compatible delivery microcatheter for all of the current flow diverters except for the Surpass flow diverter,

for which a technique to place a stent without an intracranial exchange maneuver has been described.[27] The stent is certainly an additional cost of the procedure. However, placement of a stent results in a comparable increase in cost with regard to the other adjunctive methods used to increase the efficiency of flow diverters such as intrasaccular flow diverters,[4] Medina[28] embolization device, regular coils,[29] or telescopic placement of another flow diverter. Because of the concern related to cost, we suggest that stent placement within a flow diverter should be selective and limited to bailout situations such as those listed in the previous section of our article and to those aneurysms that are expected to have a lower rate of occlusion by placement of a single flow diverter (eg, large and giant aneurysms).

The main limitations of this study include its retrospective nature and relatively small sample size. None of the stents we deployed inside flow diverter have been approved for such use, and this technique is an off-label use of these stents. Finally, only 1 type of flow diverter was examined in this study, and other types of flow diverters need to be studied to verify the proposed relation of device apposition and aneurysm occlusion.

CONCLUSIONS

Our study demonstrated, for the first time, the possible consequences of stent placement within a flow diverter. Our findings were based on the comparison of aneurysms treated by a bare flow diverter and those in which a laser-cut stent was placed within a flow diverter for a variety of different reasons. The trend toward earlier occlusion in the stented arm is promising and calls for scrutiny of the previously reported animal studies that put forward subtle flow-diverter malapposition as a cause of flow-diverter failure. Our findings need to be verified in larger cohorts, preferably from multicenter registries, and cannot be generalized to routine clinical scenarios or all neurointerventional practices. However, operators may individually consider stent placement within a freshly deployed flow diverter in selected situations as in our cases, bearing in mind that aside from bailing out a troubled flow-diversion procedure, stent placement may potentially help with occlusion rates without significantly increasing the risk of the procedure.

REFERENCES

1. Akgul E, Onan HB, Akpinar S, et al. **The DERIVO embolization device in the treatment of intracranial aneurysms: short- and mid-term results.** *World Neurosurg* 2016;95:229–40 CrossRef Medline
2. Becske T, Kallmes DF, Saatci I, et al. **Pipeline for uncoilable or failed aneurysms: results from a multicenter clinical trial.** *Radiology* 2013;267:858–68 CrossRef Medline
3. Bhogal P, AlMatter M, Hellstern V, et al. **The combined use of intraluminal and intrasaccular flow diversion for the treatment of intracranial aneurysms: report of 25 cases.** *Neurointervention* 2018; 13:20–31 CrossRef Medline
4. Lescher S, Du Mesnil de Rochemont R, Berkefeld J. **Woven Endobridge (WEB) device for endovascular treatment of complex unruptured aneurysms-a single center experience.** *Neuroradiology* 2016;58:383–90 CrossRef Medline
5. Amuluru K, Al-Mufti F, Roth W, et al. **Anchoring Pipeline flow diverter construct in the treatment of traumatic distal cervical carotid artery injury.** *Intervent Neurol* 2017;6:153–62 CrossRef Medline
6. Kuhn AL, Wakhloo AK, Gounis MJ, et al. **Use of self-expanding stents for better intracranial flow diverter wall apposition.** *Interv Neuroradiol* 2017;23:129–36 CrossRef Medline
7. Rahal JP, Dandamudi VS, Heller RS, et al. **Use of concentric Solitaire stent to anchor Pipeline flow diverter constructs in treatment of shallow cervical carotid dissecting pseudoaneurysms.** *J Clin Neurosci* 2014;21:1024–28 CrossRef Medline
8. Kühn AL, Rodrigues KM, Wakhloo AK, et al. **Endovascular techniques for achievement of better flow diverter wall apposition.** *Interv Neuroradiol* 2018;25:344–47 CrossRef Medline
9. Topcuoglu OM, Arat A, Peker A, et al. **Intermediate catheter placement distal to the cerebral aneurysm during flow diversion embolization with the Surpass device.** *J Neurointerv Surg* 2018;10:e35 CrossRef Medline
10. De Vries J, Boogaarts J, Van Norden A, et al. **New generation of flow diverter (Surpass) for unruptured intracranial aneurysms: a prospective single-center study in 37 patients.** *Stroke* 2013;44:1567–77 CrossRef Medline
11. Shapiro M, Becske T, Nelson PK. **Learning from failure: persistence of aneurysms following Pipeline embolization.** *J Neurosurg* 2017; 126:578–85 CrossRef Medline
12. Kaya T, Daglioglu E, Gurkas E, et al. **Silk device for the treatment of intracranial aneurysms, Part 2: factors related to clinical and angiographic outcome.** *Turk Neurosurg* 2016;26:533–37 CrossRef Medline
13. Foin N, Gutierrez-Chico JL, Nakatani S, et al. **Incomplete stent apposition causes high shear flow disturbances and delay in neointimal coverage as a function of strut to wall detachment distance: implications for the management of incomplete stent apposition.** *Circ Cardiovasc Interv* 2014;7:180–89 CrossRef Medline
14. Marosfoi M, Langan ET, Strittmatter L, et al. **In situ tissue engineering: endothelial growth patterns as a function of flow diverter design.** *J Neurointerv Surg* 2017;9:994–98 CrossRef Medline
15. King RM, Brooks OW, Langan ET, et al. **Communicating malapposition of flow diverters assessed with optical coherence tomography correlates with delayed aneurysm occlusion.** *J Neurointerv Surg* 2018;10:693–97 CrossRef Medline
16. US Food and Drug Administration. **Summary of Safety and Effectiveness Data: Surpass Embolization Device** 2018; P170024. https://www.accessdata.fda.gov/cdrh_docs/pdf17/P170024B.pdf. Accessed May 12, 2019
17. Souteyrand G, Amabile N, Mangin L, et al. **Mechanisms of stent thrombosis analysed by optical coherence tomography: insights from the national PESTO French registry.** *Eur Heart J* 2016; 37:1208–16 CrossRef Medline
18. Berge J, Biondi A, Machi P, et al. **Flow-diverter Silk stent for the treatment of intracranial aneurysms: 1-year follow-up in a multicenter study.** *AJNR Am J Neuroradiol* 2012;33:1150–55 CrossRef Medline
19. Klisch J, Turk A, Turner R, et al. **Very late thrombosis of flow-diverting constructs after the treatment of large fusiform posterior circulation aneurysms.** *AJNR Am J Neuroradiol* 2011;32:627–32 CrossRef Medline
20. Oishi H, Teranishi K, Nonaka S, et al. **Symptomatic very delayed parent artery occlusion after flow diversion stent embolization.** *Neurol Med Chir (Tokyo)* 2016;56:350–53 CrossRef Medline
21. Potts MB, Shapiro M, Zumofen DW, et al. **Parent vessel occlusion after Pipeline embolization of cerebral aneurysms of the anterior circulation.** *J Neurosurg* 2017;127:1333–41 CrossRef Medline
22. Srinivasan VM, Carlson AP, Mokin M, et al. **Prolapse of the Pipeline embolization device in aneurysms: incidence, management, and outcomes.** *Neurosurg Focus* 2017;42:E16 CrossRef Medline
23. Shapiro M, Raz E, Becske T, et al. **Building multidevice Pipeline constructs of favorable metal coverage: a practical guide.** *AJNR Am J Neuroradiol* 2014;35:1556–61 CrossRef Medline
24. Chalouhi N, Tjoumakaris S, Starke RM, et al. **Comparison of flow diversion and coiling in large unruptured intracranial saccular aneurysms.** *Stroke* 2013;44:2150–54 CrossRef Medline

25. Zhang Y, Zhou Y, Yang P, et al. **Comparison of the flow diverter and stent-assisted coiling in large and giant aneurysms: safety and efficacy based on a propensity score-matched analysis.** *Eur Radiol* 2016;26:2369–77 CrossRef Medline
26. Briganti F, Leone G, Cirillo L, et al. **Postprocedural, midterm, and long-term results of cerebral aneurysms treated with flow-diverter devices: 7-year experience at a single center.** *Neurosurg Focus* 2017;42:E3 CrossRef Medline
27. Ocal O, Arat A, Peker A, et al. **Better wall apposition of Surpass device with Atlas stent: a new and easy technique. In:** *Proceedings of the 14th Congress of the World Federation of Interventional and Therapeutic Neuroradiology.* Budapest, Hungary. October 16–19, 2017
28. Aguilar Perez M, Bhogal P, Martinez Moreno R, et al. **The Medina Embolic Device: early clinical experience from a single center.** *J Neurointerv Surg* 2017;9:77–87 CrossRef Medline
29. Nossek E, Chalif DJ, Chakraborty S, et al. **Concurrent use of the Pipeline Embolization Device and coils for intracranial aneurysms: technique, safety, and efficacy.** *J Neurosurg* 2015;122:904–11 CrossRef Medline

Novel Models for Identification of the Ruptured Aneurysm in Patients with Subarachnoid Hemorrhage with Multiple Aneurysms

H. Rajabzadeh-Oghaz, J. Wang, N. Varble, S.-I. Sugiyama, A. Shimizu, L. Jing, J. Liu, X. Yang, A.H. Siddiqui, J.M. Davies, and H. Meng

ABSTRACT

BACKGROUND AND PURPOSE: In patients with SAH with multiple intracranial aneurysms, often the hemorrhage pattern does not indicate the rupture source. Angiographic findings (intracranial aneurysm size and shape) could help but may not be reliable. Our purpose was to test whether existing parameters could identify the ruptured intracranial aneurysm in patients with multiple intracranial aneurysms and whether composite predictive models could improve the identification.

MATERIALS AND METHODS: We retrospectively collected angiographic and medical records of 93 patients with SAH with at least 2 intracranial aneurysms (total of 206 saccular intracranial aneurysms, 93 ruptured), in which the ruptured intracranial aneurysm was confirmed through surgery or definitive hemorrhage patterns. We calculated 13 morphologic and 10 hemodynamic parameters along with location and type (sidewall/bifurcation) and tested their ability to identify rupture in the 93 patients. To build predictive models, we randomly assigned 70 patients to training and 23 to holdout testing cohorts. Using a linear regression model with a customized cost function and 10-fold cross-validation, we trained 2 rupture identification models: RIM_C using all parameters and RIM_M excluding hemodynamics.

RESULTS: The 25 study parameters had vastly different positive predictive values (31%–87%) for identifying rupture, the highest being size ratio at 87%. RIM_C incorporated size ratio, undulation index, relative residence time, and type; RIM_M had only size ratio, undulation index, and type. During cross-validation, positive predictive values for size ratio, RIM_M, and RIM_C were 86% ± 4%, 90% ± 4%, and 93% ± 4%, respectively. In testing, size ratio and RIM_M had positive predictive values of 85%, while RIM_C had 92%.

CONCLUSIONS: Size ratio was the best individual factor for identifying the ruptured aneurysm; however, RIM_C, followed by RIM_M, outperformed existing parameters.

ABBREVIATIONS: AR = aspect ratio; CFD = computational fluid dynamics; D = maximum diameter; H = height (perpendicular); H_{max} = maximum height; IA = intracranial aneurysm; NWSS = normalized wall shear stress; OSI = oscillatory shear index; RIM = rupture identification model; RRS = rupture resemblance score; RRT = relative residence time; SR = size ratio; UI = undulation index; WSS = wall shear stress

Approximately 30% of patients with intracranial aneurysms (IAs) present with multiple aneurysms.[1] Correct identification of the ruptured IA in a patient with SAH is critical for treatment planning.[2] Identifying the ruptured IA is increasingly important in an era of increased endovascular treatment because the source of hemorrhage cannot be confirmed visually and aneurysms are usually treated individually. Hemorrhage pattern on initial CT scans is the primary indicator of the bleeding source, as demonstrated by Orning et al,[3] who reported that a definitive hemorrhage pattern (localized to 1 IA) could accurately delineate the ruptured IAs. However, in approximately half of patients with multiple aneurysms, the hemorrhage pattern cannot

Received December 5, 2018; accepted after revision August 23, 2019.

From the Canon Stroke and Vascular Research Center (H.R.-O., N.V., A.H.S., J.M.D., H.M.) and Departments of Mechanical and Aerospace Engineering (H.R.-O., N.V., H.M.) and Biostatistics (J.W.), University at Buffalo, Buffalo, New York; Department of Neuroanesthesia (S.-I.S.), Kohnan Hospital, Sendai, Japan; Department of Neurosurgery (S.-I.S., A.S.), Tohoku University Graduate School of Medicine, Sendai, Japan; Department of Interventional Neuroradiology (L.J., J.L., X.Y., H.M.), Beijing Neurosurgical Institute, Beijing Tiantan Hospital, Capital Medical University, Beijing, China; Departments of Neurosurgery (A.H.S., J.M.D.), Bioinformatics (J.M.D.), and Radiology (A.H.S.), Jacobs School of Medicine and Biomedical Sciences, University at Buffalo, Buffalo, New York; and Jacobs Institute (A.H.S., J.M.D), Buffalo, New York.

This work was supported by National Institutes of Health grants R01NS091075 and R03NS090193 and Canon Medical Systems. J.M. Davies was supported by the National Center for Advancing Translational Sciences of the National Institutes of Health (award KL2TR001413 to the University at Buffalo). This work is also supported by National Key Research and Development Plan of China (grant 2016YFC1300800), the National Natural Science Foundation of China (grants 81220108007, 81371315, 81471167, and 81671139), and the Special Research Project for Capital Health Development (grant 2018-4-1077).

Please address correspondence to Hui Meng, PhD, Canon Stroke and Vascular Research Center, Clinical Translational Research Center, 875 Ellicott St, Buffalo, NY 14203; e-mail: huimeng@buffalo.edu

Indicates open access to non-subscribers at www.ajnr.org
Indicates article with supplemental on-line appendix and tables.
Indicates article with supplemental on-line photos.
http://dx.doi.org/10.3174/ajnr.A6259

delineate the ruptured IA.[3] In such cases, rupture identification relies on angiographic findings, such as IA size, shape, and location.[2,3] Several studies have reported misidentification of the ruptured aneurysm, which has been attributed to the small size or benign shape of the ruptured IA.[2-8] Therefore, developing more reliable means of identifying the ruptured IA has clinical value in patients with multiple IAs, especially when the hemorrhage pattern cannot delineate the ruptured IA.

Several morphologic and hemodynamic parameters have been found to differ significantly between ruptured and unruptured aneurysm cohorts in patients with multiple IAs, albeit with conflicting findings.[9-15] These studies have generally relied on univariate and multivariate regression analyses of pooled data of ruptured and unruptured IAs. Although such methods model the general probability of aneurysm rupture, they are not tailored for identifying which aneurysm ruptured in patients with SAH with multiple aneurysms. To that end, the ability of aneurysmal metrics for identification of the ruptured aneurysm should be evaluated by comparing all IAs within each patient, and models trained by associating the coexisting IAs within each patient should be developed.

In this study, we retrospectively analyzed IAs in patients with SAH presenting with multiple aneurysms to test the performance of existing morphologic and hemodynamic parameters and to build new composite models for identifying the ruptured aneurysm in patients with multiple aneurysms. The performance of the new models was compared against existing morphologic and hemodynamic parameters along with aneurysm location and type (sidewall or bifurcation) and a previously developed rupture-classification model, the rupture resemblance score (RRS).[16] Our findings may assist clinicians in better identifying the ruptured IA in patients with SAH presenting with multiple aneurysms.

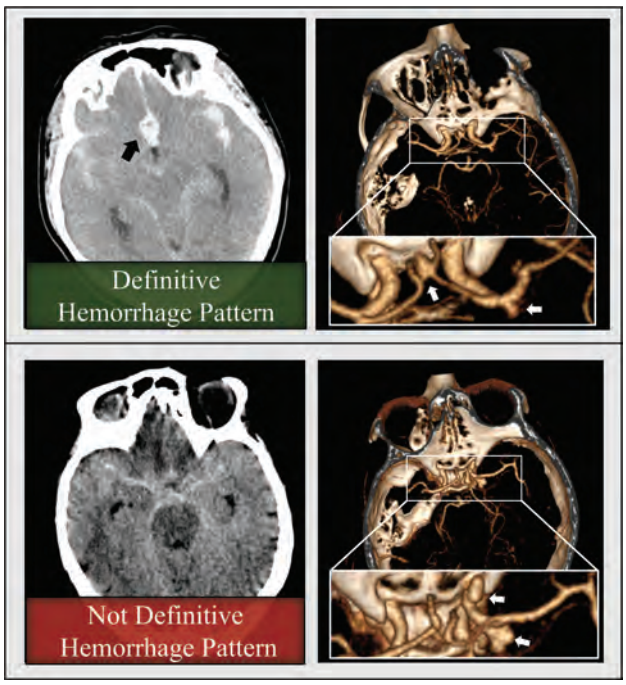

FIG 1. *Top*, A 62-year-old woman who presented with SAH (*left image*, noncontrast CT scan) was found to have anterior communicating artery and MCA aneurysms (*white arrows*, *right image*, CTA). A focal hematoma in the anterior circulation (*black arrow*, *left image*) delineated the anterior communicating artery aneurysm as the source of bleeding, which was confirmed at surgery. *Bottom*, A 59-year-old woman presented with SAH (*left image*, noncontrast CT scan). She was found to have 2 large lobulated right ICA aneurysms (*white arrows*, *right image*, CTA). The source of the rupture could not be identified from the hemorrhage pattern (this patient was excluded from our study). Both aneurysms were treated endovascularly.

MATERIALS AND METHODS

Ethics Approval

This study was approved by the institutional review board of the University at Buffalo (IRB: 30–510704: Virtual Intervention of Intracranial Aneurysms).

Data Collection

We retrospectively collected cerebrovascular images and medical records from consecutive series of patients with aneurysmal SAH treated at 3 stroke centers located in China (Beijing Tiantan Hospital, Capital Medical University, Beijing, China), Japan (Kohnan Hospital, Sendai, Japan), and the United States (Gates Vascular Institute, Buffalo, NY). Inclusion criteria mandated that patients had a ruptured IA and at least 1 unruptured aneurysm and that all aneurysms were saccular. For the patients who underwent a craniotomy for aneurysm clipping, the ruptured aneurysm was confirmed through microscopic visual assessment. For patients who underwent endovascular or no treatment, we included only those with a definitive hemorrhage pattern on CT (localized to 1 IA). Examples of definitive and nondefinitive hemorrhage patterns are provided in Fig 1, respectively. All patients included in the current study underwent 3D rotational DSA preoperatively, which was used for aneurysm-geometry reconstruction. In general, the voxel sizes of images obtained at the 3 centers were similar, with little variation during the acquisition period: Chinese center, 0.280 mm; Japanese center, 0.227–0.226 mm; and US center, 0.256–0.223 mm. The images and data were anonymized, and the study received institutional review board approval. The operators who conducted image segmentation and morphologic and hemodynamic evaluations were blinded to aneurysm rupture status.

Image Segmentation and Computational Fluid Dynamics

The 3D-DSA images of all patients were segmented using an open-source Vascular Modeling Toolkit (VMTK; http://www.vmtk.org). VMTK is a semiautomated tool that uses a level-set method to place lumen contours at regions with maximum gradient intensity.[17] After segmentation, a surface mesh for IAs with surrounding parent vessels was generated using the threshold-based marching cubes algorithm.[17]

Computational fluid dynamics (CFD) simulations were performed at 2 different centers (China: Beijing Tiantan Hospital, Capital Medical University, Beijing, China and Gates Vascular Institute, Buffalo, NY). For the Chinese data base, CFD was performed using ICEM-CFD software (ANSYS, Canonsburg, Pennsylvania) for mesh generation and CFX 14.0 software (ANSYS) for CFD simulation. For the US and Japanese

databases, CFD was performed using STAR-CCM+ (Siemens, Erlangen, Germany) for both mesh generation and CFD simulations. All geometries were converted to computational domains using the same meshing setup: tetrahedral volumetric mesh, minimum element size of 0.1 mm, and 3 refined prism layers. All CFD simulations were performed using the same numeric setup, assumptions, and boundary conditions, including rigid wall, Newtonian behavior of blood flow, location-based inflow rate,[18] and distribution of outlet flow based on the Murray law.[19] Complete details of CFD simulations, including the sensitivity of the hemodynamic results to the CFD solvers, are given in the On-line Appendix and On-line Figs 1 and 2.

Morphologic Parameters

Aneurysmal morphology was calculated using AView,[20-22] a computational workflow for morphologic and hemodynamic assessment of IAs. The definitions of the 13 morphologic indices are illustrated in On-line Fig 3. Maximum diameter (D) is the maximum distance between any 2 points on the aneurysm sac. Maximum height (H_{max}) is the maximum distance between the sac and the center of the neck plane. Height (H) is the maximum perpendicular distance from the neck plane to the sac. Size ratio (SR) has 2 definitions in the literature,[23,24] so does aspect ratio (AR),[23,25] and we applied both. SR_D is the ratio of D to the average parent vessel diameter, and SR_{Hmax} is the ratio of H_{max} to the average parent vessel diameter. AR_{Hmax} and AR_H are the ratios of H_{max} and H to the average neck diameter, respectively. Aneurysm number[26] is the neck ratio (the ratio of neck diameter to the average parent vessel diameter) multiplied by the pulsatility index based on parent artery location obtained from the literature.[27,28] Undulation index (UI) represents the degree of aneurysm surface irregularity. Ellipticity index represents deviation of the IA from a perfect hemisphere. Nonsphericity index represents deviation of the IA from a perfect hemisphere while also considering surface undulations.[23] Surface area and volume of the IAs were calculated as well. We also classified aneurysms as bifurcation or sidewall. Bifurcation IAs are those that arise at the apex of a split from a main (proximal) artery into ≥2 daughter (distal) arteries.

Hemodynamic Parameters

After obtaining the flow field in each IA, we calculated the aneurysm-averaged values for the following 10 hemodynamic parameters: time-averaged wall shear stress (WSS), which is the WSS magnitude averaged over the aneurysm sac; normalized WSS (NWSS), which is WSS further normalized by the spatiotemporal average wall shear stress of the parent vessel; maximum and minimum WSS and NWSS, which are the maximum or minimum value of WSS that occurred on the aneurysm sac; oscillatory shear index (OSI), which measures the directional change of the WSS through the cardiac cycle; relative residence time (RRT), which quantifies the stasis of blood near the aneurysm wall; low shear area, which is the percentage of the sac area exposed to low WSS (defined as <10% of the averaged parent vessel WSS); and finally, complex flow, which is defined as an aneurysmal flow structure that contains >1 separate vortex core line.[18,29] This parameter is binary: 1 for complex flow structure and 0 for simple flow structure. These parameters are defined in On-line Table 1 and illustrated in On-line Fig 4.

Because multiple operators performed numeric analyses, we conducted a post hoc study to quantify the intraclass correlation coefficient among operators using our protocol for calculating morphologic and hemodynamic parameters and found excellent agreement. Details are provided in the On-line Appendix, On-line Table 2, and On-line Fig 5.

Rupture Resemblance Score

We also calculated the RRS, a rupture classification model that was trained based on a database of 204 ruptured and unruptured IAs.[30] RRS can provide a rupture probability for an IA based on IA morphology and hemodynamics, which can be used to gauge the similarity of an IA to a cohort of ruptured IAs. The equation for the calculation of RRS is provided in the On-line Appendix.

Description of Ruptured and Unruptured Aneurysms

For all IAs, we described location, type (bifurcation versus sidewall), morphology, hemodynamics, and RRS. Continuous variables were presented as means with SDs. Conditional logistic regression[31] was used to assess differences between ruptured and unruptured cohorts. Discrete variables were presented as numbers, and a χ^2 test was used to determine significant differences between ruptured and unruptured cohorts. A P value of <.01 was considered significant.

Testing the Performance of Existing Rupture Predictive Parameters in Identifying the Ruptured IA

We further investigated the performance of each parameter for identifying each patient's ruptured IA. For aneurysm location, rupture prediction was based on rupture site frequencies as reported by Nehls et al[2] (anterior communicating artery, 62% of IAs identified at this location were ruptured; basilar artery, 50%; PICA, 50%; posterior communicating artery, 38%; posterior cerebral artery, 33%; anterior cerebral artery, 33%; ICA, 32%; and MCA, 27%), and the aneurysm with the highest rupture frequency was assumed to be ruptured. If the ruptured IA and a coexisting unruptured IA were located on the same artery or arteries with the same rupture frequency, we assumed that identifying the ruptured aneurysm was not possible, and this was considered a false prediction.

Aneurysm type was used as a predictor of a ruptured aneurysm based on the assumption that bifurcation aneurysms rupture more frequently than sidewall aneurysms, especially small bifurcation aneurysms.[32] Aneurysmal flow pattern was used as a predictor of a ruptured aneurysm based on the assumption that ruptured IAs more frequently contain a complex flow structure.[29] If the ruptured IA and a coexisting unruptured IA were of the same type or had the same flow pattern, we assumed that the rupture site was unidentifiable, and this was considered a false prediction.

For quantitative predictive parameters, the patient's IAs were compared and the IA with the highest value was assumed to be the ruptured IA. For parameters that are generally lower in ruptured aneurysms (eg, NWSS), the aneurysm with the lowest value was assumed to be the ruptured one.

We compared rupture prediction results with actual (confirmed through an operation or definitive hemorrhage pattern) aneurysm rupture status. The performance of each metric was quantified as a positive predictive value, which is the number of patients with correct identification of ruptured IAs divided by the total number of patients.

Generating Rupture Identification Models

After testing the performance of individual rupture predictors, we generated composite models that were trained to provide a higher score for the ruptured IA in patients with SAH with multiple IAs, which we called the rupture identification model (RIM). First, we randomly assigned 70 patients to a training cohort and 23 patients to a holdout testing cohort. To distribute equal weight, we centered all variables to 0 (subtraction of the mean) and scaled them (division by the SD). All variables were then used to generate all possible linear combinations, and we removed those with collinear variables (Pearson correlation >0.5, moderate correlation; On-line Table 3). We used a linear regression model with a customized cost function, which maximizes the positive predictive value and the differences between ruptured and coexistent unruptured IAs within each patient, to fit the remaining models. The best performing model during 10-fold cross-validation was identified. The resulting model, which was trained by all variables, was termed RIM_C, with the subscript C indicating the need for CFD to obtain hemodynamic parameters. We also trained a second model by excluding hemodynamic variables, termed RIM_M, with the subscript M indicating that it is a morphologic parameter and does not require CFD analysis. In the end, we evaluated the final models on the holdout testing cohort as well.

The workflow, access link to the model training code, and additional details of model generation are provided in the On-line Appendix and On-line Fig 6. Statistical analysis and model fitting were performed using an in-house code developed in R statistical and computing software (Version 1.0.44; https://www.r-project.org/).

RESULTS

Clinical Information

Table 1 summarizes the clinical information of the 93 patients with 206 IAs included in this study: Chinese center (59 patients, 130 IAs), Japanese center (17 patients, 38 IAs), and US center (17 patients, 38 IAs). The average patient age was 60 ± 13 years; 74% of all patients were women. The ruptured aneurysm was identified through craniotomy in 35 patients (38%) and a definitive hemorrhage pattern in 58 patients (62%). Seventy-six patients (82%) had 2 IAs, 15 (16%) had 3 IAs, 1 (1%) had 4 IAs, and 1 (1%) had 5 IAs.

Description of Ruptured and Unruptured Aneurysms

On-line Table 4 shows the number of IAs at each location, IA type (bifurcation or sidewall), morphology, hemodynamics, and RRS for all IAs in the ruptured and unruptured cohorts. Eighty-two (40%) of all IAs were located along the ICA, 57 (70%) of which were unruptured. The anterior circulation was associated with the highest rupture frequency: Seven of 10 (70%) IAs located on the anterior cerebral artery and 16 of 22 (73%) IAs located at the anterior communicating artery were ruptured. Only 6 IAs were located in the posterior circulation. Most ruptured IAs were bifurcation aneurysms (71%).

Table 1: Clinical information for patients with SAH with multiple IAs

Clinical Information	
Demographics and comorbidities (n = 93)	
Age (mean) (yr)	60 ± 13
Female sex	69 (74%)
Hypertension	59 (63%)
Smoking history	35 (38%)
Coronary artery disease	7 (8%)
Hyperlipidemia	28 (30%)
Diabetes mellitus	13 (14%)
Polycystic kidney disease	1 (1%)
Received treatment	
Clipping	35 (38%)
Endovascular	53 (57%)
No treatment	5 (5%)
Aneurysm multiplicity	
2 Aneurysms	76 (82%)
3 Aneurysms	15 (16%)
4 Aneurysms	1 (1%)
5 Aneurysms	1 (1%)

Except for the nonsphericity index and ellipticity index, the morphologic indices of the ruptured and unruptured cohorts were significantly different. Aneurysmal hemodynamics also differed, with ruptured IAs being exposed to lower WSS, higher RRT, and larger low shear area than the unruptured IAs. Complex flow patterns were present in 62% of ruptured IAs and 20% of unruptured IAs. The RRS was significantly higher in the ruptured cohort ($P < .001$).

Performance of Existing Parameters in Identifying the Ruptured Aneurysm

All parameters were further analyzed to test their ability in identifying the ruptured aneurysm by calculating the percentage of correctly identified ruptured IAs. We found that the positive predictive value considerably varied by individual parameters from 31% to 87%. SR_{Hmax} and H_{max} had the highest performance, identifying the ruptured IA in 87% and 85% of patients, respectively (Table 2). RRT identified the ruptured IA in 76% of patients and exhibited the best hemodynamic parameter performance. Figure 2 shows SR_{Hmax} and time-averaged RRT distributions on the aneurysm sac for ruptured and unruptured IAs in 3 representative patients. RRS identified the ruptured IA in 80% of the patients.

Rupture Identification Models

The 2 models, RIM_C and RIM_M, tailored to identify the ruptured aneurysm in patients with SAH with multiple IAs, achieved positive predictive values of 93% ± 4% and 90% ± 4%, respectively, during 10-fold cross-validation.

1)
$$RIM_C = 0.45\ SR_{Hmax} + 0.17\ UI + 0.21\ RRT + 0.17\ (Bifurcation)$$

Table 2: Performance of existing aneurysmal parameters in the prediction of ruptured aneurysm in patients with SAH with multiple IAs[a]

Parameter	Positive Predictive Value
Location	52%
Type	31%
Morphology	
D	82%
H_{max}	85%
H	81%
SR_D	83%
SR_{Hmax}	87%
AR_{Hmax}	80%
AR_H	74%
Aneurysm No.	63%
Undulation index	80%
Nonsphericity index	49%
Ellipticity index	40%
Surface area	80%
Volume	80%
Hemodynamics	
WSS	67%
Maximum WSS	55%
Minimum WSS	75%
NWSS	71%
Maximum NWSS	51%
Minimum NWSS	74%
OSI	68%
RRT	76%
LSA	75%
Complex flow	50%
RRS	80%

[a] For WSS, Minimum WSS, NWSS, Maximum NWSS, and Minimum NWSS, we hypothesized that among IAs belonging to each patient, the IA with the lowest value is the ruptured IA. For the rest of the variables, we hypothesized that the IA with the highest value is the ruptured IA.

2)
$$RIM_M = 0.65\ SR_{Hmax} + 0.16\ UI + 0.19\ (Bifurcation),$$

where *Bifurcation* equals 1 if an aneurysm is a bifurcation type and 0 if it is a sidewall type.

In the hold-out testing cohort, RIM_C and RIM_M could identify the ruptured IA in 92% and 85% of the 23 patients, respectively. Figure 3 shows the performance of RIM_C and RIM_M in the 10-fold cross-validation and hold-out testing cohorts.

DISCUSSION

Identification of the bleeding site is essential to management of aneurysmal SAH because one of the early steps in clinical care is to secure the rupture site to prevent rebleeding. It is often unfeasible to secure all aneurysms discovered in the same setting, so clinicians prioritize treating the highest risk aneurysm first. Misidentification of the ruptured IA may result in disastrous rebleeding of the ruptured lesion and mortality.[2-8] In approximately 50% of patients, the hemorrhage pattern on CT images makes positive identification of the source of bleeding questionable, in which case clinicians often rely on angiographic findings.[2,3] In a study by Orning et al,[3] the ruptured aneurysm was misidentified in 16.2% of patients who had nondefinitive hemorrhage patterns. To create a more reliable aneurysmal metric for identifying the causative lesion, we generated 2 models (RIM_C and RIM_M) that identify the ruptured site in patients with multiple IAs better than existing aneurysmal parameters.

Recent studies have reported using high-resolution MR imaging of the vessel wall for identifying the ruptured aneurysm among multiples.[33,34] However, the reliability of such an approach is not yet established because 28.5% of stable unruptured IAs also demonstrated wall-enhancement features.[35] Moreover, such imaging requires a long acquisition time, which limits its clinical application and requires cooperative or intubated patients.[36] Consequently, the standard of care for identification of ruptured IAs in patients with multiple aneurysms still relies on CT and angiographic findings.

Controversy exists in the literature regarding whether aneurysm size or shape is more reliable for identifying the ruptured IA in patients with multiple IAs. Nehls et al[2] noted that irregular shape, defined as "multilobulated, contained a nipple, or were markedly elongated," is a better predictor of the ruptured aneurysm than aneurysm size, "greatest dimension." Conversely, Shojima et al[37] reported that aneurysm size, "largest diameter," predicts ruptured aneurysms better than irregular shape, which was defined as an aneurysm with a daughter sac or "an irregular protrusion of the aneurysm wall." We believe such opposing opinions exist because "irregular shape" was not clearly defined and is subject to interrater variations.[22] To avoid such a problem, we quantified aneurysm shape by calculating 3 shape indices, UI, nonsphericity index, and ellipticity index.[23] Among them, UI was the only parameter that was different between ruptured and unruptured IAs, and identified the ruptured IAs in 80% of patients. However, all definitions of aneurysm size, including H_{max} and D, outperformed UI in identifying the ruptured IA, indicating that aneurysm size is more reliable than aneurysm shape for ruptured IA identification.

Previous studies have investigated the morphologic and hemodynamic differences between ruptured and unruptured aneurysms in patients with multiple IAs, mainly through regression analysis, which is more suitable for modeling event probabilities.[9,10,12-14,37] In the current study, the ruptured aneurysm was identified by directly comparing the IAs within each patient. We noted that morphology outperformed hemodynamics in identifying ruptured IAs. Among the morphologic parameters that we studied, SR_{Hmax} had the highest performance, better than traditional indices such as aneurysm size (D, H_{max}) and AR_{Hmax}. SR_{Hmax} incorporates H_{max} and vessel diameter, which is a surrogate for aneurysm location, another variable previously found to be well-correlated with IA rupture.[38]

In a recent study, 17 research groups were asked to use their developed rupture classification models and identify the ruptured aneurysm in a single patient with SAH with 5 IAs. However, only 4 groups could correctly identify the true ruptured aneurysm.[39] In our study, we observed that some individual morphologic parameters, including SR_{Hmax} and H_{max}, outperformed RRS, a previously developed rupture classification model.[16] This finding indicates that existing rupture classification models, including RRS, may not be tailored to such a specific problem, namely, the identification of the ruptured

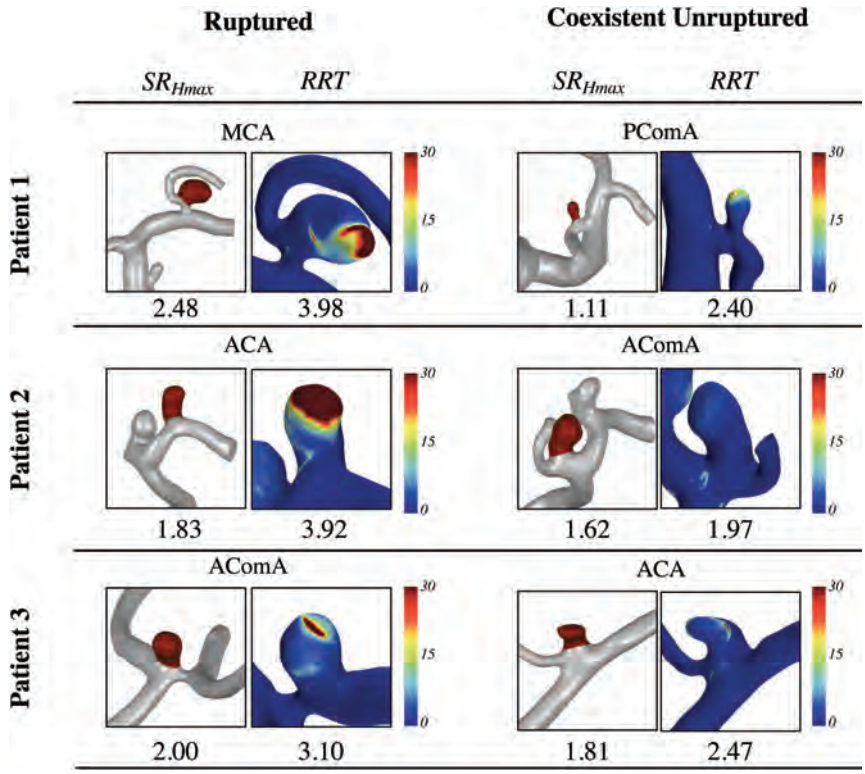

FIG 2. Size ratio (SR_{Hmax}) and relative residence time for all IAs in 3 representative cases (each patient had 1 ruptured and 1 unruptured IA). The number for the RRT is the spatiotemporal aneurysm averaged over the aneurysm sac.

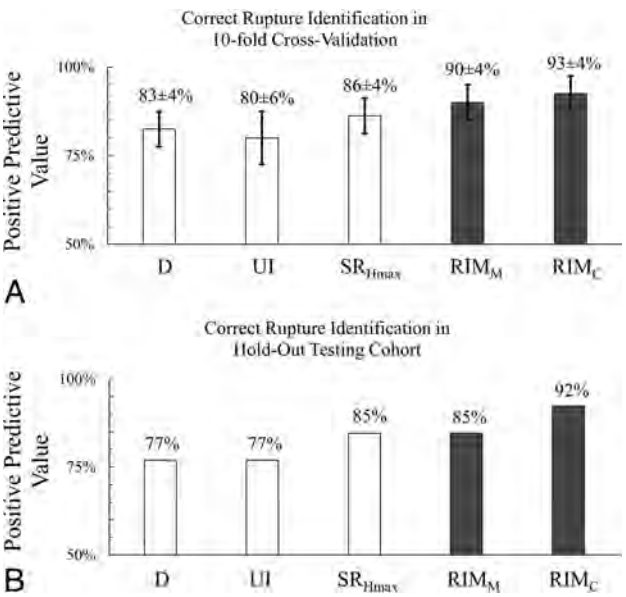

FIG 3. Comparison of rupture identification models (RIM_C and RIM_M) with the 3 existing rupture-risk predictors in identifying the ruptured IA in patients with SAH with multiple IAs in 10-fold cross-validation (*A*) and the holdout testing cohort (*B*).

IA in patients with multiple IAs. A plausible explanation is that those models were built on the basis of pooled data of individuals with multiple and single IAs. A previous study indicated that the characteristics or natural history of IAs in patients with multiple aneurysms might be different from those with a single IA.[40] For instance, it was reported that posterior circulation aneurysms were less frequent in patients with multiple IAs than in patients with a single aneurysm, which we also observed in our study (only 3% of IAs were located at the posterior circulation). Moreover, previous models were trained to discriminate ruptured cohorts from unruptured cohorts without associating the coexisting IAs within each patient. Such factors were considered when generating the RIM_C and RIM_M. The RIM_C model incorporated aneurysm SR_{Hmax}, UI, RRT, and bifurcation type. SR_{Hmax} and UI represent aneurysm size and shape, respectively, which both are established morphologic metrics for identification of ruptured IAs. RRT is a hemodynamic parameter that incorporates both WSS and OSI. IAs with high RRTs are exposed to high near-wall flow stasis, which could promote inflammatory cell infiltration and aneurysm wall degradation, thereby increasing the risk of aneurysm rupture.[41] Bifurcation type is a surrogate for locations with high risk of rupture, including the anterior communicating artery, PICA, and posterior communicating artery.[2,42]

As an alternative model that does not require hemodynamic parameters, RIM_M incorporates only morphologic factors, SR_{Hmax}, UI, and bifurcation. Although RIM_C slightly outperformed RIM_M, we believe that RIM_M will be more user-friendly in clinical settings by reducing the need for intensive CFD simulations.

Our novel predictive models (RIM_M, RIM_C) can be helpful in patients with SAH with hemorrhage patterns that are not definitive. In such cases, instead of solely relying on aneurysm size, shape, or location to delineate the ruptured source, the composite rupture identification models may provide more reliable identification.

Limitations

First, our study had a small sample size and was limited to saccular aneurysms, which could explain the low percentage of posterior circulation aneurysms (3%). Second, definitive hemorrhage patterns were used to identify the rupture source in some of our cases, but only craniotomy can reveal the true rupture status; therefore, there is a possibility of misidentification. Third, our cases came from 3 different centers, and there could be a difference in their aneurysm rupture patterns due to genetics. Fourth, we used several widely used simplifications to perform CFD simulations such as a rigid wall, Newtonian

blood, and generalized boundary conditions to make the computations tractable. Fifth, although we found excellent agreement among users in calculating morphologic and hemodynamic parameters, this was contingent on users following the protocol described in this study. It is unclear how well the rupture identification models will hold if different imaging modalities, segmentation methods, or CFD settings are used. Finally, we used only linear regression models because they were easier to customize for our specific problem. In addition, it was easier to interpret the components (eg, weights) of the final models. In future studies, the application of nonlinear models, such as artificial neural network and random forest, could be explored to account for possible nonlinear interaction among variables.

CONCLUSIONS

To identify ruptured IAs in patients with SAH with multiple IAs, SR_{Hmax} is the best predictor among individual morphologic parameters, including location and type, and hemodynamic parameters. However, composite models (RIM_C and RIM_M), specifically designed for identifying the ruptured IA in patients with multiple IAs, outperformed all individual parameters. Between the 2 models, RIM_C, which incorporated aneurysm hemodynamics, had a better positive predictive value in identifying ruptured IAs, than RIM_M. These findings may help to improve clinical identification of the ruptured IAs in patients with SAH presenting with multiple aneurysms.

Disclosures: Hui Meng—*RELATED*: *Grant*: National Institutes of Health and Canon Medical Systems, *Comments*: National Institutes of Health grant R01NS091075 R03NS090193, and Canon Medical Systems Corporation grants [no grant number]. Co-founder, Neurovascular Diagnostics, Inc.* Adnan H. Siddiqui—*RELATED*: *Grant*: National Institutes of Health/National Institute of Neurological Disorders and Stroke 1R01NS071075, Virtual Intervention of Intracranial Aneurysms; *UNRELATED*: *Consultancy*: Amnis Therapeutics, Boston Scientific, Canon Medical Systems, Cerebrotech Medical Systems, Cerenovus, Corindus, Endostream Medical, Guidepoint Global Consulting, Imperative Care, Integra, Medtronic, MicroVention, Northwest University, Data and Safety Monitoring Board Chair for the HEAT trial, Penumbra, Q'Apel Medical, Rapid Medical, Rebound Therapeutics, Serenity Medical, Silk Road Medical, StimMed, Stryker, Three Rivers Medical, Vassol, W.L. Gore and Associates; *Stock/Stock Options*: Amnis Therapeutics, BlinkTBI, Buffalo Technology Partners, Cardinal Consultants, Cerebrotech Medical Systems, Cognition Medical, Endostream Medical, Imperative Care, International Medical Distribution Partners, Neurovascular Diagnostics, Q'Apel Medical, Rebound Therapeutics, RIST Neurovascular, Serenity Medical, Silk Road Medical, StimMed, Synchron, Three Rivers Medical, Viseon Spine; Jason M. Davies—*RELATED*: *Grant*: National Center for Advancing Translational Sciences of the NIH (award number KL2TR001413), University at Buffalo. Speakers' bureau: Penumbra; Honoraria: Neurotrauma Science; *Other*: Cerenovus, Medtronic, MicroVention, Penumbra, Medical University of South Carolina, *Comments*: National Principal Investigator/Steering Committee for Cerenovus LARGE Trial and ARISE II Trial; Medtronic SWIFT PRIME and SWIFT DIRECT trials; MicroVention FRED Trial and CONFIDENCE study; Medical University of South Carolina POSITIVE Trial; Penumbra Separator 3D trial, COMPASS trial, INVEST trial. *Money paid to the institution.

ACKNOWLEDGMENTS

We thank Paul H. Dressel, BFA, for figure preparation and W. Fawn Dorr, BA, and Debra J. Zimmer for editorial assistance.

REFERENCES

1. Juvela S. **Risk factors for multiple intracranial aneurysms.** *Stroke* 2000;31:392–97 CrossRef Medline
2. Nehls DG, Flom RA, Carter LP, et al. **Multiple intracranial aneurysms: determining the site of rupture.** *J Neurosurg* 1985;63:342–48 CrossRef Medline
3. Orning JL, Shakur SF, Alaraj A, et al. **Accuracy in identifying the source of subarachnoid hemorrhage in the setting of multiple intracranial aneurysms.** *Neurosurgery* 2018;83:62–68 CrossRef Medline
4. Hino A, Fujimoto M, Iwamoto Y, et al. **False localization of rupture site in patients with multiple cerebral aneurysms and subarachnoid hemorrhage.** *Neurosurgery* 2000;46:825–30 CrossRef Medline
5. Liu Z, Wei LF, Wang RM, et al. **Misdiagnosis of rupture sites of multiple intracranial aneurysms: special report of two cases.** *Scientific Research and Essays*, 2010;5:3794–98
6. Lee KC, Joo JY, Lee KS. **False localization of rupture by computed tomography in bilateral internal carotid artery aneurysms.** *Surg Neurol* 1996;45:435–40; discussion 40–41 CrossRef Medline
7. Zderkiewicz E, Pawlik Z, Czochra M, et al. **Clinical signs pointing to the source of hemorrhage in multiple intracranial aneurysms.** *Med Sci Monit* 2002;8:Cr83–86 Medline
8. Koyama T, Tanaka Y, Kobayashi S, et al. **Surgery of basilar aneurysms associated with unexpected rupture of an internal carotid artery aneurysm.** *Neurosurg Rev* 2000;23:168–70 CrossRef Medline
9. Bjorkman J, Frosen J, Tahtinen O, et al. **Irregular shape identifies ruptured intracranial aneurysm in subarachnoid hemorrhage patients with multiple aneurysms.** *Stroke* 2017;48:1986–89 CrossRef Medline
10. Jing L, Fan J, Wang Y, et al. **Morphologic and hemodynamic analysis in the patients with multiple intracranial aneurysms: ruptured versus unruptured.** *PLoS One* 2015;10:e0132494 CrossRef Medline
11. Doddasomayajula R, Chung B, Mut F, et al. **Hemodynamic characteristics of ruptured and unruptured multiple aneurysms at mirror and ipsilateral locations.** *AJNR Am J Neuroradiol* 2017;38:2301–07 CrossRef Medline
12. Bhogal P, AlMatter M, Hellstern V, et al. **Difference in aneurysm characteristics between ruptured and unruptured aneurysms in patients with multiple intracranial aneurysms.** *Surg Neurol Int* 2018;9:1. CrossRef Medline
13. Backes D, Vergouwen MD, Velthuis BK, et al. **Difference in aneurysm characteristics between ruptured and unruptured aneurysms in patients with multiple intracranial aneurysms.** *Stroke* 2014;45:1299–303 CrossRef Medline
14. Jeon HJ, Lee JW, Kim SY, et al. **Morphological parameters related to ruptured aneurysm in the patient with multiple cerebral aneurysms (clinical investigation).** *Neurol Res* 2014;36:1056–62 CrossRef Medline
15. Berg P, Beuing O. **Multiple intracranial aneurysms: a direct hemodynamic comparison between ruptured and unruptured vessel malformations.** *Int J Comput Assist Radiol Surg* 2018;13:83–93 CrossRef Medline
16. Xiang J, Yu J, Choi H, et al. **Rupture resemblance score (RRS): toward risk stratification of unruptured intracranial aneurysms using hemodynamic-morphological discriminants.** *J Neurointerv Surg* 2015;7:490-95 CrossRef Medline
17. Antiga L, Piccinelli M, Botti L, et al. **An image-based modeling framework for patient-specific computational hemodynamics.** *Med Biol Eng Comput* 2008;46:1097–12 CrossRef Medline
18. Xiang J, Natarajan SK, Tremmel M, et al. **Hemodynamic–morphologic discriminants for intracranial aneurysm rupture.** *Stroke* 2011;42:144–52 CrossRef Medline
19. Murray CD. **The physiological principle of minimum work, I: the vascular system and the cost of blood volume.** *Proc Natl Acad Sci U S A* 1926;12:207–14 CrossRef Medline
20. Rajabzadeh-Oghaz H, Varble N, Davies JM, et al. **Computer-assisted adjuncts for aneurysmal morphologic assessment: toward more precise and accurate approaches.** *Proc SPIE Int Soc Opt Eng* 2017; 10134 CrossRef Medline
21. Xiang J, Antiga L, Varble N, et al. **A View: an image-based clinical computational tool for intracranial aneurysm flow visualization**

and clinical management. *Annals of biomedical engineering.* 2016;44:1085–96 Medline
22. Rajabzadeh-Oghaz H, Varble N, Shallwani H, et al. **Computer-assisted three-dimensional morphology evaluation of intracranial aneurysms.** *World Neurosurg* 2018;119:e541–50 CrossRef Medline
23. Dhar S, Tremmel M, Mocco J, et al. **Morphology parameters for intracranial aneurysm rupture risk assessment.** *Neurosurgery* 2008; 63:185–97 CrossRef Medline
24. Rahman M, Smietana J, Hauck E, et al. **Size ratio correlates with intracranial aneurysm rupture status: a prospective study.** *Stroke* 2010;41:916-20 CrossRef Medline
25. Raghavan ML, Ma B, Harbaugh RE. **Quantified aneurysm shape and rupture risk.** *J Neurosurg* 2005;102:355–62 CrossRef Medline
26. Asgharzadeh H, Borazjani I. **Effects of Reynolds and Womersley numbers on the hemodynamics of intracranial aneurysms.** *Comput Math Methods Med* 2016;2016:1 CrossRef Medline
27. Tsivgoulis G, Sharma VK, Hoover SL, et al. **Applications and advantages of power motion-mode Doppler in acute posterior circulation cerebral ischemia.** *Stroke* 2008;39:1197–204 CrossRef Medline
28. Steinmeier R, Laumer R, Bondar I, et al. **Cerebral hemodynamics in subarachnoid hemorrhage evaluated by transcranial Doppler sonography, Part 2: pulsatility indices: normal reference values and characteristics in subarachnoid hemorrhage.** *Neurosurgery* 1993; 33:10–18 discussion 18–19 CrossRef Medline
29. Byrne G, Mut F, Cebral J. **Quantifying the large-scale hemodynamics of intracranial aneurysms.** *AJNR Am J Neuroradiol* 2014;35:333–38 CrossRef Medline
30. Xiang J, Yu J, Snyder KV, et al. **Hemodynamic–morphological discriminant models for intracranial aneurysm rupture remain stable with increasing sample size.** *J Neurointervent Surg* 2016;8:104–10 CrossRef Medline
31. Gail MH, Lubin JH, Rubinstein LV. **Likelihood calculations for matched case-control studies and survival studies with tied death times.** *Biometrika* 1981;68:703–07 CrossRef
32. Feng X, Ji W, Qian Z, et al. **Bifurcation location is significantly associated with rupture of small intracranial aneurysms (< 5 mm).** *World Neurosurg* 2017;98:538–45 CrossRef Medline
33. Matouk CC, Mandell DM, Gunel M, et al. **Vessel wall magnetic resonance imaging identifies the site of rupture in patients with multiple intracranial aneurysms: proof of principle.** *Neurosurgery* 2013; 72:492–96; discussion 496 CrossRef Medline
34. Mandell DM, Mossa-Basha M, Qiao Y, et al. **Intracranial Vessel Wall MRI: Principles and Expert Consensus Recommendations of the American Society of Neuroradiology.** *AJNR Am J Neuroradiol* 2017;38:218–29 CrossRef Medline
35. Edjlali M, Gentric JC, Régent-Rodriguez C, et al. **Does aneurysmal wall enhancement on vessel wall MRI help to distinguish stable from unstable intracranial aneurysms?** *Stroke* 2014;45:3704–06 CrossRef Medline
36. Lindenholz A, van der Kolk AG, Zwanenburg JJM, et al. **The use and pitfalls of intracranial vessel wall imaging: how we do it.** *Radiology* 2018;286:12–28 CrossRef Medline
37. Shojima M, Morita A, Nakatomi H, et al. **Size is the most important predictor of aneurysm rupture among multiple cerebral aneurysms: post hoc subgroup analysis of Unruptured Cerebral Aneurysm Study Japan.** *Neurosurgery* 2018;82:864–69 CrossRef Medline
38. Ma D, Tremmel M, Paluch RA, et al. **Size ratio for clinical assessment of intracranial aneurysm rupture risk.** *Neurol Res* 2010; 32:482–86 CrossRef Medline
39. Berg P, Voß S, Janiga G, et al. **Multiple Aneurysms AnaTomy CHallenge. 2018 (MATCH), Phase II: rupture risk assessment.** *Int J Comput Assist Radiology Surg* 2019 May 3. [Epub ahead of print] CrossRef Medline
40. Lee YJ, Parreira T, Matouk CC, et al. **Clinical characteristics and preferential location of intracranial mirror aneurysms: a comparison with non-mirror multiple and single aneurysms.** *Neuroradiology* 2015;57:35–40 CrossRef Medline
41. Meng H, Tutino VM, Xiang J, et al. **High WSS or low WSS? Complex interactions of hemodynamics with intracranial aneurysm initiation, growth, and rupture: toward a unifying hypothesis.** *AJNR Am J Neuroradiol* 2014;35:1254–62 CrossRef Medline
42. Varble N, Rajabzadeh-Oghaz H, Wang J, et al. **Differences in morphologic and hemodynamic characteristics for "PHASES-Based" intracranial aneurysm locations.** *AJNR Am J Neuroradiol* 2017; 38:2105–10 CrossRef Medline

Transitioning to Transradial Access for Cerebral Aneurysm Embolization

C. Chivot, R. Bouzerar, and T. Yzet

ABSTRACT

BACKGROUND AND PURPOSE: Despite several retrospective studies showing the safety and efficacy of transradial access for cerebral angiography, neurointerventionalists are apprehensive about implementing TRA for neurointerventions. This reluctance is mainly due to anatomic factors, technical factors, and a long learning curve (relative to transfemoral access). We present here our experience of TRA transition for cerebral aneurysm embolization. Our aim was to demonstrate the feasibility and safety of radial access for consecutive embolizations of ruptured and unruptured cerebral aneurysms.

MATERIALS AND METHODS: We performed a retrospective review of a prospective data base on cerebral aneurysm embolizations. Between April and December 2018, radial access was considered for all consecutive patients referred to our institution for cerebral aneurysm embolization. Technical success was defined as radial access with insertion of the sheath and completion of the intervention without a crossover to conventional femoral access. The primary safety end point was the in-hospital plus 30-day incidence of radial artery occlusion. Secondary end points included intraoperative complications and neurologic complications at discharge and in the following 30 days.

RESULTS: Seventy-one patients with a cerebral aneurysm underwent 73 embolization procedures at our institution. The first-choice access route was the radial artery in 62 patients (87.3%) and the femoral artery in 9 (12.6%). Thirty-four embolizations were performed using coils, 22 used a balloon-assisted coil technique, 6 used a stent-assisted coil technique, and 2 used a flow diverter. Crossover to femoral access was observed in 2 patients (3.1%). Four patients developed coil-induced thrombi requiring intra-arterial tirofiban injections. In 1 case, an aneurysm ruptured during the operation but did not have a clinical impact. No cases of radial artery occlusion or hand ischemia were observed.

CONCLUSIONS: A transition to radial access for cerebral aneurysm embolization is feasible and does not increase the level of risk associated with the procedure.

ABBREVIATIONS: POD = postoperative day; TFA = transfemoral access; TRA = transradial access

Transradial access (TRA) for transcatheter coronarography has been performed for >25 years, and several studies have found that it is safer than transfemoral access (TFA).[1–8] The European Society of Cardiology recommends TRA as the first-line approach for coronary diagnosis and therapy because this method is associated with a lower hemorrhage risk, a shorter length of hospital stay, a shorter period of immobilization, lower costs, and greater levels of patient satisfaction.[9] Despite these clear benefits, TRA is underused in neuroradiology; surgeons tend to reserve it for posterior fossa aneurysm embolization or after TFA has failed. This reluctance is mainly due to anatomic factors, technical factors, and a long learning curve (relative to TFA). A small radial artery diameter is an anatomic factor of major concern, puncture is considered more difficult than in TFA, and a small diameter prevents the use of large catheters required for interventions (eg, flow diverters). With regard to technical factors, the lack of dedicated equipment for TRA is a major issue because the catheter transition zones are adjusted for TFA; therefore, stability may be a problem during TRA. The literature data show that in cardiology, a 50-case learning curve is required to decrease the complications and crossover rates.[10]

It is likely that the learning curve in neuroradiology would be the same, though the number of patients treated is obviously lower than in cardiology. Consequently, the longer time needed to gain sufficient experience might explain the surgeons'

Received June 20, 2019; accepted after revision August 13.

From the Departments of Radiology (C.C., T.Y.) and Image Processing (R.B.), Amiens University Hospital, Amiens, France.

Please address correspondence to Cyril Chivot, MD, Department of Radiology, Hôpital Sud, Centre Hospitalier Universitaire d'Amiens, Ave René Laennec, F-80054, Amiens Cedex 01, France; e-mail: chivot.cyril@chu-amiens.fr

http://dx.doi.org/10.3174/ajnr.A6234

reluctance to use TRA. Nevertheless, TRA has true value in neuroradiology because a growing proportion of stent placements require dual-antiplatelet therapy, increasing the risk of hemorrhagic complications at the puncture site. The proportion of patients with obesity is also increasing, and TRA is easier and safer than TFA in this population.[11] Last, the most important benefit of using TRA is greater comfort for the patient.

In view of the many reported advantages of TRA (notably with regard to feasibility and safety in diagnostic cerebral angiography[12,13]), our institution began transitioning all its diagnostic cerebral angiography examinations to TRA. Next, after a few months of practice, we decided to use TRA for all cerebral embolization procedures. Two recent cohort studies[12,13] found that TRA was safe for the embolization of unruptured cerebral aneurysms, though the patients were probably selected and not consecutive. The objective of the present study was thus to determine the feasibility and safety of a transition to TRA for consecutive embolizations of ruptured or unruptured cerebral aneurysms.

MATERIALS AND METHODS

We reviewed our prospective data base on cerebral aneurysm embolizations performed between April and December 2018. During this period, TRA was considered for all consecutive patients addressed for cerebral aneurysm embolization at our institution. This retrospective, single-center study was approved by the institutional review board. The board waived the need for informed consent.

The Endovascular Procedure

All embolizations were performed with the patient under general anesthesia by the same surgeon (C.C.) with 5 years of experience in TFA cerebral embolization. Before puncture, a Barbeau test was performed to check the patency of the superficial palmar arch. Radial access was suitable only for patients with Barbeau A–C waveforms.

The patient's arm was positioned on a swivel-arm board at his or her side. Access to the radial artery was obtained using an anterior or counter-puncture technique at the start of our series and using sonographic guidance for the last 20 patients. Once the 6F radial sheath had been placed, we injected a medication cocktail (2.5 mg of verapamil and 250 μg of nitroglycerine) directly through it. Intravenous heparin (50 U/kg) was administered to maintain an activated clotting time between 250 and 350 seconds.

A 6F sheath was placed in the right (preferably) radial artery, and supra-aortic vessels were catheterized by advancing a 6F Envoy catheter (Codman & Shurtleff, Raynham, Massachusetts) or a Benchmark catheter (Penumbra, Almeda, California) over a 130-cm 5F Simmons 2-shaped catheter (Penumbra for anterior circulation, or over a 125-cm 5F Berenstein diagnostic catheter [Penumbra]) for the posterior circulation, as described previously by Snelling et al.[14]

For flow-diverter placement (Pipeline Flex; Covidien, Irvine, California), a 0.088-inch-internal-diameter guide catheter was inserted sheathlessly with an intermediate catheter (Sofia; MicroVention, Tustin, California) after ensuring that the diameter of the radial artery was >2.5 mm. When the diameter was <2.5 mm, TFA was preferred.

For remodeling techniques, a dual-lumen balloon catheter (Scepter C or XC; MicroVention) and a microcatheter (Excelsior SL 10; Stryker, Kalamazoo, Michigan) were placed in the same guide catheter (Envoy; DePuy Synthes, Warsaw, Indiana; or Benchmark), and coils were deployed through the microcatheter using standard techniques.

Stents (Neuroform Atlas, Stryker; or LEO Baby stent, Balt Extrusion, Montmorency, France) were placed through the microcatheter (Excelsior SL 10) using standard techniques.

Outcome

Technical success was defined as TRA with insertion of the sheath and completion of the cerebral aneurysm procedure without crossover to conventional TFA.

The safety end point was the in-hospital plus 30-day incidence of radial artery occlusion. This was evaluated 24 hours after the procedure, at discharge, and on postoperative day (POD) 30. The secondary end points included the in-hospital incidence of access site hematoma, pseudoaneurysm, arteriovenous fistula, infection, or neurologic complications requiring an operation, together with a composite of these. At each follow-up visit, the access site was inspected. The secondary end points also included cerebral thromboembolic and hemorrhagic complications and vessel injury. Patients underwent a physical examination by a neurologist 24 hours after the procedure, at discharge, and on POD 30.

RESULTS

Between April and December 2018, seventy-one patients with cerebral aneurysms underwent 73 embolization procedures (all performed by the same operator) at our institution. The first-choice access route was the radial artery in 62 patients (87.3%) and the femoral artery in 9 (12.6%). The study populations' baseline clinical and radiologic characteristics are summarized in Table 1. In the subset of 62 patients treated with TRA, 33 were treated on an emergency basis for a ruptured aneurysm, and 29 underwent scheduled embolization for an unruptured aneurysm. Two patients had a second embolization after recanalization: One procedure was performed with coils, and the other, with flow diverters.

Intervention Site

Of the 64 embolization procedures with TRA performed in the 62 cases, 56 and 8 (87.5% and 12.5%) involved the anterior and posterior circulations, respectively. The left internal carotid artery was used in 33 cases (51.5%), followed by the right ICA in 23 (35.9%), the left vertebral artery in 7 (10.9%), and the right vertebral artery in 1 (1.5%). The right and left radial arteries were used in 52 and 12 cases, respectively (Fig 1). The left radial artery was chosen in 7 cases to catheterize a dominant left vertebral artery, in 3 cases because a right arterial line was already in place (Fig 2), and in 2 cases because the right radial artery was occluded (due to several radial coronarographies).

Interventions Performed

Thirty-four embolizations were performed using coils, 22 used a balloon-assisted coiling technique, 6 used a stent-assisted coiling technique, and 2 used a flow diverter (Table 2). Eight patients

required ≥2 TRAs: 2 for intra-arterial injection of milrinone, 2 for a second embolization, and 4 for diagnostic cerebral angiography before embolization. The mean dose-area product was 75.7 Gy × cm^2, which is equivalent to the mean value obtained with TFA in our center during the previous year (75.6 Gy × cm^2).

Table 1: Demographic and baseline clinical characteristics of the study population

	Ruptured (*n* = 33)	Unruptured (*n* = 29)
Age (mean) (range) (yr)	52.6 (31–79)	54.5 (37–77)
Female	16	16
BMI (mean)	27.4	27.5
Arterial hypertension	17 (51.5%)	18 (62%)
Current smoking	22 (66.6%)	17 (58.6%)
Diabetes mellitus	2 (6%)	3 (10.3%)
Alcohol abuse	6 (18.1%)	2 (6.8%)
Dyslipidemia	5 (15.5%)	9 (31%)
Family history of aneurysm	2 (6%)	2 (6.8%)
Antithrombotic medications	2 (6%)	12 (41.3%)
WFNS score		
I	13 (39.3%)	
II	10 (30.3%)	
III	1 (3%)	
IV	3 (9%)	
V	6 (18.1%)	
Fisher scale		
1	1 (3%)	
2	2 (6%)	
3	13 (39.3%)	
4	16 (48.4%)	
Hydrocephalus	10 (30.3%)	
Aneurysm site		
AcomA	17 (51.5%)	13 (44.8%)
PcomA	2 (6%)	4 (13.7%)
Paraclinoid	2 (6%)	3 (10.3%)
PICA	1 (3%)	1 (3.4%)
Tip of the basilar artery	1 (3%)	5 (17.2%)
Terminus of the carotid artery	0 (0%)	1 (3.4%)
Pericallosal artery	2 (6%)	0 (0%)
Middle cerebral artery bifurcation	8 (24.2%)	2 (6.8%)
Aneurysm length (mean) (range) (mm)	7 (2.5–12)	7.4 (4–28)

Note:—BMI indicates body mass index; WFNS, World Federation of Neurologic Societies; AcomA, anterior communicating artery; PcomA, posterior communicating artery.

Feasibility

Two (3.1%) attempted TRA procedures required crossover to TFA. The reasons for failure included the detection of a right axillary artery occlusion during the procedure and an acute angle between the origin of the left common carotid artery and the left subclavian artery. In the latter patient, left radial access was used because a right artery line had been placed by the anesthesiologist.

For 9 patients, TRA was not initially attempted during the embolization procedure: One of these patients did not show a pulse after 2 minutes of radial artery compression (Barbeau type D), 1 patient had a right dialysis fistula, and 2 patients had right arterial lines placed by the anesthesiologist after several attempts to puncture the left radial artery had failed. Femoral access was also used for flow-diverter placement in 3 subjects. In 2 cases, this was due to a small radial artery (diameter, <2.5 mm). In the other case, this was due to the discovery of an aberrant origin of the right subclavian artery (arteria lusoria) during diagnostic cerebral angiography with radial access a few months before embolization. Last, femoral access was chosen in 2 other cases because of the occurrence of a radial artery spasm during diagnostic cerebral angiography with a 4F sheath performed a few months before embolization.

Safety

No cases of radial artery occlusion, hand ischemia, or other sequelae were observed at the puncture site. In 1 patient, however, persistent arterial bleeding at the puncture site was observed whenever the TR Band compression device was deflated (Terumo, Tokyo, Japan); hence, the device was left partially inflated for 24 hours. No radial artery occlusion was noted during follow-up. With regard to intraoperative complications, 4 patients developed coil-induced thrombi requiring an intra-arterial tirofiban injection. There were no neurologic sequelae after resolution of the thrombi. In 1 case, an aneurysm ruptured in a patient referred for embolization of a ruptured anterior communicating artery, but it did not have a clinical effect.

Five of the 33 patients with a ruptured aneurysm died (World Federation of Neurologic Societies score, 5) a few days or weeks

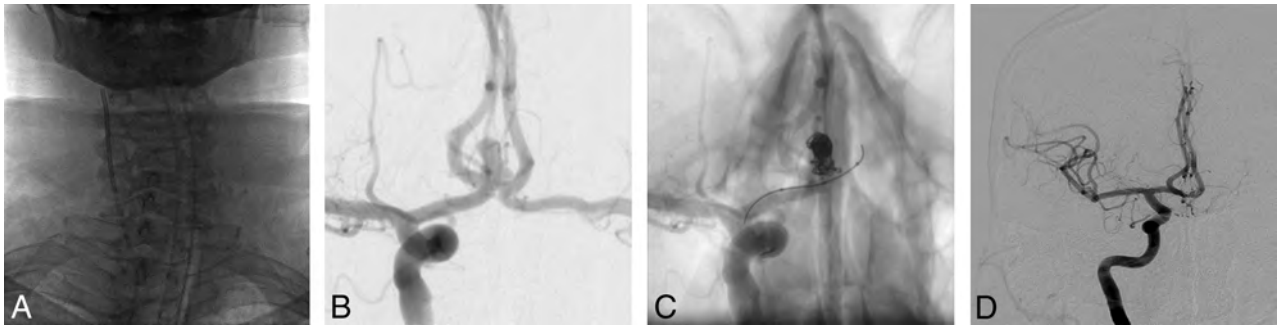

FIG 1. A middle-aged patient presenting with a ruptured bilobed aneurysm of the anterior communicating artery (measuring 6.8 × 4.8 mm), treated using balloon-assisted coiling via TRA. *A*, The right ICA was catheterized with a guide catheter via right TRA. *B*, An angiogram of the right ICA highlights the anterior communicating artery aneurysm. *C*, An angiogram of the right ICA, with a dual-lumen balloon and microcatheter in place. *D*, An angiogram of the right ICA shows the total occlusion of the aneurysm.

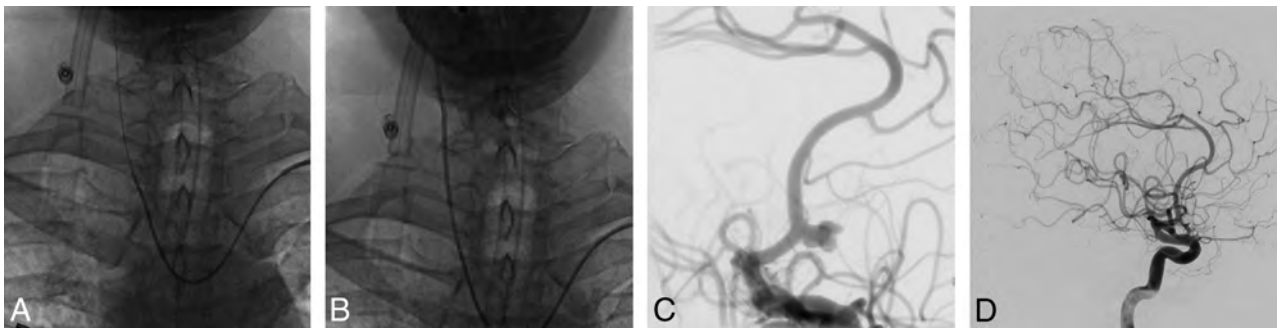

FIG 2. A middle-aged patient presenting with a ruptured aneurysm of the anterior communicating artery (measuring 7 × 4 mm), treated using coiling via left TRA. *A*, The right common carotid artery was catheterized using a Simmons shaped catheter via left TRA; then, a guiding catheter (*B*) was advanced over it. *C*, An angiogram of the right ICA highlights the irregular aneurysm of the anterior communicating artery. *D*, An angiogram of the right ICA shows the total occlusion of the aneurysm.

Table 2: Characteristics of the procedures

	Ruptured (*n* = 33)	Unruptured (*n* = 31)
TRA side		
Right	26 (78.7%)	26 (83.8%)
Left	7 (21.2%)	5 (16.1%)
Aneurysm side		
Right	16 (48.4%)	15 (48.4%)
Left	17 (51.5%)	16 (51.6%)
Crossover	2 (3.1%)	0 (0%)
Embolization technique		
Coiling	21 (63.6%)	13 (41.9%)
Balloon-assisted technique	12 (36.4%)	10 (32.2%)
Stent-assisted technique	0 (0%)	6 (19.3%)
Flow diverter	0 (0%)	2 (6.4%)
Intraoperative thromboembolic complications	2 (6%)	2 (6.4%)
Intraoperative rupture	1 (3%)	0 (0%)

after the embolization procedure due to progression of the initial hemorrhage. Eight patients (including 2 patients with TRA) received an intra-arterial milrinone injection for cerebral vasospasm. One patient underwent 3 TRA procedures for intracranial milrinone injection. On POD 30, three patients had an mRS score of 3 and 25 patients had an mRS score of <2. In all embolized patients with an unruptured aneurysm (*n* = 29), the mRS was the same at discharge and on POD 30.

DISCUSSION

A large number of comparative, randomized trials in the field of cardiology have shown that morbidity and mortality rates are significantly lower for TRA than for TFA.[1-7] Recently, several groups have transitioned from TFA to TRA for diagnostic cerebral angiography, with good surgical results and a patient preference for radial access.[12] Despite these encouraging results, most neurointerventionists consider TRA appropriate only for interventions within the posterior circulation and in cases of TFA failure. However, the safety profile of TRA is a strong argument for the transition because heparin is administered during all neurointervention procedures, and stent-assisted coiling or flow-diverter procedures requiring dual-antiplatelet therapy are increasingly frequent.

Some case reports and cohort studies[12,14-16] have demonstrated the feasibility of transradial cerebral aneurysm embolization in selected cases, rather than for consecutive patients. Goland et al[16] reported 40 complication-free cerebral aneurysm embolizations with right TRA. Thirty-three aneurysms were ruptured and 7 were unruptured, 35 were treated with coils, and 5 were treated with a flow diverter. Snelling et al[14] reported 33 cases of TRA for unruptured aneurysm embolizations (performed with balloon-assisted coiling in 3 cases, coiling in 12 cases, a flow diverter in 11 cases, stent-assisted coiling in 6 cases, and vessel sacrifice in 1 case). There were 5 crossovers: 2 due to radial artery spasms, 2 due to tortuosity of the left common carotid artery, and 1 due to tortuosity of the subclavian artery. With regard to neurologic complications, 1 patient developed an in-stent thrombus postoperatively; this was treated with intra-arterial thrombolysis with no permanent sequelae.

Neither Goland et al[16] nor Snelling et al[14] (Table 3) reported symptomatic radial artery occlusions, though the frequency of asymptomatic radial artery occlusion—a very important factor in complete transitions to TRA—was not specified. Indeed, the patency of the radial artery is crucial for follow-up or further embolization. At POD 30, we did not observe any radial artery occlusion, even in the 8 patients having undergone ≥2 TRA procedures. In the cardiology literature, the estimated frequency of radial artery occlusion is 5%.[17] This complication is caused by the absence of intraoperative unfractionated heparin, a procedure lasting for 3 hours, a radial inner diameter/sheath outer diameter ratio of <1.0, and the use of conventional hemostasis techniques rather than patent hemostasis techniques.[17-20]

Furthermore, the complication rates observed during our transition phase did not differ from those reported in the literature. With regard to thrombus formation, we observed 2 cases in the ruptured aneurysm group and 2 cases in the unruptured group. All 4 were resolved by tirofiban treatment, and there were no subsequent neurologic symptoms. In the literature on TFA, the rates of thromboembolic complications and

Table 3: Main series of TRA for intracranial aneurysm treatment

	Snelling et al[14]	Chen et al[15]	Goland et al[16]	Chivot et al
n	33	49	40	64
Type of treatment				
Flow diverter	11	49	5	2
Coils	12	0	35	34
Balloon-assisted coiling	3	0	0	22
Stent-assisted coiling	6	0	0	6
Vessel sacrifice	1	0	0	0
Permanent neurologic complications	0	0	0	0
Crossover	15.1% (5/33)	20.40% (10/49)	0	3.1% (2/64)
Failure reasons				
Radial artery spasm	2	2	0	0
LICA tortuosity	0	4	0	0
LCCA origin angle	2	4	0	1
Subclavian tortuosity	1	0	0	0
Subclavian occlusion	0	0	0	1

Note:—LICA indicates left internal carotid artery; LCCA, left common carotid artery.

intraoperative rupture associated with coiling for unruptured aneurysms were 7.3% and 2.0%, respectively.[21] For ruptured aneurysms, the rates of thromboembolic complications and intraoperative rupture were higher: 13.3% and 3.7%, respectively.[21]

Nonetheless, the transition to TRA requires some adjustments. First, the anesthesia team must be asked not to touch the right radial wrist for patients admitted for ruptured aneurysm. Right TRA is more suitable for cerebral embolization when the aneurysm is located on the left because the angle between the left subclavian and left common arteries is often more acute than the angle between the innominate and left arteries. At the start of our transition, we did not use the left radial artery. However, after having gained experience, we are comfortable using the left radial artery, primarily if the aneurysm is located on the right side. The left side is also very useful for posterior circulation aneurysms because the left radial artery allows direct access to the often-dominant left vertebral artery. The drawback associated with conventional left-sided access is the arm position when working on the right side of the patient. Indeed, during conventional radial access, it is difficult to maintain the arm in the supine position on the abdomen during general anesthesia because the limb tends to rotate downward. Fortunately, this problem can be solved by dorsal radial (snuffbox) access because the hand then rests in its natural position, with the palm facing the hip. The second adjustment consists of asking the intensive care team to reduce potential trauma by limiting the number of right radial artery punctures for blood gas analysis and preferring the left side.

At present, the flow-diverter procedure is the main challenge in TRA for cerebral embolization. Given the stiffness of the flow diverter, an additional proximal support is required for deployment, and a long sheath with an intermediate catheter is often essential. The long sheaths typically used in neuroradiology (such as the Neuron Max, Penumbra; and the Axs Infinity, Stryker) have an outer diameter of 2.7 mm, which limits their use for TRA. Furthermore, the diameter of the radial artery appears to vary significantly with sex, body mass index, and ethnicity.[22] Velasco et al[23] evaluated the right radial artery in 100 young adult volunteers from Texas (40 men, 60 women; mean age, 35 years; mean body mass index, 27 kg/m^2). These researchers reported that the mean vessel diameter was 2.22 $\pm$ 0.35 mm, which is smaller than the measurements reported in populations in China (2.38 $\pm$ 0.56 mm),[24] Singapore (2.45 $\pm$ 0.45 mm),[25] and South Korea (2.60 $\pm$ 0.41 mm).[26] Velasco et al also found that 42% of patients had an arterial diameter greater than that of a 5F arterial sheath (2.28 mm), 20% had a diameter greater than that of a 6F sheath (2.62 mm), and only 5% had a radial artery diameter greater than that of a 7F sheath (2.95 mm). Saito et al[27] noted that the radial artery was large enough for a 6F sheath in only 72.6% of female Asian patients and 85.7% of male Asian patients. The researchers also observed that for a 7F sheath, the radial inner diameter/sheath outer diameter ratio was >1 for 71.5% of male patients and 40.3% of female patients. For an 8F sheath, these proportions were, respectively, 44.9% and 24.0%. Last, a ratio of <1 was associated with an increased frequency of radial artery occlusion. Considering the female predominance in cerebral aneurysm populations and the smaller radial artery diameter observed in Western populations and females, the 088 Triaxial system would probably not be the preferred system for flow diverter procedures.

Indeed, Chen et al[15] reported that a transradial flow-diverter procedure was feasible in the absence of an 088 Triaxial system. In 15 of 49 cases (31%), the researchers used a quadriaxial 071- or 072-inch system (with 5 failures, 33.3%), and in 9 cases (18%), they used a biaxial intermediate catheter without a guiding catheter or sheath. The 088 Triaxial system was used in only 15 of the 49 cases (31%), and there were 3 failures (20%). The crossover rate in the study of Chen et al was 20.4%; the crossovers were prompted by an acute left common carotid artery angle in 4 patients, tortuosity of the left common carotid artery and the ICA in 5 patients, and a severe radial artery spasm in 2 patients. The crossover rate for the flow-diverter procedure currently reported in the literature is too high to generalize TRA for this purpose, but we think that for selective cases, a flow diverter is an option with a low rate of crossover. In our opinion, TRA can be the first-choice technique if we need to set up a flow diverter in the posterior circulation or at the level of the left carotid artery in case of a bovine arch configuration. For all other cases, the choice will depend on the difficulties encountered during the TRA diagnostic angiography.

Indeed, a few weeks before the flow-diverter procedure, we systematically check the radial artery diameter to determine which device to use and we perform a TRA diagnostic angiography to assess the operational feasibility.

In our series, we selected patients according their radial artery diameter and now prefer the 088 Triaxial System. We believe that failure rates for flow-diverter procedures will decrease with the introduction of softer, more easily navigable stents, along with radial-specific access systems.

Other potential drawbacks of TRA are related to the catheter length and the degree of radiation exposure. An insufficiently long catheter may be a real issue in very tall patients, patients with tortuosities, and cases of distal TRA where the puncture site is located 3 or 4 cm below the usual puncture site. Fortunately, the use of a 125-cm intermediate catheter and a microcatheter (such as the 167-cm Headway Duo; MicroVention) may solve this issue.[28] According to the cardiology literature, TRA is associated with greater radiation exposure (relative to TFA) in both diagnostic and interventional coronarography, though the difference falls with time and practice.[29,30] In the present series, the mean dose-area product was below the reference level[31] and was equivalent to the dose recorded using TFA in the preceding years. To minimize operator radiation exposure, one must position the right arm alongside the right leg (rather than abducted from the leg) so that the upper shield can be placed in the position used for TFA.[32]

Limitations

Our study had several limitations, most of which were related to the retrospective design and the small sample size. This was a single-center study with 1 operator. Therefore, potential major differences in operator training might mean that it is not be possible to generalize our results to other catheterization centers. However, the operator here had limited prior experience in TRA (31 diagnostic cerebral angiographies), and the complication rate during the transition phase was low. Accordingly (and as reported in the cardiology literature[33]), we consider that a learning curve with 30 diagnostic cerebral angiography procedures is required to become familiar with radial access and the associated difficulties before cerebral embolization can be safely performed.

CONCLUSIONS

Our results showed that a transition to TRA for cerebral aneurysm embolization is feasible and does not increase the level of risk associated with the procedure. We were able to treat 87.3% of our patients via the TRA, with an acceptable overall rate of adverse events and a low rate of complications related to the access.

REFERENCES

1. Mamas MA, Tosh J, Hulme W, et al. **Health economic analysis of access site practice in England during changes in practice: insights from the British Cardiovascular Interventional Society.** *Circ Cardiovasc Qual Outcomes* 2018;11:e004482 CrossRef Medline
2. Jolly SS, Yusuf S, Cairns J, et al. **Radial versus femoral access for coronary angiography and intervention in patients with acute coronary syndromes (RIVAL): a randomised, parallel group, multicentre trial.** *Lancet* 2011;377:1409–20 CrossRef Medline
3. Alnasser SM, Bagai A, Jolly SS, et al. **Transradial approach for coronary angiography and intervention in the elderly: a meta-analysis of 777,841 patients.** *Int J Cardiol* 2017;228:45–51 CrossRef Medline
4. Chase AJ, Fretz EB, Warburton WP, et al. **Association of the arterial access site at angioplasty with transfusion and mortality: the M.O. R.T.A.L study (Mortality benefit Of Reduced Transfusion after percutaneous coronary intervention via the Arm or Leg).** *Heart* 2008;94:1019–25 CrossRef
5. Valgimigli M, Gagnor A, Calabró P, et al; MATRIX Investigators. **Radial versus femoral access in patients with acute coronary syndromes undergoing invasive management: a randomised multicentre trial.** *Lancet* 2015;385:2465–76 CrossRef Medline
6. Brueck M, Bandorski D, Kramer W, et al. **A randomized comparison of transradial versus transfemoral approach for coronary angiography and angioplasty.** *JACC Cardiovasc Interv* 2009;2:1047–54 CrossRef Medline
7. Wang YB, Fu XH, Wang XC, et al. **Randomized comparison of radial versus femoral approach for patients with STEMI undergoing early PCI following intravenous thrombolysis.** *J Invasive Cardiol* 2012;24:412–16 Medline
8. Kok MM, Weernink MG, von Birgelen C, et al. **Patient preference for radial versus femoral vascular access for elective coronary procedures: the PREVAS study.** *Catheter Cardiovasc Interv* 2018;91:17–24 CrossRef Medline
9. Neumann FJ, Sousa-Uva M, Ahlsson A, et al. **2018 ESC/EACTS guidelines on myocardial revascularization.** *Eur Heart J* 2019;40:87–165 CrossRef Medline
10. Ball WT, Sharieff W, Jolly SS, et al. **Characterization of operator learning curve for transradial coronary interventions.** *Circ Cardiovasc Interv* 2011;4:336–41 CrossRef Medline
11. Benamer H, Louvard Y, Sanmartin M, et al. **A multicentre comparison of transradial and transfemoral approaches for coronary angiography and PTCA in obese patients: the TROP registry.** *EuroIntervention* 2007;3:327–32 CrossRef Medline
12. Snelling BM, Sur S, Shah SS, et al. **Transradial cerebral angiography: techniques and outcomes.** *J Neurointerv Surg* 2018;10:874–81 CrossRef Medline
13. Brunet MC, Chen SH, Sur S, et al. **Distal transradial access in the anatomical snuffbox for diagnostic cerebral angiography.** *J Neurointerv Surg* 2019;11:710–13 CrossRef Medline
14. Snelling BM, Sur S, Shah SS, et al. **Transradial approach for complex anterior and posterior circulation interventions: technical nuances and feasibility of using current devices.** *Oper Neurosurg (Hagerstown)* 2019;17:293–302 CrossRef Medline
15. Chen SH, Snelling BM, Shah SS, et al. **Transradial approach for flow diversion treatment of cerebral aneurysms: a multicenter study.** *J Neurointerv Surg* 2019;11:796–800 CrossRef Medline
16. Goland J, Doroszuk GF, Garbugino SL, et al. **Transradial approach to treating endovascular cerebral aneurysms: case series and technical note.** *Surg Neurol Int* 2017;8:73 CrossRef
17. Feldman DN, Swaminathan RV, Kaltenbach LA, et al. **Adoption of radial access and comparison of outcomes to femoral access in percutaneous coronary intervention: an updated report from the national cardiovascular data registry (2007-2012).** *Circulation* 2013;127:2295–306 CrossRef Medline
18. Aykan AÇ, Gökdeniz T, Gül I, et al. **Comparison of low dose versus standard dose heparin for radial approach in elective coronary angiography?** *Int J Cardiol* 2015;187:389–92 CrossRef Medline
19. Pancholy SB. **Comparison of the effect of intra-arterial versus intravenous heparin on radial artery occlusion after transradial catheterization.** *Am J Cardiol* 2009;104:1083–85 CrossRef Medline
20. Pancholy S, Coppola J, Patel T, et al. **Prevention of radial artery occlusion-patent hemostasis evaluation trial (PROPHET study): a randomized comparison of traditional versus patency documented hemostasis after transradial catheterization.** *Catheter Cardiovasc Intervent* 2008;72:335–40 CrossRef Medline

21. Pierot L, Wakhloo AK. **Endovascular treatment of intracranial aneurysms: current status.** *Stroke* 2013;44:2046–54 CrossRef Medline
22. Peruga JP, Peruga JZ, Kasprzak JD, et al. **Ultrasound evaluation of forearm arteries in patients undergoing percutaneous coronary intervention via radial artery access: results of one-year follow-up.** *Kardiol Pol* 2015;73:502–10 CrossRef Medline
23. Velasco A, Ono C, Nugent K, et al. **Ultrasonic evaluation of the radial artery diameter in a local population from Texas.** *J Invasive Cardiol* 2012;24:339–41 Medline
24. Nie B, Zhou YJ, Yang Q, et al. **Safety and feasibility of repeated percutaneous transradial coronary intervention in the same route.** *Chin Med J (Engl)* 2012;125:221–25 Medline
25. Loh YJ, Nakao M, Tan WD, et al. **Factors influencing radial artery size.** *Asian Cardiovasc Thorac Ann* 2007;15:324–26 CrossRef Medline
26. Yan Z, Zhou Y, Zhao Y, et al. **Anatomical study of forearm arteries with ultrasound for percutaneous coronary procedures.** *Circ J* 2010;74:686–92 CrossRef Medline
27. Saito S, Ikei H, Hosokawa G, et al. **Influence of the ratio between radial artery inner diameter and sheath outer diameter on radial artery flow after transradial coronary intervention.** *Catheter Cardiovasc Intervent* 1999;46:173–78 CrossRef Medline
28. Gross BA, Kenmuir CL, Ares WJ, et al. **Pericallosal aneurysm coiling with a "hubbed" 167 cm 0.013" Headway duo via a transradial approach.** *J Clin Neurosci* 2018;53:273–75 CrossRef Medline
29. Plourde G, Pancholy SB, Nolan J, et al. **Radiation exposure in relation to the arterial access site used for diagnostic coronary angiography and percutaneous coronary intervention: a systematic review and meta-analysis.** *Lancet* 2015;386:2192–203 CrossRef Medline
30. Sciahbasi A, Frigoli E, Sarandrea A, et al. **Radiation exposure and vascular access in acute coronary syndromes: the RAD-Matrix trial.** *J Am Coll Cardiol* 2017;69:2530–37 CrossRef Medline
31. Miller DL, Kwon D, Bonavia GH. **Reference levels for patient radiation doses in interventional radiology: proposed initial values for U.S. practice.** *Radiology* 2009;253:753–64 CrossRef Medline
32. Sciahbasi A, Frigoli E, Sarandrea A, et al. **Determinants of radiation dose during right transradial access: Insights from the RAD-MATRIX study.** *Am Heart J* 2018;196:113–18 CrossRef Medline
33. Hess CN, Peterson ED, Neely ML, et al. **The learning curve for transradial percutaneous coronary intervention among operators in the United States: a study from the National Cardiovascular Data Registry.** *Circulation* 2014;129:2277–86 CrossRef Medline

MR Imaging of the Extracranial Facial Nerve with the CISS Sequence

J.P. Guenette, N. Ben-Shlomo, J. Jayender, R.T. Seethamraju, V. Kimbrell, N.-A. Tran, R.Y. Huang, C.J. Kim, J.I. Kass, C.E. Corrales, and T.C. Lee

ABSTRACT

BACKGROUND AND PURPOSE: MR imaging is not routinely used to image the extracranial facial nerve. The purpose of this study was to determine the extent to which this nerve can be visualized with a CISS sequence and to determine the feasibility of using that sequence for locating the nerve relative to tumor.

MATERIALS AND METHODS: Thirty-two facial nerves in 16 healthy subjects and 4 facial nerves in 4 subjects with parotid gland tumors were imaged with an axial CISS sequence protocol that included 0.8-mm isotropic voxels on a 3T MR imaging system with a 64-channel head/neck coil. Four observers independently segmented the 32 healthy subject nerves. Segmentations were compared by calculating average Hausdorff distance values and Dice similarity coefficients.

RESULTS: The primary bifurcation of the extracranial facial nerve into the superior temporofacial and inferior cervicofacial trunks was visible on all 128 segmentations. The mean of the average Hausdorff distances was 1.2 mm (range, 0.3–4.6 mm). Dice coefficients ranged from 0.40 to 0.82. The relative position of the facial nerve to the tumor could be inferred in all 4 tumor cases.

CONCLUSIONS: The facial nerve can be seen on CISS images from the stylomastoid foramen to the temporofacial and cervicofacial trunks, proximal to the parotid plexus. Use of a CISS protocol is feasible in the clinical setting to determine the location of the facial nerve relative to tumor.

The facial nerve, which exits the skull base at the stylomastoid foramen and then branches within the parotid gland, is the primary motor nerve for facial expression. According to a recent systematic review, >20% of patients undergoing primary parotidectomy experience immediate postoperative facial weakness, while almost 4% experience permanent facial weakness, even with the use of intraoperative facial nerve monitoring.[1] With an incidence of parotid gland tumors of 4.8 per 100,000 individuals per year[2] or an incidence of approximately 15,500 per year in the United States, it can be inferred that thousands of patients may experience facial nerve injury during parotid operations each year in the United States alone. Iatrogenic facial nerve injury also regularly occurs during oral, maxillofacial, and cosmetic surgery.[3] Moreover, due to concern for facial nerve injury, it is generally considered unsafe to perform image-guided core biopsy of deep head and neck lesions if traversal of the retromandibular/parotid space is required.[4] Image-guided cryoablation of head and neck tumors, a relatively new treatment approach,[5] is similarly limited. On the opposite end of the treatment spectrum, face transplant requires facial nerve anastomosis[6] or facial nerve transfer[7] to enable motor function of the transplanted structures.

MR imaging can be used to visualize the intracranial cisternal and canalicular portions of the facial nerve[8] as well as the segments of the facial nerve in the temporal bone.[9] However, the intraparotid facial nerve distal trunk and branches are not consistently visible on conventional MR or CT images,[10-12] even when the MR imaging signal and resolution are maximized using a localized surface coil.[13] Currently, no MR imaging method is routinely used to image the facial nerve. However, the CISS sequence has previously been demonstrated to enable visualization of the

Received March 25, 2019; accepted after revision August 27.

From the Divisions of Neuroradiology (J.P.G., J.J., V.K., N.-A.T., R.Y.H., C.J.K., T.C.L.) and Otolaryngology—Head and Neck Surgery (N.B.-S., J.I.K., C.E.C), Brigham & Women's Hospital, Harvard Medical School, Boston, Massachusetts; and Siemens Medical Solutions USA (R.T.S.), Boston, Massachusetts.

This work was supported by the American Society of Head and Neck Radiology through the 2017 William N. Hanafee Research Grant. Jagadeesan Jayender, PhD, was supported by the National Institute of Biomedical Imaging and Bioengineering, National Institutes of Health, through grant No. P41EB015898.

Paper previously presented, in part, at: Annual Meeting of the American Society of Head and Neck Radiology, September 26–30, 2018; Savannah, Georgia.

Please address correspondence to Jeffrey P. Guenette, MD, Division of Neuroradiology, Brigham & Women's Hospital, 75 Francis St, Boston, MA 02115; e-mail: jpguenette@bwh.harvard.edu; @gunetty

Indicates open access to non-subscribers at www.ajnr.org
Indicates article with supplemental on-line table.
Indicates article with supplemental on-line photos.

http://dx.doi.org/10.3174/ajnr.A6261

intracranial portions of the facial nerve[14] as well as the recurrent laryngeal and vagus nerves in the neck.[15] Anecdotal evidence has also shown that the extraforaminal segments of the cranial nerves can be visualized with the CISS sequence.[16] We therefore hypothesized that the CISS sequence may have a role in routine preoperative evaluation of the extracranial facial nerve.

The aims of this study were 2-fold: 1) to determine the extent of the extracranial facial nerve that can be confidently and routinely visualized with a CISS sequence protocol; and 2) to identify the potential clinical utility of incorporating the CISS protocol in routine parotid tumor imaging for preoperative evaluation of nerve location.

MATERIALS AND METHODS

Twenty healthy subjects were enrolled in this prospective study, which was designed to determine the extent of the extracranial facial nerve that can be confidently and routinely visualized with a CISS sequence protocol. All healthy individuals were eligible for participation with the following exclusion criteria: younger than 18 years of age, pregnant, history of head and neck cancer, history of parotid gland pathology including parotitis, and inability to have an MR imaging examination. All healthy subjects underwent a 1-hour 3T MR imaging examination of the face between December 2017 and June 2018. All subjects provided informed consent. This prospective study was approved by our institutional review board and was performed in compliance with Health Insurance Portability and Accountability Act.

In addition, to identify the potential clinical utility of incorporating the CISS protocol in routine parotid tumor imaging, a retrospective review was performed of images obtained on consecutive patients with parotid tumors in the clinical setting between August 2018 and October 2018, when the CISS sequence was included as part of a proposed new parotid tumor MR imaging protocol. This retrospective study was separately approved by our institutional review board and was also performed in compliance with the Health Insurance Portability and Accountability Act with waiver of informed consent.

Imaging Protocol

All MR imaging examinations were performed on a Magnetom Prisma 3T MR imaging system with a 64-channel head/neck coil (Siemens, Erlangen, Germany). An axial CISS sequence was performed without intravenous contrast from the stylomastoid foramen to the lower aspect of the parotid gland, which, for practicality and repeatability, can be approximated from the mid-basiocciput to the cranial aspect of the extrinsic tongue muscles (Fig 1). Multiple slightly variant CISS protocols were performed on the first 10 healthy subjects. A single protocol was subjectively identified as the most promising; therefore, that protocol was included in all subsequent subject examinations. The protocol parameters are included in the Table. Of note, when the CISS protocol was added to the clinical parotid MR imaging protocol, the FOV was inadvertently decreased to 180 mm, resulting in higher spatial resolution but a lower signal-to-noise ratio compared with the images acquired with a 240-mm FOV in the healthy subjects.

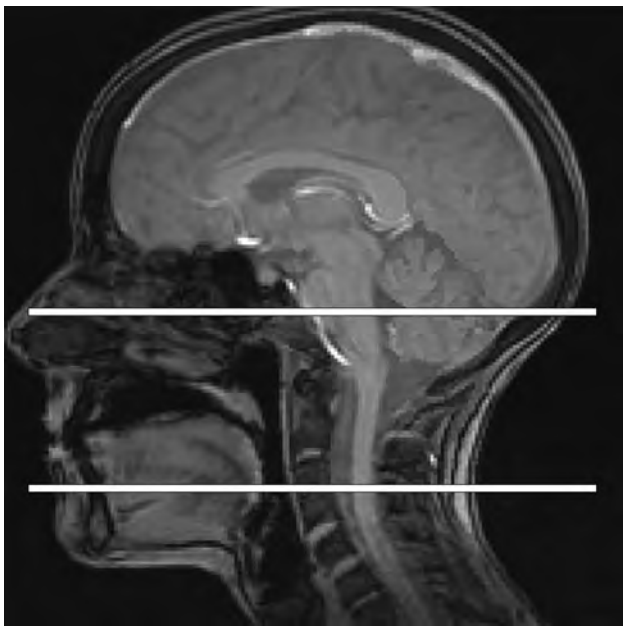

FIG 1. Sagittal midline localizer MR image. *Horizontal white lines* through the basisphenoid and cranial aspect of the extrinsic tongue muscles serve as an accurate approximation for the CISS craniocaudal slab selection when imaging the facial nerve.

Parameters for CISS sequence

Parameter	
TR	4.97 ms
TE	2.19 ms
Averages	1
Section thickness	0.8 mm
FOV	240 × 240
Matrix	320 × 320
Voxel size	0.8 × 0.8 × 0.8 mm
Bandwidth	521 Hz/pixel
Flip angle	33°
Elliptic scanning	On
Acquisition time	4:44 minutes

Facial Nerve Segmentation

Four observers independently segmented the facial nerve from the stylomastoid foramen (Fig 2) to the most distal aspect of the intraparotid branches that they could confidently identify. The observers were a neuroradiologist with 7 years of postfellowship dedicated clinical neuroradiology experience (observer 1), a neuroradiologist with 3 years of postfellowship dedicated clinical neuroradiology experience (observer 2), a first-year radiology resident (observer 3), and a fourth-year medical student (observer 4). All nerve segmentations were performed in the open-source image-processing software 3D Slicer (Version 4.8.1; www.slicer.org). The segmentations were performed in the 3D Slicer editor module. This module allows simultaneous visualization of the axial 0.8-mm images, coronal 0.8-mm reformatted images, and sagittal 0.8-mm reformatted images. The observers were allowed to build the segmentation using all 3 planes. Image manipulation or postprocessing, such as the creation of minimum intensity projection images, was

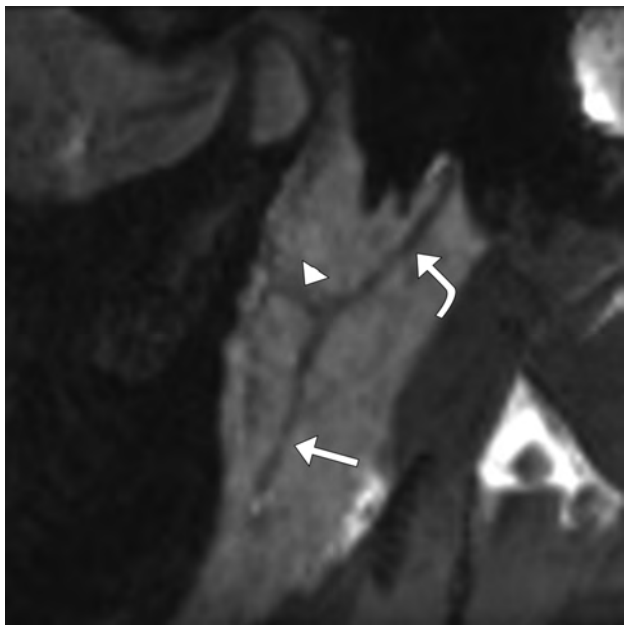

FIG 2. Representative sagittal-oblique CISS minimum intensity projection MR image shows the visible course of the facial nerve trunk (*curved arrow*) from the stylomastoid foramen to the distal aspects of the temporofacial (*arrowhead*) and cervicofacial (*arrow*) trunks.

not allowed, to best simulate the practical clinical environment in which such tools may not be available.

Facial Nerve Segmentation Comparisons

All segmentations were reviewed to determine the number of branches identified. To determine similarity of the tracings, we compared segmentations by calculating average Hausdorff distance values[17] and Dice coefficients.[18] Average Hausdorff distance values provide a measurement of the average distance of the points in one segmentation to the corresponding closest points in another segmentation. Dice coefficients provide a measurement of the degree of overlap of the segmentation volumes. In addition, the length of each segmentation from the stylomastoid foramen to the most distal aspect of the cervicofacial trunk was measured and compared. The segmentations of the more senior neuroradiologist (observer 1) were used as the reference for all comparisons.

Retrospective Review of Clinical Examinations

The CISS images were reviewed and facial nerves were followed by a single observer to evaluate whether the position of the facial nerve could be identified relative to the known tumor. The observed purported relative location of the nerve was communicated to the surgeon before the operation. Following the operation, the surgeon confirmed the actual location of the nerve relative to the tumor.

RESULTS

Twenty healthy subjects (15 men, 5 women; 30.4 ± 7.7 years of age; age range, 20–50 years) were enrolled. The optimized CISS protocol, as described in the Materials and Methods section, was performed on 16 of the healthy subjects (12 men, 4 women; 31.4 ± 8.5 years of age; age range, 20–50 years). Due to imaging time constraints, protocol optimization, and the testing of several other sequences, this sequence was not performed in 4 subjects. A total of 32 facial nerves, 2 per healthy subject, were thus imaged.

The CISS images were retrospectively reviewed for 4 consecutive patients who underwent clinical MR imaging examinations with a parotid protocol for a known parotid mass. These patients were the following: a 55-year-old man with a recurrent right parotid Warthin tumor, an 83-year-old woman with a left parotid poorly differentiated carcinoma with sarcomatoid features, a 32-year-old woman with a left parotid pleomorphic adenoma, and a 75-year-old woman with a right parotid Warthin tumor.

All images are available for review and further analysis through the Harvard Dataverse.[19]

Facial Nerve Segmentation Comparisons

The primary bifurcation of the facial nerve into the superior temporofacial and inferior cervicofacial trunks was visible on all 128 segmentations (32 nerves each segmented by 4 observers) along with at least the proximal aspect of these 2 trunks (Fig 3). The classically taught more distal 5 branches were not visualized on the segmentations.

The mean of the average Hausdorff distances was 1.2 mm (range, 0.3–4.6 mm) overall, 0.9 mm (range, 0.3–3.3 mm) when comparing observers 1 and 2, 1.7 mm (range, 0.3–4.6 mm) when comparing observers 1 and 3, and 1.0 mm (range, 0.3–2.1 mm) when comparing observers 1 and 4. Dice coefficients ranged from 0.40 to 0.82 with means of 0.64, 0.57, and 0.59 when comparing observer 1 with observers 2, 3, and 4, respectively. Segmentation lengths varied on average by 5.8 ± 4.8 mm overall, 5.7 ± 4.9 mm (18% ± 17%) when comparing observers 1 and 2, 5.1 ± 4.6 mm (16% ± 14%) when comparing observers 1 and 3, and 6.6 ± 4.9 mm (21% ± 15%) when comparing observers 1 and 4. All Hausdorff distances, dice coefficients, length difference percentages, and segmentation volume difference percentages are reported in the On-line Table. Graphic demonstration of the interobserver data distributions is presented in On-line Figs 1–4.

All measurement data are available for review and further analysis through the Harvard Dataverse.[19]

Retrospective Review of Clinical Examinations

The main facial nerve trunk and/or the temporofacial or cervicofacial trunk could be followed from the stylomastoid foramen to the level of the tumor in all cases, and the relative position of the facial nerve to the tumor could be inferred in all cases (Fig 4). The facial nerve location relative to the tumor was confirmed by the operating surgeon for the 3 patients who underwent tumor resection. One patient has elected observation of a Warthin tumor; therefore, surgical confirmation of nerve location has not been obtained.

DISCUSSION

In this study, 4 observers of variable expertise were each able to trace the facial nerve on the CISS images from the stylomastoid foramen through the primary bifurcation and along at least the

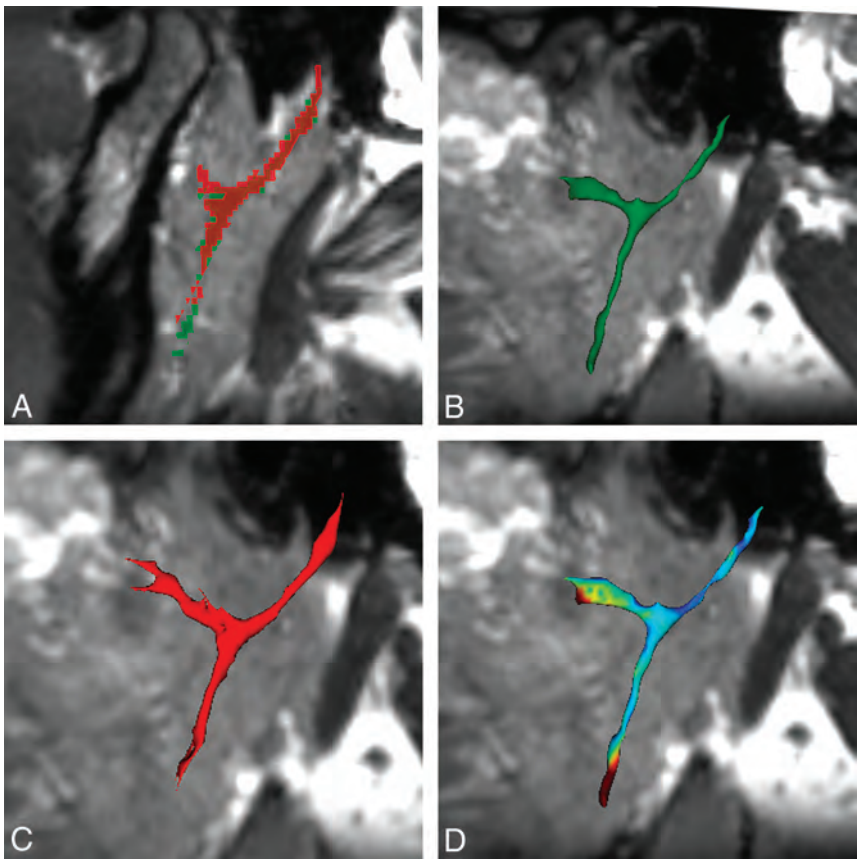

FIG 3. Representative segmentations of the left facial nerve of subject 20 with an average Hausdorff distance of 0.64, Dice coefficient of 0.60, length difference of <1%, and segmentation volume difference of 8%. *A*, Segmentations of observer 1 (*green outline*) and observer 4 (*red outline*) superimposed on the CISS image show similar agreement along the main nerve root, bifurcation, and proximal aspects of the temporofacial and cervicofacial roots, with more distal variability along the cervicofacial root, even despite the similar length segmented. *B*, 3D rendering of the observer 1 segmentation. *C*, 3D rendering of the observer 4 segmentation. *D*, Dice overlap map shows the spectrum of agreement, with blue being good agreement and red being poor agreement.

proximal temporofacial and cervicofacial trunks in all 32 facial nerves of the healthy subjects. The average Hausdorff distance of 1.2 mm is very close to the 0.8-mm isotropic voxel dimensions of the CISS images, indicating that the observers' nerve tracings varied, on average, by only 1.5 voxels. The Dice coefficients, which are a measure of segmentation overlap, are reasonable, given that segmentations in 3D Slicer are voxel-based and the facial nerve frequently crosses through portions of several voxels on a single section leading to inherent section-by-section segmentation variability. In addition, the location of the facial nerve primary or secondary trunks could be inferred relative to the tumor in the 4 patients scanned with the CISS protocol, and this location was confirmed in the 3 patients who underwent an operation. Although the more distal facial nerve branches were not visualized, surgeons typically identify the facial nerve proximal to the tumor, create a dissection plane along the nerve trunks, and may never identify the smaller parotid plexus rootlets or distal branches, so the portions of nerve visualized in this study should be adequate for surgical planning in most cases.

Comparison with Current Literature on Facial Nerve Imaging

This study advances prior published work that has also aimed to identify and evaluate the extracranial facial nerve. It has been known since the early and mid-1990s that the proximal extracranial facial nerve trunk can be routinely visualized and that gadolinium-based contrast is not helpful.[10,11] Steady-state imaging with the gradient-recalled acquisition in steady state sequence[12] and double-echo steady-state with water excitation sequence[20] have previously been reported for facial nerve imaging with more inconsistent identification of the cervicofacial and particularly temporofacial trunks, though the double-echo steady-state with water excitation sequence has recently been shown to allow accurate categorization of tumor location to the superficial or deep parotid lobes.[21] Our success in this study may be attributable to the use of more technologically advanced hardware. Use of a PSIF-DWI sequence to visualize at least a portion of the cervicofacial and temporofacial branches has more recently been described,[13] and the images obtained with the CISS protocol (eg, Fig 2) seem comparable with the published PSIF-DWI, which was obtained with a small surface coil and postprocessed into MPR and MIP images. As part of this study, we attempted PSIF-DWI but could not replicate the prior results. Moreover, our goal was to enable facial nerve imaging as part of a routine MR imaging examination, and we considered the use of a localized surface coil or manual postprocessing to be insufficient.

Anecdotally, we were able to visualize the facial nerve with 3D T1 sampling perfection with applications-optimized contrasts by using different flip angle evolutions (SPACE sequence; Siemens) images, but further protocol optimization and more rigorous testing would be needed for comparison with the CISS protocol. We could not discern any contrast between the facial nerve and surrounding parotid gland tissue with the pointwise encoding time reduction with radial acquisition (PETRA) sequence, which has been used to visualize the nerve through the temporal bone.[9]

Inherent Facial Nerve Anatomy Imaging Limitations

Confident identification of the more distal branches of the facial nerve seems to be hindered primarily by 3 factors: 1) the small size of the nerve fibers in the intervening parotid plexus that are below the resolution of current practical clinical imaging; 2)

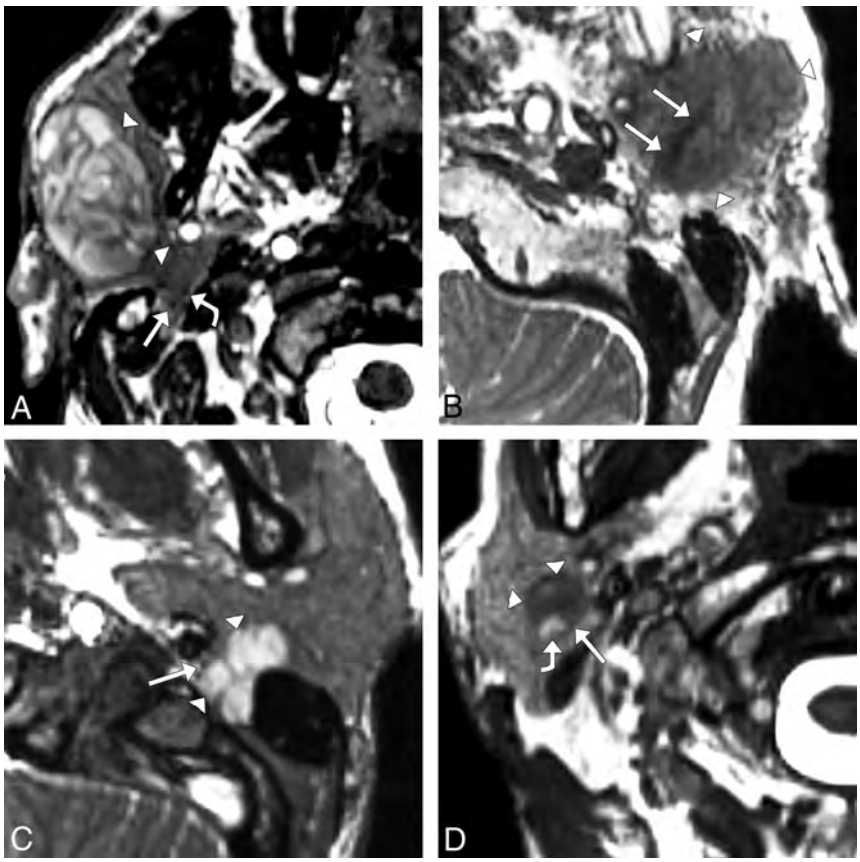

FIG 4. Axial CISS images in patients with parotid gland tumors. *A*, A 55-year-old man with a right parotid gland, 35 × 22 × 44 mm (anteroposterior × transverse × craniocaudal) Warthin tumor (*arrowheads*) and temporofacial (*straight arrow*) and superiorly displaced cervicofacial (*curved arrow*) trunks of the facial nerve (*straight arrow*), apparently deep to the tumor and just posterior to the retromandibular vein. In the operating room, the distal branches of the facial nerve were confirmed to be in the plane of the tumor with distal divisions displaced above and below the tumor and with superior displacement of the parotid plexus. *B*, An 83-year-old woman with left parotid gland, 23 × 21 × 29 mm poorly differentiated carcinoma with sarcomatoid features (*arrowheads*) and an apparently expanded facial nerve with irregular margins (*arrows*) coursing through the tumor, suggestive of perineural tumor invasion. A radical parotidectomy was performed, and pathology analysis confirmed extensive perineural invasion. *C*, A 32-year-old woman with a left parotid gland 18 × 19 × 24 mm pleomorphic adenoma (*arrowheads*) extending into the stylomastoid foramen and anteromedially displacing the facial nerve (*arrow*). Due to these imaging findings, a postauricular infratemporal fossa surgical approach was used, confirming the location of the nerve and confirming impingement of the nerve as it entered the stylomastoid foramen. *D*, A 75-year-old man with a right parotid gland, 12 × 11 × 19 mm Warthin tumor (*arrowheads*) just superficial to and between the distal, small-caliber, low-signal cervicofacial trunk of the facial nerve (*straight arrow*) and high-signal retromandibular vein (*curved arrow*). This patient has elected observation, and there is thus no surgical confirmation of facial nerve location.

variant terminal branch anatomy, including variation in the number and location of the branches, which precludes identification based on location; and 3) difficulty discriminating small nerve fibers, small ducts, and small vessels. A comprehensive overview of the parotid plexus, also known as the pes anserinus, and variant facial nerve anatomy has been recently published on the basis of a study of 158 human cadaver dissections.[22] On the basis of this work and prior work, it is known that the facial nerve exits the skull base at the stylomastoid foramen and then divides into a superior temporofacial trunk and an inferior cervicofacial trunk, usually within the parotid gland. These trunks then divide into many small rootlets, which form a parotid plexus.[22] These parotid plexus rootlets ultimately join into the 5 classically taught branches: temporal, zygomatic, buccal, marginal mandibular, and cervical. However, these branches are variable and are often present in duplicate or triplicate.[22]

Study Limitations

The major primary limitation of this study is the absence of a criterion standard comparison. The scientifically ideal study would corroborate intraoperative nerve mapping with preoperative and intraoperative MR imaging nerve delineation, but the ethical approval of such a study would depend on the involved added surgical/anesthesia time and risk. As with other similar studies, we contend that this study is an adequate surrogate, given the known course of the facial nerve and the easily identifiable expected location of the proximal extracranial nerve at the stylomastoid foramen. Another limitation of the technical portion of this study is that all imaging examinations were performed on a single MR imaging system that is currently one of the highest caliber systems on the market with high gradients; therefore, the results may not be replicable on older systems or systems from other vendors with similar, but not identical, sequences. In addition, the CISS protocol used in our clinical examination was inadvertently performed with a 180-mm FOV, instead of the 240-mm FOV used in the healthy subjects. Returning to the higher signal-to-noise 240-mm FOV may or may not improve visualization of the facial nerve in patients.

In this study, only 4 patients with parotid tumors were imaged with the CISS facial nerve sequence, and only 3 of these patients underwent an operation with subsequent surgical confirmation of facial nerve location. Consequently, although delineation of the facial nerve was possible in each of these patients, the generalizability in a routine patient population remains unknown. There may also be inherent limitations with the CISS sequence. Although discrimination of the low-signal facial nerve from large, generally high-signal blood vessels is relatively straightforward, some larger veins and many smaller blood vessels also have low signal. The signal of the parotid duct system is also variable, with high

signal in some subjects and low signal in others. High signal in the ducts could perhaps be obtained routinely by preparing a subject with a lemon mouth swab, as previously reported for MR sialography.[23] The small fibrous septations between gland lobules are at the limits of resolution of the CISS images as performed and, therefore, are also difficult to distinguish from nerve as the nerve roots decrease in size and branch into the plexus.

CONCLUSIONS

The results of this study suggest that the facial nerve can be routinely followed from the stylomastoid foramen to the temporofacial and cervicofacial trunks, proximal to the parotid plexus, with a CISS imaging protocol. Moreover, use of a CISS protocol is feasible in the clinical setting to determine the location of the primary and secondary trunks of the facial nerve relative to a tumor.

Disclosures: Jeffrey P. Guenette—*RELATED*: *Grant:* American Society of Head and Neck Radiology, *Comments*: 2017 William N, Hanafee Research Grant.* Ravi Teja Seethamraju—*UNRELATED*: *Employment*: Siemens Medical Solutions USA; *Patents (Planned, Pending or Issued)*: Siemens Healthineers; *Stock/Stock Options*: Siemens Healthineers. Jagadeesan Jayender—*RELATED*: *Grant*: National Institutes of Health, *Comments*: P41EB015898*; *UNRELATED*: *Board Membership*: Navigation Sciences; *Consultancy*: Navigation Sciences, HMDmd; *Grants/Grants Pending*: National Institutes of Health, Siemens, *Comments*: R01DK119269 and R01EB025964, research grant from Siemens Medical USA*; *Patents (Planned, Pending or Issued)*: system and method for a tissue resection margin measurement device*; *Royalties*: Navigation Sciences*; *Stock/Stock Options*: Navigation Sciences, HMDmd. *Money paid to the institution.

REFERENCES

1. Sood AJ, Houlton JJ, Nguyen SA, et al. **Facial nerve monitoring during parotidectomy: a systematic review and meta-analysis.** *Otolaryngol Head Neck Surg* 2015;152:631–67 CrossRef Medline
2. Pinkston JA, Cole P. **Incidence rates of salivary gland tumors: results from a population-based study.** *Otolaryngol Head Neck Surg* 1999;120:834–40 CrossRef Medline
3. Hohman MH, Bhama PK, Hadlock TA. **Epidemiology of iatrogenic facial nerve injury: A decade of experience.** *Laryngoscope* 2014; 124:260–65 CrossRef Medline
4. Gupta S, Henningsen JA, Wallace MJ, et al. **Percutaneous biopsy of head and neck lesions with CT guidance: various approaches and relevant anatomic and technical considerations.** *Radiographics* 2007;27:371–90 CrossRef Medline
5. Guenette JP, Tuncali K, Himes N, et al. **Percutaneous image-guided cryoablation of head and neck tumors for local control, preservation of functional status, and pain relief.** *AJR Am J Roentgenol* 2017;208:453–58 CrossRef Medline
6. Frautschi R, Rampazzo A, Bernard S, et al. **Management of the salivary glands and facial nerve in face transplantation.** *Plast Reconstr Surg* 2016;137:1887–97 CrossRef Medline
7. Audolfsson T, Rodríguez-Lorenzo A, Wong C, et al. **Nerve transfers for facial transplantation: a cadaveric study for motor and sensory restoration.** *Plast Reconstr Surg* 2013;131:1231–40 CrossRef Medline
8. Rabinov JD, Barker FG, McKenna MJ, et al. **Virtual cisternoscopy: 3D MRI models of the cerebellopontine angle for lesions related to the cranial nerves.** *Skull Base* 2004;14:93–99; discussion 99 CrossRef Medline
9. Guenette JP, Seethamraju RT, Jayender J, et al. **MR imaging of the facial nerve through the temporal bone at 3T with a noncontrast ultrashort echo time sequence.** *AJNR Am J Neuroradiol* 2018; 39:1903–06 CrossRef Medline
10. McGhee RB, Chakeres DW, Schmalbrock P, et al. **The extracranial facial nerve: high resolution three-dimensional Fourier transform MR imaging.** *AJNR Am J Neuroradiol* 1993;14:465–72 Medline
11. Dailiana T, Chakeres D, Schmalbrock P, et al. **High-resolution MR of the intraparotid facial nerve and parotid duct.** *AJNR Am J Neuroradiol* 1997;18:165–72 Medline
12. Takahashi N, Okamoto K, Ohkubo M, et al. **High-resolution magnetic resonance of the extracranial facial nerve and parotid duct: demonstration of the branches of the intraparotid facial nerve and its relation to parotid tumours by MRI with a surface coil.** *Clin Radiol* 2005;60:349–54 CrossRef Medline
13. Chu J, Zhou Z, Hong G, et al. **High-resolution MRI of the intraparotid facial nerve based on a microsurface coil and a 3D reversed fast imaging with steady-state precession DWI sequence at 3T.** *AJNR Am J Neuroradiol* 2013;34:1643–48 CrossRef Medline
14. Blitz AM, Choudhri AF, Chonka ZD, et al. **Anatomic considerations, nomenclature, and advanced cross-sectional imaging techniques for visualization of the cranial nerve segments by MR imaging.** *Neuroimaging Clin N Am* 2014;24:1–15 CrossRef Medline
15. Seethamraju RT, Jagadeesan J, Kimbrell V, et al. **Motion compensated high resolution MR imaging of vagus and recurrent laryngeal nerves with novel phase-based navigation sequences.** In: *Proceedings of the Annual Meeting & Exhibition of the International Society for Magnetic Resonance in Medicine*. Singapore; May 7–13, 2016
16. Wen J, Desai NS, Jeffery D, et al. **High-resolution isotropic three-dimensional MR imaging of the extraforaminal segments of the cranial nerves.** *Magn Reson Imaging Clin N Am* 2018;26:101–19 CrossRef Medline
17. Klein A, Andersson J, Ardekani BA, et al. **Evaluation of 14 nonlinear deformation algorithms applied to human brain MRI registration.** *Neuroimage* 2009;46:786–802 CrossRef Medline
18. Besse PC, Guillouet B, Loubes J-M, et al. **Review and perspective for distance-based clustering of vehicle trajectories.** *IEEE Trans Intell Transport Syst* 2016;17:3306–17 CrossRef
19. Guenette JP. **Facial Nerve Imaging Pilot Study Data.** *Harv Dataverse* CrossRef Accessed September 29, 2019
20. Qin Y, Zhang J, Li P, et al. **3D double-echo steady-state with water excitation MR imaging of the intraparotid facial nerve at 1.5T: a pilot study.** *AJNR Am J Neuroradiol* 2011;32:1167–72 CrossRef Medline
21. Fujii H, Fujita A, Kanazawa H, et al. **Localization of parotid gland tumors in relation to the intraparotid facial nerve on 3D double-echo steady-state with water excitation sequence.** *AJNR Am J Neuroradiol* 2019;40:1037–42 CrossRef Medline
22. Bendella H, Spacca B, Rink S, et al. **Anastomotic patterns of the facial parotid plexus (PP): a human cadaver study.** *Ann Anat* 2017; 213:52–61 CrossRef Medline
23. Kalinowski M, Heverhagen JT, Rehberg E, et al. **Comparative study of MR sialography and digital subtraction sialography for benign salivary gland disorders.** *AJNR Am J Neuroradiol* 2002;23:1485–92 Medline

Diagnostic Accuracy and Scope of Intraoperative Transoral Ultrasound and Transoral Ultrasound–Guided Fine-Needle Aspiration of Retropharyngeal Masses

T.H. Vu, M. Kwon, S. Ahmed, M. Gule-Monroe, M.M. Chen, J. Sun, B.D. Fornage, J.M. Debnam, and B. Edeiken-Monroe

ABSTRACT

SUMMARY: The use of transoral sonography–guided fine-needle aspiration for intraoperative localization of retropharyngeal masses has been described by Fornage et al. The purpose of this study was to assess the accuracy of this technique. We reviewed the images and medical records of 26 patients with a retropharyngeal lesion suspicious for a metastatic lymph node of Rouviere identified on CT and/or PET/CT. There were 14 patients with a history of thyroid cancer, 7 with mucosal squamous cell carcinoma, 1 with renal cell carcinoma, 1 with parotid acinic cell cancer, 1 with metastatic colon adenocarcinoma, and 2 with no history of cancer. Intraoperative transoral sonography was performed using a commercially available endovaginal transducer. A transoral sonography–guided fine-needle aspiration was performed with a 25-cm-long 20-ga Chiba needle through a needle guide attached to the transducer shaft. Cytopathologic results were categorized as malignant, benign, or nondiagnostic. Transoral sonography and transoral sonography–guided fine-needle aspiration were performed in all patients. A diagnostic specimen was obtained in 25 of 26 (96%) patients with a 100% overall accuracy. Twelve patients underwent subsequent transoral resection of the retropharyngeal mass. In each patient, surgical pathology confirmed the fine-needle aspiration biopsy result. In 4 patients, transoral sonography–guided injection of methylene blue was used to facilitate intraoperative localization of the metastatic retropharyngeal mass. Transoral sonography and transoral sonography–guided fine-needle aspiration of suspicious masses in the retropharyngeal space are highly accurate procedures for identification and cytologic evaluation of benign and metastatic lymph nodes of Rouviere and for presurgical localization.

ABBREVIATIONS: PTC = papillary thyroid carcinoma; RCC = renal cell carcinoma; SCC = squamous cell carcinoma; TOUS = transoral ultrasound; FNA = fine-needle aspiration

The lymph nodes of Rouviere are an uncommon-but-well-known location for regional spread of head and neck cancers. CT and, to a lesser extent, MR imaging have been the preferred techniques for identification of retropharyngeal adenopathy and for image-guided biopsy.[1] A preliminary report by Fornage et al[2] of direct transoral sonography (TOUS) imaging and TOUS-guided fine-needle aspiration (FNA) on a small series of patients suggested the validity of the role of ultrasound in the localization, evaluation, and biopsy of retropharyngeal lesions and to facilitate transoral presurgical localization. The purpose of this report was to evaluate the accuracy of diagnostic and presurgical localization of TOUS imaging and TOUS-FNA on suspected retropharyngeal adenopathy.

MATERIALS AND METHODS

This retrospective study, conducted between February 1, 2007 and June 30, 2016, included the images and medical records of 26 patients (10 females and 16 males) with suspicious retropharyngeal lesions detected on CT and/or on PET/CT and subsequently sampled by TOUS-FNA. The study was approved by our institutional review board and was compliant with Health Insurance Portability and Accountability Act regulations.

Summary statistics of patients and tumor characteristics were based on the frequency, mean, SD, median, and range.

TOUS Examination

The TOUS examinations were performed in the operating room in the presence of the surgeon. The patients received general anesthesia and were intubated. The oral cavity and oropharynx were opened and stabilized with a standard McIvor-type oral retractor in preparation for placement of an endocavitary transducer.

Received April 1, 2019; accepted after revision August 12.

From the Section of Neuroradiology (T.H.V., M.K., S.A., M.G.-M., M.M.C., J.M.D., B.E.-M.) and Section of Breast Imaging (B.D.F.), Department of Diagnostic Radiology, and Department of Biostatistics (J.S.), University of Texas MD Anderson Cancer Center, Houston, Texas.

Please address correspondence to Thinh Vu, MD, Department of Diagnostic Imaging, University of Texas MD Anderson Cancer Center, 1400 Pressler St, Unit 1482, Houston, TX 77230-1402; e-mail: thinh.vu@mdanderson.org

Indicates article with supplemental on-line table.

http://dx.doi.org/10.3174/ajnr.A6236

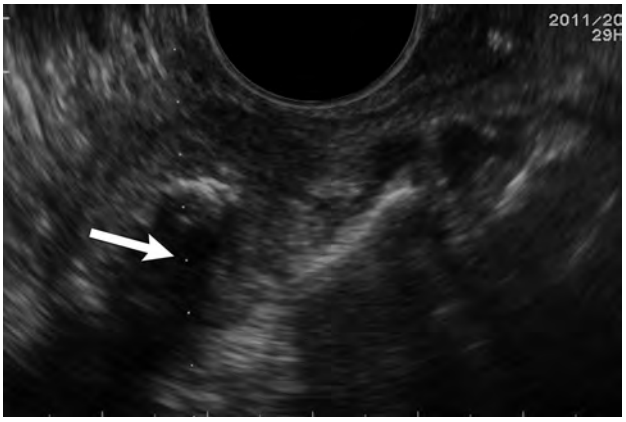

FIG 1. Biopsy line. Transverse sonography before biopsy of a partially calcified right retropharyngeal mass demonstrates a biopsy line and expected path of the biopsy needle through the lesion (*white arrow*).

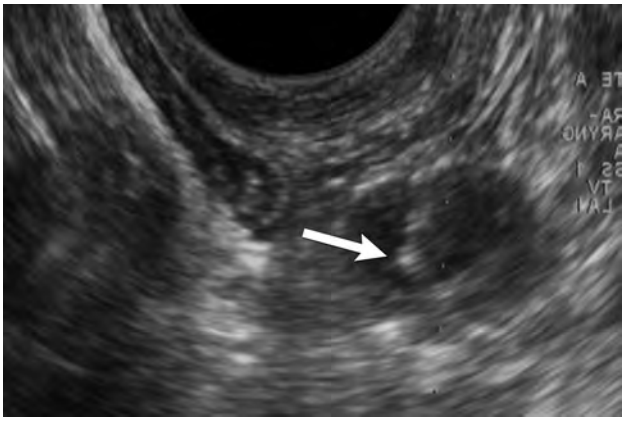

FIG 2. Needle tip visualization. Transverse sonography during biopsy of a left retropharyngeal lesion demonstrates the needle and needle tip (*white arrow*) accurately placed within the lesion.

Intraoperative TOUS imaging was performed with 1 of 2 commercially available endocavitary (endorectal or endovaginal) transducers. These included a sonography scanner (Prosound α 10; Hitachi-Aloka, Twinsburg, Ohio) equipped with a 3.0- to 8.5-MHz endorectal transducer (UST-675P; Hitachi-Aloka) or a 2.5- to 7.5-MHz endovaginal transducer (UST-9118; Hitachi-Aloka). Both transducers had an outer diameter of 2.3 cm at the tip (scan head) and offered an end-firing 180° FOV.

Each endocavity transducer was fitted with a dedicated transducer cover (NeoGuard; CIVCO Medical Solutions, Coralville, Iowa), which was placed after a small amount of sterile coupling gel was deposited on the scan head. No coupling gel was necessary on the outside of the transducer cover because the normal pharyngeal mucosa secretions are sufficient to obtain images of diagnostic quality.

All examinations included gray-scale ultrasound and power Doppler imaging. Each lesion was measured, and when possible, measurements were performed in 2 orthogonal dimensions. Recorded ultrasound characteristics of the retropharyngeal lesions included size, echogenicity, echotexture, the presence of cystic areas, and/or calcifications and vascular flow.

Power Doppler imaging demonstrated the internal vascularity of the retropharyngeal lesions and identified the location of the internal carotid artery and the internal jugular vein.

Sonography-Guided FNA Biopsy of Retropharyngeal Masses

In preparation for a TOUS-FNA, a metallic needle guide was attached securely along the shaft of the endocavitary transducer. The needle guides included an MP-2748 for the UST-9118 endovaginal transducer or an MP-2452 for the UST- 675P endorectal transducer (Hitachi-Aloka). A 25-cm 20-ga Chiba Biopsy Needle (Cook Medical, Bloomington, Indiana) was used to accommodate the length of the needle guide.

A TOUS-FNA was performed in all patients by a neuroradiologist experienced in interventional sonography of the soft tissues of the neck. The transducer, with the needle guide attached, was inserted into the oral cavity and placed in direct contact with the pharyngeal mucosa. A built-in electronic biopsy line was activated to indicate the expected trajectory of the biopsy needle. The position of the transducer was adjusted so that the biopsy line would cross the sonographic image of the suspicious retropharyngeal mass (Fig 1).

The needle was inserted through the guide and was directed transversely through the pharyngeal wall. The needle entered the sector FOV and appeared on the sonography image as a bright echogenic line. Visualization of the needle tip was critical to allow the operator to keep the needle tip at a safe distance from the internal carotid artery and internal jugular vein as the needle was guided along the planned path to the targeted mass (Fig 2). Cellular material was aspirated from the retropharyngeal mass by applying moderate (1–2 mL) continuous negative pressure for approximately 10 seconds with the needle tip kept within the targeted retropharyngeal mass.

During the aspiration, the needle was moved forward and backward to mechanically tear off and aspirate sheaths of cells from the lesion and to increase the volume of the aspirate. The aspiration was completed when the suction was released. The needle-syringe assembly was withdrawn from the needle guide, and the aspirate was placed immediately and carefully on the slides to avoid crushing or drying the aspirated cells.

The slides were stained with a Romanowsky stain (Diff-Quick; Fisher Scientific, Pittsburgh, Pennsylvania) technique. A cytopathologist provided a preliminary diagnosis within approximately 30 minutes. The final diagnosis was based on the cytopathologic diagnosis and/or clinical follow-up. In 1 patient, a transoral core biopsy was performed after the TOUS-guided FNA at the request of the cytologist due to suspicion of lymphoma on the FNA aspirate and the need for a core biopsy to test for lymphoma markers. The core biopsy was performed by transoral guidance with the same apparatus used to guide the FNA.

Methylene blue (<1 mL) was injected with the use of TOUS guidance into the malignant lymph node found in 4 patients to facilitate intraoperative localization. The methylene blue was injected using the same needle guide through which the transoral biopsy was performed. Immediate successful transoral intraoperative resection of the metastatic adenopathy was performed without complications.

Benign retropharyngeal lesions, documented by TOUS-FNA, were subsequently monitored clinically and/or by imaging.

RESULTS

The median age of the patients in this series was 53 years (range, 3–74 years). Twelve lesions (7 benign; 5 malignant) were located in the left retropharyngeal region, and 14 lesions (8 benign; 6 malignant) were in the right retropharyngeal region. The mean size of the retropharyngeal lesions was 1.6 ± 0.8 cm, ranging from 0.6 to 4.0 cm in the longest dimension, with a median size of 1.4 cm. The mean size of the malignant retroperitoneal adenopathy was 1.6 cm. The mean size of the benign retroperitoneal adenopathy was 1.6 cm.

The sonographic echotexture of the lesions was 22 hypoechoic, 2 anechoic, and 2 hyperechoic. Twenty-two lesions did not exhibit normal hilar architecture, and 4 lesions had an echogenic hilum. Twenty-two lesions were solid, and 4 were cystic or had internal cystic change. Twenty-three lesions were noncalcified, and 3 contained internal calcifications. Doppler examination of the lesions showed 18 lesions without disorganized flow and 8 lesions with disorganized flow.

The 26 retropharyngeal lesions were detected by CT (n = 20) and/or PET/CT (n = 6). A TOUS-guided biopsy of the suspicious retropharyngeal lesions was performed in each of the 26 patients with the needle accurately positioned under sonographic guidance within the retropharyngeal lesion. All TOUS-FNAs were well-tolerated. There were no immediate or delayed complications during or after the biopsies.

Twenty-five of 26 TOUS-FNA aspirates were diagnostic. One TOUS-FNA was nondiagnostic, and 1 TOUS-FNA was inadequate to exclude lymphoma. In the patient in whom aspiration was inadequate to exclude lymphoma, a TOUS core biopsy was performed, which revealed reactive hyperplasia of the lymph node but no evidence of lymphoma. In the 1 patient with nondiagnostic TOUS-FNA, direct smears demonstrated a few benign mucosal epithelial cells and rare connective tissue elements. No evidence of lymph node sampling was present. Follow-up MR imaging showed that the node remained stable but prominent in size (1.0 cm). The patient died of recurrent squamous cell carcinoma (SCC) in the maxillary sinus and, therefore, was lost to follow-up.

The final diagnosis of the TOUS-FNA was consistent with the preliminary diagnosis in all 25 patients who underwent diagnostic aspirations. Surgical pathology results were obtained in 10 (38%) of the 26 patients. In the 16 (62%) patients who did not undergo surgical intervention, clinical or imaging follow-up supported the final diagnosis. This included the 1 patient who underwent TOUS-FNA in a lymph node detected on PET/CT that subsequently regressed on follow-up evaluation. One of the 26 patients was lost to follow-up after TOUS-FNA and core biopsy revealed a reactive lymph node on cytology.

Results from the TOUS-FNAs are summarized in the On-line Table.

Patient Population

The primary diseases in the 26 patients included papillary thyroid carcinoma (PTC) (n = 14), mucosal SCC (n = 7), parotid acinic cell carcinoma (n = 1), metastatic colorectal cancer (n = 1), renal cell carcinoma (RCC) (n = 1), and no cancer history in 2 patients.

Benign retropharyngeal lesions were documented in 14 patients. These included patients with PTC (n = 6), mucosal SCC (n = 4), parotid acinic cell carcinoma (n = 1), metastatic colorectal cancer (n = 1), and no history of malignancy (n = 2). In all the cases in which cytology was negative for PTC, thyroglobulin assays were not performed on the aspirates once we had an adequate cellular sample. Among patients with benign TOUS-FNAs, the retropharyngeal lesions of interest included the following:

- One patient with PTC whose initial cytology was of concern for reactive adenopathy versus lymphoma. A TOUS core biopsy confirmed benign reactive hyperplasia with no evidence of lymphoma.
- One patient with no history of malignancy, whose retropharyngeal mass was incidentally visualized on CT performed at another facility for dysphagia. The TOUS-FNA diagnosed a ganglion cyst that was resected transorally.
- A second patient with no previous history of malignancy was a 3-year-old male child with a calcified right retropharyngeal mass found incidentally on a neck CT. A TOUS-FNA revealed dense acellular calcific debris. The lymph node was resected, and the histology was concordant with the initial cytologic finding with no tumor present.
- One patient had a base of tongue SCC; the patient's left retropharyngeal/parapharyngeal space mass was FDG-avid on staging PET/CT. TOUS-FNA revealed a salivary gland neoplasm with cystic degeneration. This was surgically resected, and the final histology was consistent with basal cell adenoma of salivary gland origin.

Metastatic retropharyngeal adenopathy was documented in 11 patients. These included patients with PTC (n = 8), mucosal SCC (n = 2), and metastatic adenopathy from undiagnosed PTC in the patient with RCC (n = 1). Among patients with metastatic TOUS-FNAs, the retropharyngeal masses of interest included the following:

- One patient with RCC in whom TOUS-FNA revealed a malignant lymph node from an undiagnosed PTC.
- One patient with PTC whose metastatic adenopathy included a cystic lymph node. The lymph node metastasis was diagnosed by elevated thyroglobulin assay on the aspirate.

One patient with a history of recurrent facial SCC had a nondiagnostic TOUS-FNA of a prominent 1.0-cm right lateral retropharyngeal node detected on PET/CT. Follow-up MR imaging showed that the lymph node remained stable but prominent in size (1.0 cm). The patient experienced recurrent SCC in the maxillary sinus and died of this disease within 2 years of the documented retropharyngeal metastatic adenopathy (and was thus lost to follow-up).

Illustrative Cases

True-Positive Cytology.

- A right 3.0 × 2.0 × 1.5 cm retropharyngeal lymph node of concern was detected on staging CT in a 65-year-old man

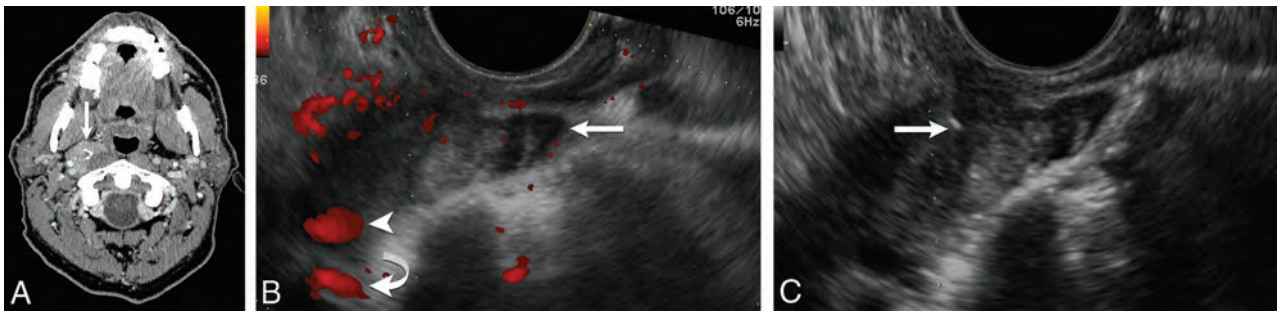

FIG 3. True-positive cytology. A 65-year-old man with a history of papillary thyroid cancer and a right retropharyngeal mass. *A*, Axial contrast-enhanced CT scan shows an enlarged right retropharyngeal node (*arrow*) with internal calcification. *B*, Transverse power Doppler sonography shows the lesion (*arrow*) and its relationship to the internal carotid artery (*arrowhead*) and internal jugular vein (*curved arrow*). *C*, Transverse sonography during biopsy of the mass documents placement of needle tip (*white arrow*) within the lesion before and during aspiration. Cytology revealed metastatic papillary thyroid cancer.

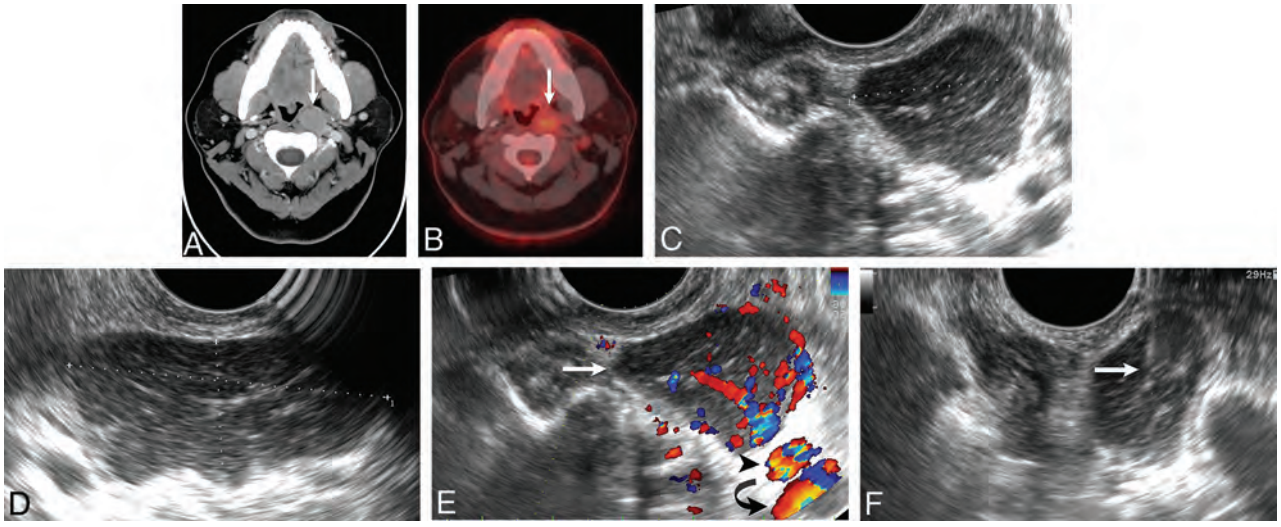

FIG 4. True-negative cytology. A 38-year-old woman with a history of papillary thyroid cancer and left retropharyngeal mass. *A*, Axial contrast-enhanced CT scan shows an enlarged left retropharyngeal node (*arrow*). *B*, Axial PET/CT shows that the enlarged left retropharyngeal node has mild FDG avidity (*arrow*). Transverse (*C*) and sagittal oblique (*D*) sonography reveals an enlarged hypoechoic left lateral retropharyngeal node measuring 2.5 × 4.3 × 1.9 cm. *E*, Transverse color Doppler sonography shows the vascular flow of the lesion (*white arrow*) and its relationship to the internal carotid artery (*black arrowhead*) and internal jugular vein (*black curved arrow*). *F*, Transverse sonography during biopsy of the mass documents placement of needle tip (*arrow*) within the lesion before and during aspiration. Cytology revealed benign reactive hyperplasia.

with a history of PTC. A TOUS-FNA was performed, and cytology showed metastatic PTC. The patient subsequently underwent transoral robotic resection of the lesion aided by localization with methylene blue inserted by TOUS guidance. Histology confirmed the cytologic diagnosis of metastatic PTC (Fig 3).

True-Negative Cytology.

- A large 4.3 × 2.5 × 1.9 cm left lateral retropharyngeal mass was found on restaging CT and PET/CT in a 38-year-old woman with a history of PTC. TOUS-FNA was performed, and cytology revealed benign reactive hyperplasia. There was clinical concern for lymphoma; therefore, a core biopsy was performed. The diagnosis of lymphoma was excluded, and the diagnosis was confirmed as a benign reactive lymph node (Fig 4).

DISCUSSION

The retropharyngeal space is a known area of local regional metastasis of head and neck cancers. It is defined as a potential midline space located between the pharyngeal constrictor muscle anteriorly and prevertebral muscles posteriorly. It is bordered by the pharyngeal mucosal space anteriorly, the carotid space laterally, and the prevertebral portion of the perivertebral space posteriorly. It communicates with the parapharyngeal space and contains adipose tissue and lymph nodes known as the nodes of Rouviere.

The success of the TOUS route to evaluate the retropharyngeal space previously reported included a small number of patients.[2] Our study included an expanded number of patients to evaluate the reliability and accuracy of TOUS and of the TOUS-guided biopsy technique. Surgical pathology or imaging follow-up or both were used as the standard of reference.

Imaging techniques used to identify, evaluate, and localize the lymph nodes of Rouviere included CT and MR imaging using the anterior and retromandibular approach and sonography using the transoral approach. Standard 2D ultrasound of the retropharyngeal region is limited by the overlying osseous structures. The advantages of TOUS include evaluation of the retropharyngeal lesion in the transverse and sagittal planes; identification of sonographic characteristics suggestive of papillary thyroid cancer such as intranodal vascularity, calcification, and cystic change; definition of the relationship between the retropharyngeal lesion and the internal carotid artery and internal jugular vein; and graded compression of the pharyngeal wall with the transducer to assess the presence or absence of a fat plane between the lesion and the carotid artery, which provides critical information for the operating surgeon.

The TOUS imaging and biopsy technique permits a pathologic diagnosis of retropharyngeal adenopathy and facilitates minimally invasive transoral resection. This system provides a reasonable replacement for the more challenging CT-guided needle biopsy. The needle guide attached to the endocavitary sonography transducer defines the expected trajectory of the biopsy needle and facilitates placement of the biopsy needle tip within the targeted lesion.

Two of the retropharyngeal lymph nodes that underwent TOUS-FNA were of particular interest and demonstrated the usefulness of this procedure in differing clinical scenarios. One was in a patient with PTC in whom the preliminary cytology of the TOUS-FNA suggested a reactive lymph node versus concern for lymphoma. A core biopsy was required to evaluate lymphoma. The TOUS-guided core biopsy excluded lymphoma and confirmed the diagnosis of benign reactive lymphoid hyperplasia obtained on TOUS-FNA. The second patient had RCC, and TOUS-FNA showed that the retropharyngeal adenopathy was due to unsuspected undiagnosed PTC.

Accurate preoperative imaging is required to assess the need for surgical intervention and surgical guidance. TOUS allows aspiration of the retropharyngeal mass to distinguish benign from malignant disease. TOUS assists in the surgical approach by demonstrating the relationship between a retropharyngeal lesion and the adjacent vasculature to guide the surgeon.

More than half of the patients in our series (n = 14) who underwent TOUS-FNA of the retropharyngeal nodes had a history of PTC. The importance of this procedure is to determine the status of the neck nodes, which is an important prognostic factor in patients with well-differentiated thyroid cancer.[3,4] In addition, aggressive surgical resection of the retropharyngeal metastasis is the preferred treatment because it correlates with a decreased cancer-specific mortality rate and improved disease-free survival. Surgical intervention was facilitated in our series by injection of methylene blue through the TOUS-FNA apparatus at the time of biopsy-proved metastatic adenopathy.

In our experience, evaluation of retropharyngeal adenopathy with TOUS-FNA yields an accurate cytologic evaluation (100%) and diagnostic yield (96%) without complications. Our diagnostic yield was higher than that achieved in previously reported series in which evaluation and biopsy of a retropharyngeal or parapharyngeal mass were performed by CT or MR imaging either from a retromandibular or paramaxillary approach without conscious sedation or general anesthesia. Maghami et al[5] and Lai et al[6] used MR imaging to guide the diagnostic biopsy of retropharyngeal masses in 78% and 71% of patients, respectively. Sherman et al[7] reported a diagnostic accuracy of 85% in 27 patients using CT to guide the biopsy of parapharyngeal space lesions. Our high diagnostic yield and accuracy rates are likely due to our FNA technique. A needle guide attached to the probe assisted in alignment of the needle with the probe scan plane and allowed visualization of the trajectory of the needle tip as it is moved toward the target during the procedure.

A limitation of this study is that all TOUS and TOUS-FNA procedures were performed in the operative theater with the patient under general anesthesia, which may add increased risk to the patient. In addition, this procedure involves the assistance of a surgeon to open the oral cavity to allow adequate exposure to the posterior oropharyngeal wall for sonographic scanning and biopsy. However, these limitations may be negated because the intraoral approach, in the operating room in the presence of the surgeon, allows immediate intraoral surgical excision rather than the more challenging extraoral transcervical approach.

CONCLUSIONS

A TOUS-guided biopsy is a safe, feasible, accurate, and reliable diagnostic procedure to differentiate benign from malignant retropharyngeal adenopathy and provides guidance for minimally invasive transoral resection.

ACKNOWLEDGMENTS

The authors thank our Department of Scientific Publications at the University of Texas MD Anderson Cancer Center, Houston, Texas, for their kind assistance in editing.

REFERENCES

1. Connor SE, Chaudhary N. **CT-guided percutaneous core biopsy of deep face and skull-base lesions.** *Clin Radiol* 2008;63:986–94 CrossRef Medline
2. Fornage BD, Edeiken BS, Clayman GL. **Use of transoral sonography with an endocavitary transducer in diagnosis, fine-needle aspiration biopsy, and intraoperative localization of retropharyngeal masses.** *AJR Am J Roentgenol* 2014;202:W481–86 CrossRef Medline
3. Mazzaferri EL, Jhiang SM. **Long-term impact of initial surgical and medical therapy on papillary and follicular thyroid cancer.** *Am J Med* 1994;97:418–28 CrossRef Medline
4. Stojadinovic A, Shoup M, Nissan A, et al. **Recurrent differentiated thyroid carcinoma: biological implications of age, method of detection, and site and extent of recurrence.** *Ann Surg Oncol* 2002;9:789–98 CrossRef Medline
5. Maghami EG, Bonyadlou S, Larian B, et al. **Magnetic resonance imaging–guided fine-needle aspiration biopsies of retropharyngeal lesions.** *Laryngoscope* 2001;111:2218–24 CrossRef Medline
6. Lai A, Maghami E, Borges A, et al. **MRI-guided access to the retropharynx.** *J Magn Reson Imaging* 2003;17:317–22 CrossRef Medline
7. Sherman PM, Yousem DM, Loevner LA. **CT-guided aspirations in the head and neck: assessment of the first 216 cases.** *AJNR Am J Neuroradiol* 2004;25:1603–07 Medline

Armed Kyphoplasty: An Indirect Central Canal Decompression Technique in Burst Fractures

A. Venier, L. Roccatagliata, M. Isalberti, P. Scarone, D.E. Kuhlen, M. Reinert, G. Bonaldi, J.A. Hirsch, and A. Cianfoni

ABSTRACT

BACKGROUND AND PURPOSE: Burst fractures are characterized by middle column disruption and may feature posterior wall retropulsion. Indications for treatment remain controversial. Recently introduced vertebral augmentation techniques using intravertebral distraction devices, such as vertebral body stents and SpineJack, could be effective in fracture reduction and fixation and might obtain central canal clearance through ligamentotaxis. This study assesses the results of armed kyphoplasty using vertebral body stents or SpineJack in traumatic, osteoporotic, and neoplastic burst fractures with respect to vertebral body height restoration and correction of posterior wall retropulsion.

MATERIALS AND METHODS: This was a retrospective assessment of 53 burst fractures with posterior wall retropulsion and no neurologic deficit in 51 consecutive patients treated with armed kyphoplasty. Posterior wall retropulsion and vertebral body height were measured on pre- and postprocedural CT. Clinical and radiologic follow-up charts were reviewed.

RESULTS: Armed kyphoplasty was performed as a stand-alone treatment in 43 patients, combined with posterior instrumentation in 8 and laminectomy in 4. Pre-armed kyphoplasty and post-armed kyphoplasty mean posterior wall retropulsion was 5.8 and 4.5 mm, respectively ($P < .001$), and mean vertebral body height was 10.8 and 16.7 mm, respectively ($P < .001$). No significant clinical complications occurred. Clinical and radiologic follow-up (1–36 months; mean, 8 months) was available in 39 patients. Three treated levels showed a new fracture during follow-up without neurologic deterioration, and no retreatment was deemed necessary.

CONCLUSIONS: In the treatment of burst fractures with posterior wall retropulsion and no neurologic deficit, armed kyphoplasty yields fracture reduction, internal fixation, and indirect central canal decompression. In selected cases, it might represent a suitable minimally invasive treatment option, stand-alone or in combination with posterior stabilization.

ABBREVIATIONS: AKP = armed kyphoplasty; BKP = balloon kyphoplasty; PWR = posterior wall retropulsion; SAIF = Stent-Screw Assisted Internal Fixation; VAS = Visual Analog Scale; VBH = vertebral body height; VBS = vertebral body stenting; SJ = SpineJack

Thoracolumbar burst fractures can result from axial-load high-energy trauma or even from minor trauma if bone is weakened by osteoporosis or neoplasm. Burst fractures are characterized by a high degree of osseous fragmentation, outward fragment dispersion, and middle column disruption and may be associated with posterior wall retropulsion (PWR) in the central canal. Burst fractures are considered unstable, carrying a risk for immediate or delayed neurologic compromise.[1]

In practice, treatment of burst fractures, especially without neurologic injury, remains controversial, with indications ranging from conservative[2] to complex combined ventral and dorsal surgical approaches.[3] Conservative treatment may imply long periods of diminution of the activities of daily living. Moreover, burst fractures carry the risk of progressive focal kyphosis and neurologic deterioration.[4] Conversely, surgical treatment should stabilize the vertebral body, restoring vertebral body height (VBH) and alignment, correcting kyphosis, and decompressing the central canal,[5,6] thereby reducing pain and allowing early mobilization.

To address these goals, traditional pedicle-screw instrumentation allows indirect fracture and kyphosis reduction,[7,8] and via a dorsal approach, the central canal can be decompressed by

Received April 9, 2019; accepted after revision August 28.

From the Departments of Neurosurgery (A.V., P.S., D.E.K., M.R.) and Neuroradiology (L.R., M.I., A.C.), Neurocenter of Southern Switzerland, Lugano, Switzerland; Department of Neuroradiology (G.B.), Papa Giovanni XXIII Hospital, Bergamo, Italy; Department of Neurosurgery (G.B.), Clinica Igea, Milan, Italy; Department of Neuroradiology (J.A.H.), Massachusetts General Hospital, Harvard Medical School, Boston, Massachusetts; and Department of Neuroradiology (A.C.), Inselspital, University Hospital of Bern, Bern, Switzerland.

Please address correspondence to Alice Venier, MD, Neurocenter of Southern Switzerland, Via Tesserete, 46, 6900 Lugano, Switzerland; e-mail: alice.venier@eoc.ch

http://dx.doi.org/10.3174/ajnr.A6285

laminectomy and posterior wall fragment impaction[9,10] or indirectly restored through a posterior external cantilever and distraction maneuver, exploiting ligamentotaxis of the posterior longitudinal ligament.[11] Nevertheless, stabilization of the anterior column remains crucial in these fractures to avoid loss of correction and instrumentation failure.[12] Surgical anterior instrumentation with strut grafting, mesh cage, and plates has proved effective in stabilizing the anterior column[13,14] but requires a more invasive approach, which could be associated with increased morbidity.[15]

A minimally invasive approach would be desirable and might represent a balanced compromise. Cement augmentation, mainly with a balloon kyphoplasty (BKP) technique, as a stand-alone or in combination with posterior instrumentation, has been proposed as an option,[16–19] but it might be not very effective in correcting kyphosis, due to the potential loss of height restoration at balloon deflation.[20,21] Moreover, in the presence of PWR, BKP might be unable to clear the canal and is even considered relatively contraindicated due to the risk of epidural cement leakage and further displacement of bony fragments in the central canal, potentially leading to worsening of the neurologic condition.[22,23] More recently introduced percutaneous intrasomatic distraction devices, such as SpineJack (SJ; Stryker, Kalamazoo, Michigan) and vertebral body stents (VBSs; DePuy-Synthes, Johnson & Johnson, Raynham, Massachusetts) used to perform an armed kyphoplasty (AKP) might be able to overcome the deflation effect of BKP and allow a minimally invasive stabilization of the vertebral body.[24,25] An effective internal vertebral body fracture reduction and fixation might, in turn, allow a ligamentotaxis effect and canal clearance.

In this study, we retrospectively assessed the results of AKP using VBS or SJ, with or without posterior instrumentation, in traumatic, osteoporotic, and neoplastic burst fractures with regard to correction of PWR and restoration of VBH.

MATERIALS AND METHODS

Patient Population

All the patients who underwent AKP at Neurocenter of Southern Switzerland between August 2013 and December 2017 were considered for the study. Inclusion criteria were the following: 1) the presence of traumatic, osteoporotic (spontaneous or related to minor trauma), or neoplastic burst fracture without neurologic deficits, 2) the presence of a retropulsed bone fragment in the central canal documented on the preprocedural CT, and 3) a postprocedural CT scan obtained within 10 days of treatment. The local ethics committee approved this study.

Procedure

AKP was performed with the patient under general anesthesia using VBS (Figs 1–3) or SJ (Figs 3 and 4) under biplane fluoroscopic guidance. The procedure was conducted using standard techniques for either device.[24,25] VBS AKP was performed stand-alone or with the additional insertion of pedicular screws anchoring the stents in accordance with the recently reported Stent-Screw Assisted Internal Fixation (SAIF) technique (Figs 2 and 3).[26] Intraoperative myelography was used in selected cases of lumbar fractures to monitor central canal stenosis during the procedure. When deemed necessary, AKP was performed in combination with surgical posterior stabilization, either with percutaneous or open surgery with or without decompressive laminectomy (Fig 4), but without additional distraction or posterior wall fragment impaction. When deemed appropriate by the operator in patients with osteoporosis, prophylactic vertebral augmentation was performed at the adjacent levels.[27] The individual treatment decision and approach were chosen via a multidisciplinary spine board.

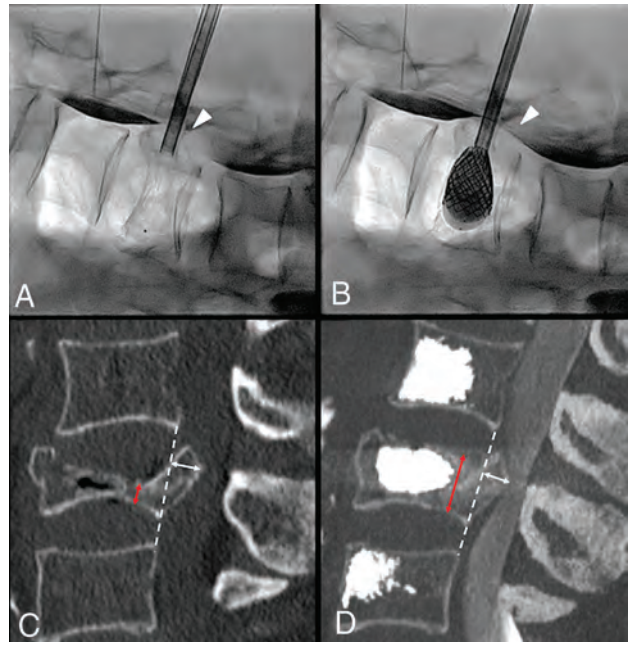

FIG 1. Severe L3 vertebral body collapse (*A*) in a 74-year-old woman with osteopenia following minor trauma. Intraoperative myelogram through intradural injection of contrast agent at L1–L2 (*arrow*, *A*) shows an opacification defect of the dural sac dorsal to the retropusled fragment at L3 (*arrowhead*, *A*). On fracture reduction through balloon-expanded vertebral body stents (*B*), the myelogram shows greater opacification of the dural sac at L3 (*arrowhead*, *B*), a real-time indirect sign of ligamentotaxis and partial central canal clearance. *C* and *D*, Preoperative and postoperative midsagittal CT images used for measurement of vertebral body height at the maximum point of collapse (*red arrows*) and of posterior wall retropulsion (*white arrows*) perpendicular to the *dashed white line* connecting the postero-inferior corner of the cranial vertebral body and the postero-superior corner of the caudal one, representing the expected original posterior wall, now intersecting the PWR.

Measurements

PWR and VBH were measured on pre- and postprocedural CT scans by 2 readers, a neuroradiologist and a neurosurgeon, in consensus. Images were reformatted with orthogonal multiplanar reconstructions, with a section thickness of 2 mm, interval of 2 mm, and bone algorithm, on a PACS system. A straight line was drawn on the midsagittal plane from the posterior-inferior corner of the cranial to the posterior-superior corner of the caudal adjacent vertebral bodies, ideally representing the original position of the normal prefracture posterior wall of the target level. This line intersected the retropulsed fractured posterior

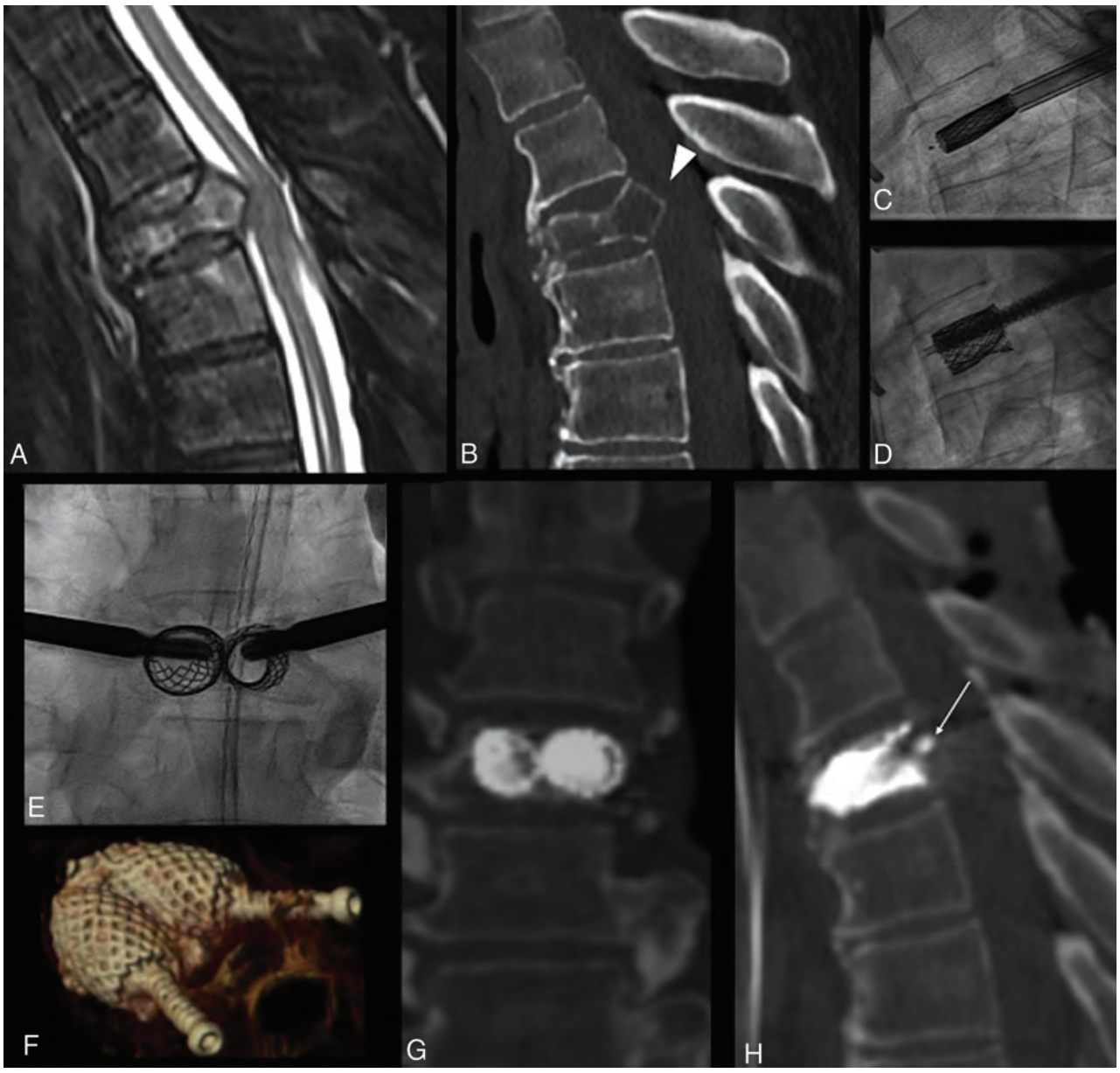

FIG 2. Lung cancer metastatic T4 fracture in a 67-year-old man, with disabling back pain. MR imaging (*A*) and CT (*B*) show a lytic lesion, with vertebral body collapse and retropulsion of an osseous fragment (*arrowhead*, *B*), causing spinal cord compression, but the patient was neurologically intact. The patient underwent armed kyphoplasty with the SAIF technique (*C–E*) with bilateral stent and screw implant, with a decompressive surgery backup plan on standby. The procedure was uneventful, and the patient showed no neurologic worsening. Postoperative CT (*F–H*) shows a 3D view of the stent-screw-cement complex (*F*) and, most notably, the vertebral body height restoration and correction of posterior wall retropulsion (*arrow*, *H*) through ligamentotaxis. The patient was ambulating the same day and could undergo radiation treatment during the following days.

wall. The PWR was then measured perpendicularly from this posterior wall line on the midsagittal image (Fig 1). VBH measurement was obtained on the midsagittal image from the superior-to-inferior endplates at the most collapsed point (Fig 1).

Statistical Analysis

Statistical analysis was performed using SPSS 20.0 (IBM, Armonk, New York).

For non-normally distributed variables, we used the related-samples Wilcoxon signed rank test to compare the median preoperative-versus-postoperative degree of PWR and to compare median preoperative-versus-postoperative VBH. Visual Analog Scale (VAS) scores for pain intensity at baseline, at 1 month, and at 6 months' follow-up were also compared using the same nonparametric test.

Follow-Up

Every patient underwent plain film and CT of the spine within 10 days from treatment to evaluate the procedure results. Clinical assessment after the procedure was mainly directed to assess for

neurologic deterioration. In a subgroup of patients, extended imaging and clinical follow-up were available and were reviewed to evaluate long-term target-level stability results, new vertebral fractures, neurologic status stability, and other clinical conditions requiring a new treatment. The VAS pain score (0–10) assessment preprocedure and at 1 and 6 months postprocedure was available for a subgroup of patients.

RESULTS

Patient Population

Of 193 patients, 94 patients were excluded because the fracture was not associated with a retropulsed bone fragment; 48 were excluded because either a pre- or a postprocedure CT scan was not available for analysis. The patient population, fulfilling all inclusion criteria, therefore included 51 patients (female/male ratio: 34:17; age range, 46–90 years; mean, 73 years) with thoracic (20/53) or lumbar (33/53) fractures. The most frequently treated levels were T12 and L1 (23/53). Two patients were treated at 2 levels. The fractures were traumatic in 32/53, osteoporotic in 12/53, and neoplastic in 9/53 cases.

Procedure

AKP was performed with VBS at 46/53 levels and with SJ at 7/53 levels. VBS AKP was performed with the SAIF technique at 33/46 levels. Intraoperative lumbar myelography was performed in 4 cases (Fig 1).

Concurrent posterior surgical stabilization with pedicular screws and rods was performed in 8/51 patients along with decompressive laminectomy in 4/8.

In 1 case, an epidural cement leak occurred causing L4 radicular pain, which promptly resolved after steroid nerve block. One patient experienced transient and completely reversible paraparesis, without evidence of worsening central canal compromise and without epidural cement leaks on postprocedure CT and MR imaging. No further intraprocedural clinical complications occurred. No other patient showed worsening neurologic status after the procedure or at follow-up.

PWR and VBH

There was a statistically significant difference between the degree of PWR preoperatively (mean, 5.8 ± 2mm; range, 2–10 mm) and postoperatively (mean, 4.5 ± 1.9 mm; range, 0–9.4 mm; $P < .001$), and there was a statistically significant difference between the VBH preoperatively (mean, 10.7 ± 4.4 mm; range, 2–21 mm) and postoperatively (mean, 16.5 ± 3.8 mm; range, 7.7–23.6 mm; $P < .001$). When we compared pre- and postoperative CT scans, the PWR difference ranged between +2 and −4 mm (mean, −1.2 mm) and the mean gain of VBH was 5.8 mm.

Individual case analysis showed that 41/53 levels had PWR correction, 6/53 had unchanged PWR, and 6/53 had worsened PWR postoperatively, while 51/53 had some degree of VBH restoration and 2/53 showed reduced VBH at postprocedure CT.

Follow-Up

Beyond the postprocedure clinical assessment, spine plain films, and CT within 10 days, 39/51 patients (41/53 levels) had an extended clinical and imaging follow-up, at least with standing spine plain films, at multiple and variable time points, ranging from 1 to 36 months postprocedure (mean, 8 months). In 19/41 (46%) levels, the postprocedure VBH was fully maintained; in 19/41 (46%), mild subsidence of the superior or inferior endplates was noted (Fig 3) with no convincing impact on alignment and kyphosis, while in 3/41 (8%), a recurrent VBH collapse of the target level was noted. In the follow-up group, 22/41 levels were studied with a cross-sectional imaging technique (8 with MR imaging and CT, 11 with CT, and 3 with MR imaging), and PWR could be assessed. Fourteen of 22 showed stability of the PWR correction compared with the postoperative CT, while 8/22 showed a recurrence in PWR. Of these 8 cases, 2 were associated with refracture of the target level, while 6 were associated with subsidence of the treated vertebra at follow-up. No retreatment was necessary at AKP-treated target levels. Clinical follow-up showed no neurologic deterioration.

Preprocedural and follow-up VAS pain scores were available for 31/51 patients. The mean VAS score at baseline was 8.5 ± 1.1 (range, 6–10); at 1-month follow-up, it was 4.0 ± 2.1 (range 0–9); and at 6 months' follow-up, it was 2.8 ± 1.8 (range, 0–7). In this cohort, the VAS scores at baseline versus 1 month and versus 6 months were significantly different ($P < .001$).

DISCUSSION

In this study, AKP using recently introduced vertebral body fracture internal distraction devices such as VBS and SJ was safely able to obtain VBH restoration and PWR correction in traumatic (Figs 3 and 4), osteoporotic (Figs 1 and 3), and neoplastic burst fractures (Fig 2). It was used as a stand-alone minimally invasive procedure in most cases or in combination with a posterior surgical approach (Fig 4), but without the need to perform any direct form of PWR correction. This minimally invasive approach had only 2 periprocedural complications, both with benign clinical resolution; showed durable results at follow-up; and required no re-intervention on the target level.

There is no definite consensus on the management of burst fractures with PWR. Some authors support a conservative approach in neurologically intact patients, claiming the possible spontaneous remodeling and resorption of the posterior wall osseous fragment encroaching the central canal,[28] while others suggest a variety of surgical approaches, including decompressive laminectomy, stabilization of the anterior column combined with a dorsal instrumentation,[13,15] and direct or indirect repositioning of retropulsed bone fragments.[9,10]

The goals of treatment are to obtain early patient mobilization and a painless, balanced, stable vertebral column with maximum spine mobility and optimal neurologic function. In neurologically intact patients, the different surgical techniques are not necessarily superior to a nonoperative approach.[6] These results might be influenced by the potentially significant morbidity and increased cost of an anterior column reconstructive surgery and by the failure rate of stand-alone posterior surgical fracture reduction and stabilization.[11,12] A safe, effective, and durable minimally invasive solution to reduce and stabilize the fracture might perform differently and better approach the ideal treatment goals.

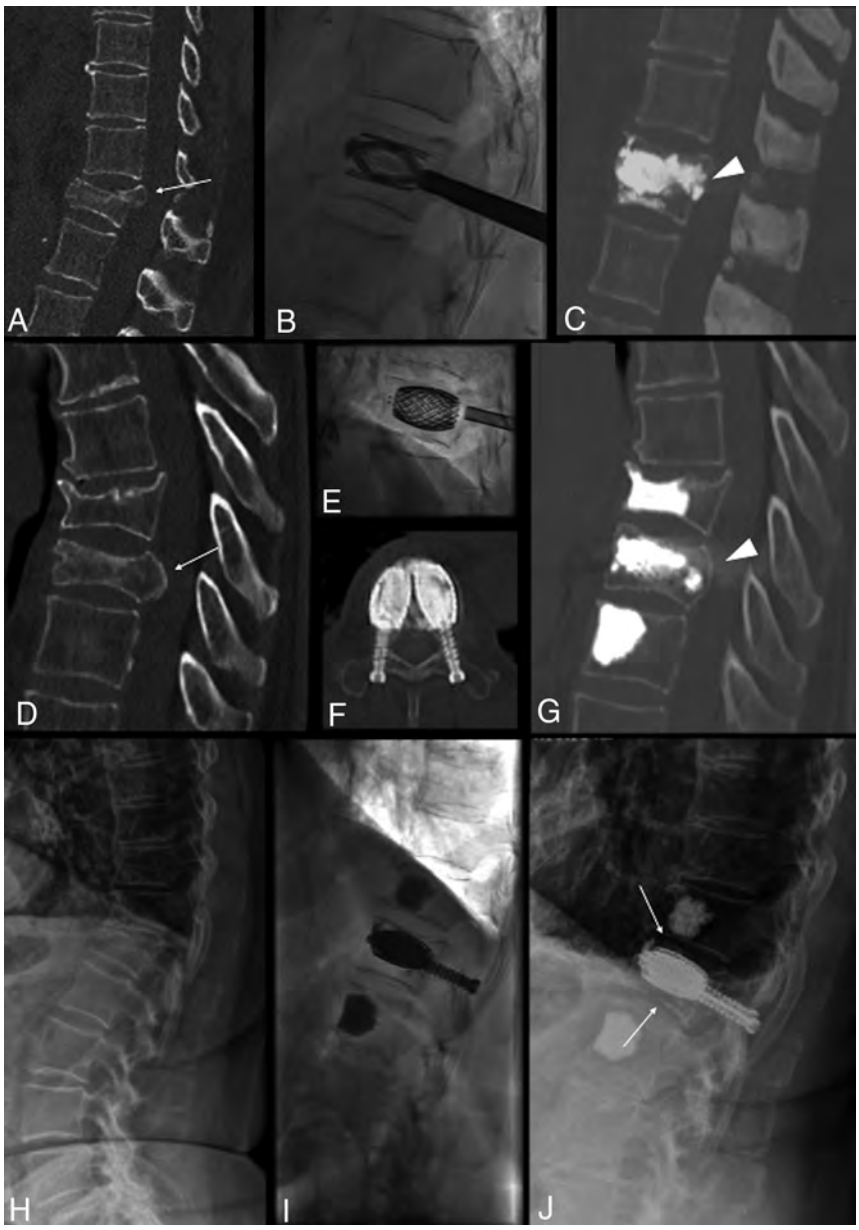

FIG 3. Three different cases (*A–C*), (*D–G*), and (*H–J*). *A–C*, Treatment with the SpineJack of a traumatic incomplete burst fracture of T12 in a 55-year-old man with posterior wall retropulsion (*arrow*, *A*) and junctional kyphosis. Postoperative CT shows vertebral height restoration, central canal clearance through retropulsed fragment correction (*arrowhead*, *C*), and kyphosis correction. *D–G*, Treatment with the SAIF technique of a traumatic T10 fracture in a 78-year-old man with osteoporosis with >50% height loss and posterior wall retropulsion (*arrow*, *D*), with effective height restoration and posterior wall reposition (*arrowhead*, *G*). *H–J*, Treatment of an L1 osteoporotic fracture with bone subsidence (*arrows*, *J*) around the cement cast at 1-month follow-up, not compromising alignment and curvature. The patient was asymptomatic.

BKP has been used to treat burst fractures, especially in a combined approach with dorsal instrumentation,[17,18] but its potential to effectively obtain VBH restoration has been questioned[20,21] and might even be relatively contraindicated.[29] With all that in mind, in clinical practice, BKP is likely used relatively frequently, given the extreme pain and functional limitations of patients for extended times. VBS and SJ have been reported as an alternative to BKP to reduce the deflation effect and potentially guarantee more reliable height restoration in wedge-shaped or incomplete burst compression fractures.[30-32] A recent randomized controlled trial showed better kyphosis correction, maintained at 12 months for SJ versus BKP in osteoporotic compression fractures.[33] A cadaveric study[34] has shown the ability of SJ to reposition the retropulsed posterior wall of a burst fracture model and substantially maintain this gain after cyclic recompression, while posterior instrumentation alone did not maintain central canal clearance, but the potential of AKP to restore VBH and correct the PWR in burst fractures has not been investigated in vivo. In fact, most studies reporting the use of VBS and SJ have focused on wedge compression fractures of an osteoporotic nature,[25,30,31] and fewer have dealt with incomplete burst fractures.[32] Within these studies, pain outcome was typically the primary end point, while kyphosis or VBH correction was secondary. In general, repositioning of the posterior fragments is underrepresented in most evaluations.[34]

AKP can effect VBH restoration, avoiding height loss due to deflation effect, and is increasingly used as a standalone measure to reconstruct and restore axial-load capability in traumatic, osteoporotic, and malignant fractures.[26,35] As a consequence of the internal fracture distraction and kyphosis reduction, AKP appears to allow ligamentotaxis correction of the PWR without the need to perform external distraction through a posterior instrumentation or even more invasive maneuvers of fragment repositioning through direct impaction. In this study, we included 8 neoplastic fractures that had a retropulsed bone fragment (Fig 2), while we did not include cases with epidural nonosseous soft-tissue masses. An epidural soft-tissue mass might, in fact, behave differently from an osseous PWR and would have been more difficult to measure on postoperative CT. Intraoperative myelography, already described in the setting of vertebral augmentation procedures at risk for central canal encroachment,[36] was used in only a minority of cases in this series, but it seemed potentially useful in selected patients to have a visual control under fluoroscopy of the PWR and to directly demonstrate the effect of ligamentotaxis during fracture reduction (Fig 1).

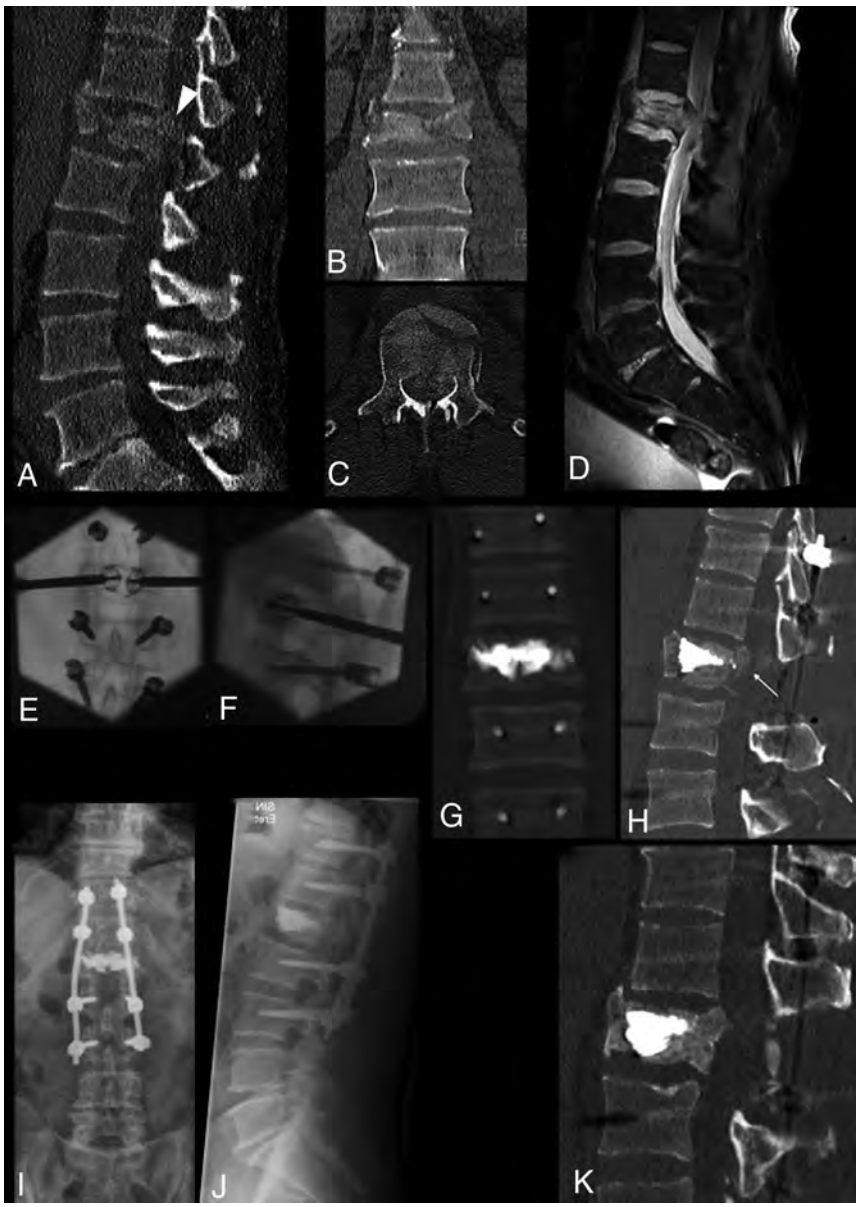

FIG 4. Complete burst fracture of L1 following high-energy trauma in a 40-year-old man with marked vertebral body fragmentation (*A–C*) and posterior wall retropulsion (*arrowhead*, *A*). Sagittal fat-saturated proton density MR image (*D*) shows an epidural hematoma and compression of the conus medullaris, but the patient was neurologically intact. The patient underwent surgical treatment in a hybrid operation room, including, in sequence, L1 decompressive laminectomy, pedicular screw placement, fracture reduction and vertebral body augmentation with percutaneous bilateral SpineJack, and posterior stabilization with spinal rods (*E* and *F*). Postprocedural CT (*G* and *H*) shows fracture and kyphosis reduction and, most important, central canal clearance (*arrow*, *H*) through ligamentotaxis. Notably, no maneuvers of direct fragment impaction or of posterior fracture distraction were performed. Follow-up imaging with standing plain films at 6 months (*I* and *J*) and with CT at 12 months (*K*) shows preserved vertebral body height and alignment and osseous healing around the cement cast. In this case, a more invasive procedure of corpectomy and anterior column stabilization could be successfully avoided by armed kyphoplasty.

We found a statistically significant difference between the mean degree of PWR and VBH pre- and postoperatively, which suggests the biomechanical effectiveness of the technique.

Besides the statistically significant postoperative changes of PWR and VBH, we found 2 cases in which VBH was reduced postoperatively, 6 cases with worsened PWR, and 6 cases with unchanged PWR. Explanations for such technical failures are not clear. Worsening PWR can certainly be an undesired effect of the internal vertebral body distraction, as generally feared, if ligamentotaxis does not occur; but fracture, VBH, and PWR might have also negatively evolved in the time lapse between preoperative imaging and the procedure. Unchanged PWR might also be related to osseous healing and/or nonefficient ligamentotaxis, which might not have allowed fragment repositioning. In addition, the group of patients we analyzed was heterogeneous, having included traumatic, osteoporotic, and malignant fractures, which theoretically may respond differently to AKP. While it is difficult to relate the technical efficacy in VBH restoration and PWR correction observed in this cohort to a definite measure of clinical benefit, PWR is still considered a relative contraindication to vertebral augmentation. Not infrequently, it represents an argument for open stabilization surgery. The results of this study might serve to mitigate the fear that AKP might worsen the status of neurologically intact patients with burst fractures. In the group of patients with available VAS assessment, there was significant and sustained pain reduction as expected compared with previously published larger series using similar treatment techniques.[36] In the 41 levels with available follow-up, the results obtained with AKP were confirmed to be stable at a mean follow-up of 8 months (range, 1–36 months) because in 38/41, the postoperative VBH was either stable or showed only minimal endplate subsidence (Fig 3); only in 3 cases did we encounter a refracture of the vertebral body treated with AKP, with VBH loss. As to a PWR correction, 14/22 patients who had cross-sectional imaging follow-up available showed stable PWR at follow-up. Some degree of PWR recurrence was noted in 8/30, associated with recurrent collapse (2/8) or subsidence. Patients with refracture of the target level and/or PWR recurrence presented with mild or no new symptoms at clinical follow-up, did not show neurologic deterioration, and did not require any further invasive treatment.

One might consider subsidence of the endplates and minimal PWR recurrence as nearly physiologic changes after AKP, namely because the surrounding fractured and weakened bone of the vertebral body on weight-bearing loading remodels and might undergo resorption phenomena against the new rigid internal scaffold, represented by VBS and SJ with polymethylmethacrylate, but usually these outcomes do not have clinical significance. The 3 new collapses reported in this series occurred in elderly patients treated for traumatic (1/3) and osteoporotic (2/3) fractures, all in the context of nontreated osteopenia. The importance of a thorough management of frequently underlying osteopenia or osteoporosis in patients at risk remains critical to reduce new fracture risk or hardware failure.[37]

AKP was performed using VBS in 46 levels, and SJ, in the remaining 7. We tend to use SJ for AKP when bone mass is preserved, especially in young patients with traumatic mechanism of fracture and impacted morphology of the fracture, to the impacted morphology needs a powerful internal fracture distraction, while we rather use VBS in bone of poor quality with a high degree of vertebral body fragmentation, osteoporosis, and lytic lesions, in which the vertebral body rather needs an internal scaffold to restore its stability and axial-load capability.[38]

There are several limitations to the present study, including its retrospective design, the small size and heterogeneity of the sample, and nonsystematic follow-up. There might have been a selection bias in the studied patient series, but the decision to treat with AKP versus a standard surgical approach was reached for every individual patient by a multidisciplinary spine board. The inclusion in this series of patients treated in combination with a posterior surgical approach underscores the possibility of treating even severe burst fractures with AKP, avoiding surgical stabilization of the anterior column and more invasive maneuvers to clear the central canal.

Given the small number of patients and confounding factors, including concurrent surgical interventions, fracture etiology heterogeneity, and technical differences in performing the AKP procedure, the conclusions of our analysis need to be confirmed in larger prospective studies.

CONCLUSIONS

AKP appears to represent a viable technique to treat neurointact burst fractures with PWR, in combination with posterior instrumentation or in selected cases as a stand-alone procedure, being able to effect VBH restoration and indirect central canal decompression through PWR correction. This minimally invasive approach should offer durable results and thus represents an alternative to avoid more invasive anterior column stabilization interventions and retropulsed bone fragment reposition techniques.

Disclosures: Pietro Scarone—*UNRELATED*: *Consultancy*: Depuy Synthes J&J Medical Devices.* Joshua A. Hirsch—*UNRELATED*: *Board Membership*: Ceranovus (Data and Safety Monitoring Board service), Relievant (Data Monitoring Committee service); *Consultancy*: Medtronic, *Comments*: ongoing consulting. *Money paid to the institution.

REFERENCES

1. Denis F. **Spinal instability as defined by the three-column spine concept in acute spinal trauma.** *Clin Orthop Relat Res* 1984:65–76 Medline
2. Mumford J, Weinstein JN, Spratt KF, et al. **Thoracolumbar burst fractures: the clinical efficacy and outcome of nonoperative management.** *Spine (Phila Pa 1976)* 1993;18:955–70 CrossRef
3. Payer M. **Unstable burst fractures of the thoraco-lumbar junction: treatment by posterior bisegmental correction/fixation and staged anterior corpectomy and titanium cage implantation.** *Acta Neurochir (Wien)* 2006;148:299–306; discussion 306 CrossRef Medline
4. Rajasekaran S. **Thoracolumbar burst fractures without neurological deficit: the role for conservative treatment.** *Eur Spine J* 2010;19:40–47 CrossRef Medline
5. Khurjekar Hk K, Kardile M. **Treatment algorithm for unstable burst fracture.** *International Journal of Spine* 2016;1:27–32
6. Scheer JK, Bakhsheshian J, Fakurnejad S, et al. **Evidence-based medicine of traumatic thoracolumbar burst fractures: a systematic review of operative management across 20 years.** *Global Spine J* 2015;5:73–82 CrossRef Medline
7. Aebi M, Etter C, Kehl T, et al. **Stabilization of the lower thoracic and lumbar spine with the internal spinal skeletal fixation system: indications, techniques, and first results of treatment.** *Spine (Phila Pa 1976)* 1987;12:544–51 CrossRef
8. Dick W, Kluger P, Magerl F, et al. **A new device for internal fixation of thoracolumbar and lumbar spine fractures: the "fixateur interne."** *Paraplegia* 1985;23:225–32 CrossRef Medline
9. Oro J, Watts C, Gaines R. **Vertebral body impactor for posterior lateral decompression of thoracic and lumbar fractures: technical note.** *J Neurosurg* 1989;70:285–86 CrossRef Medline
10. Park SH, Kim SD, Moon BJ, et al. **Short segment percutaneous pedicle screw fixation after direct spinal canal decompression in thoracolumbar burst fractures: an alternative option.** *J Clin Neurosci* 2018;53:48–54 CrossRef Medline
11. Whang PG, Vaccaro AR. **Thoracolumbar fracture: posterior instrumentation using distraction and ligamentotaxis reduction.** *J Am Acad Orthop Surg* 2007;15:695–701 CrossRef Medline
12. Lakshmanan P, Jones A. Mehta **Recurrence of kyphosis and its functional implications after surgical stabilization of dorsolumbar unstable burst fractures.** *Spine J* 2009;9:1003–09 CrossRef Medline
13. Machino M, Yukawa Y, Ito K, et al. **Posterior/anterior combined surgery for thoracolumbar burst fractures–posterior instrumentation with pedicle screws and laminar hooks, anterior decompression and strut grafting.** *Spinal Cord* 2011;49:573–79 CrossRef Medline
14. Zhang S, Thakur JD, Khan IS, et al. **Anterior stabilization for unstable traumatic thoracolumbar spine burst fractures.** *Clin Neurol Neurosurg* 2015;130:86–90 CrossRef Medline
15. Oprel PP, Tuinebreijer WE, Patka P, et al. **Combined anterior-posterior surgery versus posterior surgery for thoracolumbar burst fractures: a systematic review of the literature.** *Open Orthop J* 2010;4:93–100 CrossRef Medline
16. Kruger A, Zettl R, Ziring E, et al. **Kyphoplasty for the treatment of incomplete osteoporotic burst fractures.** *Eur Spine J* 2010;19:893–900 CrossRef Medline
17. Korovessis P, Hadjipavlou A, Repantis T. **Minimal invasive short posterior instrumentation plus balloon kyphoplasty with calcium phosphate for burst and severe compression lumbar fractures.** *Spine (Phila Pa 1976)* 2008;33:658–67 CrossRef Medline
18. Korovessis P, Repantis T, Petsinis G, et al. **Direct reduction of thoracolumbar burst fractures by means of balloon kyphoplasty with calcium phosphate and stabilization with pedicle-screw instrumentation and fusion.** *Spine (Phila Pa 1976)* 2008;33:E100–08 CrossRef Medline
19. Verlaan JJ, Somers I, Dhert WJ, et al. **Clinical and radiological results 6 years after treatment of traumatic thoracolumbar burst fractures with pedicle screw instrumentation and balloon assisted endplate reduction.** *Spine J* 2015;15:1172–78 CrossRef Medline
20. Lee JH, Lee DO, Lee JH, et al. **Comparison of radiological and clinical results of balloon kyphoplasty according to anterior height loss**

in the osteoporotic vertebral fracture. *Spine J* 2014;14:2281–89 CrossRef Medline
21. Disch AC, Schmoelz W. **Cement augmentation in a thoracolumbar fracture model: reduction and stability after balloon kyphoplasty versus vertebral body stenting.** *Spine (Phila Pa 1976)* 2014;39: E1147–53 CrossRef Medline
22. Walter J, Haciyakupoglu E, Waschke A, et al. **Cement leakage as a possible complication of balloon kyphoplasty–is there a difference between osteoporotic compression fractures (AO type A1) and incomplete burst fractures (AO type A3.1)?** *Acta Neurochir* 2012;154:313–19 CrossRef Medline
23. Saliou G, Rutgers DR, Kocheida EM, et al. **Balloon-related complications and technical failures in kyphoplasty for vertebral fractures.** *AJNR Am J Neuroradiol* 2010;31:175–79 CrossRef Medline
24. Rotter R, Martin H, Fuerderer S, et al. **Vertebral body stenting: a new method for vertebral augmentation versus kyphoplasty.** *Eur Spine J* 2010;19:916–23 CrossRef Medline
25. Renaud C. **Treatment of vertebral compression fractures with the cranio-caudal expandable implant SpineJack(R): technical note and outcomes in 77 consecutive patients.** *Orthop Traumatol Surg Res* 2015;101:857–59 CrossRef Medline
26. Cianfoni A, Distefano D, Isalberti M, et al. **Stent-screw-assisted internal fixation: the SAIF technique to augment severe osteoporotic and neoplastic vertebral body fractures.** *J Neurointerv Surg* 2018;11:603–09 CrossRef Medline
27. Diel P, Freiburghaus L, Roder C, et al. **Safety, effectiveness and predictors for early reoperation in therapeutic and prophylactic vertebroplasty: short-term results of a prospective case series of patients with osteoporotic vertebral fractures.** *Eur Spine J* 2012;21:792–99 CrossRef Medline
28. de Klerk LW, Fontijne WP, Stijnen T, et al. **Spontaneous remodeling of the spinal canal after conservative management of thoracolumbar burst fractures.** *Spine (Phila Pa 1976)* 1998;23:1057–60 CrossRef Medline
29. Chandra RV, Meyers PM, Hirsch JA, et al. **Vertebral augmentation: report of the Standards and Guidelines Committee of the Society of NeuroInterventional Surgery.** *J Neurointerv Surg* 2014;6:7–15 CrossRef Medline
30. Noriega DC, Rodríguez-Monsalve F, Ramajo R, et al. **Long-term safety and clinical performance of kyphoplasty and SpineJack(R) procedures in the treatment of osteoporotic vertebral compression fractures: a pilot, monocentric, investigator-initiated study.** *Osteoporos Int* 2019;30:637–45 CrossRef Medline
31. Werner CM, Osterhoff G, Schlickeiser J, et al. **Vertebral body stenting versus kyphoplasty for the treatment of osteoporotic vertebral compression fractures: a randomized trial.** *J Bone Joint Surg Am* 2013;95:577–84 CrossRef Medline
32. Hartmann F, Griese M, Dietz SO, et al. **Two-year results of vertebral body stenting for the treatment of traumatic incomplete burst fractures.** *Minim Invasive Ther Allied Technol* 2015;24:161–66 CrossRef Medline
33. Noriega D, Maestretti G, Renaud C, et al. **Clinical performance and safety of 108 SpineJack implantations: 1-year results of a prospective multicentre single-arm registry study.** *Biomed Res Int* 2015;2015:1. CrossRef Medline
34. Kruger A, Oberkircher L, Figiel J, et al. **Height restoration of osteoporotic vertebral compression fractures using different intravertebral reduction devices: a cadaveric study.** *Spine J* 2015;15:1092–98 CrossRef Medline
35. Cianfoni A, Distefano D, Pravata E, et al. **Vertebral body stent augmentation to reconstruct the anterior column in neoplastic extreme osteolysis.** *J Neurointerv Surg* 2019;11:313–18 CrossRef Medline
36. Cianfoni A, Raz E, Mauri S, et al. **Vertebral augmentation for neoplastic lesions with posterior wall erosion and epidural mass.** *AJNR Am J Neuroradiol* 2015;36:210–18 CrossRef Medline
37. Bae JS, Park JH, Kim KJ, et al. **Analysis of risk factors for secondary new vertebral compression fracture following percutaneous vertebroplasty in patients with osteoporosis.** *World Neurosurg* 2017;99:387–94 CrossRef Medline
38. Cianfoni A, Distefano D, Pravata E, et al. **Vertebral body stent augmentation to reconstruct the anterior column in neoplastic extreme osteolysis.** *J Neurointer Surg* 2019;11:313–18 CrossRef Medline

Unintended Consequences: Review of New Artifacts Introduced by Iterative Reconstruction CT Metal Artifact Reduction in Spine Imaging

D.R. Wayer, N.Y. Kim, B.J. Otto, A.M. Grayev, and A.D. Kuner

ABSTRACT

SUMMARY: Metal hardware serves as a common artifact source in spine CT imaging in the form of beam-hardening, photon starvation, and streaking. Postprocessing metal artifact reduction techniques have been developed to decrease these artifacts, which has been proved to improve visualization of soft-tissue structures and increase diagnostic confidence. However, metal artifact reduction reconstruction introduces its own novel artifacts that can mimic pathology.

ABBREVIATION: MAR = metal artifact reduction

Metal artifacts are an obstacle to obtaining high-fidelity CT images in postoperative spine imaging, which is increasingly problematic as the number of instrumented spinal fusions grows. There were approximately 463,200 spinal fusions in 2014 in the United States,[1] a 12% increase compared with 2011[2] and nearly triple the amount from 1998.[3] Unfortunately, up to one-third of patients experience no improvement or worsening of symptoms following surgical intervention[4] and require appropriate spine imaging.[4-7]

The main artifacts introduced by metallic spinal implants include beam-hardening, photon starvation, and streaking,[8] which diminish overall image quality and impair the identification of pathology.[9,10] Metal artifact reduction (MAR; GE Healthcare, Milwaukee, Wisconsin) postprocessing techniques have been developed[11] to recover image quality and detail in affected areas and to diminish the artifacts themselves.[12] Unfortunately, MAR introduces different artifacts that can mimic pathology, which radiologists need to recognize.[12,13] The purpose of this article was to review MAR-related artifacts seen on GE Healthcare scanners. While only 1 manufacturer is included in this article, many of the concepts are applicable to different vendor products that use similar techniques.

Received June 6, 2019; accepted after revision August 16.

From the Department of Radiology (D.R.W., N.Y.K., B.J.O., A.M.G., A.D.K.), University of Wisconsin, Madison, Wisconsin; and the University of Wisconsin School of Medicine and Public Health (A.D.K.), Madison, Wisconsin.

Paper previously presented at: Zachary Clark Radiology Research Symposium, May 4, 2019, Madison, Wisconsin; and Annual Meeting of the American Society of Neuroradiology, May 18–23, 2019, Boston, Massachusetts.

Please address correspondence to Anthony D. Kuner, MD, University of Wisconsin School of Medicine and Public Health, Clinical Science Center, 600 Highland Ave, Madison, WI 53792-3252; e-mail: akuner@uwhealth.org

http://dx.doi.org/10.3174/ajnr.A6238

MAR Technique and Its Benefits

MAR is an automated postprocessing, projection-based technique developed by GE Healthcare that addresses metal artifacts in 3 stages. First, metal artifacts are identified in the source tomogram projection using a density threshold. Second, the data lost from metal artifacts are reconstructed into an inpainted projection with corrected data, which is generated by estimation from artifact-free areas. Finally, the corrected projection is formed by combining the inpainted projection and the original projection, which reveal details of structures obscured by artifacts.[14,15]

MAR reconstruction has been shown to significantly improve visualization of obscured soft-tissue structures and diagnostic confidence compared with the standard weighted filtered back-projection reconstruction method.[12] Paraspinal soft tissues adjacent to the fusion hardware are obscured on traditional images, while the MAR image allows adequate visualization of the underlying structures (Fig 1). Despite the clear benefits of applying MAR to decrease metal artifacts, MAR introduces its own unique artifacts.

MAR-Related Artifacts and Limitations

MAR-induced artifacts have been described in the hip and elbow,[15] but there are limited descriptions of these artifacts in the spine[12,16] where MAR artifacts frequently mimic pathology. The primary artifacts include the following: perihardware lucency, pedicle screw lucency, factitious subarachnoid material on myelography, and misrepresentation of intraosseous cement.

Perihardware Lucency. Perihardware lucency (Fig 2*A*, white arrow) is concerning because it usually signifies loosening of the hardware; however, this is not visualized in the non-MAR images

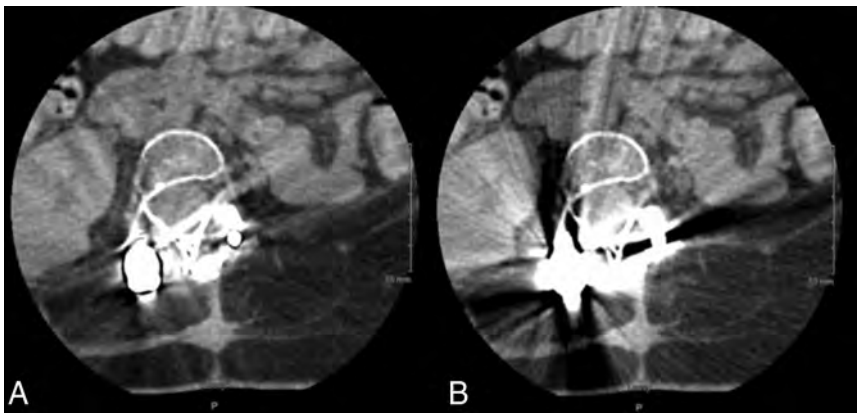

FIG 1. Axial lumbar CT images of a 15-year-old boy with spinal muscular atrophy type II who underwent posterior spinal fusion of T2–L5 due to severe scoliosis. *A*, MAR images demonstrating improved visualizations of soft tissues surrounding the hardware. *B*, Uncorrected images show artifacts covering soft tissues surrounding the hardware.

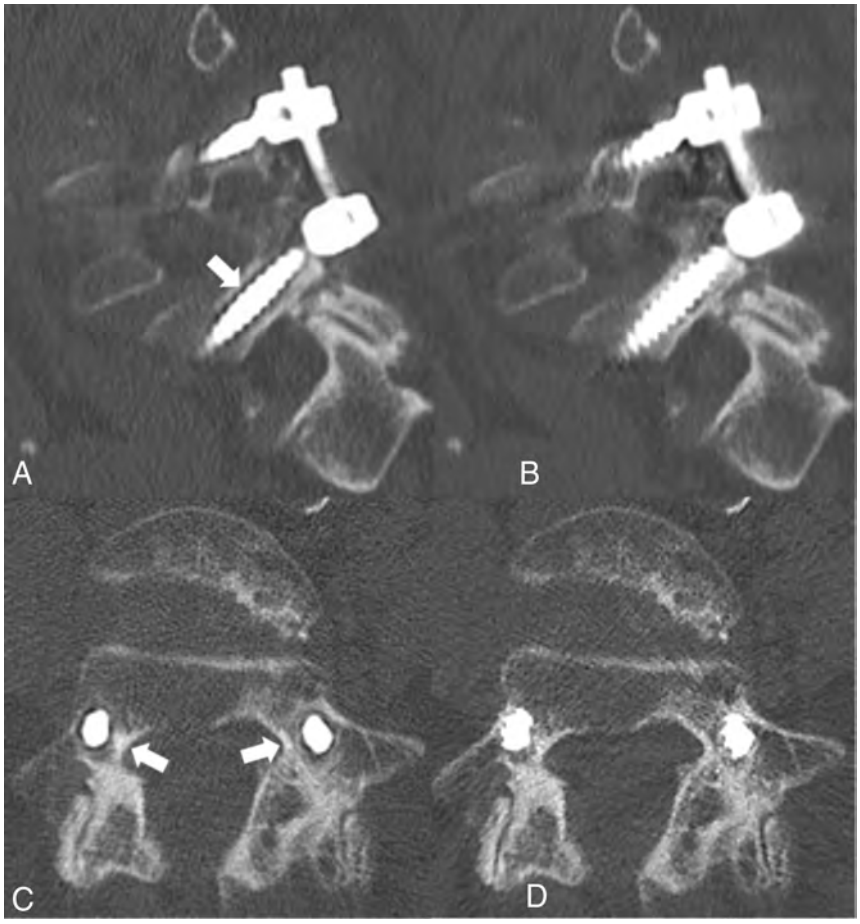

FIG 2. *A*, Sagittal CT image of posterior lumbar spinal fusion with the MAR technique applied shows lucency surrounding the L5 pedicle screw as indicated by the *white arrow*. *B*, Image *A* without the MAR protocol applied, *C*, Axial CT image shows bilateral pedicle screws with the MAR technique applied, demonstrating lucency surrounding the bilateral pedicle screws (*white arrows*). If the MAR images were viewed alone, these lucencies could be mistaken for hardware loosening. *D*, Image *C* without the MAR protocol applied.

(Fig 2*B*). More troublesome is that these artifacts persist in multiple planes as shown in the axial plane (Fig 2*C*, -*D*).

Pedicle Screw Lucency. Pedicle screw lucency occurs when the implanted hardware fatigues and fractures (Fig 3*A*, white arrow), which is not seen on the non-MAR image (Fig 3*B*). This artifact is not uniform throughout the MAR series, and adjacent images demonstrate that adjacent screws are unaffected.

Subarachnoid Material on Myelography. Factitious subarachnoid material can be seen on myelograms when MAR is applied, particularly in areas of concentrated intrathecal contrast. There is hypodense material in the dorsal spinal canal (Fig 4*A*, white arrow), which is not seen on the non-MAR image (Fig 4*B*). This artifact could be mistaken for arachnoiditis, tumor, or layering debris and may lead to unnecessary further work-up.

Intraosseous Cement Abnormal Distribution. Postvertebroplasty cement configuration can appear irregular and fragmented with indistinct margins (Fig 5*A*, white arrow) and an internal heterogeneous pattern of vertebral body filling; however, in the non-MAR image (Fig 5*B*), the bone cement has a normal uniform distribution with clearly defined margins.

CONCLUSIONS

MAR is a useful imaging reconstruction technique that can minimize metal artifacts, thus improving soft-tissue visualization and diagnostic confidence in the setting of spinal hardware;[12] however, it is critical to understand the generated artifacts to render a correct interpretation. One limitation of this article is that we exclusively used GE Healthcare scanners. While MAR techniques of different vendors may have overlap in method (ie, projection modification is used by GE Healthcare and Philips Healthcare), each vendor ultimately has its own proprietary algorithm.[17] All can potentially

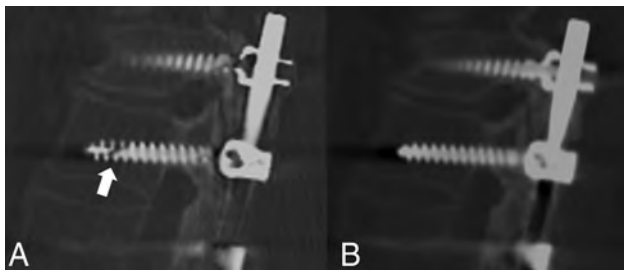

FIG 3. *A*, Sagittal CT image of posterior spinal fusion of the MAR protocol demonstrating lucency through the pedicle screw (*white arrow*). This lucency clearly mimics a fracture, hence could be called a "pseudofracture" if non-MAR images are not available. *B*, Image without the MAR application shows a normal appearance of the pedicle screw.

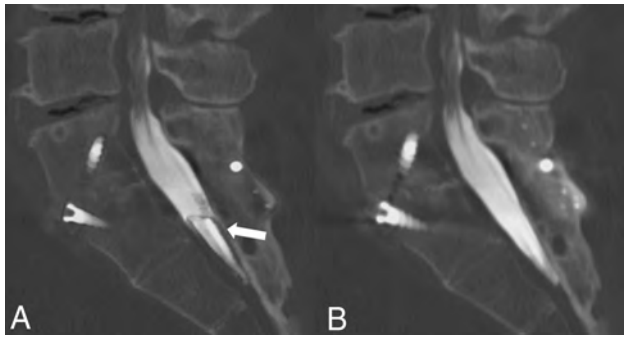

FIG 4. *A*, Sagittal MAR CT image with fusion hardware in the lumbar and sacral spine demonstrates apparent hypodense material (*white arrow*) in the dorsal spinal canal not seen in the non-MAR image. This filling defect could be mistaken for arachnoiditis, tumor, or layering debris and lead to unnecessary further work-up. *B*, Non-MAR image without evidence of material within the spinal canal.

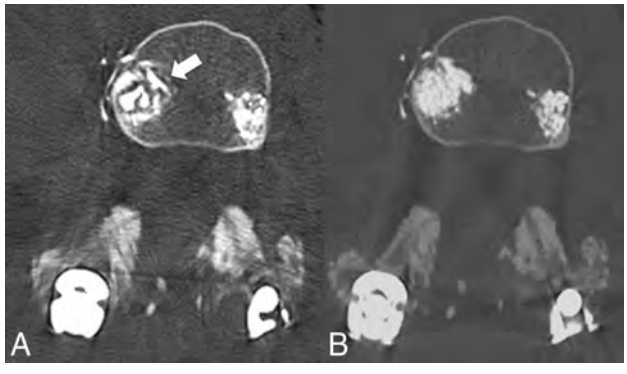

FIG 5. *A*, Axial CT image with MAR applied demonstrating an irregular fragmented appearance of bone cement with indistinct margins (*white arrow*). *B*, Non-MAR counterpart image with normal appearance of bone cement with accurate representation of vertebral filling.

simulate undersampling due to oversmoothing by the MAR algorithm in areas where dense objects interface with bone, as shown in previous phantom modeling demonstrating distortion of hardware.[17]

At our institution, we include a set of standard images along with the MAR postprocessed images (from a single CT acquisition) on the PACS to allow confident identification of MAR artifacts and true pathology or postoperative complication. Given the widespread use of MAR techniques and the implication of misinterpreting artifacts, it is crucial that radiologists recognize these artifacts exist.

Disclosures: Allison M. Grayev—*UNRELATED*: *Royalties*: McGraw Hill, *Comments*: Author.

REFERENCES

1. McDermott KW, Freeman WJ, Elixhauser A. Overview of Operating Room Procedures During Inpatient Stays in U.S. Hospitals, 2014: Statistical Brief #233. In: *Healthcare Cost and Utilization Project (HCUP) Statistical Briefs*. Rockville: Agency for Healthcare Research and Quality; 2017
2. Weiss AJ, Elixhauser A, Andrews RM. Characteristics of Operating Room Procedures in U.S. Hospitals, 2011: Statistical Brief #170. In: *Healthcare Cost and Utilization Project (HCUP) Statistical Briefs*. Rockville: Agency for Healthcare Research and Quality; 2014
3. Rajaee SS, Bae HW, Kanim LEA, et al. **Spinal fusion in the United States: analysis of trends from 1998 to 2008.** *Spine* 2012;37:67–76 CrossRef Medline
4. Skolasky RL, Wegener ST, Maggard AM, et al. **The impact of reduction of pain after lumbar spine surgery: the relationship between changes in pain and physical function and disability.** *Spine* 2014;39:1426–32 CrossRef Medline
5. Chan C, Peng P. **Failed back surgery syndrome.** *Pain Med* 2011; 12:577–606 CrossRef Medline
6. Young PM, Berquist TH, Bancroft LW, et al. **Complications of spinal instrumentation.** *Radiographics* 2007;27:775–89 CrossRef Medline
7. Baber Z, Erdek MA. **Failed back surgery syndrome: current perspectives.** *J Pain Res* 2016;9:979–87 CrossRef Medline
8. Barrett JF, Keat N. **Artifacts in CT: recognition and avoidance.** *Radiographics* 2004;24:1679–91 CrossRef Medline
9. Stradiotti P, Curti A, Castellazzi G, et al. **Metal-related artifacts in instrumented spine: techniques for reducing artifacts in CT and MRI: state of the art.** *Eur Spine J* 2009;18:102–08 CrossRef Medline
10. White LM, Buckwalter KA. **Technical considerations: CT and MR imaging in the postoperative orthopedic patient.** *Semin Musculoskelet Radiol* 2002;06:5–17 CrossRef Medline
11. Gjesteby L, Man BD, Jin Y, et al. **Metal artifact reduction in CT: where are we after four decades?** *IEEE Access* 2016;4:5826–49 CrossRef
12. Kotsenas AL, Michalak GJ, DeLone DR, et al. **CT metal artifact reduction in the spine: can an iterative reconstruction technique improve visualization?** *AJNR Am J Neuroradiol* 2015;36:2184–90 CrossRef Medline
13. Zhou P, Zhang C, Gao Z, et al. **Evaluation of the quality of CT images acquired with smart metal artifact reduction software.** *Open Life Science* 2018;13:155–62 CrossRef
14. GE Healthcare. GE Healthcare. Smart Metal Artifact Reduction (MAR). 2013 https://www.gehealthcare.com/products/computed-tomography/radiation-therapy-planning/metal-artifact-reduction. Accessed May 30, 2019
15. Katsura M, Sato J, Akahane M, et al. **Current and novel techniques for metal artifact reduction at CT: practical guide for radiologists.** *Radiographics* 2018;38:450–61 CrossRef Medline
16. Wang Y, Qian B, Li B, et al. **Metal artifacts reduction using monochromatic images from spectral CT: evaluation of pedicle screws in patients with scoliosis.** *Eur J Radiol* 2013;82:e360–66 CrossRef Medline
17. Huang JY, Kerns JR, Nute JL, et al. **An evaluation of three commercially available metal artifact reduction methods for CT imaging.** *Phys Med Biol* 2015;60:1047–67 CrossRef Medline

Celebrating 35 Years of the AJNR

November 1984 edition

Magnetic Resonance Demonstration of Multiple Sclerosis Plaques in the Cervical Cord

Kenneth R. Maravilla[1]
Jeffrey C. Weinreb
Richard Suss
Ray L. Nunnally

Magnetic resonance imaging (MRI) has been shown to be far more sensitive than computed tomography (CT) in the detection of multiple sclerosis plaques within the brain. Unlike CT, MRI is also able to detect multiple sclerosis in the brainstem and cerebellum. This report is the first description of MRI of multiple sclerosis plaques within the cervical spinal cord. Twenty-one patients with clinically typical multiple sclerosis had characteristic plaques within the brain. In 10 patients one or more plaques were identified in the cervical spinal cord. Plaques in the spinal cord were detected only in the upper cervical region using the 30-cm head radiofrequency coil. No lesions were identified using the larger-diameter body coil because of poorer signal-to-noise ratio. Further improvement in visualization of plaques in the lower cervical and thoracic spinal cord may depend on development of high-quality surface coils.

Multiple sclerosis (MS) is a widespread demyelinating disease of the central nervous system consisting of lesions widely separated in location as well as time of onset. MS has traditionally been a diagnosis of exclusion that has required evaluation of patients with multiple imaging studies including computed tomography (CT) of the head and myelography whenever symptoms attributable to a spinal cord lesion are present.

In recent years, an improved battery of nonimaging studies has been developed that greatly aids in establishing the clinical diagnosis of MS [1, 2]. These tests include visual, auditory, and somatosensory-evoked potentials. Cervical cerebrospinal fluid (CSF) analysis, including measurement of IgG and CSF electrophoresis for the detection of oligoclonal bands, is also extremely helpful. However, while these sophisticated tests increase the sensitivity and accuracy for diagnosing MS, they have several limitations. They are not positive in 100% of patients with MS, and patients with other diseases may have elevated IgG and oligoclonal bands within the CSF leading to false-positive diagnoses. In addition, even though the diagnosis of MS can be implied using a comprehensive battery of ne studies, these tests do not provide the information needed for localizing M determining the number and size of lesions, and determining their sites bution. This is important not only for diagnosis but also for determination of the disease and subsequent prognosis. Moreover, this type of infor crucial in following patients, determining their response to therapy, and in e the efficacy of proposed new treatment regimens. Efforts to obtain this in have been greatly hampered by the inability to reliably image MS plaques

CT of the brain, especially with high-dose intravenous contrast enha has been used to detect some MS plaques [3–5], but CT also ha limitations. Small, low-density plaques often are not visualized on the C and even large periventricular plaques may not be seen since their de approximate that of CSF within the ventricles, and they may be insepar the outline of the ventricular wall [6]. Partial-volume effects between CS periventricular plaques further diminish the sensitivity of CT. Some dem

This article appears in the November/December 1984 issue of AJNR and the February 1985 issue of AJR.

Received May 7, 1984; accepted June 14, 1984.

[1] All authors: Department of Radiology, University of Texas, Health Science Center at Dallas, 5323 Harry Hines Blvd., Dallas, TX 75235. Address reprint requests to K. R. Maravilla, NMR Imaging Center.

AJNR 5:685–690, November/December 1984
0195-6108/84/0506-0685

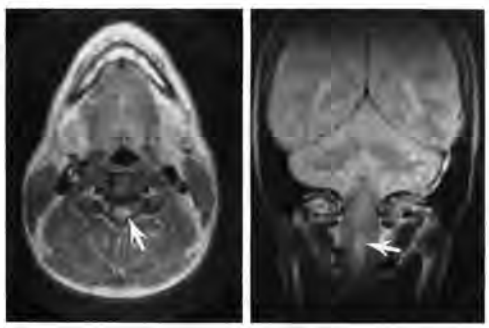

A B

CT of Acquired Immunodeficiency Syndrome

Enrique M. Bursztyn[1]
Benjamin C. P. Lee
James Bauman

Thirty patients with acquired immunodeficiency syndrome were examined by computed tomography. In addition to systemic disease, these patients had a variety of neurologic symptoms and signs. Cerebral toxoplasmosis (six cases) was generally manifested by ring-enhancing lesions with surrounding decreased attenuation. Lymphoma (one case) exhibited a solid enhancing nodule, and progressive multifocal leukoencephalopathy (two cases) showed periventricular decreased attenuation. Atrophy (13 cases) was very common and invariably indicated a poor prognosis; the autopsy examinations of the latter cases showed degeneration of gray and white matter with features similar to cytomegalic inclusion encephalitis and subacute sclerosing encephalopathy of measles.

In the spring of 1981, the Centers for Disease Control began to report in alarming numbers healthy homosexual men with infections and Kaposi sarcoma [1–3]. The etiology of this acquired immunodeficiency syndrome (AIDS) is unknown, but has since been reported increasingly outside the homosexual community, in intravenous drug abusers [4–6], Haitians [7], women who are not themselves drug abusers but have sexual contact with addicts [8], and hemophiliacs and other recipients of blood products [9]. Only pulmonary and gastrointestinal changes have been reported in the radiologic literature [10–26]. We are unaware of a comprehensive review of the central nervous system (CNS) manifestations in AIDS. Over the past 2 years we have had the opportunity to study computed tomographic (CT) scans of a number of such patients. It appears that, although a wide spectrum of changes is seen, certain appearances may be characteristic of this disorder. Our study is a report of such changes.

Materials and Methods

Thirty patients with the diagnosis of AIDS admitted to the New York Hospital and Memorial Sloan-Kettering Cancer Center were scanned on a GE 8800 or Technicare 2020 scanner; intravenous contrast material was administered in all cases. Patients were from 26–50 years of age; 22 were sexually active homosexuals, two were intravenous drug abusers who denied homosexuality, and six did not state sexual orientation. Most were admitted for evaluation of underlying malignancy and for overwhelming systemic *Pneumocystis carinii* and cytomegalic viral infections. The indications for CT evaluation were decreased mental status in 18 cases and confusion and changes in the level of consciousness in 12. CT lesions were confirmed by biopsy, autopsy, or clinical response to therapy (table 1).

Results

Six different types of CT abnormalities were observed (table 1):

1. Ring-enhancing lesions with surrounding low attenuation were seen in four cases; three cases had single lesions, one multiple. There was slight mass effect or mass effect disproportional to the size of the area of decreased attenuation

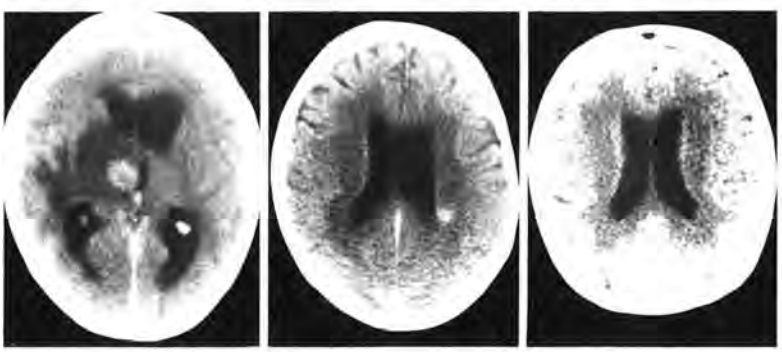

1 2 3

Impact on Quality of Neuroradiology Interpretations by Caseload

I congratulate Patel et al[1] for their careful examination and publication of risk factors in their article "Risk Factors for Perceptual-versus-Interpretive Errors in Diagnostic Neuroradiology" and the *American Journal of Neuroradiology* for publishing it. This article is particularly meaningful to neuroradiologists because it is specific to our practice. Their finding that errors are linked to the number of cases read per hour by staff confirms what every neuroradiologist who has taken weekend call at a busy hospital system has long suspected. However, there is nothing quite like data since there is some disagreement within our specialty about what constitutes an appropriate workload that has been ongoing for years, even while it has steadily increased during my professional career.

A reasonable question from those outside of radiology is, "Why would radiologists ever read at a rate that could impact quality?" While it is hard to explain this to those involved in quality control in other high-risk industries like aviation, most of us really have no idea what our true error rates are either as individuals or as a group. Moreover, much like those imaginary children Garrison Keeler tells us about from Lake Woebegone, we all think we are above average. This approach is not unique to radiology, however; and in some surgical practices, it results in unrealistically favorable complication rates being quoted to patients during informed consent that were taken from published reports by the best surgeons in the world. The validation provided in this article provides a carefully established link between the reading rate and quality that has been suspected but rarely documented.

What is striking in this report, however, is the actual number of cases read per hour, 5 versus 6, where the error rate increased. Considering the standard practice at many hospitals of operating their MR imaging and CT scanners all weekend but with reduced faculty, that threshold I would expect is routinely and predictably exceeded. What currently is used to determine staffing in the neuroradiology section by many hospital administrations are the "benchmarks" derived from data from the radiology departments of other hospitals. The peril in this approach is that it is entirely possible that it could, and some would say has, led to everyone reading too many cases per day but at least consistently so.

http://dx.doi.org/10.3174/ajnr.A6229

I have lately wondered if we are capable of regulating our own workplace in a way that protects the best interests of both our patients and staff. Unlike many industries that try to match staffing with planned increases in workload, it has been my experience that radiology departments willingly or unwillingly take on the work of a new scanner, outpatient center, or whole hospital with no added faculty as though their radiologists had not enough to do previously. Perhaps it will take outside regulation much like airline pilots and truck drivers who are not allowed to work beyond some fixed time limit, since we seem unable or unwilling to make the case within our hospitals or even among ourselves that quality suffers when caseloads become excessive.

Many readers I expect will challenge the findings of this article as they might apply to their own practice because the findings are not relevant to their particular case mix or workplace infrastructure. Some will say that they are well within the safety zone, figuring that they read about 50 cases in a 10-hour workday. Nevertheless, certainly in any academic practice, that calculation fails to take into account time spent answering questions on the phone, responsibility for teaching, and, heaven forbid, lunch. Until we have some guidance from our leadership or spend the time and money to calculate our actual individual miss rate as it relates to caseload—I expect it varies among neuroradiologists—this article represents an important step in the right direction, and I commend the authors and the journal for that.

REFERENCE

1. Patel SH, Stanton CL, Miller SG, et al. **Risk factors for perceptual-versus-interpretative errors in diagnostic neuroradiology.** *AJNR Am J Neuroradiol* 2019;40:1252–56 CrossRef Medline

A. Mamourian
Departments of Neurology, Neurosurgery, and Radiology
Penn State–Hershey Medical Center
Hershey, Pennsylvania

Professor Emeritus
Department of Radiology, Division of Neuroradiology
Hospital of the University of Pennsylvania
Philadelphia, Pennsylvania